



*TEAM tAO*

---

品



金

石

林



現見  
康珍藏





6 August 2004

# Science

Vol. 305 No. 5685  
Pages 737-900 \$10

Spirit  
at Gusev Crater

AAAS





## SPIRIT AT GUSEV CRATER

A portion of the "Mission Success" panorama acquired by the Pancam instrument onboard the Mars Exploration Rover Spirit on 8 January 2004, around 10:30 a.m. local solar time. The view is to the east; the Columbia Hills in the distance are about 2.5 km away and 100 to 200 m in height. This is an approximate true-color rendering of the scene generated from Pancam's 750-nm, 530-nm, and 480-nm filters. [Photo: NASA/JPL/Cornell]

Volume 305  
6 August 2004  
Number 5685

793 Touch and Go

### RESEARCH ARTICLES AND REPORTS

794 The Spirit Rover's Athena Science Investigation at Gusev Crater, Mars

S. W. Squyres et al.

800 Pancam Multispectral Imaging Results from the Spirit Rover at Gusev Crater

J. F. Bell III et al.

807 Surficial Deposits at Gusev Crater Along Spirit Rover Traverses

J. A. Grant et al.

810 Wind-Related Processes Detected by the Spirit Rover at Gusev Crater, Mars

R. Greeley et al.

811 Spirit at Gusev Crater: Plates

821 Localization and Physical Properties Experiments Conducted by Spirit at Gusev Crater

R. E. Arvidson et al.

824 Textures of the Soils and Rocks at Gusev Crater from Spirit's Microscopic Imager

K. E. Herkenhoff et al.

827 Magnetic Properties Experiments on the Mars Exploration Rover Spirit at Gusev Crater

P. Bertelsen et al.

829 Chemistry of Rocks and Soils in Gusev Crater from the Alpha Particle X-ray Spectrometer

R. Gellert et al.

833 Mineralogy at Gusev Crater from the Mössbauer Spectrometer on the Spirit Rover

R. V. Morris et al.

837 Initial Results from the Mini-TES Experiment in Gusev Crater from the Spirit Rover

P. R. Christensen et al.

842 Basaltic Rocks Analyzed by the Spirit Rover in Gusev Crater

H. Y. McSween et al.

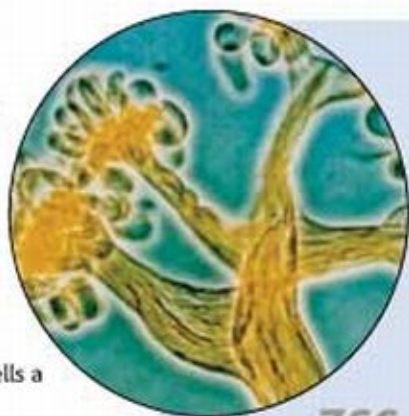
Related News story page 770

### DEPARTMENTS

- 747 SCIENCE ONLINE  
749 THIS WEEK IN SCIENCE  
753 EDITORIAL by Helga Nowotny  
European Research Momentum  
754 EDITORS' CHOICE  
758 CONTACT SCIENCE  
759 NETWATCH  
880 NEW PRODUCTS  
881 SCIENCE CAREERS

### NEWS OF THE WEEK

- 760 ELECTION 2004  
The Calculus of Making Stem Cells a Campaign Issue
- 761 RESEARCH PROTESTS  
Britain Unveils a Plan to Curb Animal Rights 'Extremists'
- 762 NEUROBIOLOGY  
Untangling Alzheimer's by Paring Plaques Bolsters Amyloid Theory
- 762 NANOTECHNOLOGY  
Yellow Light for Nanotech
- 763 ASTROPHYSICS  
Dark-Matter Sighting Ends in Shock
- 763 SCIENCE SCOPE
- 764 PALEONTOLOGY  
X-ray Scan Shows Oldest Known Bird Had a Bird Brain
- 764 SCIENTIFIC PUBLISHING  
Seeking Advice on 'Open Access,' NIH Gets an Earful
- 765 IN MEMORIAM  
Philip Hauge Abelson, 1913–2004



766



779

### NEWS FOCUS

- 766 EVOLUTIONARY BIOLOGY  
The Birth of a Nucleus
- 768 PROFILE: EDWARD HAMMOND  
Activist Throws a Bright Light on Institutes' Biosafety Panels
- 770 PLANETARY SCIENCE  
Rainbow of Martian Minerals Paints Picture of Degradation  
related Spirit at Gusev Crater section page 793
- 772 MEETING  
Basic and Clinical Immunology  
An Old Favorite Is Resurrected: Regulatory T Cells Take the Stage  
And Action! Dendritic Cells Go Live  
Genes Crisscross Disease Lines
- 774 RANDOM SAMPLES
- LETTERS
- 776 Creating a European Research Council Initiative for Science in Europe (ISE). Predators and Prey in the Channel Islands P. Dratch, T. Coonan, D. Graber; K. M. Helgen. Response G. W. Roemer, R. Woodroffe, F. Courchamp
- 778 Corrections and Clarifications
- BOOKS ET AL.
- 779 NEUROSCIENCE  
The Psychology of Art and the Evolution of the Conscious Brain R. L. Solso, reviewed by V. S. Ramachandran
- 780 Nota Bene on His Brother's Keeper A Story from the Edge of Medicine

Contents continued



## PERSPECTIVES

782 **NEUROSCIENCE**  
Probing the Neural Basis of Body Ownership *M. Botvinick* *related Report page 875*

783 **CHEMISTRY**  
The Modest Undressing of a Silicon Center *G. Bertrand* *related Report page 849*

785 **PHYSICS**  
Only Skin Deep *W. Barnes and R. Sambles* *related Report page 847*

786 **IMMUNOLOGY**  
NK Cells Lose Their Inhibition *P. Parham* *related Report page 872*

## REVIEW

788 **PHYSICS**  
Metamaterials and Negative Refractive Index *D. R. Smith, J. B. Pendry, M. C. K. Wiltshire*

## SCIENCE EXPRESS [www.sciencexpress.org](http://www.sciencexpress.org)

**GEOLOGY:** Evidence for Deep Magma Injection Beneath Lake Tahoe, Nevada-California  
*K. D. Smith, D. von Seggern, G. Blewitt, L. Preston, J. G. Anderson, B. P. Wernicke, J. L. Davis*  
A swarm of small earthquakes in 2003 deep beneath east-central California was surprisingly coincident with changes in elevation at the surface and might reflect magma movement in the lowermost crust.

**CELL BIOLOGY:** Mitochondrial Fusion Intermediates Revealed in Vitro

*S. Meeusen, J. M. McCaffery, J. Nunnari*

Mitochondria, the double membrane-bound organelles that generate cellular energy, fuse with one another using quite different mechanisms for joining the inner and outer membranes.

**MOLECULAR BIOLOGY:** Small Interfering RNA-Induced Transcriptional Gene Silencing in Human Cells

*K. V. Morris, S. W.-L. Chan, S. E. Jacobsen, D. J. Looney*

Small interfering RNAs can silence genes in human cells as they do in plants, yeast, and flies, possibly by methylating DNA.

**VIROLOGY:** Src Mediates a Switch from Microtubule- to Actin-Based Motility of Vaccinia Virus

*T. P. Newsome, N. Scaplehorn, M. Way*

Vaccinia virus co-opts a host protein that initiates polymerization of actin, which then enhances spread of the virus from cell to cell.

## TECHNICAL COMMENT ABSTRACTS

778 **APPLIED PHYSICS**  
Comment on "Observation of the Inverse Doppler Effect"

*E. J. Reed, M. Soljagic, M. Ibanescu, J. D. Joannopoulos*

*full text at [www.sciencemag.org/cgi/content/full/305/5685/778b](http://www.sciencemag.org/cgi/content/full/305/5685/778b)*

Response to Comment on "Observation of the Inverse Doppler Effect"

*N. Seddon, T. Bearpark*

*full text at [www.sciencemag.org/cgi/content/full/305/5685/778c](http://www.sciencemag.org/cgi/content/full/305/5685/778c)*

## BREVIA

846 **DEVELOPMENTAL BIOLOGY:** Multiplex Detection of RNA Expression in *Drosophila* Embryos

*D. Kosman, C. M. Mizutani, D. Lemons, W. G. Cox, W. McGinnis, E. Bier*

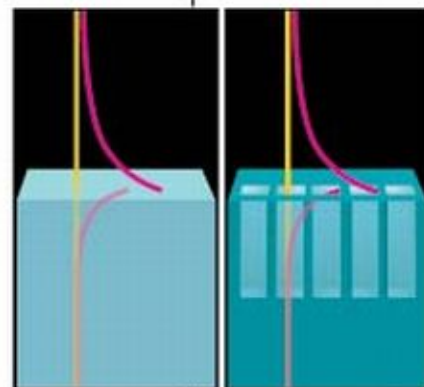
An improved, highly sensitive in situ hybridization method allows detection of five or more mRNA expression patterns simultaneously.

## REPORTS

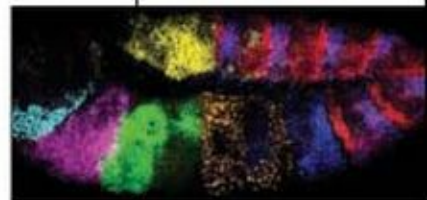
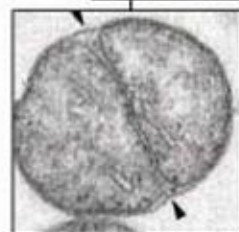
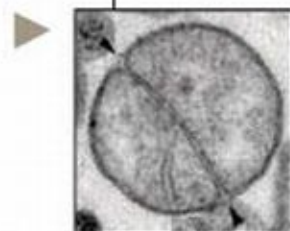
847 **PHYSICS:** Mimicking Surface Plasmons with Structured Surfaces

*J. B. Pendry, L. Martin-Moreno, F. J. Garcia-Vidal*

Manipulation of the size and spacing of minute holes in the surface of a metal influences the oscillation of free surface electrons, which can interact with light at subwavelength scales. *related Perspective page 785*



785  
& 847



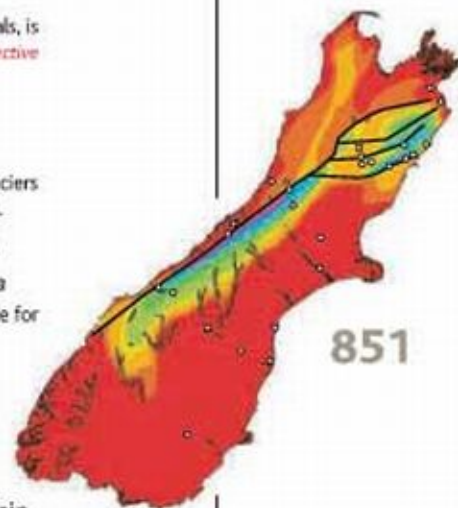
846

Contents continued ►



## REPORTS CONTINUED

- 849 **CHEMISTRY:** The  $(\text{Me}_5\text{C}_5)\text{Si}^+$  Cation: A Stable Derivative of  $\text{HSi}^+$   
*P. Jutzi, A. Mix, B. Rummel, W. W. Schoeller, B. Neumann, H.-G. Stammer*  
 A stable compound with an elusive silicon species, having one lone electron pair and two vacant orbitals, is successfully synthesized and used to produce another compound with a Si-Si double bond. *related Perspective page 763*
- 851 **CLIMATE CHANGE:** Climatic Control of Riverine and Seawater Uranium-Isotope Ratios  
*L. F. Robinson, G. M. Henderson, L. Hall, I. Matthews*  
 Uranium isotope ratios from New Zealand rivers, used to interpret a climate record, imply that glaciers advanced in New Zealand about 13,000 years ago because of more snowfall, not colder temperatures.
- 855 **PLANT SCIENCE:** A Plant Vacuolar Protease, VPE, Mediates Virus-Induced Hypersensitive Cell Death  
*N. Hatsugai, M. Kuroyanagi, K. Yamada, T. Meshi, S. Tsuda, M. Kondo, M. Nishimura, I. Hara-Nishimura*  
 A protein-cleaving enzyme that resides in the large interior vacuole of plant cells is primarily responsible for programmed cell death in plants and is similar to the one in animals.
- 858 **STRUCTURAL BIOLOGY:** Structural Basis of Mitochondrial Tethering by Mitofusin Complexes  
*T. Koshiba, S. A. Detmer, J. T. Kaiser, H. Chen, J. M. McCaffery, D. C. Chan*  
 Coiled coils of a mitochondrial outer-membrane protein bind to one another, initiating the process by which these membrane-bound organelles fuse within the cell.
- 862 **SIGNAL TRANSDUCTION:** The Semaphorin 4D Receptor Plexin-B1 Is a GTPase Activating Protein for R-Ras  
*I. Oinuma, Y. Ishikawa, H. Katoh, M. Negishi*  
 Axons stop growing and retreat when receptors on their tips encounter repulsive signals in the environment and activate a regulatory protein inside the cell.
- 866 **STRUCTURAL BIOLOGY:** The Binding Mode of Etoposide A on  $\alpha$ ,  $\beta$ -Tubulin by Electron Crystallography  
*J. H. Nettles, H. Li, B. Cornett, J. M. Krahn, J. P. Snyder, K. H. Downing*  
 A new class of drug inhibits cancer cell growth by stabilizing microtubules, as does the drug Taxol, but it interacts with different residues within the binding site.
- 869 **GENETICS:** Multiple Rare Alleles Contribute to Low Plasma Levels of HDL Cholesterol  
*J. C. Cohen, R. S. Kiss, A. Pertsemlidis, Y. L. Marcel, R. McPherson, H. H. Hobbs*  
 Rare mutations in just a few genes can cause low levels of good cholesterol in blood, contrary to the notion that many genes control HDL levels.
- 872 **IMMUNOLOGY:** HLA and NK Cell Inhibitory Receptor Genes in Resolving Hepatitis C Virus Infection  
*S. I. Khakoo, C. L. Thio, M. P. Martin, C. R. Brooks, X. Gao, J. Astemborski, J. Cheng, J. J. Goedert, D. Vlahov, M. Hilgartner, S. Cox, A.-M. Little, G. J. Alexander, M. E. Cramp, S. J. O'Brien, W. M. C. Rosenberg, D. L. Thomas, M. Carrington*  
 People who can successfully fight off a hepatitis C virus infection tend to have innate immune cells with certain genetic types of receptors. *related Perspective page 766*
- 875 **NEUROSCIENCE:** That's My Hand! Activity in Premotor Cortex Reflects Feeling of Ownership of a Limb  
*H. H. Ehrsson, C. Spence, R. E. Passingham*  
 The brain activity of subjects experiencing an illusion in which they feel that a rubber hand is their own reveals the neural basis of one aspect of self-consciousness. *related Perspective page 782*
- 877 **BEHAVIOR:** Brood Parasitic Cowbird Nestlings Use Host Young to Procure Resources  
*R. M. Kilner, J. R. Madden, M. E. Hauber*  
 Parents will feed a parasitic cowbird chick more generously if some of the parents' own chicks are also in the nest, explaining why cowbirds refrain from killing all of the rival chicks.



851



877



ADVANCING SCIENCE. SERVING SOCIETY

SCIENCE (ISSN 0036-8075) is published weekly on Friday, except the last week in December, by the American Association for the Advancement of Science, 1200 New York Avenue, NW, Washington, DC 20005. Periodicals Mail postage (publication No. 494660) paid at Washington, DC, and additional mailing offices. Copyright © 2004 by the American Association for the Advancement of Science. The title SCIENCE is a registered trademark of the AAAS. Domestic individual membership and subscription (51 issues) \$130 (\$74 allocated to subscription). Domestic institutional subscription (51 issues) \$500. Foreign postage extra. Mexico, Caribbean (surface mail) \$55; other countries (air assist delivery) \$65. First class, airmail, student, and emeritus rates on request. Canadian rates with GST available upon request, GST #R125488122. Publications Mail Agreement Number 1064624. Printed in the U.S.A.

Change of address: allow 4 weeks, giving old and new addresses and 8-digit account number. Postmaster: Send change of address to Science, P.O. Box 10111, Danbury, CT 06815-1011. Single copy sales: \$10.00 per issue (paid) includes surface postage; bulk rates on request. Authorization to photocopy material for internal or personal use under circumstances not falling within the fair use provisions of the Copyright Act is granted by AAAS to libraries and other users registered with the Copyright Clearance Center (CCC) Transactional Reporting Service, provided that \$10.00 per article is paid directly to CCC, 222 Rosewood Drive, Danvers, MA 01923. The identification code for Science is 0036-8075/05 \$10.00. Science is indexed in the *News & Guide to Periodical Literature* and in several specialized indexes.

Contents continued ▶



**Motherly Love Coddles the Brain**

For rat pups, mom's care leaves a lasting impression.

**Whale-Eating Worms Discovered**

Two new species make a meal of whale skeletons on the ocean floor.

**Beer of Kings**

High in the Andes, archaeologists find what may be the oldest large-scale brewery.



Radio frequency chips time distance runners.

science's next wave [www.nextwave.org](http://www.nextwave.org) CAREER RESOURCES FOR YOUNG SCIENTISTS

**GLOBAL/US: This Time, We Mean It** *A. Kotok*

Radio frequency identification helps runners and race organizers keep more accurate performance times.

**GLOBAL/CANADA: Getting Ice Time** *A. Fazekas*

Two researchers working on safety on the ice reflect on career prospects in Canadian sports science.

**GLOBAL/NETHERLANDS: Clap Your Skates—Innovation in the Ice and Inline World** *D. Hol and T. Vrijenhoek*

The invention of clapskates turned the ice speedskating world upside down.

**US: Let's Do the Numbers** *J. Austin*

Who's buying, who's selling, and who's just browsing in the scientific job market?

**GERMANY: Science Down Under** *M. Hommel*

Despite the advantages of staying in Germany or going to the United States, she went and did a postdoc in Australia.

**MiSciNET: Genetics and Culture Shock** *C. Parks*

Howard Hughes investigator Carlos Bustamante talks about adjusting to American culture and research after leaving his native Peru.

science's sage ke [www.sageke.org](http://www.sageke.org) SCIENCE OF AGING KNOWLEDGE ENVIRONMENT

**REVIEW: Murine Models of Life Span Extension** *J. K. Quarrie and K. T. Riabowol*

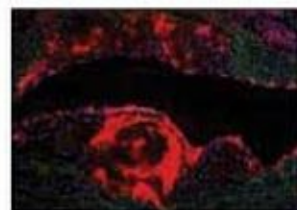
What can mice with defects in specific signaling molecules tell us about mammalian aging?

**News Focus: Suppressed RAGE** *M. Leslie*

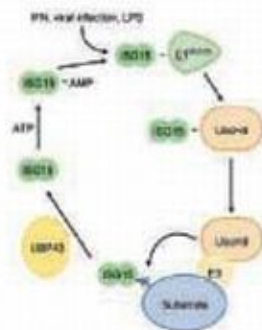
Cell-surface receptor battles compounds that promote aging by thwarting its alter ego.

**News Focus: The Thing That Wouldn't Leave** *R. J. Davenport*

Immune cells that flock to fat-laden blood vessels stay when they should go.



Monocytes wear out their welcome.



Protein regulation by isgylation.

science's stke [www.stke.org](http://www.stke.org) SIGNAL TRANSDUCTION KNOWLEDGE ENVIRONMENT

**PERSPECTIVE: AcK-knowledge Reversible Acetylation** *T. Cohen and T.-P. Yao*

New roles for protein acetylation in regulating apoptosis and formation of the immune synapse are described.

**PERSPECTIVE: Ubiquitylation and Isgylation—Overlapping Enzymatic Cascades Do the Job** *O. Staub*

Ubiquitin and ubiquitin-like proteins may be attached to target proteins by the same E3 ligases.

Separate individual or institutional subscriptions to these products may be required for full-text access.



## European Research Momentum

Last year, a *Science* Editorial (29 August 2003) surveyed recent developments in European science and research policy. It highlighted the call for a restructuring that would double support for science, with a renewed focus on basic research, better priority-setting, regional centers of excellence, integration of European Union (EU) science policy with respect to broader issues, and a new balance between basic and applied research. It hinted at the formation of a European Research Council (ERC) as a partial answer to dissatisfactions expressed by researchers with the EU's Framework Programmes for research funding.

One year later, the dynamics look truly impressive. The EU has become larger, and the European Constitution, agreed on in June 2004, makes explicit reference to research and a convergent European Research Area "in which researchers, scientific knowledge and technology circulate freely." This gives EU research policy a more solid base and broadens its scope, making research a "shared competence." The last Communication of the outgoing EU Commissioner for Research, M. Philippe Busquin, entitled *Science and Technology, the Key to Europe's Future*, contains an outline of Framework Programme 7 (FP7), a proposal based on a prospective EU research budget that would be doubled. Politically, the importance of research has received recognition. New financial instruments have been designated that allow, for instance, reallocation of funds from highways to research infrastructures. None of these developments should be taken for granted. Our common efforts need to be directed to ensure that the new EU Commission and the newly elected European Parliament will build on this momentum.

One of the six objectives of FP7, to begin in 2007, supports basic research and an ERC that would encompass all disciplines, including the humanities and social sciences. The ERC mission would be to generously support the very best researchers, making them truly competitive on a global scale. This is a welcome development after a vigorous public debate. But if basic research, investigator-driven and conducted solely through competition based on scientific excellence, is to be effectively organized, the Competitiveness Council, presided over by Maria van der Hoeven, Minister for Education, Culture and Science (the Netherlands), must ensure an autonomous ERC that fits these objectives. An ERC should also help to create working conditions at least as good as those in the United States for young and talented researchers in Europe.

But an ERC is no miracle cure, nor can it compensate for other deficiencies. The challenge is to create a European knowledge base for research and innovation in which human resources, adequate infrastructures, and mechanisms to encourage excellence receive the necessary sustained boost. Political support for a better balance between basic and applied research stems from recognition of the impact of basic research on economic performance. Comparing research institutions in the United States with those in Europe shows the overall greater mission orientation of the U.S. federal R&D system and the concomitant importance attached to management. In contrast, research in Europe is still often seen as belonging to the separate categories of "basic" and "applied," and we seem to put more effort into inventing rules for management than into having management meet objectives. We should not be surprised that the general climate for university/industry cooperation and for innovation is more favorable in the United States.

A key to the overall challenges is the transformation of European universities, which in the end will determine whether support for basic research through EU mechanisms will have the desired effects. Throughout Europe, there is clear recognition that brakes of a political, financial, and administrative nature on universities have to be removed. Some countries, such as Germany, are discussing the creation of elite universities. Many cultural mindsets will have to change. European science needs a two-pronged approach if the present momentum is to lead to robust organizational solutions: sound research policies and much hard work on local and national levels.

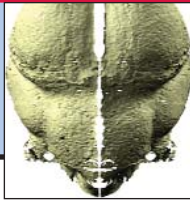
Finally, European research and innovation policies must be rooted in a broader-based culture that truly integrates European citizens. Such a culture of science must also address the public's occasional skepticism, and even its refusal, of such a climate. This month, the EuroScience Open Forum 2004 (Stockholm), with its deliberately provocative yet cheerful embrace of controversial issues, is not only timely but indispensable. It alerts us that focus and momentum must be kept at this crucial period of transition.

**Helga Nowotny**

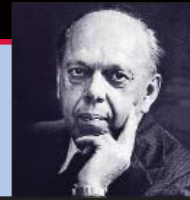
Helga Nowotny is director of Society in Science: The Branco Weiss Fellowship and chair of the European Research Advisory Board.

The challenge is to create a European knowledge base for research and innovation.





PAGE 764  
*Archaeopteryx's*  
bird brain



765  
Philip Abelson:  
An appreciation

### ELECTION 2004

## The Calculus of Making Stem Cells a Campaign Issue

Most scientists predict that it will be at least several years before human embryonic stem cells are used to treat disease. But Democratic presidential candidate John F. Kerry is betting that the political payoff from his support for stem cell research will be much quicker.

Last week, the Kerry campaign took the unusual step of elevating a complicated bit of science policy to a top-tier election issue.

Kerry used his televised nomination speech to attack the Bush Administration's handling of science and promised to lift restrictions on government-funded stem cell research that his opponent, President George W. Bush, imposed in 2001. "What if we have a president who believes in science,

so we can unleash the wonders of discovery like stem cell research to treat illness and save millions of lives?," Kerry asked in the 29 July address to the Democratic National Convention in Boston, Massachusetts. Two days earlier, Ron Reagan, the son of the late Republican president, addressed the convention to extol the promises of embryonic stem cell research.

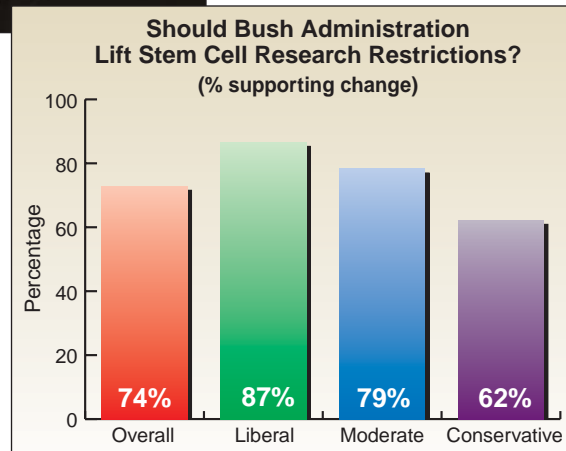
Kerry's barbed rhetoric drew a quick response from Bush campaign officials. "Ridiculous. ... We have a commitment to science," said deputy policy director Megan Hauck. She noted that the Administration has overseen increased funding for research and relied on input from both scientific and religious leaders to craft a "compromise" that provides federal funding for some embryonic stem cell research.

Many science and patient groups welcomed Kerry's remarks, saying they signaled success in attracting attention to their key concerns. "For science and stem cells to make it [into Kerry's speech] shows that these issues have made it to the political major leagues," says Kevin Wilson, public policy director of the American Society for

Cell Biology in Bethesda, Maryland. But, Wilson and others warned, the high-profile embrace could also create problems, from unrealistic public expectations for quick stem cell cures to strained relationships with Republican allies. "I had hoped that we could keep stem cell research separate from election-year politics. ... Politicization of this critical issue will only serve to

alienate more potential supporters," predicted Senator Orrin Hatch, a Utah Republican who has led efforts to reverse the White House policy.

Many polling experts, however, say Kerry's move is smart electoral politics, given surveys



**Political science.** Kerry hopes to benefit from public sentiment reflected in this Opinion Research Corp. poll ( $n=1017$ ).

showing that more than two-thirds of voters—including many conservatives—support loosening Bush's 3-year-old stem cell policy, which limits federally funded researchers to using just a few dozen existing stem cell lines. The White House has held firm against relaxing the restrictions, in part for fear of alienating conservative Christian voters who oppose destroying human embryos to harvest stem cells.

Such complicated science issues rarely rise to prominence in national elections. But the death of former president Reagan, along with public criticism of Bush's policy from his widow Nancy and son, helped focus public attention on the issue. And that spotlight presented Kerry—who has long opposed the Administration's restrictions on stem cell research and raised the issue in his stump speeches—with an opportunity to make a "double-edged" case, says Matthew Nisbet, a communications professor at Ohio State University in Columbus who has studied public opinion on stem cell research. "It allowed Kerry to highlight a major policy difference between the candidates on a health issue that is relevant to millions of Americans," he says. It also allowed him to reinforce reservations that undecided voters may already have about Bush being "an ideologue who doesn't listen to experts who hold other views."

Still, Nisbet warns that many voters are "queasy" about the moral issues raised by stem cell research. And the Bush campaign believes those voters will be reassured by the current policy, which Hauck says "balances our need to respect human life and move ahead with research."

Other analysts say Kerry's claim that Bush's policy is delaying cures may appeal to sought-after suburban women voters, while the suggestion that Bush doesn't believe in science could appeal to white males with technical training. "This is a message crafted with an eye toward demographics," says one Democratic strategist.

Amid the sound bites, some researchers worry that public expectations for stem cell therapies will become too great. Kerry's speech "was electrifying," says cell biologist George Daley of Harvard Medical School in Boston, Massachusetts. "But it

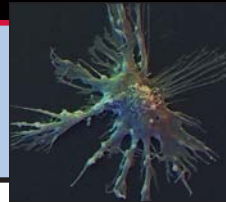
puts a heavy responsibility on scientists to provide accurate information and not over-hype." Voters, meanwhile, are expected to have plenty of opportunity to make up their own minds. Analysts on both sides expect the candidates to be asked questions about their stem cell policies in the upcoming debates.

— DAVID MALAKOFF

With reporting by David Grimm and Constance Holden.

CREDITS: (TOP TO BOTTOM) BROOKS KRAFFT/CORBIS; SOURCE: CIVIL SOCIETY INSTITUTE/OPINION RESEARCH CORPORATION, 16 JUNE 2004 POLL





## RESEARCH PROTESTS

## Britain Unveils a Plan to Curb Animal-Rights 'Extremists'

**CAMBRIDGE, U.K.**—Britain is weighing tough new measures to crack down on intimidating tactics used by a radical minority of animal-rights activists. In a report published on 30 July, the government proposes new criminal penalties for protests that cause “harassment, alarm, or distress,” to be enforced by a newly created special police unit and network of 43 prosecutors. The move comes in the wake of animal-rights campaigns that contributed to the University of Cambridge’s decision to abandon a primate research facility this year and now threaten to derail construction of a building at the University of Oxford.

Leaders of the research community welcomed the plan: “It’s great that the Home Office is doing something about this at long last,” says neuroscientist E. Barry Keverne, chair of the Royal Society’s Committee on Animals in Research. But antivivisection groups suggest that ratcheting up penalties won’t deter their protests.

In addition to outlawing harassment of people at home, the government seeks to make it an offense for protesters to return within 3 months to a place they’ve been ordered to leave. The government also plans to extend antiharassment laws to apply to all employees of an organization rather than specific individuals and may outlaw acts that cause economic damage to research-related operations. The government did not seek—but is considering—a single law targeting animal-rights extremists.

Scientists hope the new measures will be more effective than past efforts at deterring threatening behavior. Personal intimidation, such as calling researchers “torturers” in letters to neighbors, has increased in the last 18 months, says Mark Matfield, executive director of the Research Defence Society (RDS), which represents scientists engaged in animal research. RDS reports that 50 suppliers for animal research facilities have pulled out of contracts this year alone. Over the past year, instances of damage to property—mostly involving corrosive substances

\* *Animal Welfare: Human Rights—Protecting people from animal rights extremists.* [www.homeoffice.gov.uk](http://www.homeoffice.gov.uk)

thrown at vehicles—have doubled, and protests at the homes of company directors have increased by 45%, according to the Association of the British Pharmaceutical Industry. “It does make it difficult to get anything done,” says Keverne.

Matfield says protesters have turned their attention from heavily guarded private facilities to “softer targets”: the universities. In January, a planned primate research facility

“The government has pledged to support the project; we just hope that that would include financial support,” she says, adding that there are no plans to use troops to assist the project, as some newspaper reports have suggested.

A recent Royal Society survey (*Science*, 18 June, p. 1731) found that security against animal-rights extremism was costing universities \$320,000 per year on average. The National Association of Pension Funds, whose members control about 20% of the U.K. stock market, are considering establishing a \$46 million fund to reward information on extremists. Seeking to offset the impact of protests, three big drug companies—GlaxoSmithKline, AstraZeneca, and Pfizer—last week announced a \$7.3 million fund for animal research in U.K. universities over the next 4 years.

The protesters say they’re unimpressed. Cogswell sees the tougher measures as a “knee-jerk reaction” to complaints from pharmaceutical companies. “The government needs to think carefully why people are engaging in actions,” he says, arguing that



**On the march.** After the University of Cambridge canceled a primate research center this year, protesters targeted a lab building at Oxford.

at Cambridge University was abandoned after protests led by the group Stop Primate Experiments at Cambridge escalated security costs (*Science*, 30 January, p. 605). “It gave the activists a victory they hadn’t had for 5 years,” says Matfield. The university is now seeking to carry out primate studies at existing laboratories, an official says.

The animal activist group, now calling itself Speak, has since set its sights on an animal research facility being built at Oxford University. Construction of the \$33 million laboratory ground to a halt last month when the main contractors pulled out following threats to staff and shareholders and damage to property (*Science*, 23 July, p. 463). Speak co-founder Robert Cogswell says that the group was not involved in any illegal acts.

A spokesperson for the university describes the delay as a “temporary hiccup.”

many are disappointed over its failure to deliver a promised inquiry into animal research. “The more people feel disempowered, the more they’re going to take the law into their own hands.” However, he’s confident that opponents can stop the Oxford facility “by legal means.”

Ian Gibson, chair of the U.K. Parliament’s science and technology committee, doubts that the new measures will stop the most determined extremists, but he hopes they’ll “give some breathing space” for debate. Matfield and Aisling Burnand, CEO of the BioIndustry Association, suggest that the government may need to adopt even stronger measures. To move quickly, the government has opted primarily to amend existing legislation, but the new law banning protests at individuals’ homes will require approval by Parliament.

—FIONA PROFFITT



## NEUROBIOLOGY

# Untangling Alzheimer's by Paring Plaques Bolsters Amyloid Theory

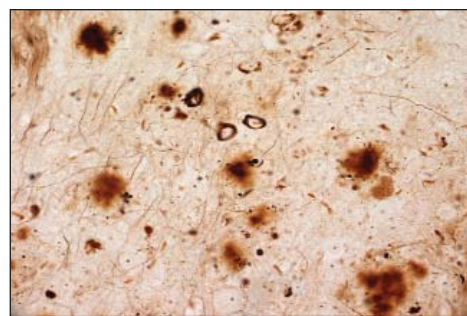
Consider it a potential biomedical bargain—two therapies for the price of one. New research in mice suggests that targeting one of the two molecular aggregates gumming up brains with Alzheimer's disease also rids tissue of the other, as long as treatment starts early enough. This finding and a recent analysis of an interrupted Alzheimer's vaccine trial in people have brought new life to the idea of immunotherapy for the debilitating disease.

An ongoing debate within the Alzheimer's disease community centers on the importance of brain plaques, extracellular clumps of a protein fragment called  $\beta$  amyloid, and tangles, filaments of the protein tau that form inside neurons. In the 5 August issue of *Neuron*, a team led by neuroscientist Frank LaFerla of the University of California, Irvine, reports that antibodies against  $\beta$  amyloid can wash mice brains free of amyloid plaques—and mutant tau before it tangles. Some researchers have argued that plaques instigate the formation of tangles, but there's been little solid evidence for that. "This is the most complete

confirmation that accumulation of  $\beta$  amyloid can lead to accumulation of tau and eventually to tangles," says neuroscientist Michael Hutton of the Mayo Clinic College of Medicine in Jacksonville, Florida.

Researchers have had difficulty testing the relative roles of plaques and tangles, because until last year, no one had generated mice that develop both. LaFerla and his colleagues recently endowed mice with a triple threat: a mutant copy of the gene for amyloid precursor protein (APP), a mutated gene for presenilin-1, which helps chop APP into  $\beta$  amyloid, and a mutant form of the tau gene. These rodents develop plaques and tangles in the cortex, amygdala, and hippocampus, just as people with Alzheimer's disease do. The plaques precede tangles, consistent with the idea that  $\beta$ -amyloid buildup starts brains off on the road to dementia.

In the new work, the team injected antibodies against  $\beta$  amyloid into the hippocampus of their transgenic mice once the animals were 1 year old. Three days after the in-



**Double trouble.**  $\beta$ -amyloid plaques (diffuse black structures) and tau tangles (open, black circles) mar this slice of mouse brain.

jection, plaques in the injected animals had disappeared. Between 5 and 7 days after the injection, tau, which in the mice had aggregated within neurons but not yet formed tangles, also had melted away.

LaFerla's group tested the antibody treatment on another set of triple-mutant mice; these animals have two copies of each mutant gene and develop tangles in under a year. The antibodies erased plaques in 6- and 12-month-old animals. They also cleared pre-tangle tau aggregates in the 6-month-old animals but couldn't budge the tangles in year-old mice. "Once tau forms tangles, it can't be removed," says LaFerla.

The rodent work seems to mirror recent findings in autopsies of brains from people involved in a vaccine trial for Alzheimer's disease. In 2000, investigators showed that immunizing mice with amyloid itself could rid mouse brains of plaques. In 2002, however, clinicians abruptly halted a human study of the vaccine when a small percentage of patients developed brain inflammation. Last month, at the 9th International Conference on Alzheimer's Disease and Related Disorders in Philadelphia, Pennsylvania, Sid Gilman of the University of Michigan, Ann Arbor, described the brains of four people with mild to moderate Alzheimer's disease who had received the vaccine and subsequently died from unrelated causes. Each brain showed an almost complete lack of  $\beta$  amyloid; the tangles remained, however.

LaFerla's work "goes hand-in-hand with the vaccine trial," says neurobiologist Virginia Lee of the University of Pennsylvania in Philadelphia. The mouse and human data suggest that a vaccine would be most therapeutic if researchers treat patients in very early stages of the disease, before tau forms tangles.

Still, Lee admits, that remains a bit of a "pipe dream," because such patients can't yet be identified. Nevertheless, biotech companies are redesigning amyloid vaccines to make them safer and considering new clinical trials. Apparently, the reported death of Alzheimer's disease immunotherapy was an exaggeration.

—MARY BECKMAN

Mary Beckman is a writer in southeastern Idaho.

## NANOTECHNOLOGY

## Yellow Light for Nanotech

**LONDON, U.K.**—Although "gray goo" made of self-replicating "nanorobots" is unlikely to doom the planet, some kinds of nanomaterials could be hazardous and require a closer look, according to a 12-month study\* published last week by the U.K. Royal Society and the Royal Academy of Engineering. Overall, however, the report concludes that most nanotechnologies pose no new risk and no general moratorium is needed.

Many products that incorporate nanoparticles, such as computer chips and self-cleaning windows, are no cause for new concern, said Cambridge University mechanical engineer Ann Dowling, who led the study, at a press conference last week. But because some chemicals are more toxic in their nano form and can penetrate cells more readily, nanomaterials should be subjected to toxicity studies "without delay," she said. Panel member Anthony Seaton, an expert in occupational and respiratory medicine at Aberdeen University in the U.K., added, "At the moment, it would be wrong to pretend we know much about the toxicology of nanoparticles."

\* *Nanoscience and nanotechnologies: Opportunities and uncertainties.* [www.nanotec.org.uk/finalReport.htm](http://www.nanotec.org.uk/finalReport.htm)

The panel concluded that nanoparticles and nanotubes—tiny tubes of carbon that have many potential uses, such as in friction-reducing oil additives and electronic displays—should be tested and regulated as new chemicals under existing U.K. and E.U. legislation. "We believe no new bodies are needed to regulate nanotechnologies," Dowling said, but existing bodies should review their regulations, and manufacturers should publicly disclose test results. Only large quantities of new materials would need to be tested; small-scale producers such as laboratories would not be affected. Nanotechnologists seem pleased with the panel's conclusions. Physician Michael Horton of the London Centre for Nanotechnology says, "The report was entirely right in its optimistic caution."

U.K. science minister David Sainsbury commissioned the study in July 2003 following alarmist reports in the media about inhaling toxic particles and the perils of self-replicating gray goo. The Royal Society and the Royal Academy will hold a public meeting to discuss the report on 29 September, and the government says it will respond by the end of the year.

—FIONA PROFFITT

## ASTROPHYSICS

## Dark-Matter Sighting Ends in Shock

Rumors have been flying for months among astrophysicists that a new telescope in Africa had spotted particles of “dark matter” destroying one another at the heart of our galaxy. Now, the telescope’s German-led team confirms that it has detected gamma rays blazing directly from the Milky Way’s core. But the signal looks more like a shock wave from ordinary matter, the team reported last week at a meeting\* in Heidelberg, Germany. Dark matter may be “the most interesting possible source of gamma rays,” says physicist Werner Hofmann of the Max Planck Institute for Nuclear Physics in Heidelberg. “But it is not the most natural explanation for what we see.”

Hofmann and a team of about 100 researchers used the High Energy Stereoscopic System (HESS), an array of four telescopes completed in December 2003 at a dark high-altitude site in central Namibia. Unlike conventional telescopes, which spy their targets directly, HESS watches for the traces of gamma rays and cosmic rays plowing into Earth’s

barely make their presence felt. When two WIMPs collide, they should spit out a flurry of other particles and gamma rays. Those immolations should happen most often at the Milky Way’s core, where WIMPs are thought to swarm in a dense knot around the galaxy’s supermassive black hole.

The steady gamma ray signal seen by HESS does indeed come from a tiny area at the galaxy’s center. But there are problems with a dark-matter interpretation, Hofmann says. First, the pattern of energy looks like a classic shock wave, created by ordinary atomic nuclei slamming into ambient material in space. A likely source is the remnant of a violent supernova next to the galactic center, where strong magnetic fields have trapped and accelerated particles for thousands of years, Hofmann says.

Moreover, the gamma rays are so powerful that if they came from WIMPs, their masses—expressed in terms of energy—would be at least 12 trillion electron volts. That’s 10 to 100 times higher than predicted



**Seeing sparks.** The new HESS telescope array in Namibia sees gamma rays from energetic processes at the core of the Milky Way—but probably not dark-matter annihilation.

atmosphere. The impacts spark cascades of millions of secondary particles, which emit faint meteorlike trails of bluish light called Cerenkov radiation. HESS’s multiple eyes, each covering more than 100 square meters, are designed to trace those trails back to their origins. “I’m really impressed and amazed by their sensitivity,” says astrophysicist Dan Hooper of the University of Oxford, U.K. Adds astrophysicist Paolo Gondolo of the University of Utah in Salt Lake City: “HESS is the best gamma ray telescope working now. It has the resolution necessary to test for the presence of dark matter.”

Theory maintains that the Milky Way is engulfed by a vast halo of dark matter, outweighing the ordinary matter in stars and planets by a factor of 10 or more. In one popular scenario, the dark matter consists primarily of “weakly interacting massive particles,” or WIMPs, that suffuse space but

by nearly all models of supersymmetry, a popular framework that extends physics to higher energies. “One clearly has to prefer a more normal explanation,” Hofmann says.

For now, Hooper agrees: “I won’t completely write off an ultraexotic dark-matter particle, but it will take a lot more evidence to convince me.”

Researchers should keep an open mind, says physicist Joel Primack of the University of California, Santa Cruz. Thus far, the HESS team has analyzed data from mid-2003, when just two telescopes were operating. Now, with all four scopes running, HESS might see different types of gamma rays from the putative supernova remnant and the adjacent core of the galaxy. “It’s likely HESS can disentangle the two,” Primack says.

Nor is Primack deterred by the surprisingly high WIMP mass implied by HESS. “The surprise is based on our prejudices of what supersymmetry might do,” he says. “But we’re absolutely ignorant. We simply do not know.”

—ROBERT IRION

## Asia Girds for Bird Flu Battle

**BANGKOK**—Southeast Asian governments are escalating the battle against a highly pathogenic strain of avian influenza, H5N1, planning a regional network and wider vaccination of farm birds. Both initiatives came out of a meeting held here last week by the United Nations Food and Agriculture Organization (FAO).

Last winter, H5N1 raged through eight Asian countries, killing at least 24 people and prompting farmers to kill more than 100 million birds. The outbreak subsided in May only to resurface in late June (*Science*, 16 July, p. 321). Health authorities worry that the virus could change to a form easily transmitted among humans, touching off a global pandemic.

Hans Wagner, an FAO officer in Bangkok, says 10 countries—Cambodia, East Timor, Indonesia, Laos, Malaysia, Myanmar, Papua New Guinea, Thailand, the Philippines, and Vietnam—have agreed to form a flu network. FAO will help with staff training, laboratory, and field surveillance capabilities and has pledged \$1.2 million to start networks in South and East Asia. Long-term efforts will be needed to control H5N1, because “the evidence is starting to show there is now no possibility of easily eradicating this disease,” says Joseph Domenech, chief of FAO’s Animal Health Service. FAO and others are expected to urge wider use of poultry vaccines, which are controversial because of their uncertain efficacy and added cost. Each bird must be inoculated at least twice, at a cost of about 5 cents per shot plus labor.

—DENNIS NORMILE

## Gene Therapy Pioneer Denies Sexual Abuse Charges

A gene therapy pioneer has denied allegations that he sexually abused a young girl. William French Anderson, 67, this week pled not guilty to six charges of child molestation brought by prosecutors in Pasadena, California. The incidents allegedly took place between 1997 and 2001, when Anderson was the girl’s mentor and martial arts instructor.

Anderson, who led the first approved human gene therapy trial in 1990, is free on a \$600,000 bond pending trial. The University of Southern California has placed him on leave from his position as director of the Gene Therapy Laboratory at the Keck School of Medicine in Los Angeles.

“It is a nightmare being falsely accused,” Anderson told the *Los Angeles Times* on 3 August. “I did not do the things that I am charged with.”

—DAVID MALAKOFF

\* International Symposium on High Energy Gamma-Ray Astronomy, 26 to 30 July.



## PALEONTOLOGY

# X-ray Scan Shows Oldest Known Bird Had a Bird Brain

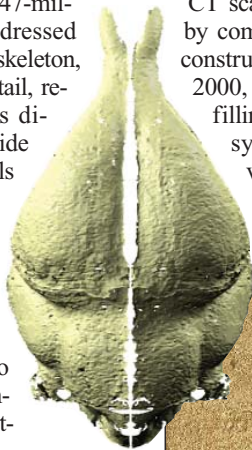
Ever since its discovery in 1861, *Archaeopteryx* has been the classic example of a transitional fossil. With an impressive array of modern-looking feathers, the 147-million-year-old fossil is clearly dressed like a bird. But almost all of its skeleton, from its teeth to its long, bony tail, resembles that of a carnivorous dinosaur. Now, the first look inside the head of *Archaeopteryx* reveals a fundamentally birdlike brain, well suited for flying. The new anatomy will help explain the evolutionary transition from dinosaurs to birds and the evolution of flight, says Lawrence Witmer, a paleontologist at Ohio University College of Osteopathic Medicine in Athens: "It's a critical piece of the puzzle."

Paleontologist Angela Milner of the Natural History Museum in London, U.K., and colleagues inspected the brain of the so-called London specimen of *Archaeopteryx*, one of seven known fossils of the magpie-sized creature. Although the brain itself isn't preserved, during life the brain pressed against the skull, leaving an impression of its lobes.

Working with paleontologist Tim Rowe and his imaging team at the University of Texas, Austin, the researchers scanned the

20-millimeter-long braincase with an industrial computerized tomography (CT) scanner, which has a higher resolution than medical CT scanners. They assembled the images by computer into a three-dimensional reconstruction of the brain (*Science*, 9 June 2000, p. 1728), touching up damage and filling in missing sections by reversing symmetrical portions that had survived intact.

*Archaeopteryx's* brain turned out to be much like that of mod-



**High minded.** Computer reconstruction (inset) shows that *Archaeopteryx's* brain was wired for flight.

ern birds, the group reports this week in *Nature*. For starters, it's big relative to body mass. With a volume of about 1.6 milliliters, the brain was three times larger than those of living reptiles. But it wasn't full-fledged: Modern birds, for their body size, have brains that are 33% to 500% larger than *Archaeopteryx's*.

Birdlike features of the anatomy include enlarged cerebral lobes (relative to the width of the brain), compared with its reptile relatives. In living birds, these lobes process sensory information from the inner ear and muscles. "It's the command and control center for flight," Milner explains. That center was likely kept busy: Feeding into it were the optic lobes, each enlarged almost to the size of the cerebellum and located on the sides of brain—just as they are in birds and pterosaurs. (In reptiles, they're on top of the brain.)

Also sending flight information were the semicircular canals of the inner ear, which help an animal sense its orientation in space. Animals with larger loops relative to body size, such as birds—including *Archaeopteryx*, the CT shows—tend to be more nimble (*Science*, 31 October 2003, p. 770). "*Archaeopteryx* was agile, quick, and jerky in its movements," says Witmer, who likens the extent of its acrobatics more to those of a chicken than a falcon or swallow. Even though *Archaeopteryx* lacked some of the skeletal features to fly like an eagle, it appears to have evolved all the brains for it.

—ERIK STOKSTAD

## SCIENTIFIC PUBLISHING

## Seeking Advice on 'Open Access,' NIH Gets an Earful

The National Institutes of Health is forging ahead with plans to require that papers from NIH-funded research be made freely available. Last week, in a hastily called meeting, NIH director Elias Zerhouni told journal publishers he is not happy with the "status quo" and is under pressure from the public to expand access to research results. He got an earful from scientific societies worried that any mandatory plan will drive their journals under.

The discussion was sparked by a July report from the House Appropriations Committee instructing NIH to consider requiring its grantees to deposit manuscripts in PubMed Central, its full-text Internet archive, when they are accepted by a journal. PubMed Central would post them 6 months after the journal published them, or immediately after publication if the author's NIH grant pays for any publication charges (*Science*, 23 July, p. 458).

In response, Zerhouni held an invitation-only meeting on 28 July with 44 participants,

many from scientific societies, as well as commercial and open-access journals. "There really is a strong advocacy for this" from scientists and universities as well as patients, explains NIH Office of Science Policy Director Lana Skirboll. Zerhouni also thinks an archive of NIH-funded research would help the agency manage its grants portfolio.

Many journals already make content freely available within a year or 6 months, but imposing a time limit could doom some journals, participants warned. Martin Frank, executive director of the American Physiological Society, noted after the meeting that publishers are already tinkering with having the author pay publication costs in exchange for immediate open access, and he argues that a single policy mandated by NIH "doesn't take into account the broad diversity of publishing." Says Frank: "Let me do the experiment."

Another concern is that posting manuscripts could be confusing: Would the PubMed Central version or the published

paper be the document of record? Some publishers suggested that instead, MEDLINE, the NIH abstracts database, could include links to full-text papers on journals' sites. Zerhouni, however, said he's concerned that some journal archives won't remain stable over the long term.

Critics also question whether NIH should divert funds from research to expand PubMed Central, which now costs \$2.5 million a year and contains papers from about 150 journals. Frank estimates that it would cost \$50 million to post full-text articles for all 4500 journals in MEDLINE.

Skirboll says NIH expects to hold at least one more meeting, this time with patient groups, then post a proposal for comment in the NIH grants guide, probably by December. Even when the plan is final, it can be modified if it causes harm, she adds. "Policies are not laws. ... Anything NIH puts in place, we will evaluate."

—JOCELYN KAISER

CREDIT: NATURAL HISTORY MUSEUM; (INSET) P. D. ALONSO ET AL., NATURE 430, 666-669 (AUGUST 2004)

## IN MEMORIAM

## Philip Hauge Abelson, 1913–2004

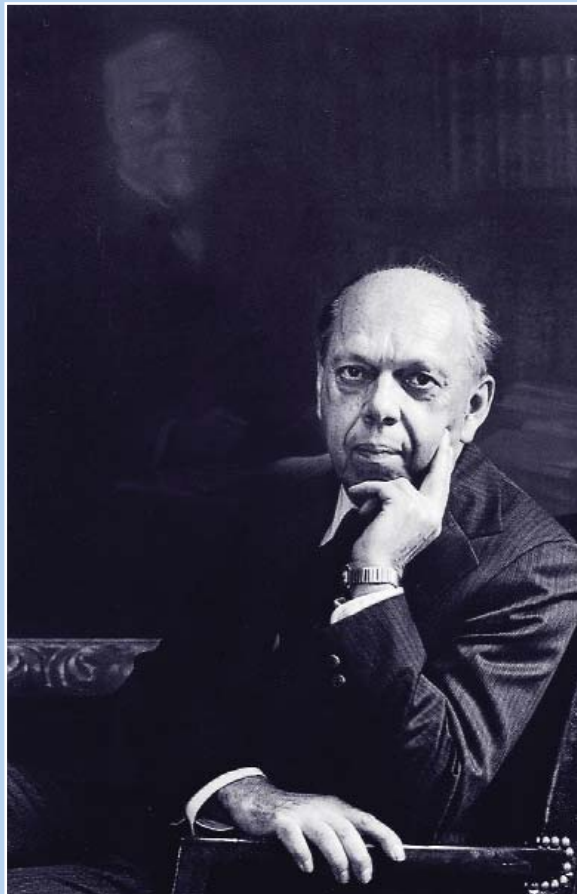
Philip H. Abelson, for 23 years the editor of *Science*, passed away on 1 August at 91. For us relative newcomers as well as those whom he brought here, his loss marks the end of an era. As an extraordinary role model here at *Science*, he cared about the full breadth of scientific work, having himself made major contributions in fields from nuclear physics to geology. As a colleague, he offered a thoughtfully dispensed supply of good counsel. And to the pages of this magazine, he brought an enhanced focus on the convergence of science and public policy—evident not only in the News pages but in his crisply opinionated editorials on research policy, regulation, and higher education.

Some disagreed with some of Phil's editorials, as he expected, and so the Letters column grew as a forum for discussion and debate over the important scientific issues of the day. After Dan Koshland succeeded him in 1985, the two adopted a friendly custom of dueling editorials—one week one, the next week the other. I suspect Dan and I are equally impressed, as his successors, with the size of the program Phil had ahead of himself as he took over. In his first editorial (*Science*, 19 October 1962), he modestly described himself as the “custodian of a uniquely valuable property.” What this custodian then announced was a plan to reduce publication time to 2 months—and to close News and Comment on Tuesday, print on Wednesday, and mail by midnight!

The Abelson scientific biography is an extraordinary saga, touching many of the important figures and scientific institutions that dominated American science during the 20th century. After graduating from Washington State University, he began his doctoral program in physics at the University of California, Berkeley, working with Ernest O. Lawrence on nuclear research and collaborating with Nobel Prize winner Luis Alvarez—and, as always, with the support and help of his wife Neva. During the year after he received his Ph.D., he worked with Edwin McMillan, bombarding uranium with neutrons in the Berkeley cyclotron to create neptunium. By that time, the Manhattan Project was getting

under way, and a system for separating and concentrating uranium-235 was needed. Abelson worked on a thermal diffusion technique, and the method he developed in Philadelphia was later enlarged to make the huge facility in Oak Ridge, Tennessee, that produced the first bomb-grade material.

Phil spent much of his later career at the Carnegie Institution of Washington, where he was director of the Geophysics Laboratory from 1953 until his appointment as president of the institution in 1971, a position he



held until 1978. I hope it will not escape the reader that for most of the time he was doing these things he was also the editor of *Science*. Maxine Singer, who watched much of Phil's Carnegie career as he moved from rank to rank, may have hit on an explanation for his polyvalence: “Until a few months ago when illness struck, Phil was a remarkable resource for learning what was going on across an amazing array of scientific fields; I have never known anyone who read and thought so broadly and deeply.”

Comments from Phil's colleagues at *Science* portray two different values. One, from Editorial, said: “He was an unabashed, passionate advocate for science and scientific progress.” He was an optimist who once edited a volume of essays—they were actually editorials—entitled *Enough of Pessimism*. As a member of our Senior Editorial Board during the past several years, he frequently reminded us of the importance of technology—the instrumental innovation that drives science forward. In a way, he was a hybrid scientist-engineer: a scientist who earned his engineering stripes on the battlefield in the course of a rich, technology-intensive career.

The other characterization, from a longtime member of the News department, described Phil as having reached the “generativity” stage: mature and confident enough of his own place to invest his energy in helping others succeed. All three of his successors have benefited from Phil's presence and his support. Although he was a willing and helpful critic, he did not mind divergence of views. On the contrary, he often encouraged pieces with which he fundamentally disagreed. The only thing he insisted on was that we get the facts right and honor the data.

His own editorials were clear, rich with content, and sometimes angry. He didn't like government regulation much, particularly when it involved regulation of science, and when I was at the Food and Drug Administration doing some of that, his editorials occasionally made me wince. But his arguments were honest, asking only to be judged on their merits. The last paragraph of one of his editorials, written in 1976 when society was concerned about the unanticipated risks associated with new technologies, is revealing. After surveying the cost-benefit pendulum of innovation, he comes down against the pessimists: “One would not advocate that we become a nation of Panglosses. However, enough of pessimism. It leads nowhere but to paralysis and decay.”

Paralysis and decay? Not on your life—not for a man who walked 4 miles every day before breakfast.

**DONALD KENNEDY**  
Editor-in-Chief



When and how did the command and control center of the eukaryotic cell arise?

# The Birth of the Nucleus

**LES TREILLES, FRANCE**—What stands between us and *Escherichia coli* is the nucleus. Eukaryotic cells—the building blocks of people, plants, and amoebae—have these specialized, DNA-filled command centers. Bacteria and archaea, the prokaryotes, don't. The nucleus's arrival on the scene may have paved the way to the great diversity of multicellular life seen today, so the membrane-bound organelle fascinates scientists probing the evolution of modern organisms. "The question of the origin of the cell nucleus is intimately linked to the question of our own origin," says Patrick Forterre, a molecular biologist at the University of Paris-Sud in Orsay, France.

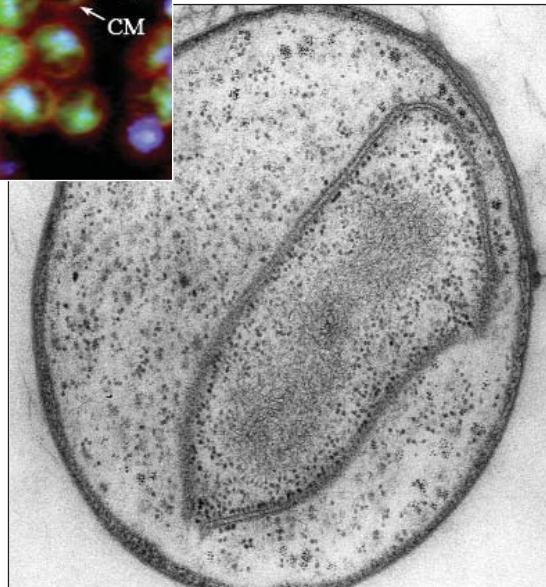
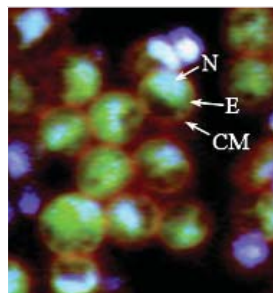
Last month, Forterre and two dozen microbiologists, evolutionary biologists, cell biologists, and others met\* here to hash out leading theories about the origin of the nucleus. One camp holds that the organelle is the result of a microbial merger. Another contends that residual nuclei hidden away in some bacteria indicate that the crucial innovation is far older than commonly thought. Perhaps the most radical theory of all puts viruses at the center of this cellular development.

At the meeting's end, the discussions of the origin of the nucleus had left biologists with a key insight: They had underestimated the complexity of the eukaryotic cell's 1.5-billion-year-old precursor. The data presented indicated that this ancestral cell had more genes, more structures, and more diverse biochemical processes than previously imagined.

But when it came to accounting for how the nucleus was born, no single hypothesis bubbled to the top. "It's like a puzzle," says Forterre. "People try to put all the pieces together, but we don't know who is right or if there is still some crucial piece of informa-

tion missing."

Biologists have long considered the nucleus the driving force behind the complexity of eukaryotic cells. The Scottish botanist Robert Brown discovered it 180 years ago while studying orchids under a microscope. In his original paper, Brown called the novel cellular structure both an areola and a nucleus, but the latter name stuck. Now, as then, the organelle's complexity inspires awe. The nucleus is a "huge evolutionary novelty," says Eugene Koonin of the National Center for Biotechnology Information in Bethesda, Maryland.



**Precocious prokaryote.** Bacteria aren't supposed to have nuclei, but *Gemmata obscuriglobus* does. A closer look shows DNA (N, blue) inside a proper nuclear envelope (E, green), as well as a cytoplasmic membrane (CM, red).

Each nucleus in a eukaryotic cell consists of a double lipid-based membrane punctuated by thousands of sophisticated protein complexes called nuclear pores, which control molecular traffic in and out of the organelle. Inside, polymerases and other specialized enzymes transfer DNA's protein-coding message to RNA. Other proteins modify the strands of RNA to ensure that they bring an accurate message to the ribosomes outside the nucleus. The nucleus also contains a nucleolus, a tightly packed jumble of RNA and

proteins that are modified and shipped out of the nucleus to build ribosomes.

The picture is far different in bacteria, in which DNA, RNA, ribosomes, and proteins operate together within the main cell compartment. It's a free-for-all in that as soon as the DNA code is transcribed into RNA, nearby proteins begin to translate that RNA into a new protein. In eukaryotes, "the double membrane [of the nucleus] uncoupled transcription and translation" and resulted in better quality control, says John Fuerst, a microbiologist at the University of Queensland, Australia. As a result, RNA is modified as needed before it comes into contact with a ribosome outside the nucleus.

The nuclear distinction between prokaryotes and eukaryotes shaped early speculation about the development of complex life. Until the 1970s, two competing theories dominated the debate over early eukaryotic evolution. According to one, a subset of bacteria slowly developed eukaryotic features, such as the nucleus. In the other, eukaryotes came first, but over time, some of them lost the nucleus and evolved a cell wall, spawning modern-looking bacteria.

Then the Woesean revolution struck. By looking at DNA sequence differences in the same gene across hundreds of microorganisms, Carl Woese, a microbiologist at the University of Illinois, Urbana-Champaign, showed that "bacteria" were actually two kingdoms, the bacteria proper and the archaea, which apparently arose some 2 billion years ago, millions of years before eukaryotes. The initial genetic analyses indicated that archaea were more closely related to eukaryotes than were bacteria. This kinship hinted that eukaryotes came from the seemingly simple archaeal stock.

Recent comparisons of fully sequenced microbial genomes have, however, added a twist to this story: Eukaryotes contain both archaeal and bacterial genes. Archaeal genes tend to run processes involving DNA and RNA, so-called information functions; the bacterial genes are responsible for metabolic and housekeeping chores. From the jumble of genes, some evolutionary biologists have concluded that this division of labor arose from the ancient symbiotic partnership between bacteria and archaea, a partnership that gave rise to eukaryotes.

\* "The Origin of the Nucleus" was held in Les Treilles, France, from 7 to 13 July.

### Friendly mergers

Such a partnership may have been enough to create the nucleus, according to Purificación López-García and David Moreira of the University of Paris-Sud. The two evolutionary biologists speculate that the original union between bacteria and archaea grew from metabolic requirements. The nucleus, they further argue, arose as a way for these endosymbionts to keep their metabolic chemistries from interfering with one another. "You needed the [nuclear] membrane because you have two competing pathways," López-García explains.

In 1998, she and Moreira proposed that in life's earliest days, methane-making archaea sometimes lived within bacteria that depended on fermentation for sustenance: the so-called syntrophic model. The relationship worked for the archaea because fermentation yielded a resource they needed, namely hydrogen. The bacterium may have benefited because fermentation requires that hydrogen concentrations remain low.

López-García and Moreira hypothesize that Earth's changing environmental conditions ultimately prompted a shift in the symbiosis. The archaeum gradually lost its appetite for hydrogen, ceased making methane, and instead relied more on the bacterial host for other nutrients. The archaeum's membrane, which had been critical for methanogenesis, became superfluous. At the same time, the outer bacterial membrane invaginated the cellular compartment, eventually surrounding the archaeal DNA but excluding the ribosomes. The change was advantageous to the bacteria, because in separating ribosomes from the microbial chromosomes, it helped ensure more accurate conveyance of the DNA's message. This set-up persisted and ultimately evolved into the eukaryotic nucleus, says López-García. And what remained of the archaeal cytoplasm became the nucleolus.

The researchers suggest that modern methanogenic archaea bearing a resemblance to eukaryotes are possible descendants of the ancient methanogens that entered into the nucleus-generating symbiosis with bacteria. These archaea and eukaryotes have similar genes encoding proteins involved with DNA and RNA. For example, they share genes for histones, proteins that help stabilize chromosomes. In contrast, bacteria don't have histones.

Another modern microbe, the myxobacterium, may resemble the ancient bacterial host in which the nucleus evolved. Like eukaryotic cells, myxobacteria communicate with other cells, move, and can form multicellular complexes. Myxobacteria "have complex structures that are very striking" and reminiscent of eukaryotic cells, López-García notes. These bacteria also have cell-

signaling molecules, such as kinases and G proteins, in common with eukaryotes.

### Self-starters

López-García and Moreira's proposal assumes that bacteria and archaea appear earlier on the tree of life than eukaryotes, but Fuerst holds that the reverse is true. He is



**Fruitful partnership.** A bacterium akin to this myxobacterium may have paired off with an archaeum, eventually evolving a nucleus.

convinced that eukaryote-like cells were around before bacteria and archaea or emerged right at the time when these prokaryotes split off to form separate kingdoms of their own. Fuerst points to an unusual group of bacteria that he's studied for the past decade. These remarkable microbes have nuclei, or something akin to them, and may resemble the early cells that evolved into modern eukaryotes, according to Fuerst.

Found in soil and fresh water, these microbes, called planctomycetes, have cell walls that are not quite as rigid as those of other bacteria. As early as 1984, researchers had suggested that some planctomycetes also have internal membranes. In 2001, Fuerst and his colleagues, using sophisticated electron microscopy techniques, confirmed the existence of these membranes, even revealing double ones like those of a nucleus. Those observations "turn the dogma that 'prokaryotes have no internal membranes' upside down," says Philip Bell, a yeast biologist at Macquarie University in Sydney, Australia.

Using sophisticated electron microscopy techniques, Fuerst and his colleagues have now verified that there are discrete membrane-bound compartments within two planctomycetes, *Gemmata obscuriglobus* and *Pirellula marina*. One compartment, pushed up along the periphery, seems to have

very little in it. A second sits in the center of the microbe and holds a dense collection of genetic material—RNA and DNA mixed with DNA- and RNA-processing proteins. The stuff in between—the cytoplasm—is full of proteins, ribosomes, and RNA.

At least one planctomycete has a double internal membrane around its DNA instead of the more typical single membrane. The membrane is not continuous but consists of pieces of folded membranes linked together. The gaps between the folds could indicate how nuclear pores got their start, says Fuerst.

Explaining these structures has always posed a sticking point for nuclear evolution. Without pores, the nucleus can't function. But nothing similar to these complex channels had been seen in bacteria before. At the meeting, however, Fuerst showed dramatic electron micrographs of craterlike spots in the internal membranes of planctomycetes. These depressions closely resemble nuclear pores, he says. Although nuclear pore genes are hard to compare, Fuerst is encouraged that a preliminary look at a planctomycete genome hints that the bacteria have primitive versions of eukaryotic genes for some key nuclear pore proteins.

"If you combine all the evidence, it makes a consistent picture," he asserts. "*Gemmata* is a valid model for a non-symbiotic origin of the eukaryotic nucleus."

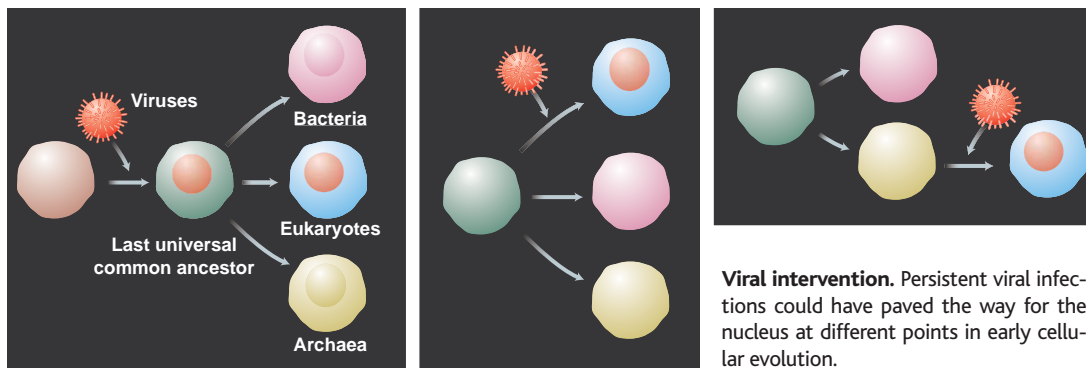
It may not be alone. There's a recently discovered phylum of sponge-dwelling bacteria that also seem to have nuclei, says Fuerst, and there are likely more, yet-to-be-discovered microbes with similar features. Bacteria with nuclear pores and internal membranes, features typically considered eukaryote-specific, suggest that the nucleus was born much earlier than traditionally thought. If Fuerst's scenario is correct, "then the nucleus actually precedes eukaryotes," says Koonin.

In fact, this compartment could date back to the last universal common ancestor (LUCA), a putative organism from which eukaryotes, bacteria, and archaea eventually emerged, says Fuerst. If that's the case, certain LUCA features, such as the nucleus, were retained in eukaryotes but lost to some degree in most archaea and bacteria. Indeed, that seems to be the case, as eukaryotic cells possess features now seen in each of these groups.

### Hostile takeover

A third option for the origin of the nucleus revolves around viruses. "Viruses predated the divergence between the three domains of life," says David Prangishvili, a virologist at the University of Regensburg, Germany. He argues that viruses were already quite common in the primordial soup and only later became dependent on cells to survive. When these early cells came along, "viruses played





**Viral intervention.** Persistent viral infections could have paved the way for the nucleus at different points in early cellular evolution.

a critical role in the evolution of the complex [eukaryotic] system,” adds Forterre.

Viruses do have the ability to set up permanent residency in a cell, infecting but not killing the host. Thus they and their genes can stay around and influence a cell’s evolution. Bell, Forterre, Prangishvili, and Luis Villarreal, a virologist at the University of California, Irvine, each have a different proposal for how viruses were important to the evolution of the nucleus. Their supporting data are provocative, but circumstantial and controversial. “I do not believe [it],” says Jacomine Krijnse-Locker of the European Molecular Biology Laboratory in Heidelberg, Germany. “The idea of the viruses ‘inventing’ [eukaryotic cells] from scratch is hard for me to conceive.”

When viruses persist in cells instead of killing them, cells “can acquire a whole new set of genes in one event,” counters Villarreal. While in residence over millions of years, the new viral genes could have supplanted bacterial or archaeal genes, replacing, for instance, proteins that process DNA. These extra genes could also evolve to play new roles in the cell.

Villarreal points out that there are intriguing similarities between nuclei and viruses, which are basically packets of DNA surrounded by a protein coat—and often by a membrane. In red algae, for example, a nucleus can move from cell to cell, much like an infectious virus. And in general, cell nuclei and viruses lack protein- and lipid-producing pathways within their borders. Both contain linear chromosomes, whereas most bacterial chromosomes are circular. Both disassemble their “membrane” during replication. Both transcribe DNA but don’t translate mRNA within their boundaries. As they replicate within a cell, some poxviruses even make a membrane around their DNA using the endoplasmic reticulum of the infected cell. The eukaryotic cell uses this same material to build its nucleus.

Large, complex DNA viruses, which include poxviruses and the African swine fever virus, likely bear the closest resemblance to the putative viral ancestor of the nucleus, Bell suggests. DNA strands in these viruses have primitive telomeres, protective DNA se-

quences found at the ends of eukaryotic chromosomes.

Bell speculates that a virus living in an archaeum set the stage for the nucleus. Ultimately, viral DNA and archaeal DNA merged inside the virus, and the new genome later shed genetic material from both. In the end, “the unique genetic architecture of the eukaryote is a result of superimposing a viral genetic architecture on an archaeal genetic architecture,” Bell argues.

“If this is true, then we are all basically descended from viruses,” remarks Forterre.

genome sequences become available, such as those of several planctomycetes, Fuerst and others plan to search for more genetic similarities between these bacteria and eukaryotes. Meanwhile, García-López anxiously awaits sequenced genomes of myxobacteria and plans to compare them with the genes of eukaryotes.

Overall, says Forterre, it’s “a really exciting time to tackle questions which were previously only considered seriously by a few theorists.”

—ELIZABETH PENNISI

## Profile Edward Hammond

# Activist Throws a Bright Light on Institutes’ Biosafety Panels

Edward Hammond’s aggressive sleuthing has triggered a debate on the oversight of the growing field of biodefense research

**AUSTIN, TEXAS**—In late January, Edward Hammond sent out a blizzard of faxes to almost 400 research institutes from Honolulu to New York. His request was straightforward enough: He asked for the minutes of the last two meetings of each organization’s Institutional Biosafety Committee (IBC).

Hammond, who directs the Sunshine Project, a small nonprofit organization based in Austin, wondered whether the IBCs fulfill their oversight role for certain types of biology experiments as prescribed by guidelines from the National Institutes of Health (NIH). In particular, he questioned whether they would publicly share their deliberations. Such openness, he says, is vital to prevent biodefense research from going astray.

Today, Hammond is fighting testy e-mail battles with his targets over their tardy responses. How to answer his query has become a hot topic among biosafety officers and university lawyers. Some universities have sent him minutes, but with almost every detail blanked out, arguing that the

redacted information is private, proprietary, or security-sensitive. More important, Hammond has concluded that the IBC system, designed in the 1970s to review recombinant DNA research, is in disarray. He claims that dozens of IBCs, many of them at the nation’s research powerhouses, aren’t staffed properly, don’t seriously review proposals, or never meet at all. Outraged, he has filed complaints with NIH, asking it to cut off funding retroactively to 19 institutions. Dozens more complaints are on the way.

NIH officials are investigating the charges, but there’s no reason to assume that the entire system is broken, says Allan Shipp of NIH’s Office of Biotechnology Activities (OBA), which oversees IBCs. Most IBCs are “very earnest in their attempts and desire to fulfill their responsibilities,” he says.

Some researchers who have followed Hammond’s quest—he posts alleged violations frequently on his Web site—disagree. “Frankly, I’ve been surprised by the number and magnitude of the deviations from the

CREDITS: P. HURY/SCIENCE; SOURCE: P. FORTERRE

guidelines that he has identified,” says molecular biologist Richard Ebright of Rutgers University in Piscataway, New Jersey. To him, the results are an indictment of OBA as well. “If many institutions do not have IBCs in place for a long period of time, or their IBCs don’t schedule meetings, then that office is not functioning,” he says.

Hammond’s critics say he doesn’t distinguish between correct paperwork and biosafety itself. The latter is a topic he doesn’t know much about, argues Stefan Wagener, president of the American Biological Safety Association. Many also dislike the confrontational tone of his prolific correspondence. “He’s an irritant sometimes,” says virologist C. J. Peters of the University of Texas Medical Branch in Galveston. “He’s fond of trouble, but the kind of information that he’s after doesn’t make us much safer.”

**Just answer the question**

In a café near his tiny office, the San Antonio native, who graduated in Latin American studies and community and regional planning, explains the motivation behind his crusade. Safety isn’t Hammond’s main concern. He sympathizes with biodefense activists who, fearful of escaping germs, rail against planned high-level biosafety labs in their neighborhoods, but he’s more interested in another issue: transparency. “The public has a right to know,” he says, “that’s what it’s really all about.” He is unapologetic about being aggressive. “You have to be tough to be heard,” he says. “If you are working with Ebola, the public has a right to ask questions.”

Without appropriate public oversight, Hammond argues, biodefense spending could easily cross over into offensive research. Some recent studies—such as the creation of the poliovirus from scratch and the partial resurrection of the 1918 pandemic flu virus—trigger a vicious cycle, he asserts: Under the guise of defending against potential threats, researchers generate new ones, requiring new countermeasures.

German biologist Jan van Aken founded the Sunshine Project—exposure to sunlight can inactivate many biological weapons—in 1999 to investigate activities that could undermine the 1972 Biological and Toxin Weapons Convention. In 2000, he joined with Hammond and his wife Susana Pimiento, a lawyer from Colombia, to set up a U.S. branch.

The group’s \$100,000 annual budget is funded by liberal-leaning charities such as the Ben & Jerry’s Foundation and individual donors.

One of Hammond’s first targets was the U.S. program—still ongoing—to use pathogenic fungi to eradicate opium poppy, cannabis, and coca crops in South America and Asia. Using the Freedom of Information Act, he has unearthed “a tremendous amount of information” about that effort, says Mark Wheelis, an arms control researcher at the University of California, Davis, who serves on Sunshine’s advisory committee. Hammond has also dug into the Pentagon’s secretive research into so-called nonlethal weapons, which include psychoactive and anesthetic drugs. These weapons may violate the 1993 Chemical Weapons Convention. “He has done an immense service to the arms control community,” says Wheelis. “Most of us simply don’t have the time to chase those documents.”

**Minutes Man**

Now Hammond has become a watchdog of the biodefense business, and he’s using the IBCs to get a foot in the door. Set up in the 1970s in response to worries about genetic engineering, IBCs review studies involving recombinant DNA at

every institute that receives NIH funding. NIH rules require them to have members from outside the institute and make meeting min-

utes accessible. Although recombinant DNA work is their official mandate, many institutes have also charged IBCs with looking at other potentially hazardous work.

Hammond concedes that most of the vast stacks of the documents he has received don’t contain anything very exciting. It’s what he hasn’t received, however, that upsets him.

Take Mount Sinai Medical Center in New York City, which has dozens of projects that entail recombinant DNA work, including studies with Ebola and Lassa fever viruses. Yet its IBC has met only once and reviewed three proposals since 2001. The committee’s minutes—which Mount Sinai provided to Hammond and subsequently to *Science*—consist simply of the research proposals and signed letters of approval from the IBC. A Mount Sinai spokesperson provided *Science* with a list of reasons why experiments that Hammond says should have been reviewed are, in fact, exempt from the guidelines.

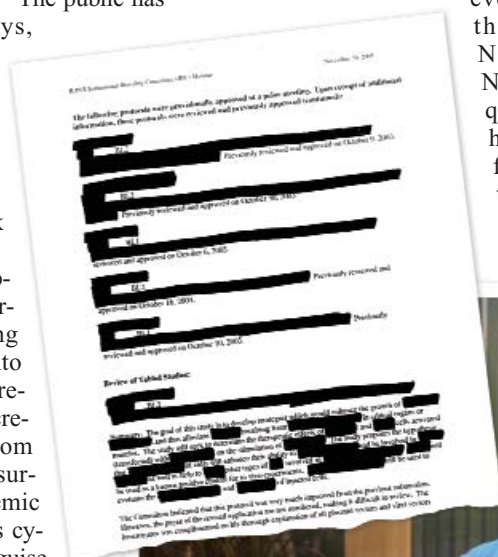
IBC meetings are an equally rare event at Rockefeller University in New York City, where the panel last met in September 2003, after a 5-year hiatus. The Rockefeller IBC reviews all proposals—some 161 since 2000—electronically, explains Amy Wilkerson, associate vice president for research support. She, however, has declined to share any electronic records with Hammond, who says this is at odds with the spirit of the IBC system.

At Tulane University in New Orleans, Louisiana, Hammond’s January fax was simply ignored, as was a follow-up by certified mail. When he faxed a final, more threatening request on 7 July, the university responded with a four-line letter saying it “has no documents responsive to your request.”

OBA will investigate each of Hammond’s complaints, says Shipp. In May, it put out a memo instructing IBCs that minutes should contain, at a minimum, “the major points of discussion and the committee’s rationale for particular decisions.” Mount Sinai told *Science* it will change its practices accordingly and will also honor a recent NIH suggestion that its IBC meet at least once a year.

Hammond’s efforts come at a key time for IBCs. In March, the U.S. government announced plans to have them review any experiments that could play into the hands of bioterrorists (*Science*, 12 March, p. 1595). From the responses Hammond has received, Ebright says, “it’s clear that they’re not prepared for this extra burden.”

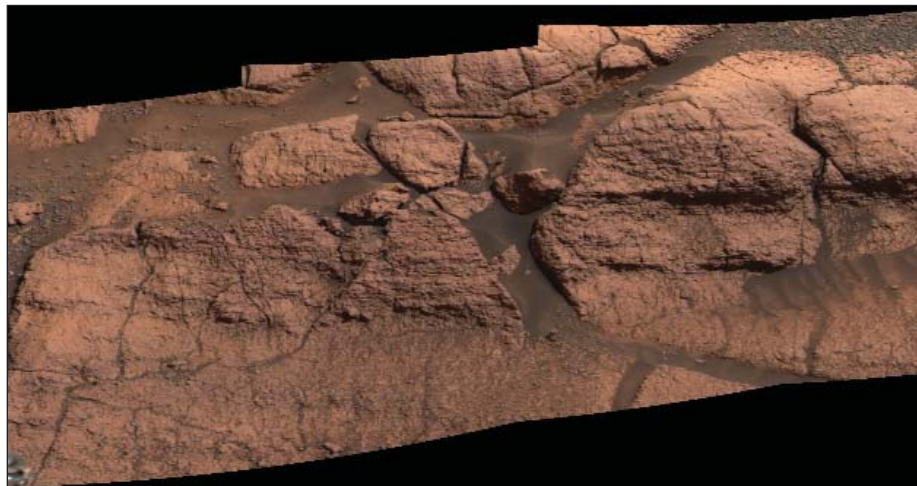
—MARTIN ENSERINK



**Blackout.** Edward Hammond’s request for minutes of biosafety meetings produced heavily redacted documents—or nothing, in some cases.

CREDITS: (BOTTOM) LAM HA/SIPA





## Rainbow of Martian Minerals Paints Picture of Degradation

Better spectroscopic observations from Europe's Mars Express and analyses by NASA's rovers are revealing a diversity of minerals that tells of water shaping the planet

To a geologist, there's nothing like getting your hands on a rock to see what it is made of. But spectroscopists can get some sense of the makeup of a distant planet's rocks by splitting the light that comes off the planet's surface into the squiggly lines of a spectrum. The peaks and valleys of those spectra, properly interpreted, can reveal the planet's mineralogical composition. Spectra of Earth can splash a riot of color across the wavelengths from the blue of the visible to the far infrared, revealing "a mineralogical museum," notes planetary scientist John Mustard of Brown University in Providence, Rhode Island. Mars, on the other hand, had presented spectroscopists with not much more than "little bumps" to mull over. "Perhaps Mars is mineralogically impoverished," Mustard mused a couple of years ago.

Fortunately for Mustard and his colleagues, they are finally seeing a spectral diversity on Mars that, although it doesn't rival Earth's, tells a far more complete story of how water came to chemically alter much of the martian surface. Mars, it turns out, is not so much mineralogically impoverished as incompletely studied. With a new spectrometer now in orbit aboard Mars Express, instruments on the Opportunity and Spirit rovers getting up close to rocks (see special section, p. 793, for the first published results from Spirit), and yet more capable spectrometers on the way, "we have a real opportunity to put the whole of Mars together," says planetary spectroscopist Jessica Sunshine of SAIC Inc. in Chantilly, Virginia.

The emerging picture is of a salt-laden, often corroded planet that had standing water early in its history. Volcanic emanations made that water acidic enough to leach salt from the rock and lay it down in thick beds, and water beneath the surface seems to have altered rock as well. Most of the planet is now covered by weathering products of yellow-brown dust or rock rinds. But the nature of the weathering and to what extent it has continued to the present are still being debated; even the new and improved spectral squiggles are leaving room for interpretation.

### Salty Mars

It was a unique bit of spectral color that brought the Opportunity rover to the shallow sea deposits of Meridiani Planum in the first place. As the Thermal Emission Spectrometer (TES) on Mars Global Surveyor scanned the planet strip by narrow strip beginning in 1999, the planet looked pretty simple. The better part of it is bright, dust-covered regions. In TES spectra of the infrared radiation emitted by the surface—the so-called midinfrared of 5- to 50-micrometer wavelengths—the dark areas are volcanic rock that has low or medium amounts of silica, the basic ingredient of rock. But one area on the equator about the size of Oklahoma had a booming spectral signal of the iron-oxide mineral hematite. Hoping to land on a once-buried lakebed or hydrothermal deposit—common places to find hematite on Earth—mission controllers set the Opportunity rover down on Meridiani Planum last January.

**Pages in a book.** Thin layers of salt-laden sediment speak of an ancient acidic sea on Mars.

Opportunity found the hematite expected from remote sensing, but not in any of the expected geologic settings. The hematite had formed in marblelike concretions while buried in dirty, salt-laden deposits laid down as a shallow sea or a series of puddles evaporated (*Science*, 5 March, p. 1450). When the rover applied its analytical instruments directly to the centimeters-thick deposit of little Eagle crater, the outcrop turned out to be almost half sulfate salts. Small amounts of sulfate had been inferred from martian soil sulfur analyses since the Viking landers of the late 1970s, but remote sensing had seen nary a wisp of sulfates from orbit. Opportunity is now inching down the steep interior of the large crater Endurance and finding meter after meter of the same sulfate-rich evaporite as at Eagle crater. Presumably it goes down the entire 300 meters of the light-toned, layered stratum seen from orbit underlying Meridiani Planum.

Now sulfates—as well as other weathering products—are turning up all across Mars. In late December, the European Space Agency's Mars Express went into orbit carrying the Visible and Infrared Mineralogical Mapping Spectrometer (OMEGA) among its seven instruments. It is the first-ever spectrometer spanning the near-infrared wavelengths of 0.35 to 5.2 micrometers to make it safely into Mars orbit and operate for more than a few weeks. Its 10-times-finer spatial resolution and near-infrared wavelengths sensitive to altered, fine-grained material revealed far more "color" on Mars than spectroscopists could see before.

In March at the Lunar and Planetary Science Conference (LPSC) in Houston, Yves Langevin of the University of Paris South (UPS) in Orsay and the OMEGA team reported the detection of a magnesium sulfate mineral called kieserite. This sulfate "seems to be ubiquitous in low-lying regions" where



**Iron berries.** The distinctive spectrum of hematite-rich balls lured in the Opportunity rover.

CREDITS: NASA/JPL/CORNELL

water might have collected and evaporated, he said, such as at the bottom of a canyon of the Valles Marineris. OMEGA also detected clays, produced by the water weathering of silicate rock, and serpentine, the weathering product of olivine.

At last month's biennial scientific assembly of the Committee on Space Research in Paris, OMEGA principal investigator Jean-Pierre Bibring of UPS mapped out the distribution of both magnesium and calcium sulfates in the tiny fraction of Mars covered by OMEGA so far. They appear not only where ancient waters may have collected but also in some, although not all, of the layered deposits beyond Meridiani Planum. Layered deposits have of late become the leading geological mystery on Mars (*Science*, 8 December 2000, p. 1879). Some geologic force—water, wind, volcano, or impact—laid down light-toned material inside impact craters and in other low-lying regions. The Opportunity and OMEGA discoveries seem to show that at least some of the mysterious layered deposits were formed beneath standing water: ponds, lakes, or oceans.

#### Ancient age of corrosive ponds

To geochemists, a sulfate-salty Mars tells a story of a young planet corroded by acid. In a 1987 paper, the late Roger Burns detailed the geochemical consequences of a young, volcanically active Mars. Sulfuric acid derived from volcanic emissions would have mixed with any water that was about and chemically eroded rock to produce a variety of sulfates, in particular a potassium iron hydroxy sulfate called jarosite.

The Opportunity rover's Mössbauer instrument did in fact identify jarosite in the evaporite at Eagle crater. Because the Meridiani Planum rocks are some of the oldest seen on the planet, that's "a compelling case for acidic water on [early] Mars and lots of it," says geologist Jeffrey Kargel of the U.S. Geological Survey in Flagstaff, Arizona. In recognition of Burns's foresight, Opportunity team members named the largest evaporite outcrop of Endurance crater Burns Cliff.

Water on early Mars as acidic as gastric juices could not only have helped corrode Mars and contribute to sedimentary deposits, but it could have played a pivotal role in martian climate. Signs that running water cut valleys during the first billion years or so of martian history—when life was beginning on Earth—have convinced most researchers that early Mars was "warm and wet," or at least not so cold that all water was continually locked up as ice. But the young sun was not stoked to its full heat and brilliance in the first billion years of its life, so climate modelers have had to invoke some sort of extra heating

early on, such as a strong greenhouse, to explain the warmth.

A dense carbon dioxide atmosphere could have boosted the early martian greenhouse, but the gas is not geochemically inert; it too forms an acid with water and corrodes rock to form carbonate salts. Locked up in carbonates, carbon dioxide couldn't warm the planet. With enough volcanoes erupting, however, sulfuric acid could have frustrated carbonate formation, kept the carbon dioxide as a gas, and propped up the martian greenhouse, notes planetary geologist Jeffrey Moore of NASA's Ames Research Center in Mountain View, California. The huge Tharsis volcanic complex and a host of other Hawaiian-style volcanoes on Mars suggest that there was lots of eruptive activity into martian middle age.

#### Questions of color

Although OMEGA is bringing a broader spectral view to martian remote sensing and the two rovers are providing some much-needed ground truth for orbiting instruments, they certainly haven't settled many debates on the nature of the martian surface. A central question is what, if anything, water was doing after the early "warm and wet" era. For example, exactly what TES data reveal about the darker, dust-free regions covering much of Mars remains unsettled. Do their spectral signatures divide them into areas of rock of either low or moderate silica content? Or are they fresh rock and alteration-coated rock? Although the answers remain unclear, the case for alteration—perhaps in the middle history of Mars—does seem to be gaining ground.

Other chemical rock alteration cannot yet be tied to early Mars. Early on, Spirit found two kinds of "crud," as one team member describes weathering products, coating many rocks in Gusev crater that neither its remote-sensing Mini-TES instrument nor its two contact analyzers could make heads or tails of (*Science*, 9 April, p. 196). And now Spirit has identified hematite in rocks of the Columbia Hills that are utterly unlike those of Meridiani Planum. Severe, wet alteration of some sort of rock in the Columbia Hills seems to have occurred, says rover team member Raymond Arvidson of Washing-

ton University in St. Louis, but details remain murky.

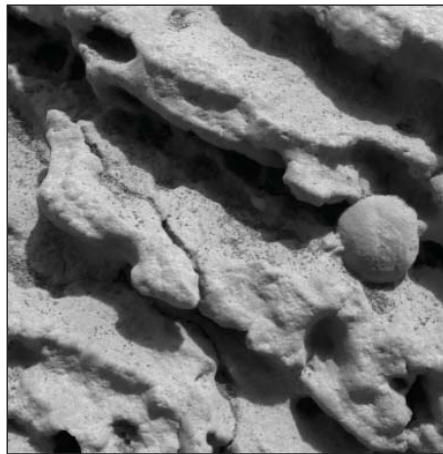
The soil of Gusev crater is generating another debate over how much weathering occurred when. The rover science team concludes that the soil is mostly local volcanic rock pulverized by impacts or sandblasted off exposed rock by the wind, with a bit of windblown dust added in. Exposure to the martian elements that weathered large Gusev rocks apparently has failed to weather away even the vulnerable olivine exposed in the soil.

Three nonteam spectroscopists—Melissa Lane of the Planetary Science Institute in Tucson, Arizona; Darby Dyar of Mount Holyoke College in South Hadley, Massachusetts; and Janice Bishop of NASA Ames—argued at the LPSC that the soil's rock has in fact completely rotted away to crud. Lane, who was a student of Philip Christensen of Arizona State University in Tempe, the TES, THEMIS, and Mini-TES PI, argued that Mini-TES analyses did not compare Gusev soil spectra with enough spectra of known compounds. She found that hydrous iron sulfate—another acid weathering product predicted by Burns—is as good a match to absorptions that Christensen and his colleagues

attribute to trace carbonate and loosely bound water. And Mössbauer specialist Dyar—who along with Bishop was a student of Burns—argued that Mössbauer soil spectra match hydrous iron sulfate just as well as they do olivine. So, what the rover team takes to be unaltered rock, Lane and her colleagues see as alteration products formed well after warm and wet Mars.

Resolving such differences could require many sorts of observations by both remote sensing and rover-manipulated analyzers, says planetary spectroscopist Carlé Pieters of Brown University. "It's clear you need multiple pieces of information," she says. In the past, instruments have been flown one at a time, she notes, but that is changing with the current rovers, Mars Express, and the upcoming NASA 2010 Mars Science Laboratory rover and the 2006 Mars Reconnaissance Orbiter. Even so, she says, understanding martian dust, soil, and weathering—and thus water's role in martian history—will probably require the return of samples.

—RICHARD A. KERR



**Invisible.** Meridiani Planum's abundant sulfates were spectrally unrecognizable from orbit.



MONTREAL, CANADA—More than 7000 researchers gathered here from 18 to 23 July for the International Congress of Immunology and the Annual Conference of the Federation of Clinical Immunology Societies.

## An Old Favorite Is Resurrected: Regulatory T Cells Take the Stage

When roughly 1000 people packed a convention center hall here for talks on a mysterious class of T cells, it was clear that 20 years after falling out of favor, regulatory T cells have made a stunning comeback. The cells, which make up roughly 5% to 10% of T cells in people, suppress the function of other T cells and may help physicians control a range of infections, autoimmune diseases, and organ transplant rejection. That no one understands exactly how these cells rein in the immune system or how to harness their powers doesn't appear to have dampened enthusiasm one bit. "It's over the top at the moment," says immunologist Anne O'Garra of the National Institute for Medical Research in London.

Regulatory T cells, formerly called suppressor T cells, first attained popularity in the early 1970s. But by the mid-1980s, they'd lost their appeal, in part because they were so difficult to isolate and grow. Aided by improved technology in the last 5 years, immunologists led by Shimon Sakaguchi of Kyoto University in Japan found new markers with which to identify the cells, such as the surface proteins CD4 and CD25, and the field was reborn. What scientists learned was remarkable: In test tubes and mouse studies, regulatory T cells seemed to ease inflammation and regulate other immune cells implicated in autoimmune diseases such as type 1 diabetes. In some experiments, they also prevented transplanted organs in mice from being rejected.

At the meeting, David Hafler of Harvard University suggested that patients with multiple sclerosis, an autoimmune disease, have normal numbers of regulatory T cells positive for CD4 and CD25, but the cells are sluggish, unable to rein in other T cells as they normally would. Fiona Powrie of the University of Oxford, U.K., meanwhile, reported that CD25 cells given to mice with a version of inflammatory bowel disease infiltrate the animals' guts and reverse inflammation.

Although CD25 is the most popular marker for regulatory T cells, there's a major catch: All activated T cells express it, so it's only useful when studying inactive or "naïve" cells that haven't been challenged by, say, a pathogen. Another popular marker, FoxP3, a transcription factor, is present only inside the cell, not on its surface. Because it's tough to spot and

manipulate, FoxP3 can have limited usefulness in identifying and sorting regulatory T cells.

Two groups, one led by O'Garra and the other led by Maria Grazia Roncarolo, who directs the San Raffaele Telethon Institute for Gene Therapy in Milan, Italy, now propose that the secreted cytokine interleukin-10 (IL-10) provides a good marker with which to identify regulatory T cells. O'Garra reported that IL-10-making T cells that displayed regulatory abilities didn't always express much Fox P3, raising questions about its appropriateness as a marker. Roncarolo, meanwhile, reported that IL-10 regulatory T cells blocked the development of diabetes in mice that are susceptible to it.

It remains unclear how regulatory T cells suppress the immune system and whether they falter in people with autoimmune diseases. Ethan Shevach of the National Institute of Allergy and Infectious Diseases, who has helped lead the comeback of regulatory T cells, revealed new data suggesting that the cells destroy B cells in test tubes; if this occurs in live animals, it could represent another route by which regulatory T cells suppress immune activity. "It's extremely exciting," says O'Garra, who believes the work has "major implications" in explaining the suppressive nature of regulatory T cells.

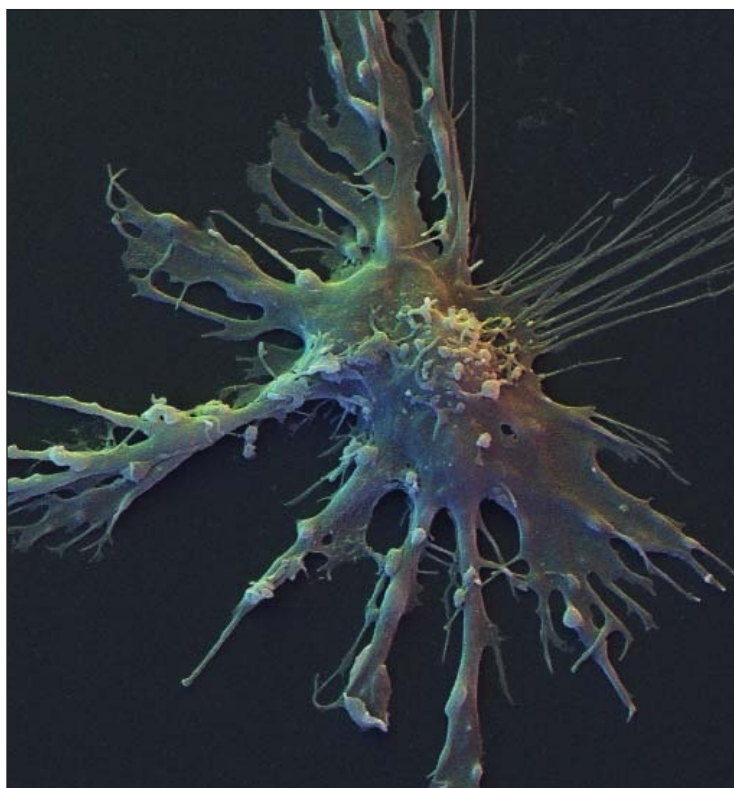
These findings have some immunologists itching to test regulatory T cells in clinical trials, although others caution that such efforts would be premature, given the confusion still swirling around the cells. "Hopefully," says Harvard immunologist Harald von Boehmer, "they'll allow clinicians to do what they haven't been able to do for 30 years: manipulate immunity."

## And Action! Dendritic Cells Go Live

While regulatory T cells were fodder for gossip at evening cocktail parties, some of the most provocative news concerned another type of immune cell, the dendritic cell. By educating T cells as to appropriate targets, dendritic cells help the immune system maintain a tenuous but crucial balance between attacking pathogens and sparing the body's own tissue.

Because how cells behave in a petri dish may not reflect their typical actions in a live animal, a handful of immunology teams are now setting up reality shows starring dendritic cells. Using expensive high-tech imaging systems, they've developed intricate methods to visualize the cells in living mice. For example, 7 months ago, Ulrich von Andrian of Harvard University and his colleagues delineated how dendritic cells move as

CREDIT: DAVID SCHARF



**Close-up view.** Immunologists are starting to deconstruct the elaborate dance between dendritic cells like this one and T cells.

they perform one of their major functions: alerting T cells to a pathogen invasion. He found that the cells move briskly through certain parts of the lymph nodes and often interact only briefly with T cells.

Now a second group, led by Michael Dustin of New York University and Michel Nussenzweig of Rockefeller University in New York City, has offered a glimpse into how dendritic cells accomplish their second major function: ensuring that the body tolerates its own tissue. The team genetically altered mice to express a fluorescent protein in their dendritic cells, which made these immune sentinels easier to spot under a microscope. Then the investigators anesthetized the animals and carefully separated a flap of skin containing a lymph node—where many dendritic cells are found—from each rodent's thigh.

In live images of this system, they watched immature dendritic cells, which hadn't yet been primed by an antigen, form dense networks of almost motionless cells. T cells entering the lymph node reached this network and then quite literally stood still for over an hour, apparently communing with the dendritic cells.

Nussenzweig speculates that the network is an efficient way for immature dendritic cells, which closely monitor the lymph node environment, to pick up certain "self" antigens that enter lymph tissue—and in turn shut down potentially self-reactive T cells. In that way, they may protect the body from autoimmunity.

Why cells clump together in such nearly still networks isn't clear. "There's a world to be discovered" about dendritic cell behavior, says von Andrian.

On the clinical side, Jacques Banchereau, director of the Baylor Institute for Immunology Research in Dallas, Texas, presented new data implicating dendritic cells in a crippling form of arthritis, systemic onset juvenile idiopathic arthritis (SOJIA). Working with blood samples from children with this condition, he's found an upregulation of genes affecting an immune protein called interleukin-1. IL-1 is known to activate dendritic cells.

An IL-1-suppressing drug called Anakinra is on the market for use in rheumatoid arthritis, but it hasn't met with much success, notes Banchereau. When he and his institute colleague Virginia Pascual tested it on nine children with SOJIA, however, eight showed complete regression of disease, and the ninth was also helped. This suggests that unlike rheumatoid arthritis, SOJIA appears dependent on IL-1 and dendritic cell malfunction, concludes Banchereau.

## Genes Crisscross Disease Lines

Scientists have spent decades hunting for genes behind immune disorders, with relatively little success. But a new genetic tool and some recent studies suggest they're making progress at nailing down some elusive genes, including those that affect more than one disease.

The tool is the increasingly popular technique of RNA interference (RNAi), a relatively quick and simple method to dampen or shut off the expression of individual genes using small RNAs. Immunologist Luk Van Parijs of the Massachusetts Institute of Technology (MIT) recently completed one of the first RNAi gene screens focused on immunity. His lab selected 168 genes whose expression in immune cells is regulated by growth factors but whose roles in overall immune function—and dysfunction—remain unclear.

Using RNAi to quash one or more genes in mouse embryos and adult animals, the investigators examined hundreds of mice, including ones from strains already predisposed to cancer or type I diabetes. Van Parijs was excited to find that knocking out some of the immune genes slowed or sped the onset of those conditions. For example, in a strain of cancer-prone mice, RNAi was used to blunt the effects of a gene in the NF- $\kappa$ B family, which encode proteins that control gene expression. Van Parijs reported that tumor growth was accelerated in the animals, although he hasn't discovered why. The screen also indicated that genes controlling regulatory T cells influence the progression of type I diabetes.

Other researchers have begun to find that genes with a role in one autoimmune disease may contribute to other, related conditions. For example, John Rioux, director of inflammatory disease research at MIT's Whitehead Institute, is finding hints that lupus is tied to variations in *IBD5*, a gene previously implicated in inflammatory bowel disease.

Rioux is also working with Whitehead postdoc Emily Walsh on a dense genetic map that they hope will point to other lupus genes. Walsh focuses on haplotypes, stretches of DNA that can vary slightly between sets of individuals and encompass multiple genes. She has homed in on a suspect already, for example—a haplotype previously linked to an in-

creased risk of lupus. It includes an immune-related *HLA* gene that has a known role in the condition, but there may be other connections, she says: "It smells like there are independent [genetic] effects" on this haplotype.

Another immune gene that apparently crosses disease boundaries is *PTPN22*, says Linda Wicker of the University of Cambridge, U.K. Like other labs, her group jumped on the gene earlier this year when it was linked with type I diabetes. In June, geneticist Peter Gregersen of the North Shore–Long Island Jewish Research Institute in New York reported tying the gene to



**Fingering the culprits.** Genes behind one autoimmune disorder, like painful rheumatoid arthritis, are beginning to be tied to seemingly disparate diseases, like type 1 diabetes or lupus.

rheumatoid arthritis. A month later, rheumatologist Timothy Behrens and his colleagues at the University of Minnesota, Twin Cities, implicated it in lupus.

Wicker is studying three other genes that seem to protect mice from diabetes with a combined power larger than their individual effects would suggest. Like many of her colleagues, she contends that immunologists and geneticists need to recognize that small variations in a gene, which may shift gene expression patterns or tweak a protein's amino acids, can spur autoimmune disease as readily as the complete loss of a gene's function. "Subtle changes ... can really make a big difference through years of inflammation," she says.

Wicker's team had studied the gene encoding interleukin-2 for years, painstakingly searching for different expression patterns in type I diabetes and finding none. Now she's discovering subtle variations in gene expression just in CD8 T cells that she thinks could explain the gene's potential effect on type I diabetes.

With the drought in gene-hunting for immune diseases over, says Wicker, "we can try to move on and figure out the biology."

—JENNIFER COUZIN



## Creating a European Research Council

**IT IS A VERY POSITIVE DEVELOPMENT IN THE EU** that many governments now recognize that basic, not just targeted, research is vital for a knowledge-based society. This realization lays the foundations for innovation, long-term growth, and improvement of quality of life. The enlarged EU, a newly elected European Parliament, and a new Commission should now grasp the historic opportunity to establish without delay a European Research Council (ERC), with full participation of the scientific community.

Many learned societies, organizations of scientists, universities, European research organizations, and large laboratories have contributed extensively to the emerging consensus that Europe needs to fund basic research, including the social sciences and humanities, not only at a national level but also at the European level. An ERC supported by the scientific community is needed to ensure that the best research is funded, to combat the prevailing fragmentation of research efforts, and to provide long-term commitment of science policy in Europe toward the development of its science base at the highest level. Such an ERC must be independent and must adhere to strict criteria of scientific excellence and originality. Its budget must be commensurate with the ambition of achieving a proper balance with European targeted programs.

Expanding and strengthening basic research in Europe is also in the interest of industrial innovation and competitiveness. Europe's knowledge society requires a strong science base in all countries, new human resources for science and technology, better science education, and a renewed priority for science communication and scientific culture, and it will benefit from a wider dialogue between scientists and citizens and, hence, a broader social constituency for its scientific and technological development. The role of the universities in this respect should be recognized.

Basic science has no frontiers. With only national and no significant European mechanisms for the support of basic research, universities and research institutes have not been able to muster the resources to provide the necessary scale and scope for their best scientists and their teams. Stronger cooperation across Europe is needed in most areas. In the recent past, Europe has lost significant ground vis-à-vis the United States. For instance, Europe's share in high-impact publi-

cations is deteriorating in most areas, its performance in Nobel prizes is fading, and its capability to attract top scientists from abroad, or even to retain its own talents, is dangerously declining. It is therefore a matter of urgency to strengthen basic research in Europe and to provide the next generation of scientists with the proper means and working environment. Failure to do so may lead to an irreparable loss of talent.

**“ The enlarged EU, a newly elected European Parliament, and a new Commission should now grasp the historic opportunity to establish without delay a European Research Council (ERC)...”**

The Commission has done much preparatory work on the ERC. A first communication on Basic Science was published in January and a second in June. We welcome these important initiatives and in particular the very positive role that the EC Commissioner for Research, Philippe Busquin, has played in this respect. New opportunities, however, also carry the danger of fostering complacency. That would be a grave mistake, as much work lies ahead of us. In times of uncertain and possibly more limited financial prospects than hoped for, other important, highly visible political issues may easily obscure the long-term benefits of basic research. Furthermore, governments should not be tempted to reduce national funding for basic science if an ERC is established.

We call upon those who are entrusted by Europe's people to create the conditions for Europe's long-term future to act on the conviction that science is a cornerstone of European society. Providing funds for researchers, engaged in basic research, at the European level through an ERC is an important milestone in achieving a knowledge-based society. Scientists and their organizations, universities, and research institutes are today united and ready to continue their efforts to make the ERC a reality. This appeal, launched by the Initiative for Science in Europe (ISE), is endorsed in a personal capacity by the Presidents, Chairs, and

## Letters to the Editor

Letters (~300 words) discuss material published in *Science* in the previous 6 months or issues of general interest. They can be submitted through the Web ([www.submit2science.org](http://www.submit2science.org)) or by regular mail (1200 New York Ave., NW, Washington, DC 20005, USA). Letters are not acknowledged upon receipt, nor are authors generally consulted before publication. Whether published in full or in part, letters are subject to editing for clarity and space.

Directors General of 52 European organizations in all scientific disciplines.

**INITIATIVE FOR SCIENCE IN EUROPE (ISE): EUROPEAN LIFE SCIENCES FORUM (ELSF), EUROPEAN MOLECULAR BIOLOGY LABORATORY (EMBL), EUROPEAN MOLECULAR BIOLOGY ORGANIZATION (EMBO), EUROPEAN PHYSICAL SOCIETY (EPS), EUROPEAN PLANT SCIENCE ORGANIZATION (EPSO), EUROPEAN SCIENCE FOUNDATION (ESF), EUROPEAN UNIVERSITY ASSOCIATION (EUA), EUROSCIENCE, FEDERATION OF EUROPEAN BIOCHEMICAL SOCIETIES (FEBS), GROUP OF EUROPEAN NOBEL LAUREATES, STIFTERVERBAND FÜR DIE DEUTSCHE WISSENSCHAFT (CHAIRIED BY PROFESSOR JOSÉ MARIANO GAGO, FORMER PORTUGUESE MINISTER OF SCIENCE AND TECHNOLOGY). OTHER SUPPORTING ORGANIZATIONS: ACADEMIA EUROPAEA, ALL EUROPEAN ACADEMIES (ALLEA), ASSOCIATION OF EUROPEAN GEOLOGICAL SOCIETIES (AEGS), EUROPEAN ANTHROPOLOGICAL ASSOCIATION (EAA), EUROPEAN ASSOCIATION OF ARCHAEOLOGISTS (EAA), EUROPEAN ASSOCIATION OF EXPERIMENTAL SOCIAL PSYCHOLOGY (EAESP), EUROPEAN ASSOCIATION OF LAW AND ECONOMICS (EAL), EUROPEAN ASSOCIATION OF PHARMA BIOTECHNOLOGY (EAPB), EUROPEAN ASSOCIATION OF RESEARCH AND TECHNOLOGY ORGANIZATIONS (EARTO), EUROPEAN ASSOCIATION OF SOCIAL ANTHROPOLOGISTS (EASA), EUROPEAN ASTRONOMICAL SOCIETY (EAS), EUROPEAN BIOPHYSICAL SOCIETIES ASSOCIATION (EBSA), EUROPEAN CYSTIC FIBROSIS SOCIETY (ECFS), EUROPEAN COLLOID AND INTERFACES SOCIETY (ECIS), EUROPEAN CONSORTIUM FOR POLITICAL RESEARCH (ECPR), EUROPEAN FEDERATION OF BIOTECHNOLOGY (EFB), EUROPEAN FEDERATION OF IMMUNOLOGICAL SOCIETIES (EFIS), EUROPEAN FEDERATION OF ORGANIZATIONS FOR MEDICAL PHYSICS (EFOMP), EUROPEAN FEDERATION OF PSYCHOLOGISTS' ASSOCIATIONS (EFPA), EUROPEAN GEOSCIENCES UNION (EGU), EUROPEAN GROUP FOR ATOMIC SPECTROSCOPY (EGAS), EUROPEAN HIGH PRESSURE RESEARCH GROUP (EHPRG), EUROPEAN LIFE SCIENTIST ORGANIZATION (ELSO), EUROPEAN MATHEMATICAL SOCIETY (EMS), EUROPEAN MATERIALS RESEARCH SOCIETY (E-MRS), EUROPEAN NETWORK OF IMMUNOLOGY INSTITUTES (ENII), EUROPEAN NUCLEAR SOCIETY (ENS), EUROPEAN OPTICAL SOCIETY (EOS), EUROPEAN SOCIETY OF GENE THERAPY (ESGT), EUROPEAN SOCIETY OF HUMAN GENETICS (ESHG), EUROPEAN SOCIETY FOR NEUROCHEMISTRY (ESN), EUROPEAN SOCIOLOGICAL ASSOCIATION (ESA), EUROPEAN SOUTHERN OBSERVATORY (ESO), EUROPEAN SYNCHROTRON RADIATION FACILITY**

(ESRF), FEDERATION OF EUROPEAN CHEMICAL SOCIETIES (FECS), FEDERATION OF EUROPEAN MATERIALS SOCIETIES (FEMS), FEDERATION OF EUROPEAN MICROBIOLOGICAL SOCIETIES (FEMS), FEDERATION OF EUROPEAN NEUROSCIENCE SOCIETIES (FENS), FEDERATION OF EUROPEAN PHARMACOLOGICAL SOCIETIES (EPHAR), MARIE CURIE FELLOWSHIP ASSOCIATION (MCFA), "SAUVONS LA RECHERCHE" (SLR).

## Predators and Prey in the Channel Islands

**IN THEIR BREVIA, "REMOVING PROTECTED populations to save endangered species"** (28 Nov., p. 1532), F. Courchamp *et al.* use a predator-prey model on Santa Cruz Island to make the case for lethal removal of golden eagles (*Aquila chrysaetos*) from Channel Islands National Park. In the model, as nonnative feral pigs (*Sus scrofa*) are removed, eagles increasingly target native foxes (*Urocyon littoralis*) and could drive them to extinction if mitigating measures are not taken. But in fact, some of the underlying factors in this model do not represent actual conditions.

Eagles are protected under the Bald and Golden Eagle Protection Act and the Endangered Species Act. In March, the fox subspecies on each of the northern Channel Islands were listed as endangered, and measures to prevent fox extinction and ultimately provide for recovery are being taken. Between 1999 and 2002, foxes were captured and brought into captivity on all three of the northern Channel Islands, to be held until the threat from eagles is further reduced or eliminated, and to increase wild fox populations through captive breeding and release. A working group of 90 professionals advises the fox recovery effort. Since 1999, 35 golden eagles have been captured and relocated to northern California. Despite employment of the most effective known golden eagle capture techniques, some eagles evade capture and continue to breed and prey on foxes.

Running a captive breeding program on three island locations is not without its own risks, particularly from disease, loss of genetic variation, and changes in behavior. For those reasons, and to learn more about the efficacy of restoration in the face of a novel predator,

foxes were released from the breeding facilities on Santa Cruz and Santa Rosa Islands starting in December 2003. On Santa Cruz, five of the nine foxes released were killed by golden eagles, and the remaining four were returned to captivity. On Santa Rosa, one of the released foxes died of eagle predation, seven remain in the wild, and a pair of the released foxes has produced two pups. Captive-bred foxes seem much more susceptible to eagle predation. In contrast, annual survivorship of the remaining wild foxes on Santa Cruz was 80% in 2003, as determined by radiotelemetry.

Even with a high population of pigs present, the island foxes released from captivity experienced a high predation rate, suggesting that they were the preferred food for some eagles or the more accessible food in some areas. Moreover, the removal of the pigs on Santa Cruz is necessary for the recovery of nine endangered or threatened plants. Bald eagles (*Haliaeetus leucocephalus*), which were the dominant raptor species on the islands until the 1950s, coexisted with abundant fox populations. They have recently been reintroduced to Santa Cruz Island. Mature bald eagles and the absence of all feral prey should make

the northern Channel Islands less attractive to golden eagles.

Image not available for online use.

Image not available for online use.

Image not available for online use.

In the California Channel Islands, golden eagles (*Aquila chrysaetos*) prey on feral pigs (*Sus scrofa*) and island foxes (*Urocyon littoralis*). The fox population is in decline.

Island foxes were brought into captivity because of predation by golden eagles. Because foxes are successfully breeding in captivity, the immediate threat of extirpation is low, even with pig removal. Although Courchamp *et al.*'s model there-

fore has limited application, the policy issue of lethally removing a protected predator is entirely relevant to fox recovery. Such lethal removal of golden eagles may be the only management action which, in the end, permits recovery of island foxes. It can now be reviewed and evaluated under the process by which federal agencies safeguard species and landscapes.

PETER DRATCH,<sup>1</sup> TIM COONAN,<sup>2</sup> DAVID GRABER<sup>3</sup>

<sup>1</sup>National Park Service, Biological Resources Management Division, 1201 Oakridge Drive, Fort Collins, CO 80526, USA. <sup>2</sup>Channel Islands National Park, 1901 Spinnaker Drive, Ventura, CA 93001, USA. <sup>3</sup>Sequoia & Kings Canyon National Parks, 47050 Generals Highway, Three Rivers, CA 93271-9651, USA.

**IN THEIR BREVIA "REMOVING PROTECTED populations to save endangered species"** (28 Nov., p. 1532), F. Courchamp *et al.* describe a remarkable ecological scenario from California's Channel Islands, where the introduction of pigs enabled colonization by golden eagles, resulting in the decline of an endemic island fox via eagle predation. Courchamp *et al.* predict that without the complete removal of eagles, eradication of pigs would amplify threats posed by the eagles to the foxes. They have called the actual and predicted dynamics of this system "unexpected" and "unique" (1). Although highly illuminating, this example may represent a special case of a scenario more common than the authors appreciate.

The original human settlers of Polynesia encountered islands with rich avifaunas, limited reptile and bat faunas, and plentiful inshore marine resources (2, 3).

These resources alone were probably insufficient to sustain resident human populations (3). Instead, humans spread throughout Polynesia by transporting horticulture and animal husbandry from Near Oceania, introducing many plants and several animals (pigs, dogs, and chickens) throughout the Pacific (3).

Subsequently, pigs were the only large nonhuman mammal in Pacific ecosystems, existing on various islands in domesticated and feral states. They were certainly exploited for food, but the extent to which humans relied on them is uncertain (4, 5). Nevertheless, they were intentionally translocated throughout Polynesia in tandem with human expansion (4) and may have played a role in successful human establishment throughout the region.

Anthropogenic impacts of human colonization and expansion in the Pacific ulti-



## LETTERS

mately resulted in the extinction of thousands of native insular bird and reptile species (2). In potentially assisting human colonization, pigs may have played an indirect role in these declines. Interestingly, some islands where pigs were introduced but later became extinct (4) suffered extremely high levels of avifaunal extinction (6). The situation in the Channel Islands may represent an analogous case, singularly unique in that the apex predators in this case are golden eagles rather than humans.

KRISTOFER M. HELGEN

Department of Environmental Biology, University of Adelaide, Adelaide, SA 5000, Australia. E-mail: kristofer.helgen@adelaide.edu.au.

### References

1. G. W. Roemer, C. J. Donlan, F. Courchamp, *Proc. Natl. Acad. Sci. U.S.A.* **99**, 791 (2002).
2. D. W. Steadman, *Science* **267**, 1123 (1995).
3. P. V. Kirch, *The Lapita Peoples* (Blackwell, Malden, MA, 1997).
4. M. S. Allen, E. Matisoo-Smith, A. Horsburgh, *Int. J. Osteoarchaeol.* **11**, 4 (2001).
5. P. V. Kirch, *On the Road of the Winds* (Univ. of California Press, Berkeley, 2000).
6. D. W. Steadman, P. V. Kirch, *Proc. Natl. Acad. Sci. U.S.A.* **87**, 9605 (1990).

## Response

**DRATCH ET AL. ARGUE THAT OUR MODEL OF** apparent competition involving golden eagles, feral pigs, and critically endangered island foxes “has limited application,” because “underlying factors... do not represent actual conditions.” We contend that its implications for island fox conservation are crucial.

Our model—like all models—is an abstraction that cannot predict what will happen, but only suggests what may happen. Our model was derived from another that accurately depicted fox decline following golden eagle colonization (1). We took great care to parameterize it to reflect conditions both before and after the translocation of golden eagles. Hence, our model was based on the best available data. We acknowledge that our formulation ignored the recent reintroduction of bald eagles, but we caution that deterrence of golden eagles by bald eagles is speculative (2). Although we support bald eagle reintroduction, we do not believe that decisions concerning fox recovery should hinge on the assumption that this undocumented management action will work.

Although we are reassured by the persistence of foxes in captivity and acknowledge the National Park Service’s (NPS) efforts in averting extinction, captive populations are no substitute for wild ones. Further, the NPS has delayed several conservation measures that could have improved the chances of recovery (3), and the recent unsuccessful releases of captive foxes on Santa Cruz Island described by Dratch *et al.* were conducted against the advice of the “working group of 90 professionals” (4). Finally, the NPS already had

information on the “efficacy of restoration in the face of a novel predator.” In 2002, they released three captive-borne foxes on Santa Cruz Island and two were killed by golden eagles (3). Such decisions point to the need for the NPS to base resource management in the National Parks on sound science (5).

We have previously advocated—with great regret—the lethal removal of golden eagles that have proven too elusive to capture (6). We are encouraged that Dratch *et al.* agree that this measure may be necessary, but we are concerned that they may not view this action as urgent. Whether pig eradication alone will prompt the extinction or recovery of wild foxes can only be known for certain by trying it—our research shows that the risk of extinction is high. The precautionary principle therefore suggests that immediate, and complete, removal of golden eagles is the measure needed to spur recovery of the critically endangered island fox.

Helgen suggests that domestic/feral pigs “may have played a role in successful human establishment” throughout Polynesia and “may have played an indirect role” in the declines of insular bird and reptile species via apparent competition. We find Helgen’s hypothesis both clever and thought provoking, but we also note that apparent competition is difficult to elucidate and often overlooked as an important process in communities and ecosystems (7, 8). We considered the case on the Channel Islands to be “unique” because we were able to show that apparent competition was responsible for the trophic reorganization of this vertebrate community and that it ultimately led to the near extinction of an endemic insular carnivore (1). In contrast, although it is highly likely that pigs played some role in the extinctions of insular fauna in the Polynesian region, it is difficult to be sure whether these past extinction events were due to apparent competition, or to direct effects such as predation and habitat modification (9–11).

The value of our study was essentially

threefold: We were able to reveal the mechanism responsible as it occurred, we linked this mechanism with a loss in biodiversity that resulted from the introduction of an exotic species, and we then projected possible effects of management actions. The community reorganization was “unexpected”: No one predicted that golden eagles would colonize the islands as a consequence of the pigs’ presence. Our model projections were likewise “unexpected”: Removing pigs at first seemed a logical solution to the problem, yet our model suggested that this might cause eagles to focus more on the remaining foxes, increasing the latter’s probability of extinction.

GARY W. ROEMER,<sup>1</sup> ROSIE WOODROFFE,<sup>2</sup> FRANCK COURCHAMP<sup>3</sup>

<sup>1</sup>Department of Fishery and Wildlife Sciences, New Mexico State University, Las Cruces, NM 88003, USA.

<sup>2</sup>Department of Wildlife, Fish and Conservation Biology, University of California, Davis, CA 95616, USA. <sup>3</sup>Ecologie, Systématique & Evolution, Université Paris-Sud, 91405 Orsay, France.

### References

1. G. W. Roemer, C. J. Donlan, F. Courchamp, *Proc. Natl. Acad. Sci. U.S.A.* **99**, 791 (2002).
2. G. W. Roemer, T. J. Coonan, D. K. Garcelon, J. Bascompte, L. Laughrin, *Anim. Cons.* **4**, 307 (2001).
3. G. W. Roemer, C. J. Donlan, *Endangered Species UPDATE* **21**, 23 (2004).
4. T. J. Coonan, *Findings of the Island Fox Conservation Working Group, June 24–26, 2003* (National Park Service, Channel Islands National Park, Ventura, CA, 2003).
5. J. Kaiser, *Science* **288**, 34 (2000).
6. IUCN/Species Survival Commission, “CSG scientists call for urgent action to save the endangered island fox,” press release 27 November 2003 (available at [www.canids.org/bulletins/Island\\_fox.htm](http://www.canids.org/bulletins/Island_fox.htm)).
7. R. Holt, J. Lawton, *Annu. Rev. Ecol. Syst.* **25**, 495 (1994).
8. R. Morris, O. Lewis, H. Godfray, *Nature* **428**, 310 (2004).
9. I. Owens, P. Bennett, *Proc. Natl. Acad. Sci. U.S.A.* **97**, 12144 (2000).
10. F. Courchamp, M. Pascal, J.-L. Chapuis, *Biol. Rev.* **78**, 347 (2003).
11. D. Steadman, P. Martin, *Earth Sci. Rev.* **61**, 133 (2003).

## CORRECTIONS AND CLARIFICATIONS

**Letters:** “The health benefits of eating salmon” by C. M. Rembold (23 July, p. 475). The credit for the image accompanying this letter was inadvertently omitted. The credit should be Pat Wellenbach/AP.

## TECHNICAL COMMENT ABSTRACTS

### COMMENT ON “Observation of the Inverse Doppler Effect”

Evan J. Reed, Marin Soljagic, Mihai Ibanescu, John D. Joannopoulos

Seddon and Bearpark (Reports, 28 November 2003, p. 1537) presented a creative and exciting observation of a reversed Doppler effect when an electromagnetic shock propagates through a transmission line. We find that the physical origin of this anomalous effect is fundamentally different from the one suggested by Seddon and Bearpark (that  $v_{\text{phase}}v_{\text{group}} < 0$ ) but that the experimental results can be properly validated with the correct theory. Full text at [www.sciencemag.org/cgi/content/full/305/5685/778b](http://www.sciencemag.org/cgi/content/full/305/5685/778b)

### RESPONSE TO COMMENT ON “Observation of the Inverse Doppler Effect”

N. Seddon, T. Bearpark

We thank Reed *et al.* for their comments and alternative interpretation of the experimentally observed inverse Doppler shift. However, we believe that the wave propagation and reflection processes presented in the original paper accurately describe the physical mechanisms in this experiment.

Full text at [www.sciencemag.org/cgi/content/full/305/5685/778c](http://www.sciencemag.org/cgi/content/full/305/5685/778c)

## Comment on “Observation of the Inverse Doppler Effect”

Seddon and Bearpark present a creative and exciting observation of a reversed Doppler effect when an electromagnetic shock propagates through a transmission

line (1). We find that the physical origin of this anomalous effect is fundamentally different from the one suggested by Seddon and Bearpark (that  $v_{\text{phase}}v_{\text{group}} < 0$ ), but that the experimental results can be properly validated with the correct theory.

The system studied by Seddon and Bearpark falls into the general class of systems that involve a propagating shocklike excitation in a periodic medium, for which we have predicted reversed Doppler effects using a different theoretical framework (2). For this system, an extended Brillouin zone scheme should be used, rather than the periodic BZ scheme considered by Seddon and Bearpark (3). In their analysis, a phase-matching condition  $v_{\text{shock}} = v_{\text{phase}}$  leads to the conclusion that radiation

emitted by the shock has a  $\Psi_0$  (wave vector) value in the second BZ, where  $v_{\text{phase}}v_{\text{group}} < 0$ . Although the condition  $v_{\text{shock}} = v_{\text{phase}}$  predicts the correct emission frequency  $\omega_0$ , the suggestion that this emitted radiation has a  $\Psi$  value in the second BZ is not founded. The discretized nature of this system precludes unique measurement of  $v_{\text{phase}}$  (assignment of  $\Psi$  to a particular BZ) by measuring voltages or other quantities at points that are spatially periodically related.

Radiation well characterized by plane waves in the first band of periodic systems is poorly characterized by plane waves with wave-vector values outside the first BZ. Imposing a periodicity on the vacuum dispersion reveals a region similar to that of the Seddon and Bearpark transmission-line system, where  $v_{\text{phase}}v_{\text{group}} < 0$ , that is clearly unphysical (Fig. 1). Applied to vacuum, the analysis of Seddon and Bearpark [equation 1 in (1)] incorrectly predicts that a reversed Doppler shift can occur in that system. Away from the cutoff frequency, physical values of wave vector  $\Psi$  in the experiment of Seddon and Bearpark fall within the first BZ, where  $v_{\text{phase}}v_{\text{group}} > 0$ .

We have shown (2) that the phase of the reflection coefficient of the shock front is time dependent, unlike that of a normal moving reflecting surface assumed by Seddon and Bearpark in equation 1. This key feature is the actual origin of the inverse Doppler effect and explains how it can be observed in a region in which  $v_{\text{phase}}v_{\text{group}} > 0$ . The condition on the magnetic field at the shock-front location  $x = x_0 + v_s t$  is

$$H_0 u_{k_0}(x_0 + v_s t) e^{i(k_0 v_s t - \omega_0 t)} + H_r u_{k_r}(x_0 + v_s t) e^{i(k_r v_s t - \omega_r t)} e^{i \frac{2\pi}{a} v_s t} = 0$$

where  $u_{k_0}$  and  $u_{k_r}$  are the periodic parts of the Bloch states for the incident and reflected radiation of wave vectors  $k_0$  and  $k_r$ , respectively, and the phase term  $e^{i \frac{2\pi}{a} v_s t}$  is the phase of the reflection coefficient at the shock-front leading edge (2). This reflection coefficient can have multiple reflection phase-frequency components in some regimes (2). When  $k_r$  and  $k_0$  are chosen in the first BZ so that  $u_{k_0}$  and  $u_{k_r}$  have no nodes, the approximation  $u_{k_0} \approx u_{k_r}$  leads to

$$k_0 v_s - \omega_0 - k_r v_s + \omega_r - \frac{2\pi}{a} v_s = 0$$

which predicts results in direct agreement with the experimental observations. By contrast, when  $k_0$  is (incorrectly) measured in the second Brillouin zone as in the analysis of

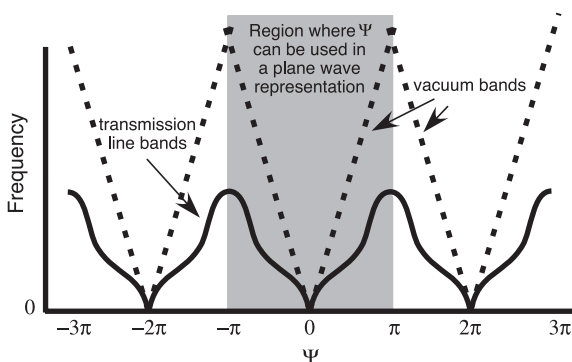


Fig. 1. Depicted is a periodic Brillouin zone schematic of the qualitatively similar dispersion relations for vacuum (dotted line) and the transmission line of the Seddon and Bearpark experiment (solid line). Both dispersion relations have an unphysical region where  $v_{\text{phase}}v_{\text{group}} < 0$  outside the first Brillouin zone.

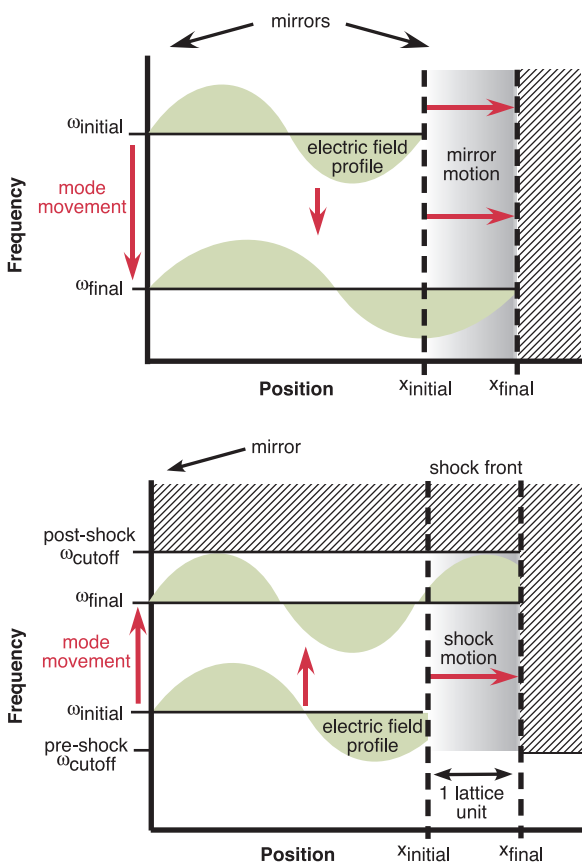


Fig. 2. Schematic frequency as a function of position for the normal Doppler shift from a moving metallic mirror (top) and the reversed Doppler shift in a transmission line (bottom). Radiation of frequency  $\omega_{\text{initial}}$  is confined between a fixed mirror on the left and a moving mirror (top) or shock front (bottom) on the right side. In the top panel, as the right mirror slowly (adiabatically) moves to the right, the number of nodes of the radiation is preserved, giving rise to a frequency-lowering effect. A Doppler shift occurs upon each reflection of the radiation from the moving mirror. In this case, the Doppler shift is in the negative direction, which is the usual Doppler shift. In the periodic transmission line in the bottom panel, the cutoff frequency is increased from the preshock  $\omega_{\text{cutoff}}$  to the postshock  $\omega_{\text{cutoff}}$  as the shock propagates. As the shock propagates slowly (adiabatically) to the right through one lattice unit of the transmission line, an extra node is added to the field profile by the shift of the reflection phase of the shock front through  $2\pi$ . The addition of an extra node results in a frequency increase despite the increase in cavity length, providing an inverse Doppler shift.



Seddon and Bearpark,  $k'_0 = k_0 - \frac{2\pi}{a}$ , which gives  $k'_0 v_s - \omega_0 - k_r v_s + \omega_r = 0$

This equation is equivalent to equation 1 of Seddon and Bearpark and explains the good agreement achieved between their theory and their experimental data. The use of an unphysical phase velocity fortuitously cancels with the neglect of the time-dependent shock-wave reflection coefficient, producing the correct result.

A schematic depiction (Fig. 2) provides additional insight on the origin of the inverse Doppler effect in the Seddon and Bearpark system. First, we consider the origin of the normal Doppler shift (Fig. 2A); in this case, the right-hand mirror moves to the right slowly enough that the electromagnetic mode evolves adiabatically, so that the nodal structure of the mode is preserved and the frequency is lowered as the cavity length increases. A normal Doppler shift (with a negative sign) occurs each time the light reflects from the moving mirror. By contrast, in the transmission-line system of Seddon and Bearpark, which produces an inverse Doppler effect (Fig. 2B), the system has a cutoff frequency,  $\omega_{\text{cutoff}}$ . As the shock propagates to the right through one lattice unit, a node is added to the electric-field profile by the shift of the reflection phase of the shock front, and the frequency shifts up. The addition of a node tends to

increase the frequency, and the increase of the cavity length tends to decrease the frequency, but the frequency-increasing effect has greater magnitude in this particular case. The Doppler shift has a positive sign, which is an inverse Doppler shift. Modes must move up in frequency because they all start out in the frequency range from zero to the preshock  $\omega_{\text{cutoff}}$  and all end (after the shock has propagated through the entire transmission line) in the frequency range from 0 to the postshock  $\omega_{\text{cutoff}}$  which is higher than the preshock  $\omega_{\text{cutoff}}$ . Physically, incident radiation resonantly couples into individual units of the transmission line as their frequencies move up through the incident radiation frequency. The radiation is re-emitted at a later time and at a higher frequency.

Although the theory of (2) and the theory of Seddon and Bearpark happen to predict the same results in the experimental conditions published by Seddon and Bearpark, differing results are predicted in other regimes of the Seddon and Bearpark system. For example, their analysis predicts that if radiation is emitted within the first BZ by altering the shock speed or by other means, no anomalous effect will occur because the first BZ has  $v_{\text{phase}} v_{\text{group}} > 0$ . However, our analysis predicts that an anomalous effect will still occur in this case because of the time-dependent phase of the shock-wave

reflection coefficient. Our analysis also predicts that multiple frequencies may be reflected from the shock as the shock-front thickness is decreased, whereas the Seddon and Bearpark analysis provides no mechanism for more than one frequency to be emitted. These predictions can be tested within the computational model of Seddon and Bearpark and may also be realizable within their experiment.

*Evan J. Reed*

*Marin Soljagic*

*Mihai Ibanescu*

*John D. Joannopoulos*

*Department of Physics*

*Massachusetts Institute of Technology*

*Cambridge, MA 02139*

*E-mail: evan@mit.edu (E.J.R.)*

#### References and Notes

1. N. Seddon, T. Bearpark, *Science* **302**, 1537 (2003).
2. E. J. Reed, M. Soljagic, J. D. Joannopoulos, *Phys. Rev. Lett.* **91**, 133901 (2003).
3. C. Kittel, *Introduction to Solid State Physics* (Wiley, New York, 1996).
4. This work was supported by the Lawrence Livermore National Laboratory Energetic Materials Center and the Materials Research Science and Engineering Center program of the National Science Foundation under Grant No. DMR-9400334.

12 April 2004; accepted 30 June 2004

## Response to Comment on "Observation of the Inverse Doppler Effect"

The explanation of the observed Doppler shift (*I*) hinges on the existence, or otherwise, of waves in the second Brillouin zone (BZ) of the transmission line system. We agree with Reed *et al.* (2) that the second BZ is unphysical in the case of the vacuum. However, we believe that the transmission line used in the Doppler experiment has characteristics that allow the generation of waves in the second BZ of this system.

Waves (space harmonics) may be excited in the second BZ of suitable periodic systems by injecting a pump signal with a propagation velocity that is synchronous with the phase velocity of the required space harmonic. This technique is well established in the field of microwave tube technology, in which an electron beam provides the pump energy (3). For example, backward wave oscillators (BWO), which exhibit normal dispersion in the first BZ and anomalous dispersion in the second BZ, produce microwave output by excitation of a wave (spatial harmonic) in the second BZ (3). As the velocity of the electron beam is reduced, the phase velocity of the excited wave is reduced continuously across the BZ boundary to give a continuous transition from generation of waves with

$v_{\text{group}}v_{\text{phase}} > 0$  (first BZ) to generation of waves with  $v_{\text{group}}v_{\text{phase}} < 0$  (second BZ). The BWO clearly demonstrates that the generation of waves in the second BZ of periodic systems is not unphysical when a pumping pulse is used to generate the synchronous wave.

Formation of a wave with  $v_{\text{group}}v_{\text{phase}} > 0$  in the second BZ of the transmission line used in the inverse Doppler experiment in (*I*) has been analyzed previously (4). The system used in the Doppler experiment has the same essential features as the BWO; spatial dispersion is provided by cross-link capacitors in the transmission line and by a corrugated waveguide in the BWO. An electrical pump pulse in the transmission line experiment performs the same function as the electron beam in the BWO, which is generation of a synchronous wave. The transmission line is analyzed as a discrete periodic system, whereas the BWO is usually analyzed as a continuous periodic system. The analysis of purely discrete systems leads to mathematical uncertainty as to the phase velocity of waves that are measured at periodically related points, as pointed out by Reed *et al.* However, practical experience shows that generation of waves in the second BZ of pumped periodic systems is physical, as described above.

Both our analysis and that of Reed *et al.* agree with the experimental observations that both the oscillation frequency and the group velocity of the generated wave vary continuously as the pump-pulse velocity is reduced. However, stipulation that the generated wave can exist only in the first BZ requires that the generated wave undergo a discontinuous change of phase velocity at the BZ boundary, from  $+v_p$  to  $-v_p$ . We maintain that that assertion is not physically correct and that the phase velocity of the generated wave changes continuously to generate a wave in the second BZ, as demonstrated in the BWO and described in previous analyses of the transmission-line system (4).

**N. Seddon  
T. Bearpark**

*Optics and Laser Technology Department  
Advanced Technology Centre  
BAE Systems  
Post Office Box 5  
Filton, Bristol BS34 7QW, UK  
E-mail: nigel.seddon@baesystems.com*

### References and Notes

1. N. Seddon, T. Bearpark, *Science* **302**, 1537 (2003).
2. E. J. Reed, M. Soljagic, M. Ibanescu, J. D. Joannopoulos, *Science* **305**, 778 (2004); [www.sciencemag.org/cgi/content/full/305/5685/778b](http://www.sciencemag.org/cgi/content/full/305/5685/778b).
3. S. H. Gold, G. S. Nusinovich, *Rev. Sci. Instrum.* **68**, 3945 (1997).
4. A. M. Belyantsev, A. B. Kozyrev, *Sov. Phys. Tech. Phys.* **45**, 747 (2000).
5. This work was funded by the BAE Systems Advanced Technology Centre Long-Look Programme.

5 May 2004; accepted 7 July 2004



## NEUROSCIENCE

### Beauty or Brains?

V. S. Ramachandran

What is art? There are probably as many views on that subject as there are human beings. Consider the following aphorisms: “Art is the lie that reveals the truth” (Picasso). “Art is the magic of the soul” (Goethe). “The Godlike rendered visible” (Carlyle). “The...desire to find ourselves again among the phenomena of the external world” (Wagner). Or my own, “That which allows us to transcend our mortality by giving us a foretaste of eternity” (I). All are quite vague—especially to readers of *Science*—yet we sense intuitively that there must be some truth to each of them.

The main themes of *The Psychology of Art and the Evolution of the Conscious Brain* are the two most nebulous topics in psychology, and one can’t help admiring Robert Solso (a cognitive scientist at the University of Nevada, Reno) for rushing in where angels fear to tread. In the 1950s, C. P. Snow pointed out that the “two cultures” (science and the humanities) are separated by a huge gap, which many have considered impossible to close. But during the last ten years there has been a growing realization that neuroscience provides an interface that may allow us to bridge the gap.

A final understanding of visual art (the focus of Solso’s book) will, I believe, come from a more thorough grasp of the psychological laws of perception and object recognition, of the evolutionary logic that drives these laws, and of the physiology of the connections between visual and limbic structures in the brain. How successful is Solso at developing this framework?

There have been two recent groundbreaking books on neuroaesthetics: one by Semir Zeki, who coined the term (2), and one by Marge Livingstone (3). Both emphasize neuroscience more than aesthetics, so the fresh psychological perspective Solso’s book brings to the topic is welcome.

Solso wisely avoids overarching philosophical issues concerning aesthetics. He has chosen, instead, to concentrate on the

phenomenologies of visual experience and visual illusions and their relevance to art and consciousness. Making skillful use of visual illusions, he points out that they are not mere curiosities but can provide crucial insights into normal visual function and may even help explain aspects of art.

Like Zeki and Livingstone, Solso avoids the question of whether there are such things as artistic universals. We know there have been hundreds of artistic styles: classical Greek, Renaissance, Chola (Indian), Tellem, Dogon, Impressionism, Cubism; the list is endless. Yet despite this staggering surface diversity, could there be some universal laws (or at least broadly applicable rules of thumb) that cut across cultural boundaries and may be hardwired? Such a notion is likely to provoke a strong reaction from artsy types who argue that the very notion of a science of art or artistic universals is an oxymoron. They hold that science is a quest for universal laws, whereas art is the exact opposite—it is the ultimate celebration of one’s individuality.

These days, I can take a toothbrush, throw it on a silver tray, and proclaim, “I call this art, therefore it is art.” (Or Damien Hirst can say the same of a cow pickled in formalin.) For this reason, we would be better off speaking of the laws of aesthetics rather than laws of art (which is a much more loaded term). Such laws of aesthetics may have been hardwired into the visual areas of our brains (as well as the connections between them and limbic emotional circuits) to defeat camouflage, segment the visual scene, and discover and orient to object-like entities. Before the visual-processing stream culminates in the climactic “aha” of recognition, there are probably several mini-ahas along the way. One could posit that the goal of visual art is to generate as many such mini-ahas and ahas as possible by using cleverly contrived visual patterns (4). Although hardly a complete

description of visual aesthetics, this is a start.

One criticism that I have heard of all such enterprises—whether Zeki’s, Livingstone’s, Solso’s, or my own—is that they do not explain the true essence of art because they are too “reductionist.” (That term has come to acquire pejorative connotations among psychologists, philosophers, and other social scientists.) After all, what could a Calder mobile possibly have in common with a Picasso painting or a Chola bronze Nataraja? This objection is based on the logical fallacy that surface diversity implies an equal diversity of causes, a notion that is the very antithesis of science. And even if 90% of the variance seen in art is driven by fad, fancy, and culture (or, worse yet, by the auctioneer’s hammer), it is the remaining 10% (influenced partly by genes and partly by environmental universals) that interests scientists. The culturally driven ineffable 90% is already being studied by art historians, who have written thousands of tomes on the topic, whereas only a handful of people—

**The Psychology of Art and the Evolution of the Conscious Brain**  
by Robert L. Solso

MIT Press, Cambridge, MA, 2004. 296 pp. \$45, £29.95. ISBN 0-262-19484-8.



“A psychological view of motion and color.” Claude Monet’s *Impression: Sunrise* (1872).

including Rudolf Arnheim (5) and Ernst Gombrich (6) in the mid-20th century—have attempted to discover these universal laws. Spelling out such laws does not in any way detract from the originality of the individual artist, for how she deploys the laws or which ones she chooses to emphasize in a given work is entirely up to her. Indeed, many of these universal laws of aesthetics cut across not only cultural boundaries but species boundaries as well. After all, we find birds and butterflies beautiful despite the fact that they evolved to be pretty to their own kind and we diverged from them millions of years ago.

The reviewer is at the Center for Brain and Cognition, University of California, San Diego, 9500 Gilman Drive, La Jolla, CA 92093-0109, USA. E-mail: vramacha@ucsd.edu

Even though Solso's book is sprinkled with dazzling insights, it sometimes reads like a hodgepodge and (despite the promise made in the preface) there is no punch line nor even an attempt at a framework or new theory. But the author is hardly to be blamed for these shortcomings. The science of art and consciousness is still very much in its infancy, and it is unfair to expect more than an impressionistic survey. Maybe the day will come when the pieces fit together; we will then have taken a big step toward bridging the two cultures.

To understand any aspect of the human mind (be it art, humor, dreams, color vision, or consciousness), three criteria must be fulfilled: answers to the questions what, why, and how (4). The first requires a clear statement of what the law or principle is (e.g., the law of grouping—fragments in the visual scene that share a certain feature, such as color, depth, or motion, are mentally grouped). Explaining why the law has the form that it does may involve determining its survival value, if any (grouping defeats camouflage and allows the efficient detection of

objects). And third, we need to identify the underlying neural mechanism. (Grouping is achieved by interactions between visual neurons that are tuned to the same feature, for example, the same direction of motion or same color). Little does the salesman at Nordstrom picking a color for your scarf that matches your skirt realize that he is tapping into a brain principle that evolved to detect lions behind foliage by grouping yellow lion fragments together and sending an aha jolt to your limbic structures. Most previous attempts at neuroaesthetics have failed because they tend to focus exclusively on one question—what (black-box psychology), why (evolutionary psychology, with the “just-so” stories it is notorious for), or how (naïve neuro-reductionism)—without recognizing that in biology we need to address all three. This requirement is obvious when spelled out, but it is rarely put to practice.

Processes like grouping, segmentation, and symmetry detection might be intrinsically pleasurable to the visual system because they facilitate detection and orienting toward objects, whereas other principles might be re-

quired to make the recognition and categorization of objects pleasurable. For instance, a gull chick will beg for food by pecking at the red spot on its mother's long yellow beak. Niko Tinbergen found that a long stick with three red stripes on it is, paradoxically, much more effective at stimulating fervent begging than a beak, even though it does not resemble one. Such ultranormal stimuli must excite beak-detecting visual neurons in the chick's brain more powerfully than an actual beak does, because of certain accidental features of these neurons' wiring (perhaps embodying the rule “the more red contour the better”). So if gulls had art galleries, they might hang this abstract pattern on the wall, worship it, pay millions of dollars for it (even call it a Picasso), yet not understand why—given that the strange pattern doesn't even resemble anything. I would argue that the same situation holds for nonrealistic or semi-abstract art that we humans enjoy. Artists such as Picasso and Henry Moore, through intuition or trial and error, arrived at the figural primitives of our perceptual grammar and contrived patterns that stimulate our visual neurons even

#### NOTA BENE: BIOMEDICINE

## A Bridge Too Far?

**A**claimed science writer Jonathan Weiner's latest book tells the story of one family and its battle against the fatal neurodegenerative disease amyotrophic lateral sclerosis (ALS). In ALS, also known as Lou Gehrig's disease after the American baseball star whose career and life were cut short by the illness, the body's motor neurons disintegrate, leading to paralysis and death, usually within two years of diagnosis.

*His Brother's Keeper* portrays the agony and desperation of a family's search for a cure, but is ultimately weakened by the author's close involvement in the story he tells. The book opens with an introduction to the Heywood family, their idyllic life in Newtonville (a suburb of Boston), and the strong ties that unite the parents, John and Peggy, with their three handsome sons, Jamie, Stephen, and Ben. Each brother pursued a different path in life: Jamie, ambitious and entrepreneurial, followed in his father's footsteps, studying mechanical engineering at MIT. Stephen, the mellow dreamer, ventured off to see the world on his motorbike. Ben, though trained in engineering, sought

his fortune in Hollywood as a movie producer. In 1996, 27-year-old Stephen returned from his travels, settled down to life as a carpenter, and began to renovate a tumbledown shack in Palo Alto. That house was almost finished and ready to sell at a handsome profit when the upbeat story came to an abrupt halt. Stephen suddenly began to experience weakness in his right hand and arm; seemingly simple tasks—turning a key in a lock, holding a hammer, or arm-wrestling his brother—became insurmountable. Within two years, Robert Brown, a neurologist at Massachusetts General Hospital and a leading ALS researcher, would deliver the grim diagnosis to Stephen and his family, a diagnosis that they had already guessed.

Up to this point, *His Brother's Keeper* could be the story of any family struck with the horror of watching a beloved member waste away from a neurodegenerative disease. Where this story differs is in the response of a grief-stricken Jamie to the devastating news. Deciding that scientific research on ALS was progressing far too slowly to save Stephen, Jamie—despite his lack of formal training in biology—set out to design his own gene therapy protocol to commute his brother's death sentence. He left his well-paid position as director of technology transfer at the Neurosciences Institute (a La Jolla, California, research think tank) and returned with his wife to his parents' home, where Stephen and his girlfriend also now lived.

To raise money to develop the therapy that he was convinced would save Stephen, Jamie launched a nonprofit organization—the ALS Therapy Development Foundation—from the basement of his parents' house. From mechanical engineer to genetic engineer is a bold leap indeed, but Jamie was unstoppable, resolved that only he could win this life-or-death battle. He used every connection he had, every ounce of his charm, and most of his own and his family's money in the drive to achieve his goal.

Jamie decided on gene therapy as the quickest route to Stephen's salvation and selected *EAAT2* (which encodes a glutamate transporter) as the therapeutic gene to be injected into his brother's spinal cord. His choice was based on research by Jeffrey Rothstein, an ALS researcher at Johns Hopkins, but we are not told the rationale for selecting this gene over other more obvious candidates. With his charm and energy, Jamie recruited a number of well-respected scientists to help him in his quest, including Matt During, a daring but controversial gene therapy researcher at Thomas Jefferson University.

At this point, Weiner, a Pulitzer-Prize-winning author, became part of the entourage, as both scribe (he was writing a story about Jamie and Stephen for the *New Yorker*) and bit player in the unfolding Heywood family drama. The remainder of the book follows Jamie's efforts, working with During and his lab, to design the *EAAT2* gene therapy protocol, test it in mice with

**His Brother's Keeper**  
A Story from the  
Edge of Medicine  
by Jonathan Weiner

Ecco, New York, 2004.  
368 pp. \$26.95, C\$36.95.  
ISBN 0-06-001007-X.



more effectively than natural or real objects. They have created the equivalent, for our brain, of what the stick with stripes is for the gull chick.

Another criticism of Solso's approach might be that he is merely elucidating principles of perception rather than the essence of art. But I would reject that claim. It is based on a, now largely discredited, "bucket brigade" model of vision, a sequential hierarchical model that ascribes our aesthetic response only to the very last stage—the big jolt of recognition. In my view (and Solso would probably agree), there are minijolts at each stage of visual segmentation before the final aha. Indeed the very act of perceptual groping for object-like entities may be pleasurable in the same way a jigsaw puzzle is. Art, in other words, is visual foreplay before the final climax of recognition.

In Solso's intriguing discussion of consciousness, he contrasts the representational functions of art with the metarepresentational function of consciousness. Yet his attempts to link visual art with consciousness are not entirely convincing. It is as if he is saying that

you have to be conscious in order to appreciate art and therefore the two topics must be closely related. That is a dubious argument because the two may have nothing in common other than the fact that they are both mysterious. It is a line of reasoning that is no more illuminating than to be told that we are conscious when we laugh and therefore laughter must be related to, and can lead to an understanding of, consciousness. The author's claims that "both mind and art are part of a single physical universe" and "art and mind are of a single reality" do not do much to enhance our understanding of either art or mind. Indeed, many would argue that much of art's appeal is unconscious rather than conscious. The various components of the aesthetic impulse surely include a set of early unconscious mechanisms (such as the perceptual problem-solving aspect) that are themselves pleasurable, as well as components (such as the final recognition jolt) that do make it into consciousness.

Despite these minor shortcomings, *The Psychology of Art and the Evolution of the Conscious Brain* is a valuable contribution.

Fun to read and encyclopedic in its range, the book should be of interest to scholars in many disciplines: psychologists, neuroscientists, and even philosophers (who would do well to heed Darwin's advice, "He who understands baboon would do more toward metaphysics than Locke"). Perhaps we will never fully explain art—especially its unique capacity to enable us to transcend ourselves or to "discern eternity looking through time" (Carlyle). But thanks to Arnheim, Gombrich, Zeki, Livingstone, and, now, Solso, we can say as Holmes did to Watson, "The game is afoot."

#### References

1. V. S. Ramachandran, "The Emerging Mind," BBC Reith lectures, 2003.
2. S. Zeki, *Inner Vision: An Exploration of Art and the Brain* (Oxford Univ. Press, Oxford, 1999).
3. M. Livingstone, *Vision and Art: The Biology of Seeing* (Abrams, New York, 2002).
4. V. S. Ramachandran, *A Brief Tour of Human Consciousness* (Pi, New York, 2004).
5. R. Arnheim, *Art and Visual Perception: A Psychology of the Creative Eye* (Univ. California Press, Berkeley, 1954).
6. E. H. Gombrich, *Art and Illusion: A Study in the Psychology of Pictorial Representation* (Pantheon, New York, 1960).

ALS, and obtain Food and Drug Administration (FDA) approval in the shortest possible time.

The book is oddly disturbing. Weiner repeatedly admits that he is dazzled by Jamie's determination and manic energy and by what he seems to be able to accomplish through sheer force of will. Several times, the author—grappling with his mother's supranuclear palsy (another neurodegenerative disease)—notes his inability to remain objective. Amidst the usual rationale for writing the Heywoods' story, Weiner acknowledges that he harbored a faint hope that if gene therapy could cure Stephen, then perhaps it could also cure his mother. Weiner needed to stay objective about the story he was writing, and particularly about Jamie (who was fast becoming the focal point of his narrative), but he could not.

As Weiner dissects Jamie's motives for setting up the foundation and his increasing obsession with gene therapy, we glimpse an unsettling cowboy entrepreneurial streak that melds with Jamie's genuine love for his brother. Weiner details the internal strife that wracks Jamie as he weighs whether the foundation should remain nonprofit or be converted to a company that would make money for him if the gene therapy protocol proved to be an effective treatment for ALS. (In the end, Jamie reluctantly kept the foundation nonprofit.) Also troubling are the desperate short cuts that Jamie takes to speed through his plan in time to save Stephen. The fact is that scientific research is generally a slow, painstaking process that only rarely can be accelerated by determination, anguish, anger, or brute force.

There is no doubt, however, that Jamie's intense efforts have brought together researchers from different fields who would not normally talk to one another. Certainly he is correct in predicting that better communication among scientists and more fluid exchange of research findings between different disciplines should accelerate the pace of research. Complex scientific problems—

and surely developing effective therapies to treat neurodegenerative diseases resides in this category—require big solutions.

If it accomplishes nothing else, the Heywoods' story demonstrates how much gene therapy was oversold to the public in the 1990s as a quick cure for just about everything. Ironically, perhaps



The Heywood brothers.

Jamie's smartest idea came after his gene therapy strategy stalled in the wake of the tragic death of a young patient receiving gene therapy treatment for another disease. He swiftly changed direction, abandoned gene therapy, and set up an animal facility to screen FDA-approved drugs for possible effectiveness in treating ALS. Given that large pharmaceutical companies are not interested in ALS or other orphan diseases that affect too few patients to make a

profit, this screening strategy may be the quickest route to finding new drugs to treat ALS. Although it remains possible that gene therapy and stem cell therapy may be of value for treating certain neurodegenerative diseases, including ALS, these treatments are unlikely to enter routine clinical use anytime soon.

*His Brother's Keeper* is the story of family unity, brotherly love, and unwavering courage as a young man faces imminent death from an incurable disease. The book's real hero is Stephen, the gentle stoic. Even as he remains supportive of Jamie's efforts and faintly hopeful, he is probably the most realistic of the Heywoods. Stephen's determination to live his life to the fullest for as long as he can—despite his rapidly deteriorating condition, he marries his sweetheart and becomes a doting father—should provide comfort and inspiration for other ALS patients and their families.

—ORLA SMITH

## Probing the Neural Basis of Body Ownership

Matthew Botvinick

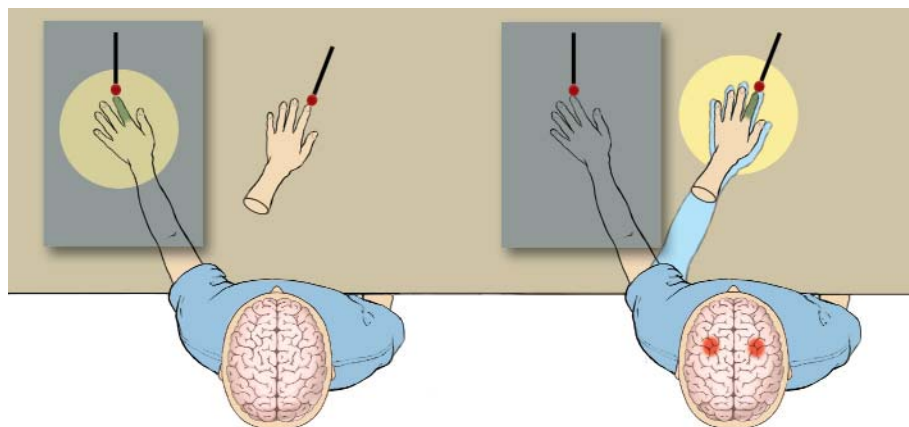
In the cognitive sciences, the most challenging phenomena are often the ones we take for granted in our everyday lives. An excellent example is body ownership. Ask any child whether his hands belong to him, and the answer is likely to be “Of course.” But how do we distinguish our bodies, but not other objects, as belonging to ourselves, and what is the basis for the associated feeling of identification or ownership? The problem of the bodily self has long intrigued philosophers (1) and psychologists (2), yet only recently has it attracted the interest of neuroscientists. On page 875 of this issue, Ehrsson *et al.* (3) present an elegant functional neuroimaging study in which they probe the neural underpinnings of the bodily self.

An important idea underlying the Ehrsson study is that the body is distinguished from other objects by its involvement in the correlation or matching of special patterns of intersensory information. For example, there is a reliable correspondence between what our body position looks like and what it feels like. Visual input about body posture relates directly to information about proprioception, our intrinsic sense of position. Another important correspondence is between vision and touch—when we see an object contact our body surface, we anticipate a corresponding tactile sensation. Importantly, it is only the body, not other objects, that registers such intersensory correlations. Thus, the integration of visual, tactile, and proprioceptive information about the body can be thought of as self-specifying (4).

Evidence for a link between self-specifying intersensory correlations and bodily self-identification comes from diverse sources. Developmental psychologists, for example, have shown that the ability to register self-specifying correlations is present very early in life, alongside behaviors that appear to reflect self-recognition (such as touching one’s face when looking into a mirror, after having had a mark un-

obtrusively placed on one’s cheek) (2, 4). Convergent evidence for a link between self-identification and intersensory correlations comes from a bizarre neurological syndrome known as somatoparaphrenia. In patients with this syndrome, damage to the right parietal lobe—a brain region that is crucial for intersensory integration—causes the individuals to deny ownership of

probe. Under these conditions, the subject experiences an illusion in which the felt touch is brought into alignment with the seen touch, the way a ventriloquist’s voice is brought together with the puppet’s mouth. There is a compelling sense that one is feeling the probe as it touches the rubber hand, as if one is feeling “with” the rubber hand. Psychophysical experiments have shown that the rubber hand illusion is based on an overriding of proprioceptive input by visual information (7). However, the illusion involves not just a spatial realignment of the proprioceptive map onto the visual map, but also a feeling of ownership—subjects describing the illusion spontaneously report that the rubber hand feels as if it is “their hand.”



**This hand is my hand.** Activation of the premotor cortex during the rubber hand illusion. In the illusion, normal individuals experience an artificial limb (rubber hand) as if it were part of their own body. (Left) The subject observes a facsimile of a human hand (the rubber hand) while one of his own hands is hidden from view (gray square). Both the artificial hand and the subject’s hand are stroked, repeatedly and synchronously, with a probe. The green and yellow areas indicate the tactile and visual receptive fields, respectively, for neurons in the premotor cortex (red circles). (Right) The subject experiences an illusion in which the felt touch (green) is brought into alignment with the seen touch (illusory position of arm; blue). This brings the visual receptive field (yellow) into alignment with the rubber hand, resulting in activation of premotor cortex neurons.

their left arm or leg (5). The somatoparaphrenic patient may even insist that his own limb has been replaced by someone else’s or that the limb is “fake” (6).

Surprisingly, just the opposite phenomenon can be induced in neurologically normal individuals, causing them to experience an artificial limb as if it were part of their own body. This is precisely what happens in the so-called “rubber hand illusion” (7). Here, the subject observes a facsimile of a human hand while one of his own hands is hidden from view (see the figure). Both the artificial hand and the subject’s hand are then stroked, repeatedly and synchronously, with a

In their neuroimaging study, Ehrsson and co-workers investigated the pattern of brain activity that underlies this feeling of ownership. The researchers induced the rubber hand illusion while subjects underwent functional magnetic resonance imaging (fMRI). This revealed that the illusion is accompanied by activation of a frontal lobe region called the premotor cortex (see the figure). Control conditions indicated that this activation could not be attributed simply to viewing the rubber hand, or to seeing it touched. Furthermore, premotor cortex activation correlated with the strength of the illusion, and the timing of activation fit with the illusion’s onset.

The author is at the Center for Cognitive Neuroscience, University of Pennsylvania, Philadelphia, PA 10104-6241, USA. E-mail: mmb@mail.med.upenn.edu



Based on these observations, Ehrsson and colleagues conclude that “neural activity in the premotor cortex reflects the feeling of ownership of a seen hand” (3).

As the authors note, their findings square well with the idea that self-identification depends on the integration of multi-sensory information. The premotor cortex receives strong inputs from parietal regions that integrate visual, tactile, and proprioceptive information (8). In addition, animal studies have shown that the premotor cortex contains neurons with combined visual and tactile receptive fields. Interestingly, these visuo-tactile neurons appear to encode visual inputs by using a reference frame that is body-part centered (9)—that is, the cells respond both when a specific area of the body is touched, and when an object is seen approaching that same area. It seems plausible that such body-part-centered neurons might be directly responsible for the Ehrsson *et al.* findings. We know that, as part of the rubber hand illusion, proprioceptive information is distorted such that the position of one's own hand is remapped to the position of the viewed rubber hand (7). Presumably, when this happens, hand-centered visual receptive fields undergo the same shift, becoming aligned with the artificial hand (10). If this is the case, then viewing the probe as it approaches the rubber hand would activate hand-centered neurons in the premotor cortex (see the figure).

The foregoing account appears to explain why activation of the premotor cortex occurs during the illusion, but what does it tell us about the feeling of ownership? The intersensory matching theory seems to imply that this feeling is simply the subjective correlate of the neural events involved in registering self-specifying intersensory correlations. Understood in this way, the intersensory matching theory is, like other recent accounts of self-representation (11), quasi-reductive. The theory's claim is that, at the neural level, body ownership simply is the registration of self-specifying intersensory correlations. The fact that the relevant neural events correlate with the subjective experience of body ownership is critical to the theory, but the theory does not attempt to explain it.

The intersensory matching theory has an intuitive appeal, and the accumulated empirical data (including those of Ehrsson and colleagues) make it increasingly compelling. However, it also faces some interesting challenges. For example, if we accept that the activation of body-part-centered neurons is a hallmark of self-identification, then it should not be possible to observe such activation in the absence of ownership feelings. However, neurophysiological studies have shown that, during tool use, neu-

rons with body-part-centered visual receptive fields (this time, neurons in the parietal lobe) are activated when objects approach not only the hand but the tool itself (12). From this finding, we would predict that tools are represented as belonging to the bodily self. However, although this may be true in some weak sense, the feeling of ownership that we have for our bodies clearly does not extend to, for example, the fork we use at dinner. Apparently, the activation of neurons with (usually) body-part-centered receptive fields may not be entirely sufficient to evoke a feeling of ownership.

Another issue facing the intersensory matching theory concerns the nature of the correlations involved. Although certain correlations can be understood as self-specifying, others appear similar in form but do not give rise to a feeling of ownership. For example, the rubber hand illusion can be considered analogous to the illusion of ventriloquism. Ventriloquism, too, is driven by familiar intersensory (visual-auditory) correlations (13). Yet this illusion has nothing to do with feelings of ownership. What makes the rubber hand illusion different? It is clear how self-specifying intersensory correlations might set our bodies apart from other objects, but what is it about these sensory maps that leads us to identify with our bodies, to link them with our sense of self? Perhaps the answer has to do with our ability to make our bodies move, and thus with our subjective sense of agency (14). Perhaps it has to do with spe-

cific relationships between interoceptive senses (such as proprioception) and exteroceptive ones (such as vision) (4).

Evaluating these possibilities and others pertaining to body ownership will require a willingness to engage phenomena that are, at least in part, irreducibly subjective. This willingness has been rare among experimentalists. The work of Ehrsson and colleagues provides an encouraging indication that this attitude may be changing, opening up fascinating new avenues of scientific inquiry.

#### References

1. J. L. Bermudez, A. Marcel, N. Eilan, *The Body and the Self* (MIT Press, Cambridge, MA, 1995).
2. P. Rochat, *The Self in Infancy: Theory and Research* (Elsevier, Amsterdam, 1995).
3. H. Henrik Ehrsson, C. Spence, R. E. Passingham, *Science* **305**, 875 (2004); published online 1 July 2004 (10.1126/science.1097011).
4. P. Rochat, T. Striano, *Infant Behav. Dev.* **23**, 513 (2000).
5. D. Boisson, J. Luaute, *Ann. Med.-Psychol.* **162**, 55 (2004).
6. O. Sachs, *A Leg to Stand On* (Harper, New York, 1993).
7. M. Botvinick, J. Cohen, *Nature* **391**, 756 (1998).
8. M. S. Graziano, M. M. Botvinick, in *Common Mechanisms in Perception and Action*, vol. 19, Attention and Performance, W. Prinz, B. Hommel, Eds. (Oxford Univ. Press, Oxford, UK, 2002).
9. M. S. A. Graziano, X. Hu, C. G. Gross, *J. Neurophysiol.* **77**, 2268 (1997).
10. A. Farnè, F. Pavani, F. Meneghello, E. Ladavas, *Brain* **123**, 2350 (2000).
11. D. M. Wegner, *The Illusion of Conscious Will* (MIT Press, Cambridge, MA, 2002).
12. A. Iriki, M. Tanaka, S. Obayashi, Y. Iwamura, *Neurosci. Res.* **40**, 163 (2001).
13. M. Radeau, *Curr. Psychol. Cogn.* **13**, 3 (1994).
14. E. Van den Bos, M. Jeannerod, *Cognition* **85**, 177 (2002).

#### CHEMISTRY

## The Modest Undressing of a Silicon Center

Guy Bertrand

The periodic table helps chemists systematize their thinking about the chemical reactivity of groups of elements on the basis of their valence. This approach is useful so long as one is aware of the “first-row anomaly” (1), which is mainly the result of the atomic orbital structure of these elements. In group 14, a large gap in physical properties and chemical behavior exists between carbon, the nonmetal of major importance to life, and silicon, the semimetal that drives the computer revolution. Among the most striking

differences between these two elements is their opposite coordination behavior. Silicon has the propensity to form hypercoordinate (more than four neighbors) species (2), including heptacoordinate and even octacoordinate silicon complexes, which is not possible with carbon. Similarly, whereas carbon easily gives low-coordinate derivatives (tricoordinate and dicoordinate species such as alkenes and alkynes), which are the basic components of the synthetic chemist's toolbox, silicon rarely forms analogous species (3). Another important difference is the difficulty for silicon to maintain a bare positive charge, such as in  $R_3Si^+$  (4), whereas numerous carbocations  $R_3C^+$  are known to be stable (where R can be any of a wide range

The author is at UCR-CNRS Joint Research Chemistry Laboratory (UMR 2282), Department of Chemistry, University of California, Riverside, CA 92521, USA. E-mail: gbertran@mail.ucr.edu

## PERSPECTIVES

of substituents). On the other hand, both elements are usually tetravalent, and it is very difficult to prepare stable low-valent species such as carbenes ( $R_2C$ ) (5) and silylenes ( $R_2Si$ ) (6). On page 849 of this issue, Jutzi *et al.* (7) show that the ease with which silicon can achieve hypercoordination allows for the isolation of the pentamethylcyclopentadienyl silicon cation ( $Cp^*Si^+$ ), a derivative of the cationic, low-coordinate, low-valent species  $HSi^+$ .

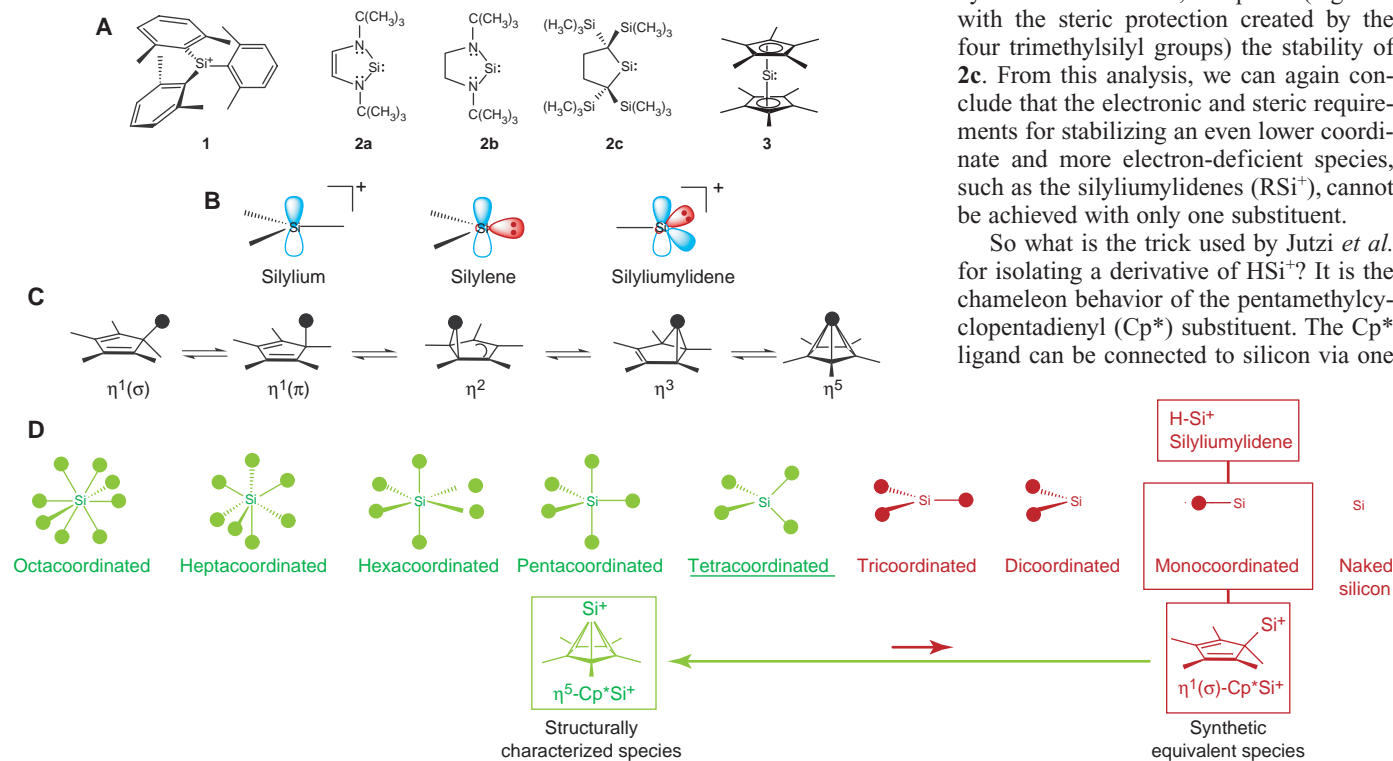
Aside from naked silicon atoms, which are extremely reactive,  $HSi^+$  is the smallest possible silicon moiety. This molecule has only four valence electrons, of which two are needed to make the Si-H  $\sigma$  bond; consequently, a lone pair of electrons and two vacant orbitals are located on the silicon atom. Although  $HSi^+$  has been identified in the solar spectrum (as a gas-phase species), it is safe to predict that the observation in the condensed phase of such a positively charged, electron-deficient, low-coordinate compound will not be possible, at least under usual experimental conditions. The dif-

ficulties met by researchers in isolating both silylium ions ( $R_3Si^+$ ) and silylenes ( $R_2Si$ ) are combined in the case of silyliumylidenes ( $RSi^+$ ).

Silicon is more electropositive, more polarizable, and larger than carbon, and therefore it should be easier to form a silyl cation rather than analogous carbon-based cations. This is indeed the case in the gas phase, but not at all in the condensed phase. The instability is kinetic in origin and results from the high electrophilicity of  $R_3Si^+$  ions, which in solution or in the solid state interact with almost all  $\pi$ - and  $\sigma$ -electron donors, including arenes. The isolation of the only known free silylium ion **1** (see the figure), more than 100 years after a carbocation ( $Ph_3C^+$ , where Ph is phenyl), has been made possible by the use of three bulky substituents that could keep both solvent molecules and counterions at a distance from the silicon atom beyond the range of complexation (8). Clearly, such steric protection cannot be achieved by the lonely substituent of silyliumylidenes ( $RSi^+$ ).

Although attempts to prepare the parent carbene ( $CH_2$ ) by dehydration of methanol had been reported as early as the 1830s, the quest for stable carbenes as well as silylenes has for a long time been considered hopeless. During the 1970s and 1980s several of these species were observed in matrices at temperatures of 77 K or below, confirming their inherent instability. It was only in 1988 that a stable carbene was isolated (9); part of the chemical community believes that the first room-temperature isolation of a silylene (**2a** in the figure) was described in 1994 (10). The possible involvement of the aromaticity (six- $\pi$ -electron ring system) in the stabilization of silylene **2a** has been a matter of controversy. Undoubtedly,  $\pi$ -electron donation from the two nitrogen lone pairs into the vacant orbital on silicon plays a crucial role. Indeed, the corresponding saturated silylene **2b** was isolated later. Moreover, a stable dialkylsilylene **2c** has been prepared (11). Although the electron donation from the neighboring C-Si  $\sigma$  bonding orbital is far weaker than the electronic perturbation by amino substituents, it explains (together with the steric protection created by the four trimethylsilyl groups) the stability of **2c**. From this analysis, we can again conclude that the electronic and steric requirements for stabilizing an even lower coordinate and more electron-deficient species, such as the silyliumylidenes ( $RSi^+$ ), cannot be achieved with only one substituent.

So what is the trick used by Jutzi *et al.* for isolating a derivative of  $HSi^+$ ? It is the chameleon behavior of the pentamethylcyclopentadienyl ( $Cp^*$ ) substituent. The  $Cp^*$  ligand can be connected to silicon via one



**A challenging isolation.** (A) The positively charged silicon center of the only structurally characterized silylium ion **1** is shielded by bulky substituents; the formally vacant orbital of the very rare stable dicoordinate silylenes **2** benefits from electron donation from the neighboring groups, whereas the silylene **3** is stabilized by hypercoordination. (B) It is equally difficult for silicon to bear a positive charge, as in silylium ions, and a lone pair and a vacant orbital as in silylenes. In silyliumylidenes, the silicon center bears a positive charge, a lone pair, and not one but two vacant orbitals that easily explain their high instability. (C) The pentamethylcyclopentadiene ligand can provide one, two, three, or even five

electrons to fulfill the electronic needs of the bonded atom. (D) Silicon is usually tetracoordinate but has a strong tendency for hypercoordination (five to eight) but not low coordination (one to three). In  $HSi^+$ , there are only four valence electrons and the silicon is almost naked, preventing its isolation. In contrast, in the silyliumylidene isolated by Jutzi *et al.*, the bottom part of the molecule is sterically shielded by the  $Cp^*$  ligand, which also provides five electrons, giving a total of eight valence electrons for the molecule. Note that the hypercoordinate  $\eta^5-Cp^*Si^+$  chemically behaves as the monocoordinate  $\eta^1(\sigma)-Cp^*Si^+$ , a derivative of the silyliumylidene  $HSi^+$ .



carbon ( $\eta^1$ ), but also via up to five carbons ( $\eta^5$ ), to adjust to the electronic requirement at the bonded atom (see the figure) (12). The same approach has already been used to prepare what is considered by some in the chemical community to be the first stable silylene (13). Indeed, the so-called decamethylsilicocene **3** (by analogy with ferrocene) features a divalent silicon center with a lone pair, as expected for a silylene; however, it is not dicoordinate but hypercoordinate. This compound shows the reactivity of a nucleophilic silylene because the  $\pi$ -bonded ( $\eta^5$ ) Cp\* ligands easily rearrange to  $\sigma$ -bonded ( $\eta^1$ ) substituents. For example, it reacts with iodine ( $I_2$ ) to give the tetravalent tetracoordinate adduct Cp<sub>2</sub>SiI<sub>2</sub>.

Along this line, the Cp\*Si<sup>+</sup> cation can indeed be considered as a derivative of HSi<sup>+</sup>, but it is important to realize that the silicon is not monocoordinate but pentacoordinate; therefore, this compound is not truly electron deficient, and it even respects the octet rule. As with the silicocene **3**, its reactivity is that expected for silyliumidenes, and it is therefore an excellent

building block for preparing a variety of silicon compounds. It is easy to imagine that, starting from such a monocoordinate compound, all the other coordination states can be reached step by step. It would be especially interesting if a wide range of Cp\*-substituted silylenes (Cp\*SiR) and silylium ions (Cp\*SiR<sub>2</sub><sup>+</sup>) becomes available.

It would be a gross oversimplification to assume that the chemistry of the heavier group 14 elements (germanium, tin, and lead) resembles the chemistry of silicon. Going down the periodic table, *s/p* hybridization is more and more difficult, leading to what is known as the “inert *s*-pair effect,” in which only the *p* electrons are used in the bonding. One of the consequences is the ease with which these elements form low-valent species. Lead even prefers to form divalent PbR<sub>2</sub> compounds rather than tetravalent PbR<sub>4</sub> compounds. Therefore, it is not surprising that the germanium, tin, and lead analogs of Cp\*Si<sup>+</sup> are already known (14). At the opposite extreme, it is difficult to imagine that Cp\*C<sup>+</sup> would be stable because of the reluctance

of carbon to be hypercoordinate: The carbon would be almost totally and not modestly naked, as the silicon is in Cp\*Si<sup>+</sup>.

#### References and Notes

- W. Kutzelnigg, *Angew. Chem. Int. Ed. Engl.* **23**, 272 (1984).
- D. Kost, I. Kalikhman, in *The Chemistry of Organosilicon Compounds*, Z. Rappoport, Y. Apeloig, Eds. (Wiley, Chichester, UK, 1998), vol. 2, part 2, pp. 1339–1346.
- P. P. Power, *Chem. Rev.* **99**, 3463 (1999).
- C. A. Reed, *Acc. Chem. Res.* **31**, 325 (1998).
- D. Bourissou, O. Guerret, F. P. Gabbaï, G. Bertrand, *Chem. Rev.* **100**, 39 (2000).
- M. Haaf, T. A. Schmedake, R. West, *Acc. Chem. Res.* **33**, 704 (2000).
- P. Jutzi *et al.*, *Science* **305**, 849 (2004); published online 1 July 2004 (10.1126/science.1099879).
- K.-C. Kim *et al.*, *Science* **297**, 825 (2002).
- A. Igau, H. Grützmacher, A. Baceiredo, G. Bertrand, *J. Am. Chem. Soc.* **110**, 6466 (1988).
- M. Denk *et al.*, *J. Am. Chem. Soc.* **116**, 2691 (1994).
- M. Kira, S. Ishida, T. Iwamoto, C. Kabuto, *J. Am. Chem. Soc.* **121**, 9722 (1999).
- P. Jutzi, *Pure Appl. Chem.* **75**, 483 (2003).
- P. Jutzi, D. Kanne, C. Krüger, *Angew. Chem. Int. Ed. Engl.* **25**, 164 (1986).
- P. Jutzi, N. Burford, *Chem. Rev.* **99**, 969 (1999).
- I thank the American Chemical Society Petroleum Research Fund (38192-AC4) and Rhodia Inc. for support.

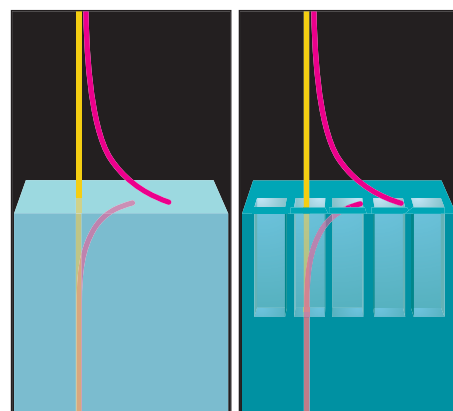
## PHYSICS

# Only Skin Deep

William Barnes and Roy Sambles

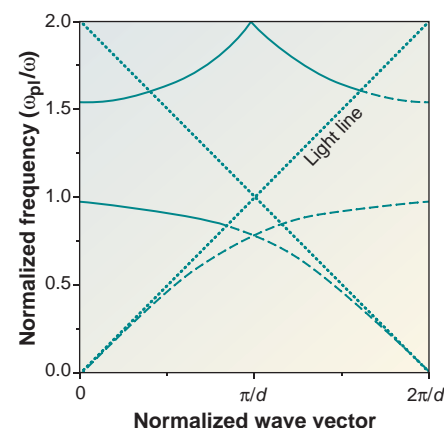
In recent years, there has been an explosion of interest in controlling the interaction between light and matter by introducing structure on length scales equal to or smaller than the wavelength of the light involved. Functionality is thus as much a property of geometry as of material parameters—a concept sometimes referred to as metamaterials. In the 1980s, Yablonovitch (1) and John (2) showed that by introducing three-dimensional periodicity on the scale of the wavelength of light, one can alter how light interacts with the material, specifically by blocking the propagation of light to make photonic band gap (PBG) materials. More recently, by introducing structure smaller than the wavelength of light involved, synthetic “left-handed” materials have been created that have the fascinating property of negative refraction (3). Pendry *et al.* now show on page 847 of this issue how in theory we may be able to exploit another aspect of structure on the subwavelength scale, this time to create a new family of surface electromagnetic modes (4).

Wavelength-scale periodic structures with even a very small refractive index contrast may lead to the strong selective reflection of light and photonic stop-bands. However, producing a truly three-dimensional PBG material that reflects over a range of wavelengths for all directions is very challenging. Indeed,



**Metamaterials create surface modes.** Typical surface plasmon-polariton modes have enhanced fields at the interface between a metal and a dielectric, with the fields decaying away exponentially with distance from the interface (left). At microwave frequencies, the penetration of the field into the metal is very small, and an effective penetration depth is achieved by introducing subwavelength holes into the surface that allow an exponential field to exist (center). The dispersion of these modes, including scattering attributable to the periodic nature of the holes, is shown (right) for a hole/period ratio ( $a/d$ ) of 0.95. For this hole/period ratio there is a band gap just above the newly created surface plasmon frequency  $\omega_{\text{sp}}$ . Nonradiative regions are shown as dashed curves.

practical applications of the PBG idea have been most fruitfully pursued in restricted dimensions, notably in the photonic crystal fiber and in two-dimensional planar slabs. An interesting variant is to apply the same idea to surface waves. In 1996 our group demonstrated that a full PBG for surface plasmon-polariton (SPP) modes could be made by introducing periodic texture into the metallic surface that supports SPPs (5). In the latest development by Pendry *et al.* (4), surface structure is used not just to control surface modes but also to create them.



The authors are in the School of Physics, University of Exeter, Exeter EX4 4QL, UK. E-mail: w.l.barnes@exeter.ac.uk

SPPs are surface modes that propagate at metal-dielectric interfaces and constitute an electromagnetic field coupled to oscillations of the conduction electrons at the metal surface. The fields associated with the SPP are enhanced at the surface and decay exponentially into the media on either side of the interface. In the visible domain, there is a very short penetration depth of the field into the metal and a relatively short penetration depth into the dielectric, thus allowing one to concentrate light on a scale much smaller than the wavelength involved (6). In the microwave regime, metals have a very large complex refractive index ( $n + ik$ ), where  $n$  and  $k$  are the real and imaginary parts, respectively, and  $-n \sim k \sim 10^3$ . The SPP mode is then very nearly a plane wave that extends huge distances into the dielectric but only very short distances into the metal. Metals in the microwave domain are therefore frequently treated as ideal conductors, thus reflecting microwaves perfectly, which limits the usefulness of applying near-field concepts being developed in the visible domain to the microwave regime. What Pendry *et al.* have shown is that by puncturing the metal surface with subwavelength holes, some of the field may penetrate the (effective) surface. This changes the field-matching situation at the bounding surface and leads to a new effective surface plasmon resonance frequency. Note that this frequency is given by the geometry of the surface and may there-

fore be chosen anywhere within the microwave spectrum.

This idea uses the fact that the holes (which cannot be slits) in the metal are hollow metallic waveguides and therefore have a cutoff frequency, a frequency below which no propagating modes in the guide are allowed and any incident fields fall off exponentially with distance down the hole. Below the cutoff frequency of the holes, only an evanescent field exists on the metal side of the interface, but it is just this kind of field that is required for a surface mode (see the figure, center). In this way it is now possible, the authors suggest, to design and synthesize a surface with particular surface mode properties.

Many intriguing questions are opened up when one explores the consequences of this approach. The right side of the figure is an extended dispersion diagram (with the influence of the periodicity  $d$  included) of the surface modes given by Pendry *et al.* in their figure 2, with the square holes having size  $a$ . For the hole/spacing ratio chosen ( $a/d = 0.95$ ), the normalized resonant frequency is  $1/0.95$ . It is apparent that by virtue of scattering from the periodic structure, there is a frequency region in which these new modes are above the light line and are thus radiative; it should therefore be possible to observe these modes in reflectivity experiments, assuming the relevant coupling conditions can be met. Further, for frequencies below the point

where the scattered mode crosses the light line (normalized frequencies below 0.92 for the system in the figure), the modes will be delta functions (and thus unobservable) unless one allows some finite conductivity for the metal and/or fills the holes with a dielectric having some absorption (a power loss channel is required). We can also see that there now exists the possibility of scattered modes interacting and possibly forming band gaps at the Brillouin zone boundary, adding further richness to the modes supported by such a structure.

In the past few years, metamaterials have shown how new functionality can be provided and new physics explored when we start to design materials at the subwavelength level—for example, through the construction of “left-handed” materials displaying negative refraction. The idea put forward here by Pendry *et al.* appears to extend our repertoire of new photonic materials. This heralds a very exciting future for research in electromagnetic surfaces using waves that are only skin deep.

#### References

1. E. Yablonovitch, *Phys. Rev. Lett.* **58**, 2059 (1987).
2. S. John, *Phys. Rev. Lett.* **58**, 2486 (1987).
3. R. A. Shelby, D. R. Smith, S. Schultz, *Science* **292**, 77 (2001).
4. J. B. Pendry, L. Martín-Moreno, F. J. García-Vidal, *Science* **305**, 847 (2004); published online 8 July 2004 (10.1126/science.1098999).
5. S. C. Kitson, W. L. Barnes, J. R. Sambles, *Phys. Rev. Lett.* **77**, 2670 (1996).
6. W. L. Barnes, A. Dereux, T. W. Ebbesen, *Nature* **424**, 824 (2003).

## IMMUNOLOGY

# NK Cells Lose Their Inhibition

Peter Parham

Hepatitis C virus (HCV) is quietly colonizing the vast, plentiful archipelago that we call the human species (1, 2). For those infected, the immediate effects are mild and attract little attention. The evidence of infection is obtained only later, either in the form of virus-specific immunity or liver disease. About 20% of infected individuals clear the virus. For the rest—now numbering ~180 million persons worldwide—the infection and its accompanying immune reactions persist for decades and can lead to liver cancer or liver failure. There is no vaccine for HCV, but for those on the chase, it helps to know what factors distinguish a successful immune response from one that just blunders around. One such

factor is a forceful cytotoxic T cell response aimed at viral peptides presented by a range of HLA class I molecules expressed by immune cells and many other cell types (3, 4). On page 872 of this issue, Khakoo *et al.* (5) report that another function of HLA class I molecules—the regulation of a type of immune cell called a natural killer (NK) cell—may also influence the fate of HCV infection.

NK cells are the lymphocytes that secrete cytokines and kill infected cells at early stages of a primary viral infection. Such speed is possible because NK cells abound in blood as differentiated effectors that are ready to go. On entering infected tissue, NK cells are activated by antigen-presenting cells called dendritic cells through surface receptors that sense microbial products or cellular stress (6). In contrast, in healthy tissue the activation pathways are kept in check by signals coming

from inhibitory receptors (see the figure). In NK cells, this control is mediated by one or more inhibitory receptors that recognize self HLA class I molecules. Such inhibitory receptors include CD94:NKG2A, which binds to HLA-E, and certain members of the killer-cell immunoglobulin-like receptor (KIR) family, which bind to HLA-A, -B, or -C. Whereas CD94:NKG2A and HLA-E are conserved, HLA-A, B, C, and their corresponding KIR receptors are highly polymorphic (7). This variability and their functional interactions imbue KIR and HLA class I molecules with considerable potential as biomarkers of disease progression.

With this objective, Khakoo *et al.* determined the KIR and HLA genotypes of 1037 individuals, who were exposed to HCV and had raised a virus-specific immune response. Comparison of the 352 individuals who resolved infection to the 685 with persisting HCV revealed a difference in the distribution of HLA-C ligands and their inhibitory KIR2DL receptors. The HLA-C locus encodes two forms of KIR2DL ligand defined by the presence of either asparagine (HLA-C1) or lysine

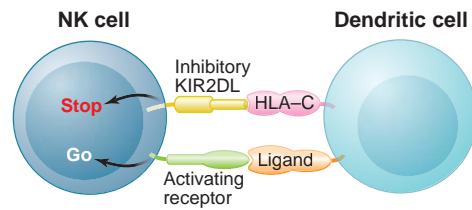
The author is in the Department of Structural Biology, Stanford University School of Medicine, Stanford, CA 94305, USA. E-mail: peropa@stanford.edu



(HLA-C2) at position 80 in the protein's sequence. HLA-C1 allotypes are the ligands for the KIR2DL2 and KIR2DL3 receptors, whereas HLA-C2 allotypes are the ligands for the KIR2DL1 receptor. Khakoo *et al.* show that individuals who are homozygous for HLA-C1 and KIR2DL3 resolve HCV infection more frequently than individuals with other genotypes (see the figure).

Given that the KIR and HLA genes are on different chromosomes, the correlation itself is evidence that the underlying mechanism for the resolution of HCV infection involves HLA-C1 binding to KIR2DL3. At first this seems paradoxical; how does inhibiting an NK cell help in viral clearance? A consideration of the alternatives was the key to solving this puzzle. Khakoo *et al.* make the case that in HLA-C1:KIR2DL3 homozygotes there is a relatively weak inhibition of NK cells by HLA-C. Their brief goes like this: HLA-C1 homozygosity necessitates that the HLA-C2 ligand be absent, so its KIR2DL receptor (which most people have) is nonfunctional. Likewise, KIR2DL3 homozygosity necessitates that KIR2DL2 be absent, because KIR2DL2 and KIR2DL3 behave as alleles (see the figure). KIR2DL3 has a lower affinity for HLA-C1 than does KIR2DL2 (8), so HLA-C1-mediated inhibition of NK cells is inherently weaker in KIR2DL3 homozygotes than in either KIR2DL3/2DL2 heterozygotes or KIR2DL2 homozygotes. Hence, HLA-C1:KIR2DL3 homozygotes are predicted to be rich in NK cells using KIR2DL3 as their inhibitory receptor for self HLA class I. For these NK cells, the inhibitory control will be weaker than for other NK cells, so they will be more easily activated by viral infection. In short, Khakoo *et al.* propose that in responding to HCV infection, individuals homozygous for HLA-C1:KIR2DL3 more effectively activate NK cells than individuals with other genotypes.

Although HCV appears to be unique to humans, its origins and history are mysterious (9). Transmission occurs mainly through direct contact with infected blood—for example, through transfusion of contaminated blood or blood products, or injections or accidental wounds using contaminated syringe needles. These two modes of infection differ in the quantity of virus delivered: Blood transfusions



Inhibitory receptor	HLA-C ligand		Affinity of interaction
KIR2DL1	Lysine 80	C2	Strong
KIR2DL2	Asparagine 80	C1	Intermediate
KIR2DL3	Asparagine 80	C1	Weak

Two common arrangements of KIR2DL genes on chromosome 19



**Taking the brakes off NK cells. (Top)** The activity of NK cells is determined by the integration of signals coming from activating receptors and inhibitory receptors such as KIR2DL. **(Middle)** The three interactions between HLA-C1 and HLA-C2 and KIR2DL receptors that inhibit NK cells. The weak interaction between KIR2DL3 and HLA-C1 can be easily overcome such that individuals with this genotype more readily resolve infection with hepatitis C virus than infected individuals of other genotypes (5). **(Bottom)** The two common chromosomal arrangements of KIR2DL genes.

contain “high doses” of virus, which likely exceed by orders of magnitude the “low doses” accompanying injection with a contaminated needle. The patient panel studied by Khakoo *et al.* comprised 490 individuals infected by blood infusion and 533 infected by injection. Although the frequency of resolved infection was the same in both groups, the dramatic association between HLA-C1:KIR2DL3 homozygosity and resolution of HCV infection was seen only in the group infected by injection.

The two modes of infection differ also in the anatomy of the infection site. Infection by injection is likely to begin as a local affair, like many normal infections, in which an inflammatory response involving NK cells starts at the site of injection and spreads to the draining lymphoid tissue to stimulate B and T cells. Later, as HCV reaches the liver, its preferred site of replication, further stimulation of the immune response could take place. In contrast, in a blood transfusion, massive quantities of HCV are introduced directly into the systemic circulation, from where the virus may quickly reach the liver and also the

spleen. The amount of virus also may be sufficient to suppress NK cell functions by binding directly to these cells (10, 11). All of this is necessarily speculative, because HCV biology is poorly understood. The main point is that HCV and human immunity may well behave differently after the two modes of infection, as is implied by their differential association with KIR2DL3:HLA-C1. While in this cautionary vein, one should note that KIR receptors are expressed by some T cells (12), and they too might contribute to the effect of KIR2DL3:HLA-C1 on HCV infection.

HCV is periodically compared to HIV and judged a Cinderella (13). Both are rapidly evolving RNA viruses that have exploited modern mores and medicine to make their way around the world. Although HIV captures more attention, HCV captures more bodies: 180 million compared to 40 million for HIV. The rates of morbidity and mortality for HCV are lower than those for HIV and, unlike HIV, a substantial proportion of those infected get rid of the virus. This enhances the survival of the host species, but also of the virus, by maintaining a reservoir of subjects that can spawn future HCV infections. It also gives immunologists hope that vaccines will be developed to prevent and control HCV infection. In treating acute myelogenous leukemia with allogeneic stem cell transplantation, it is possible to improve the clinical outcome by temporarily releasing NK cells from the inhibition caused by interactions of KIR2DL receptors with HLA-C expressed by dendritic or other cells (14). Is it also possible that a similar strategy of inducing NK cells to lose their inhibition could encourage the resolution of HCV infection? What that would require is some sort of “lager” for lymphocytes that would not affect the liver.

#### References

1. World Health Organisation, *Wkly. Epidemiol. Rec.* **72**, 341 (1997).
2. V. Racanelli, B. Rehermann, *Trends Immunol.* **24**, 456 (2003).
3. S. Cooper *et al.*, *Immunity* **10**, 439 (1999).
4. F. Lechner *et al.*, *J. Exp. Med.* **191**, 1499 (2000).
5. S. I. Khakoo *et al.*, *Science* **305**, 872 (2004).
6. A. Moretta, *Nat. Rev. Immunol.* **2**, 957 (2002).
7. M. Uhrberg *et al.*, *Immunity* **7**, 753 (1997).
8. C. C. Winter, J. E. Gumperz, P. Parham, E. O. Long, N. Wagtmann, *J. Immunol.* **161**, 571 (1999).
9. P. Simmonds, *Philos. Trans. R. Soc. London B* **356**, 1013 (2001).
10. S. Crotta *et al.*, *J. Exp. Med.* **195**, 35 (2002).
11. C.-T. K. Tseng, G. R. Klimpel, *J. Exp. Med.* **195**, 43 (2002).
12. M. R. Snyder, C. M. Weyand, J. J. Goronzy, *Trends Immunol.* **25**, 25 (2004).
13. J. Cohen, *Science* **285**, 26 (1999).
14. L. Ruggeri *et al.*, *Science* **295**, 2097 (2002).

## Metamaterials and Negative Refractive Index

D. R. Smith,<sup>1</sup> J. B. Pendry,<sup>2</sup> M. C. K. Wiltshire<sup>3</sup>

Recently, artificially constructed metamaterials have become of considerable interest, because these materials can exhibit electromagnetic characteristics unlike those of any conventional materials. Artificial magnetism and negative refractive index are two specific types of behavior that have been demonstrated over the past few years, illustrating the new physics and new applications possible when we expand our view as to what constitutes a material. In this review, we describe recent advances in metamaterials research and discuss the potential that these materials may hold for realizing new and seemingly exotic electromagnetic phenomena.

Consider light passing through a plate of glass. We know that light is an electromagnetic wave, consisting of oscillating electric and magnetic fields, and characterized by a wavelength,  $\lambda$ . Because visible light has a wavelength that is hundreds of times larger than the atoms of which the glass is composed, the atomic details lose importance in describing how the glass interacts with light. In practice, we can average over the atomic scale, conceptually replacing the otherwise inhomogeneous medium by a homogeneous material characterized by just two macroscopic electromagnetic parameters: the electric permittivity,  $\epsilon$ , and the magnetic permeability,  $\mu$ .

From the electromagnetic point of view, the wavelength,  $\lambda$ , determines whether a collection of atoms or other objects can be considered a material. The electromagnetic parameters  $\epsilon$  and  $\mu$  need not arise strictly from the response of atoms or molecules: Any collection of objects whose size and spacing are much smaller than  $\lambda$  can be described by an  $\epsilon$  and  $\mu$ . Here, the values of  $\epsilon$  and  $\mu$  are determined by the scattering properties of the structured objects. Although such an inhomogeneous collection may not satisfy our intuitive definition of a material, an electromagnetic wave passing through the structure cannot tell the difference. From the electromagnetic point of view, we have created an artificial material, or metamaterial.

The engineered response of metamaterials has had a dramatic impact on the physics, optics, and engineering communities, because metamaterials can offer electromagnet-

ic properties that are difficult or impossible to achieve with conventional, naturally occurring materials. The advent of metamaterials has yielded new opportunities to realize physical phenomena that were previously only theoretical exercises.

### Artificial Magnetism

In 1999, several artificial materials were introduced, based on conducting elements designed to provide a magnetic response at microwave and lower frequencies ( $f$ ). These nonmagnetic structures consisted of arrays of wire loops in which an external applied magnetic field could induce a current, thus producing an effective magnetic response.

The possibility of magnetism without inherently magnetic materials turns out to be a natural match for magnetic resonance imaging (MRI), which we use as an example of a potential application area for metamaterials. In an MRI machine there are two distinct magnetic fields. Large quasi-static fields, between 0.2 and 3 tesla in commercial machines, cause the nuclear spins in a patient's body to align. The spins are resonant at the local Larmor frequency, typically between 8.5 and 128 MHz, so that a second magnetic field in the form of a radio frequency (RF) pulse will excite them, causing them to precess about the main field. Images are reconstructed by observing the time-dependent signal resulting from the precession of the spins. Although the resolution of an MRI machine is obtained through the quasi-static fields, precise control of the RF field is also vital to the efficient and accurate operation of the machine.

Any material destined for use in the MRI environment must not perturb the quasi-static magnetic field pattern, thus excluding the use of all conventional magnetic materials. However magnetic metamaterials that respond to time-varying fields but not to static fields can be used to

alter and focus the RF fields without interfering with the quasi-static field pattern.

All measurements are made on a length scale much smaller than a wavelength, which is 15 m at 20 MHz. On a subwavelength scale, the electric and magnetic components of electromagnetic radiation are essentially independent; so to manipulate a magnetic signal at RF, we need only control the permeability of the metamaterial: The dielectric properties are largely irrelevant.

The metamaterial design best suited to MRI applications is the so-called Swiss roll ( $I$ ) manufactured by rolling an insulated metallic sheet around a cylinder. A design with about 11 turns on a 1-cm-diameter cylinder gives a resonant response at 21 MHz. Figure 1A shows one such cylinder. The metamaterial is formed by stacking together many of these cylinders.

In an early demonstration, it was shown that Swiss roll metamaterials could be applied in the MRI environment (2). A bundle of Swiss rolls was used to duct flux from an object to a remote detector. The metamaterial used in these experiments was lossy, and all the positional information in the image was provided by the spatial encoding system of the MRI machine. Nevertheless, it was clear from this work that such metamaterials could perform a potentially useful and unique function.

### Metamaterials and Resonant Response

Why does a set of conductors shaped into Swiss rolls behave like a magnetic material? In this structure, the coiled copper sheets have a self-capacitance and self-inductance that create a resonance. The currents that flow when this resonance is activated couple strongly to an applied magnetic field, yielding an effective permeability that can reach quite high values. At the resonant frequency, a slab of Swiss roll composite behaves as a collection of magnetic wires: A magnetic field distribution incident on one face of the slab is transported uniformly to the other, in the same way that an electric field distribution would be transported by a bundle of electrically conducting wires. In real materials of course, there is loss, and this limits the resolution of the transfer to roughly  $d/\sqrt{\text{Im}(\mu)}$ , where  $d$  is the thickness of the slab and  $\text{Im}(\mu)$  is the imaginary part of the permeability. This field transference was demonstrated (3) by arranging an antenna in the shape of the letter M as the source and mapping the transmitted magnetic field distribution (the fields near a current-

<sup>1</sup>Department of Physics, University of California, San Diego, 9500 Gilman Drive, La Jolla, CA 92093-0319, USA. E-mail: drs@physics.ucsd.edu <sup>2</sup>Department of Physics, Imperial College London, London SW7 2AZ, UK. E-mail: j.pendry@imperial.ac.uk <sup>3</sup>Imaging Sciences Department, Imperial College London, Hammersmith Hospital, Du Cane Road, London W12 0HS, UK. E-mail: michael.wiltshire@imperial.ac.uk



carrying wire are predominantly magnetic). On resonance, the Swiss roll structure transmitted the incident field pattern across the slab (Fig. 1B), and the resolution matched that predicted by theory.

The image transference was also demonstrated in an MRI machine (4). Here, the same M-shaped antenna was used both as the source of the RF excitation field and as the detector for the signal, and the metamaterial was tested twice over. First, it had to transmit the excitation field without degradation of spatial information so that the required spin pattern was excited in the sample. Second, the signal from that spin pattern had to be conveyed faithfully back to the receiver. This experiment demonstrated that a high-performance metamaterial could act as a magnetic face plate and convey information from one side to the other without loss of spatial information (Fig. 1C).

Medical imaging is but one example of the potential utility of artificial magnetic materials. Although artificial magnetic metamaterials

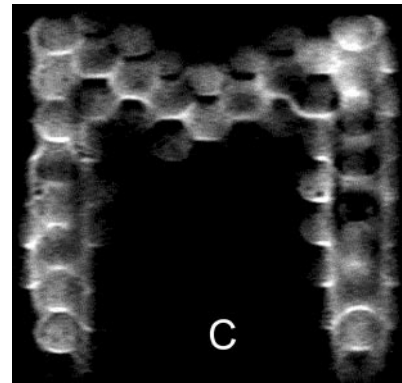
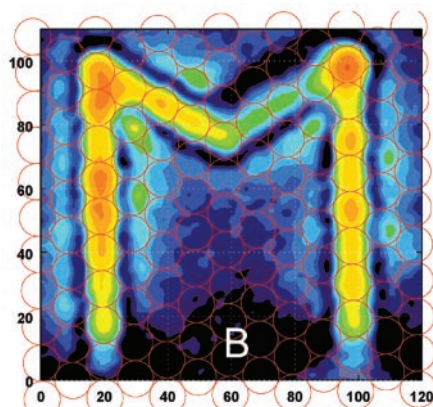
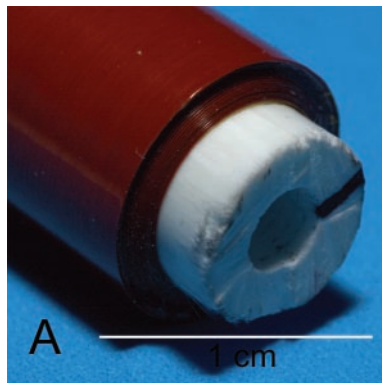


**Fig. 1.** (A) A single element of Swiss roll metamaterial. (B) An array of such elements is assembled into a slab and the RF magnetic field from an M-shaped antenna, placed below the slab, is reproduced on the upper

surface. The red circles show the location of the rolls, which were 1 cm in diameter. (C) The resulting image taken in an MRI machine, showing that the field pattern is transmitted back and forth through the slab.

have unique properties, at these lower frequencies magnetism is also exhibited by existing conventional materials. As we look to higher frequencies, on the other hand, conventional magnetism tails off and artificial magnetism may play an increasingly important role.

A frequency range of particular interest occurs between 1 and 3 THz, a region that represents a natural breakpoint between magnetic and electric response in conventional materials. At lower frequencies, inherently magnetic materials (those whose magnetism results from unpaired electron spins) can be found that exhibit resonances. At higher frequencies, nearly all materials have electronic resonances that result from lattice vibrations or other mechanisms and give rise to electric response. The mid-THz region represents the point where electric response is dying out from the high-frequency end and magnetic response is dying out from the low-frequency end: Here, nature does not provide any strongly dielectric or magnetic materials.

Metamaterials, on the other hand, can be constructed to provide this response. At higher frequencies, the split ring resonator (SRR), another conducting structure, can be conveniently used to achieve a magnetic response (1). The SRR consists of a planar set of concentric rings, each ring with a gap. Because the SRR is planar, it is easily fabricated by lithographic methods at scales appropriate for low frequencies to optical frequencies.

Recently, an SRR composite designed to exhibit a magnetic resonance at THz frequencies was fabricated (5). The size of the SRRs was on the order of 30  $\mu\text{m}$ , 10 times smaller than the 300- $\mu\text{m}$  wavelength at 1 THz. Scattering experiments confirmed that the SRR medium had a magnetic resonance that could be tuned throughout the THz band by slight changes to the geometrical SRR parameters.

Both the Swiss roll metamaterial and the THz SRR metamaterial illustrate the advantage of developing artificial magnetic

response. But metamaterials can take us even further, to materials that have no analog in conventional materials.

### Negative Material Response

A harmonic oscillator has a resonant frequency, at which a small driving force can produce a very large displacement. Think of a mass on a spring: Below the resonant frequency, the mass is displaced in the same direction as the applied force. However, above the resonant frequency, the mass is displaced in a direction opposite to the applied force. Because a material can be modeled as a set of harmonically bound charges, the negative resonance response translates directly to a negative material response, with the applied electric or magnetic field acting on the bound charges corresponding to the force and the responding dipole moment corresponding to the displacement. A resonance in the material response leads to negative values

for  $\epsilon$  or  $\mu$  above the resonant frequency.

Nearly all familiar materials, such as glass or water, have positive values for both  $\epsilon$  and  $\mu$ . It is less well recognized that materials are common for which  $\epsilon$  is negative. Many metals—silver and gold, for example—have negative  $\epsilon$  at wavelengths in the visible spectrum. A material having either (but not both)  $\epsilon$  or  $\mu$  negative is opaque to electromagnetic radiation.

Light cannot get into a metal, or at least it cannot penetrate very far, but metals are not inert to light. It is possible for light to be trapped at the surface of a metal and propagate around in a state known as a surface plasmon. These surface states have intriguing properties which are just beginning to be exploited in applications (6).

Whereas material response is fully characterized by the parameters  $\epsilon$  and  $\mu$ , the optical properties of a transparent material are often more conveniently described by a different pa-

rameter, the refractive index,  $n$ , given by  $n = \sqrt{\epsilon\mu}$ . A wave travels more slowly in a medium such as glass or water by a factor of  $n$ . All known transparent materials possess a positive index because  $\epsilon$  and  $\mu$  are both positive.

Yet, the allowed range of material response does not preclude us from considering a medium for which both  $\epsilon$  and  $\mu$  are negative. More than 35 years ago Victor Veselago pondered the properties of just such a medium (7). Because the product  $\epsilon\mu$  is positive, taking the square root gives a real number for the index. We thus conclude that materials with negative  $\epsilon$  and  $\mu$  are transparent to light.

There is a wealth of well-known phenomena associated with electromagnetic wave propagation in materials. All of these phenomena must be reexamined when  $\epsilon$  and  $\mu$  are simultaneously negative. For example, the Doppler shift is reversed, with a light source moving toward an observer being down-shifted in frequency. Likewise, the

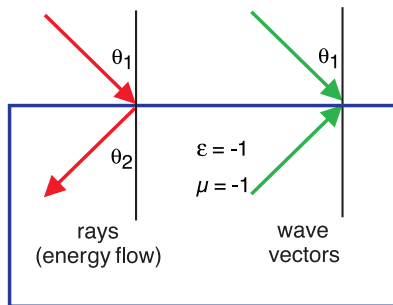


**Fig. 2.** Negative refraction in operation: On the left, a ray enters a negatively refracting medium and is bent the wrong way relative to the surface normal, forming a chevron at the interface. On the right, we sketch the wave vectors: Negative refraction requires that the wave vector and group velocity (the ray velocity) point in opposite directions.

Cherenkov radiation from a charge passing through the material is emitted in the opposite direction to the charge's motion rather than in the forward direction (7).

The origin of this newly predicted behavior can be traced to the distinction between the group velocity, which characterizes the flow of energy, and the phase velocity, which characterizes the movement of the wave fronts. In conventional materials, the group and phase velocities are parallel. By contrast, the group and phase velocities point in opposite directions when  $\epsilon < 0$  and  $\mu < 0$  (Fig. 2).

The reversal of phase and group velocity in a material implies a simply stated but profound consequence: The sign of the refractive index,  $n$ , must be taken as negative.

After the early work of Veselago, interest in negative index materials evaporated, because no known naturally occurring material exhibits a frequency band with  $\mu < 0$  and also possesses  $\epsilon < 0$ . The situation changed in 2000, however, when a composite structure based on SRRs was introduced and shown to have a frequency band over which  $\epsilon$  and  $\mu$  were both negative (8). The negative  $\mu$  occurred at frequencies above the resonant frequency of the SRR structure. The negative  $\epsilon$  was introduced by interleaving the SRR lattice with a lattice of conducting wires. A lattice of wires possesses a cutoff frequency below which  $\epsilon$  is negative (9); by choosing the parameters of the wire lattice such that the cutoff frequency was significantly above the SRR resonant frequency, the composite was made to have an overlapping region where both  $\epsilon$  and  $\mu$  were negative. This prelim-

inary experiment showed that Veselago's hypothesis could be realized in artificial structures and kicked off the rapidly growing field of negative index metamaterials.

### Negative Refraction and Subwavelength Resolution

Experimentally, the refractive index of a material can be determined by measuring the deflection of a beam as it enters or leaves the interface to a material at an angle. The quantitative statement of refraction is embodied in Snell's law, which relates the exit angle of a beam,  $\theta_2$ , as measured with respect to a line drawn perpendicular to the interface of the material, to the angle of incidence,  $\theta_1$ , by the formula

$$\sin(\theta_1) = n \sin(\theta_2)$$

The refractive index determines the amount by which the beam is deflected. If the index is positive, the exiting beam is deflected to the opposite side of the surface normal, whereas if the index is negative, the exiting beam is deflected the same side of the normal (Fig. 2).

In 2001, a Snell's law experiment was performed on a wedge-shaped metamaterial designed to have a negative index of refraction at microwave frequencies (10). In this experiment, a beam of microwaves was directed onto the flat portion of the wedge sample, passing through the sample undeflected, and then refracting at the second interface. The angular dependence of the refracted power was then measured around the circumference, establishing the angle of refraction.

The result of the experiment (Fig. 3) indicated quite clearly that the wedge sample refracted the microwave beam in a manner consistent with Snell's law. Figure 3B shows the detected power as a function of angle for a Teflon wedge ( $n = 1.5$ , blue curve) compared to that of the NIM wedge (red curve). The location of the peak corresponding to the

negative index material (NIM) wedge implies an index of  $-2.7$ .

Although the experimental results appeared to confirm that the metamaterial sample possessed a negative refractive index, the theoretical foundation of negative refraction was challenged in 2002 (11). It was argued that the inherent frequency-dispersive properties of negative index materials would prevent information-carrying signals from truly being negatively refracted. The theoretical issue was subsequently addressed by several authors (12–14), who concluded that, indeed, time-varying signals could also be negative refracted.

Since this first demonstration of negative refraction, two more Snell's law experiments have been reported, both using metamaterial wedge samples similar in design to that used in the first demonstration. These experiments have addressed aspects not probed in the first experiment. In one of the experiments, for example, spatial maps of the electromagnetic fields were made as a function of distance from the wedge to the detector. In addition, wedge samples were used with two different surface cuts to confirm that the angle of refraction was consistent with Snell's law (15). In the second of these experiments, the negatively refracted beam was measured at much farther distances from the wedge sample (16). Moreover, in this latter experiment, the metamaterial sample was carefully designed such that material losses were minimized and the structure presented a better impedance match to free space; in this manner, much more energy was transmitted through the sample, making the negatively refracted beam easier to observe and much less likely to be the result of any experimental artifacts. These additional measurements have sufficed to convince most that materials with negative refractive index are indeed a reality.

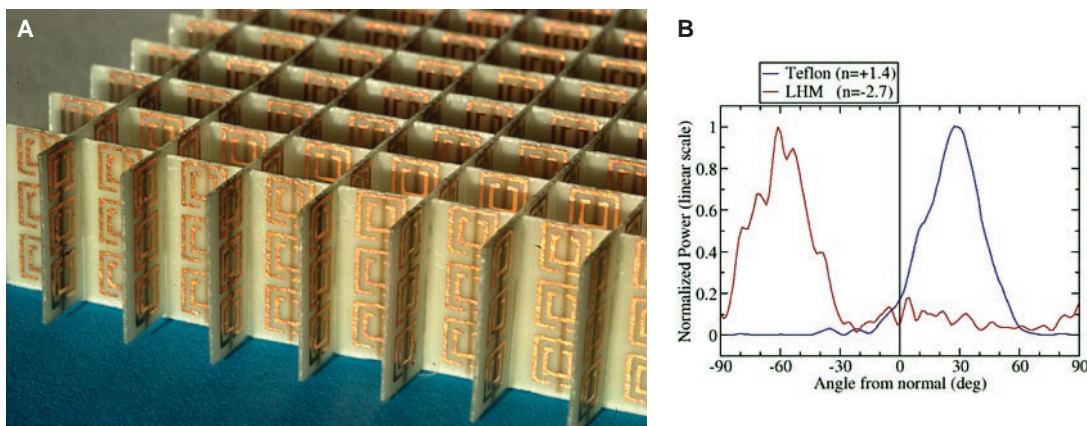


**Fig. 3.** (A) A negative index metamaterial formed by SRRs and wires deposited on opposite sides lithographically on standard circuit board. The height of the structure is 1 cm. (B) The power detected as a function of angle in a Snell's law experiment performed on a Teflon sample (blue curve) and a negative index sample (red curve).



Having established the reality of negative refraction, we are now free to investigate other phenomena related to negative index materials. We quickly find that some of the most long-held notions related to waves and optics must be rethought! A key example is the case of imaging by a lens. It is an accepted convention that the resolution of an image is limited by the wavelength of light used. The wavelength limitation of optics imposes serious constraints on optical technology: Limits to the density with which DVDs can be written and the density of electronic circuitry created by lithography are manifestations of the wavelength limitation. Yet, there is no fundamental reason why an image should not be created with arbitrarily high resolution. The wavelength limitation is a result of the optical configuration of conventional imaging.

Negative refraction by a slab of material bends a ray of light back toward the axis and thus has a focusing effect at the point where the refracted rays meet the axis (Fig. 4A). It was recently observed (17) that a negative index lens exhibits an entirely new type of focusing phenomenon, bringing together not just the propagating rays but also the finer details of the electromagnetic near fields that are evanescent and do not propagate (Fig. 4B). For a planar slab of negative index material under idealized conditions, an image plane exists that contains a perfect copy of an object placed on the opposite side of the slab. Although realizable materials will never meet the idealized conditions, nevertheless these new negative index concepts

show that subwavelength imaging is achievable, in principle; we need no longer dismiss this possibility from consideration.

This trick of including the high-resolution but rapidly decaying part of the image is achieved by resonant amplification of the fields. Materials with either negative permittivity or negative permeability support a host of surface modes closely related to surface plasmons, commonly observed at metal surfaces (6), and it is these states that are resonantly excited. By amplifying the decaying fields of a source, the surface modes restore them to the correct amplitude in the image plane.

The term lens is a misnomer when describing focusing by negative index materials. Recent work (18, 19) has shown that a more accurate description of a negative index material is negative space. To clarify, imagine a slab of material with thickness  $d$  for which

$$\epsilon = -1 \text{ and } \mu = -1$$

Then, optically speaking, it is as if the slab had grabbed an equal thickness of empty space next to it and annihilated it. In effect, the new lens translates an optical object a distance  $2d$  down the axis to form an image.

The concept of the “perfect lens” at first met with considerable opposition (20, 21), but the difficulties raised have been answered by clarification of the concept and its limitations (22, 23), by numerical simulation (24, 25), and in the past few months by experiments.

In a recent experiment, a two-dimensional version of a negative index material has been assembled from discrete elements arranged on a

planar circuit board (26). A detail of the experiment (Fig. 4C) shows the location of a point source and the expected location of the image. Figure 4D shows the experimental data, where the red curve is the measured result and lies well within the green curve, the calculated diffraction-limited result. A more perfect system with reduced losses would produce better focusing.

The conditions for the “perfect lens” are rather severe and must be met rather accurately (23). This is a particular problem at optical frequencies where any magnetic activity is hard to find. However, there is a compromise that we can make if all the dimensions of the system are much less than the wavelength: As stated earlier, over short distances the electric and magnetic fields are independent. We may choose to concentrate entirely on the electric fields; in which case it is only necessary to tune to  $\epsilon = -1$  and we can ignore  $\mu$  completely. This “poor man’s” lens will focus the electrostatic fields, limited only by losses in the system. Thus, it has been proposed that a thin slab of silver a few nanometers thick can act as a lens (17). Experiments have shown amplification of light by such a system in accordance with theoretical predictions (27).

### Photonic Crystals and Negative Refraction

Metamaterials based on conducting elements have been used to demonstrate negative refraction with great success. However, the use of conductors at higher frequencies, especially optical, can be problematic because of losses. As an alternative, many researchers have been investigating the potential of negative refraction in the periodic structures known as photonic crystals (28). These materials are typically composed of insulators and therefore can exhibit very low losses, even at optical frequencies.

In photonic crystals, the size and periodicity of the scattering elements are on the order of the wavelength rather than being much smaller. Describing a photonic crystal as a homogeneous medium is inappropriate, so it is not possible to define values of  $\epsilon$  or  $\mu$ . Nevertheless, diffractive phenomena in photonic crystals can lead to the excitation of waves for which phase and group velocities are reversed in the same manner as in negative index metamaterials. Thus, under the right conditions, negative refraction can be observed in photonic crystals.

In 2000, it was shown theoretically that several photonic crystal configurations could exhibit the same types of optical phenomena predicted for negative index materials, including negative refraction and imaging by a planar surface (23).

Since then, several versions of photonic crystals have been used to demonstrate neg-

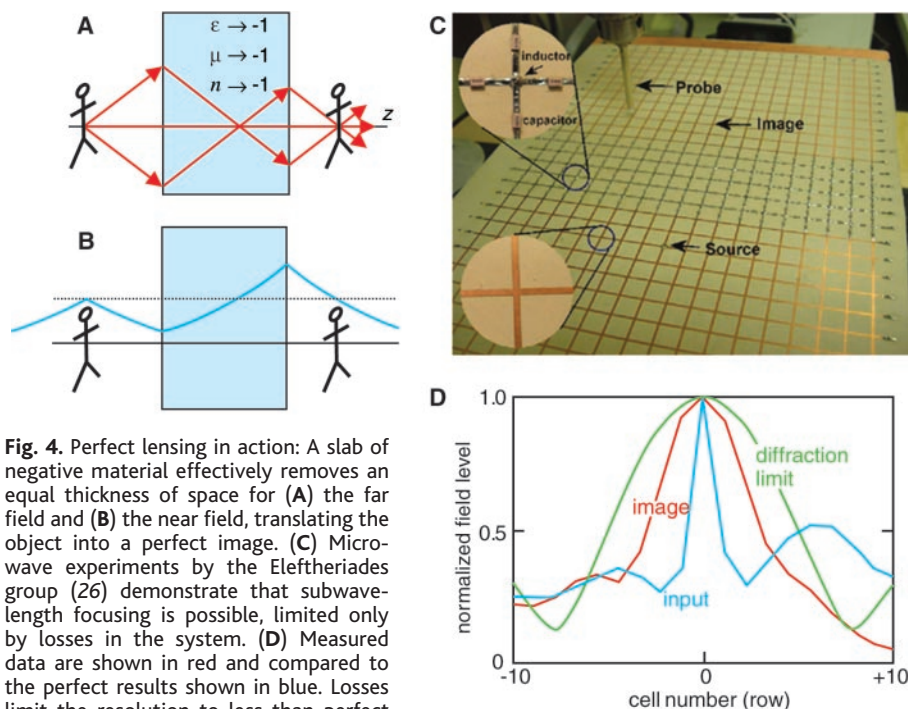


**Fig. 4.** Perfect lensing in action: A slab of negative material effectively removes an equal thickness of space for (A) the far field and (B) the near field, translating the object into a perfect image. (C) Microwave experiments by the Eleftheriades group (26) demonstrate that subwavelength focusing is possible, limited only by losses in the system. (D) Measured data are shown in red and compared to the perfect results shown in blue. Losses limit the resolution to less than perfect but better than the diffraction limit shown in green.

active refraction. For example, a metallic photonic crystal, formed into the shape of a wedge, was used in a Snell's law experiment (29). In an alternative approach, the shift in the exit position of a beam incident at an angle to one face of a flat dielectric photonic crystal slab was used to confirm the effective negative refractive index (30). Although these experiments have been performed at microwave frequencies, the same negative refracting structures scaled to optical frequencies would possess far less loss than the metamaterials based on conducting elements.

Photonic crystals have also been used to demonstrate focusing (31). Images as sharply defined as  $\lambda/5$  can be obtained at microwave frequencies with the use of photonic crystal slab lenses (32). The work in photonic crystals is an example of where the identification of new material parameters has prompted the development of similar concepts in other systems.

### New Materials, New Physics

We rely on the electromagnetic material parameters such as the index, or  $\epsilon$  and  $\mu$ , to replace the complex and irrelevant electromagnetic details of structures much smaller than the wavelength. This is why, for example, we can understand how a lens focuses light without concern about the motion of each of the atoms of which the lens is composed. With the complexity of the material removed from consideration, we are free to use the material properties to design applica-

tions or study other wave propagation phenomena with great flexibility.

The past few years have illustrated the power of the metamaterials approach, because new material responses, some with no analog in conventional materials, are now available for exploration. The examples presented here, including artificial magnetism, negative refraction, and near-field focusing, are just the earliest of the new phenomena to emerge from the development of artificial materials. As we move forward, our ability to realize the exotic and often dramatic physics predicted for metamaterials will now depend on the quality of metamaterials.

### References and Notes

1. J. B. Pendry, A. J. Holden, D. J. Robbins, W. J. Stewart, *IEEE Trans. Microwave Theory Tech.* **47**, 2075 (1999).
2. M. C. K. Wiltshire *et al.*, *Science* **291**, 849 (2001).
3. M. C. K. Wiltshire, J. V. Hajnal, J. B. Pendry, D. J. Edwards, C. J. Stevens, *Opt. Express* **11**, 709 (2003).
4. M. C. K. Wiltshire *et al.*, *Proc. Int. Soc. Mag. Reson. Med.* **11**, 713 (2003).
5. T. J. Yen *et al.*, *Science* **303**, 1494 (2004).
6. W. L. Barnes, A. Dereux, T. W. Ebbesen, *Nature* **424**, 824 (2003).
7. V. G. Veselago, *Sov. Phys. Usp.* **10**, 509 (1968).
8. D. R. Smith, W. J. Padilla, D. C. Vier, S. C. Nemat-Nasser, S. Schultz, *Phys. Rev. Lett.* **84**, 4184 (2000).
9. J. B. Pendry, A. J. Holden, W. J. Stewart, I. Youngs, *Phys. Rev. Lett.* **76**, 4773 (1996).
10. R. Shelby, D. R. Smith, S. Schultz, *Science* **292**, 77 (2001).
11. P. M. Valanju, R. M. Walsler, A. P. Valanju, *Phys. Rev. Lett.* **88**, 187401 (2002).
12. D. R. Smith, D. Schurig, J. B. Pendry, *Appl. Phys. Lett.* **81**, 2713 (2002).
13. J. Pacheco, T. M. Grzegorzczak, B.-I. Wu, Y. Zhang, J. A. Kong, *Phys. Rev. Lett.* **89**, 257401 (2002).
14. J. B. Pendry, D. R. Smith, *Phys. Rev. Lett.* **90**, 029703 (2003).
15. A. A. Houck, J. B. Brock, I. L. Chuang, *Phys. Rev. Lett.* **90**, 137401 (2003).
16. C. G. Parazzoli, R. B. Greegor, K. Li, B. E. C. Koltenbah, M. Tanielian, *Phys. Rev. Lett.* **90**, 107401 (2003).
17. J. B. Pendry, *Phys. Rev. Lett.* **85**, 3966 (2000).
18. J. B. Pendry, S. A. Ramakrishna, *J. Phys. Cond. Matter* **15**, 6345 (2003).
19. A. Lakhtakia, *Int. J. Infrared Millimeter Waves* **23**, 339 (2002).
20. N. Garcia, M. Nieto-Vesperinas, *Phys. Rev. Lett.* **88**, 207403 (2002).
21. G. W. 't Hooft, *Phys. Rev. Lett.* **87**, 249701 (2001).
22. J. T. Shen, P. M. Platzman, *Appl. Phys. Lett.* **80**, 3286 (2002).
23. D. R. Smith *et al.*, *Appl. Phys. Lett.* **82**, 1506 (2003).
24. P. Kolinko, D. R. Smith, *Opt. Express* **11**, 640 (2003).
25. S. A. Cummer, *Appl. Phys. Lett.* **82**, 1503 (2003).
26. A. Grbic, G. V. Eleftheriades, *Phys. Rev. Lett.* **92**, 117403 (2004).
27. Z. W. Liu, N. Fang, T. J. Yen, X. Zhang, *Appl. Phys. Lett.* **83**, 5184 (2003).
28. M. Notomi, *Phys. Rev. B* **62**, 10696 (2000).
29. P. V. Parimi *et al.*, *Phys. Rev. Lett.* **92**, 127401 (2004).
30. E. Cubukcu, K. Aydin, E. Ozbay, S. Foteinopoulou, C. M. Soukoulis, *Nature* **423**, 604 (2003).
31. P. V. Parimi, W. T. Lu, P. Vodo, S. Sridhar, *Nature* **426**, 404 (2003).
32. E. Cubukcu, K. Aydin, E. Ozbay, S. Foteinopoulou, C. M. Soukoulis, *Phys. Rev. Lett.* **91**, 207401 (2003).
33. J.B.P. thanks the European Commission (EC) under project FP6-NMP4-CT-2003-505699 for financial support. D.R.S. also acknowledges support from Defense Advanced Research Projects Agency (DARPA) (DAAD19-00-1-0525), and D.R.S. and J.B.P. received support from DARPA/Office of Naval Research Multidisciplinary Research Program of the University Research Initiative grant N00014-01-1-0803. Additionally J.B.P. acknowledges support from the Engineering and Physical Sciences Research Council, and M.C.K.W., from the EC Information Societies Technology (IST) program Development and Analysis of Left-Handed Materials (DALHM), project number IST-2001-35511.

**Science**

**Functional Genomics Web Site**

- Links to breaking news in genomics and biotech, from *Science*, *ScienceNOW*, and other sources.
- Exclusive online content reporting the latest developments in post-genomics.
- Pointers to classic papers, reviews, and new research, organized by categories relevant to the post-genomics world.
- *Science's* genome special issues.
- Collections of Web resources in genomics and post-genomics, including special pages on model organisms, educational resources, and genome maps.
- News, information, and links on the biotech business.

[www.sciencegenomics.org](http://www.sciencegenomics.org)



## INTRODUCTION

# Touch and Go

**T**he escapades of the Mars Exploration Rover Spirit have given new meaning to the expression “touch and go.” Spirit landed on the floor of Gusev crater on 4 January 2004 universal time. This special issue presents the research results of the first 90 sols (martian solar days).

Although the entry, descent, and landing of Spirit were perilous, science operations began soon after, when the mast of the rover popped up and the two instruments on the mast, the panoramic camera (Pancam) and the miniature Thermal Emission Spectrometer (mini-TES) scoped out the morphology and gross mineralogy of the landing site. Pancam and mini-TES provided scouting reports and detailed investigations throughout the 90 sols. On sol 12, the fully unfolded and fully loaded rover left its landing shell to begin unprecedented mobile exploration. Besides the mast, with two instruments and a suite of magnets to analyze magnetic particles, Spirit has a robotic arm with a microscopic imager to view textural details, an alpha-particle x-ray spectrometer to measure elemental abundances, a Mössbauer spectrometer to distinguish iron-bearing minerals, and a Rock Abrasion Tool (RAT).



Spirit drove about 600 meters from the Columbia Memorial Station to the rim of Bonneville crater in 90 sols. Along the way, the rover performed quick analyses, called touch-and-go operations, in which the instruments on the arm touched and analyzed a feature, but no brushing or grinding was done. At more interesting features such as the rocks Adirondack, Humphrey, and Mazatzal, Spirit stayed longer, using the RAT and the other instruments to acquire more data.

Exploration has changed since the era of nautical exploration by large sailing vessels, when “touch and go” is thought to have originated to describe a ship’s keel touching the seafloor briefly but not getting stuck. Certainly Spirit’s exploration has been successful, as the following 11 papers describe, taking some of the peril and fear out of touch-and-go operations, although robotic space exploration remains difficult and human space exploration remains distant. Spirit is still going strong, extending its mission to over 200 sols and setting the distance record driven by a rover on another planet to over 3000 meters as of 28 July. There is more to come. You go girl!

LINDA ROWAN

## CONTENTS

RESEARCH ARTICLES  
AND REPORTS

- 794 **The Spirit Rover’s Athena Science Investigation at Gusev Crater, Mars** S. W. Squyres *et al.*
- 800 **Pancam Multispectral Imaging Results from the Spirit Rover at Gusev Crater** J. F. Bell II *et al.*
- 807 **Surficial Deposits at Gusev Crater Along Spirit Rover Traverses** J. A. Grant *et al.*
- 810 **Wind-Related Processes Detected by the Spirit Rover at Gusev Crater, Mars** R. Greeley *et al.*
- 811 **Spirit at Gusev Crater: Plates**
- 821 **Localization and Physical Properties Experiments Conducted by Spirit at Gusev Crater** R. E. Arvidson *et al.*
- 824 **Textures of the Soils and Rocks at Gusev Crater from Spirit’s Microscopic Imager** K. E. Herkenhoff *et al.*
- 827 **Magnetic Properties Experiments on the Mars Exploration Rover Spirit at Gusev Crater** P. Bertelsen *et al.*
- 829 **Chemistry of Rocks and Soils in Gusev Crater from the Alpha Particle X-ray Spectrometer** R. Gellert *et al.*
- 833 **Mineralogy at Gusev Crater from the Mössbauer Spectrometer on the Spirit Rover** R. V. Morris *et al.*
- 837 **Initial Results from the Mini-TES Experiment in Gusev Crater from the Spirit Rover** P. R. Christensen *et al.*
- 842 **Basaltic Rocks Analyzed by the Spirit Rover in Gusev Crater** H. Y. McSween *et al.*

See also News story on page 770.

# Science

# The Spirit Rover's Athena Science Investigation at Gusev Crater, Mars

S. W. Squyres,<sup>1\*</sup> R. E. Arvidson,<sup>2</sup> J. F. Bell III,<sup>1</sup> J. Brückner,<sup>3</sup> N. A. Cabrol,<sup>4</sup> W. Calvin,<sup>5</sup> M. H. Carr,<sup>6</sup> P. R. Christensen,<sup>7</sup> B. C. Clark,<sup>8</sup> L. Crumpler,<sup>9</sup> D. J. Des Marais,<sup>10</sup> C. d'Uston,<sup>11</sup> T. Economou,<sup>12</sup> J. Farmer,<sup>7</sup> W. Farrand,<sup>13</sup> W. Folkner,<sup>14</sup> M. Golombek,<sup>14</sup> S. Gorevan,<sup>15</sup> J. A. Grant,<sup>16</sup> R. Greeley,<sup>7</sup> J. Grotzinger,<sup>17</sup> L. Haskin,<sup>2</sup> K. E. Herkenhoff,<sup>18</sup> S. Hviid,<sup>19</sup> J. Johnson,<sup>18</sup> G. Klingelhöfer,<sup>20</sup> A. Knoll,<sup>21</sup> G. Landis,<sup>22</sup> M. Lemmon,<sup>23</sup> R. Li,<sup>24</sup> M. B. Madsen,<sup>25</sup> M. C. Malin,<sup>26</sup> S. M. McLennan,<sup>27</sup> H. Y. McSween,<sup>28</sup> D. W. Ming,<sup>29</sup> J. Moersch,<sup>28</sup> R. V. Morris,<sup>29</sup> T. Parker,<sup>14</sup> J. W. Rice Jr.,<sup>7</sup> L. Richter,<sup>30</sup> R. Rieder,<sup>3</sup> M. Sims,<sup>10</sup> M. Smith,<sup>31</sup> P. Smith,<sup>32</sup> L. A. Soderblom,<sup>18</sup> R. Sullivan,<sup>1</sup> H. Wänke,<sup>3</sup> T. Wdowiak,<sup>33</sup> M. Wolff,<sup>34</sup> A. Yen<sup>14</sup>

The Mars Exploration Rover Spirit and its Athena science payload have been used to investigate a landing site in Gusev crater. Gusev is hypothesized to be the site of a former lake, but no clear evidence for lacustrine sedimentation has been found to date. Instead, the dominant lithology is basalt, and the dominant geologic processes are impact events and eolian transport. Many rocks exhibit coatings and other characteristics that may be evidence for minor aqueous alteration. Any lacustrine sediments that may exist at this location within Gusev apparently have been buried by lavas that have undergone subsequent impact disruption.

Spirit landed in Gusev crater on 4 January 2004 UTC. It was followed 21 days later by Opportunity, which landed on Meridiani Planum. Both vehicles landed using a variant of the airbag landing system that was developed for the Mars Pathfinder mission, deploying the rovers after the landers had come to rest on the surface (1). The primary scientific objective of their mission is to explore two sites on the martian surface where water may once have been present, and to assess past environmental conditions at those sites and their suitability for life. Here we provide an overview of the results from the 90-sol (2) nominal mission of Spirit.

Like Opportunity, Spirit carries a copy of the Athena science payload (3) (Fig. 1). The topography, morphology, and mineralogy of the scene around the rover have been revealed by two remote sensing instruments: a panoramic camera (Pancam) and a miniature thermal emission spectrometer (Mini-TES). Pancam (4) is a stereo camera whose filters provide 11 unique color spectral bandpasses over the spectral region from 0.4 to 1.1  $\mu\text{m}$ , as well as two other filters for direct imaging of the Sun. Mini-TES (5) produces high spectral resolution (10  $\text{cm}^{-1}$ ) infrared image cubes with a wavelength range of 5 to 29  $\mu\text{m}$ . The Pancam cameras and the Mini-TES scanning mirrors are mounted atop a mast (3) at a height of  $\sim 1.5$  m above the ground.

Once potential science targets have been identified using Pancam and Mini-TES, they have been studied in more detail with the use of two in situ compositional sensors mounted on a 5-degree-of-freedom robotic arm (3). These are an Alpha Particle-X-Ray Spectrometer [APXS (6)] and a Mössbauer Spectrometer (7). Radioactive  $^{244}\text{Cm}$  alpha sources

and two detection modes (alpha and x-ray) in the APXS reveal elemental abundances of rocks and soils (8). The Mössbauer Spectrometer measures the resonant absorption of gamma rays produced by a  $^{57}\text{Co}$  source to determine splitting of nuclear energy levels in  $^{57}\text{Fe}$  atoms, revealing the mineralogy and oxidation state of Fe-bearing phases. The instrument arm also carries a Microscopic Imager [MI (9)] that has been used to obtain high-resolution (30  $\mu\text{m}/\text{pixel}$ ) images of rock and soil surfaces and a Rock Abrasion Tool [RAT (10)] that can remove up to  $\sim 5$  mm of material over a circular area 45 mm in diameter. Finally, the payload includes the Magnetic Properties Experiment consisting of seven magnets that have attracted fine-grained magnetic materials for viewing by payload instruments (11).

The rover itself uses a six-wheel rocker-bogie suspension system and onboard autonomous navigation and hazard avoidance capability, allowing traverse distances of tens of meters per sol (1). Navigation and hazard avoidance are aided by two monochromatic navigation cameras (Navcams) mounted on the mast, and by four hazard avoidance cameras (Hazcams) mounted in fore- and aft-facing stereo pairs on the rover body (12). Prelanding mission success criteria dictated that at least one of the rovers should travel a minimum of 600 m over its lifetime, with a goal of 1 km. The design surface lifetime for both vehicles was 90 sols.

The landing site chosen for Spirit lies within Gusev crater, a flat-floored crater that is 160 km in diameter and of Noachian age. The southern rim of Gusev is breached by Ma'adim Vallis, one of the largest branching valley networks on the planet. Gusev is expected to have acted as a settling pool for

sediment carried by the water that cut Ma'adim before it overflowed and exited through a gap in the northern rim of the

<sup>1</sup>Department of Astronomy, Cornell University, Ithaca, NY 14853, USA. <sup>2</sup>Department of Earth and Planetary Sciences, Washington University, St. Louis, MO 63130, USA. <sup>3</sup>Abteilung Kosmochemie, Max-Planck-Institut für Chemie, Postfach 3060, D-55128 Mainz, Germany. <sup>4</sup>NASA Ames/SETI Institute, Moffett Field, CA 94035, USA. <sup>5</sup>Department of Geological Sciences, University of Nevada, Reno, NV 89557, USA. <sup>6</sup>U.S. Geological Survey, Menlo Park, CA 94025, USA. <sup>7</sup>Department of Geological Sciences, Arizona State University, Tempe, AZ 85287, USA. <sup>8</sup>Lockheed Martin Corporation, Littleton, CO 80127, USA. <sup>9</sup>New Mexico Museum of Natural History and Science, Albuquerque, NM 87104, USA. <sup>10</sup>NASA Ames Research Center, Moffett Field, CA 94035, USA. <sup>11</sup>Centre d'Etude Spatiale des Rayonnements, 31028 Toulouse Cedex 4, France. <sup>12</sup>Enrico Fermi Institute, University of Chicago, Chicago, IL 60637, USA. <sup>13</sup>Space Science Institute, Boulder, CO 80301, USA. <sup>14</sup>Jet Propulsion Laboratory, California Institute of Technology, Pasadena, CA 91109, USA. <sup>15</sup>Honeybee Robotics, New York, NY 10012, USA. <sup>16</sup>Center for Earth and Planetary Studies, Smithsonian Institution, Washington, DC 20560, USA. <sup>17</sup>Department of Earth, Atmospheric and Planetary Sciences, Massachusetts Institute of Technology, Cambridge, MA 02139, USA. <sup>18</sup>U.S. Geological Survey, Flagstaff, AZ 86001, USA. <sup>19</sup>Max-Planck-Institut für Aeronomie, D-37191 Katlenburg-Lindau, Germany. <sup>20</sup>Johannes Gutenberg-Universität, Staudinger Weg 9, D-55099 Mainz, Germany. <sup>21</sup>Botanical Museum, Harvard University, Cambridge, MA 02138, USA. <sup>22</sup>NASA Glenn Research Center, Cleveland, OH 44135, USA. <sup>23</sup>Department of Atmospheric Sciences, Texas A&M University, College Station, TX 77843, USA. <sup>24</sup>Department of Civil and Environmental Engineering and Geodetic Science, Ohio State University, Columbus, OH 43210, USA. <sup>25</sup>Niels Bohr Institute, Ørsted Laboratory, DK-2100 Copenhagen 0, Denmark. <sup>26</sup>Malin Space Science Systems, San Diego, CA 92191, USA. <sup>27</sup>Department of Geosciences, State University of New York, Stony Brook, NY 11794, USA. <sup>28</sup>Department of Earth and Planetary Sciences, University of Tennessee, Knoxville, TN 37996, USA. <sup>29</sup>NASA Johnson Space Center, Houston, TX 77058, USA. <sup>30</sup>Institut für Raumsimulation, Deutsches Zentrum für Luft- und Raumfahrt (DLR), Dj-51170 Köln, Germany. <sup>31</sup>NASA Goddard Space Flight Center, Greenbelt, MD 20771, USA. <sup>32</sup>Lunar and Planetary Laboratory, University of Arizona, Tucson, AZ 85721, USA. <sup>33</sup>Department of Physics, University of Alabama, Birmingham, AL 35294, USA. <sup>34</sup>Space Science Institute, Martinez, GA 30907, USA.

\*To whom correspondence should be addressed. E-mail: squyres@astro.cornell.edu



crater. Exploration of the floor of Gusev therefore was anticipated to offer opportunities to study sediments that were derived from the southern highlands of Mars and deposited in a lacustrine environment (13).

Given the great length and depth of Ma'adim Vallis and the shallow depth and flat floor of Gusev crater, the quantity of lacustrine sediments filling the crater is likely to be substantial (14–16). The aqueous sedimentation events at Gusev probably occurred more than 3 billion years ago, however, and we recognized before landing that any water-lain deposits could have been buried by more recent volcanic and/or eolian materials (13). Small impact craters are common across the floor of Gusev, and the interiors and ejecta of such craters may provide access to material from stratigraphic horizons below the surface. The floor of Gusev also has a number of small hills, possibly erosional remnants that could preserve higher stratigraphic horizons that were never buried or were exhumed. We therefore anticipated that the rover's mobility could be important in accessing crater and hill material at the Gusev site that might be different from whatever materials dominate the plains.

**The Rover traverse.** Spirit touched down in the eastern portion of the Gusev crater landing ellipse, at a latitude of 14.5692°S and a longitude of 175.4729°E as defined in the planetocentric IAU 2000 coordinate frame (Fig. 2). The landing site, now named Columbia Memorial Station (17), lies in a region of locally low albedo on the floor of Gusev crater that we interpret to be a zone that has seen recent removal of some fine, loose particulates by dust devils. The first Navcam images of the site (Fig. 3) revealed a rock-strewn plain with low hills on the horizon. The largest impact crater within Spirit's reach, which we observed in the first Pancam panorama (Plate 1), was the Bonneville (18) impact crater (about 210 m in diameter), which lies about 300 m to the northwest of Columbia Memorial Station. The highest hills within Spirit's possible reach, the Columbia Hills (Plate 4), have summit altitudes about 100 m above the plains and lie about 2.6 km to the southeast of the landing site.

During the first 11 sols, we acquired full panoramas of the scene around the lander with Pancam (19) and Mini-TES (20). Egress from the lander took place on sol 12. After a brief initial investigation of the soil immediately adjacent to the lander with all of the instruments on the arm (21–23), we drove Spirit on sol 15 to the nearest large (~50 cm wide) rock, Adirondack (Plate 9). We then investigated Adirondack with all of the arm instruments, including use of the RAT to brush and abrade the rock surface (Plate 9B). Because of a flight software anomaly that occurred on sol 18, temporarily halting normal science operations, we

did not command Spirit to drive away from Adirondack until sol 36.

The traverse path of Spirit from Columbia Memorial Station through the end of the nominal mission on sol 91 (Plate 14) consisted of a drive toward the northeast to the rim of Bonneville crater, in situ investigation of the Bonneville rim region and remote sensing of the crater floor, and then a turn toward the southeast and the beginning of the long drive toward the Columbia Hills. The traverse to and then away from Bonneville yielded the first transect through the ejecta deposits of an impact crater on another planet. Along the way we made several extended stops during which we investigated high-priority science targets with the full Athena payload. In addition, all traverse sols included the use of Pancam and Mini-TES, and many also included brief “touch and go” measurements with the MI, APXS, and/or Mössbauer Spectrometer on targets of opportunity (3).

Spirit drove away from Adirondack on sol 36, arriving at a low circular depression (probably a small impact crater) named Laguna Hollow on sol 45. During sols 46 to 49 we used the rover's wheels to excavate a trench in the soil of Laguna Hollow (Plate 7). We resumed the drive toward Bonneville on sol 50, stopping on sol 54 at a large boulder named Humphrey (Plate 10A). Sols 55 to 60 were spent investigating Humphrey in detail, including brushing (Plate 10B) and grinding (Plate 10C) with the RAT, acquisition of compositional data at several steps in the process, and acquisition of a mosaic of MI images (Plate 12). We resumed the drive toward the rim of Bonneville on sol 61, and arrived there on sol 67 (Plate 3).

Sols 68 to 77 were spent performing detailed remote sensing with Pancam (Plate 5) and Mini-TES (Plate 6) of the interior of Bonneville, as well as exploration of the Bonneville rim that included trenching and in situ

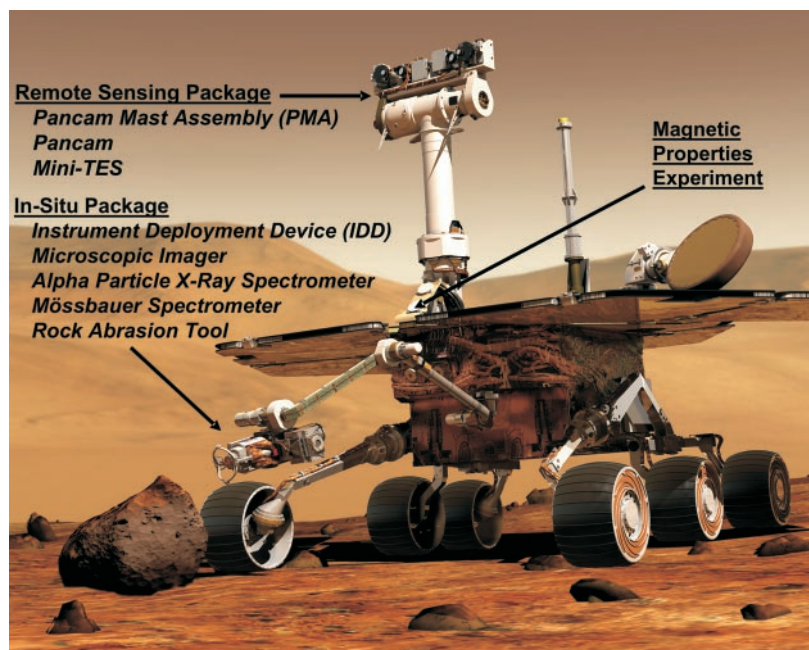


Fig. 1. The MER rover, showing the location of the various elements of the Athena science payload.

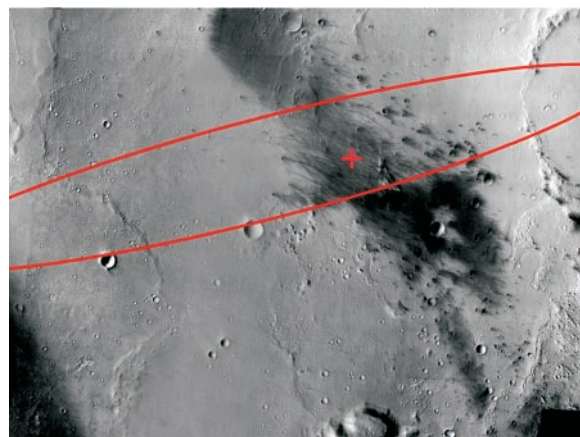


Fig. 2. A Mars Odyssey THEMIS (Thermal Emission Imaging System) visible-wavelength image of the floor of Gusev crater, showing the location of the Spirit target ellipse and the actual landing location (cross). Scale across the image is ~70 km.

investigation of an eolian drift named Serpent. Because the remote sensing of Bonneville did not reveal features within the crater that merited detailed investigation, we turned Spirit toward the southeast and the Columbia Hills. Sols 78 to 86 were spent performing a detailed analysis, with the full payload, of a light-toned rock named Mazatzal (Plates 11A to 11C, Plate 13). Through the end of the nominal mission at sol 91, we continued to drive Spirit toward the Columbia Hills.

The path of the traverse was documented using the navigation capabilities aboard the rover. Localization experiments included triangulation based on landmarks seen on the horizon in Pancam and Navcam images, together with a formal least-squares bundle adjustment using features delineated in overlapping images, wheel odometry, rover gyro and accelerometer data, and Pancam observations of the Sun (24). Results indicate that the total length of the rover traverse during the 90-sol primary mission was 637 m as measured by wheel odometry, 506 m as assessed from formal localization performed for the locations where image data were acquired, and 316 m by straight-line distance.

**Soils.** The soils on the Gusev crater plains explored by Spirit are ubiquitous; they

cover flat regions as well as depressions that we have termed hollows (see below), and also exist as discrete drifts of probable eolian origin (24–26). A thin cover of dust-sized particles of likely airborne origin covers much of the soil and rocks observed around Columbia Memorial Station and during traverses to and from the rim of Bonneville crater. Mini-TES emissivity spectra show that the dust cover rather closely mimics the typical dust spectrum retrieved from Mars Global Surveyor (MGS) TES data (20), and 11-color Pancam reflectivity spectra of the dust cover are consistent with previous telescopic and spacecraft measurements of classical bright regions (19). Exceptions to the dust-covered soils include inferred upwind sides of some drifts that expose darker materials, presumably because of preferential scouring on these drift faces. The thin nature of the dust cover on soils is evident from examination of rover tracks that commonly expose underlying darker materials (e.g., Plate 2). Microscopic imaging of undisturbed soils suggests that the dust deposits exist as aggregates of finer particles (21). The continuing nature of dust accumulation is evident from monitoring the degradation of power with time from the solar panels, in addition to

slight reddening of the Pancam calibration target and other components on the rover deck (19). A mean decrease in solar array energy output of 0.2% per sol is inferred over the 90-sol primary mission (24).

The composition of Gusev soils determined from Spirit APXS data is similar to the composition determined from measurements at the Pathfinder and Viking sites (22), consistent with homogenization of soils by wind on regional and global scales. Sulfur and chlorine are enhanced relative to fresh rock surfaces at Gusev, although the bulk soil compositions are dominated by basaltic materials. Mössbauer observations of soils show the presence of olivine, pyroxene, and magnetite, as well as oxidized iron phases (containing  $\text{Fe}^{3+}$ , ferric iron) (23). In addition, low concentrations of carbonates and sulfates are implied by Mini-TES data (20). Mini-TES data for dark soils exposed in wheel tracks, in the dark materials in the trench excavated in Laguna Hollow, and in the disturbed areas in Serpent drift show basaltic signatures typical of those inferred for selected dark areas from MGS TES data (20, 24). Pancam spectra of soils are also consistent with fine-grained, ferric-rich, poorly crystalline phases (19).

Soils disturbed during landing by retraction of the airbags, by traversing, and during trenching and scuffing by the wheels tend to look cloddy, implying some cohesive strength in the upper few centimeters (24). Sources of cohesion may include a small amount of cementation or electrostatic forces between soil particles. The Laguna Hollow trench suggests cohesion to the depth of the trench, which was about 6 to 7 cm. The composition of the trench interior is similar to the undisturbed surface, except for a lower ferric iron oxide content, consistent with a layer of more ferric iron-rich dust on the surface than in the subsurface (19).

Grain sizes for soils inferred from Mini-TES thermophysical measurements (e.g., Plate 6) suggest that the hollows are filled with the finest grained materials, with an average particle size in the silt to fine-sand range (20). Drifts are seen from imaging data to be covered with a monolayer of particles with medium to coarse sand sizes. This layer appears to be an armor that protects the bedform from erosion and redeposition. There is also a suggestion in some of the highest resolution Pancam images of the plains near Columbia Memorial Station that rock clasts are sitting on a coarse sand layer, with both materials variably covered with dust (Fig. 4).

**Rocks.** Dark, fine-grained rocks, many of them vesicular, litter the Spirit landing site. Many rocks are variably mantled with high-albedo material. Although many of the rocks observed along Spirit's traverse during the

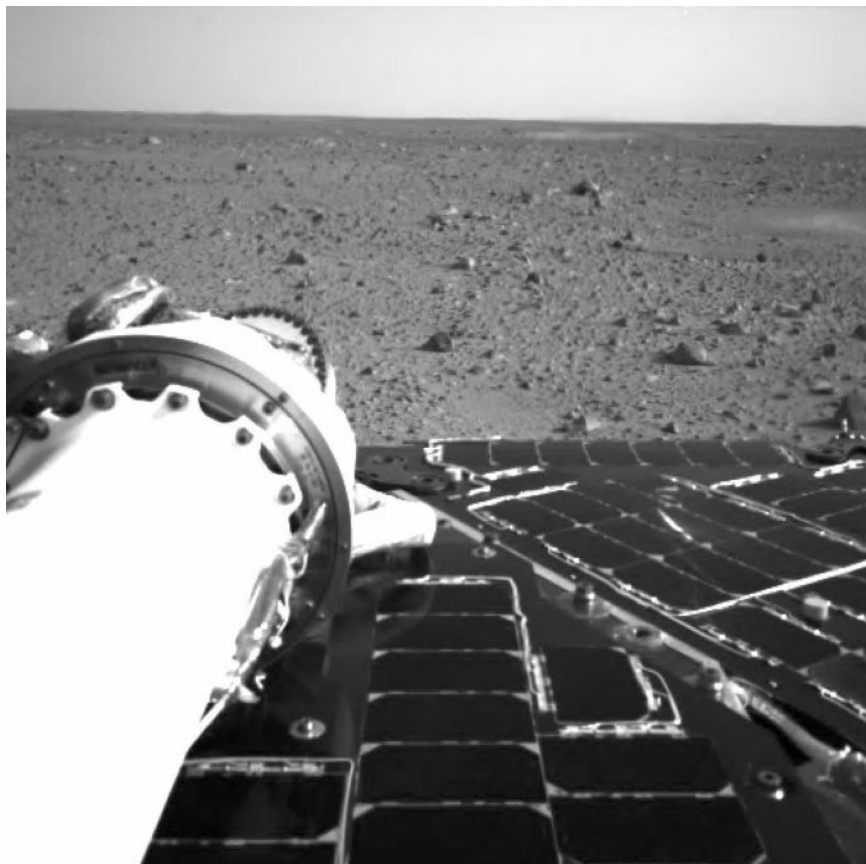


**Fig. 3.** The first image of the martian surface acquired by Spirit. It is a Navcam image acquired on sol 1, reduced in resolution to  $512 \times 512$  pixels and obtained before deployment of the Pancam Mast Assembly. (Image ID 2N126467960)



nominal mission were probably excavated from Bonneville crater, no breccias or obvious shock effects have been noted in any images.

Rocks are variably coated with bright materials, particularly on flat facets and on low rocks that are partially embedded in soils and have been shaped by the wind. Some rocks (e.g., Adirondack, Plate 9) have a distinctive two-toned appearance; upper portions look relatively fresh and dark, whereas lower portions are brighter and coated. Other rocks, particularly ones with upper surfaces that lie close to ground level, are completely covered with bright coatings (e.g., Mazatzal, Plate 11A).

Pancam and Mini-TES spectra of the dark surfaces of all rocks at the Gusev site observed to date are consistent with the spectra of basaltic rocks (19, 20). The texture and composition of Adirondack, Humphrey, and Mazatzal were analyzed using the full Athena payload, including use of the RAT to produce brushed and abraded surfaces.

These rocks are volcanic materials of basaltic composition (27). Rock interiors viewed in MI images contain dark megacrysts, possibly olivine (Plates 12 and 13). The presence of olivine is confirmed by Mössbauer spectra (23); these spectra also reveal pyroxene and magnetite. Rock compositions extrapolated from APXS spectra of natural, brushed, and abraded APXS measurements correspond to olivine-rich basalts (22). Calculated norms, which conform to the redox state measured by the Mössbauer Spectrometer, suggest that the rocks contain olivine, plagioclase, and pyroxenes, with accessory magnetite, ilmenite, and phosphate. The normative mineral compositions are similar to those in basaltic martian meteorites, although the bulk chemical compositions are different. Basaltic lavas at Gusev may have formed by partial melting of an ancient mantle source that was not previously depleted by formation of the crust.

The rocks also show evidence of fractures and vugs filled to varying degrees with bright materials, perhaps of aqueous origin. Pancam and MI images of Mazatzal show unambiguous evidence of multiple coatings: a dark, smooth layer sandwiched between two thin, light-toned layers (Plate 13). MI images of an oblique RAT cut into Humphrey reveal a subsurface layer with distinct fine-grained texture (Plate 12). These coatings probably represent alteration, as do veins, filled fractures, and amygdules in the interiors of three separate rocks. APXS chemical compositions of the alteration materials are distinct from those of the rock interiors and do not lie along mixing lines between rock and Gusev soils (22). The dark coating on Mazatzal and the higher albedo materials seen in the interiors of all three rocks may result from reactions

with aqueous fluids; light coatings on rock exteriors could be cemented dust.

The three rocks that were abraded by the RAT required grinding energy per unit volume that suggests mechanical strengths somewhat less than those of hard terrestrial basalts (24). This finding is also consistent with the view that the outer portions of these rocks have undergone some degree of alteration.

**Geologic processes.** Evolution of the surface materials that we have observed at Gusev crater has been dominated by impact processes. Impact craters ranging in size from a few meters to hundreds of meters and larger (e.g., Thyra crater, located ~20 km to the east) are responsible for much of the low relief on the plains and for the blocky rubble that mantles the surface. Shallow circular depressions, or hollows, represent the smallest, most modified members of the crater population. Formation of the hollows and emplacement of associated ejecta (recognized as accumulations of blocks on and distal to the hollow rims) have disrupted the surface, promoting erosion by the wind, deflating the surface and leaving perched rocks in the ejecta. Hollow interiors have experienced geologically rapid modification, as demonstrated by trenching that revealed uniform infilling by comparatively unaltered and dust-free sediments that may bury many rocks.

Ejecta deposits associated with Bonneville were seen along the traverse, and surface expression of the ejecta is in line with expectations for a relatively pristine impact structure (28). Most of the ejecta clasts retain angular to subangular shapes. Rock abundance and rock size increase toward the rim of Bonneville by factors of approximately 2

and 5, respectively. The largest blocks are more than 2 m in their longest dimension, which suggests that they were impact-fragmented from blocks as large as 6 to 7 m in length and at least 10 m beneath the gardened regolith surface (29).

Wind-related features observed at Gusev include depositional features such as ripples and mantles of dust on rocks, as well as erosional features on rocks, such as beveled sides, facets, and grooves (Fig. 5). Wind-blown sediments include dust, sand, and granules. Bedforms consist primarily of meter-size ripples in which the crests have a surface layer of well-rounded coarse sands and the troughs consist of poorly size-sorted sands. MI images show that the sands have a bimodal size distribution (21), with modes centered on fine sand (0.1 to 0.3 mm in diameter) and coarse sand to granules (1 to 3 mm in diameter). The larger grains are subangular to rounded, and appear to be lithic fragments. The presence of surface crusts on the deposits and bedforms, the inclusion of dust on the bedforms, and the absence of sand dunes and steep slip faces all suggest that the sand is not currently active.

Wind direction indicators are abundant. The axes of ripples and other bedforms are oriented east-northeast to west-southwest and are slightly asymmetric with the steeper slope on the east-southeast side, suggesting formative winds from the west-northwest. Lower albedo portions of most drift deposits and rocks face west-northwest. Drift deposits around some rocks—indicators of wind directions similar to ones seen at the Mars Pathfinder site (30)—are tapered toward the southeast. Wind-abraded rocks (ventifacts, Fig. 5)



**Fig. 4.** A Pancam color image of soil in Gusev crater, showing regularly spaced clasts and coarse sand, all coated with dust. The image was acquired on sol 12 at around 15:30 LST, using the Pancam's L2 (750 nm), L5 (530 nm), and L6 (480 nm) filters, and is an approximate true-color rendering. Scale across the image is ~50 cm. (Image ID 2P127444032)

suggest formative winds from the northwest. RAT operations on Adirondack and Humphrey produced rock cuttings that were asymmetrically distributed toward the southeast (Plates 10 and 11). All of these results are consistent with predictions (31) of afternoon winds in Gusev crater that blow from the northwest, and with the analysis of the orientations of wind-related features seen from orbit (32).

Many of the rocks at the Gusev site show evidence for partial or complete burial followed by exhumation. These include the two-toned rocks discussed above, ventifacts that originate from a common horizon (suggesting that the lower part of the rock was shielded), and rocks that appear to be perched on top of other rocks. In addition, some rocks appear to be undercut (i.e., the soil has been removed from beneath their edges). Taken together, these observations suggest that surface deflation, perhaps highly localized, of 5 to 60 cm has occurred.

Eolian activity clearly has been subordinate to impacts in shaping the surface. The dominant role of impact has contributed to destruction or burial of any primary morphology associated with alluvial or lacustrine infilling of Gusev crater. Moreover, the pristine basaltic lithology and the absence of evidence for phyllosilicates or other aqueous weathering products in the Mini-TES, APXS, and Mössbauer data argue either that water-lain deposits are absent from surficial deposits or that any association with standing water was short-lived.

Although volcanic materials dominate the deposits observed at Gusev, no obvious volcanic source has been identified, either from

the surface or from orbit. Instead, the rocks may be derived from lavas that are inferred to cover the floor of Gusev farther to the northeast (33) and may also have extended into the landing region, where they were later disrupted by impact. We have observed a few rocks whose textures resemble a'a and pahoehoe, the characteristic forms of lava flow surfaces seen at young terrestrial volcanoes such as Kilauea; again, these findings are consistent with substantial impact disruption and mixing.

**Comparison to landing site predictions.** Prelanding predictions of the physical properties of the Gusev landing site (13) are broadly consistent with our observations. The landing location has a bulk TES thermal inertia of  $300$  to  $350 \text{ J m}^{-2} \text{ s}^{-0.5} \text{ K}^{-1}$ , suggesting a surface dominated by duricrust to cemented soil-like materials or cohesionless sand and granules, which is consistent with the observed thermal inertias and soil characteristics at Gusev (20, 21). Spirit landed in the darkest portion of the Gusev landing ellipse (albedo  $\sim 0.19$ ) characterized by dust devil tracks, and then traversed into a higher albedo area that included Bonneville (albedo  $\sim 0.26$ ). The albedo measured by Pancam is comparable (19), which suggests that albedo in Gusev can be used as a proxy for the amount of bright atmospheric dust on the surface. The rock abundance derived from orbital thermal differencing techniques at the Gusev landing site is  $\sim 7\%$ , similar to rock counts within 10 m of Columbia Memorial Station that yield  $\sim 5\%$ . This value is within the  $\pm 5\%$  uncertainty of the orbital estimate (34), although the abundance of rocks has varied by perhaps factors of 2 to 4 along the nominal mission traverse. Orbital estimates

of slope at scales of 1 km and 100 m (from Mars Orbiter Laser Altimeter topography) and 5 m (from Mars Orbiter Camera stereogrammetry and photogrammetry and from radar roughness) indicate that Gusev is comparable to or smoother than the Viking Lander 1 and Mars Pathfinder sites at all three scales (13), consistent with the relatively flat and moderately rocky plain seen in the Pancam and Navcam images.

**Atmospheric science.** Upward-looking Mini-TES spectra reveal the vertical thermal structure of the atmosphere between about 20 and 2000 m above the surface, as well as column-integrated infrared aerosol optical depth, water vapor abundance, and aerosol particle size. The retrieved temperature profiles show the development of a near-surface superadiabatic layer during the afternoon and a deep inversion layer at night (Fig. 6). Upward-looking Mini-TES stares, in which spectra are collected every 2 s for up to an hour, show warm and cool parcels of air moving through the Mini-TES field of view on a time scale of 30 s.

Direct solar imaging with Pancam provides a measurement of visible-wavelength optical depth, whereas near-Sun and sky brightness surveys help reveal the physical

**Fig. 5.** A Pancam image of ventifacts on the wind-scoured surface of the rock Mazatzal. The image was acquired on sol 78 at around 10:40 LST using the Pancam's L7 (1000 nm) filter. Scale across the image is  $\sim 50$  cm. (Image ID 2P133283852)

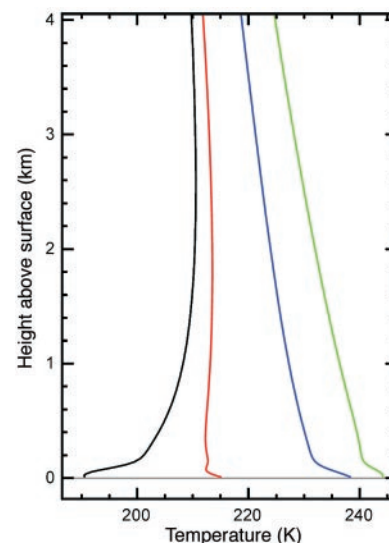
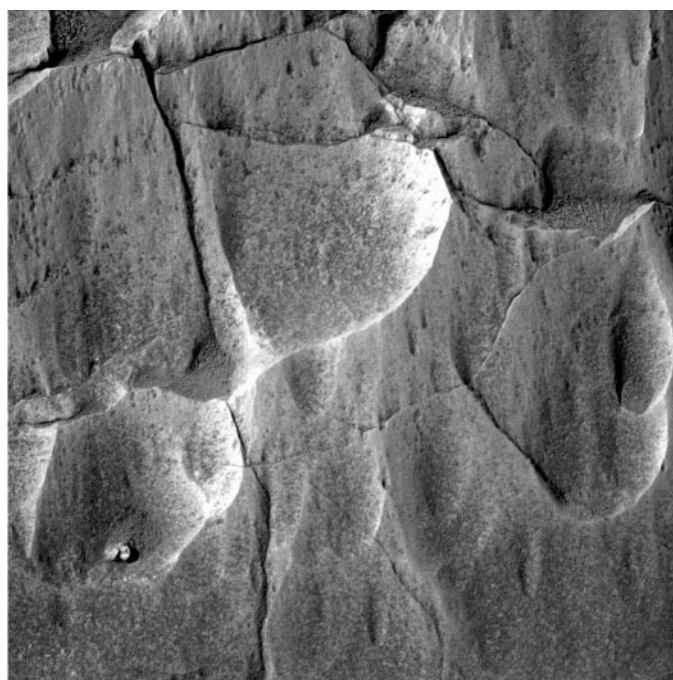


**Fig. 6.** Atmospheric temperature as a function of height above the surface, as observed by Mini-TES. Temperature profiles were taken on sol 72, 12:55 hours (blue); sol 73, 05:20 hours (black); sol 73, 10:00 hours (red); and sol 73, 15:45 hours (green). There is a large diurnal variation in atmospheric temperatures, especially near the surface. In the afternoon (blue and green profiles), near-surface temperatures drop very rapidly with height, forming a superadiabatic layer more than 100 m deep; at night (black profile), strong surface cooling leads to an inversion layer at least 2 km thick. The mini-TES instrument is sensitive to atmospheric temperatures up to about 2 km above the surface. Temperatures above that height are based on concurrent MGS TES observations (35).



properties, scattering properties, and vertical structure of particles suspended in the atmosphere. We have monitored the fallout of dust after a large regional dust storm that occurred in December 2003 and the further clearing associated with the transition into the southern hemisphere fall season (35). Visible-wavelength dust optical depth at Gusev crater dropped from a value of 0.90 soon after landing to 0.56 on sol 91.

**Magnetic properties.** Each rover carries three permanent magnets designed to attract dust from the martian atmosphere, as well as four small magnets designed to attract rock dust produced during RAT operations. Pancam observations of these magnets indicate that particles fine enough to be suspended in the martian atmosphere are typically composed of more than one mineral phase, and that most of the particles, perhaps all of them, are magnetic in the sense that they are attracted to permanent magnets (36). A ferrimagnetic mineral (magnetite, titanomagnetite, or maghemite), present at about 2 weight percent in the dust collected, is most consistent with the observations. Hematite alone cannot be responsible for the magnetism of the dust particles. The fact that the RAT magnets collected low-albedo dust during grinding suggests that the rocks contain substantial ferrimagnetic mineral, consistent with the Mössbauer observations of magnetite.

**Summary.** Gusev crater was chosen as the landing site for Spirit because there is evidence that it once contained a lake (13). However, to date we have found no evidence for lacustrine sedimentation at the Spirit landing site. The morphologic, lithologic, and mineralogic features observed can be explained by local impact disruption of volcanic rocks, followed by eolian modification. Any lacustrine sediments at Gusev were buried by volcanic activity, and Spirit to date has sampled only the impact-disrupted products of this volcanism, plus soils that represent a mixture of locally derived and globally mixed fine-grained materials.

We cannot rule out the possibility that some of the materials that we have observed at the Spirit landing site were transported into Gusev by water that flowed through Ma'adim Vallis. Many of the rocks at our landing site are small enough to have been transported into Gusev via some kind of hyperconcentrated, water-charged debris flow. However, we have seen little direct evidence (e.g., rounded blocks, imbrication, percussion marks, block-to-block variations in lithology)

to support this view. Moreover, the obvious relationships between block properties and distance from Bonneville crater clearly implicate impact as important, if not dominant, in producing the block distributions that we see.

It is also plausible that fluvial/lacustrine processes transported fine-grained sediments as far into Gusev crater as our landing site. These materials may have remained unconsolidated after deposition, never forming sedimentary rocks, and they may have mixed with volcanic fragments by impact processes. If so, then some of the fine-grained soils that we see may actually be sediments that were transported by fluvial processes into Gusev crater. We have seen no direct evidence to support this hypothesis, however.

Regardless of whether fluvial or lacustrine processes have played any role in emplacement of the rocks and soils that we have seen, water probably has been involved (although to a limited degree) in the formation of the veins, filled vugs, and surface coatings that are associated with rocks at the Spirit landing site. This view is particularly supported by the high concentrations in the veins, vugs, and coatings of elements such as S, Cl, and Br that are easily mobilized by water. The light-toned coatings on some rocks may have formed while the low-lying portions of rocks were buried by drift migration or by frost deposited in periods of high obliquity. In such a scenario, as water migrated upward by capillary action between soil grains or along rock surfaces, evaporation left salts behind that acted as cementing and coating agents on rock surfaces.

#### References and Notes

1. J. A. Crisp *et al.*, *J. Geophys. Res.* **108**, 8061, doi:10.1029/2002JE002038 (2003).
2. A martian solar day has a mean period of 24 hours 39 minutes 35.244 seconds, and is referred to as a sol to distinguish this from a roughly 3% shorter solar day on Earth. A martian sidereal day, as measured with respect to the fixed stars, is 24h 37m 22.663s, as compared with 23h 56m 04.0905s for Earth. See [www.giss.nasa.gov/tools/mars24](http://www.giss.nasa.gov/tools/mars24) for more information.
3. S. W. Squyres *et al.*, *J. Geophys. Res.* **108**, 8062, doi:10.1029/2003JE002121 (2003).
4. J. F. Bell III *et al.*, *J. Geophys. Res.* **108**, 8063, doi:10.1029/2003JE002070 (2003).
5. P. R. Christensen *et al.*, *J. Geophys. Res.* **108**, 8064, doi:10.1029/2003JE002117 (2003).
6. R. Rieder *et al.*, *J. Geophys. Res.* **108**, 8066, doi:10.1029/2003JE002150 (2003).
7. G. Klingelhöfer *et al.*, *J. Geophys. Res.* **108**, 8067, doi:10.1029/2003JE002138 (2003).
8. The term martian soil is used here to denote any loose, unconsolidated materials that can be distinguished from rocks, bedrock, or strongly cohesive sediments. No implication of the presence or absence of organic materials or living matter is intended.

9. K. E. Herkenhoff *et al.*, *J. Geophys. Res.* **108**, 8065, doi:10.1029/2003JE002076 (2003).
10. S. Gorevan *et al.*, *J. Geophys. Res.* **108**, 8068, doi:10.1029/2003JE002061 (2003).
11. M. B. Madsen *et al.*, *J. Geophys. Res.* **108**, 8069, doi:10.1029/2002JE002029 (2003).
12. J. Maki *et al.*, *J. Geophys. Res.* **108**, 8071, doi:10.1029/2003JE002077 (2003).
13. M. P. Golombek *et al.*, *J. Geophys. Res.* **108**, 8072, doi:10.1029/2003JE002074 (2003).
14. N. A. Cabrol, E. A. Grin, G. Dawidowicz, *Icarus* **123**, 269 (1996).
15. N. A. Cabrol, E. A. Grin, R. Landheim, *Icarus* **132**, 362 (1998).
16. N. A. Cabrol, E. A. Grin, R. Landheim, R. O. Kuzmin, R. Greeley, *Icarus* **133**, 98 (1998).
17. Columbia Memorial Station was named to honor the crew of Space Shuttle Columbia, who perished on 1 February 2003. The name Columbia Memorial Station refers both to the lander itself and to the martian terrain that it occupies.
18. Names have been assigned to areographic features by the Mars Exploration Rover (MER) team for planning and operations purposes. The names are not formally recognized by the International Astronomical Union.
19. J. F. Bell III *et al.*, *Science* **305**, 800 (2004).
20. P. R. Christensen *et al.*, *Science* **305**, 837 (2004).
21. K. E. Herkenhoff *et al.*, *Science* **305**, 824 (2004).
22. R. Gellert *et al.*, *Science* **305**, 829 (2004).
23. R. V. Morris *et al.*, *Science* **305**, 833 (2004).
24. R. E. Arvidson *et al.*, *Science* **305**, 821 (2004).
25. J. A. Grant *et al.*, *Science* **305**, 807 (2004).
26. R. Greeley *et al.*, *Science* **305**, 810 (2004).
27. H. Y. McSween *et al.*, *Science* **305**, 842 (2004).
28. J. A. Grant, P. H. Schultz, *J. Geophys. Res.* **98**, 11025 (1993).
29. H. J. Melosh, *Impact Cratering* (Oxford Univ. Press, Oxford, 1989).
30. R. Greeley *et al.*, *J. Geophys. Res.* **104**, 8573 (1999).
31. S. R. C. Rafkin, T. I. Michaels, *J. Geophys. Res.* **108**, 8091, doi:10.1029/2002JE002027 (2003).
32. R. Greeley *et al.*, *J. Geophys. Res.* **108**, 8077, doi:10.1029/2002JE002006 (2003).
33. K. A. Milam *et al.*, *J. Geophys. Res.* **108**, 8078, doi:10.1029/2002JE002023 (2003).
34. P. R. Christensen, *Icarus* **68**, 217 (1986).
35. M. D. Smith, *Icarus* **167**, 148 (2004).
36. P. Bertelsen *et al.*, *Science* **305**, 827 (2004).
37. We are deeply indebted to the many hundreds of engineers and scientists—far too numerous to name here—who made the Mars Exploration Rover Project and the Athena Science Investigation possible. Funding for the MER Project, including most of the Athena payload, was provided by NASA. The APXS and Mössbauer instruments were funded by the German Aerospace Center (DLR), and the magnet array was funded by the Danish government. The MER Project was led with skill and dedication by P. Theisinger, and the development of the MER flight system was led with equal skill and dedication by R. Cook and B. Goldstein. J. Rademacher managed the development of the Mini-TES, APXS, and Mössbauer payload elements. M. Schwochert led the engineering teams for Pancam and the Microscopic Imager, and S. Kondos and M. Johnson managed the development of the Rock Abrasion Tool. To all of them, and to the hundreds of members of the MER family who have made this adventure such a joy and privilege to be part of, we express our heartfelt and lasting thanks.

#### Plates Referenced in Article

[www.sciencemag.org/cgi/content/full/305/5685/794/](http://www.sciencemag.org/cgi/content/full/305/5685/794/)

DC1

Plates 1 to 7 and 9 to 14

11 May 2004; accepted 9 July 2004

# Pancam Multispectral Imaging Results from the Spirit Rover at Gusev Crater

J. F. Bell III,<sup>1\*</sup> S. W. Squyres,<sup>1</sup> R. E. Arvidson,<sup>2</sup> H. M. Arneson,<sup>1</sup> D. Bass,<sup>3</sup> D. Blaney,<sup>3</sup> N. Cabrol,<sup>4</sup> W. Calvin,<sup>5</sup> J. Farmer,<sup>6</sup> W. H. Farrand,<sup>7</sup> W. Goetz,<sup>8</sup> M. Golombek,<sup>3</sup> J. A. Grant,<sup>9</sup> R. Greeley,<sup>6</sup> E. Guinness,<sup>2</sup> A. G. Hayes,<sup>1</sup> M. Y. H. Hubbard,<sup>1</sup> K. E. Herkenhoff,<sup>10</sup> M. J. Johnson,<sup>1</sup> J. R. Johnson,<sup>10</sup> J. Joseph,<sup>1</sup> K. M. Kinch,<sup>11</sup> M. T. Lemmon,<sup>12</sup> R. Li,<sup>13</sup> M. B. Madsen,<sup>8</sup> J. N. Maki,<sup>3</sup> M. Malin,<sup>14</sup> E. McCartney,<sup>1</sup> S. McLennan,<sup>15</sup> H. Y. McSween Jr.,<sup>16</sup> D. W. Ming,<sup>17</sup> J. E. Moersch,<sup>16</sup> R. V. Morris,<sup>17</sup> E. Z. Noe Dobrea,<sup>1</sup> T. J. Parker,<sup>3</sup> J. Proton,<sup>1</sup> J. W. Rice Jr.,<sup>6</sup> F. Seelos,<sup>2</sup> J. Soderblom,<sup>1</sup> L. A. Soderblom,<sup>10</sup> J. N. Sohl-Dickstein,<sup>1</sup> R. J. Sullivan,<sup>1</sup> M. J. Wolff,<sup>7</sup> A. Wang<sup>2</sup>

Panoramic Camera images at Gusev crater reveal a rock-strewn surface interspersed with high- to moderate-albedo fine-grained deposits occurring in part as drifts or in small circular swales or hollows. Optically thick coatings of fine-grained ferric iron-rich dust dominate most bright soil and rock surfaces. Spectra of some darker rock surfaces and rock regions exposed by brushing or grinding show near-infrared spectral signatures consistent with the presence of mafic silicates such as pyroxene or olivine. Atmospheric observations show a steady decline in dust opacity during the mission, and astronomical observations captured solar transits by the martian moons, Phobos and Deimos, as well as a view of Earth from the martian surface.

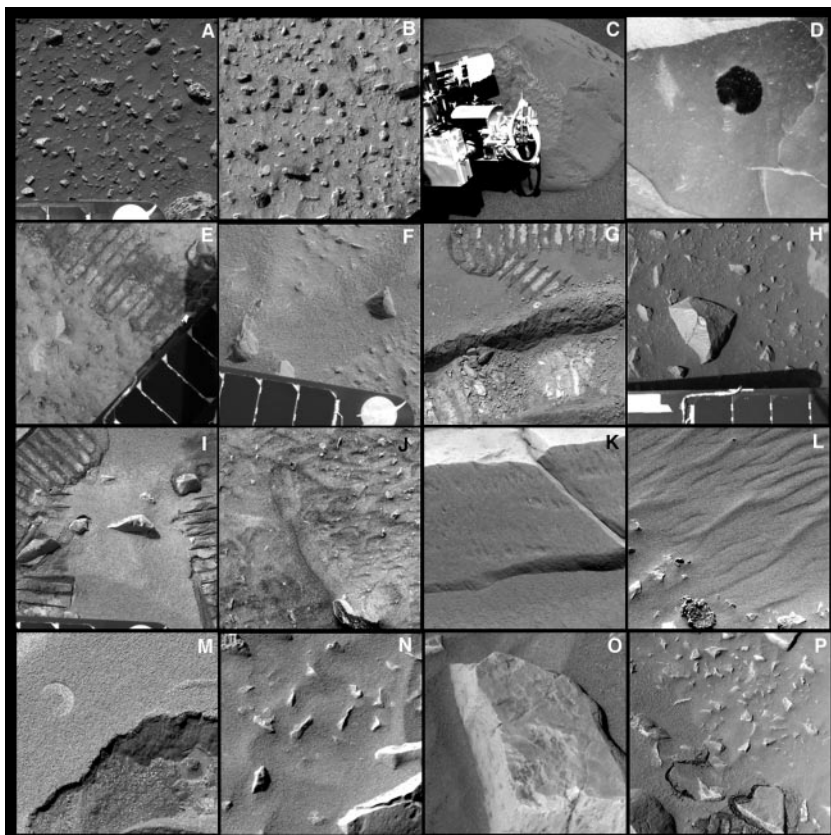
On 4 January 2004 universal time coordinated, the Mars Exploration Rover, Spirit, landed on Mars at 14.5692°S, 175.4729°E, within the crater Gusev, a 160-km-diameter Noachian-age impact crater. Previous orbital remote sensing data have been used to hypothesize that Gusev crater may be partially infilled by ancient lacustrine sedi-

ments (1, 2). We acquired high spatial resolution multispectral panoramic images of the landing site and its environs to characterize the morphology, composition, and physical and atmospheric properties of the region. Our primary objective is to relate these characteristics to the origin and evolution of the martian crust, with particular

emphasis on the search for evidence of liquid water in this region in the past.

**Instrumentation and calibration.** Panoramic Camera (Pancam) is a digital imaging system consisting of two 1024 pixel by 1024 pixel charge-coupled device (CCD) cameras with a 30-cm stereo separation and 0.27 mrad per pixel resolution, mounted on a mast assembly ~1.5 m above the martian surface (3). Each camera has an eight-position filter wheel and is capable of obtaining narrow-band color images of the surface or sky in 11 distinct narrow bands or direct neutral-density filter images of the Sun for opacity determinations at two wavelengths. Because of downlink bandwidth limitations, most images were compressed before downlink with the use of a

**Fig. 1.** Close-up of examples of rocks, clasts, and fine-grained deposits in the region directly in front of the rover (at Pancam's highest resolution). The features are ~1.6 m from the camera, and each image is about 40 to 50 cm across. The smallest features visible in the images are ~0.8 to 1.0 mm across. (A) Sol 12, sequence P2269, filter L7 (430 nm). (B) Sol 12, sequence P2269, filter L2 (754 nm). (C) Sol 30, sequence P2558, filter L7 (430 nm). (D) Sol 33, sequence P2563, filter L2 (754 nm). (E) Sol 36, sequence P2282, filter L2 (754 nm). (F) Sol 39, sequence P2593, filter L2 (754 nm). (G) Sol 50, sequence P2420, filter L7 (430 nm); (H) Sol 50, sequence P2566, filter R1 (430 nm). (I) Sol 51, sequence P2425, filter L2 (754 nm). (J) Sol 54, sequence P2581, filter L2 (754 nm). (K) Sol 63, sequence P2530, filter R1 (430 nm). (L) Sol 66, sequence P2514, filter R1 (430 nm). (M) Sol 74, sequence P2560, filter L7 (430 nm). (N) Sol 75, sequence P2562, filter L7 (430 nm). (O) Sol 76, sequence P2566, filter R1 (430 nm). (P) Sol 90, sequence P2514, filter R1 (430 nm).





high-quality but lossy wavelet-based compression algorithm (4). Bandwidth and power limitations also forced many multi-spectral observations to be acquired with

the use of only a subset (typically 5 or 6) of the 13 narrow-band surface filters.

Calibration was achieved through a combination of preflight laboratory measure-

ments and daily measurements of an onboard reflectance calibration target (3). The calibration target was observed to gradually redden over time because of the accumulation of

<sup>1</sup>Cornell University, Ithaca, NY 14853–6801, USA.

<sup>2</sup>Washington University, St. Louis, MO 63130, USA.

<sup>3</sup>Jet Propulsion Laboratory–California Institute of Technology, Pasadena, CA 91109, USA.

<sup>4</sup>National Aeronautics and Space Administration (NASA) Ames Research Center–Search for Extraterrestrial Intelligence Institute, Moffett Field, CA 94035, USA.

<sup>5</sup>University of Nevada, Reno, NV 89501, USA.

<sup>6</sup>Arizona State University, Tempe, AZ 85287, USA.

<sup>7</sup>Space Science Institute, Boulder, CO 80301, USA.

<sup>8</sup>University of Copenhagen, DK-2100 Copenhagen Ø, Denmark.

<sup>9</sup>National Air and Space Museum, Washington, DC 20560, USA.

<sup>10</sup>U.S. Geological Survey, Flagstaff, AZ 86001, USA.

<sup>11</sup>Aarhus University, DK-8000 Aarhus C, Denmark.

<sup>12</sup>Texas A&M University, College Station, TX 77843, USA.

<sup>13</sup>Ohio State University, Columbus, OH 43210, USA.

<sup>14</sup>Malin Space Science Systems, Incorporated, San Diego, CA 92191, USA.

<sup>15</sup>State University of New York at Stony Brook, Stony Brook, NY 11794, USA.

<sup>16</sup>University of Tennessee, Knoxville, TN 37996, USA.

<sup>17</sup>NASA Johnson Space Center, Houston, TX 77058, USA.

<sup>18</sup>University of Tennessee, Knoxville, TN 37996, USA.

<sup>19</sup>University of Tennessee, Knoxville, TN 37996, USA.

<sup>20</sup>University of Tennessee, Knoxville, TN 37996, USA.

<sup>21</sup>University of Tennessee, Knoxville, TN 37996, USA.

<sup>22</sup>University of Tennessee, Knoxville, TN 37996, USA.

<sup>23</sup>University of Tennessee, Knoxville, TN 37996, USA.

<sup>24</sup>University of Tennessee, Knoxville, TN 37996, USA.

<sup>25</sup>University of Tennessee, Knoxville, TN 37996, USA.

<sup>26</sup>University of Tennessee, Knoxville, TN 37996, USA.

<sup>27</sup>University of Tennessee, Knoxville, TN 37996, USA.

<sup>28</sup>University of Tennessee, Knoxville, TN 37996, USA.

<sup>29</sup>University of Tennessee, Knoxville, TN 37996, USA.

<sup>30</sup>University of Tennessee, Knoxville, TN 37996, USA.

<sup>31</sup>University of Tennessee, Knoxville, TN 37996, USA.

<sup>32</sup>University of Tennessee, Knoxville, TN 37996, USA.

<sup>33</sup>University of Tennessee, Knoxville, TN 37996, USA.

<sup>34</sup>University of Tennessee, Knoxville, TN 37996, USA.

<sup>35</sup>University of Tennessee, Knoxville, TN 37996, USA.

<sup>36</sup>University of Tennessee, Knoxville, TN 37996, USA.

<sup>37</sup>University of Tennessee, Knoxville, TN 37996, USA.

<sup>38</sup>University of Tennessee, Knoxville, TN 37996, USA.

<sup>39</sup>University of Tennessee, Knoxville, TN 37996, USA.

<sup>40</sup>University of Tennessee, Knoxville, TN 37996, USA.

<sup>41</sup>University of Tennessee, Knoxville, TN 37996, USA.

<sup>42</sup>University of Tennessee, Knoxville, TN 37996, USA.

<sup>43</sup>University of Tennessee, Knoxville, TN 37996, USA.

<sup>44</sup>University of Tennessee, Knoxville, TN 37996, USA.

<sup>45</sup>University of Tennessee, Knoxville, TN 37996, USA.

<sup>46</sup>University of Tennessee, Knoxville, TN 37996, USA.

<sup>47</sup>University of Tennessee, Knoxville, TN 37996, USA.

<sup>48</sup>University of Tennessee, Knoxville, TN 37996, USA.

<sup>49</sup>University of Tennessee, Knoxville, TN 37996, USA.

<sup>50</sup>University of Tennessee, Knoxville, TN 37996, USA.

<sup>51</sup>University of Tennessee, Knoxville, TN 37996, USA.

<sup>52</sup>University of Tennessee, Knoxville, TN 37996, USA.

<sup>53</sup>University of Tennessee, Knoxville, TN 37996, USA.

<sup>54</sup>University of Tennessee, Knoxville, TN 37996, USA.

<sup>55</sup>University of Tennessee, Knoxville, TN 37996, USA.

<sup>56</sup>University of Tennessee, Knoxville, TN 37996, USA.

<sup>57</sup>University of Tennessee, Knoxville, TN 37996, USA.

<sup>58</sup>University of Tennessee, Knoxville, TN 37996, USA.

<sup>59</sup>University of Tennessee, Knoxville, TN 37996, USA.

<sup>60</sup>University of Tennessee, Knoxville, TN 37996, USA.

<sup>61</sup>University of Tennessee, Knoxville, TN 37996, USA.

<sup>62</sup>University of Tennessee, Knoxville, TN 37996, USA.

<sup>63</sup>University of Tennessee, Knoxville, TN 37996, USA.

<sup>64</sup>University of Tennessee, Knoxville, TN 37996, USA.

<sup>65</sup>University of Tennessee, Knoxville, TN 37996, USA.

<sup>66</sup>University of Tennessee, Knoxville, TN 37996, USA.

<sup>67</sup>University of Tennessee, Knoxville, TN 37996, USA.

<sup>68</sup>University of Tennessee, Knoxville, TN 37996, USA.

<sup>69</sup>University of Tennessee, Knoxville, TN 37996, USA.

<sup>70</sup>University of Tennessee, Knoxville, TN 37996, USA.

<sup>71</sup>University of Tennessee, Knoxville, TN 37996, USA.

<sup>72</sup>University of Tennessee, Knoxville, TN 37996, USA.

<sup>73</sup>University of Tennessee, Knoxville, TN 37996, USA.

<sup>74</sup>University of Tennessee, Knoxville, TN 37996, USA.

<sup>75</sup>University of Tennessee, Knoxville, TN 37996, USA.

<sup>76</sup>University of Tennessee, Knoxville, TN 37996, USA.

<sup>77</sup>University of Tennessee, Knoxville, TN 37996, USA.

<sup>78</sup>University of Tennessee, Knoxville, TN 37996, USA.

<sup>79</sup>University of Tennessee, Knoxville, TN 37996, USA.

<sup>80</sup>University of Tennessee, Knoxville, TN 37996, USA.

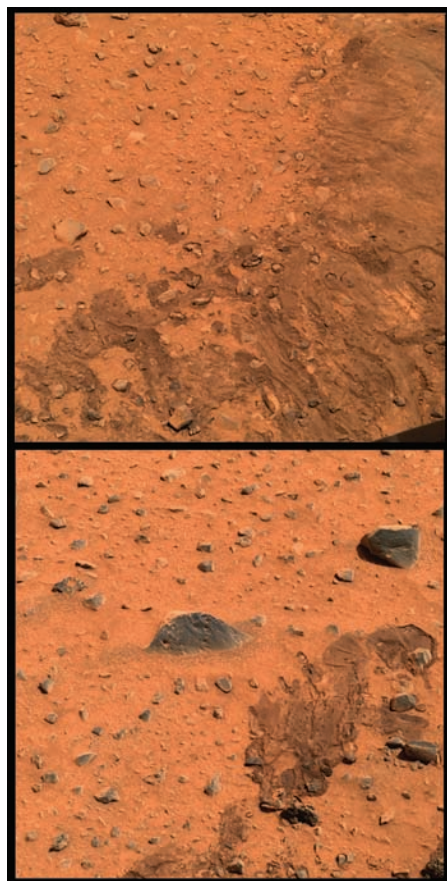


**Fig. 2.** Examples of gravel armor and crusted fines observed in Pancam images of airbag scape marks near the lander. (Top) Sol 11, sequence P2536, 10:45 local solar time (LST); (bottom) sol 7, sequence P2530, 13:20 LST. Both images are approximate true color renderings generated with the use of Pancam's 600 nm, 530 nm, and 480 nm filters.

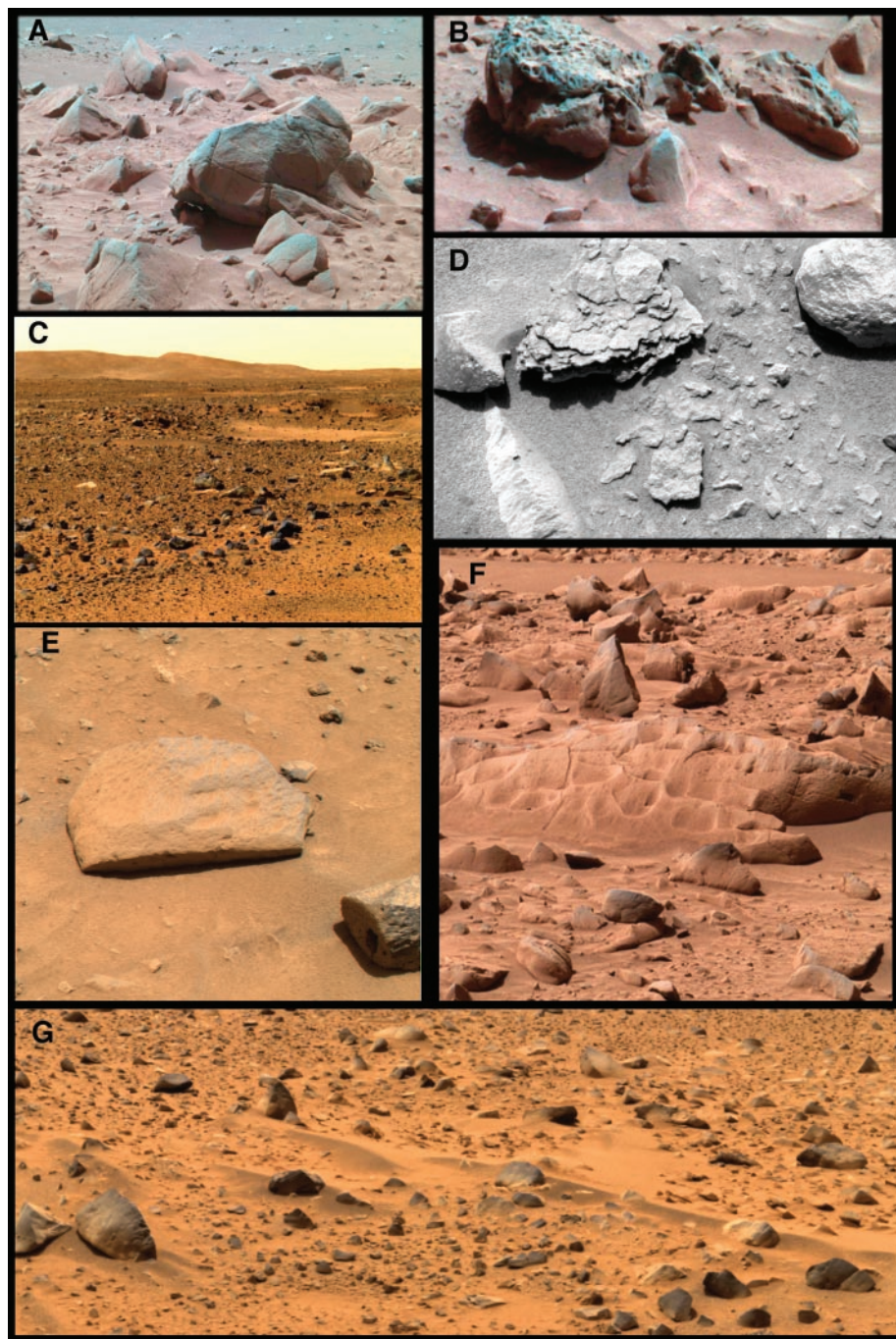


**Fig. 3.** Examples of the variety of rock forms observed by Pancam at the Gusev site. (A) A 77-cm-wide fractured block from sol 68 imaging near the rim of Bonneville crater. (B) A 25-cm-wide rock (left of frame) also imaged on sol 68, showing both vesicular and smooth morphologies. (C) Sol 49 view of the boundary between Laguna Hollow (near field) and the surrounding plains, showing typical increased rock abundance near the periphery of the hollow. (D) Image of the 5-cm-wide platy rock Mimi from sol 42. (E) The rocks Sashimi (center, 30 cm long, and 18 cm wide) and Sushi (lower right, 10 cm wide) imaged near the lander on sol 14. Sashimi is moderately pitted and exhibits ventifact-like aeolian scour marks; Sushi is heavily pitted, including a large angular pit in the exposed interior of the left side of the rock. (F) The low-lying rock Mazatzal, imaged on sol 76. The rock is ~2.1 m long and ~45 cm high. (G) View from sol 5 of small rocks and aeolian bedforms near the lander, showing that the most rounded-looking rocks near the lander are also typically the darkest. The small rock next to the bedform at center is ~15 cm across.



settling airborne dust on its surface. The degree of reddening and its influence on the image calibration has been modeled with the use of a simple two-layer Hapke model of a thin layer of dust with spectral properties like those determined by the Viking and Pathfinder landers (5–7) on top of the silicone-based calibration target materials (3). The model was verified and validated by using results from the Sweep Magnet experiment (8). With this time-variable dust correction applied, the cameras' absolute radiance calibration is estimated to be within ~5 to 10% accuracy on the basis of comparison with sky radiance models and direct imaging of the Sun (9, 10). The relative reflectance (radiance factor or  $I/F$ , where  $I$  is the measured scene radiance and  $\pi F$  is the solar irradiance at the top of the martian atmosphere) is estimated to be within ~5 to 10% absolute accuracy and ~1 to 3% relative filter-to-filter precision.

During the course of Spirit's 90-sol (11) primary mission, more than 9300 Pancam images, totaling more than 750 Mbytes of data, were acquired and downlinked. Among these images were sets of large multispectral panoramas acquired from the initial landing site, from halfway along the traverse to a nearby crater informally known as Bonneville (12), and from the rim of Bonneville itself. These panoramas were acquired with the use of a subset of Pancam filters designed to provide stereo coverage, span the full wavelength range of the instrument, and cover key wavelengths that could provide tactical time scale information on potential drive directions and/or in situ instrument target choices.

**Regional-scale observations.** The panoramic views of the landing site and traversed regions (Plates 1 to 3) show a generally flat plain with about 5% of the area covered by relatively small (tens of cm size or smaller) rocks. Most of the rocks are angular to subangular, and a small number are rounded. The 210-m-diameter rim of Bonneville crater could be seen about 300 m northeast of the lander. More distant features include a ridge of low-lying (~100 to 150 m high) hills, called the Columbia Hills (Plate 4), ~3 to 4 km east of the lander and isolated knobs and mesas ranging from ~8 km to ~26 km south to southwest of the lander near the mouth of Ma'adim Vallis. There were more rocks on the Bonneville crater ejecta blanket, with ~10% of the area covered by rocks (13, 14). The local relief around the landing site exhibits meter-scale undulations interspersed with small (< 200-m diameter), low-relief (< 15-m depth) impact craters and much smaller (tens of m in diameter) circular hollows. Full resolution, losslessly compressed Pancam images reveal morphologic, albedo, and color variations within

the Columbia Hills that may indicate scarps, terraces, or layers such as those identified in Mars Global Surveyor (MGS) Mars Orbiter Camera images (1, 2, 15).

**Rocks and fines.** Clastic materials imaged by Pancam at the landing site encompass a range of morphologies and physical properties (Fig. 1). Examples of fines include thin reddish aeolian dust coatings, fine-grained soil particles (16), sand, granules, and gravel. Bedforms hypothesized to be ripples formed of coarse sand and granules ~0.5 to several mm in size were identified on the basis of Pancam albedo and color variations; this hypothesis was verified with the use of Microscopic Imager (MI) images (17, 18). Most fines observed at the landing site show some cohesion on the basis of how the material holds together when disturbed by the rover wheels, airbag bounces, and drag marks or the Mössbauer spectrometer contact plate (18). There is also some evidence for layering of finer-grained materials above and below an armor of what appear to be gravel, pebbles, and cobbles (Fig. 2). The coarser layers may have formed by accretion of aeolian fine-grained dust on the basis of images from regions where larger particles are not seen beneath the surface (e.g., Plate 7), or they may represent deflation lag deposits on the basis of images from other regions

where larger particles are seen beneath the surface [e.g., within trenches or the Serpent bedform (18, 19)].

Many rocks at the landing site are fractured or fragmented, and some are pitted and may contain vesicles (Fig. 3). Some rocks are partially buried by fines, whereas others are perched on the surface. Rounded rocks are rare and are generally darker and display signs of wind erosion rather than any unambiguous indications of a fluvial origin. No sedimentary rocks or impact breccias have been identified at the site.

**Photometric observations.** Calibrated Pancam images from sequences acquired with the use of a broadband filter (L1,  $739 \pm 338$  nm bandpass) were used to estimate the albedo of the landing site region to be  $0.25 \pm 0.05$  (20). This is a moderately high albedo for Mars, comparable to the MGS Thermal Emission Spectrometer (TES) bolometric albedo of the Viking Lander 1 site ( $0.26 \pm 0.05$ ), slightly higher than the albedo of the Viking Lander 2 ( $0.23 \pm 0.01$ ) or the MPF ( $0.22 \pm 0.01$ ) sites but within the uncertainties of previous orbital and telescopic estimates of the albedo of the Gusev landing error ellipse [ $\sim 0.23$  (17)]. Some of the uncertainty on the Pancam albedo estimate comes from albedo variations visible in images of the landing site region. The lander itself is within a slightly lower-albedo

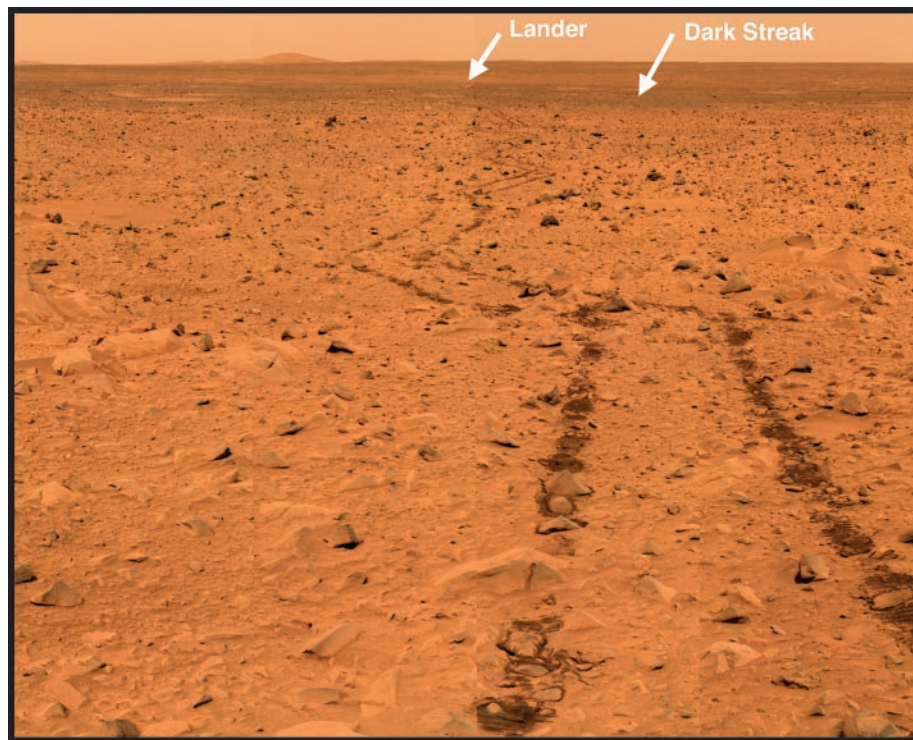


**Fig. 4.** Pancam mosaic acquired from near the rim of Bonneville crater, looking back to the southwest along the traverse path toward the lander (center, top). This view shows the lander to be within a wind or dust devil streak with a lower albedo than the more distant Gusev plains or the near-field crater ejecta deposit. This is an approximate true color rendering of a mosaic acquired around 10:20 LST on sol 66 with the use of Pancam's 750 nm, 530 nm, and 480 nm filters.



( $0.20 \pm 0.02$ ) wind streak or dust devil track that trends northwest to southeast across the center of Gusev crater. During the first 90 sols, the rover crossed albedo boundaries associated with this lower-albedo wind streak and the higher-albedo ( $0.30 \pm 0.02$ ) hollows and the ejecta deposits of Bonneville crater (Fig. 4). These albedo extremes are consistent with the lowest ( $\sim 0.19$ ) and highest ( $\sim 0.26$ ) albedos measured by TES within the Gusev landing region error ellipse (14).

Pancam multispectral images acquired at different times of day document reflectance variations related to surface properties such as texture, porosity, and grain size (21, 22). For example, photometric observations of regions near the shadow cast by the Pancam mast assembly indicated a strong opposition effect in some soil and rock surfaces, and specular brightenings seen in some brushed and/or compacted surfaces suggest very fine-grained soils or smooth, reflective mineral surfaces in the rocks. Photometric observations were coordinated to occur during or within 1 sol of space-

craft overflights by the Mars Odyssey, Mars Express, and MGS orbiters to provide ground truth observations of visible and near-infrared (IR) reflectance as a function of illumination and viewing geometries.

**Multispectral observations.** The multispectral panoramas acquired from the Columbia Memorial Station and along Spirit's traverse (Plates 1 to 3) show broad classes of color units detectable at and near the landing site. For example, in the initial 360° mission success panorama (Plate 8), rocks or parts of rocks that are less dusty appear bluer than average, as do lower-albedo, possibly coarser-grained soils. A red/blue color ratio metric was often used to distinguish less dusty from more dusty rocks (none of the rocks were observed to be completely dust-free). The general spectral and color classes seen near the station include (i) high-albedo (0.25 to 0.35) red soils and drifts, (ii) moderate-albedo (0.20 to 0.25) red soils, such as those in the hollows, (iii) moderate- to high-albedo (0.20 to 0.30) red rock surfac-

es, (iv) moderate- to low-albedo (0.15 to 0.20) red drifts and far-field soils, (v) low-albedo (0.10 to 0.15) red disturbed soil deposits, and (vi) low-albedo (0.10 to 0.15) gray rock surfaces.

Less-compressed 13-filter (11-color) Pancam multispectral observations of selected targets provide additional constraints on the mineralogy associated with these spectral classes. Moderate- and high-albedo soil spectra (e.g., Figs. 5, A and B, and 6, A and B) are similar to telescopic and spacecraft measurements of martian dust (14, 23, 24) and are characteristic of fine-grained, poorly crystalline ferric iron oxides (25, 26). A weak absorption centered near 860 to 930 nm in most high-albedo soil spectra can be used to constrain the ferric iron oxide mineralogy; however, a unique mineral identification cannot be assigned for this feature on the basis of Pancam data alone. Candidates to explain the near-IR band include fine-grained hematite, goethite, ferrihydrite, maghemite, or schwertmannite (25, 26). The spectra of lower-

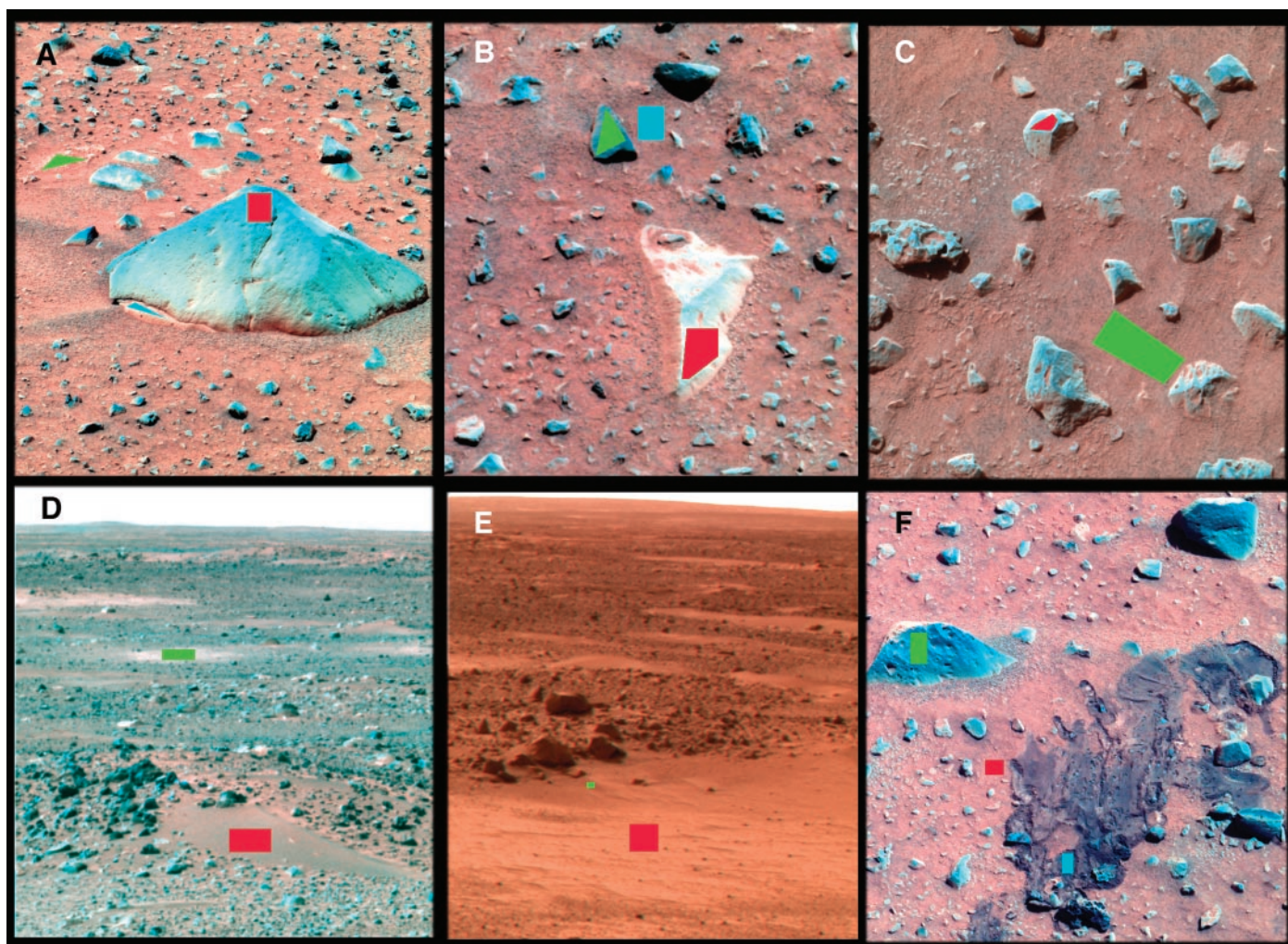


Fig. 5. Context images for Pancam spectra displayed in Fig. 6. All images are false-color composites using Pancam's 750 nm, 530 nm, and 480 nm filters. (A) Sol 14, target Adirondack; (B) sol 26, target Blanco; (C) sol 12,

targets within the instrument arm work volume; (D) sol 9, position 1 within the 120 survey sequence; (E) sol 9, position 8 within the 120 survey sequence; and (F) sol 7, target Magic Carpet.

albedo undisturbed soils at the site (e.g., Figs. 5, D and F, and 6, D and F) can be modeled by a simple scaling of bright soil spectra, suggesting that the iron-bearing mineralogy of these regions is similar to that of the bright dust deposits but that the grain size of the materials is larger. Such a grain-size variation is also consistent with the interpretation of albedo boundaries seen on small aeolian ripple deposits at the site (17). Pancam images were also obtained of three different sets of magnets carried by Spirit that were designed to provide constraints on the composition and physical properties of magnetic dust grains (27). Initial results of the imaging and other measurements on

the magnets indicates that essentially all of the airborne dust is magnetic and that the dust particles must be composite, multi-mineral-phase grains (8).

Pancam spectra of rock surfaces display a continuum of characteristics between light-toned red rock surfaces with spectra similar to bright soils (e.g., Figs. 5, A and B, and 6, A and B), likely indicating a fine-grained ferric iron oxide dust covering or coating, to much lower-albedo gray surfaces that are spectrally distinct (Figs. 3; 5, C and F; and 6, C and F). Specifically, the lowest albedo rock surfaces (naturally occurring or in regions of brushing and grinding) have a higher reflectance in the bluest wavelengths than the soils

and dust, show an overall negative spectral slope from 750 nm to 1000 nm, and exhibit a weak near-IR absorption feature that is centered at a longer wavelength than the near-IR feature seen in the dust. These spectral characteristics are consistent with a lower relative percentage of ferric iron phases (less dust and/or soil cover) in these parts of the rocks and with ferrous iron silicates such as pyroxene or olivine to explain the longer-wavelength near-IR band (28–33). These spectral characteristics are also consistent with the Mössbauer spectrometer observations of rock surfaces (34, 35), and similar spectral characteristics were observed in a rare “black rock” spectral class of materials at the MPF landing site (33).

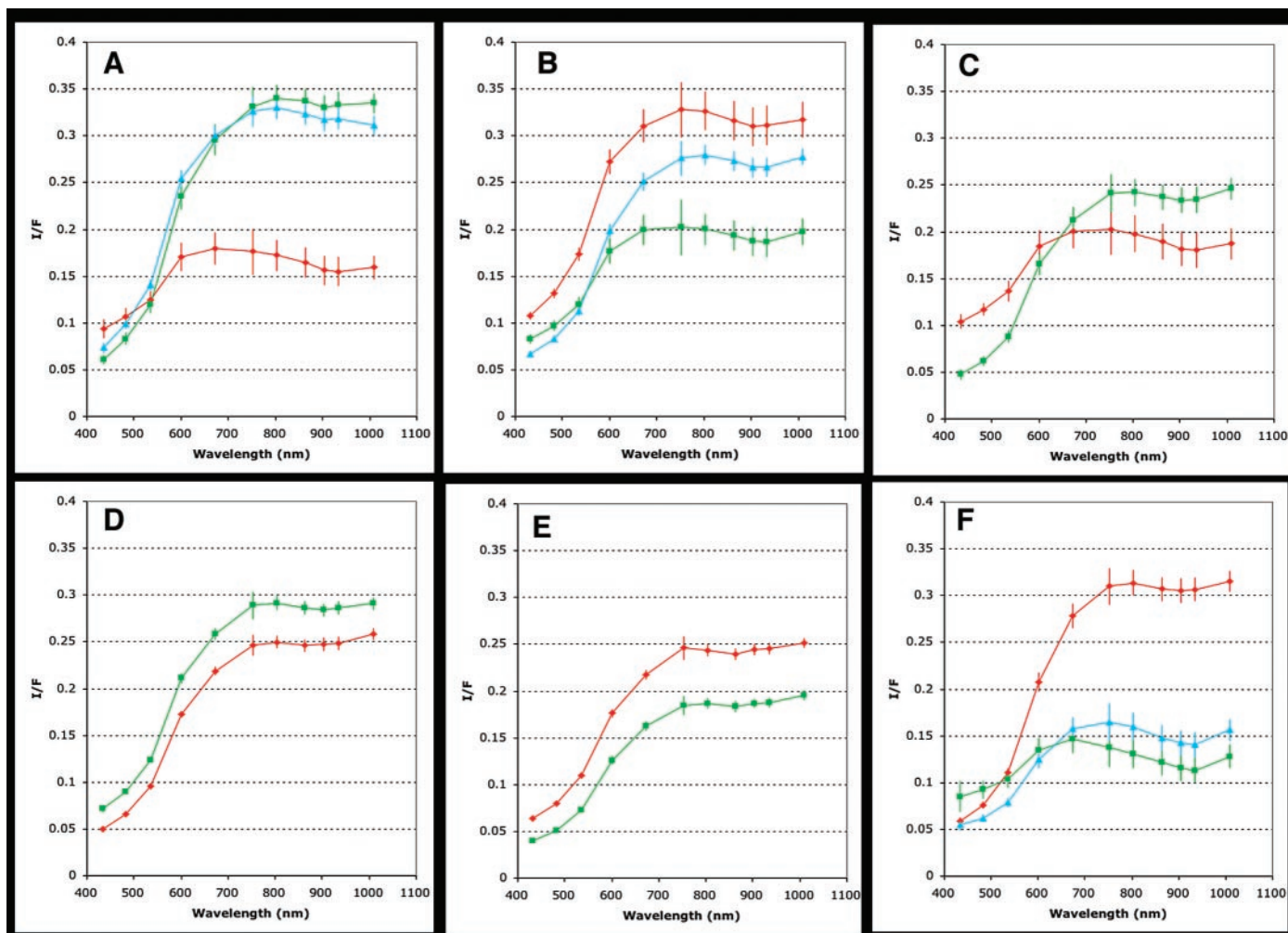


**Fig. 6.** Thirteen-filter Pancam spectra showing the range of spectral diversity seen within rocks and soils at the Gusev site. Each colored spectrum comes from the region of interest of the same

color in the corresponding frame of Fig. 5. No corrections for local topography effects (incidence angle variations) are included in these spectra.

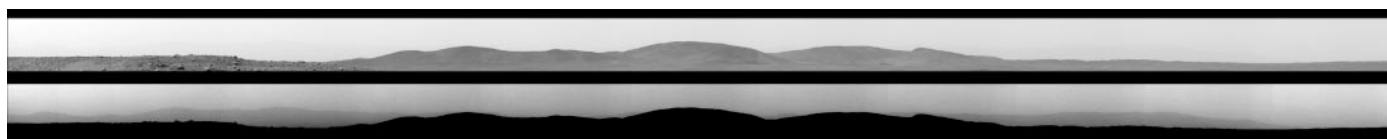


**Fig. 7.** Pancam panorama from sol 85, sequence P2365, blue filter (430 nm). (Top) The Columbia Hills are prominent “foreground” objects ~3 km from the rover. (Bottom) With a harsher contrast enhancement, the rim of Gusev crater, ~80 km from the rover, can be seen in the distance.



Pancam images and spectra of soils that were disturbed by the airbags or during trenching activities (Figs. 5F and 6F and Plate 7) reveal low-albedo materials that have more in common spectrally with dark

rock surfaces than with dark soils. Specifically, the lower albedo, lower red/blue ratio, stronger near-IR spectral slope, and deeper near-IR absorption feature are consistent with a lower  $\text{Fe}^{3+}/\text{Fe}^{2+}$  ratio in the

disturbed soils relative to undisturbed soils. The Pancam spectral data from the trench that was dug in Laguna Hollow (19) (Plate 7) show that the uppermost more oxidized (ferric iron-rich) layer of the soil in the hollow is quite thin, because this dust-like spectral signature is not seen in the spectra of the walls or the floor of the trench. This result is also consistent with Mössbauer spectra of the trench (34, 35), which showed the surface soils to be more oxidized than the trench interior. The dusty soils may have an even higher  $\text{Fe}^{3+}/\text{Fe}^{2+}$  ratio than inferred from the Mössbauer data, because the surface observed by Pancam (the upper few micrometers of the surface) is much thinner than the Mössbauer penetration depth.

Three of the rocks that were studied in detail with the in situ instruments included a small two-toned angular rock near the lander named Adirondack (Plate 9), a large partly dust-covered rock halfway along the traverse to Bonneville named Humphrey (Plate 10), and a long but low-lying light-toned rock named Mazatzal along the traverse near the rim of Bonneville (Plate 11). Pancam images of these rocks were used to select MI, Mössbauer,  $\alpha$  particle x-ray spectrometer (APXS), and Rock Abrasion Tool (RAT) target regions on the basis of both morphologic and color considerations. Brushing and grinding into each of these rocks removed the bright red dust covering and any light-toned coatings and revealed their intrinsic gray color and near-IR spectral properties to be consistent with the presence of ferrous iron minerals such as pyroxene, olivine, and magnetite (19, 28). The Pancam data on these freshly exposed rock interiors are consistent with the APXS, Mössbauer, and Mini-TES results, which indicate that these rocks are all olivine-bearing basalts (28, 33, 35) and that the light-toned veins seen in MI images of freshly exposed rock interiors are not simply fractures filled with reddish dust (Plates 12 and 13).

**Atmospheric and astronomical observations.** Daily (or many times daily) images of the Sun were obtained with the use of 440-nm and 880-nm neutral density filters in order to derive and monitor atmospheric dust opacity. The visible wavelength dust opacity at the start of the mission was  $\sim 0.9$ , a relatively high value that was likely related to enhanced global-scale dust storm activity that occurred during November and December 2003. By sol 90, the opacity had fallen to  $\sim 0.5$  (10, 36). The atmosphere had cleared enough by sol 85 to allow Pancam imaging of the walls of Gusev crater, some 80 km from the landing site (Fig. 7). Time-lapse observations of sunrise and sunset were also acquired in order to



**Fig. 8.** Navcam presunrise image of the eastern horizon and sky, acquired at 04:47 LST on sol 63, with an overlaid Pancam image of the Earth acquired a few minutes later with the use of the broadband L1 filter. The Earth is the faint "star" in the center of the frame.

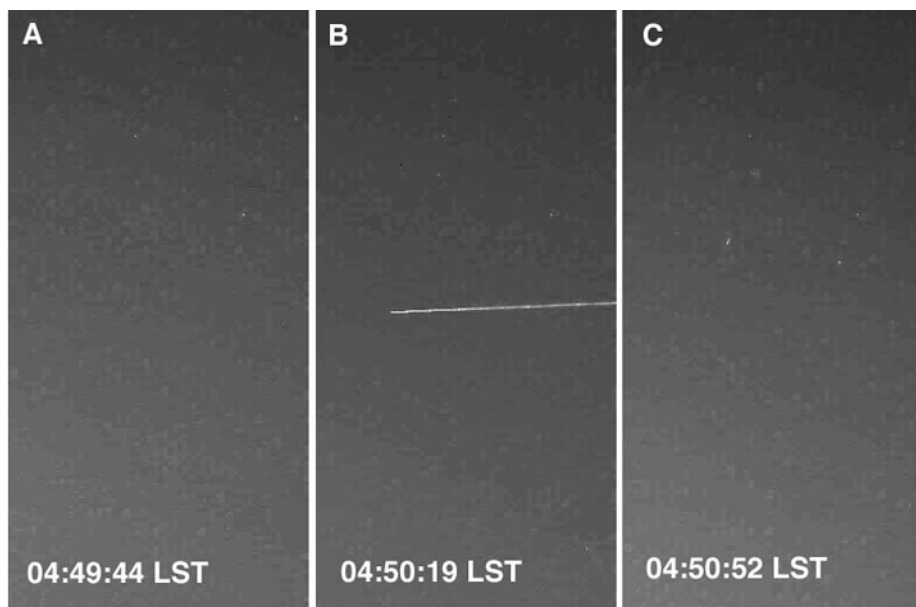
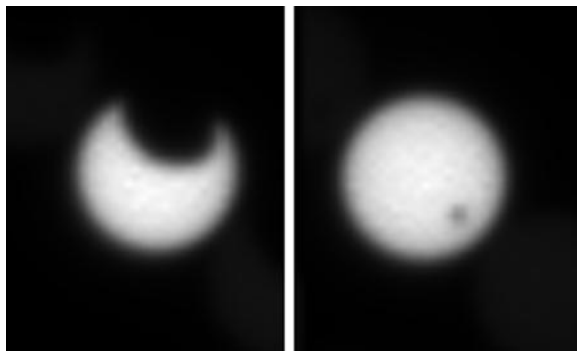


**Fig. 9.** Three sequential raw Pancam images acquired as part of the Earth-imaging sequence on sol 63. (A) Image 2P131930902ESF1300P2733L4M1, acquired at 04:49:44 LST. (B) Image 2P131930937ESF1300P2733L5M1, acquired at 04:50:19 LST and showing an anomalously bright streak that may be a meteor trail. (C) Image 2P131930972ESF1300P2733L6M1, acquired at 04:50:52 LST. All three images were pointed at the same region of the sky and had an exposure time of 15 s.

**Fig. 10.** Pancam solar filter images of Phobos and Deimos in midtransit. (Left) Phobos event observed on sol 104 (18 April 2004); (right) Deimos event observed on sol 68 (13 March 2004).



derive and monitor the vertical extent of dust in the atmosphere and to search for evidence of morning or evening twilight water ice clouds that are expected to begin forming as southern fall transitions into winter (37). During one of the cloud search sequences on sol 63, the Earth was observed in the presunrise twilight sky (Fig. 8). During that same imaging sequence, a long, anomalously bright streak was observed in one long-exposure Pancam image (Fig. 9). The streak's orientation is not consistent with the known or inferred paths of any Mars-orbiting spacecraft except perhaps Viking Orbiter 2, and thus the streak may represent a lucky observation of a meteor trail (38). Daytime sky observations and nighttime astronomical observations of stars and Deimos were acquired to search for evidence of clouds. As of the end of the primary mission (areocentric longitude of the Sun  $\sim 15^\circ$ , corresponding to early southern hemisphere autumn), no unambiguous clouds were detected at the landing site in Gusev, nor had any dust devils been detected either in dedicated dust devil search sequences or in serendipitous horizon imaging.

Lastly, Spirit's near-equatorial landing latitude made it possible to observe solar transits by the martian moons. Two transits were captured by Pancam from the Gusev site: one set of images of Deimos passing across the solar disk on sol 68 and one grazing Phobos transit event on sol 104 (Fig. 10) (39). Discrepancies between the predicted transit contact times and phase angles and those that were observed are being used to

update the orbital ephemeris parameters of both satellites (neither of which have been carefully monitored in decades) (40). These calculations will provide dynamical information on the satellites' orbital evolutions as well as increased accuracy for future spacecraft imaging of the moons (42).

#### References and Notes

- M. P. Golombek *et al.*, *J. Geophys. Res.* **108**, 10.1029/2003JE002074 (2003).
- N. Cabrol *et al.*, *J. Geophys. Res.* **108**, 10.1029/2002JE002026 (2003).
- J. F. Bell III *et al.*, *J. Geophys. Res.* **108**, 10.1029/2003JE002070 (2003).
- J. N. Maki *et al.*, *J. Geophys. Res.* **108**, 10.1029/2003JE002077 (2003).
- M. E. Ockert-Bell *et al.*, *J. Geophys. Res.* **102**, 9039 (1997).
- J. F. Bell III *et al.*, *J. Geophys. Res.* **105**, 1721 (2000).
- J. R. Johnson *et al.*, *Icarus* **163**, 330 (2003).
- P. Bertelsen *et al.*, *Science* **305**, 827 (2004).
- M. T. Lemmon, personal communication.
- M. J. Wolff, Athena Science Team, *Proc. Lunar Planet. Sci.* **XXXV**, abstr. 2171 (2004) [CD].
- A martian solar day has a mean period of 24 hours 39 min 35.244 s and is referred to as a sol to distinguish this from a roughly 3%-shorter solar day on Earth. A martian sidereal day, as measured with respect to the fixed stars, is 24 hours 37 min 22.663 s, as compared with 23 hours 56 min 04.0905 s for Earth. See <http://www.giss.nasa.gov/tools/mars24/> for more information.
- Names have been assigned to areographic features by the Mars Exploration Rover (MER) team for planning and operations purposes. The names are not formally recognized by the International Astronomical Union.
- J. A. Grant *et al.*, *Science* **305**, 807 (2004).
- M. Golombek *et al.*, *Lunar Planet. Sci.* **XXXV**, abstr. 2185 (2004) [CD].
- M. C. Malin, Athena Science Team, *Lunar Planet. Sci.* **XXXV**, abstr. 2170 (2004) [CD].
- The term martian soil is used here to denote any loose unconsolidated materials that can be distinguished from rocks, bedrock, or strongly cohesive sediments. No implication of the presence or absence

of organic materials or living matter is intended [see, for example, (6)].

- R. Greeley *et al.*, *Science* **305**, 810 (2004).
- K. E. Herkenhoff *et al.*, *Science* **305**, 824 (2004).
- R. E. Arvidson *et al.*, *Science* **305**, 821 (2004).
- An estimated albedo is derived by dividing the *I/F* determined from observations calibrated with the onboard calibration target by the cosine of the solar elevation angle at the time of each observation. This albedo estimate should be comparable to the bolometric Lambert albedo values derived from orbital observations.
- B. Hapke, *Theory of Reflectance and Emittance Spectroscopy* (Cambridge Univ. Press, New York, 1993).
- J. R. Johnson *et al.*, *J. Geophys. Res.* **104**, 8809 (1999).
- T. B. McCord *et al.*, *J. Geophys. Res.* **87**, 3021 (1982).
- J. F. Bell III *et al.*, *J. Geophys. Res.* **102**, 9109 (1997).
- R. V. Morris *et al.*, *J. Geophys. Res.* **94**, 2760 (1989).
- R. V. Morris *et al.*, *J. Geophys. Res.* **105**, 1757 (2000).
- M. B. Madsen *et al.*, *J. Geophys. Res.* **108**, 10.1029/2002JE002029 (2003).
- H. Y. McSween *et al.*, *Science* **305**, 842 (2004).
- Both pyroxene and olivine exhibit broad  $\text{Fe}^{2+}$  absorption bands centered near 900 to 1100 nm [e.g., (30, 37)], but because the long-wavelength sides of these bands are typically beyond the spectral range of silicon CCD detectors, it is usually not possible to uniquely identify the specific  $\text{Fe}^{2+}$ -bearing phases responsible for reflectance decreases observed in the longest-wavelength filters of instruments such as Pancam.
- J. B. Adams, *J. Geophys. Res.* **79**, 4829 (1974).
- E. A. Cloutis *et al.*, *J. Geophys. Res.* **91**, 11641 (1986).
- X. McSween *et al.*, *J. Geophys. Res.* **104**, 8679 (1999).
- J. F. Bell III *et al.*, *Icarus* **158**, 56 (2002).
- G. Klingelhöfer *et al.*, *Lunar Planet. Sci.* **XXXV**, abstr. 2184 (2004) [CD].
- R. V. Morris *et al.*, *Science* **305**, 833 (2004).
- M. Lemmon *et al.*, in preparation.
- For example, M. J. Wolff *et al.*, *J. Geophys. Res.* **104**, 9027 (1999).
- Meteor showers have been predicted to occur on Mars, e.g., (41).
- J. F. Bell III, M. Lemmon, M. Wolff, *Transits of Mars I and II* (IAU Circular 8298, 8 March 2004).
- J. F. Bell III *et al.*, in preparation.
- F. Selsis *et al.*, *Astron. Astrophys.* **416**, 783 (2004).
- We extend our sincere gratitude to the many hundreds of people who have contributed to the success of the Pancam investigation. These include the many MER engineers, managers, and support staffers at JPL; engineers and researchers at many vendor organizations; students and support staff at Cornell University, U.S. Geological Survey Flagstaff, Washington University, and other institutions; image processing and visualization experts at JPL and NASA Ames Research Center; and many of the co-investigators, collaborators, and associates on the Athena Science Team. The authors also extend special thanks to our families and loved ones for their patience and support during mission operations and throughout the many years leading up to Spirit's spectacular travels on Mars.

#### Plates Referenced in Article

[www.sciencemag.org/cgi/content/full/305/5685/800/DC1](http://www.sciencemag.org/cgi/content/full/305/5685/800/DC1)

Plates 1 to 4 and 7 to 10

1 May 2004; accepted 16 July 2004



# Surficial Deposits at Gusev Crater Along Spirit Rover Traverses

J. A. Grant,<sup>1\*</sup> R. Arvidson,<sup>2</sup> J. F. Bell III,<sup>3</sup> N. A. Cabrol,<sup>4</sup> M. H. Carr,<sup>5</sup> P. Christensen,<sup>6</sup> L. Crumpler,<sup>7</sup> D. J. Des Marais,<sup>8</sup> B. L. Ehlmann,<sup>2</sup> J. Farmer,<sup>6</sup> M. Golombek,<sup>9</sup> F. D. Grant,<sup>6</sup> R. Greeley,<sup>6</sup> K. Herkenhoff,<sup>10</sup> R. Li,<sup>11</sup> H. Y. McSween,<sup>12</sup> D. W. Ming,<sup>13</sup> J. Moersch,<sup>12</sup> J. W. Rice Jr.,<sup>6</sup> S. Ruff,<sup>6</sup> L. Richter,<sup>14</sup> S. Squyres,<sup>3</sup> R. Sullivan,<sup>3</sup> C. Weitz<sup>15</sup>

The Mars Exploration Rover Spirit has traversed a fairly flat, rock-strewn terrain whose surface is shaped primarily by impact events, although some of the landscape has been altered by eolian processes. Impacts ejected basaltic rocks that probably were part of locally formed lava flows from at least 10 meters depth. Some rocks have been textured and/or partially buried by windblown sediments less than 2 millimeters in diameter that concentrate within shallow, partially filled, circular impact depressions referred to as hollows. The terrain traversed during the 90-sol (martian solar day) nominal mission shows no evidence for an ancient lake in Gusev crater.

Gusev crater is 160 km in diameter, is of Noachian age, and lies at the terminus of the 900-km-long branching Ma'adim Vallis. The crater is partially filled by Hesperian-aged materials (1) and was selected as the landing site for the Mars Exploration Rover Spirit to search for evidence of previous liquid water flow and/or ponding that may be responsible for the crater infilling (1–8).

Landing occurred on a generally flat plain (14.5692°S, 175.4729°E) characterized by approximately circular, shallow depressions <20 m in diameter [hollows (9)] (Fig. 1A) and poorly defined ridges up to hundreds of meters long and a few meters high (Plate 1). The 210-m diameter Bonneville crater (9) is ~300 m northeast of the lander, and surface albedo increases from ~0.19 to ~0.26 to-

ward its rim as a result of increased dust mantling (10). Bonneville and its ejecta deposits comprised the primary exploration targets along the 506-m traverse during the nominal mission reported here.

The largest rocks within 20 m of the lander are <0.5 m in diameter, smaller than the largest rocks at the three previous Mars landing sites (11, 12). Rocks >1 cm cover about 5% of the surface, and the area covered by fragments >10 cm is ~50% of the total rock-covered area (12). The size-frequency distribution of rocks >1 cm generally follows the exponential model distribution based on the Viking Lander and Mars Pathfinder landing sites for 5% rock abundance (1, 11).

Most rocks >1 cm are angular (13) and of variable sphericity (13), and almost none display obvious rounding (14). The majority of rocks are intrinsically dark gray in color, but some exhibit variable dust coverings and possibly associated weathering coatings or rinds that impart a light-toned and/or reddish color, especially apparent on the lowermost 5 to 15 cm of their surfaces (10–12, 15, 16) (Plate 9). Bulk-rock compositions are consistent with picritic (olivine-rich) basalt (16).

Rocks >15 cm and within 20 m of the lander are mostly around hollows or near drift deposits, whereas they are largely absent within hollows (Fig. 1A). Rocks sitting exposed or perched on the surface are up to 10 times as numerous around the immediate exterior of hollows as elsewhere (Fig. 1A). Fractured and split rocks are also concentrated around the hollows, but lighter toned (redder) rocks are often closer to eolian drifts. Faceted rocks are five to eight times as abundant away from hollows (Fig. 1B) and are likely the result of wind erosion (15).

There are six times as many rock fragments <4 cm in diameter per m<sup>2</sup> as at the

Pathfinder landing site and 36 times as many per m<sup>2</sup> as at either of the Viking Landers (17). Rocks <2 mm comprise regolith and local drift deposits covering much of the surface. These fine sediments are characterized by bimodal size distributions having modes between 1 and 2 mm in diameter and less than about 0.5 mm in diameter (18). The coarser 1- to 2-mm grains are often rounded (14), perhaps the result of abrasion during transport. Grains <0.2 mm in diameter comprise about 30% of the samples, are typically basaltic in composition and devoid of clays and aqueous weathering products (16), but are too small to be characterized more completely (18).

The largest rocks within 10 m of the traverse to Bonneville's rim increased by a factor of five to at least 2.5 m in diameter across the crater's outer discontinuous ejecta (where the deposit incompletely buries the preimpact surface) and more proximal continuous ejecta (where the deposit completely buries the preimpact surface), which starts about 205 m and 175 m from the rim, respectively (Fig. 2). Partial burial of some of the largest rocks along Bonneville's rim precludes accurate measure of their maximum diameter, but those that are visible confirm an exponential increase in number with decreasing size. By contrast, the average size of rocks <10 to 15 cm increases by a factor of less than two, from 1.75 to 2.95 cm, along the traverse while their relative sorting decreases (Table 1).

The rim of Bonneville crater (Plates 3 and 5) rises 6.4 m above the surrounding plain, and the crater averages 10 m deep, with a maximum floor-to-rim-crest relief of 14 m. Wall slopes measured along 32 evenly spaced lines by using two different stereo panoramas average 11°, with a range between 6° and 16°. Although a cover of eolian drift mantles the crater floor and portions of the walls (10, 15), rocks poking up through the drift in a few locations suggest that most of the deposits are relatively thin (less than a meter or two thick). Crater walls are locally steepest and convex along the southeast wall, where some of the largest boulders protrude and where several small craters (12 to 15 m in diameter) excavated the eastern wall.

Several lines of evidence suggest that Bonneville was formed into unconsolidated

<sup>1</sup>Center for Earth and Planetary Studies, National Air and Space Museum, Smithsonian Institution, Washington, DC 20560, USA. <sup>2</sup>Department of Earth and Planetary Sciences, Washington University, St. Louis, MO 63130, USA. <sup>3</sup>Department of Astronomy, Space Sciences Building, Cornell University, Ithaca, NY 14853, USA. <sup>4</sup>NASA Ames/SETI Institute, Space Science Division, MS 245-3, Moffett Field, CA 94035, USA. <sup>5</sup>U.S. Geological Survey, 345 Middlefield Road, Menlo Park, CA 94025, USA. <sup>6</sup>Department of Geological Sciences, Arizona State University, Tempe, AZ 85287, USA. <sup>7</sup>New Mexico Museum of Natural History and Science, 1801 Mountain Road NW, Albuquerque, NM 87104, USA. <sup>8</sup>NASA Ames Research Center, Moffett Field, CA 94035, USA. <sup>9</sup>Jet Propulsion Laboratory, California Institute of Technology, Pasadena, CA 91109, USA. <sup>10</sup>U.S. Geological Survey, Flagstaff, AZ 86001, USA. <sup>11</sup>Department of Civil and Environmental Engineering and Geodetic Science, Ohio State University, Columbus, OH 43210, USA. <sup>12</sup>Department of Earth and Planetary Sciences, University of Tennessee, Knoxville, TN 37996, USA. <sup>13</sup>NASA Johnson Space Center, Houston, TX 77058, USA. <sup>14</sup>DLR Institute of Space Simulation, Linder Hoehe, D-51170, Cologne, Germany. <sup>15</sup>NASA Headquarters, 300 E Street S.W., Washington, DC 20560, USA.

\*To whom correspondence should be addressed. E-mail: grantj@nasm.si.edu

**Table 1.** Small rock size and sorting. Rocks <10 to 15 cm per m<sup>2</sup>, sorting based on comparison of measured variance.

Location*	Average long axis (cm)	Variance (cm)
Spirit landing site	1.75	0.99
Bonneville discontinuous ejecta	1.96	1.68
Bonneville continuous ejecta	2.95	1.91

\*Measured in 1 m<sup>2</sup> grids with standardized Pancam and end-of-drive clast surveys.

blocky debris. First, the low wall slopes indicate that coherent strata did not impede slumping during final stages of crater formation. Second, the largest rocks appear jumbled and reflect local transport after disruption of rocks up to 6 m in diameter during the late stages of crater formation (19). Third, the small craters formed into the eastern wall of Bonneville do not expose bedrock. Finally, the sharp contrast between Bonneville's ejecta deposits (Fig. 2) and surfaces beyond the ejecta (e.g., surrounding the lander) indicate that surfaces of the crater facies remain relatively pristine and are not mantled by younger debris that might mask detection of bedrock in the crater walls. We conclude that the crater formed largely in loose rubble but that the largest observed ejecta blocks may be derived from locally more competent rocks (e.g., a lava flow).

Despite shallow wall slopes relative to many pristine primary craters (20), the absence of debris chutes and subjacent talus at their base and uniformly distributed rocks on the walls imply that there has been little modification of the walls by mass wasting. In addition, relatively drift-free sections of the walls (Plates 3 and 5) retain low slopes, which demonstrates that eolian infilling is not responsible for masking steeper walls. Instead, the well-preserved character and low depth-to-diameter ratio of  $\sim 0.07$  suggests that Bonneville crater experienced meters or less of erosion and may have formed during a secondary cratering event (21).

Hollow morphology and sizes (Fig. 3) argue for an impact origin. Their spatial distribution across most surfaces is random [figure 1A in (22)] and characterized by a population that increases exponentially from 20 m down to less than 1 m (Fig. 3), consistent with that expected for small craters (23–25). Hollows have fairly uniform morphology, and the increased perched, fractured, split, and sometimes radial distribution of rocks around their margins (Fig. 1C) is consistent with emplacement as ejecta. Although the number density of hollows decreases within about 100 m of the rim of Bonneville, their detection may be impeded by relief associated with the in-

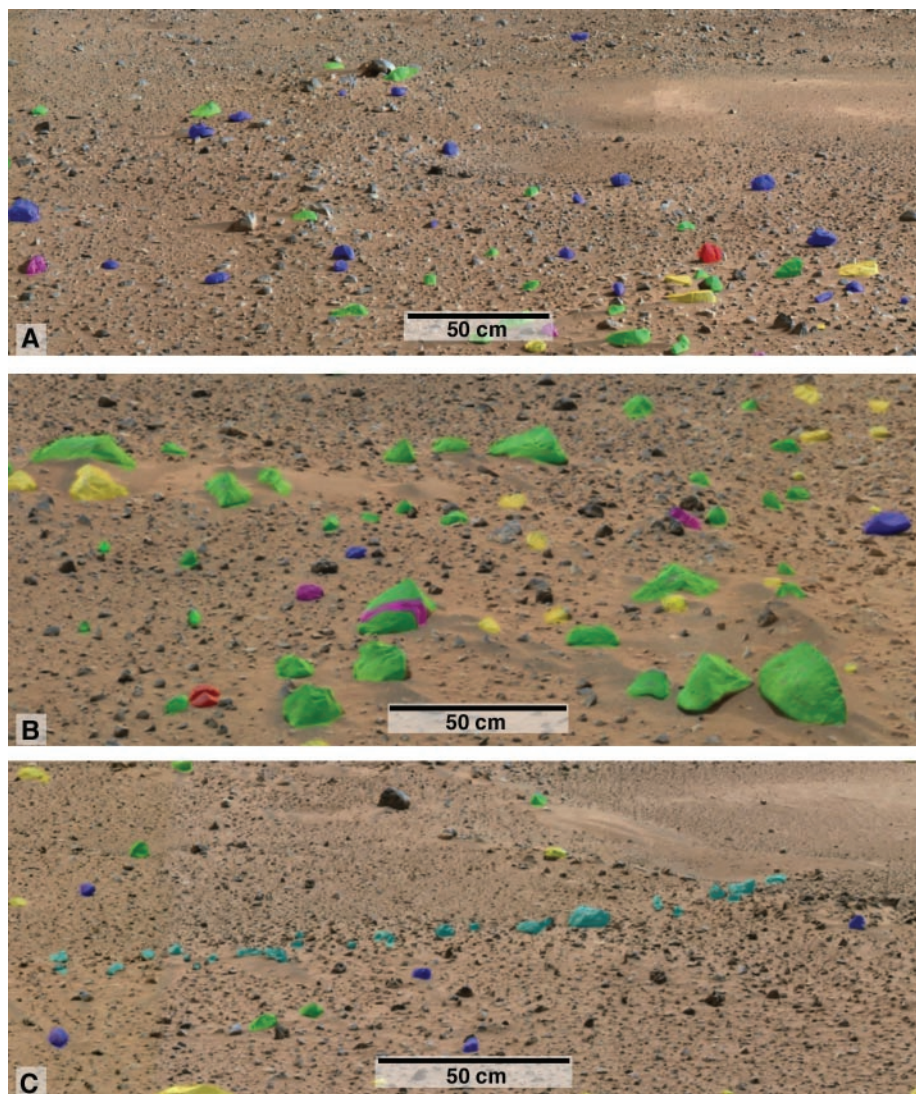


**Fig. 1.** Example rock types around the lander. (A) Perched (blue), split (red), and fractured (purple-pink) rocks are 2 to 10 times as numerous around hollows as elsewhere (azimuth shown is 160° to 195°). (B) Faceted (green) and light-toned (yellow) rocks are concentrated around drift, with faceted rocks five to eight times as numerous (azimuth shown is 70° to 95°). (C) Radial accumulation of blocks (light blue) around hollow (azimuth shown is 260° to 285°). Mapped on Pancam Mission Success panorama (mspan\_2X\_final-A1OR1\_br, approximate true color based on a scaling of 750-nm, 530-nm, and 480-nm filter data as RGB) (see Plate 1) and emphasized blocks >10 cm in diameter up to 20 m from the lander. Near-field scales are approximate.

creased number of rocks >50 cm. Increasing rock size and abundance near the rim of Bonneville likely creates a clast-supported substrate (20) that may be more difficult to excavate during small impacts and leads to limited expression of near-rim hollows. The pristine appearance of Bonneville's ejecta deposits, however, makes it unlikely that near-rim hollows were formed and completely removed by erosion.

Once formed, hollows are rapidly modified to their present form. Their excavation during an impact is accompanied by emplacement of a surrounding ejecta deposit with widely varying grain size and fractured rocks (19). Surface roughness across these landforms would be in disequilibrium

with the eolian regime (15), leading to deflation of ejected fines (fragments <2 mm in diameter), exposing fractured rocks, and creating a population of perched coarser fragments. At the same time, hollow interiors would be filled as transported fines are trapped within the depression. Trenching with Spirit's wheels in Laguna hollow near the edge of the Bonneville ejecta exposed unaltered basaltic fines (16, 22) capped by a thin layer of brighter, finer, globally pervasive dust. The absence of dust interbeds or any chemical signature of dust in sediment filling the hollows, coupled with their uniformly filled appearance, implies rapid modification to their current more stable form.



**Fig. 2.** Distal margin of Bonneville's ejecta deposit (black dashed line) from "Middle Ground" hollow. Mosaic of Pancam images 2P131526-662FFL1155P2437 and 2P131526768FFL115-5P2437 with the 430-nm blue filter.

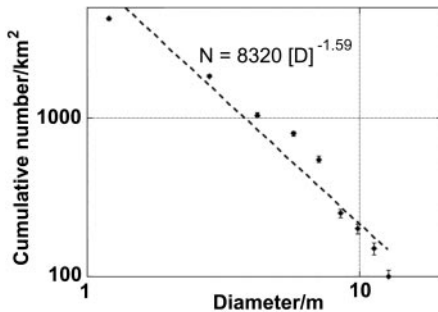


**Fig. 3.** Hollow size-frequency distribution along the traverse to Bonneville crater. Hollows are plotted in square root of 2 bins for the size range 20 m down to 1 m and reported as the number per km<sup>2</sup>. Includes 85 hollows >0.02 km<sup>2</sup>.

Surficial deposits created by impact and eolian processes are recognized in Gusev crater. Impact craters and associated ejecta deposits dominate the landscape and account for disruption of the upper ~10 m of the volcanic subsurface. The predominant role played by cratering processes in shaping the surface landforms is underscored by the impact origin of the hollows.

The shape, size, and clearly defined distribution of ejecta blocks >20 cm around Bonneville is generally consistent with observations around pristine terrestrial craters (20, 26). Minor differences between observed rock populations and that expected from a single impact event are likely the result of comminution during multiple impacts that mix dark gray and lighter toned (presumably coated and/or more weathered) rocks (10, 16, 27). Although the hollows are modified, their diameters and associated implied depths (21) suggest meters or less of infilling. Some local redistribution of

rocks <10 cm and/or winnowing of fines to form pavements [figure 4 in (28)] may account for lesser along-traverse variation in these size fragments but is also consistent with only meters of gradation at most. Hence, relief on the plains appears to be created by rubble accumulated in the aftermath of multiple impact events, and morphology diagnostic of nonimpact processes is not preserved.

All of the surficial deposits are basaltic, and their uniform composition (16) argues for a local volcanic source. If the rocks at the landing site were delivered by large impacts outside of Gusev or alluvial transport out of the Ma'adim Vallis watershed [which exceeds 200,000 km<sup>2</sup> along the main channel alone (7)], they would sample a range of terrains and have variable chemistry (at least in trace elements), which is not seen. Moreover, the size, poor sorting, and rounding of the largest rocks makes their arrival as alluvium from Ma'adim Vallis unlikely. Estimated discharge (29) and derived flow velocity (30) for Ma'adim Vallis indicate that rocks >1 m could not have been transported tens of kilometers to the landing site by clear water or hyperconcentrated flows. Finally, it is unlikely that the numerous rocks larger than 1 to 2 m could be ejecta coming from outside of Gusev, because they would not survive ballistic sedimentation (19). While no obvious fissure or other volcanic edifice is visible on the floor of Gusev crater, plains to the northeast have been interpreted as volcanics (31) that may have extended into the landing region but were broken up during subsequent impacts.

Local eolian deposits are inactive in the current setting (15). Although past eolian activity must have accounted for drift migration, formation of numerous faceted rocks, and infilling of hollows, and is another means

of creating light-toned rocks (15), the local distribution of eolian deposits indicates that eolian processes are subordinate to impact processes in shaping the surface.

While conclusive evidence for ancient water-lain deposits in Gusev remains elusive, the volcanic materials and subsequent action of impact and eolian processes may mask their signature across terrains traversed during the nominal mission. Nevertheless, the preservation of the landscape is testament to the minimal gradation occurring since Hesperian times in Gusev that may be roughly comparable to post-Hesperian gradation affecting the Mars Pathfinder landing site (32).

#### References and Notes

1. M. P. Golombek *et al.*, *J. Geophys. Res.* **108**, 8072 (2003).
2. J. A. Grant *et al.*, *Planet. Space Sci.* **52**, 11 (2004).
3. N. A. Cabrol, E. A. Grin, G. Dawidowicz, *Icarus* **123**, 269 (1996).
4. N. A. Cabrol, E. A. Grin, R. Landheim, *Icarus* **132**, 362 (1998).
5. N. A. Cabrol, E. A. Grin, R. Landheim, R. O. Kuzmin, R. Greeley, *Icarus* **133**, (1998).
6. R. O. Kuzmin, R. Greeley, R. Landheim, N. A. Cabrol, J. Farmer, *U.S. Geol. Surv., Misc. Geol. Invest. Map I-2666* (2000).
7. R. P. Irwin, T. A. Maxwell, A. D. Howard, R. A. Craddock, D. W. Leverington, *Science* **296**, 2209 (2002).
8. J. W. Rice Jr. *et al.*, *Lunar Planet. Sci.* [CD-ROM], abstract 2091 (2003).
9. Names have been assigned to areographic features by the Mars Exploration Rover (MER) team for planning and operations purposes. The names are not formally recognized by the International Astronomical Union.
10. J. F. Bell III *et al.*, *Science* **305**, 800 (2004).
11. M. P. Golombek, D. Rapp, *J. Geophys. Res.* **102**, 4117 (1997).
12. M. P. Golombek *et al.*, *J. Geophys. Res.* **108**, 8086 (2003).
13. M. R. Leeder, *Sedimentology*, George Allen and Unwin Ltd. (London, 1982).

14. R. L. Folk, *Petrology of Sedimentary Rocks*, Hemphill Publishing (Austin, TX, 1980).
15. R. Greeley *et al.*, *Science* **305**, 810 (2004).
16. H. Y. McSween *et al.*, *Science* **305**, 842 (2004).
17. M. P. Golombek *et al.*, *Lunar Planet. Sci.* [CD-ROM], abstract 2185 (2004).
18. K. E. Herkenhoff *et al.*, *Science* **305**, 824 (2004).
19. H. J. Melosh, *Impact Cratering*, Oxford Univ. Press (New York, 1989).
20. J. A. Grant, P. H. Shultz, *J. Geophys. Res.* **98**, 11025 (1993).
21. M. Hurst, M. P. Golombek, R. Kirk, *Lunar Planet. Sci.* [CD-ROM], abstract 2068 (2004).
22. R. E. Arvidson *et al.*, *Science* **305**, 821 (2004).
23. W. K. Hartmann, J. Anguita, M. A. de la Casa, D. C. Berman, E. V. Ryan, *Icarus* **149**, 37 (2001).
24. W. K. Hartmann *et al.*, *Nature* **397**, 586 (1999).
25. F. Horz, M. J. Cintala, W. C. Rochelle, B. Kirk, *Science* **285**, 2105 (1999).
26. J. A. Grant, P. H. Shultz, *J. Geophys. Res.* **98**, 15033 (1993).
27. P. R. Christensen *et al.*, *Science* **305**, 837 (2004).
28. S. W. Squyres *et al.*, *Science* **305**, 794 (2004).
29. R. P. Irwin, A. D. Howard, T. A. Maxwell, *Lunar Planet. Sci.* [CD-ROM], abstract 1852 (2004).
30. G. Komatsu, V. R. Baker, *J. Geophys. Res.* **102**, 4151 (1997).
31. K. A. Milam *et al.*, *J. Geophys. Res.* **108**, 8078 (2003).
32. M. P. Golombek, N. T. Bridges, *J. Geophys. Res.* **105**, 1841 (2000).
33. Research was supported by NASA through the Mars Exploration Rover Project. Our sincere thanks go to the Mars Exploration Rover management, staff, and engineering teams for their outstanding support and operation of Spirit.

## Plates Referenced in Article

www.sciencemag.org/cgi/content/full/305/5685/807/DC1

Plates 1, 3, 5, and 9

3 May 2004; accepted 28 June 2004

## REPORT

# Wind-Related Processes Detected by the Spirit Rover at Gusev Crater, Mars

R. Greeley,<sup>1</sup> S. W. Squyres,<sup>2</sup> R. E. Arvidson,<sup>3</sup> P. Bartlett,<sup>4</sup> J. F. Bell III,<sup>2</sup> D. Blaney,<sup>5</sup> N. A. Cabrol,<sup>6</sup> J. Farmer,<sup>1</sup> B. Farrand,<sup>7</sup> M. P. Golombek,<sup>5</sup> S. P. Gorevan,<sup>4</sup> J. A. Grant,<sup>8</sup> A. F. C. Haldemann,<sup>5</sup> K. E. Herkenhoff,<sup>9</sup> J. Johnson,<sup>9</sup> G. Landis,<sup>5</sup> M. B. Madsen,<sup>10</sup> S. M. McLennan,<sup>11</sup> J. Moersch,<sup>12</sup> J. W. Rice Jr.,<sup>1</sup> L. Richter,<sup>13</sup> S. Ruff,<sup>1</sup> R. J. Sullivan,<sup>2</sup> S. D. Thompson,<sup>1</sup> A. Wang,<sup>3</sup> C. M. Weitz,<sup>14</sup> P. Whelley,<sup>1</sup> Athena Science Team

Wind-abraded rocks, ripples, drifts, and other deposits of windblown sediments are seen at the Columbia Memorial Station where the Spirit rover landed. Orientations of these features suggest formative winds from the north-northwest, consistent with predictions from atmospheric models of afternoon winds in Gusev Crater. Cuttings from the rover Rock Abrasion Tool are asymmetrically distributed toward the south-southeast, suggesting active winds from the north-northwest at the time (midday) of the abrasion operations. Characteristics of some rocks, such as a two-toned appearance, suggest that they were possibly buried and exhumed on the order of 5 to 60 centimeters by wind deflation, depending on location.

In the current environment of Mars, wind appears to be the most frequent agent of surface modification, resulting in albedo patterns that change on time scales as short as a few weeks (1). Abundant dune forms, mantles of wind-blown deposits, and wind-eroded features are seen from orbit in many parts of Mars, including the three previous sites where successful landings have occurred. Understanding the processes that form aeolian (wind-related) features provides insight into the evolution of the martian surface, including rates of erosion and deposition. The Mars Exploration Rover (MER) Spirit landed near the middle of Gusev Crater (2–5) in a relatively low-albedo zone (6) considered to be a track left by the passage of dust devils that removed bright dust to expose a relatively darker substrate (Fig. 1A). Comparison of orbital images taken of the same area from July 2003 to January 2004 show changes in the tracks, indicating that dust devils were recently active.

Here, we describe initial analyses of aeolian features during the first ~90 sols (7) of operation. Wind-related features include sediments (some of which are organized into bedforms such as ripples), wind-abraded features on rocks, eroded zones around rock

edges, and features generated by the rover during operations that suggest active winds.

The surface at Columbia Memorial Station consists of rocks, regolith, dark granules, and fine-grained material, including dust (8, 9). Patches of red regolith range in size from 0.5 m across to as large as 15 m across. Bonneville (10) crater and many of the small depressions, called hollows, are partly filled with regolith deposits. Light-toned material was inferred to be dust, the upper surfaces of some rocks, the rover solar panels, and the Panoramic Camera (Pancam) calibration target (11). Although dust grains are too small to be resolved by the Microscopic Imager (MI) (12), previous estimates suggest that martian dust is a few micrometers in diameter (13, 14).

An MI image of a regolith patch shows a bimodal size distribution of particles (Fig. 1B) that includes coarse (1 to 3 mm) grains and finer grains smaller than a few hundred micrometers in diameter. Although some coarse grains are subangular, most are rounded, suggesting erosion during transport. We propose that the dark coarse particles are lithic fragments on the basis of their basaltic composition (16, 17) and appearance in the MI images (18).

Aprons of granular debris occur as isolated patches on the regolith and around some rocks. For example, the rock Adirondack (2) has an encircling debris apron that extends 5 to 20 cm from the edge of the rock. The aprons consist of coarse grains that have spectral properties similar to those of Adirondack and the other basaltic rocks in the area (11, 19). Therefore, some of the more angular coarse-grained material is probably derived

<sup>1</sup>Department of Geological Sciences, Arizona State University, Box 871404, Tempe, AZ 85287-1404, USA. <sup>2</sup>Department of Astronomy, Cornell University, 428 Space Sciences Building, Ithaca, NY 14853-1301, USA. <sup>3</sup>Department of Earth and Planetary Sciences, Washington University, One Brookings Drive, St. Louis, MO 63031-4899, USA. <sup>4</sup>Honeybee Robotics, 204 Elizabeth Street, New York, NY 10012, USA. <sup>5</sup>Jet Propulsion Laboratory, 4800 Oak Grove Drive, Pasadena, CA 91109-8099, USA. <sup>6</sup>Ames Research Center, Moffett Field, CA 94035-1000, USA. <sup>7</sup>Space Science Institute, University of Colorado, Boulder, CO 80301, USA. <sup>8</sup>Center for Earth and Planetary Studies, National Air and Space Museum, Smithsonian Institution, Washington, DC 20560-0315, USA. <sup>9</sup>U.S. Geological Survey, 2255 North Gemini Drive, Flagstaff, AZ 86001-1698, USA. <sup>10</sup>Niels Bohr Institute for Astronomy, Physics, and Geophysics, Center for Planetary Science and Ørsted Laboratory, University of Copenhagen, Universitetsparken 5, DK-2100 Copenhagen, Denmark. <sup>11</sup>Department of Geosciences, State University of New York at Stony Brook, Stony Brook, NY 11794-2100, USA. <sup>12</sup>Department of Earth and Planetary Sciences, University of Tennessee, 1412 Circle Drive, Room 306, Knoxville, TN 37996, USA. <sup>13</sup>Deutsches Zentrum für Luft- und Raumfahrt (German Aerospace Center)—Institute of Space Simulation, Linder Hoene, D-51170 Cologne, Germany. <sup>14</sup>National Aeronautics and Space Administration (NASA) Headquarters, Washington, DC 20546-0001, USA.

\*To whom correspondence should be addressed. E-mail: Greeley@asu.edu



from physical weathering of rocks in the area, as suggested for the Mars Pathfinder (MPF) site on the basis of spectral properties (14). Although the dark regolith within Bonneville crater was not examined in situ, the regolith has similar aprons on its surface.

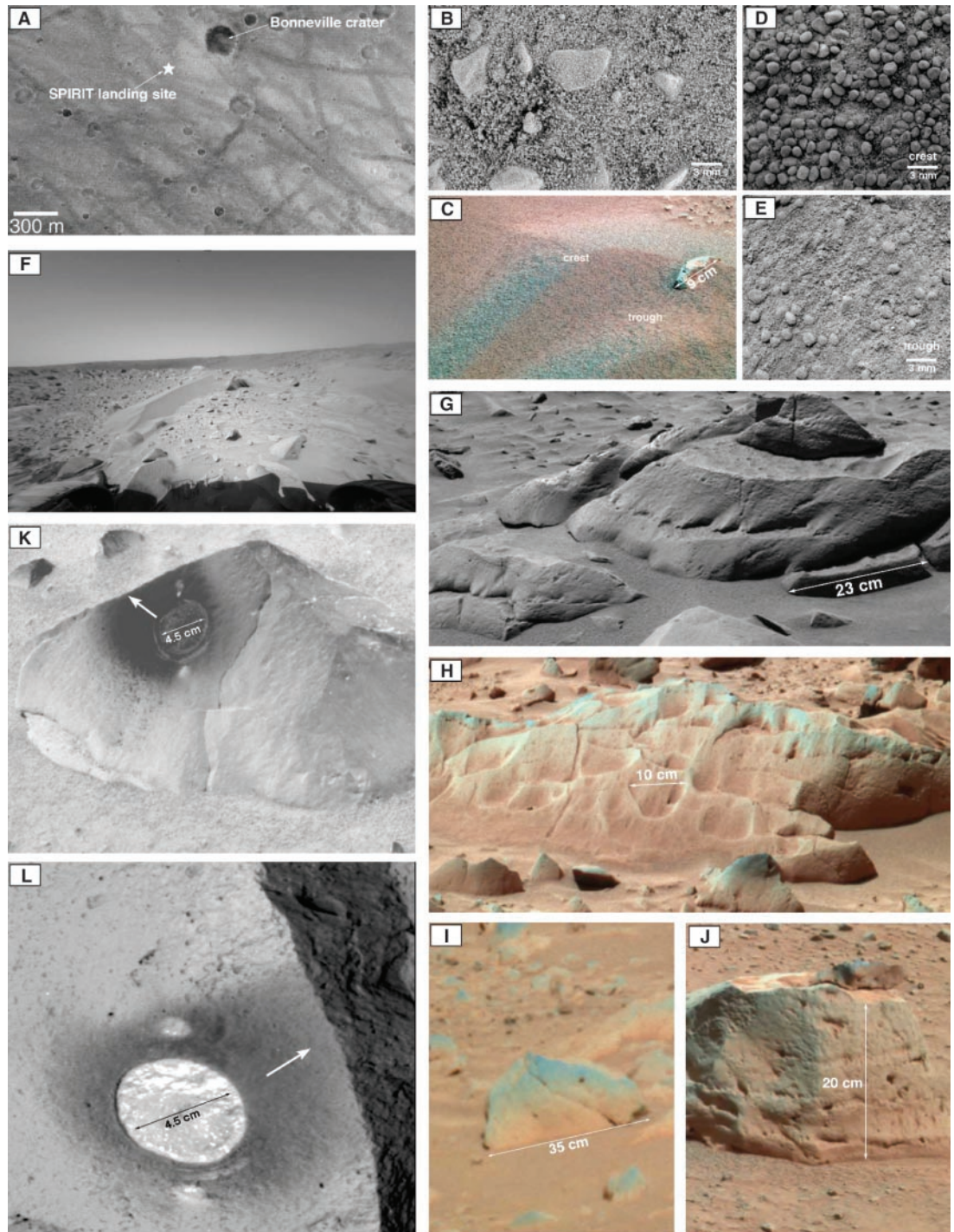
Bedforms are common at the site and range in size from 0.1 m long by 0.03 m wide by 0.02 m high to 10 m long by 2 m wide by 0.5 m high. They have wavelengths of 0.06 to 10 m,

with the larger bedforms having longer wavelengths. The larger bedforms are only seen within Bonneville crater and on the outer flanks of the crater and can be identified in orbital images. In cross section, most bedforms are slightly asymmetric, with the southeast sides being steeper and higher in albedo than the northwest sides. Thermal infrared spectral emissivity measurements (16) across meter-scale bedforms show asymmetry that correlates

with the visible-wavelength albedos. The higher albedo southeast slopes show a thermal infrared (IR) signature of dust that is equivalent to the globally homogeneous dust (20). Spectra of the lower-albedo northwest-facing slopes suggest the presence of materials compositionally similar to the rocks seen at the site and is attributed to the presence of particles similar to those composing the debris aprons.

MI images taken on one bedform named

**Fig. 1.** (A) Mars Orbiter Camera (MOC) image R12-01091. View of the Spirit site from orbit showing the Columbia Memorial Station (star) and the impact crater, Bonneville. The relative dark zones are tracks left by the passage of dust devils. One prominent track crosses Bonneville crater. (B) MI image, 2M130463156E00-900P2943M21, of regolith showing large, subangular granules set in smaller, sand-size grains. The spectral properties of the granules suggest that they are lithic fragments. (C) Pancam image, 2P129911125FFL0500-P2399L2M1, of the ripple, Arena. (D) MI image, 2M1-30001357E00F0506P2953M-2M1, of Arena crest, showing well-sorted rounded grains. (E) MI image, 2M130001-885E00F0506P2943M2M1, of Arena trough zone, showing poorly sorted grains. (F) Front Hazcam (Hazard Avoidance Camera) image, 2F132673895FFL1900P121-2L0M1, of Serpent, a 2-m bedform near the rim of Bonneville crater. (G) Pancam image, 2P131954281S-FL1300P2531L7M1, of Terrace rock with ventifact grooves originating from a common horizon. (H) Pancam image, 2P1331069-87SFL2200P2567L2M1, of Mazatzal rock, showing prominent ventifact grooves. (I) Pancam image, 2P134-272699FFL2500P2373L7M1, of two-toned rock. (J) Pancam image, 2P1299993-73FFL0506P2531R2M1, of Perched rock. (K) Pancam image, 2P129556193FFL03-29P2580L2M1, of Adirondack and (L) Pancam image, 2P131696760EEF1159P25-97L5M1, of Humphrey rock, showing the 4.5-cm areas abraded by the RAT and the distribution of the abraded cuttings (dark area) and the inferred wind direction (white arrow) at the time of abrasion.



Arena (Fig. 1, C, D, and E) show that the side with the lower slope (i.e., the windward side) has a crest that consists of a layer of well-sorted coarse particles (~1.8 mm in diameter) overlying finer grains, whereas the trough consists of a poorly sorted mixture of particles. These properties are characteristic of ripples on Earth (21, 22). Although only one bedform has been imaged to date by the MI on both its inferred windward and leeward sides, we conclude that the smaller bedforms seen at the Spirit site are ripples (22).

Some of the rocks have associated triangular-shaped deposits of regolith, similar to those seen at previous landing sites on Mars, termed wind tails. The wind tails tend to scale with the size of the rock with which they are associated, and at the MPF site the orientation of the tapered part of the wind tail is considered to point in the downwind direction (23, 24). However, unlike the MPF site, many of the drift deposits around the rocks at Gusev have a layer of coarse particles that form an armored surface, similar to the debris aprons described above.

The wheels on Spirit were used to dig into regolith deposits (9), which revealed the presence of a surface crust and poorly sorted particles. We suggest that the larger grains of debris aprons, drift deposits, and ripples have been concentrated on the surface as a lag through the winnowing action of the wind that has removed the finer sand and dust. The coarse grains on the ripple crests are further concentrated by saltation impact, typical of ripple formation on Earth. This winnowing can lead to size-sorted bedding structures.

We observed an increase in rock size and frequency around Bonneville crater, reflecting ejecta that was thrown out of the crater during an impact event (25). There is a corresponding increase in drift deposits around Bonneville (Fig. 1F), which we attribute to the increase in surface roughness. Although overall wind shear stress increases when wind encounters rougher terrain (26, 27), the fraction of the shear stress available for mobilizing particles decreases, reducing the surface flux of particles and leading to net deposition (28, 29). There is also an increase in the proportion of rocks for which the tops are dust-mantled. We attribute this to the rover traverse passing out of the recent dust devil track that cuts across the landing zone and into an area that has not been swept clean by a recent dust devil (Fig. 1A).

Many of the rocks at the Columbia Memorial Station have flat faces (facets) and/or grooves cut into their surfaces, giving them the appearance of wind-abraded rocks, or ventifacts. The facets form beveled surfaces inclined 20° to 70° from the horizontal. The grooves range in size from 2 to 50 cm long by 0.5 to 5 cm wide and occur on the facets and on irregular surfaces. Most of the facets and grooves are on the northwest sides of the rocks. Although they are similar in morphology to rocks seen at the MPF site (30), they are less common at the Spirit site.

Terrace rock (Fig. 1G) has a zone of ventifact grooves that originates at a horizon a few cm above the ground. A similar zone is seen on a smaller rock nearby. This horizon could represent a change in the properties of the rock (in which the lower part is more resistant to abrasion), a horizontal fracture in the rock that served as an initiation zone for abrasion, or an indication that the lower part of the rock was buried and shielded from abrasion. Mazatzal (Fig. 1H) is a light-toned, flat rock with ventifact grooves cut into the upper surface. We suggest that the prominent grooves resulted from the trajectories of abrading particles that struck the rock at low angles, gouging the surface, an interpretation consistent with laboratory experiments of rock abrasion under martian conditions (31, 32).

The regolith beneath some rocks has been removed, giving the rock an undercut appearance. Many of the low-lying flat rocks are partly buried in the regolith and have bright, dusty surfaces (11). In other cases, rocks are two-toned: the lower part of the rock is bright and the tops of the rocks are darker and less dusty (Fig. 1I).

In a few cases along the traverse, Spirit imaged rocks that are perched on top of other rocks (Fig. 1J). These could be (i) inclusions or fragments released by weathering from a single rock, (ii) fragments emplaced as impact ejecta, or (iii) the remnant of a former mantling deposit where the finer-grained material has been mostly removed, with the perched rock having sunk into place.

The Rock Abrasion Tool (RAT) is used to abrade and brush the surface of rocks for analyses (33). Permission experiments demonstrated that in the absence of winds the brush disperses cuttings in symmetrical trajectories radially from the abrasion area. In the presence of wind, the material is carried downwind, leaving an asymmetric pattern. Two rocks at the Spirit site, Adirondack and Humphrey, were abraded, and in the process the abraded debris was distributed asymmetrically from the abraded area. Grinding operations took place for 3 hours starting at 12:30 hours local solar time (LST) for Adirondack and for 4 hours starting at 11:30 hours LST for Humphrey. We interpret the pattern of RAT cuttings (Fig. 1, K and L) to indicate that wind was actively blowing from the northwest toward the southeast in both cases. The asymmetry is more prominent on Adirondack, suggesting higher wind speeds.

Before Spirit landed, wind regimes were predicted from mesoscale atmospheric models (33, 34) and from analyses of features seen from orbit (36). These studies suggested that strong winds occur in the afternoon at Gusev Crater, coincident with the strongest heating of the atmosphere, and that wind orientations are about radial from the central zone of the crater. In the landing area, the predicted prevailing

winds are from the north-northwest toward the south-southeast, which is along the axis of the dust devil tracks seen from orbit. At night, the winds in the area reverse direction, a result of cold air ponding in the crater.

The asymmetric distribution of the RAT cuttings are consistent with predicted afternoon winds from the northwest. Moreover, the orientations of the axes of most of the bedforms (e.g., ripples) observed from Spirit are east-northeast to the west-southwest. On the assumption that these features are ripples, their axes would be orthogonal to the winds, which could be either from the northwest or from the southeast. However, the slight asymmetry of some bedforms (with steeper faces on the southeast) suggests prevailing winds from the north-northwest on the assumption that the steep side is the slip face. The observation that the asymmetry is not pronounced could reflect the day-to-night reversing winds. The wind-abraded grooves and facets are predominantly on the northwest sides of the rocks, also consistent with winds from that direction. These features also suggest that wind abrasion resulted from winds capable of transporting particles that were derived from sources northwest of the site.

A fundamental issue is the current activity of windblown particles on Mars and at the Gusev site. Frequent observations of martian dust storms, changes in dust devil tracks at the Spirit site, and accumulated dust on the rover demonstrate that fine particles are currently entrained, transported, and deposited by the wind. However, no bedform on Mars has been seen to change size, shape, or position from either orbit or the surface. MI images of the surfaces and interiors of regolith patches and bedforms show that most of the deposits consist of poorly sorted mixtures of different grain sizes and that many of the regoliths and bedform surfaces are crusted by a thin layer (9). If the coarse grains were undergoing active saltation, the dust and finer materials should have been removed by wind winnowing. Moreover, the ventifacted rock surfaces are mantled with dust and possibly a weathering rind (9), and if grains were undergoing active saltation they should be swept clean of dust by impacts. On the basis of these observations, it is unlikely that grains other than dust are currently being transported by wind at the landing site.

Undercut rocks, perched rocks, and other features discussed above suggest that the surface within Gusev Crater has been lowered over time. We infer, for example, that the bright zone of the two-toned rocks represents the buried part, similar to two-toned rocks seen in deserts on Earth and at the MPF site (23, 24). Burial could have occurred as part of a widespread deposit or by the passage of a bedform, such as a dune. If all of these features are the result of widespread deflation, measurements of the undercut rocks, the height to the boundary between the bright and



dark parts of the two-toned rocks, the height of the largest of the bright (light-toned) rocks, and the perched rocks would suggest local deflation of 5 to 60 cm. Thus, there must have been previous deposition on this order.

#### References and Notes

1. Reviewed by R. Greeley, N. Lancaster, S. Lee, P. Thomas, in *Mars*, H. H. Kieffer, B. Jakosky, Eds. (Univ. of Arizona Press, Tucson, AZ, 1992), pp. 730–766.
2. S. W. Squyres *et al.*, *Science* **305**, 794 (2004).
3. J. A. Crisp *et al.*, *J. Geophys. Res.* **108**, 10.1029/2002JE002038 (2003).
4. M. P. Golombek *et al.*, *J. Geophys. Res.* **108**, 10.1029/2003JE002074 (2003).
5. M. P. Golombek *et al.*, *Lunar Planet. Sci.* **XXXV**, abstr. 2185 (2004).
6. At 0.19 (36), the landing site has the lowest albedo as determined from orbit of the entire landing ellipse. From analysis of broadband (0.4 to 1.0  $\mu\text{m}$ ) images from the MER Pancam; the average albedo measured from the surface is  $0.25 \pm 0.05$  (70).
7. A martian solar day has a mean period of 24 hours 39 min 35.244 s and is referred to as a sol to distinguish this from a roughly 3% shorter solar day on Earth. A martian sidereal day, as measured with respect to the fixed stars, is 24 hours 37 min 22.663 s, as compared with 23 hours 56 min 04.0905 s for Earth. See [www.giss.nasa.gov/tools/mars24/](http://www.giss.nasa.gov/tools/mars24/) for more information.
8. "Dust" is an imprecise term but is commonly used for material on Earth that is smaller than about 40  $\mu\text{m}$  and that is transported primarily in suspension. Estimates for dust on Mars suggest diameters of a few micrometers, although these particles are thought to stick together in some cases, possibly by electrostatic charges, to form aggregates of larger sizes (37).
9. R. E. Arvidson *et al.*, *Science* **305**, 821 (2004).
10. Names have been assigned to areographic features by the Mars Exploration Rover (MER) team for planning and operations purposes. The names are not formally recognized by the International Astronomical Union.
11. J. F. Bell III *et al.*, *Science* **305**, 800 (2004).
12. K. E. Herkenhoff *et al.*, *J. Geophys. Res.* **108**, 10.1029/2003JE002076 (2003).
13. J. B. Pollack *et al.*, *J. Geophys. Res.* **82**, 4479 (1977).
14. P. H. Smith *et al.*, *Science* **278**, 1758 (1997).
15. M. G. Tomasko, L. R. Dose, M. Lemmon, P. H. Smith, E. Wegryn, *J. Geophys. Res.* **104**, 8987 (1999).
16. P. R. Christensen *et al.*, *Science* **305**, 837 (2004).
17. H. Y. McSween *et al.*, *Science* **305**, 842 (2004).
18. K. E. Herkenhoff *et al.*, *Science* **305**, 824 (2004).
19. J. F. Bell *et al.*, *Icarus* **158**, 56 (2002).
20. J. L. Bandfield, *J. Geophys. Res.* **107**, 10.1029/2001JE001510 (2002).
21. R. P. Sharp, *J. Geol.* **71**, 617 (1963).
22. Ripples are bedforms composed of sand and granules that are moved by surface creep induced by the impact of saltating sands, whereas dunes are larger bedforms typically composed of finer sands and not formed directly by saltation processes.
23. R. Greeley *et al.*, *J. Geophys. Res.* **104**, 8573 (1999).
24. M. P. Golombek, N. T. Bridges, *J. Geophys. Res.* **105**, 1841 (2000).
25. J. A. Grant *et al.*, *Science* **305**, 807 (2004).
26. R. Greeley, J. D. Iversen, *Wind as a Geological Process: Earth, Mars, Venus, and Titan* (Cambridge Univ. Press, Cambridge, 1985).
27. R. Greeley, J. D. Iversen, *Geophys. Res. Lett.* **14**, 925 (1987).
28. M. R. Raupach, *Boundary-Layer Meteorol.* **60**, 375 (1992).
29. M. R. Raupach, D. A. Gillette, J. F. Lyles, *J. Geophys. Res.* **98**, 3023 (1993).
30. N. T. Bridges *et al.*, *J. Geophys. Res.* **104**, 8595 (1999).
31. R. Greeley *et al.*, *J. Geophys. Res.* **87**, 10009 (1992).
32. N. T. Bridges *et al.*, *Planet. Space Sci.* **52**, 199 (2004).
33. S. P. Gorevan *et al.*, *J. Geophys. Res.* **108**, 10.1029/2003JE002061 (2003).
34. S. R. C. Raffin, T. I. Michaels, *J. Geophys. Res.* **108**, 10.1029/2002JE002027 (2003).
35. D. Toigo, M. I. Richardson, *J. Geophys. Res.* **108**, 10.1029/2003JE002064 (2003).
36. R. Greeley *et al.*, *J. Geophys. Res.* **108**, 10.1029/2002JE002006 (2003).
37. M. T. Mellon, B. M. Jakosky, H. H. Kieffer, P. R. Christensen, *Icarus* **148**, 437 (2000).
38. R. Greeley, *J. Geophys. Res.* **84**, 6248 (1979).
39. Our work was supported by NASA by contracts through the Jet Propulsion Laboratory.

10 May 2004; accepted 23 June 2004

#### REPORT

# Localization and Physical Properties Experiments Conducted by Spirit at Gusev Crater

R. E. Arvidson,<sup>1</sup> R. C. Anderson,<sup>2</sup> P. Bartlett,<sup>3</sup> J. F. Bell III,<sup>4</sup> D. Blaney,<sup>2</sup> P. R. Christensen,<sup>5</sup> P. Chu,<sup>3</sup> L. Crumpler,<sup>6</sup> K. Davis,<sup>3</sup> B. L. Ehlmann,<sup>1</sup> R. Fergason,<sup>5</sup> M. P. Golombek,<sup>2</sup> S. Gorevan,<sup>3</sup> J. A. Grant,<sup>7</sup> R. Greeley,<sup>5</sup> E. A. Guinness,<sup>1</sup> A. F. C. Haldemann,<sup>2</sup> K. Herkenhoff,<sup>8</sup> J. Johnson,<sup>8</sup> G. Landis,<sup>9</sup> R. Li,<sup>10</sup> R. Lindemann,<sup>2</sup> H. McSween,<sup>11</sup> D. W. Ming,<sup>12</sup> T. Myrick,<sup>3</sup> L. Richter,<sup>13</sup> F. P. Seelos IV,<sup>1</sup> S. W. Squyres,<sup>4</sup> R. J. Sullivan,<sup>4</sup> A. Wang,<sup>1</sup> J. Wilson<sup>3</sup>

The precise location and relative elevation of Spirit during its traverses from the Columbia Memorial station to Bonneville crater were determined with bundle-adjusted retrievals from rover wheel turns, suspension and tilt angles, and overlapping images. Physical properties experiments show a decrease of 0.2% per Mars solar day in solar cell output resulting from deposition of airborne dust, cohesive soil-like deposits in plains and hollows, bright and dark rock coatings, and relatively weak volcanic rocks of basaltic composition. Volcanic, impact, aeolian, and water-related processes produced the encountered landforms and materials.

During the first few Mars solar days (sols) (1) of operations, we determined the landed location in inertial coordinates by analyzing Spirit-to-Earth two-way X-band Doppler transmissions and two passes of ultrahigh-frequency two-way Doppler between Spirit and the Mars Odyssey orbiter. The equivalent location in the International Astronomical Union (IAU) 2000 body-centered reference frame is 14.571892°S, 175.47848°E. The location with respect to surface features was derived by the correlation of hills and craters observed in images taken by the Pancam, the Entry Descent and Landing (EDL) Camera, and the Mars Orbital Camera. On the basis of these analyses, the landing site is located at 14.5692°S, 175.4729°E in IAU

2000 coordinates, ~300 m north-northwest of the radiometric solution. This offset is consistent with the map tie errors between inertially derived coordinate systems and those derived from image-based coverage of the planet.

Localization experiments during traverses focused on systematic acquisition of forward- and backward-looking overlapping images, on-board inertial measurement unit (IMU) observations to derive rover tilt, and tracking the number of wheel turns to provide wheel-based odometry. These observations were employed in a least-squares bundle adjustment to solve for the position and orientation of Spirit in local Cartesian coordinates at discrete locations during traverses (Fig. 1 and Plate 14). In addition,

measurements of differential rocker and bogie angles in the suspension system, together with IMU data, were used to reconstruct the elevation of each wheel at a 2- to 8-Hz sample rate relative to the start of each traverse (Fig. 1).

Localization results were extracted for 33 traverse segments from the Columbia Memori-

<sup>1</sup>Department of Earth and Planetary Sciences, Washington University, St. Louis, MO 63130, USA. <sup>2</sup>Jet Propulsion Laboratory, California Institute of Technology, Pasadena, CA 91109, USA. <sup>3</sup>Honeybee Robotics, 204 Elizabeth Street, New York, NY 10012, USA. <sup>4</sup>Department of Astronomy, Space Sciences Building, Cornell University, Ithaca, NY 14853, USA. <sup>5</sup>Department of Geological Sciences, Arizona State University, Tempe, AZ 85287, USA. <sup>6</sup>New Mexico Museum of Natural History and Science, Albuquerque, NM 87104, USA. <sup>7</sup>Center for Earth and Planetary Studies, National Air and Space Museum, Smithsonian Institution, Washington, DC 20560, USA. <sup>8</sup>U.S. Geological Survey, Flagstaff, AZ 86001, USA. <sup>9</sup>National Aeronautics and Space Administration (NASA) Glenn Research Center, Cleveland, OH 44135, USA. <sup>10</sup>Department of Civil and Environmental Engineering and Geodetic Science, Ohio State University, Columbus, OH 43210, USA. <sup>11</sup>Department of Earth and Planetary Sciences, University of Tennessee, Knoxville, TN 37996, USA. <sup>12</sup>NASA Johnson Space Center, Houston, TX 77058, USA. <sup>13</sup>Deutsche Luft und Raumfahrt Institut für Raumsimulation, Linder Hoehe, Köln, DJ-51170, Germany.



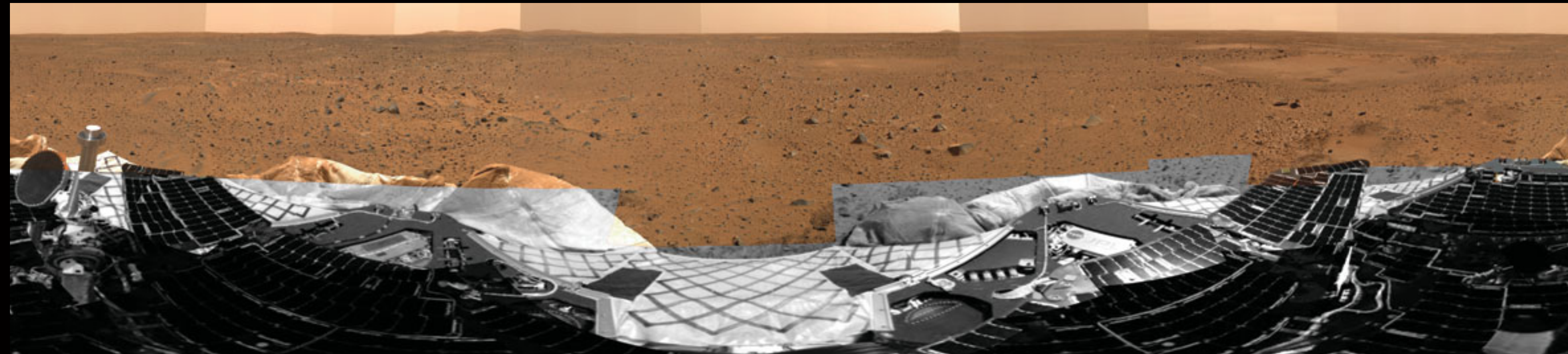


PLATE 1



PLATE 2



PLATE 3

**PLATE 1:** Pre-standup (sols 3,4,5) Mission Success panorama color composite (Red = 750 nm, Green = 530 nm, Blue = 480 nm) overlaid onto a Navcam monochrome view of parts of the lander and rover deck. Colors processed to represent only an approximate rendering of true color.

**PLATE 2:** "Legacy 1" panorama color composite, acquired from a point about halfway along the traverse to Bonneville crater on sols 59,60,61. Red = 750 nm, Green = 530 nm, Blue = 480 nm. Colors were calibrated relative to the Pancam calibration target and represent only an approximate rendering of true color.

**PLATE 3:** Bonneville panorama color composite acquired on sols 68 and 69. Red = 750 nm, Green = 530 nm, Blue = 480 nm. Colors were calibrated relative to the Pancam calibration target and represent only an approximate rendering of true color.

**PLATE 4:** Low-compression view of Columbia Hills, acquired on sol 8. False-color composite (red = 750 nm, Green = 530 nm, Blue = 480 nm).

**PLATE 5:** Enlargement of Bonneville crater from Plate 3.

**PLATE 6:** Mini-TES diurnal temperature series maps of Bonneville crater. Temperatures are scaled from blue = 210K to red = 285K and observations are shown from five local solar times of day (top to bottom) near 10:00, 12:00, 14:00, 15:00, and 17:00.

**Science**



PLATE 4



PLATE 5

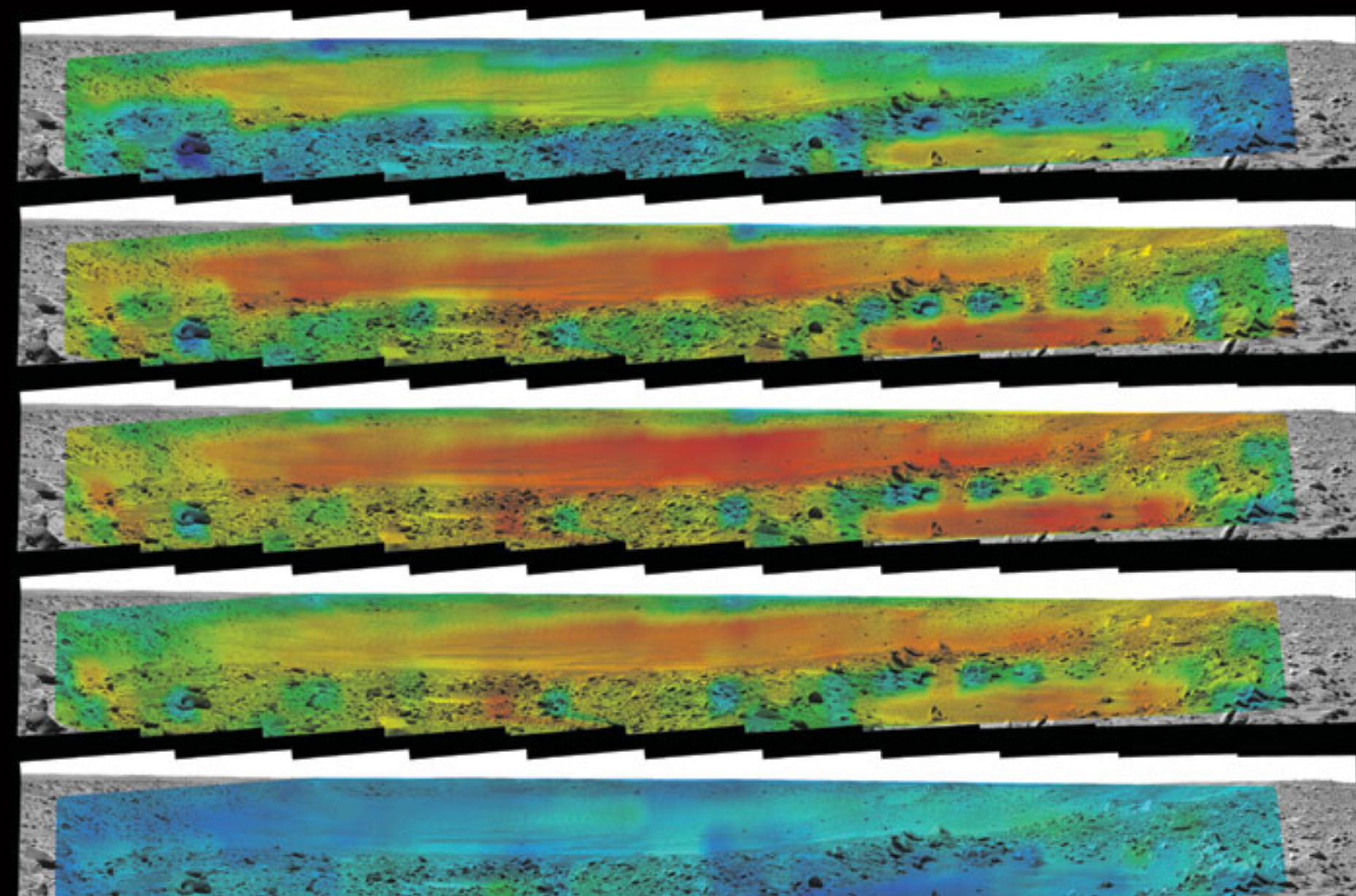


PLATE 6





PLATE 7

PLATE 7: Pancam mosaic of the trench dug at Laguna Hollow on sol 47. Red = 750 nm, Green = 530 nm, Blue = 480 nm. Colors processed to represent only an approximate rendering of true color.

PLATE 8: False color composite of pre-standup Mission Success panorama. Red corresponds to the 750/480 nm ratio (stretched from 2.0 to 6.0), Green corresponds to the I/F at 750 nm (stretched from 0.0 to 0.45), and Blue corresponds to the 480/750 nm ratio (stretched from 0.1 to 0.5).

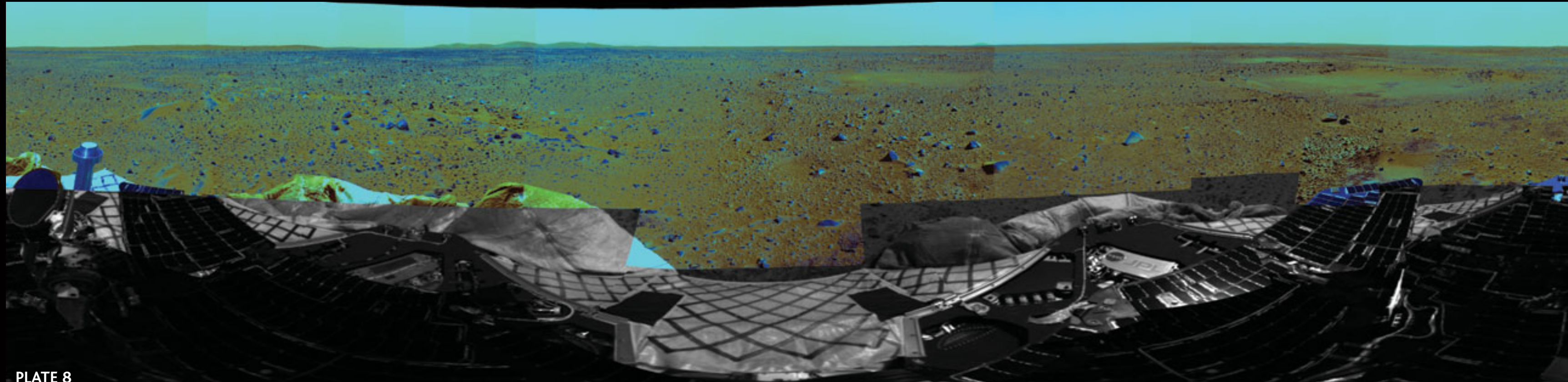


PLATE 8



PLATE 9A

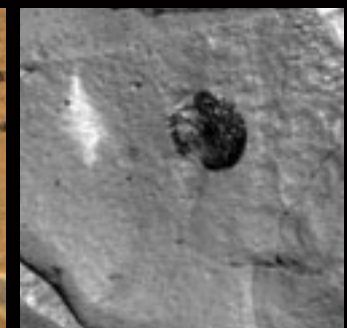


PLATE 9B



PLATE 9C

PLATE 9: (a) Pancam image of Adirondack from sol 14, prior to any instrument arm work. RGB composite from 750, 530, and 480 nm filters; (b) Sol 33 Pancam image of Adirondack, after brushing with the RAT. Blue filter (430 nm) image; (c) Sol 35 Pancam image of Adirondack, after completion of the RAT grinding activity. RGB composite from Pancam's 750, 530, and 480 nm filters.

PLATE 10: (a) Pancam image of Humphrey from sol 54, prior to any instrument arm work; (b) Sol 55 Pancam image of Humphrey, after brushing 3 times with the RAT; (c) Sol 60 Pancam image of Humphrey, after completion of the RAT grinding activity. All images are RGB composite from Pancam's 750, 530, and 480 nm filters.



PLATE 10A



PLATE 10B



PLATE 10C

Plate 11: (a) Pancam image of Mazatzal from sol 76, before any robotic arm work; (b) Sol 81 Pancam image of Mazatzal, after brushing 2 spots with the RAT; (c) Sol 82 Pancam image of Mazatzal, after completion of the first RAT grinding activity. All images are RGB composite from Pancam's 750, 530, and 480 nm filters.



PLATE 11A



PLATE 11B



PLATE 11C

PLATE 12: MI/Pancam merged mosaic of Humphrey RAT hole from sol 60.

PLATE 13: MI/Pancam merged mosaic of the first Mazatzal RAT hole from sol 82.

PLATE 14: Spirit traverse path graphic, showing the rover's route during the primary mission from the Columbia Memorial Station northeast to Bonneville crater then southeast along the crater's rim.



PLATE 12



PLATE 13

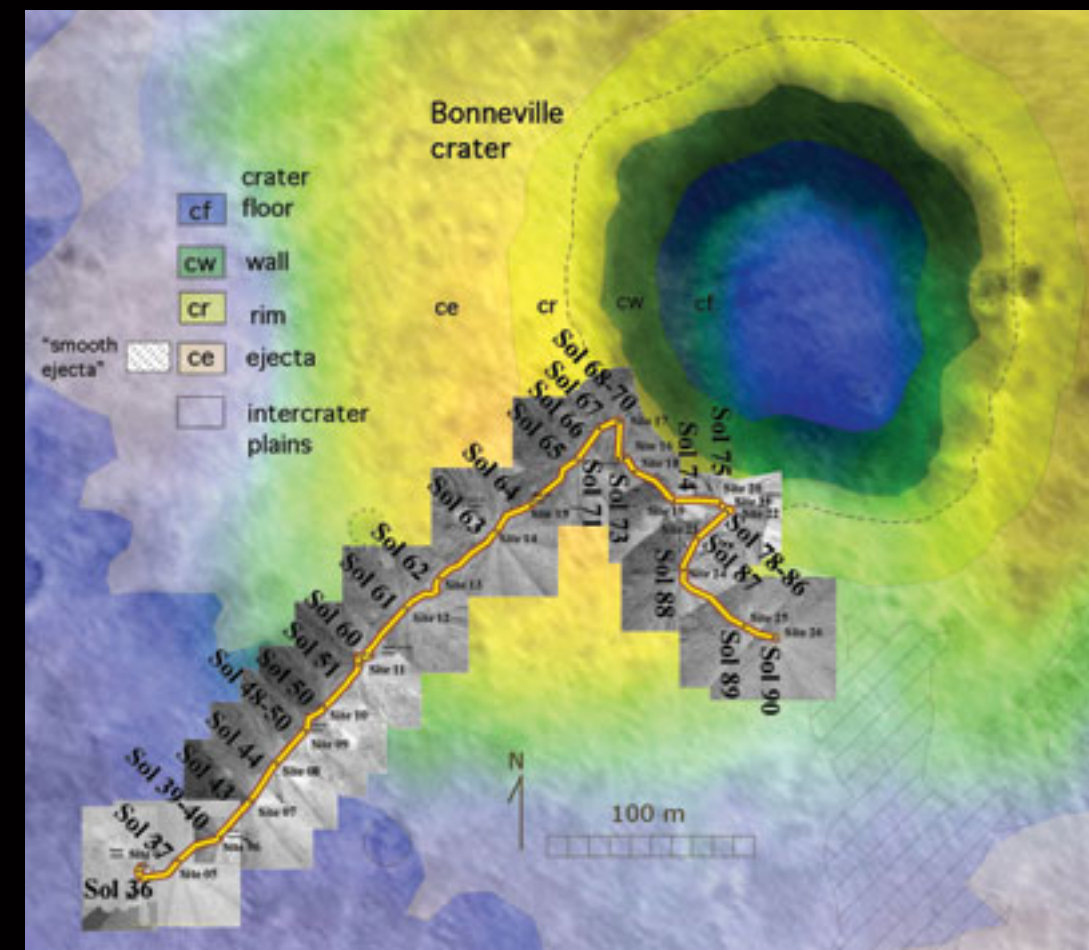


PLATE 14



al station to the rock Route 66 (2) (Fig. 1). The terrain from the landing site to the location of the rock Humphrey in Middle Ground hollow is flat and level, with a relative-elevation decrease of only 1 m over the horizontal distance of 197 m between localization stations. From Humphrey to the crater rim, the relative elevation increased 7.4 m over a distance of 135 m between stations, consistent with the increased slope expected as the rim of Bonneville crater was approached. From the crater rim to the rock Mazatzal, the relative elevation decreased 0.6 m over a distance of 80 m, consistent with the traverse azimuths that kept the vehicle near the rim. Finally, the distance from Mazatzal to Route 66 is 95 m, with a decrease in relative elevation of 3 m, consistent with travel away from the rim. Based on wheel odometry, Spirit traversed 637 m from Columbia Memorial station to the rock Route 66 and the summed distance between the 33 stations is 507 m. Notably, the bundle adjustments increased positional accuracy by 2% relative to the use of wheel odometry alone.

Rocks litter the landscape at the landing site and are larger and more abundant near the Bonneville crater rim (3). Soil (4) deposits dominated by particles <1 mm in diameter cover the plains and occasionally are found as aeolian drifts (3, 5, 6). Soil deposits not within hollows or on hollow rims are covered with an evenly spaced set of angular to smooth rocks ranging in size from granules (2 to 4 mm) to pebbles (4 to 16 mm). Furthermore, soils are covered with a thin (<1-mm) layer of bright

red dust. These dust deposits are easily disturbed, as shown by airbag bounce marks generated during landing and observations that wheel motions associated with traversing removed the dust covers and exposed darker, underlying deposits (Fig. 1). The short-circuit current monitor solar cell showed a decrease in current of 0.2% per sol (corrected for seasonal variations in Mars-Sun distance and solar elevation angle) over the first 93 sols of operation, showing airborne dust accumulation on the rover solar panels comparable to that observed during the Pathfinder mission (7). The ubiquitous nature of the dust cover on soils, combined with discernable dust accumulation rates, serves as evidence that the Gusev site has accumulated dust deposits for a number of years.

Soil deposits typically display surface crusts a few millimeters thick beneath the thin dust covers. For example, airbag retraction scars include thin crustal plates a few centimeters in width that were laterally displaced as the deflated airbags were retracted after landing. Surface crusts also have been observed in wheel track disturbances, especially where rocks wobbled by wheels created moats as small amounts of adjacent crust were displaced. Imaging of wheel tracks shows well-defined soil casts indicative of materials with a range of grain sizes, from coarse sand (0.5 to 1 mm) to diameters too fine to be discerned with the 30  $\mu\text{m}$ /pixel spatial resolution of the Microscopic Imager (MI) (Fig. 2A). Imaging data also show that smooth indentations were produced by the Mössbauer Spectrometer contact plate as it pushed into

soils before the contact switch initiated, stopping movement at  $\sim 1$  N of applied force (Fig. 2A). The finer grains were molded into interstices of the larger grains when displaced by the wheels and faceplate, producing well-defined soil casts. Unfortunately, no in situ measurements have been done yet on cloddy soils that are dust free. Thus, it is impossible to determine whether the cloddy nature is due to enrichment of cementing agents such as iron oxides or sulfates.

To explore the degree to which soil properties change with depth, a 6- to 7-cm-deep trench was excavated with the right front wheel in Laguna hollow on sol 47. Trench walls in Laguna hollow have slopes of up to 65°, values steeper than the angle of repose for most granular materials ( $\sim 30^\circ$ ). This result indicates the presence of slightly cohesive soils throughout the upper 6 to 7 cm beneath the surface, although the exact degree of cohesion is difficult to estimate with certainty. An additional experiment excavated into the drift Serpent (Fig. 2B). The surface layer of the drift consists of closely packed, very coarse sand-sized particles ( $\sim 1$  to 2 mm in diameter) overlying finer grained soils. The very coarse sand armors the surface and protects the drift from aeolian erosion and transport of the underlying particles. The armor is covered with the thin dust deposit that is typical of the soil surfaces examined during Spirit's traverses and observations. The slightly cohesive nature of the upper portion of the drift soil is evident based on the presence of clods produced by the excavations (Fig. 2).

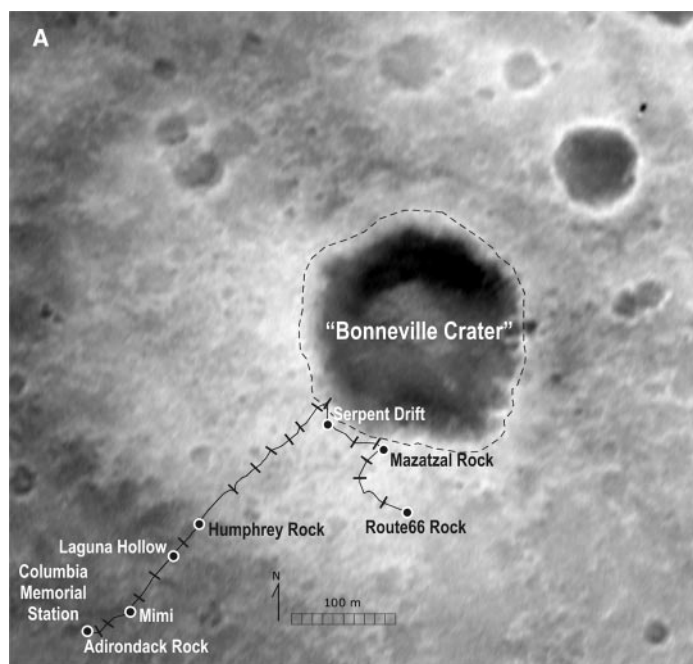


**Fig. 1. (A)** MER EDL Camera image acquired from 1430 m above the surface shows Spirit's localization-derived traverses and positions for physical property experiments during the first 93 sols in Gusev crater. Tick marks along traverse path show localization stations. Some stations that are close together are not plotted to avoid clutter.

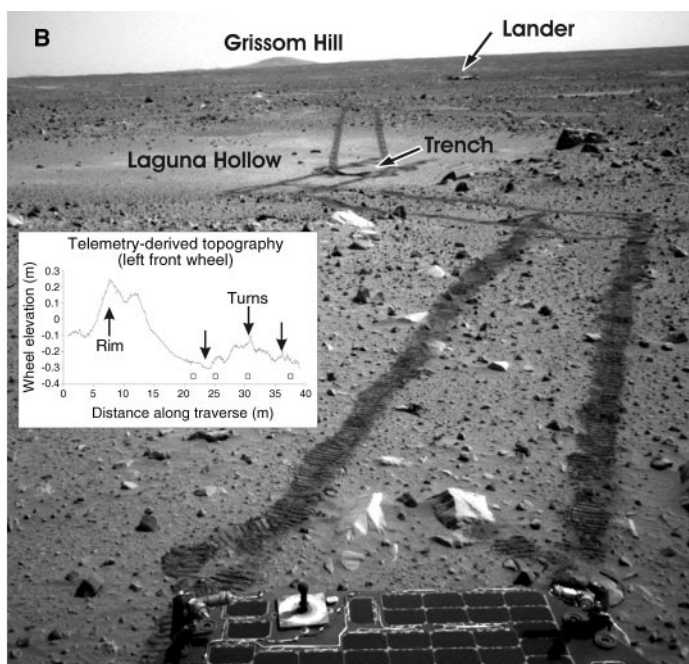


Image identification is 2E126462405EDN000F0006NOM1. **(B)** Navcam image (2N130812149EFF1000P1901L0M1) of Laguna hollow with tracks that are about 10 cm wide. The inset shows a vertical topographic profile across the hollow as derived from rover tilt and wheel suspension data.



With regard to standard terramechanical analyses, estimates of soil-bearing strength of  $\sim 5$  kPa, cohesive strength of  $\sim 1$  kPa, and an angle of internal friction of  $\sim 20^\circ$  were derived from wheel sinkage depths in a hollow adjacent to the lander traversed on sol 15 (8). More resistant deposits (with less sinkage), such as those found in the egress area traversed on sol 12 and in the region in front of the drift Arena crossed on sol 42, provided values of  $\sim 200$  kPa, 15 kPa, and  $25^\circ$ , respectively, for the same parameters. These values are comparable to the range of soil values found from analyses of Viking Lander and Pathfinder physical properties data (9).

Rocks ranging up to boulder sizes were observed during Spirit's traverses (Fig. 1). Rocks tend to be massive in appearance, al-

though a few rocks, including Mimi (Fig. 2A), have a layered appearance. The layered rocks are interpreted to be weathered in place by mechanical spalling along lines of weakness. Low-lying rocks (less than  $\sim 25$  cm tall) of the more typical massive variety in many cases appear to have been faceted by wind action and tend to be light-toned relative to surrounding soils, e.g., Mazatzal rock on the rim of Bonneville crater (Fig. 3). Additionally, these rocks are commonly embedded in soil deposits. All rocks show strong variations in brightness with lighting and viewing geometries in imaging data. At small phase angles, flat surfaces of individual rocks tend to be brighter and redder in visible wavelengths relative to corners or edges or tops, consistent with the presence of brighter coat-

ings that are optically thicker on the facets as opposed to the corners or edges. These observations imply that rocks are coated with bright, red materials preferentially on smooth, flat facets. Accumulation of airborne dust is a plausible mechanism for formation of these bright coatings.

Rock Abrasion Tool (RAT) deployments were made on Adirondack ( $\sim 20$ -cm-high light-toned rock), Humphrey ( $\sim 50$ -cm-high rock, variable brightness), and Mazatzal ( $\sim 20$ -cm-high, faceted, light-toned rock) (Figs. 1 and 3). After initial brushing experiments designed to remove loose deposits, the RAT was used to grind into the rock facets, extending 2.7 and 2.1 mm (based on RAT motor drive data) into Adirondack and Humphrey, respectively. For Mazatzal, two rattings were conducted with a

**Fig. 2.** (A) Pancam image (2P130088011-EFF0514P2538L2M1) of Mimi rock and rover front wheel tracks, along with an MI (2M-130169106EFF0514-P2953M2M1) inset showing the tracks in more detail. The MI inset shows the imprint of the MB contact plate (arrows) into moldable soil. The inset covers about 3 cm across. (B) Pancam image (2P13-2756681EFF1957P23-52L2M1) of Serpent drift after scuffing by the rover front wheel, with MI (2M132842-058EFF2000P2977M-2M1) inset showing dust-coated armor of very coarse sand grains over sand-sized and finer-grained particles. Soil clods are evident just to the upper right of the inset location. The MI inset covers about 1.5 cm in width on the drift.

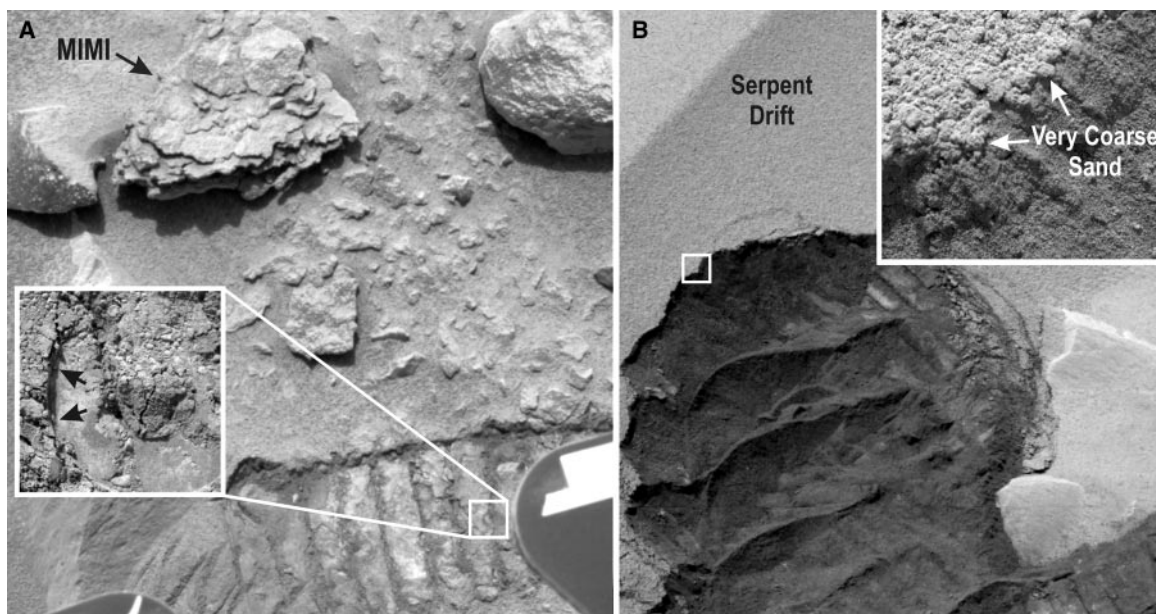
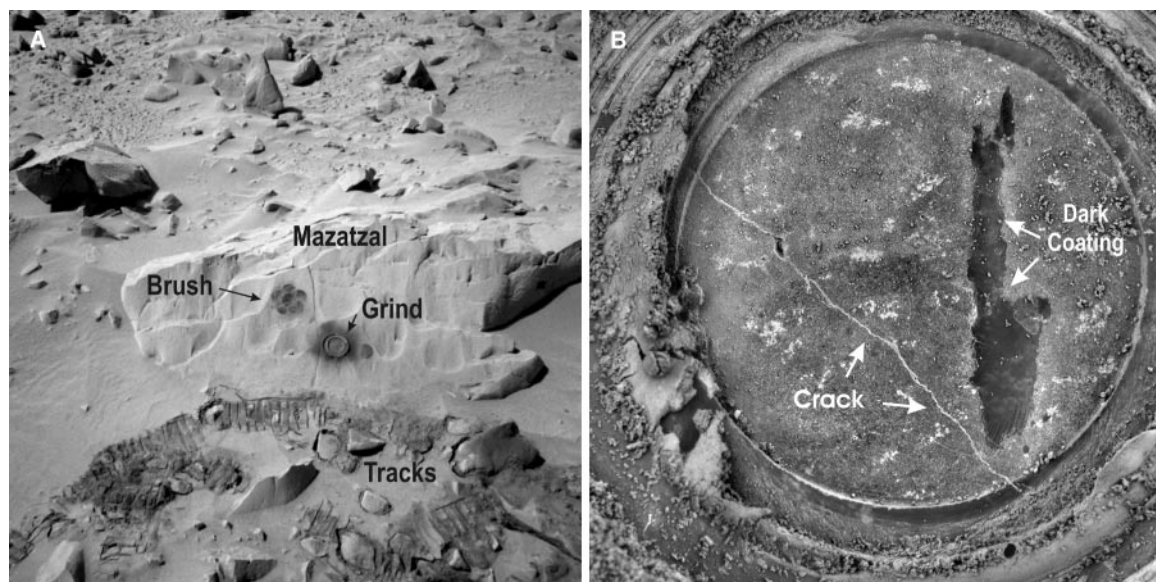


**Fig. 3.** (A) Navcam image (2N13400813-9EFF2238P1959LOM1) showing the brushed (Brush) and abraded (Grind) areas on the 2.3-m-wide Mazatzal rock. (B) Mosaic (2M-P085IOF22ORT32P2-959L456F1\_qn) of four MI images acquired of the Mazatzal RAT hole after the second grinding operation, showing that only a small amount of dark coating remains. The RAT hole is about 4.5 cm across. Black and white version of merged color Pancam and MI mosaic is shown.



3.8-mm penetration on the first attempt and a 4.1-mm penetration on the second attempt. The brushing and grinding operations on Mazatzal showed the presence of a dark, smooth, indurated coating beneath the light-toned loose coating (Fig. 3). This dark coating was largely removed by the second grinding, revealing the underlying rock surface (Fig. 3B). There is also some evidence that a second bright coating may underlie the dark coating (10, 11).

Grind motor currents, the depths achieved, and grinding areas provided estimates of the amount of energy consumed by the RAT while removing a unit volume of material. Because grind energy density is a nontraditional means of quantifying rock mechanical properties, three terrestrial rocks were abraded in the laboratory for calibration, with the use of a flight-like RAT: a fresh, nonvesicular basalt sample from Ash Fork, Arizona; a fine-grained dolostone sample collected from the Soda Mountains north of Silver Lake, California; and Cleveland Member (fissile shale) of the Ohio Formation. These experiments yielded energy densities of ~166, 83, and 11 J/mm<sup>3</sup>, respectively. For comparison, Humphrey required 83 J/mm<sup>3</sup>, whereas Adirondack and Mazatzal required 51 and 65 J/mm<sup>3</sup>, respectively. Thus, rocks abraded by Spirit required less energy per volume than the particular basalt sample ground in the tests, and comparable grind energy densities to the two terrestrial sedimentary rock samples, even though composition and mineralogy data from Spirit demonstrate that the rocks encountered are basalts (10, 12–14).

The physical properties experiments conducted by Spirit at Gusev crater show that surface soils are cloddy, rock coatings are ubiquitous, and rocks are easily abraded and thus mechanically weaker than the fresh, nonvesicular basaltic sample used in the laboratory tests. Furthermore, the abraded surfaces of the rocks at Gusev exposed vugs and cracks filled with bright material suggestive of aqueous mineralization (Fig. 3) (10, 11). There is also a suggestion of a vertical weathering profile for Humphrey rock, where the grinding direction was accomplished at a slight angle from the surface normal, thereby exposing shallow to deep surfaces (10). The presence of liquid water, even for brief periods of time, is one way to cement surface soils, form rock coatings, deposit minerals in vugs and cracks, and weather the surfaces of rocks. Liquid water might occur for brief periods when the spin axis obliquity and atmospheric relative humidity are high and precipitation occurs as snow or frost (15). A modest temperature enhancement as a result of absorption of solar radiation by underlying regolith and rocks, with “greenhouse”-related absorption of outgoing thermal radiation by the ice and snow, could generate thin films of liquid water that would mobilize soluble species and produce the features observed by Spirit. Other models are also being explored to place the physical properties experiments in an environmental context, in addition to further measurements designed to test hypotheses.

## References and Notes

1. A martian solar day has a mean period of 24 hours 39 min 35.244 s and is referred to as a sol to distinguish this from a roughly 3% shorter solar day on Earth. A martian sidereal day, as measured with respect to the fixed stars, is 24 hours 37 min 22.663 s, as compared with 23 hours 56 min 04.0905 s for Earth. See [www.giss.nasa.gov/tools/mars24](http://www.giss.nasa.gov/tools/mars24) for more information.
2. Names have been assigned to areographic features by the Mars Exploration Rover (MER) team for planning and operations purposes. The names are not formally recognized by the IAU.
3. J. A. Grant *et al.*, *Science* **305**, 807 (2004).
4. The term martian soil is used here to denote any loose unconsolidated materials that can be distinguished from rocks, bedrock, or strongly cohesive sediments. No implication of the presence or absence of organic materials or living matter is intended.
5. P. R. Christensen *et al.*, *Science* **305**, 837 (2004).
6. R. Greeley *et al.*, *Science* **305**, 810 (2004).
7. G. Landis, P. Jenkins, *J. Geophys. Res.* **105**, 1855 (2000).
8. Based on wheel track sinkage values for terrains covered by one to three MER wheels described in L. Richter and P. Hamacher, paper presented at the 13th Conference of the International Society for Terrain-Vehicle Systems, Munich, Germany, 14 to 17 September 1999.
9. H. Moore *et al.*, *J. Geophys. Res.* **104**, 8729 (1999).
10. K. E. Herkenhoff *et al.*, *Science* **305**, 824 (2004).
11. H. Y. McSween *et al.*, *Science* **305**, 842 (2004).
12. S. W. Squyres *et al.*, *Science* **305**, 794 (2004).
13. J. F. Bell III *et al.*, *Science* **305**, 800 (2004).
14. P. R. Christensen *et al.*, *Science* **305**, 837 (2004).
15. M. A. Mischna *et al.*, *J. Geophys. Res.* **108**, 5062 (2003).
16. Work funded by NASA through the Mars Exploration Rover Project. We thank the MER team of scientists and engineers, who made the landing, traverses, and science observations a reality.

4 May 2004; accepted 2 July 2004

## REPORT

# Textures of the Soils and Rocks at Gusev Crater from Spirit's Microscopic Imager

K. E. Herkenhoff,<sup>1\*</sup> S. W. Squyres,<sup>2</sup> R. Arvidson,<sup>3</sup> D. S. Bass,<sup>4</sup> J. F. Bell III,<sup>2</sup> P. Bertelsen,<sup>5</sup> N. A. Cabrol,<sup>6</sup> L. Gaddis,<sup>1</sup> A. G. Hayes,<sup>2</sup> S. F. Hviid,<sup>7</sup> J. R. Johnson,<sup>1</sup> K. M. Kinch,<sup>8</sup> M. B. Madsen,<sup>5</sup> J. N. Maki,<sup>4</sup> S. M. McLennan,<sup>9</sup> H. Y. McSween,<sup>10</sup> J. W. Rice Jr.,<sup>11</sup> M. Sims,<sup>12</sup> P. H. Smith,<sup>13</sup> L. A. Soderblom,<sup>1</sup> N. Spánovich,<sup>13</sup> R. Sullivan,<sup>2</sup> A. Wang<sup>14</sup>

The Microscopic Imager on the Spirit rover analyzed the textures of the soil and rocks at Gusev crater on Mars at a resolution of 100 micrometers. Weakly bound agglomerates of dust are present in the soil near the Columbia Memorial Station. Some of the brushed or abraded rock surfaces show igneous textures and evidence for alteration rinds, coatings, and veins consistent with secondary mineralization. The rock textures are consistent with a volcanic origin and subsequent alteration and/or weathering by impact events, wind, and possibly water.

The Microscopic Imager (MI) is a fixed-focus camera mounted on a robotic arm (1, 2). The MI was designed to function like a geologist's hand lens, acquiring images at a spatial resolution of 31  $\mu\text{m}/\text{pixel}$  (picture element) over a broad spectral range (400 to 700 nm). The MI uses the same

electronics design as the other Mars Exploration Rover (MER) cameras (3, 4), but its optics yield a field of view of 32 by 32 mm across a 1024- by 1024-pixel charge-coupled device image. The MI acquires images with only solar or skylight illumination of the target surface. A contact sensor is

used to place the MI slightly closer to the target surface than its best-focus distance of about 66 mm, which allows concave surfaces to be imaged in good focus. The depth of field of the MI is ~3 mm; coarse focusing (~2-mm precision) is achieved by moving the arm away from a rock target after contact is sensed. The MI optics are protected from the martian environment by a retractable dust cover. This cover includes a Kapton (polyimide film, DuPont, Wilmington, Delaware) window that is tinted orange to restrict the spectral bandpass to 500 to 700 nm, which allows crude color information to be obtained by acquiring images with the cover open and closed.



During the first 90 sols (5), Spirit acquired and returned 537 MI images of seven rocks, many martian soil (6) and bedform targets, and the martian sky (for calibration). Tracks and trenches created by the rover wheels were also imaged (7), as were the filter and capture magnets on the front of the rover (8).

As part of the daily MER operations process (9), targets for the MI and other arm instruments were selected by using available Pancam (10), Navcam, and Hazcam imagery (4). The MI routinely observed targets that were investigated by the other ARM instruments to study surface details, to provide context for the spectrometer data, and to examine the results of rock abrasion tool (RAT) brushing and grinding activities (2, 11, 12, 13). Many of the Mössbauer spectrometer (11) soil targets were imaged twice by the MI (before and after Mössbauer touch) to observe the physical effects of the Mössbauer contact sensor on the soil and to determine the location of the Mössbauer field of view.

A typical MI data set includes a stack of three, five, or seven MI images, acquired at 3-mm steps along the MI optical axis with the dust cover open (1). This acquisition approach helped to ensure optimum focus on targets with relief greater than the MI depth of field. The number of images in an MI stack was kept small to minimize the volume of extraneous MI data returned to Earth. Most of the MI stacks included at least one image in good focus, but uncertainties in the front Hazcam terrain model resulted in poorly focused MI images in some cases. Color information was sometimes added by acquiring an additional single-frame MI image of the same target at the nominal best-focus position with the dust cover closed. Some of the MI targets were imaged with a binocular stereo pair of left/right MI stacks or even a mosaic of MI stacks (e.g., Plates 12 and 13).

Soil materials at Gusev that have been examined by the MI show texture down to the limit of resolution, about 100  $\mu\text{m}$  (14). Soil

surfaces typically are rough at submillimeter scales but are molded to much smoother surfaces under compression by the Mössbauer contact plate and/or a rover wheel, revealing the presence of a substantial fraction of particles too small to be resolved. It is unclear how much remodeling was accomplished by compression of void space and reorganization of existing particles, or by destruction of weak particles to even smaller sizes. Soil texture was obliterated by the  $\sim 1$  N force applied by the Mössbauer contact plate (Fig. 1). If this was due to crushing of particles, the original particles must have been very weak. Some soils preserve a vertically coherent network (100 to 300  $\mu\text{m}$  scale) of tubelike and honeycomb features. These observations are con-

**Fig. 1.** MI image of soil target at Sugar Loaf Flats, showing partial annular imprint of Mössbauer contact plate. Contact plate was not parallel to soil surface, so contact was made only in the brighter part of the image. The part of MI full frame 2M1321-32632 shown here is 27 by 22 mm. Illumination from bottom.



**Fig. 2.** Merge of MI image 2M132842785 of feature Serpent (trenched), taken sol 073, with Pancam enhanced color data (602 nm, 535 nm, and 483 nm). Illumination from top; frame is 32 mm square.



<sup>1</sup>U.S. Geological Survey Astrogeology Team, Flagstaff, AZ 86001, USA. <sup>2</sup>Department of Astronomy, Space Sciences Building, Cornell University, Ithaca, NY 14853, USA. <sup>3</sup>Department of Earth and Space Sciences, Washington University, St. Louis, MO 63130, USA. <sup>4</sup>Jet Propulsion Laboratory, California Institute of Technology, Pasadena, CA 91109, USA. <sup>5</sup>Center for Planetary Science, Danish Space Research Institute and Niels Bohr Institute for Astronomy, Physics, and Geophysics, University of Copenhagen, Denmark. <sup>6</sup>NASA Ames Research Center/SETI Institute, Moffett Field, CA 94035, USA. <sup>7</sup>Max Planck Institut für Aeronomie, Katlenburg-Lindau, D-37191, Germany. <sup>8</sup>Institute of Physics and Astronomy, Aarhus University, Aarhus, Denmark. <sup>9</sup>State University of New York, Department of Geosciences, Stony Brook, NY 11794, USA. <sup>10</sup>Department of Earth and Planetary Sciences, University of Tennessee, Knoxville, TN 37996, USA. <sup>11</sup>Arizona State University, Department of Geological Sciences, Tempe, AZ 85287, USA. <sup>12</sup>NASA Ames Research Center, Moffett Field, CA 94035, USA. <sup>13</sup>University of Arizona, Lunar and Planetary Laboratory, Tucson, AZ 85721, USA. <sup>14</sup>Department of Earth and Space Sciences and McDonnell Center for Space Sciences, Washington University, St. Louis, MO 63130, USA.

\*To whom correspondence should be addressed. E-mail: kherkenhoff@usgs.gov

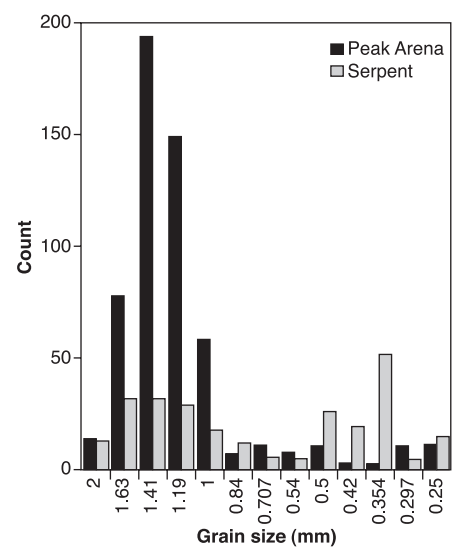


**Fig. 3.** Grain count versus size for bedform materials at Gusev crater, showing variation in modalities. Grain size increases from right to left. Data were gathered from images shown in figure 2 and figure 2C of (20).

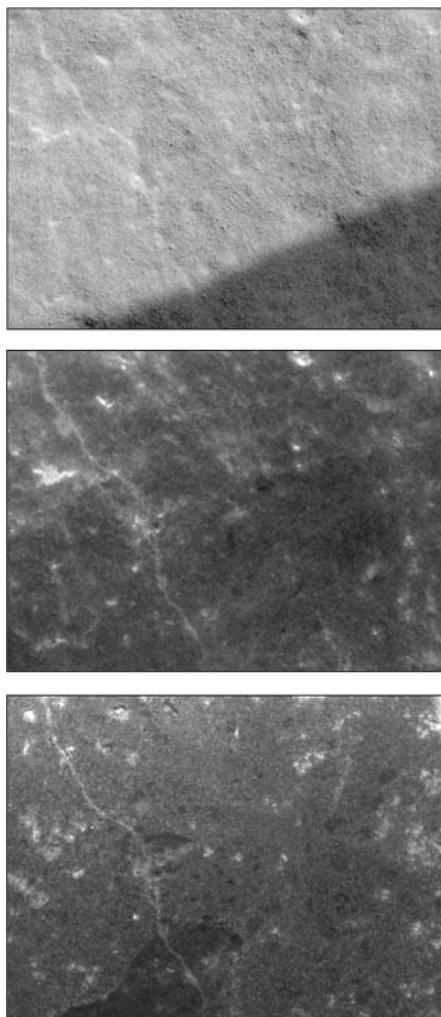


**Fig. 4.** MI images of rock called Adirondack. **(Top)** Part of image 2M127876442 showing natural surface. **(Middle)** Part of image 2M129296827 showing same area after RAT brushing. **(Bottom)** Part of image 2M129468568 showing same area after RAT grinding. Each subframe  $\sim 20$  mm across. Illumination from top, shadow at lower right in left frame; right frames show surface in complete shadow.

sistent with electrostatic cohesion or minor cementation of dust grains (15). Some of the MI images of soil or dusty rocks show linear textures that may have been formed by recent winds.

MI data were used to quantify grain-size distribution and shape in soils and bedforms at Gusev Crater. Biases and sources of measurement errors in image analyses of terrestrial sediments have been studied and quantified (16–18) and are mainly related to the resolution of the instrument, the size of individual grains, and the light-scattering effect and projected shadows on grains. Representative areas of equal size in each MI image were selected for statistical data gathering, and grains were counted by several analysts. Longest and short-

est axes of grains were measured with an average deviation of  $\pm 1$  pixel (31  $\mu\text{m}$ ) (18). Single grains were identified with confidence when their diameter was at least 120  $\mu\text{m}$  ( $\sim 4$  pixels). At this size, the error margin of  $\pm 1$  pixel still represents a significant fraction of a grain size ( $\sim 30\%$ ). Therefore, we limited our counts to grain diameters  $>210$   $\mu\text{m}$ , where confidence is high and error margin acceptable. Our results thus do not include the very fine sand to clay fractions. Grain-size classifications of the MI samples use the Wentworth scale (19).

Most of the soils at Gusev are composed of very fine grains or agglomerates of grains at the margin of MI resolution. Bedforms have coarser particles at their crests and finer grains in the troughs, like aeolian ripples on Earth (20). Particle-size frequencies of sampled ripple surfaces such as Arena (20, 21) typically are bimodal, with one mode centered between 1 and 2 mm (coarse sand to very fine granules) and the other below 210  $\mu\text{m}$  (fine to very fine sand). MI images of soil (e.g., Fig. 2) indicate that grains too small to be resolved are present, but statistics for grains smaller than 210  $\mu\text{m}$  are not included in Fig. 3. The larger grains are rigid (as opposed to agglomerates of finer grains), based upon the lack of modification by the Mössbauer contact plate. The bedform Serpent, analyzed on sol 73, has a trimodal distribution, with an additional mode centered between 500 and 250  $\mu\text{m}$  (Figs. 2 and 3). Specific shapes are associated with the coarser modes: granules are platy-rounded to ellipsoidal; medium sands are spherical. The shape of the finest sands at the margin of resolution could not be assessed. Typical soils include a mixture of grain sizes and larger clasts. Multimodalities in grain-size distribution are usually associated with multiple processes having affected the grains. In this case, the size and sphericity of the medium sand is consistent with aeolian processes (20), while the platy-rounded and ellipsoidal shapes of the granules are associated with aqueous or aeolian processes on Earth.

Rocks at the Gusev site were examined by the MI before and after brushing and grinding by the RAT (12) (Fig. 4 and Plates 12 and 13). The images of natural surfaces show a submillimeter texture that appears to be caused by cohesion of unresolved dust grains on the rocks, similar to the agglomerates seen in the soils at Gusev. Pits and veins are visible in the rocks before and after brushing or grinding, but only after dust has been removed from the rock surface can the color and reflectance of the veins be observed. MI observations of areas that have been abraded by the RAT reveal evidence for thin coatings on the rocks, which may be products of alteration by water (22). The images show min-

eral grains, probably phenocrysts, beneath the coatings. These observations are consistent with the rocks having a volcanic origin, as indicated by other Spirit observations (23).

#### References and Notes

1. K. E. Herkenhoff *et al.*, *J. Geophys. Res.* **108**, 8065 (2003).
2. S. W. Squyres, *et al.*, *J. Geophys. Res.* **108**, 8062 (2003).
3. J. F. Bell III *et al.*, *J. Geophys. Res.* **108**, 8063 (2003).
4. J. N. Maki *et al.*, *J. Geophys. Res.* **108**, 8071 (2003).
5. A martian solar day has a mean period of 24 hours 39 min 35.244 s and is referred to as a sol to distinguish it from a roughly 3% shorter solar day on Earth. A martian sidereal day, as measured with respect to the fixed stars, is 24 hours 37 min 22.663 s, as compared with 23 hours 56 min 04.0905 s for Earth. See [www.giss.nasa.gov/tools/mars24](http://www.giss.nasa.gov/tools/mars24) for more information.
6. The term martian soil is used here to denote any loose, unconsolidated materials that can be distinguished from rocks, bedrock, or strongly cohesive sediments. No implication of the presence or absence of organic materials or living matter is intended.
7. R. E. Arvidson *et al.*, *Science* **305**, 821 (2004).
8. P. Bertelsen *et al.*, *Science* **305**, 827 (2004).
9. S. W. Squyres *et al.*, *Science* **305**, 794 (2004).
10. J. F. Bell III *et al.*, *Science* **305**, 800 (2004).
11. R. V. Morris *et al.*, *Science* **305**, 833 (2004).
12. S. Gorevan *et al.*, *J. Geophys. Res.* **108**, 8068 (2003).
13. R. Gellert *et al.*, *Science* **305**, 829 (2004).
14. The ability to resolve individual grains with the MI depends on the illumination of the scene and the contrast between the grain and its surroundings. Typically, an object must subtend at least 3 pixels to be recognized in an image.
15. G. Landis *et al.*, in *Lunar and Planetary Science XXXV* (LPI Publication 1197, Lunar and Planetary Institute, Houston, CD-ROM, 2004).
16. J. B. Butler, S. N. Lane, J. H. Chandler, *J. Hydraulic Res.* **39**, 1 (2001).
17. D. M. Rubin, *J. Sed. Res.* **74**, 160 (2004).
18. We used NIH Image, version 1.63 (24).
19. C. K. Wentworth, *J. Geol.* **30**, 377 (1922).
20. R. Greeley *et al.*, *Science* **305**, 810 (2004).
21. Names have been assigned to areographic features by the Mars Exploration Rover (MER) team for planning and operations purposes. The names are not formally recognized by the International Astronomical Union.
22. H. Y. McSween *et al.*, *Science* **305**, 842 (2004).
23. P. R. Christensen *et al.*, *Science* **305**, 837 (2004).
24. J. Wagner *et al.*, in preparation.
25. The U.S. Geological Survey MER Team developed MI software and created various data products, including some of those displayed in this issue: B. Archinal, J. Barrett, K. Becker, T. Becker, D. Burr, D. Cook, T. Hare, A. Howington-Kraus, R. Kirk, E. Lee, M. Rosiek, B. Sucharski, T. Sucharski, and J. Torson (project engineer). The Ames MER team and Mark Lemmon developed software to merge focal sections and generate anaglyphs from them. The MER Rover Planners provided excellent support of the MI investigation by commanding the arm and MI dust cover. Reviews of this paper by M. Chapman, L. Keszthelyi, S. Thompson, C. Weitz, and four anonymous referees are much appreciated. The work described here was supported by the NASA Jet Propulsion Laboratory Mars Exploration Rover project. The use of trade, product, or firm names in this paper does not imply endorsement by the U. S. government.

#### Plates Referenced in Article

[www.sciencemag.org/cgi/content/full/305/5685/824/DC1](http://www.sciencemag.org/cgi/content/full/305/5685/824/DC1)  
Plates 12 and 13

6 May 2004; accepted 15 July 2004



# Magnetic Properties Experiments on the Mars Exploration Rover Spirit at Gusev Crater

P. Bertelsen,<sup>1\*</sup> W. Goetz,<sup>1</sup> M. B. Madsen,<sup>1</sup> K. M. Kinch,<sup>2</sup> S. F. Hviid,<sup>3</sup> J. M. Knudsen,<sup>1</sup> H. P. Gunnlaugsson,<sup>2</sup> J. Merrison,<sup>2</sup> P. Nørnberg,<sup>4</sup> S. W. Squyres,<sup>5</sup> J. F. Bell III,<sup>5</sup> K. E. Herkenhoff,<sup>6</sup> S. Gorevan,<sup>7</sup> A. S. Yen,<sup>8</sup> T. Myrick,<sup>7</sup> G. Klingelhöfer,<sup>9</sup> R. Rieder,<sup>10</sup> R. Gellert<sup>10</sup>

The magnetic properties experiments are designed to help identify the magnetic minerals in the dust and rocks on Mars—and to determine whether liquid water was involved in the formation and alteration of these magnetic minerals. Almost all of the dust particles suspended in the martian atmosphere must contain ferrimagnetic minerals (such as maghemite or magnetite) in an amount of ~2% by weight. The most magnetic fraction of the dust appears darker than the average dust. Magnetite was detected in the first two rocks ground by Spirit.

The history of liquid water on Mars may be reflected in the magnetic minerals present in the surface materials on Mars today: If liquid water is present in an oxidizing environment, Fe<sup>2+</sup> ions in solution will oxidize to Fe<sup>3+</sup>, and new minerals will form. In general, the magnetic minerals in the (<3- $\mu$ m-diameter) atmospheric dust particles will provide information on the formation and alteration processes that have taken place globally on Mars. The Viking Landers (1976) and the Mars Pathfinder Lander (1997) carried permanent magnets (1–3) designed to investigate the magnetic properties of the martian soil (4) and the dust particles suspended in the atmosphere. The main conclusion of these investigations was that the martian soil and dust on average must contain about 2% by weight of a strongly magnetic (ferrimagnetic) mineral. This mineral could be maghemite ( $\gamma$ -Fe<sub>2</sub>O<sub>3</sub>, saturation magnetization  $\sigma_s = 70$  A m<sup>2</sup> kg<sup>-1</sup>), or magnetite (Fe<sub>3</sub>O<sub>4</sub>,  $\sigma_s = 92$  A m<sup>2</sup> kg<sup>-1</sup>). Each of the Mars Exploration Rovers carries seven permanent magnets (5). The Magnetic Properties Experiments (MPEs) on the rovers are designed to (i) identify the magnetic mineral(s) in the dust on Mars; (ii) establish if all airborne particles contain magnetic minerals; and (iii) provide qualitative information of the magnetism of a few selected rocks (5–7).

<sup>1</sup>Center for Planetary Science, Danish Space Research Institute and Niels Bohr Institute for Astronomy, Physics and Geophysics, University of Copenhagen, DK-2100 Copenhagen, Denmark. <sup>2</sup>Department of Physics and Astronomy, University of Aarhus, DK-8000 Aarhus, Denmark. <sup>3</sup>Max Planck Institut für Aeronomie, D-37191 Katlenburg-Lindau, Germany. <sup>4</sup>Department of Earth Sciences, University of Aarhus, DK-8000 Aarhus, Denmark. <sup>5</sup>Cornell University, Department of Astronomy, Ithaca, NY 14853, USA. <sup>6</sup>U.S. Geological Survey Branch of Astrogeology, Flagstaff, AZ 86001, USA. <sup>7</sup>Honeybee Robotics Ltd., New York, NY 10012, USA. <sup>8</sup>Jet Propulsion Laboratory, California Institute of Technology, Pasadena, CA 91109, USA. <sup>9</sup>Institut für Inorganische und Analytische Chemie, Johannes Gutenberg-Universität, D-55099 Mainz, Germany. <sup>10</sup>Max-Planck-Institut für Chemie, D-55020 Mainz, Germany.

\*To whom correspondence should be addressed. E-mail: preben@fys.ku.dk

Four small cylindrical magnets are integrated into the Rock Abrasion Tool (RAT) on the rover. The purpose of the RAT magnets is to detect magnetic minerals in the abraded rock material. The two strongest RAT magnets are identical (both named 1), and the maximum value of magnetic field and magnetic field gradient is  $B = 0.28$  T and  $\nabla|B| = 350$  T m<sup>-1</sup>. The remaining two magnets are weaker:  $B = 0.10$  T and  $\nabla|B| = 120$  T m<sup>-1</sup> for type 2, and  $B = 0.07$  T and  $\nabla|B| = 80$  T m<sup>-1</sup> for type 3, respectively. The weak magnets can only attract and hold particles that have a high magnetization.

Before operations of the RAT, the RAT magnets attracted reddish magnetic particles from the atmosphere, and the spectrum of the attracted dust from sol 30 (8) is similar to the

spectrum of bright surface soil (Fig. 1). After brushing of the rock Adirondack (9), more dust is present on the RAT magnets, but the color is still reddish (the rock was covered with a thin layer of reddish dust). After grinding of the rock Humphrey, the dust attracted to the magnet is much darker and nearly black. The spectrum is consistent with the presence of magnetite and dark basaltic rock material. Because even the weak magnets have attracted a large amount of dark dust, we conclude that the rocks must contain at least a few percent of a dark ferrimagnetic mineral, probably magnetite. The result is corroborated by the Mössbauer spectra of the rocks Adirondack and Humphrey (10), which show the presence of magnetite.

The capture and filter magnets are placed at the front of the rover near the base of the Pancam mast. The two magnets attract atmospheric dust, which can be analyzed by the Pancam and by the instruments on the robotic arm (7). An image of the capture magnet acquired with the Microscopic Imager shows the dust pattern in detail (11). Both magnets (Sm<sub>2</sub>Co<sub>17</sub>) have a diameter of 25 mm and are embedded in an aluminum structure with a

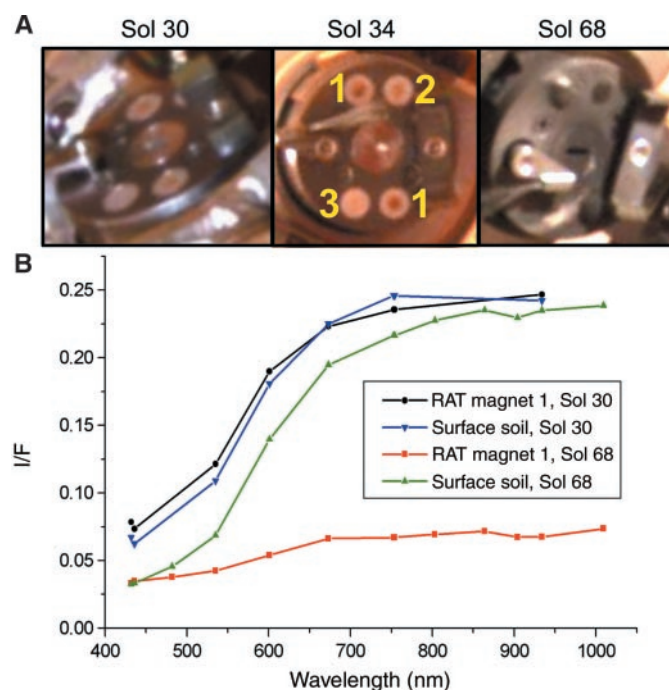


**Fig. 1.** The RAT magnets. (A) Pancam images from sol 30 (before any RAT operations), sol 34 (after brushing the rock Adirondack), and sol 68 (after grinding the rock Humphrey). The location of the individual magnets (type 1, 2, and 3) is shown with numbers. (B) Spectra of bright surface soil and dust on RAT Magnet 1 from sol 30 and sol 68. The ordinate is the calibrated reflectance.

diameter of 45 mm (5). The capture magnet (Fig. 2A, top) is very strong, with maximum values of the magnetic field and field gradient of  $B = 0.46$  T and  $\nabla|B| = 550$  T m<sup>-1</sup>. The filter magnet (Fig. 2A, bottom) is weaker:  $B = 0.2$  T and  $\nabla|B| = 34$  T m<sup>-1</sup>. The capture magnet is strong enough to attract and hold all paramagnetic and ferrimagnetic particles. The filter magnet, however, will (almost) only attract particles with a high value of magnetic susceptibility ( $\chi > 10^{-4}$ ). Therefore, the dust particles in the atmosphere will be “filtered” according to their magnetic properties.

The amount of dust on the capture magnet is higher than the amount of dust on the filter magnet (Fig. 2A) by a factor of  $\sim 2$  (a rough estimate based on the absorption at 440 nm early in the mission). This observation supports the view that the airborne particles have a saturation magnetization of about  $\sigma_s \sim 2$  A m<sup>2</sup> kg<sup>-1</sup> (5). Furthermore, small differences are observed in the visible–near infrared spectrum of the area where dust has accumulated on each magnet (Fig. 2B). The filter magnet is not yet optically saturated with dust, so the reflectivity at 440 nm is relatively high. At wavelengths above 750 nm, the dust accumulating on the filter magnet has lower

reflectance than the aluminum surface, whereas the opposite is true for the material accumulating on the capture magnet. This shows that the dust on the filter magnet is intrinsically darker than the dust on the capture magnet. The darker particles thus have higher magnetization.

The sweep magnet is on the solar panels close to the Pancam calibration target (5, 7), where it attracts dust from the atmosphere. It is a ring magnet (Sm<sub>2</sub>Co<sub>17</sub>) with an outer diameter of 9.0 mm, embedded in an aluminum structure. The maximum value of the magnetic field and field gradient at the surface of the magnet is  $B = 0.42$  T and  $\nabla|B| = 450$  T m<sup>-1</sup>. The size and direction of the magnetic field and field gradient prevent particles with magnetic susceptibility larger than  $10^{-6}$  m<sup>3</sup> kg<sup>-1</sup> from settling in the circular area inside the ring, called the sweep area (5). The sweep magnet is visible in many images of the Pancam calibration target acquired daily during the mission (Fig. 3A). The sweep magnet ring was optically saturated with red dust around sol 25 (at 440 nm). The dust on the ring shows an absorption spectrum (Fig. 3B) similar to the spectrum of the reddish bright soil on Mars (12–15). The main ab-

sorption features are due to the charge transfer band in an Fe<sup>3+</sup> compound. The lack of structure in the spectrum supports the view that the martian dust and soil are magnetic composites of multiple phases.

Outside the magnet, no magnetic force is present, and this surface will collect an amount of dust corresponding to the general sedimentation taking place everywhere. The spectrum of the area outside the magnet (Fig. 3B) shows an amount of reddening that is consistent with the reddening observed on the Pancam calibration target (12). The third spectrum—of the circular area inside the ring—is similar to the spectrum of a clean aluminum surface of the magnet. No (discernible) dust has settled in the sweep area. Indeed, this little region may be the “cleanest” part of the entire rover deck. Therefore, all airborne dust particles must be sufficiently magnetic that their paths near the magnet be controlled by the magnetic force. We note that a specially designed magnet like this could be used to keep (small) calibration targets clean in future missions.

Although we cannot yet determine which mineral is causing the magnetism of the dust particles, we can assess whether the magnetism of the suspended particles could be caused by hematite ( $\alpha$ -Fe<sub>2</sub>O<sub>3</sub>) alone. Hematite is a canted antiferromagnet above 260 K ( $\sigma_s = 0.4$  A m<sup>2</sup> kg<sup>-1</sup>), and is antiferromagnetic below 260 K. On the basis of alpha particle x-ray spectroscopy (APXS) elemental analysis of the dust, the maximum possible content of  $\alpha$ -Fe<sub>2</sub>O<sub>3</sub> in a given particle is about 18% by weight (16). Mössbauer spectroscopy of soil at the Columbia Memorial Station site shows that less than half of the iron is present as iron oxides (10). A substantial part of the iron in the soil is located in paramagnetic silicates, mostly olivine [(Mg,Fe)<sub>2</sub>SiO<sub>4</sub>]. Even if all the iron were present in hematite, the bulk magnetization would still be less than 0.08 A m<sup>2</sup> kg<sup>-1</sup>, and particles with such a low magnetization would not stick to the filter magnet in the amount shown on Fig. 2B. We therefore infer that hematite cannot be the dominant source of the magnetism present in the airborne particles.

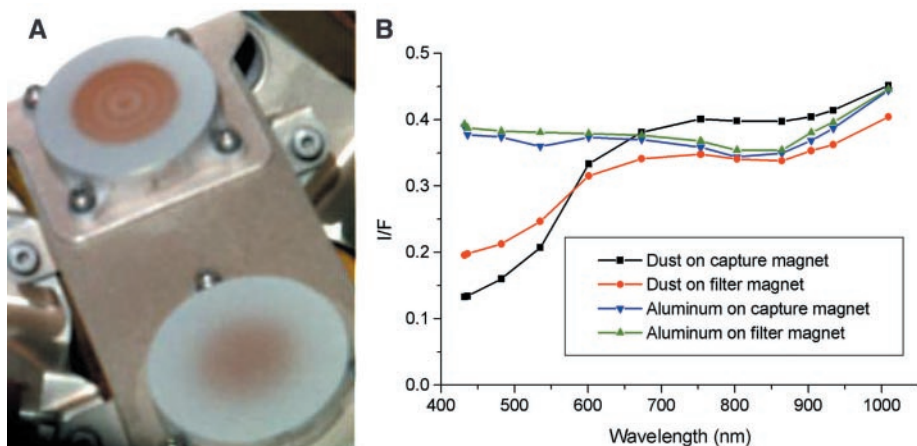
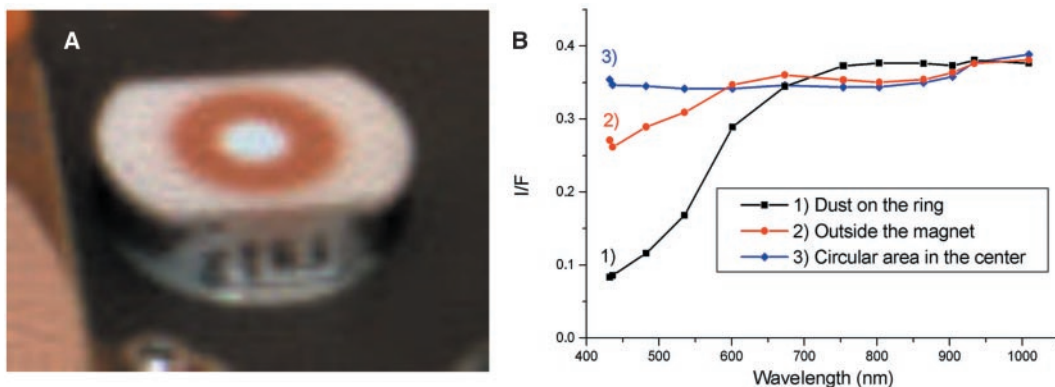


**Fig. 2.** The capture and filter magnets. (A) Pancam image recorded on sol 71. (B) Spectra of the area where dust has accumulated on the two magnets, and of the aluminum surface. The ordinate is the calibrated reflectance.

**Fig. 3.** The sweep magnet. (A) Pancam image recorded on sol 73. (B) Spectra from three areas: 1, the dust on the ring; 2, the dust outside the ring; and 3, the dust inside the ring. The ordinate is the calibrated reflectance.





Furthermore, Mössbauer spectra of soils at the Spirit site show the presence of magnetite (10). A small fraction of magnetite in the dust particles could easily explain the strong magnetization of the dust and the dust on the filter magnet being darker than that on the capture magnet.

APXS measurements and Mössbauer measurements of the dust on the filter and capture magnets will take place later in the mission in order to uniquely identify the ferrimagnetic phase in the composite particles (5).

#### References and Notes

1. R. B. Hargraves, D. W. Collinson, R. E. Arvidson, C. R. Spitzer, *J. Geophys. Res.* **82**, 4547 (1977).
2. P. H. Smith *et al.*, *J. Geophys. Res.* **102**, 4003 (1997).
3. M. B. Madsen *et al.*, *J. Geophys. Res.* **104**, 8761 (1999).
4. The term "martian soil" is used here to denote any loose, unconsolidated materials that can be distinguished from rocks, bedrock, or strongly cohesive
5. M. B. Madsen *et al.*, *J. Geophys. Res.* **108**, 8069 (2003).
6. S. Gorevan *et al.*, *J. Geophys. Res.* **108**, 8068 (2003).
7. S. W. Squyres *et al.*, *J. Geophys. Res.* **108**, 8062 (2003).
8. A sol is a martian day. Sol 1 is the day of landing. A martian solar day has a mean period of 24 hours 39 min 35.244 s and is referred to as a sol to distinguish it from a roughly 3% shorter solar day on Earth. A martian sidereal day, as measured with respect to the fixed stars, is 24 hours 37 min 22.663 s, as compared with 23 hours 56 min 04.0905 s for Earth. See [www.giss.nasa.gov/tools/mars24/](http://www.giss.nasa.gov/tools/mars24/) for more information.
9. Names have been assigned to areographic features by the Mars Exploration Rover (MER) team for planning and operations purposes. The names are not formally recognized by the International Astronomical Union.
10. R. V. Morris *et al.*, *Science* **305**, 833 (2004).
11. K. E. Herkenhoff *et al.*, *Science* **305**, 824 (2004).
12. J. F. Bell III *et al.*, *Science* **305**, 800 (2004).

13. J. F. Bell III, T. B. McCord, P. D. Owensby, *J. Geophys. Res.* **95**, 14447 (1990).
14. R. V. Morris *et al.*, *J. Geophys. Res.* **94**, 2760 (1989).
15. R. V. Morris, D. C. Golden, J. F. Bell III, H. V. Lauer Jr., J. B. Adams, *Geochim. Cosmochim. Acta* **57**, 4597 (1993).
16. R. Rieder *et al.*, *Science* **278**, 1771 (1997).
17. We are grateful for help from the skillful and dedicated Pancam team, particularly M. J. Johnson, J. Proton, H. M. Arneson, and E. McCartney. The "rover drivers" C. Leger, S. Maxwell, and E. Baumgartner made invaluable contributions to imaging of the RAT magnets. We also thank DELTA Danish Electronics, Light & Acoustics, who performed vibration testing and qualification certification of our flight instruments at no cost to the project, and the Danish Science Research Agency and the Thomas B. Thrige Foundation for the financial support that made our participation possible. We thank our colleagues at our own laboratory, particularly at the workshop, for their undivided dedication to this project.

10 May 2004; accepted 7 July 2004

#### REPORT

# Chemistry of Rocks and Soils in Gusev Crater from the Alpha Particle X-ray Spectrometer

R. Gellert,<sup>1,2\*</sup> R. Rieder,<sup>1</sup> R. C. Anderson,<sup>3</sup> J. Brückner,<sup>1</sup> B. C. Clark,<sup>4</sup> G. Dreibus,<sup>1</sup> T. Economou,<sup>5</sup> G. Klingelhöfer,<sup>2</sup> G. W. Lugmair,<sup>1</sup> D. W. Ming,<sup>6</sup> S. W. Squyres,<sup>7</sup> C. d'Uston,<sup>8</sup> H. Wänke,<sup>1</sup> A. Yen,<sup>3</sup> J. Zipfel<sup>1</sup>

The alpha particle x-ray spectrometer on the Spirit rover determined major and minor elements of soils and rocks in Gusev crater in order to unravel the crustal evolution of planet Mars. The composition of soils is similar to those at previous landing sites, as a result of global mixing and distribution by dust storms. Rocks (fresh surfaces exposed by the rock abrasion tool) resemble volcanic rocks of primitive basaltic composition with low intrinsic potassium contents. High abundance of bromine (up to 170 parts per million) in rocks may indicate the alteration of surfaces formed during a past period of aqueous activity in Gusev crater.

The alpha particle x-ray spectrometer (APXS) on the Spirit rover is an improved version of the APXS on the Sojourner rover that measured compositions of soils (1) and rocks during the 1997 Mars Pathfinder mission (2). A description of the instrument, the methodology, and an outline of the calibration procedure can be found in (3). Despite increased background count rate, because of the radioactive sources of the nearby Mössbauer spectrometer (MB) (4)

and cosmic radiation, the increased sensitivity of this instrument relative to the Pathfinder APXS allowed us to determine the abundances of trace

elements such as Ni, Zn, and Br, in addition to the major and minor rock-forming elements (Fig. 1) of circular spots 2.5 cm in diameter.

The internal control software of the APXS automatically splits the measuring time into several intervals. Repeatability and statistical significance, especially for the trace elements, was evaluated using these individual spectra. Data reduction was performed with a least-squares-fit routine developed during calibration. The in-

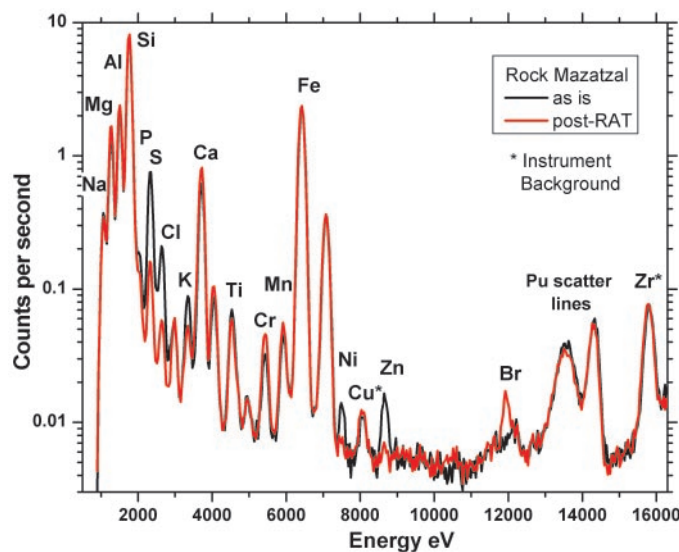


Fig. 1. X-ray spectra of rock Mazatzal before and after abrading with the RAT.

<sup>1</sup>Max-Planck-Institut für Chemie, J. J. Becher-Weg 27, D-55128 Mainz, Germany. <sup>2</sup>Institut für Anorganische und Analytische Chemie, J. Gutenberg-Universität, D-55128 Mainz, Germany. <sup>3</sup>Jet Propulsion Laboratory, Pasadena, CA 911091, USA. <sup>4</sup>Lockheed Martin Corporation, Littleton, CO 80127, USA. <sup>5</sup>Laboratory for Atmospheric and Space Research, Enrico Fermi Institute, Chicago, IL 60637, USA. <sup>6</sup>Johnson Space Center, National Aeronautics and Space Administration (NASA), Houston, TX 77058, USA. <sup>7</sup>Center for Radiophysics and Space Research, Cornell University, Ithaca, NY 14853, USA. <sup>8</sup>Centre d'Etude Spatiale des Rayonnements, F-31028, Toulouse, France.

\*To whom correspondence should be addressed. E-mail: gellert@mpch-mainz.mpg.de.

**Table 1.** Calibration results, standard deviation of analysis.

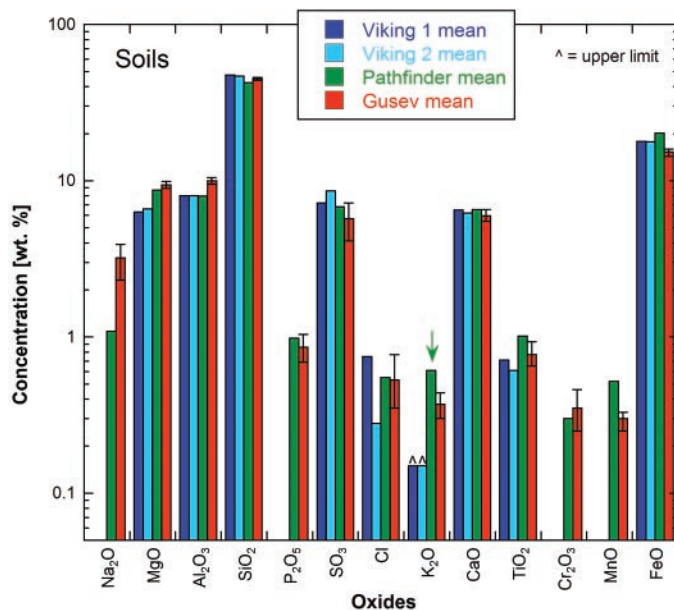
Element	Na	Mg	Al	Si	P	S	Cl	K	Ca	Ti	Cr	Mn	Fe	Ni	Zn	Br
Relative SD (%)	8.5	17.3	7.2	3.5	16.8	14.1	12.5	14.4	7.7	20.4	20	7.9	5.8	10.1	11.7	10
No. of samples	31	31	42	41	27	19	8	34	33	31	8	35	34	17	31	6

struments were calibrated with about 60 samples of widely varying composition. The relative standard deviations of the analytical results (i.e., their accuracy) for all measured elements are given in Table 1. The relative accuracy of the analyses was found to be even better when samples with similar matrices were analyzed. In these cases, systematic errors tend to cancel each other, and accuracy is mainly determined by precision. Therefore, even small variations between similar samples are significant. Instrument precision (reproducibility) is high, as can be judged from the close agreement of analyses of areas cleaned with the rock abrasion tool (RAT) (5) of the rocks Adirondack, Humphrey, and Mazatzal (6). All three rocks were also found to be similar by the rest of the Athena instrument suite (7).

The compositions of soils and rocks, analyzed during the 90-day primary mission, are presented in Tables 2 and 3. In these tables, iron was assigned to FeO, although from Mössbauer spectroscopy (8), it is known that between 10 and 50% of iron is present in the form of Fe<sup>3+</sup>. However, the resulting effect on normalization and matrix correction is less than 1%. The element compositions are normalized to 100% oxides, with the assumptions that samples are free of water and carbonates and S is present as SO<sub>3</sub>. In this way, variations in the observed X-ray intensities due to various measuring geometries are compensated.

In general, the major element compositions of the soils at the Viking 1, Viking 2, Pathfinder, and Gusev landing sites are similar (Table 2 and Fig. 2). This supports the hypothesis of a global mixing process driven by dust storms (9, 10). In the case of highly incompatible minor elements like K, the contribution from local rocks becomes apparent (green arrow in Fig. 2): the high concentration of K in the Pathfinder soil stems from local debris of the K-rich rocks at that site.

All soils at the Gusev landing site are characterized by high S and Cl concentrations, as was also observed at other landing sites on Mars (9–12). Concentrations of S in soils range from 1.3 to 3 weight %, with a fairly consistent S/Cl ratio of 4.7 ± 0.3. Pathfinder soils cover a similar range with a S/Cl ratio of 5.0 ± 0.4. Besides Cl, only P is positively correlated with S (Table 2 and Fig. 3), whereas Ni and Zn vary independently of the S abundance. In soils, major elements,

**Fig. 2.** Composition of martian soils from different landing sites. Viking data are taken from (9) (for K, only an upper limit was derived) and Pathfinder from (10, 11). "Gusev mean" is the average of APXS soil measurements (see Table 2). Error bars indicate range of soil data. Arrow, the contribution from local rocks becomes apparent.**Table 2.** Average of all 11 soils and selected individual soils, concentration in weight percent of oxides or parts per million by weight.

Oxide	Average	Deviation	Minimum	Maximum	Gusev soil	Laguna Hollow	Laguna Hollow (trench)	Gobi	Serpent scuffed
<i>Concentration (wt %)</i>									
Na <sub>2</sub> O	3.3	0.31	2.7	3.8	3.2	3.6	2.7	3.1	3.3
MgO	9.3	0.24	9.0	9.7	9.1	9.2	9.7	9.0	9.7
Al <sub>2</sub> O <sub>3</sub>	10.0	0.22	9.7	10.4	10.0	10.1	9.8	9.7	10.2
SiO <sub>2</sub>	45.8	0.44	45.1	46.5	46.1	45.7	45.7	45.1	46.4
P <sub>2</sub> O <sub>5</sub>	0.84	0.07	0.70	0.93	0.89	0.89	0.74	0.93	0.70
SO <sub>3</sub>	5.82	0.86	4.22	7.38	6.36	6.09	5.88	7.38	4.22
Cl	0.53	0.13	0.35	0.77	0.51	0.49	0.46	0.59	0.36
K <sub>2</sub> O	0.41	0.03	0.34	0.45	0.45	0.41	0.34	0.45	0.37
CaO	6.10	0.27	5.72	6.63	6.03	6.02	5.81	5.78	6.23
TiO <sub>2</sub>	0.81	0.08	0.67	0.96	0.80	0.83	0.96	0.83	0.89
Cr <sub>2</sub> O <sub>3</sub>	0.35	0.07	0.25	0.48	0.29	0.31	0.41	0.29	0.44
MnO	0.31	0.02	0.26	0.34	0.31	0.31	0.33	0.29	0.34
FeO	15.8	0.36	15.2	16.3	15.2	15.4	16.1	15.9	16.4
<i>Concentration (ppm)</i>									
Ni	450	120	260	630	550	320	480	630	450
Zn	300	80	190	440	290	300	310	440	210
Br	40	30	0	100	20	10	60	10	50

such as Mg, show negative trends with S (see Fig. 3). Along a 500-meter traverse by Spirit, no significant variation in soil composition was found. In a depression filled with fine-grained soil (Laguna Hollow), a trench about 10 cm deep was excavated. No significant differences have been observed between the composition of the top layer, the wall, and the floor of the trench. However, the scuffed interior of an eolian drift (Serpent) gave the

lowest S concentration (SO<sub>3</sub> = 4.22 wt % in Table 2) of all soil analyses.

When comparing the chemical relation between soils and rocks, we observe the following: cleaned rocks have low concentrations of Ni and Zn, similar to martian meteorites. However, the exterior of rock Mazatzal shows higher concentrations of Ni and Zn than the average soil. Only the soil Gobi, adjacent to Mazatzal, has concentra-



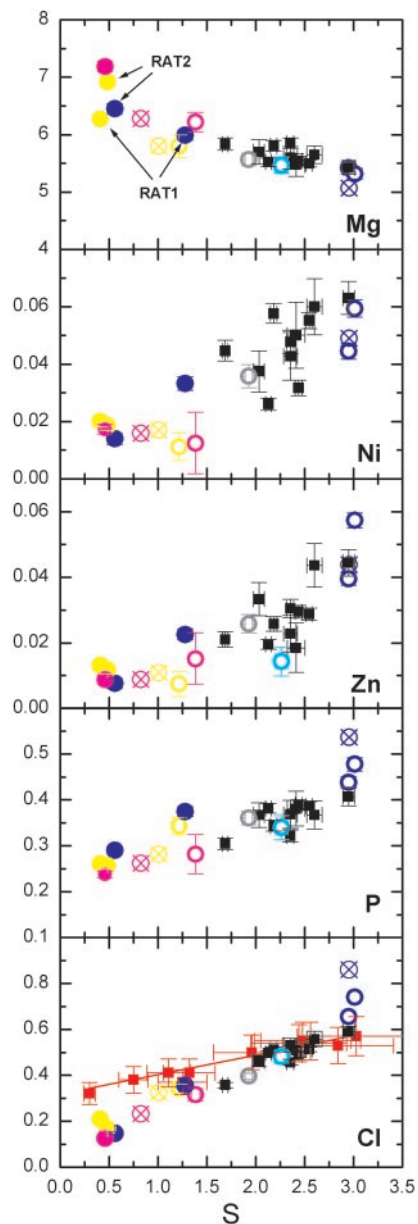


**Fig. 3.** Element versus S variation diagrams. Shown are Gusev soils (black squares), and Gusev rocks: Mazatzal (blue), Humphrey (yellow), Adirondack (magenta), Mimi (gray) and Plank (cyan). Open symbols refer to natural (untreated) surfaces; symbols marked with X refer to surfaces after brushing; filled symbols refer to analyses after grinding (RAT); Error bars refer to statistical uncertainties. Subsequent RAT grinds are indicated by RAT1 and RAT2. Natural surfaces of rocks and soils (red squares) from the Pathfinder Mission (10, 11) fall on simple mixing lines (red line). All element concentrations are given in wt %.

tions of similar magnitude. The high Ni contents of soils may be attributable to a meteoritic component and/or decomposed olivine. Enrichment of Zn in martian soils has been predicted, if magmatic degassing were responsible for differences between soils and rocks (13, 14).

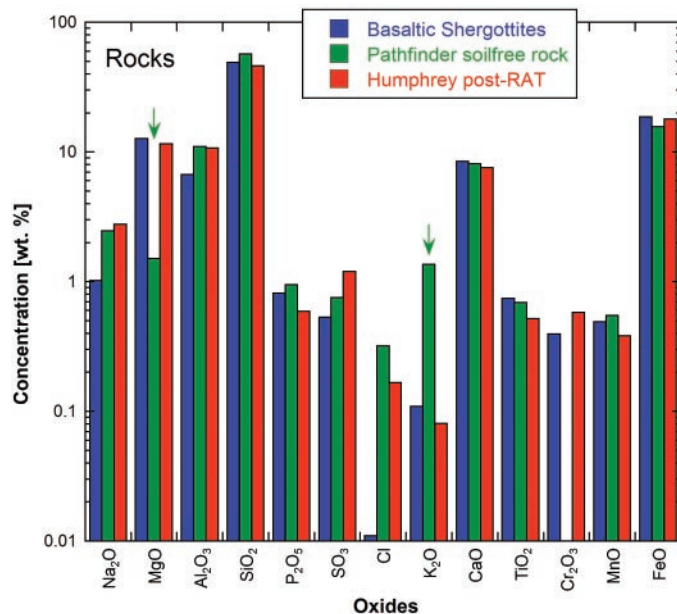


**Fig. 4.** Composition of different martian rocks. The “basaltic shergottites” are the average composition of selected shergottites (17). “Pathfinder soil-free rock” is extrapolated to an  $\text{SO}_3$  value of 0.75 wt % (10, 11). “Humphrey post-RAT” is a rock at Gusev crater, abraded by the RAT (see Table 3). Arrows, rocks that are poor in Mg, rich in K.

Earlier analyses of rock surfaces during the Pathfinder mission showed lower S and Cl concentrations when compared with soils but fall on the same correlation line, which indicates that rocks are covered with soil to a varying degree. Therefore, element versus S correlations were used to derive an extrapolated “soil-free” composition of these rocks (10, 11). However, such an extrapolation would not be possible for Gusev rocks because of the small compositional difference between rocks and soil (see Mg versus S in Fig. 3).

Concentrations of S and Cl are highly variable in natural (untreated) surfaces of the analyzed rocks. Compared with soils, these concentrations can either be lower, as in the case of the darker rocks Adirondack and Humphrey, or higher, as for the relatively bright rock Mazatzal. Gobi, the only soil with similarly high S and Cl concentrations, is located close to Mazatzal and indicates that the material covering the surface of Mazatzal came from the local soil. Rock compositions show considerable scatter after brushing off loose surface material and grinding with the RAT. This effect is most pronounced in Mazatzal. Brushing the surface did not change S but Cl and  $\text{P}_2\text{O}_5$  increased to 0.86 and 1.23 wt %, respectively, the highest values observed so far. Even more important, the concentration of Br increased from 30 to 100 parts per million. Subsequent grinding removed practically all S and Cl, whereas the concentration of Br further increased to 170 ppm (see Fig. 1 and Table 3). The only other rock with a measurable amount of Br is Humphrey. In microscopic images (15), a white vein in Mazatzal and an alteration zone in Humphrey are visible. Thus, the material in these veins or alteration zones appears to be

the carrier of the Br. Because of the lack of measurable Br in Adirondack high Br in these rocks is unlikely to be indigenous.

On their freshly ground surfaces, the compositions of Adirondack, Humphrey, and Mazatzal are similar (Table 3) and reminiscent of typical primitive basaltic rocks found on Earth (16). However, the lowest Cl and S concentrations of  $\sim 0.15$  and  $\sim 0.5$  wt %, respectively, are still higher than in basaltic martian meteorites (17). This could be because of alteration veins or residual dust in “vugs” and/or a weathering rind on the rock surfaces. In some instances, e.g., Adirondack, the surface topography of the rock prevented a complete removal of the outer layer of the rock by the RAT; this means that the APXS was viewing a mixed surface that was mostly abraded but in some places material from the outer layer remained. Thus, in addition to being covered by some loose soil material, the rocks in Gusev crater may be covered with a crust or weathering rind with a composition distinct from the rocks and soil. Dust crust-free compositions are therefore difficult to estimate, and we assume that the composition of Humphrey (after the second grind) yields the closest approximation to the indigenous, uncontaminated rock composition (except for Br).

The basaltic rocks at Gusev are primitive in a geochemical sense (18). They are rich in Mg, poor in K (see arrows in Fig. 4), and poor in Cl, similar to primitive terrestrial basalts. Their very primitive nature is also evident from the low content of incompatible elements and an Al/Ti ratio close to the value of carbonaceous chondrites type I (CI). This indicates that these rocks were produced by a high degree of partial melting of the martian mantle—as such they may even be compared

**Table 3.** Compositions of all Gusev rocks, concentration in weight % of oxides or parts per million by weight. Absolute statistical error is 2 $\cdot$  for a typical measurement of 4 hours' duration. This number can also be considered as detection limit. For Adirondack as is, Humphrey as is, and

Plank, brief (0.5 hour) measurements with higher statistical errors, typically twofold, especially for minor and trace elements. Abbreviations: As is, untreated surface; RAT, rock abrasion tool; OR, Oregon; NY, New York; ND, not detectable.

Oxide	Abs. stat. error	Adirondack			Mimi	Humphrey					Plank	Mazatzal				
		As is	Brush	RAT		As is 1	As is 2	Brush	RAT1	RAT2		Texas as is	OR as is	NY brush	NY RAT1	NY RAT2
<i>Concentration (wt %)</i>																
Na <sub>2</sub> O	0.3	2.7	3.1	2.7	3.2	3.5	3.4	3.3	3.1	2.8	3.5	3.6	3.2	2.9	3.1	3.1
MgO	0.2	10.3	10.4	11.9	9.2	9.6	9.6	9.6	10.4	11.5	9.1	9.0	8.8	8.4	9.9	10.7
Al <sub>2</sub> O <sub>3</sub>	0.2	11.1	11.4	10.9	10.1	10.7	11.2	11.2	10.9	10.6	9.8	9.2	9.0	8.6	10.0	10.8
SiO <sub>2</sub>	0.4	45.8	45.5	45.4	45.0	45.5	45.3	45.7	46.1	45.7	43.9	43.7	44.6	44.6	45.4	45.5
P <sub>2</sub> O <sub>5</sub>	0.03	0.65	0.60	0.54	0.87	0.67	0.67	0.65	0.60	0.59	0.78	1.00	1.09	1.23	0.86	0.67
SO <sub>3</sub>	0.05	3.46	2.06	1.15	5.32	3.37	3.04	2.52	1.02	1.20	5.66	7.38	7.54	7.39	3.20	1.39
Cl	0.03	0.32	0.23	0.13	0.50	0.39	0.34	0.32	0.21	0.17	0.48	0.66	0.74	0.86	0.36	0.15
K <sub>2</sub> O	0.1	0.15	0.11	0.06	0.46	0.16	0.16	0.17	0.12	0.08	0.31	0.44	0.50	0.52	0.27	0.15
CaO	0.05	7.24	7.51	7.42	6.73	7.14	7.16	7.43	7.84	7.53	6.49	5.91	6.00	6.30	7.22	7.68
TiO <sub>2</sub>	0.03	0.52	0.46	0.45	0.62	0.46	0.50	0.51	0.54	0.53	0.53	0.76	0.74	0.79	0.65	0.56
Cr <sub>2</sub> O <sub>3</sub>	0.03	0.57	0.61	0.59	0.52	0.56	0.58	0.58	0.66	0.59	0.55	0.32	0.21	0.26	0.44	0.53
MnO	0.03	0.33	0.37	0.38	0.38	0.36	0.36	0.36	0.38	0.38	0.39	0.31	0.32	0.31	0.37	0.39
FeO	0.2	17.4	17.2	18.0	16.6	17.0	17.2	17.2	17.8	18.0	18.1	17.2	16.7	17.2	17.7	18.0
<i>Concentration (ppm)</i>																
Ni	40	130	160	170	260	230	110	170	200	190	ND	445	595	490	330	140
Zn	40	150	90	90	200	130	75	110	130	120	140	395	570	440	230	75
Br	30	ND	10	0	40	ND	ND	30	35	50	ND	30	60	100	150	170

with terrestrial basaltic komatiites. Of course, like all martian rocks, they have a high Fe content, reflecting the high Fe abundance in the martian mantle.

These rocks are also similar in composition to basaltic shergottites, the only type of martian meteorites that are basalts. They also correspond to the proposed category of rocks that were needed to explain the relatively high Mg and low K content of the Pathfinder soil (10). In contrast, the existence of more evolved rocks (such as found at the Pathfinder site) is required elsewhere to explain the relatively low Mg and high K in soil at Gusev.

If we take the estimated mantle abundances (19) at face value, the primitive martian mantle should contain 0.037 wt % K<sub>2</sub>O, 0.16 wt % P<sub>2</sub>O<sub>5</sub>, and 0.14 wt % TiO<sub>2</sub>. However, in Gusev rock Humphrey (RAT 2), these incompatible elements are enriched by factors of < 2.7, 3.6, and 3.8, respectively. The lower enrichment factor for the highly incompatible element K might indicate a slightly depleted mantle source (16). In contrast, the Pathfinder rocks must have been formed by a low degree of partial melting. Relative to the martian mantle they show enrichment factors of 37, 5.9, and 4.9, respectively.

As mentioned above, excess Br has been observed in Gusev rocks (Mazatzal and Humphrey) associated with alteration zones or veins. It is also interesting to note that a substantial enhancement of Br over Cl has been reported for fracture-filling aqueous al-

teration products in olivine from the martian meteorite Nakhla (20). Although we do not yet fully understand these findings, high Br and low Cl/Br ratios may be indicative of alteration in an aqueous environment. Precipitation of chlorides, after reaching saturation, leads to a decrease of the Cl/Br ratio in residual brines, as is also known from terrestrial evaporates from salt lakes. Thus, we assume that water played a major role in Cl/Br fractionation in Gusev crater.

#### References and Notes

- The term martian soil is used here to denote any loose, unconsolidated materials that can be distinguished from rocks, bedrock, or strongly cohesive sediments. No implication of the presence or absence of organic materials or living matter is intended.
- R. Rieder *et al.*, *Science* **278**, 1770 (1997).
- R. Rieder *et al.*, *J. Geophys. Res.* **108** (no. E12), 8066 (2003).
- The influence of the Mössbauer reference and main sources, mainly scattered high-energy radiation, was investigated during the development of the APXS. The introduced background was suppressed by a factor of 10 with 1-mm tantalum shields on the APXS and the Mössbauer instruments. Nevertheless, the resulting background was still 2.5 times that of the original.
- S. P. Gorevan *et al.*, *J. Geophys. Res.* **108** (no. E12), 1029 (2003).
- Names have been assigned to areographic features by the Mars Exploration Rovers (MER) team for planning and operations purposes. The names are not formally recognized by the International Astronomical Union (IAU).
- S. W. Squyres *et al.*, *J. Geophys. Res.* **108** (no. E12), 8062 (2003).
- G. Klingelhoefer *et al.*, *Science*, this issue.
- B. C. Clark *et al.*, *J. Geophys. Res.* **87** (no. B12), 10059 (1982).
- H. Wänke, J. Brückner, G. Dreibus, R. Rieder, I. Ryabchikov, *Space Sci. Rev.* **96**, 317 (2001).
- J. Brückner, G. Dreibus, R. Rieder, H. Wänke, *J. Geophys. Res.* **108** (no. E12), 8094 (2003).
- C. N. Foley, T. Economou, R. N. Clayton, *J. Geophys. Res.* **108** (no. E12), 8096 (2003).
- B. C. Clark, A. K. Baird, *Geophys. Res. Lett.* **6**, 811 (1979).
- H. E. Newsom, J. J. Hagerty, *J. Geophys. Res.* **102**, 19345 (1997).
- K. E. Herkenhoff *et al.*, *Science*, **305**, 824 (2004).
- H. Y. McSween Jr. *et al.*, *Science*, **305**, 842 (2004).
- Selected martian meteorites to derive a mean composition for martian basalts are Shergotty, Zagami (21), Los Angeles (22), SaU 005, and Yamato 980459 (23).
- Primitive basalts are rocks with low SiO<sub>2</sub>, low K<sub>2</sub>O, and high MgO concentrations derived by large degrees of partial melting of the primitive mantle.
- H. Wänke, G. Dreibus, *Philos. Trans. R. Soc. London A Math. Phys. Sci.* **349**, 285 (1994).
- S. R. Sutton *et al.*, *Lunar Planet Sci.* **XXXIII**, abstr. no. 1278 (2002).
- A. Banin, B. C. Clark, H. Wänke, in *Mars*, H. H. Kieffer, B. M. Jakosky, C. W. Snyder, M. S. Matthews, Eds. (Univ. Arizona Press, Tucson, 1992), pp. 594–625.
- G. Dreibus, unpublished data.
- G. Dreibus, R. Haubold, W. Huisl, B. Spettel, International Symposium, Evolution of Solar System Material: A New Perspective from Antarctic Meteorites, National Institute of Polar Research, Tokyo, 3 to 5 September 2003, p. 19.
- We thank our editor, J. Bishop, and two anonymous reviewers for their critical comments and suggestions, which significantly improved the manuscript. The APXS was mainly funded by the Max-Planck-Society and by a grant from the German Space Agency (DLR), grant no. 50QM0014. G.K. and R.G. also acknowledge support from DLR grant no. 50QM0014. Funding for Athena science team members was provided by NASA contracts through Cornell and the Jet Propulsion Laboratory.

4 May 2004; accepted 13 July 2004



# Mineralogy at Gusev Crater from the Mössbauer Spectrometer on the Spirit Rover

R. V. Morris,<sup>1\*</sup> G. Klingelhöfer,<sup>2</sup> B. Bernhardt,<sup>2</sup> C. Schröder,<sup>2</sup> D. S. Rodionov,<sup>2,3</sup> P. A. de Souza Jr.,<sup>2,4</sup> A. Yen,<sup>5</sup> R. Gellert,<sup>2,6</sup> E. N. Evlanov,<sup>3</sup> J. Foh,<sup>2,7</sup> E. Kankeleit,<sup>7</sup> P. Gütllich,<sup>2</sup> D. W. Ming,<sup>1</sup> F. Renz,<sup>2</sup> T. Wdowiak,<sup>8</sup> S. W. Squyres,<sup>9</sup> R. E. Arvidson<sup>10</sup>

Mössbauer spectra measured on Mars by the Spirit rover during the primary mission are characterized by two ferrous iron doublets (olivine and probably pyroxene) and a ferric iron doublet (tentatively associated to nanophase ferric iron oxide). Two sextets resulting from nonstoichiometric magnetite are also present, except for a coating on the rock Mazatzal, where a hematite-like sextet is present. Greater proportions of ferric-bearing phases are associated with undisturbed soils and rock surfaces as compared to fresh rock surfaces exposed by grinding. The ubiquitous presence of olivine in soil suggests that physical rather than chemical weathering processes currently dominate at Gusev crater.

Miniaturized Mössbauer spectrometers (MIMOS II) (1) are part of the science payload of each Mars Exploration Rover (MER) (2–4). Mössbauer spectrometers provide quantitative information about the distribution of iron among its oxidation states, identification of iron-bearing phases, and distribution of iron among those phases. Ferrous iron ( $\text{Fe}^{2+}$ ) is present in primary silicate and oxide minerals (such as olivine, pyroxene, ilmenite, and magnetite) and many secondary minerals (such as serpentine). Although present at significant levels in some primary minerals (such as augite and magnetite), ferric iron ( $\text{Fe}^{3+}$ ) is primarily associated with the crystalline and amorphous products of oxidative alteration and weathering of primary materials. Characterizing the speciation and distribution of iron in martian rock and soil (5) constrains the primary rock type (such as olivine versus pyroxene basalt), the conditions under which primary minerals crystallized (such as the presence or absence of magnetite), the extent of alteration and weathering (such as the value of  $\text{Fe}^{3+}/\text{Fe}_{\text{total}}$ ), the type of alteration and weathering products (such as oxides versus sulfates versus silicates), and the processes for alteration and weathering (such as aqueous versus acid-sulfate). The first Mössbauer spectrum from

Mars was obtained by the Spirit rover on 17 January 2004, on soil near the lander at the Columbia Memorial Station.

Spirit's Mössbauer spectrometer (3) has 512 data channels and operates in backscatter geometry with a triangular velocity waveform at a drive frequency of  $\sim 24$  Hz and a standard calibrated velocity range of about  $\pm 12$  mm/s (3, 6). The instrument is mounted at the end of a robotic arm (1), and the arm places the spectrometer into physical contact with surface targets. Because of the diurnal temperature variation on Mars, the instrument stores spectra in 13 separate memory areas that correspond to 11 temperature intervals that are 10 K wide between 180 and 290 K, plus  $<180$  K and  $>290$  K windows. Sample temperature ( $\sim 195$  to 275 K during the primary mission) is measured with a sensor in the Mössbauer contact plate assembly that comes into physical contact with the surface during data acquisition. The target area illuminated by the incident 14.4 keV  $^{57}\text{Co}$   $\gamma$  radiation ( $\sim 150$  mCi at landing) has a diameter of  $\sim 1.5$  cm. Although both 6.4- and 14.4-keV resonantly scattered  $\gamma$  rays are detected by the instrument, we report spectra only for 14.4-keV  $\gamma$  rays here. The sampling depth in basaltic material is  $\sim 0.03$  g/cm<sup>2</sup>, or  $\sim 3$  mm for air-fall dust and  $\sim 0.2$  mm for coherent rock (3). Whenever possible, coupled observations of the same target are made by the Mössbauer spectrometer, Microscopic Imager (7), Alpha Particle X-ray Spectrometer (APXS) (8), Panoramic Camera (PanCam) (9), and Miniature Thermal Emission Spectrometer (Mini-TES) (10).

Mössbauer spectra of three rock and two soil targets in Gusev crater have similar patterns with three doublets (two  $\text{Fe}^{2+}$  and one  $\text{Fe}^{3+}$ ) and one or two magnetic sextets (Fig. 1). Peak parameters (center, width, and area) were calculated by least-squares

fitting procedures with Lorentzian line-shapes and using the parameter constraints described below. Center positions were used to calculate the Mössbauer parameters  $\delta$  (isomer shift relative to metallic iron),  $\Delta E_Q$  (quadrupole splitting), and strength of the internal magnetic hyperfine field ( $B_{\text{hf}}$ ). Peak areas provide information about the distribution of Fe among oxidation states and in iron-bearing phases in the target. Peak areas do not provide information about the proportion of the iron-bearing phases themselves, unless the concentration

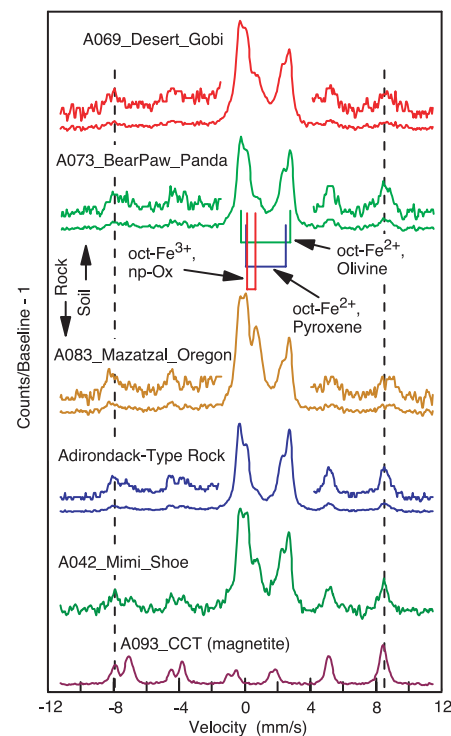


**Fig. 1.** Representative Mössbauer spectra (200 to 280 K) of rock and soil from Gusev crater and the magnetite CCT on the rover. The Gusev spectra are described by one  $\text{Fe}^{3+}$  doublet (assigned to nanophase ferric oxide), two  $\text{Fe}^{2+}$  doublets (assigned to olivine and pyroxene), and either two sextets (assigned to nonstoichiometric magnetite) or one sextet (assigned to a hematite-like phase). The spectrum of Adirondack-type rock was obtained by combining all Mössbauer data for rocks Adirondack and Humphrey. The dashed vertical lines correspond to the centers of the highest and lowest velocity peaks of magnetite.

<sup>1</sup>NASA Johnson Space Center, Houston, TX, USA. <sup>2</sup>Institut für Anorganische und Analytische Chemie, Johannes Gutenberg-Universität, Staudinger Weg 9, D-55128 Mainz, Germany. <sup>3</sup>Space Research Institute IKI, Moscow, Russia. <sup>4</sup>CVRD Group, Vitoria, Brazil. <sup>5</sup>Jet Propulsion Laboratory, California Institute of Technology, Pasadena, CA, USA. <sup>6</sup>Max Planck Institut für Chemie, Becher-Weg 27, D-55128, Mainz, Germany. <sup>7</sup>Darmstadt University of Technology, Darmstadt, Germany. <sup>8</sup>University of Alabama, Birmingham, AL, USA. <sup>9</sup>Cornell University, Ithaca, NY, USA. <sup>10</sup>Washington University, St. Louis, MO, USA.

\*To whom correspondence should be addressed. E-mail: richard.v.morris@nasa.gov

of Fe in those phases is independently known or modeled. Because mission constraints normally limited Mössbauer experiment times to  $\sim 15$  hours during the overnight period, counting statistics were not optimal for low-intensity peaks. This was always the case for the sextets and usually the case for the  $\text{Fe}^{3+}$  doublet.

Consequently, we employed more fitting constraints than is commonly done with laboratory spectra (where experiment time is not an issue) and improved counting statistics by summing spectra for the same target over all temperature intervals and by summing spectra from the same temperature over all or a subset of targets. The former produces spectra with broader lines if the values of the Mössbauer parameters are dependent on temperature. The latter does not broaden lines if the mineralogical composition is invariant.

Because we did not observe spectral asymmetry resulting from target texture, doublet peak widths and areas were constrained to be equal. The average values of  $\delta$  for the  $\text{Fe}^{3+}$  doublet for the two soil (A047\_LagunaHollow\_Trout1 and A070\_Desert\_Gobi) (11) and the three rock (A079\_Mazatzal\_NewYork, A080\_Mazatzal\_NewYork, and A083\_Mazatzal\_Oregon) spectra that have the most intense doublet and best counting statistics were the same [0.38(2) mm/s]. A value of  $\delta = 0.38$  mm/s was thus used as a constraint for all other spectra, where the  $\text{Fe}^{3+}$  doublet intensity was low and/or the counting statistics poor. The  $\text{Fe}^{2+}$  doublets were always sufficiently intense that it was not necessary to constrain their peak centers. Because the intensities of the sextet peaks are low and widths broad, it was necessary to heavily constrain their fitting parameters. Sextet peak areas were constrained in the proportion 3:2:1:1:2:3, and sextet peaks constrained to have equal areas were constrained to have equal widths. For two-sextet spectra,

we used the peak width and center parameters derived from the spectra of the rock A042\_Mimi\_Shoe, which had the most intense two-sextet spectrum, and the magnetite compositional calibration target on the rover as peak center and width constraints in other spectra. The sextet peak center and width parameters for the three targets with the single sextet (A079\_Mazatzal\_NewYork, A080\_Mazatzal\_NewYork, and A083\_Mazatzal\_Oregon) were calculated from their combined spectra. Examples of the fitting procedure for two spectra are shown in Fig. 2.

Observed peak areas are proportional to the Fe concentration,  $f$  factor (recoil-free fraction), and fractional area of each iron-bearing phase that is irradiated by the source (assuming infinite thickness for each phase). If a coating is present and is not opaque with respect to transmission of the 14.4-keV  $\gamma$  rays (like a dust coating on a rock), the subsurface also contributes in a similar manner, with reduced intensity because of attenuation of the beam by overlying material. In accordance with (12, 13), we used  $f(\text{Fe}^{3+})/f(\text{Fe}^{2+}) = 1.21$  independent of mineralogical composition to correct peak areas obtained from the fitting procedures for differences in recoil-free fractions.

Mössbauer parameters  $\delta$ ,  $\Delta E_Q$ , and  $B_{\text{hf}}$  were calculated for individual targets from spectra that were summed over the 200 to 280 K temperature intervals. The average value and standard deviation of each parameter are listed in Table 1. The standard deviations of  $\delta$  for the two  $\text{Fe}^{2+}$  doublets are comparable to the measurement and fitting uncertainties ( $\pm 0.02$  mm/s), so that these values are not dependent on temperature and/or sample-to-sample differences in the interval from 200 to 280 K.

The  $\text{Fe}^{2+}$  doublet with  $\delta \sim 1.18$  mm/s and  $\Delta E_Q \sim 3.05$  mm/s is assigned to the mineral olivine, because, for the common rock-

forming minerals, that value of  $\Delta E_Q$  is essentially mineralogically specific for olivine (14–17). Olivine has also been detected from orbiting spacecraft (18, 19) and in petrographic and Mössbauer studies of martian meteorites (20–23). We estimated the olivine composition from the temperature dependence of  $\Delta E_Q$  (Fig. 3). The Mössbauer measurements on olivine sample AREF017 ( $\text{Fo}_{90}$ ) (24) were acquired with an engineering-model MIMOS II instrument, and the fayalite ( $\text{Fo}_{00}$ ) data are from (25). The olivine identified in Gusev crater has an intermediate composition with, by extrapolation,  $\Delta E_Q \sim 2.92$  mm/s at 298 K (Fig. 3). Assuming a linear relation between  $\Delta E_Q$  and forsterite content, the Gusev olivine composition is  $\sim \text{Fo}_{60}$ . This result is consistent with APXS analyses of rocks Adirondack, Humphrey, and Mazatzal, which indicate that they are olivine-normative ( $\sim \text{Fo}_{50-60}$ ) (26), Mini-TES spectra of Adirondack and Humphrey which suggest  $\text{Fo}_{35-60}$  (10), and the ambient Mössbauer data for olivine published by (27).

The Mössbauer parameters for the second  $\text{Fe}^{2+}$  doublet ( $\delta \sim 1.18$  mm/s and  $\Delta E_Q \sim 2.12$  mm/s) are consistent with pyroxene, and we provisionally make the assignment, recognizing that other  $\text{Fe}^{2+}$ -bearing phases with comparable values of  $\Delta E_Q$  may contribute to this doublet (such as basaltic glass). The assignment is consistent with the basaltic bulk composition of rocks (26). The quadrupole splitting of the pyroxene doublet was not observed to vary in a systematic way with temperature in any of our current measurements. We are not yet able to constrain the detailed composition of the pyroxene (such as pigeonite versus augite versus orthopyroxene). We are currently addressing pyroxene composition by using two  $\text{Fe}^{2+}$  doublets instead of one for pyroxene in our fitting procedures.

The  $\text{Fe}^{3+}$  doublet ( $\delta = 0.38$  mm/s,  $\Delta E_Q \sim 0.85$  mm/s) results from octahedrally coordinated  $\text{Fe}^{3+}$  (oct- $\text{Fe}^{3+}$ ) and is not min-

**Table 1.** Average Mössbauer parameters and number of measurements ( $N$ ) for Gusev crater rock and soil and magnetite CCT on the rover (200 to 280 K).

Phase	$\delta$ (mm/s)	$\Delta E_Q$ (mm/s)	$B_{\text{hf}}$ (T)	$N$
<i>Rock</i>				
Olivine (oct- $\text{Fe}^{2+}$ )	1.18(2)*	3.05(6)	—	13
Pyroxene (oct- $\text{Fe}^{2+}$ )	1.18(2)	2.11(4)	—	13
np-Ox (oct- $\text{Fe}^{3+}$ )	0.38[2]†	0.81(10)	—	13
Hematite (oct- $\text{Fe}^{3+}$ )	0.35[2]‡	−0.07[2]‡	52.2[2]‡	1
<i>Soil</i>				
Olivine (oct- $\text{Fe}^{2+}$ )	1.17(2)	3.05(6)	—	8
Pyroxene (oct- $\text{Fe}^{2+}$ )	1.17(2)	2.14(9)	—	8
np-Ox (oct- $\text{Fe}^{3+}$ )	0.38[2]§	0.88(9)	—	8
<i>CCT (magnetite) and A042_Mimi_Shoe</i>				
Magnetite (tet- $\text{Fe}^{3+}$ )	0.30(2)	0.03(3)	51.4(3)	2
Magnetite (oct- $\text{Fe}^{2+}$ , $\text{Fe}^{3+}$ )	0.68(2)	−0.04(3)	47.8(3)	2

\*Numbers in parentheses refer to the standard deviation of the average in the final digits. Numbers in brackets refer to measurement uncertainty. † $\delta$  determined for combined A079\_Mazatzal\_NewYork, A080\_Mazatzal\_NewYork, and A083\_Mazatzal\_Oregon and used as a fitting constraint for other 10 rock spectra. ‡ $\delta$ ,  $\Delta E_Q$ , and  $B_{\text{hf}}$  determined for combined A079\_Mazatzal\_NewYork, A080\_Mazatzal\_NewYork, and A083\_Mazatzal\_Oregon. § $\delta$  determined for combined A047\_LagunaHollow\_Trout1 and A070\_Desert\_Gobi and used as a fitting constraint for other six soil spectra.

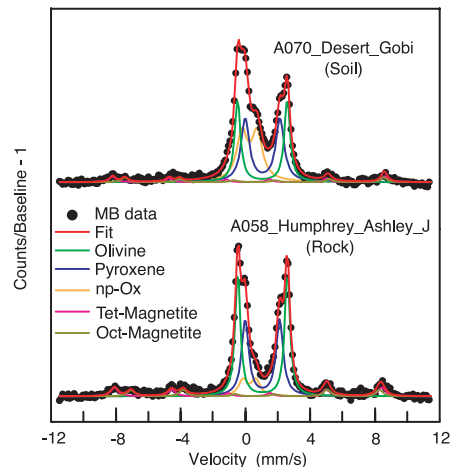


**Fig. 2.** Results of the fitting procedure for two Gusev crater Mössbauer spectra (200 to 280 K).



erologically specific. There are several reasonable pathways to explain the presence of oct- $\text{Fe}^{3+}$  doublets, however, including substitutional incorporation into silicate phases during crystallization (such as pyroxene and glass) and oxidative alteration (weathering) of  $\text{Fe}^{2+}$ -bearing-phases to form  $\text{Fe}^{3+}$ -bearing alteration products. Alteration products are favored because, as discussed in the next section, the spectral contribution of this doublet is highest in undisturbed surface soils, in dust coatings on rock, and in a coherent indurated coating on the rock Mazatzal. These martian materials are also characterized by a strong  $\text{Fe}^{3+}$  absorption edge in Pancam spectra and typically have Mini-TES spectra that are interpreted as dominated by dust (9, 10). These observations are all consistent with the presence of a fine-grained ferric oxide pigment [generically nanophase ferric oxide (np-Ox)] that is distributed through a silicate or aluminosilicate matrix (or present as a stain) and originating as a product of oxidative hydrolytic (or perhaps acid-sulfate) weathering. The  $\text{Fe}^{3+}$  doublet is probably a superposition of doublets from a number of ferric-bearing phases, which could include the superparamagnetic forms of hematite and goethite, lepidocrocite, akaganéite, schwertmannite, hydronium jarosite, ferrihydrite, and the  $\text{Fe}^{3+}$  pigment in palagonitic tephra (28–30). It is possible that the sulfur in Gusev crater soils (8) is present in part as sulfate sorbed onto fine-grained ferric oxides under acidic conditions, a process reviewed by (31).

The Mössbauer spectra of many rocks and soils (such as Adirondack-type rock and A074\_BearPaw in Fig. 1) are characterized by a two-sextet pattern whose peaks progressively overlap from low to high velocity. As shown by the spectrum of the magnetite compositional calibration target

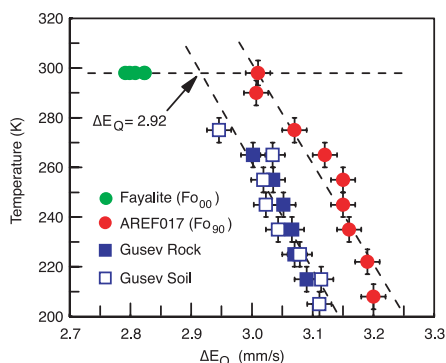


**Fig. 3.** Temperature versus quadrupole splitting  $\Delta E_Q$  for Gusev olivine. To maximize counting statistics, spectra from corresponding temperature intervals of all rocks and soils were summed before calculating  $\Delta E_Q$ . The diagonal dashed lines are linear least-squares fits. Preliminary results indicate that Gusev olivine has an intermediate composition ( $\sim\text{Fo}_{60}$ ).

(CCT) (Fig. 1), this pattern is characteristic of magnetite. In stoichiometric magnetite ( $\text{Fe}_3\text{O}_4$ ), the two sextets result from octahedral ( $\text{Fe}^{2+} + \text{Fe}^{3+}$ ) and tetrahedral ( $\text{Fe}^{3+}$ ) sites, so that the octahedral-to-tetrahedral peak area ratio is  $\sim 2$ . For magnetite inferred in Gusev crater materials, the ratio is  $\sim 1$ , implying that the magnetite is highly nonstoichiometric (ns-Mt). Deviation from stoichiometry can result from partial oxidation of  $\text{Fe}^{2+}$  to  $\text{Fe}^{3+}$  and/or substitutional impurities (such as Ti and Mg). At least one study (32) of a ns-Mt sample with a similar ratio reported that its peak centers are comparable to those for stoichiometric magnetite. To our knowledge, magnetite has not been reported in the whole-rock Mössbauer spectrum of any martian meteorite, although (20) describes a magnetite spectrum for a magnetic separate from the Nakhla martian meteorite.

A sextet that we interpret as indicative of the presence of a hematite-like phase was observed in only three spectra for the rock Mazatzal (undisturbed and brushed targets). The sextet is distinctly different from the magnetite sextets, as shown by the outer peaks at more extreme velocities as compared to magnetite (Fig. 1). The sextet appears to be associated with a coherent indurated coating that was discovered on the rock after grinding into the interior with the Rock Abrasion Tool (26, 33). Although the sextet parameters are most consistent with hematite, there are likely contributions from ns-Mt and especially maghemite to

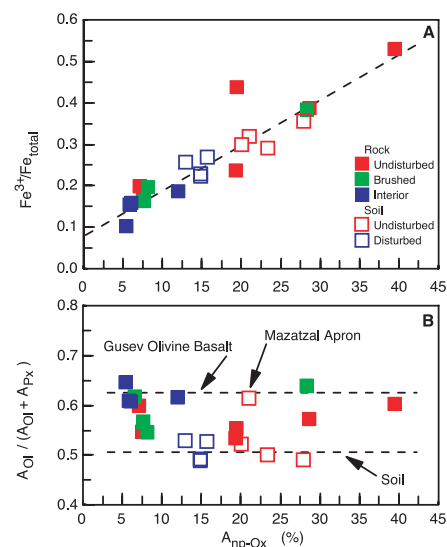


**Fig. 4.** Plot of (A)  $\text{Fe}^{3+}/\text{Fe}_{\text{total}}$  and (B)  $A_{\text{Ol}}/(A_{\text{Ol}} + A_{\text{Px}})$  as a function of  $A_{\text{np-Ox}}$  for Gusev crater rock and soil. The general trend of the data in (A) is indicated by the dashed line. The horizontal lines in (B) indicate the values of  $A_{\text{Ol}}/(A_{\text{Ol}} + A_{\text{Px}})$  for Gusev olivine basalt ( $\sim 0.63$ ) and average Gusev soil ( $\sim 0.50$ ), except for the soil target on the apron of Mazatzal. Peak areas include corrections for  $f$  factors.

the ill-defined sextet in these Mazatzal spectra. We are currently investigating more complex models for this sextet. We did not see evidence for a sextet from nonsuperparamagnetic goethite, which is commonly present in terrestrial materials (34), in the spectrum of any Gusev crater rock or soil.

The distribution of Fe among Fe-bearing phases and the values of  $\text{Fe}^{3+}/\text{Fe}_{\text{total}}$  for rocks and soils at Gusev crater (Table 2) show that the rocks are all olivine-bearing basalts and that the soil is primarily derived from olivine-bearing basalt. The soils include a trench sequence (the Laguna Hollow targets) and the interior of a dune bedform (A074\_BearPaw). We saw no evidence for a surface material in which the dominant  $\text{Fe}^{2+}$  doublet was pyroxene.

Rock interiors exposed by grinding show the least  $\text{Fe}^{3+}$  associated with np-Ox [low relative peak area ( $A_{\text{np-Ox}}$ ), implying little oxidative alteration since formation (Fig. 4A). The value of  $\text{Fe}^{3+}/\text{Fe}_{\text{total}}$  at the  $y$ -axis intercept ( $\sim 0.08$ ) is the lower limit for that ratio in unaltered rock and represents the contribution from  $\text{Fe}^{3+}$  in magnetite. The most oxidized targets are the undisturbed and brushed surfaces of the rock Mazatzal and undisturbed soils. The rock has a coherent indurated coating that has a soil-like bulk composition (8). The high values of np-Ox for the Mazatzal coating may in part be inherited from a precursor soil and in part formed during lithification of the coating. In contrast, rocks Adirondack and Humphrey probably have only thin dust coatings because the values of np-Ox for undisturbed and disturbed surfaces are the same within error. Even such thin dust coatings, however, have a large influence on Pancam and Mini-TES spectra (9, 10). Undisturbed soils are more oxidized than disturbed soils ( $\text{Fe}^{3+}/\text{Fe}_{\text{total}} \sim 0.32$  and  $0.24$ , respectively), presumably because of a thin np-Ox-rich layer of aeolian dust at the martian surface. The lower limit for the concentration of np-Ox in Gusev dust is the largest value measured for undisturbed soil (28% for A070\_Desert\_Gobi). Determination of the distribution of Fe-bearing phases in aeolian dust awaits a target whose dust thickness is demonstrably greater than the sampling depth of the 14.4-keV Mössbauer radiation ( $\sim 3$  mm).

Rock interiors have more Fe associated with olivine ( $A_{\text{Ol}}$ ) as compared to their undisturbed surfaces and to disturbed and undisturbed soil (Table 2). The  $A_{\text{Ol}}/(A_{\text{Ol}} + A_{\text{Px}})$  ratio is also higher in rock interiors ( $\sim 0.63$ ) than in soil (0.50) (Fig. 4B). Therefore, the soil occurring with the Adirondack-like basalt is a multicomponent mixture, only one of which is that basalt. Adirondack-like rocks can have a strong influence on the soil locally, however. The undisturbed soil target

Table 2. Relative peak areas (A) and Fe<sup>3+</sup>/Fe<sub>total</sub> for iron associated with specific iron-bearing phases in martian surface materials.

Target name*	Target descriptor	A <sub>O<sub>1</sub></sub> † (%)	A <sub>Px</sub> (%)	A <sub>np-Ox</sub> (%)	A <sub>ns-Mt</sub> (%)	A <sub>Hm</sub> (%)	A <sub>total</sub> (%)	Fe <sup>3+</sup> /Fe <sub>total</sub>
<i>Rock</i>								
A018_Adirondack_Blue	Undisturbed	46‡	30	7	17	0	100	0.20‡
A033_Adirondack_Blue	Post brush	44	34	8	15	0	100	0.18
A034_Adirondack_Blue	Post grind	48	31	6	15	0	100	0.17
A042_Mimi_Shoe	Undisturbed	27	21	19	33	0	100	0.44
A058_Humphrey_Ashley_J	Undisturbed	42	35	8	15	0	100	0.18
A059_Humphrey_Heyworth1	Post brush	42	35	8	15	0	100	0.20
A060_Humphrey_Heyworth2	Post grind	49	31	6	14	0	100	0.16
A076_PaperBack_Appendix	Undisturbed	40	35	19	6	0	100	0.24
A079_Mazatzal_NewYork	Undisturbed	35	26	29	0	10	100	0.39
A080_Mazatzal_NewYork	Post brush	40	22	28	0	9	100	0.38
A082_Mazatzal_NewYork	Post grind 1	49	31	12	9	0	100	0.19
A083_Mazatzal_Oregon	Undisturbed	28	19	39	0	13	100	0.53
A084_Mazatzal_NewYork	Post grind 2	57	31	5	7	0	100	0.10
<i>Soil</i>								
A014_First_Soil	Undisturbed	35	34	23	8	0	100	0.29
A043_Mimi_Tracks	Disturbed	37	33	16	14	0	100	0.27
A047_LagunaHollow_Trout1	Undisturbed	35	32	20	14	0	100	0.30
A049_LagunaHollow_Floor3	Trench	37	38	15	10	0	100	0.22
A050_LagunaHollow_WallMI only	Trench	36	38	15	11	0	100	0.23
A070_Desert_Gobi	Undisturbed	31	32	28	9	0	100	0.36
A074_BearPaw_Panda	Disturbed	37	33	13	17	0	100	0.26
A077_MazatzalFlats_Soil1	Undisturbed	39	24	21	16	0	100	0.32

\*Example of naming convention: A018\_Adirondack\_Blue refers to the Spirit sol that the Mössbauer experiment ended on (36), feature name, and target name. †Relative peak areas (A) include the *f*-factor correction  $f(\text{Fe}^{3+})/f(\text{Fe}^{2+}) = 1.21$ . Ol, olivine; Px, pyroxene; np-Ox, nanophase ferric oxide particles; ns-Mt, nonstoichiometric magnetite; Hm, hematite-like. ‡Uncertainty = ±2% absolute for A; ±0.04 for Fe<sup>3+</sup>/Fe<sub>total</sub>.

A077\_MazatzalFlats, which is located on the apron of Mazatzal rock, has higher values of  $A_{\text{O}_1}$  and  $A_{\text{O}_1}/(A_{\text{O}_1} + A_{\text{Px}})$  than other undisturbed soils (Fig. 4B). The ubiquitous presence of olivine in rock and especially in fine-grained soil is evidence that physical, rather than aqueous, chemical weathering processes dominate among the currently exposed and explored surfaces of Gusev crater.

The mineralogical composition of the strongly magnetic component in martian surface materials has been investigated since Viking with permanent magnets on landers (35). At least at Gusev crater, the Mössbauer results point to nonstoichiometric magnetite as that component. It is present in rocks and in both undisturbed and disturbed soils ( $A_{\text{ns-Mt}} \sim 14\%$ ).

#### References and Notes

- Members of the MIMOS II Consortium are G. Klingelhöfer, B. Bernhardt, P. A. de Souza Jr., J. Foh, R. Gellert, P. Gütllich, E. Kankeleit, R. V. Morris, F. Renz, D. S. Rodionov, C. Schröder, T. Wdowiak, and A. Yen.
- S. W. Squyres, et al., *J. Geophys. Res.* **108**, 10.1029/2003JE002121 (2003).
- G. Klingelhöfer et al., *J. Geophys. Res.* **108**, 10.1029/2003JE002138 (2003).
- S. W. Squyres et al., *Science* **305**, 794 (2004).
- The term "martian soil" is used here to denote any loose unconsolidated materials that can be distinguished from rocks, bedrock, or strongly cohesive sediments. No implication of the presence or absence of organic materials or living matter is intended.
- Velocity calibration was done using a spectrum of an absorber of metallic iron and hematite that was acquired in transmission geometry simultaneous with measurements on surface targets. As calculated from the error signal, the deviation of the actual velocity from the ideal waveform is <1% at the velocity extremes (±12 mm/s) and <0.2% at velocities between +6 and -6 mm/s.
- K. E. Herkenhoff et al., *Science* **305**, 824 (2004).
- R. Gellert et al., *Science* **305**, 829 (2004).
- J. F. Bell III et al., *Science* **305**, 800 (2004).
- P. R. Christensen et al., *Science* **305**, 837 (2004).
- Names have been assigned to areographic features by the MER team for planning and operations purposes. The names are not formally recognized by the International Astronomical Union.
- E. De Grave, A. Van Alboom, *Phys. Chem. Miner.* **18**, 337 (1991).
- R. V. Morris, D. C. Golden, J. F. Bell III, H. V. Lauer Jr., *J. Geophys. Res.* **100**, 5319 (1995).
- R. G. Burns, T. C. Solberg, *ACS Symp. Ser.* **415**, 262 (1990).
- C. McCammon, in *Mineral Physics and Crystallography: A Handbook of Physical Constants*, AGU Reference Shelf, vol. 2, T. J. Ahrens, Ed. (American Geophysical Union, Washington, DC, 1995), pp. 332-347.
- J. G. Stevens, A. M. Khasanov, J. W. Miller, H. Pollak, Z. Li, *Mössbauer Mineral Handbook* (Biltmore Press, Asheville, NC, 1998).
- P. A. de Souza Jr., *Lab. Robotics Automation* **11**, 3 (1999).
- J. L. Bandfield, *J. Geophys. Res.* **107**, 1626 (2002).
- T. M. Hoefen et al., *Science* **302**, 627 (2003).
- V. W. A. Vieira, T. V. V. Costa, H. G. Jensen, J. M. Knudsen, M. Olsen, *Phys. Scripta* **33**, 180 (1986).
- R. G. Burns, in *Remote Geochemical Analysis: Elemental and Mineralogical Composition*, C. M. Pieters, P. A. J. Englert, Eds. (Cambridge Univ. Press, New York 1993), pp. 539-556.
- H. Y. McSween Jr., *Meteoritics* **29**, 757 (1994).
- M. D. Dyar, *Meteor. Planet. Sci.* **38**, 1 (2003).
- This is the percentage molar ratio of Mg/(Mg+Fe) in the forsterite (Fo<sub>100</sub>) - fayalite (Fo<sub>00</sub>) series.
- M. W. Schaefer, *Nature* **303**, 325 (1983).
- H. Y. McSween Jr. et al., *Science* **305**, 842 (2004).
- O. N. Menzies, P. A. Bland, F. J. Berry, *Lunar Planet. Sci. XXXII*, abstract 1622 (2001).
- R. V. Morris et al., *J. Geophys. Res.* **94**, 2760 (1989).
- J. L. Bishop, E. Murad, *Geochem. Soc. Spec. Pub. No. 5*, 337 (1996).
- R. V. Morris et al., *J. Geophys. Res.* **105**, 1757 (2000).
- S. C. B. Myneni, in *Sulfate Minerals*, C. N. Alpers, J. L. Jambor, D. K. Nordstrom, Eds., vol. 40 of *Reviews in Mineralogy and Geochemistry* (Mineralogical Society of America, Washington, DC, 2000).
- J. M. Daniels, A. Rosencawaig, *J. Phys. Chem. Solids* **30**, 1561 (1969).
- R. E. Arvidson et al., *Science* **305**, 821 (2004).
- R. Cornell, U. Schwertmann, *The Iron Oxides: Structure, Properties, Reactions, Occurrences, and Uses* (Wiley-VCH, Weinheim, Germany, 2003).
- P. Bertelsen et al., *Science* **305**, 827 (2004).
- A martian solar day has a mean period of 24 hours 39 min 35.244 s and is referred to as a sol to distinguish this from a roughly 3% shorter solar day on Earth. A martian sidereal day, as measured with respect to the fixed stars, is 24 hours 37 min 22.663 s, as compared with 23 hours 56 min 04.0905 s for Earth. See <http://www.giss.nasa.gov/tools/mars24/> for more information.
- Development and realization for MIMOS II was funded by the German Space Agency under contract 50QM 99022. The project has been supported by the Technical University of Darmstadt and the University of Mainz. P.A. deS acknowledges support of Coordenação de Aperfeiçoamento de Pessoal de Nível Superior (CAPES) (contract PASJ 142/1999) and Companhia Vale do Rio Doce (CVRD) from Brazil. R.V.M. and D.W.M. acknowledge support of the NASA Mars Exploration Rover Project and the NASA Johnson Space Center. The support of the Russian Space agency is acknowledged. We also acknowledge the unwavering support of Jet Propulsion Laboratory engineering and operations staff.

6 May 2004; accepted 9 July 2004



# Initial Results from the Mini-TES Experiment in Gusev Crater from the Spirit Rover

P. R. Christensen,<sup>1\*</sup> S. W. Ruff,<sup>1</sup> R. L. Fergason,<sup>1</sup> A. T. Knudson,<sup>1</sup> S. Anwar,<sup>1</sup> R. E. Arvidson,<sup>2</sup> J. L. Bandfield,<sup>1</sup> D. L. Blaney,<sup>3</sup> C. Budney,<sup>3</sup> W. M. Calvin,<sup>4</sup> T. D. Glotch,<sup>1</sup> M. P. Golombek,<sup>3</sup> N. Gorelick,<sup>1</sup> T. G. Graff,<sup>1</sup> V. E. Hamilton,<sup>5</sup> A. Hayes,<sup>6</sup> J. R. Johnson,<sup>7</sup> H. Y. McSween Jr.,<sup>8</sup> G. L. Mehall,<sup>1</sup> L. K. Mehall,<sup>1</sup> J. E. Moersch,<sup>8</sup> R. V. Morris,<sup>9</sup> A. D. Rogers,<sup>1</sup> M. D. Smith,<sup>10</sup> S. W. Squyres,<sup>6</sup> M. J. Wolff,<sup>11</sup> M. B. Wyatt<sup>1</sup>

The Miniature Thermal Emission Spectrometer (Mini-TES) on Spirit has studied the mineralogy and thermophysical properties at Gusev crater. Undisturbed soil spectra show evidence for minor carbonates and bound water. Rocks are olivine-rich basalts with varying degrees of dust and other coatings. Dark-toned soils observed on disturbed surfaces may be derived from rocks and have derived mineralogy ( $\pm 5$  to 10%) of 45% pyroxene (20% Ca-rich pyroxene and 25% pigeonite), 40% sodic to intermediate plagioclase, and 15% olivine (forsterite 45%  $\pm 5$  to 10). Two spectrally distinct coatings are observed on rocks, a possible indicator of the interaction of water, rock, and airfall dust. Diurnal temperature data indicate particle sizes from 40 to 80  $\mu\text{m}$  in hollows to  $\sim 0.5$  to 3 mm in soils.

The Miniature Thermal Emission Spectrometer (Mini-TES) has provided remote measurements of mineralogy, thermophysical properties, and atmospheric temperature profile and composition of the scene surrounding the Spirit rover. The mineralogy of volcanic rocks constrains the composition, depth, and degree of partial melting of their source regions (1). Carbonates, evaporites, and oxides provide information on the role of water in the surface evolution. Oxides, such as crystalline hematite, provide insight into aqueous weathering processes, as would the occurrence of clay minerals and other weathering products. The particle size and subsurface layering provide clues to the origin of surficial materials through rock disintegration, aeolian transport, atmospheric fallout, or induration. Mini-TES spectra have also been used to determine the temperature profile in the lower boundary layer, provid-

ing evidence for convective activity, and have determined the seasonal trends in atmospheric temperature and dust and cloud opacity.

Mini-TES is a Michelson interferometer that collects infrared spectra from 5 to 29  $\mu\text{m}$  (339 to 1997  $\text{cm}^{-1}$ ) at a spectral sampling of 10.0  $\text{cm}^{-1}$  (2). Nominal spatial resolution is 20 mrad; an actuated field stop can be used to reduce the field of view to 8 mrad. The radiometric precision of the instrument is similar to prelaunch precision (2, 3). Spectra were acquired with 2 to 200 spectra summed for a single pointing location, together with 5 to 100 spectra summing for the calibration targets, to increase the radiometric precision by  $\sqrt{n}$ . Target temperature was determined by fitting a Planck function to the calibrated radiance, giving a temperature precision and accuracy of  $\pm 0.5$  K and  $\pm 2$  K, respectively, for typical nighttime and  $\pm 0.1$  K and  $\pm 0.5$  K for daytime measurements.

A full 360°, 20-mrad Mini-TES mission success panorama was acquired before egress from the Columbia Memorial Station (Fig. 1) (4). Mini-TES rasters with three by three pointing locations were collected regularly along with coregistered 13-filter Panoramic Camera (Pancam) images (5) during rover traverses to sample surface diversity. Many other rasters of various sizes and dwell lengths have been acquired, tailored to the requirements of targeted observations. The largest rocks at the Gusev crater site are typically  $< 0.4$  m in their largest dimension (6), and the hole produced by the Rock Abrasion Tool (RAT) is only 4.5 cm in diameter, or about one-third the size of the  $\sim 12$ -cm Mini-TES field of view directly in front of the rover (7).

Several targets have been observed with the use of  $5\times$  spatial oversampling and spatial deconvolution techniques to improve spectral isolation (8), together with multiple RAT brushings to clean larger areas.

**Undisturbed surficial materials.** Undisturbed surfaces in the vicinity of the station are  $\sim 5\%$  surface cover of clasts that range in size from  $\sim 1$  to 40 cm (6), with the remainder composed of finer-grained materials ( $< 100$   $\mu\text{m}$  to 3 mm), all coated with a veneer of bright dust (4, 9, 10). Mini-TES spectra of these surfaces closely match Mars Global Surveyor (MGS) TES spectra of the bright fine-grained dust that blankets low-thermal-inertia regions such as Tharsis and Arabia (Fig. 2) (11, 12). By inference from the analysis of MGS TES spectra (11), the Mini-TES spectra of undisturbed materials contain an 840- $\text{cm}^{-1}$  (11.9  $\mu\text{m}$ ) silicate transparency feature that is best matched by the framework silicates plagioclase feldspar (11), zeolite (13), or crystalline silica (14). These spectra also exhibit the spectral character near 1640  $\text{cm}^{-1}$  (6.1  $\mu\text{m}$ ) of bound water within a transparent silicate matrix. A third spectral component centered near 1480  $\text{cm}^{-1}$  (6.75  $\mu\text{m}$ ) is interpreted as due to minor ( $< 5\%$  by weight) carbonate, although other components have also been suggested (15). Carbonates produce strong emission when embedded within a silicate matrix that is nearly transparent in this spectral region. The 1480  $\text{cm}^{-1}$  absorption corresponds well to the 1450- to 1500- $\text{cm}^{-1}$  bands seen in finely particulate anhydrous carbonates (11) and most closely matches that of the Mg-carbonate magnesite (11). Mini-TES spectra contain absorption by atmospheric  $\text{CO}_2$  near 15  $\mu\text{m}$  (16) that increases roughly linearly with target distance; this spectral region is excluded in all surface analyses.

The relative mineral abundance of the entire scene from the station to the horizon was mapped with the use of a linear least squares deconvolution (17–20) of each spectrum acquired in the mission success panorama with a 40-component end-member library constructed from laboratory minerals and MGS TES and Mini-TES surface dust spectra (21, 22). Airfall

<sup>1</sup>Department of Geological Sciences, Arizona State University, Tempe, AZ 85287, USA. <sup>2</sup>Department of Earth and Planetary Sciences, Washington University, St. Louis, MO 63130, USA. <sup>3</sup>Jet Propulsion Laboratory, California Institute of Technology, Pasadena, CA 91109, USA. <sup>4</sup>Department of Geological Science, University of Nevada Reno, NV 89557, USA. <sup>5</sup>Institute of Geophysics and Planetology, University of Hawaii, Honolulu, HI 96822, USA. <sup>6</sup>Department of Astronomy, Space Sciences Building, Cornell University, Ithaca, NY 14853, USA. <sup>7</sup>U.S. Geological Survey, Flagstaff, AZ 86001, USA. <sup>8</sup>Department of Earth and Planetary Sciences, University of Tennessee, Knoxville, TN 37996, USA. <sup>9</sup>National Aeronautics and Space Administration (NASA) Johnson Space Center, Houston, TX 77058, USA. <sup>10</sup>NASA Goddard Space Flight Center, Greenbelt, MD 20771, USA. <sup>11</sup>Space Science Institute, Martinez, GA 30907, USA.

\*To whom correspondence should be addressed. E-mail: phil.christensen@asu.edu

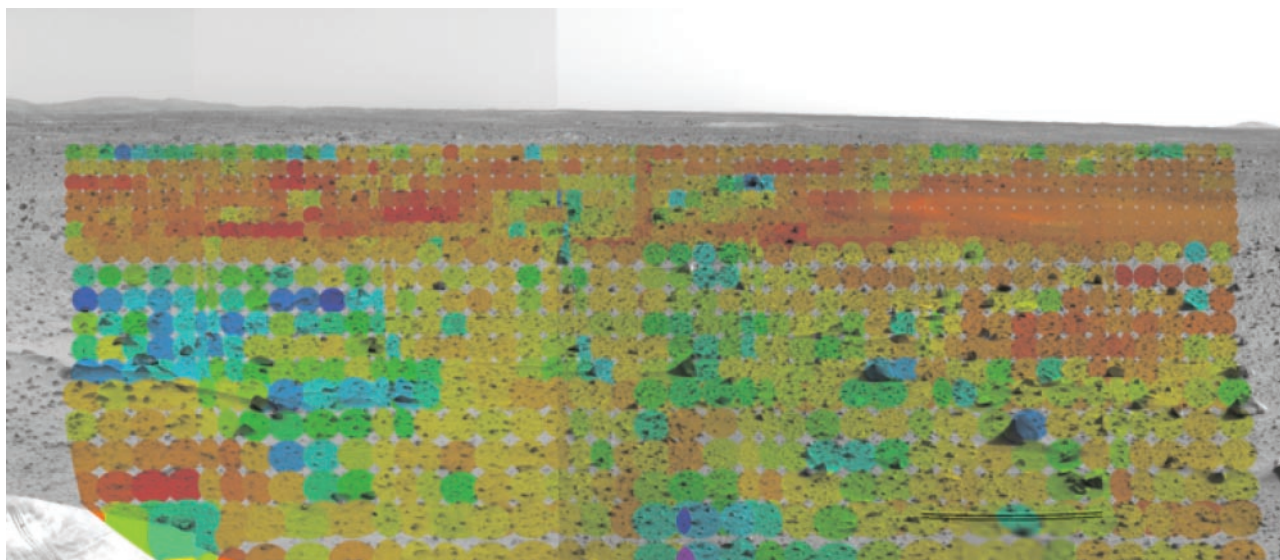
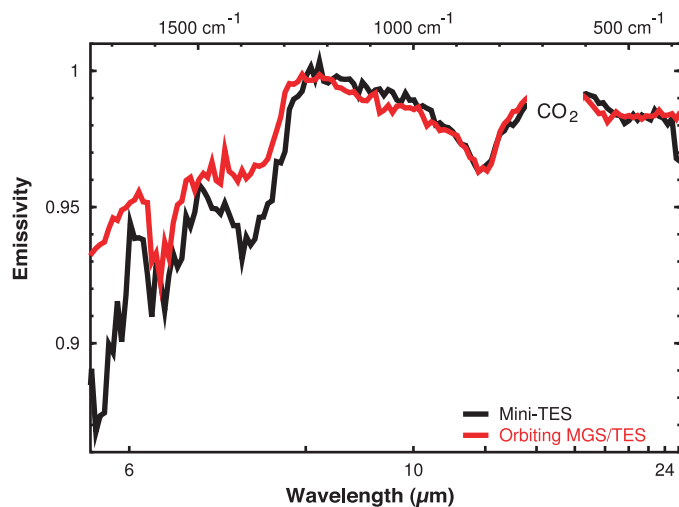


**Fig. 1.** Temperature image of a portion of the mission success pan. Each Mini-TES pointing location is shown projected onto the initial navcam panorama. Minimum temperature (blue) is 240 K; maximum temperature (red) is 290 K.

dust is ubiquitous at Gusev crater, with all rocks and undisturbed soils (23) exhibiting dust spectral features. The 1- to 13-m-diameter hollows only display the spectral features of airfall dust. Variations in undisturbed soil spectra observed through sol 90 (24) are primarily because of variable dust content together with differing viewing geometries and target orientations; no systematic compositional variations have been identified.

**Disturbed subsurface soil.** Mini-TES observed disturbed soils exposed in the rover tracks and trenching operations throughout Spirit's traverse (4, 10). Disturbed soil spectra are similar to low-albedo surface spectra derived from orbit by MGS TES (25, 26), with only minor added features consistent with airfall dust. The distinct spectral differences from dust suggest that dust is a relatively thin veneer and only a minor component of the bulk soil. Linear deconvolution of Mini-TES spectra of rover tracks indicates a basaltic soil, with a composition, normalized to remove the spectral contribution from airfall dust, of ~45% pyroxene (25% pigeonite and 20% clinopyroxene), ~40% sodic to intermediate plagioclase, and ~15% olivine (27) (Fig. 3). No goethite was detected, and the magnetite abundance was <5%. The Mini-TES-derived abundances are estimated to have accuracies of  $\sim\pm 5$  to 10% on the basis of similar analyses of laboratory and MGS TES rock and mineral mixtures (17–20, 25, 28). The olivine composition of these soils is  $\sim\text{Fo}_{45} \pm 5$  to 10 (29), which agrees with  $\alpha$  particle x-ray spectrometer (APXS)-derived normative mineralogy (1, 30). This composition is less magnesian than olivine in terrestrial

**Fig. 2.** Mini-TES spectra of the undisturbed soil component compared with an average atmosphere-removed bright-region spectrum from MGS TES (26). The deep  $840\text{-cm}^{-1}$  feature in both spectra is best matched by a transparency band in framework silicates plagioclase feldspar (11), zeolite (13), or crystalline silica (14). Bound water has a strong emission peak near  $1640\text{ cm}^{-1}$ , and carbonates produce strong emission when embedded within a silicate matrix that match the emission peak centered near  $1480\text{ cm}^{-1}$ . Both of these features are better defined in the Mini-TES spectra. Mini-TES data are from sol 3, sequence P3004.



basalts but within the range of martian meteorites (1, 31).

The disturbed soil likely gives the best Mini-TES assessment of the bulk mineralogy of Gusev materials. The derived compositions of these soils agree with the compositions of basalts derived from MGS TES, which range from 45 to 50% plagioclase, 25 to 35% Ca-rich pyroxene, 10 to 15% olivine, and 10 to 15% sheet silicates (25). The APXS results indicate that the rocks and soil have a similar composition and that the soil is primarily mechanically ground rock that has been loosely consolidated or perhaps mixed with materials from other sources, such as any aqueous-altered materials as suggested by some rinds on rocks (4, 30). Thus, the soil at Gusev is probably derived from local rocks, with only a minor component resulting from airfall dust

or surface transport (4). In this case, the Mini-TES soil mineralogy is also representative of the rock composition.

**Rocks.** The rocks at Gusev can be classified as light-toned, dark-toned, and two-toned (5). Mini-TES spectra of rocks show a variety of characteristics; representative examples of these spectral types, along with dust and disturbed soil end-members, are shown in Fig. 4. Without exception, the dark-toned rocks and the darker surfaces of two-toned rocks display similar characteristics in Mini-TES spectra (Fig. 5). The two most-studied examples are the 50-cm-wide Adirondack (32) and 70-cm-tall Humphrey. The darker, upper portion of these rocks have relatively deep spectral features (emissivity of 0.90 to 0.92) in both the middle ( $\sim 1300$  to  $800$ ) and low ( $<600$ ) wave number regions of



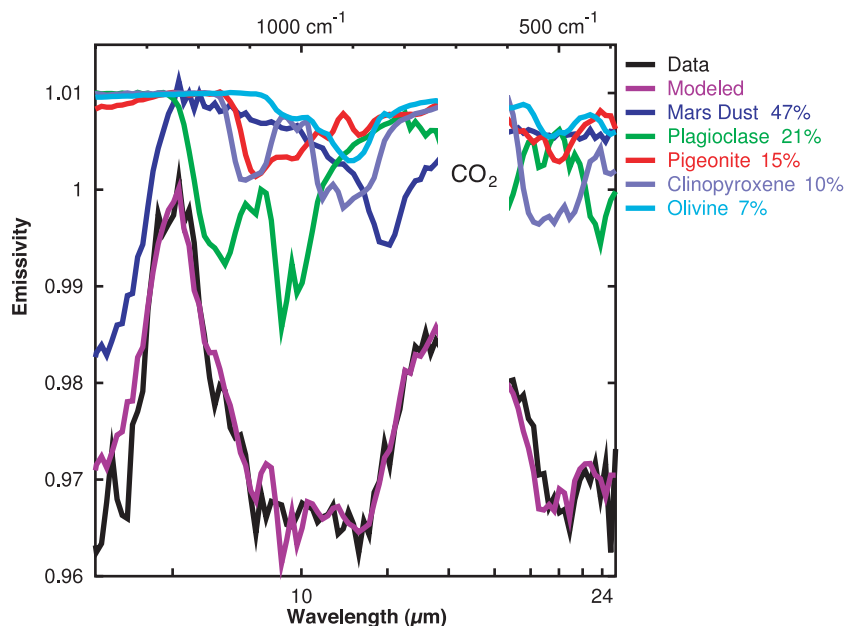


**Fig. 3.** Mineral components of disturbed soil in a rover track. Mini-TES spectrum is shown compared with the best-fit linear deconvolution model. Data are the average of 200 spectra collected on sol 89, sequence P3660, at 11:01 local solar time with an average target temperature of 267 K.

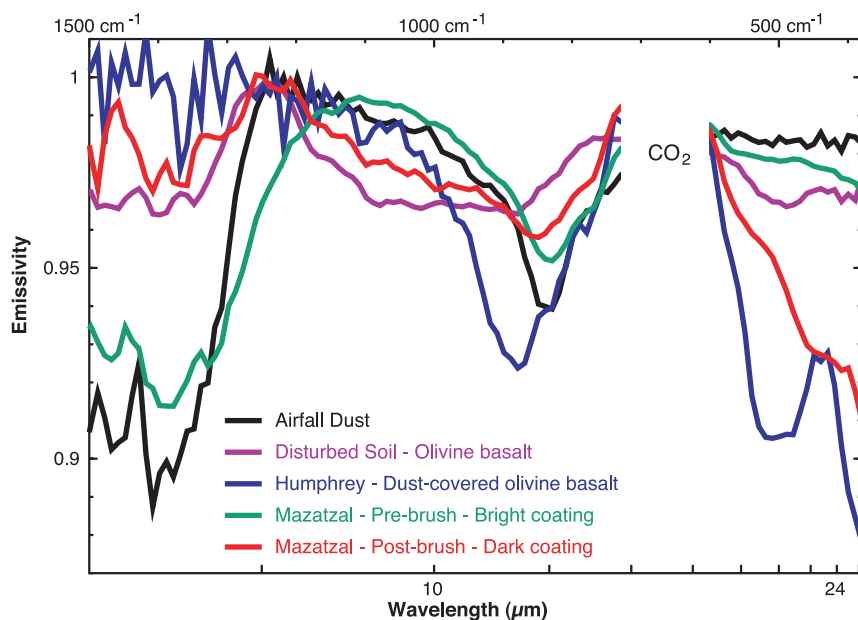


**Fig. 4.** Representative examples of the primary spectral components observed at Gusev crater.

Mini-TES spectra, whereas the high wave number region ( $>1300$ ) displays near-unity emissivity (Figs. 4 and 5). Prominent absorptions near 400 and 500  $\text{cm}^{-1}$  and the peak at  $\sim 450$   $\text{cm}^{-1}$  are consistent with olivine of intermediate composition ( $\text{Fo}_{35}$  to  $\text{Fo}_{60}$ ) (Fig. 5), an identification supported by results from the Mössbauer and APXS instruments (1, 30, 33).

Most of the spectrum, including the prominent absorption feature centered near 880  $\text{cm}^{-1}$ , can be well fit by a mixture of olivine and surface dust with lesser pyroxene and oxides (Fig. 6). The fit is poor, however,

above 1300  $\text{cm}^{-1}$ , where martian dust and laboratory fine-particulate silicates have low emission (34). This inconsistency may result from complex radiative transfer effects produced by fine-grained surface material in thermal disequilibrium with the substrate material. Alternatively, there may be a coating of unknown mineralogy on the rocks that is responsible for the 880  $\text{cm}^{-1}$  spectral band. Support for this hypothesis comes from the fact that the surfaces of rocks that display the deepest  $\sim 880$   $\text{cm}^{-1}$  band appear to be the darkest and least dusty surfaces observed at the Gusev site, according to Pancam results (5).

Excluding the spectral range above 1300  $\text{cm}^{-1}$ , the best-fit model spectra of Humphrey and Adirondack contain olivine; pyroxene is only weakly detected, plagioclase is notably absent, and there is dust on the surface (Fig. 6). The best-fit olivine is  $\text{Fo}_{40}$  to  $\text{Fo}_{45}$  and falls within the range of martian meteorites and terrestrial basalts (1, 31). The derived oxide abundances are greater than those determined by the APXS and Mössbauer instruments (1, 30, 33) and may be significantly elevated over the true volumetric abundance because of oxide's possible occurrence as a surface coating.

Light-toned rocks, such as Mazatzal, and the lighter surfaces of two-toned rocks have spectra that are different from dark-toned rocks (Fig. 4). The undisturbed Mazatzal surface has the distinctive spectral characteristics of unconsolidated surface dust, including the emissivity minimum at  $\sim 840$   $\text{cm}^{-1}$ , high, nearly featureless emissivity at low wave numbers, and a low emissivity from 1300 to 1600  $\text{cm}^{-1}$  (Fig. 4). However, Mazatzal and most light-toned rocks have an emissivity maximum that is shifted to  $\sim 1100$   $\text{cm}^{-1}$  compared with the maximum at  $\sim 1250$   $\text{cm}^{-1}$  in unconsolidated dust (Fig. 4). This spectral difference between typical airfall dust and the Mazatzal surface suggests the presence of a unique component in the coatings on light-toned surfaces.

The surface of Mazatzal was brushed with the RAT in a pattern of six placements in an effort to remove dust from an area large enough to fill the Mini-TES field of view. The 1100 to 1250  $\text{cm}^{-1}$  absorption is no longer present in the brushed-surface spectrum (Fig. 4), indicating that the component that produced this absorption was present in a relatively loose coating that was easily removed by brushing. Microscopic Imager (MI) and Pancam observations of this surface show both a red material, consistent with dust, and a bright material (5, 9) that may be related to the Mini-TES component.

The brushed surface of Mazatzal has deep, broad absorptions from 400 to 600  $\text{cm}^{-1}$  that are unique among all Gusev spectra (Fig. 4). The weak absorptions between 900 and 1200  $\text{cm}^{-1}$  are similar to those of disturbed soil and are suggestive of basalt (Fig. 4). Absorptions at long wavelengths, but not elsewhere, are characteristic of oxides [e.g., (35)]. Deconvolution of the brushed Mazatzal surface gives a mixture of oxides, dust, and plagioclase (fig. S1). Thus, the brushed surface of Mazatzal appears to be a basalt with a relatively thin ( $< \sim 50$   $\mu\text{m}$ ) (36) oxide coating. MI images of the RAT-abraded surface suggest the presence of a dark, thin coating that differs in texture from the underlying rock (9), supporting this hypothesis. The two-toned rock Humphrey was also brushed, with the only significant change being a decrease in spectral contrast. Thus, if dust contributes to

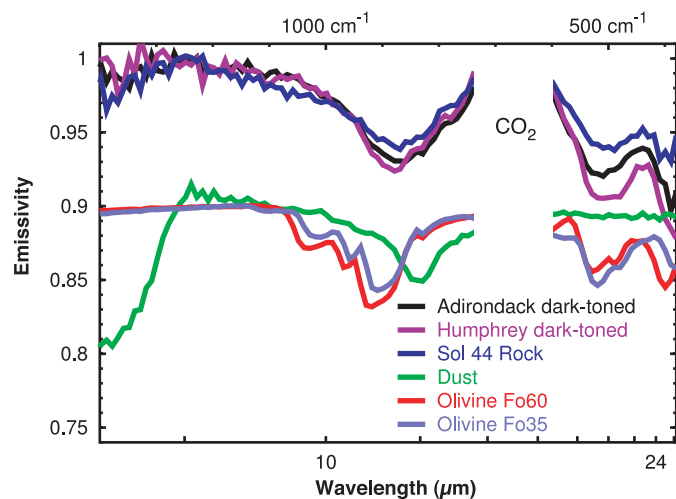
the spectral character of this rock, then sufficient dust must have remained on its surface (37, 38) and within the Mini-TES field of view for the spectral shape to be unchanged.

In summary, the Mini-TES spectra of rocks at Gusev can be tentatively explained by four components: (i) an underlying olivine basalt; (ii) a durable coating or rind, possibly oxide, with deep absorptions from 400 to 600  $\text{cm}^{-1}$  that is present on at least one rock (Mazatzal) but not present on all; (iii) a component present in the bright, readily removed coatings on light-toned rocks; and (iv) the ubiquitous unconsolidated airfall dust. The observed spectral characteristics that this model does not explain are the lack of the short wavelength absorption characteristic of dust in some rocks that otherwise appear to have a dust coating and the lack of any significant change in the spectral shape of Humphrey after its brushing.

The occurrence of coatings and rinds of unique mineralogy suggests that some degree of surface alteration has occurred. One possibility is that these rocks have been buried to modest depth, possibly by airfall dust that is periodically deposited and removed by climate variations, and that the alteration is related to the interaction of dust and water films during and/or between periods of burial (4, 10, 39, 40). Although Spirit landed in an apparent dust-devil streak with lower albedo than its surroundings (5), Gusev crater overall has high albedo and tens of micrometers of dust cover (34, 41), consistent with the ubiquitous presence of dust and coatings observed by Spirit. There is no evidence from orbital mid-infrared spectral observations of similar coatings on surfaces of classic dark regions, such as Syrtis Major, which are interpreted to be unweathered to weakly altered volcanic materials (25, 42, 43). Rocks in low-albedo regions may lack significant coatings because they have not undergone burial or surface alteration or may have been exposed to aeolian abrasion. Thus, the rocks at Gusev, although consistent with the compositions determined for the basaltic surface type (1, 25), may have undergone minor surface alteration that was different from their counterparts in low-albedo regions. The presence of both unaltered and coated rocks exposed on the martian surface may not reflect a substantially wetter environment but may be due to minor variations in near- or subsurface alteration.

**Sand.** Dark-toned particulate material has been observed in drift deposits and ripple forms (4, 6, 10). Although most accumulations of particulate material are dust-covered, some surfaces have been observed that are darker and less dusty, suggesting active removal of dust. One example is the ripple-like drift deposit Armadillo, which is darker on the inferred upwind side relative

**Fig. 5.** Mini-TES spectra of Adirondack, Humphrey, and an unnamed rock from sol 44 compared with typical Gusev dust-cover surface and laboratory olivine. Note the similarity of the three rocks to each other and the spectral match to olivine between 21 and 25  $\mu\text{m}$ . The broad rock absorption between 9 and 14  $\mu\text{m}$  can be fit by the combination of olivine and surface dust. Data are from sol 14, sequence P3110; sol 56, sequence P3175; and sol 44, sequence P3625, respectively. Laboratory and dust spectra have been offset for clarity.



to the downwind side (5, 40). Spectra from one of the darker sides display absorptions near 400 and 500  $\text{cm}^{-1}$ , similar to the inferred olivine feature observed in spectra from the darkest surfaces of rocks (Fig. 7).

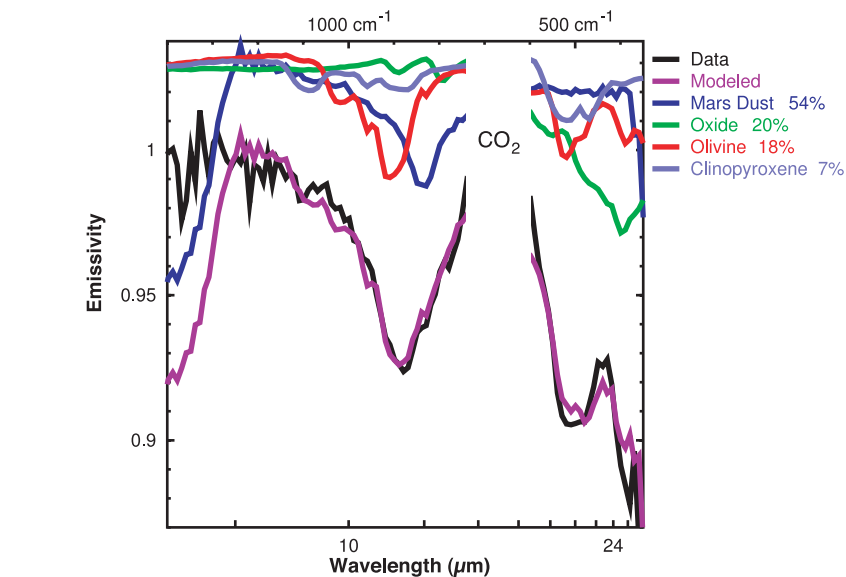


**Fig. 6.** Quantitative mineral abundance of Humphrey using the linear deconvolution of the Mini-TES spectra with a library of mineral end-members.

The spectral range above 1300  $\text{cm}^{-1}$  has higher emissivity than that of dust, consistent with the removal of most of the dust on the darker side as compared with the lighter side of the drift. Deconvolution of these spectra gives a composition of roughly equal amounts of plagioclase, clinopyroxene, olivine ( $\sim\text{Fo}_{40}$ ), and oxide. This composition is consistent with an origin from plagioclase-rich olivine basalt; high oxide abundances may indicate relatively thin surface coatings or aeolian concentrations. The spectra of these materials closely match those of the dark-toned dunes adjacent to the interior wall of Bonneville crater

as well as the average atmospherically corrected TES spectrum obtained for the Gusev site, suggesting that this dark drift or dune material occurs throughout the region.

**Thermophysical properties.** Diurnal brightness temperature measurements have been used with a model evolved from that used for Viking Infrared Thermal Mapper (IRTM) (44) and MGS TES data analysis (45) to derive the thermal inertia and average particle size for drift deposits, hollow fill material, and disturbed soil (Plate 6). Model inputs include a dust opacity of 0.4, derived from Mini-TES and Pancam, and a TES-derived albedo of 0.20 (43). Soil thermal inertias range from 150 to 430  $\text{J m}^{-2} \text{K}^{-1} \text{s}^{-1/2}$ . The 5-km resolution TES inertia for this location is 290  $\text{J m}^{-2} \text{K}^{-1} \text{s}^{-1/2}$  (43), which falls within the range observed in situ. Thermal Emission Imaging System (THEMIS)



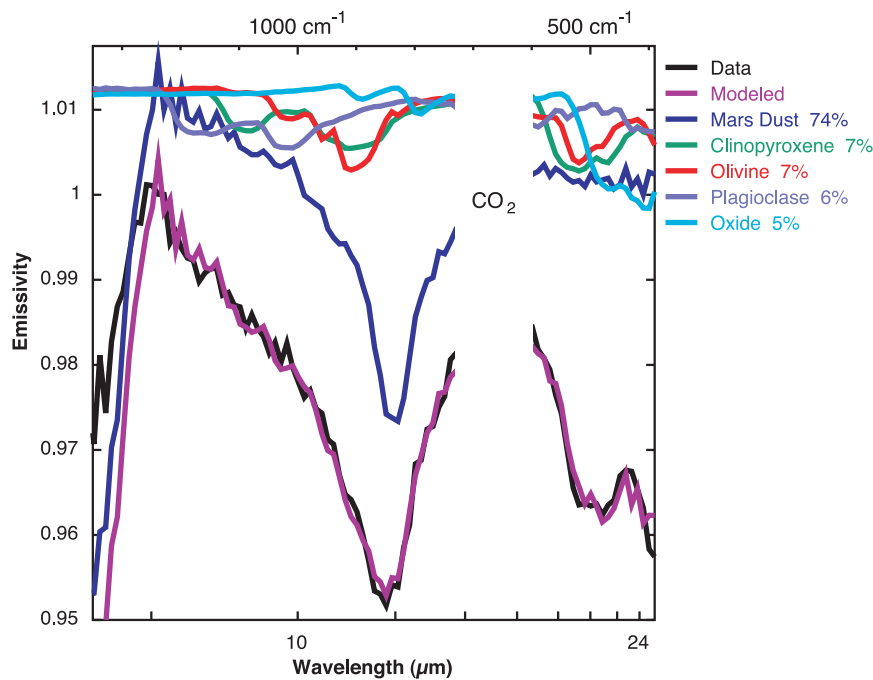


Fig. 7. Quantitative mineral abundance of dark sands in the Armadillo drift using the linear deconvolution of the Mini-TES spectra with a library of mineral end-members. Data are from sol 67, sequence P3143.

orbital data show an elevated thermal inertia of  $\sim 450 \text{ J m}^{-2} \text{ K}^{-1} \text{ s}^{-1/2}$  around Bonneville crater at 100-m scales (46) that is consistent with an increase in rock abundance from 5% to a factor of 2 to 4 higher in the crater ejecta (47) with no required change in soil properties. The hollows have the lowest inertias observed, 150 to 240  $\text{J m}^{-2} \text{ K}^{-1} \text{ s}^{-1/2}$ , corresponding to an average particle size for well-sorted, unconsolidated particles of silt (40  $\mu\text{m}$ ) to medium sand (275  $\mu\text{m}$ ) (48, 49). Drift deposits, which include ripples and dunes, have inertias of 300 to 430  $\text{J m}^{-2} \text{ K}^{-1} \text{ s}^{-1/2}$  (average particle size of  $\sim 500 \mu\text{m}$  to 1 to 3 mm) (48–50). The traverse from the landing site to Bonneville crater yielded no systematic variation in the thermal inertia of the surface of fine-grained silts to cm-sized stones.

The size-frequency distribution of rocks around the station generally follows the exponential model distribution based on the Viking Lander and MPF landing sites for 5% rock abundance (51). The area covered by rocks  $> 0.1 \text{ m}$  diameter is about half of the total, suggesting an insufficient number of rocks large enough at this spot to account for the estimate from analyses of Viking IRTM data (52). If this count is representative of the broader area observed from orbit, then the fine-component thermal inertia is probably higher than has been estimated, which is consistent with the pebble-rich and indurated or cemented soil layer or duricrust observed by Spirit (4, 6, 10). The observed thermal inertias at the surface and particle sizes (includ-

ing rock coverage) are consistent with those observed and inferred in orbital data and are in agreement with predictions made before landing (4, 53).

#### References and Notes

- H. Y. McSweeney Jr. et al., *Science* **305**, 842 (2004).
- P. R. Christensen et al., *J. Geophys. Res.* **198**, 1029/2003JE002117 (2003).
- Two-point radiometric calibration was intended to use two V-groove blackbody targets (2). The temperature sensors attached to the rover deck failed at extremely low temperatures ( $\sim -90^\circ\text{C}$ ) on the first night after landing. The calibration was modified to use prelaunch measurements of the instrument response function taken over temperature, with the instrument radiance determined from observations of the functioning target mounted in the Pancam mast assembly (PMA). On the basis of comparison with orbiting MGS TES data and modeling of the atmospheric observations, the response function has not changed from prelaunch values and the calibration approach is providing the required accuracy. The  $1-\sigma$  radiometric precision for two-spectra summing is  $\pm 1.8 \times 10^{-8} \text{ W cm}^{-2} \text{ sr}^{-1} \text{ cm}^{-1}$  between 450 and 1300  $\text{cm}^{-1}$ , increasing to  $\sim 7 \times 10^{-8} \text{ W cm}^{-2} \text{ sr}^{-1} \text{ cm}^{-1}$  at shorter (300  $\text{cm}^{-1}$ ) and longer (1800  $\text{cm}^{-1}$ ) wave numbers. The absolute radiance error is  $< 5 \times 10^{-8} \text{ W cm}^{-2} \text{ sr}^{-1} \text{ cm}^{-1}$ , decreasing to  $\sim 1 \times 10^{-8} \text{ W cm}^{-2} \text{ sr}^{-1} \text{ cm}^{-1}$ .
- S. W. Squyres et al., *Science* **305**, 794 (2004).
- J. F. Bell III et al., *Science* **305**, 800 (2004).
- J. A. Grant et al., *Science* **305**, 807 (2004).
- The Mini-TES nominal field of view is 20 mrad at infinity. For near-field observations, the field of view is the aperture diameter (6.35 cm) plus the 20 mrad divergence from the location of the telescope to the point being observed. Targets in the arm work volume are  $\sim 1.5 \text{ m}$  in front of the rover, giving a total path length of  $\sim 3 \text{ m}$  from the Mini-TES telescope. The resulting Mini-TES field of view is  $\sim 12 \text{ cm}$  at the end of the rover arm.
- S. M. Ciccollella, J. E. Moersch, *Proc. Lunar Planet. Sci.* **XXXIV**, 1836 (2003).
- K. E. Herkenhoff et al., *Science* **305**, 824 (2004).

- R. E. Arvidson et al., *Science* **305**, 821 (2004).
- J. L. Bandfield, T. D. Glotch, P. R. Christensen, *Science* **301**, 1084 (2003).
- "Dust" is used throughout to indicate the fine-grained component of surface materials with similar spectral character to regional dust deposits observed by MGS TES and interpreted to be air fallout from regional and global dust storms.
- S. W. Ruff, *Icarus* **168**, 131 (2004).
- J. L. Bishop, E. Murad, M. D. Lane, R. L. Mancinelli, *Icarus* **169**, 331 (2004).
- M. D. Lane, *Proc. Lunar Planet. Sci.* **XXXV**, abstr. 1858 (2004) [CD-ROM].
- M. D. Smith et al., in preparation.
- M. S. Ramsey, P. R. Christensen, *J. Geophys. Res.* **103**, 577 (1998).
- K. C. Feely, P. R. Christensen, *J. Geophys. Res.* **104**, 24195 (1999).
- M. B. Wyatt, V. E. Hamilton, J. H. Y. McSweeney, P. R. Christensen, L. A. Taylor, *J. Geophys. Res.* **106**, 14711 (2001).
- V. E. Hamilton, M. B. Wyatt, J. McSweeney, P. R. Christensen, *J. Geophys. Res.* **106**, 14733 (2001).
- The mineral suite used for deconvolution included a broad range of pyroxene, feldspar, olivine, oxide, and surface dust compositions. Initial studies included carbonates and sulfates that resulted in somewhat better mathematical fits but at low ( $< 2\%$ ) abundances of these minerals that were below detection limits. These minerals were subsequently removed from the library. The fits using only the remaining minerals give somewhat worse root mean square errors but provide a better determination of the abundances of the minerals that are reliably detected.
- P. R. Christensen et al., *J. Geophys. Res.* **105**, 9735 (2000).
- The term martian soil is used here to denote any loose, unconsolidated materials that can be distinguished from rocks, bedrock, or strongly cohesive sediments. No implication of the presence or absence of organic materials or living matter is intended.
- A martian solar day has a mean period of 24 hours 39 min 35.244 s and is referred to as a sol to distinguish this from a roughly 3%-shorter solar day on Earth. A martian sidereal day, as measured with respect to the fixed stars, is 24 hours 37 min 22.663 s, as compared with 23 hours 56 min 04.0905 s for Earth. See <http://www.giss.nasa.gov/tools/mars24/> for more information.
- P. R. Christensen, J. L. Bandfield, M. D. Smith, V. E. Hamilton, R. N. Clark, *J. Geophys. Res.* **105**, 9609 (2000).
- J. L. Bandfield, M. D. Smith, *Icarus* **161**, 47 (2003).
- The individual minerals fit to the spectra have been summed into mineral groups.
- J. L. Bandfield, *J. Geophys. Res.* **107**, 10.1029/2001JE001510 (2002).
- The Fo (forsterite) value is the amount of FeO in the olivine, where forsterite is the Mg end-member and fayalite is the Fe end-member.
- R. Gellert et al., *Science* **305**, 829 (2004).
- H. Y. McSweeney Jr., A. H. Treiman, in *Planetary Materials*, J. Papike, Ed. (Mineralogical Society of America, Washington, DC, 1998), chap. 6.
- Names have assigned to areographic features by the Mars Exploration Rover (MER) team for planning and operations purposes. The names are not formally recognized by the International Astronomical Union.
- R. W. Morris et al., *Science* **305**, 833 (2004).
- S. W. Ruff, P. R. Christensen, *J. Geophys. Res.* **107**, 10.1029/2001JE001580 (2002).
- V. C. Farmer, *The Infrared Spectra of Minerals* (Mineralogical Society, London, 1974).
- P. R. Christensen, S. T. Harrison, *J. Geophys. Res.* **98**, 19819 (1993).
- J. R. Johnson, P. R. Christensen, P. G. Lucey, *J. Geophys. Res.* **107**, 10.1029/2000JE001405 (2002).
- T. G. Graff, thesis, Arizona State University, Tempe, AZ (2003).
- P. R. Christensen, *J. Geophys. Res.* **91**, 3533 (1985).
- R. Greeley et al., *Science* **305**, 810 (2004).
- P. R. Christensen et al., in preparation.
- J. L. Bandfield, V. E. Hamilton, P. R. Christensen, *Science* **287**, 1626 (2000).

43. P. R. Christensen *et al.*, *J. Geophys. Res.* **106**, 23823 (2001).
44. H. H. Kieffer *et al.*, *J. Geophys. Res.* **82**, 4249 (1977).
45. M. T. Mellon, B. M. Jakosky, H. H. Kieffer, P. R. Christensen, *Icarus* **148**, 437 (2000).
46. R. L. Fergason, P. R. Christensen, *Proc. Lunar Planet. Sci.* **XXXIV**, abstr. 1785 (2003).
47. M. P. Golombek *et al.*, *Proc. Lunar Planet. Sci.* **XXXIV**, abstr. 25041 (2004).
48. H. H. Kieffer, J. S. C. Chase, E. Miner, G. Munch, G. Neugebauer, *J. Geophys. Res.* **78**, 4291 (1973).
49. M. A. Presley, P. R. Christensen, *J. Geophys. Res.* **102**, 6551 (1997).
50. K. S. Edgett, P. R. Christensen, *J. Geophys. Res.* **96**, 22,765 (1991).
51. M. P. Golombek *et al.*, *J. Geophys. Res.* **108**, 10.1029/2002JE0020235 (2003).
52. P. R. Christensen, *Icarus* **68**, 217 (1986).
53. M. P. Golombek *et al.*, *J. Geophys. Res.* **108**, 1029/2003JE002074 (2003).
54. We would like to express our deepest appreciation to all of the individuals at Raytheon Santa Barbara Remote Sensing, led by S. Silverman, and at the Jet Propulsion Laboratory whose effort and dedication have led to the successful acquisition of Mini-TES data from the surface at Gusev Crater. Funding was provided by the MER Project Science Office.

## Supporting Online Material

www.sciencemag.org/cgi/content/full/305/5685/837/DC1  
Materials and Methods  
SOM Text  
Fig. S1

## Plates Referenced in Article

www.sciencemag.org/cgi/content/full/305/5685/837/DC2  
Plate 6

21 May 2004; accepted 7 July 2004

## REPORT

## Basaltic Rocks Analyzed by the Spirit Rover in Gusev Crater

H. Y. McSween,<sup>1</sup> R. E. Arvidson,<sup>2</sup> J. F. Bell III,<sup>3</sup> D. Blaney,<sup>4</sup> N. A. Cabrol,<sup>5</sup> P. R. Christensen,<sup>6</sup> B. C. Clark,<sup>7</sup> J. A. Crisp,<sup>4</sup> L. S. Crumpler,<sup>8</sup> D. J. Des Marais,<sup>5</sup> J. D. Farmer,<sup>6</sup> R. Gellert,<sup>9</sup> A. Ghosh,<sup>1</sup> S. Gorevan,<sup>10</sup> T. Graff,<sup>6</sup> J. Grant,<sup>11</sup> L. A. Haskin,<sup>2</sup> K. E. Herkenhoff,<sup>12</sup> J. R. Johnson,<sup>12</sup> B. L. Jolliff,<sup>2</sup> G. Klingelhofer,<sup>13</sup> A. T. Knudson,<sup>6</sup> S. McLennan,<sup>14</sup> K. A. Milam,<sup>1</sup> J. E. Moersch,<sup>1</sup> R. V. Morris,<sup>15</sup> R. Rieder,<sup>9</sup> S. W. Ruff,<sup>6</sup> P. A. de Souza Jr.,<sup>16</sup> S. W. Squyres,<sup>3</sup> H. Wänke,<sup>9</sup> A. Wang,<sup>2</sup> M. B. Wyatt,<sup>6</sup> A. Yen,<sup>4</sup> J. Zipfel<sup>9</sup>

The Spirit landing site in Gusev Crater on Mars contains dark, fine-grained, vesicular rocks interpreted as lavas. Pancam and Mini-Thermal Emission Spectrometer (Mini-TES) spectra suggest that all of these rocks are similar but have variable coatings and dust mantles. Magnified images of brushed and abraded rock surfaces show alteration rinds and veins. Rock interiors contain  $\leq 25\%$  megacrysts. Chemical analyses of rocks by the Alpha Particle X-ray Spectrometer are consistent with picritic basalts, containing normative olivine, pyroxenes, plagioclase, and accessory FeTi oxides. Mössbauer, Pancam, and Mini-TES spectra confirm the presence of olivine, magnetite, and probably pyroxene. These basalts extend the known range of rock compositions composing the martian crust.

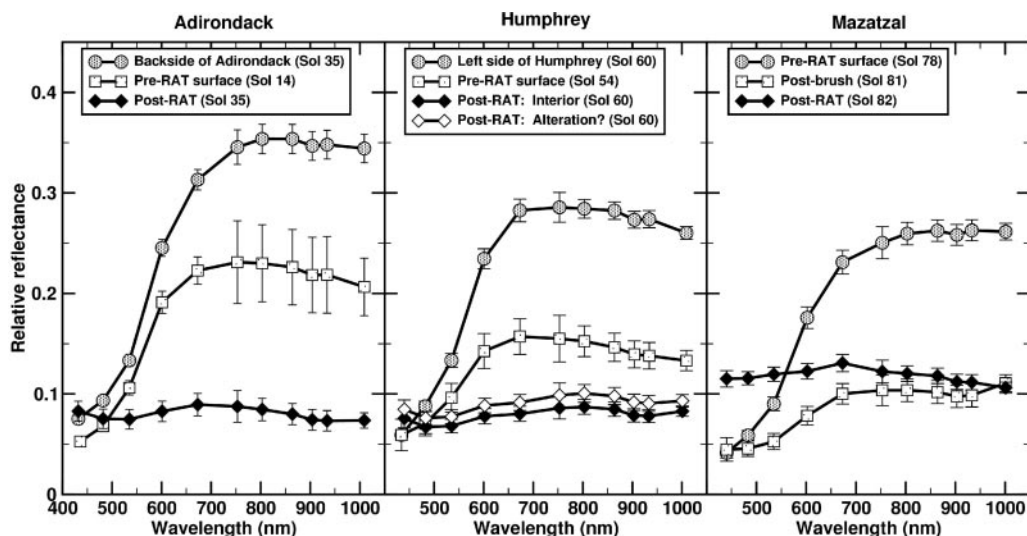
Rocks at the Spirit landing site are fine-grained with irregular vesicles and vugs, suggesting a volcanic origin. The rocks are angular and strewn across the surface, which suggests they were ejected from nearby Bonnevill crater (1) by an impact event (2).

Pancam and Mini-Thermal Emission Spectrometer (Mini-TES) spectra of rock surfaces indicate two end members, represented by dark- and light-toned rocks, with most rocks falling between these extremes. Three representative rocks, Adirondack, Humphrey,

and Mazatzal, located several hundred meters apart, have been analyzed with the Athena instruments (3). Pancam images (4) show that Adirondack and Humphrey are partly coated and that Mazatzal is uniformly coated by light-toned material (Plates 9A, 10A, and 11A). Pancam spectra (Fig. 1) of the dark portions of Adirondack and Humphrey are consistent with the presence of olivine, which has a broad (composite) absorption band near 1000 nm. A weak band center near 930 nm suggests the presence of pyroxene or contamination by ferric oxides.

The long-wavelength portion of Mini-TES spectra of dark rock surfaces resembles the Mars Global Surveyor (MGS)-TES spectra of

**Fig. 1.** Relative reflectance Pancam spectra of Adirondack, Humphrey, and Mazatzal (20). Dark-toned portions and abraded interiors (post-RAT) of rocks have flat, relatively featureless spectra consistent with basalt.





olivine-bearing basalts seen elsewhere on Mars (5). An emissivity peak at  $\sim 450\text{ cm}^{-1}$  in the spectra of dark portions of Adirondack and Humphrey is consistent with intermediate olivine (Fo36–60), but an as-yet-unidentified feature at  $\sim 875\text{ cm}^{-1}$  (also seen in orbital TES spectra of the Gusev landing site) complicates mineral deconvolution of these spectra (6).

Mini-TES spectra of the darkest portions of the rocks do not show any scattering at short thermal infrared wavelengths ( $>1300\text{ cm}^{-1}$ ) that is characteristic of micrometer-size particles, suggesting that if a coating is present, it is either coherent or a thin ( $<10\text{ }\mu\text{m}$ ) veneer of unconsolidated dust. A Microscopic Imager (MI) image of the surface of Humphrey reveals several hexagonal pits (Fig. 2), consistent with the shapes of olivine crystals. Only a coherent layer could retain mineral casts. The Rock Abrasion Tool (RAT) was used to brush and abrade rock surfaces (3), exposing dark, nearly dust-free

rocks (Plates 9B, 10B, 10C, 11B, 11C) with similar textures (Fig. 3). A smooth, dark coating, bounded above and below by thin white coatings (possibly cemented dust), was revealed in images of brushed and ground areas on Mazatzal (7). RAT abrasion of Humphrey created an oblique cut (8), and an MI image of the transition between the surface and rock interior displays a different texture (Fig. 2), interpreted as an alteration rind. Multiple, adjacent areas of Humphrey and Mazatzal were brushed to produce an area that would fill the Mini-TES field of view. The brushed Humphrey Mini-TES spectra were indistinguishable from the prebrushed rock spectra,

but the Mazatzal spectra of the prebrushed and brushed surfaces were distinct, consistent with the multiple coatings observed in MI images (6).

MI observations of the Adirondack and Mazatzal RAT holes revealed fractures filled with light-toned materials, along with dispersed patches of light-toned grains. The fracture in Mazatzal crosscuts the rock and its dark coating (Plate 11B). Humphrey contains a network of tiny, irregular light-toned veins (Figs. 2 and 3B). The absence of red coloration in high-resolution Pancam images of the fractures and veins (4) indicates that they are not filled with dust.

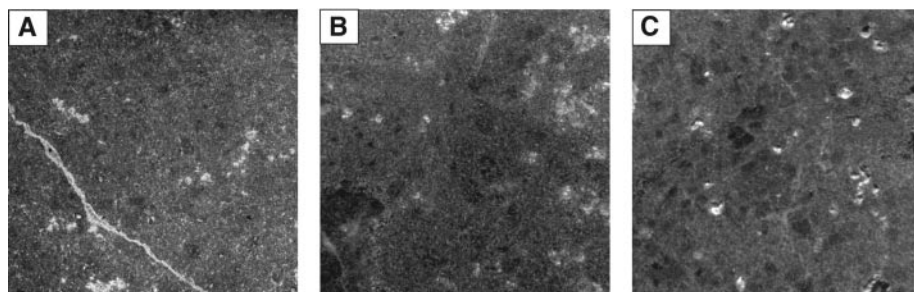


**Fig. 3.** MI subframes of rock interiors comparing the textures of (A) Adirondack (image no. 2M133914681EFF2232P2959M2M1, slightly contrast-enhanced to correct for shadowing), (B) Humphrey (image no. 2M131690279EFF1155P2939M2M1), and (C) Mazatzal (image no. 2M129468509EFF0327P2943M2M1). All three rocks contain dark megacrysts, presumably olivine. Images are  $\sim 1.2\text{ cm}$  wide.

<sup>1</sup>Department of Earth and Planetary Sciences, University of Tennessee, Knoxville, TN 37996–1410, USA.

<sup>2</sup>Department of Earth and Planetary Sciences, Washington University, St. Louis, MO 63130–4899, USA.

<sup>3</sup>Department of Astronomy, Cornell University, Ithaca, NY 14853–6801, USA. <sup>4</sup>Jet Propulsion Laboratory, California Institute of Technology, Pasadena, CA 91109–8099, USA. <sup>5</sup>NASA Ames Research Center, Moffett Field, CA 94035–1000, USA. <sup>6</sup>Department of Geological Sciences, Arizona State University, Tempe, AZ 85287–6305, USA. <sup>7</sup>Lockheed Martin Corporation, Littleton, CO 80127, USA. <sup>8</sup>New Mexico Museum of Natural History and Science, Albuquerque, NM 87104, USA. <sup>9</sup>Max Planck Institut für Chemie, D-55099 Mainz, Germany. <sup>10</sup>Honeybee Robotics, New York, NY 10012, USA. <sup>11</sup>National Air and Space Museum, Smithsonian Institution, Washington, DC 20560, USA. <sup>12</sup>U.S. Geological Survey, Flagstaff, AZ 86001–1698, USA. <sup>13</sup>Institut für Anorganische und Analytische Chemie, Johannes Gutenberg–Universität, Mainz, Germany. <sup>14</sup>Department of Geosciences, State University of New York, Stony Brook, NY 11794–2100, USA. <sup>15</sup>NASA Johnson Space Center, Houston, TX 77058, USA. <sup>16</sup>Companhia Vale do Rio Doce, 29090–900 Vitória, ES, Brazil.

<sup>17</sup>To whom correspondence should be addressed, E-mail: mcsween@utk.edu

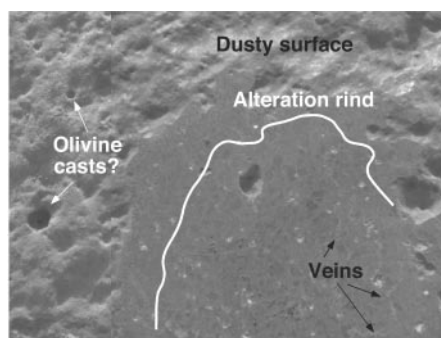


**Fig. 2.** Composite MI image (no. 2M131690279EFF1155P2939M2M1) of an oblique RAT grind into Humphrey, illustrating its natural surface containing hexagonal casts, a brushed surface, an inferred alteration rind, and an interior containing tiny, irregular veins. The view is  $\sim 3\text{ cm}$  wide.

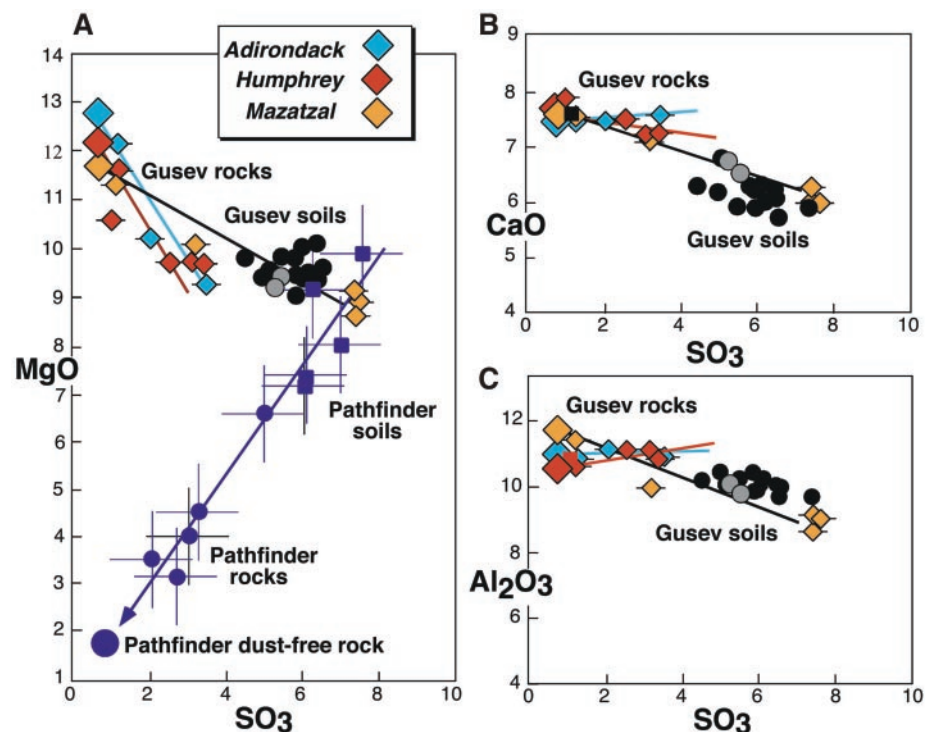


**Fig. 4.** APXS chemical variations (wt % oxides) among rocks (blue, red, and yellow diamonds), soil-coated rocks (gray circles), and soils (black circles) from Gusev: (A) MgO- $\text{SO}_3$ , also showing data for Mars Pathfinder rocks and soils (dark blue symbols) (12); (B) CaO- $\text{SO}_3$ ; and (C)  $\text{Al}_2\text{O}_3$ - $\text{SO}_3$ . Calculated compositions (Table 1) of uncoated rocks (large diamonds) are extrapolated from trends defined by analysis of natural, brushed, and abraded rocks (small diamonds), which decrease progressively in  $\text{SO}_3$ . Absolute statistical errors (17) are illustrated only for rock analyses.

Some vesicles and vugs filled with similar white material may be amygdules. The presence of multiple surface coatings and cross-cutting, fracture-filling materials may suggest alteration by several generations of fluids, although surface coatings might have formed by weathering reactions without a condensed fluid phase. The energy used in grinding a unit volume of all three rocks was lower than for a reference unaltered terrestrial basalt (7), supporting observations that these rocks are partly altered. MI images of the abraded interiors of all three rocks reveal dark megacrysts (Fig. 3), presumably olivine (9), in an aphanitic groundmass. The images are suitable for point counting, giving 9%, 25%, and 9% (by volume) megacrysts in Adirondack, Humphrey, and Mazatzal, respectively, and 13% and 14% patches of light-colored material in Adirondack and Mazatzal. Bright materials plus megacrysts sum to the same value in the three rocks, perhaps suggesting the light-toned materials are alteration products of olivine. However, the megacrysts and presumed alteration materials are distributed heterogeneously, so point counts on other areas might give differing results.

Least squares fitting of Mössbauer spectra for Adirondack, Humphrey, and Mazatzal (10) indicates the presence of olivine, pyroxene, and magnetite. Because Mössbauer spectra generally sample a greater depth (50 to 200  $\mu\text{m}$ ) than do other spectra (<100  $\mu\text{m}$ ), a weak ferric doublet may be associated with alteration rinds or veins. Estimated molar  $\text{Fe}^{2+}/\text{Fe}$  (total) values for abraded rocks are 0.84, 0.84, and  $0.90 \pm 0.04$  for Adirondack, Humphrey, and Mazatzal, respectively (10), similar to values for terrestrial basalts (0.85 to 0.90).

Alpha Particle X-ray Spectrometer (APXS) chemical variations (11) among the undisturbed, brushed, and abraded surfaces of Adirondack, Humphrey, and Mazatzal are illustrated in Fig. 4. Martian soils (12) are enriched in  $\text{SO}_3$  compared to martian meteorites and Pathfinder rocks. The natural, brushed, and abraded rock compositions do not define a mixing line with Gusev soils, as do dust-covered Mars Pathfinder rocks and soils (Fig. 4A) (13). Distinct trends for Adirondack, Humphrey, and Mazatzal indicate that coatings on Gusev rocks have compositions different from the local regolith. By extrapolating trends defined by the natural, brushed, and abraded compositions for each rock to 0.3 weight percent (wt %) residual S (0.75 wt %  $\text{SO}_3$ ), the average sulfur abundance in basaltic martian meteorites (13), the compositions of rock end members can be calculated (Table 1). Except for variations in the relative proportions of Fe oxides, the derived chemical compositions of the interiors of Adirondack, Humphrey, and Mazatzal are indistinguishable.

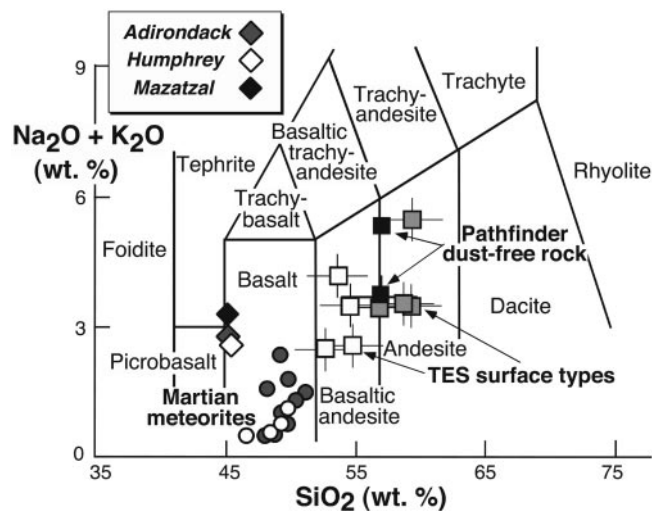


**Fig. 5.** Chemical classification diagram for volcanic rocks (14), comparing the compositions of Adirondack, Humphrey, and Mazatzal (diamonds) with those of basaltic martian meteorites (gray circles are shergottites, and open circles are nakhlites), two calibrations of the Mars Pathfinder dust-free rock (black squares), and MGS-TES surface types (open and gray squares are surface types 1 and 2, respectively). Data are from McSween *et al.* (16).

**Table 1.** Extrapolated chemical compositions of Gusev rocks and calculated norms. Rock end-member compositions were calculated by subtracting from the deepest RAT-abraded APXS composition enough of the average of brushed and natural surface APXS analyses reported by Gellert *et al.* (11) (20%, 25%, and 7% for Adirondack, Humphrey, and Mazatzal, respectively) to reduce residual S to 0.3 wt % (13). Iron was partitioned between FeO and  $\text{Fe}_2\text{O}_3$  on the basis of Mössbauer measurements (10) of molar  $\text{Fe}^{2+}/\text{Fe}$  (total) of 0.84, 0.84, and 0.90 for the three rocks, respectively. Rock compositions were recast into mineralogy by calculating norms, after removing S as FeS and Cl as NaCl. Plag, plagioclase; Or, orthoclase; Ab, albite; An, anorthite; Ne, nepheline; Di, diopside; Hy, hypersthene; Ol, olivine; Fo, forsterite; Fa, fayalite; Cr, chromite; Mt, magnetite; Ilm, ilmenite; Ap, apatite.

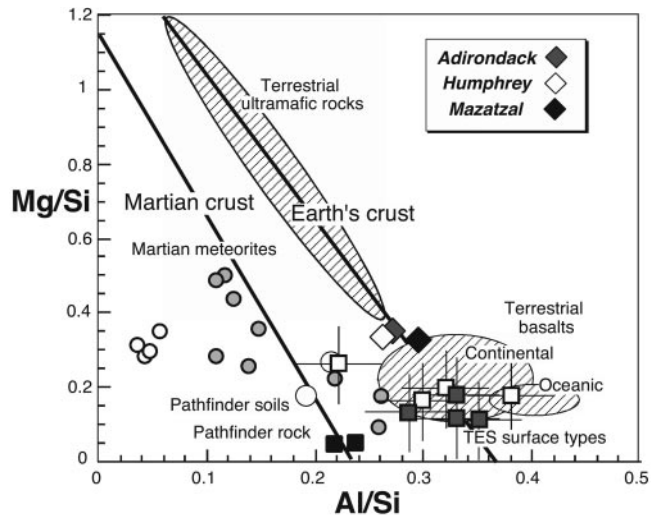
Composition	Adirondack	Humphrey	Mazatzal
<i>Oxides (wt %)</i>			
SiO <sub>2</sub>	45.4	46.1	45.7
TiO <sub>2</sub>	0.46	0.52	0.48
Al <sub>2</sub> O <sub>3</sub>	10.9	10.6	11.7
Fe <sub>2</sub> O <sub>3</sub>	3.02	2.99	1.80
Cr <sub>2</sub> O <sub>3</sub>	0.60	0.59	0.56
FeO	15.2	15.3	15.6
MnO	0.41	0.39	0.36
MgO	12.8	12.2	11.6
CaO	7.49	7.70	7.71
Na <sub>2</sub> O	2.79	2.59	3.30
K <sub>2</sub> O	0.06	0.06	0.07
P <sub>2</sub> O <sub>5</sub>	0.52	0.56	0.70
S	0.30	0.30	0.30
Cl	0.09	0.11	0.15
Total	100.0	100.0	100.1
<i>Norms (wt %)</i>			
Plag	40.6 (An <sub>43</sub> )	38.9 (An <sub>45</sub> )	44.1 (An <sub>40</sub> )
Or	0.4	0.4	0.4
Ab	22.9	21.1	26.2
An	17.3	17.5	17.5
Ne	0	0	(0.32)
Di	13.5	14.0	13.3
Hy	6.3	12.9	0
Ol	31.1 (Fo <sub>55</sub> )	26.1 (Fo <sub>52</sub> )	35.0 (Fo <sub>51</sub> )
Fo	17.1	13.7	17.8
Fa	14.0	12.4	17.2
Cr	0.9	0.9	0.8
Mt	4.4	4.3	2.6
Ilm	0.9	1.0	0.9
Ap	1.2	1.3	1.7

On an alkali-silica classification diagram for volcanic rocks (14), Gusev rocks plot near the junction between basalt, picrobasalt, and tephrite (Fig. 5). In the Irvine-Baragar classification (15), these

rocks are basalts. This olivine-rich composition is substantially more primitive than those of basaltic martian meteorites, Pathfinder rocks, and the calculated compositions of TES surface types 1 and 2 (16).



**Fig. 6.** Mg/Si versus Al/Si variations in Gusev rocks compared with other martian materials (19). Symbols are as in Fig. 5.



Gusev basalts apparently experienced very little fractionation.

Rock compositions can be recast into mineralogy by calculating norms (Table 1). The norms are dominated by olivine, pyroxene, and plagioclase, with accessory magnetite, chromite, ilmenite, and apatite. A tiny amount of nepheline in the Mazatzal norm is probably an artifact of the assigned Mössbauer oxidation state; if calculated with  $\text{Fe}^{2+}/\text{Fe}$  (total) similar to the other rocks, Mazatzal would also be hypersthene normative. The normative olivine compositions (Fo51–55) are less magnesian and plagioclase compositions (An40–45) are more sodic than comparable minerals in terrestrial basalts, but are consistent with olivine and plagioclase compositions in martian meteorites (17). This suggests that the mineralogy of martian meteorites may be generally characteristic of igneous rocks on Mars. Normative mineralogy conforms to mineralogic constraints from Mössbauer, Pancam, and Mini-TES spectra.

An estimate of the equilibrium crystallization sequence of magmas having these compositions, calculated from MELTS simulation (18) at low pressure and an oxidation state buffered by quartz-fayalite-magnetite, indicates early appearance of Cr-spinel and olivine, followed by plagioclase, clinopyroxene, orthopyroxene, and phosphate. The prediction of olivine as an abundant, early

crystallizing phase suggests the megacrysts seen in MI images are olivine phenocrysts. We cannot rule out the possibility that olivine in these rocks is cumulus or xenocrystic. However, the similar chemical compositions of the rocks, despite their textural differences, suggest that they were melts. Low Ni/Cr weight ratios ( $\sim 0.04$ ) for these rocks (11) may also argue against the addition of olivine (which has high Ni/Cr). We have also considered the possibility that these rocks were impact melts containing unmelted mineral clasts, but no breccias have been observed at Gusev and the rocks' low Ni/Cr ratios suggest no substantial added meteoritic component.

The regional geologic context for these basalts is unclear. There are no obvious effusive centers within Gusev crater, and flows into the crater from the only nearby volcano (Apolinaris Patera) are not apparent. Whatever their source, Gusev rocks do not plot on the low Al/Si trend defined by martian meteorites (Fig. 6) (19). The high Al contents of Gusev basalts could reflect melting of an ancient, relatively undepleted mantle (16), but low contents of incompatible K and P and the presence of normative olivine plus hypersthene suggest a depleted mantle source. These picritic lavas are the least fractionated materials so far encountered on

Mars. The rocks at Gusev expand the known range of volcanic compositions and the recognized extent of crustal heterogeneity. Despite orbital interpretations that large amounts of surface water shaped the Gusev landscape, the alteration of these rocks required only limited amounts of groundwater.

#### References and Notes

- Names have been assigned to aerographic features by the Mars Exploration Rover (MER) team for planning and operations purposes. The names are not formally recognized by the International Astronomical Union.
- J. A. Grant *et al.*, *Science*, **305**, 807 (2004).
- S. W. Squyres *et al.*, *Science*, **305**, 794 (2004).
- J. F. Bell III *et al.*, *Science*, **305**, 800 (2004).
- T. M. Hoefen *et al.*, *Science*, **302**, 627 (2003).
- P. R. Christensen *et al.*, *Science*, **305**, 837 (2004).
- R. E. Arvidson *et al.*, *Science*, **305**, 821 (2004).
- K. E. Herkenhoff *et al.*, *Science*, **305**, 824 (2004).
- Euhedral olivine crystals commonly have hexagonal shapes like the pits in Fig. 2, although megacrysts in rock interiors are anhedral.
- R. V. Morris *et al.*, *Science*, **305**, 833 (2004).
- R. Gellert *et al.*, *Science*, **305**, 829 (2004).
- The term martian soil is used here to denote any loose unconsolidated materials that can be distinguished from rocks, bedrock, or strongly cohesive sediments. No implication of the presence or absence of organic materials or living matter is intended.
- J. Brückner, G. Dreibus, R. Rieder, H. Wänke, *J. Geophys. Res.*, **108**, 8094 (2003).
- M. J. LeBas, R. W. LeMaitre, A. Streckeisen, B. Zanettin, *J. Petrol.*, **27**, 745 (1986).
- T. N. Irvine, W. R. A. Barragar, *Canad. J. Earth Sci.*, **8**, 523 (1971).
- H. Y. McSween, T. L. Grove, M. B. Wyatt, *J. Geophys. Res.*, **108**, 5135 (2003).
- H. Y. McSween, A. H. Treiman, in *Planetary Materials*, J. Papike, Ed. (Mineralogical Society of America, Washington, DC, 1998), chap. 6.
- M. S. Ghiorso, R. O. Sack, *Contrib. Mineral. Petrol.*, **119**, 197 (1995).
- H. Wänke, J. Brückner, G. Dreibus, R. Rieder, I. Ryabchikov, *Space Sci. Rev.*, **96**, 317 (2001).
- A martian solar day has a mean period of 24 hours 39 min 35.244 s and is referred to as a sol to distinguish this from a roughly 3%-shorter solar day on Earth. A martian sidereal day, as measured with respect to the fixed stars, is 24 hours 37 min 22.663 s, as compared with 23 hours 56 min 04.0905 s for Earth. See <http://www.giss.nasa.gov/tools/mars24/> for more information.
- Funding for Athena science team members was provided by NASA contracts through Cornell and the Jet Propulsion Laboratory.

#### Plates Referenced in Article

[www.sciencemag.org/cgi/content/full/305/5685/842/DC1](http://www.sciencemag.org/cgi/content/full/305/5685/842/DC1)  
Plates 9 to 11

3 May 2004; accepted 23 June 2004

## Multiplex Detection of RNA Expression in *Drosophila* Embryos

Dave Kosman,<sup>1</sup> Claudia M. Mizutani,<sup>1</sup> Derek Lemons,<sup>1</sup>  
W. Gregory Cox,<sup>2</sup> William McGinnis,<sup>1</sup> Ethan Bier<sup>1\*</sup>

Combinations of transcriptionally active genes control many aspects of cellular, organismal, and evolutionary diversity. Analysis of such gene networks is currently hampered by a gap between high-resolution in situ hybridization methods (1–3) and genome-wide coverage provided by microarray analysis (4). Here we report improved fluorescent in situ hybridization (FISH) methods, including a method for directly labeling RNA probes, that will help fill this gap. The key improvements are the use of bright Alexa Fluor dyes and a combination of directly labeled probes, haptenylated probes detected with secondary antibodies, and tyramide signal amplification. Figure 1A (supporting online text) shows a whole-mount *Drosophila*

embryo in which five patterning genes were detected with these methods. Multiplex labeling also allows the researcher to genotype homozygous (Fig. 1, B and C) or heterozygous (Fig. 1J) transcript null embryos (or to measure levels of target RNA in embryos treated with RNA interference), while simultaneously testing transcript levels of downstream genes.

It is possible to visualize the transcription patterns of numbers of genes by detecting nascent transcripts still associated with chromosomes at the site of RNA synthesis (2, 5). In Fig. 1D, we resolve the active transcription units of the *Dfd*, *Scr*, and *ftz* genes, spaced at ~20-kb intervals in the primary DNA sequence. The spatial separation of nascent transcript signals, along with a coding system in

which transcripts are labeled with different combinations of fluorors, has allowed the simultaneous detection of 10 transcription units per nucleus in cultured cells (6). A similar coding scheme applied to an embryo is shown in Fig. 1, E to G, in which a two-color code identifies nascent transcripts from the X-linked *sog* gene. Nearly all (99.8%,  $n = 417$ ) nuclei in *sog* expression domains have either one (males) or two (females) two-color signals. Such high coding accuracy is essential for nascent transcript multiplex FISH to have practical use in determining the precise extent and overlap of transcription patterns in embryos. With multicolor combinatorial codes, the simultaneous detection of large numbers of gene transcription patterns is feasible (6).

Another approach to multiplex detection is to reuse fluorors for spatially separated transcripts. For example, as shown in Fig. 1H, seven Hox gene transcripts can be detected with low background staining with only four fluorors. It is also possible to detect primary transcripts of microRNA genes. For example, the *miR-10* gene, located between *Dfd/Hox4* and *Scr/Hox5* in animal Hox clusters, is transcribed in the thoracic and abdominal primordia of early embryos (Fig. 1, I and J).

Multiplex detection of RNA will facilitate the assignment of unique molecular signatures to individual cells in developing embryos. These data will assist both in the construction of gene expression maps for use in gene network modeling (7) and in the decoding of *cis*-regulatory sequence information in metazoan genomes (8).

### References and Notes

1. D. Tautz, C. Pfeifle, *Chromosoma* **98**, 81 (1989).
2. G. S. Wilkie, A. W. Shermoen, P. H. O'Farrell, I. Davis, *Curr. Biol.* **9**, 1263 (1999).
3. S. C. Hughes, H. M. Krause, *Biotechniques* **24**, 530 (1998).
4. P. Tomancak *et al.*, *Genome Biol.* **3**, RESEARCH0088 (2002).
5. P. H. O'Farrell, B. A. Edgar, D. Lakich, C. F. Lehner, *Science* **246**, 635 (1989).
6. J. M. Levsky, S. M. Shenoy, R. C. Pezo, R. H. Singer, *Science* **297**, 836 (2002).
7. J. Jaeger *et al.*, *Nature*, **430**, 368 (2004).
8. A. Stathopoulos, M. Van Drenth, A. Erives, M. Markstein, M. Levine, *Cell* **111**, 687 (2002).
9. Supported by grant nos. NSF IBN0120728, NIH NS29870, and NIH 28315.

### Supporting Online Material

www.sciencemag.org/cgi/content/full/305/5685/846/DC1

Materials and Methods  
SOM Text

16 April 2004; accepted 25 June 2004

<sup>1</sup>Section of Cell and Developmental Biology, University of California–San Diego, La Jolla, CA 92093, USA.  
<sup>2</sup>Molecular Probes, Inc., 29851 Willow Creek Road, Eugene, OR 97402, USA.

\*To whom correspondence should be addressed. E-mail: ebier@ucsd.edu

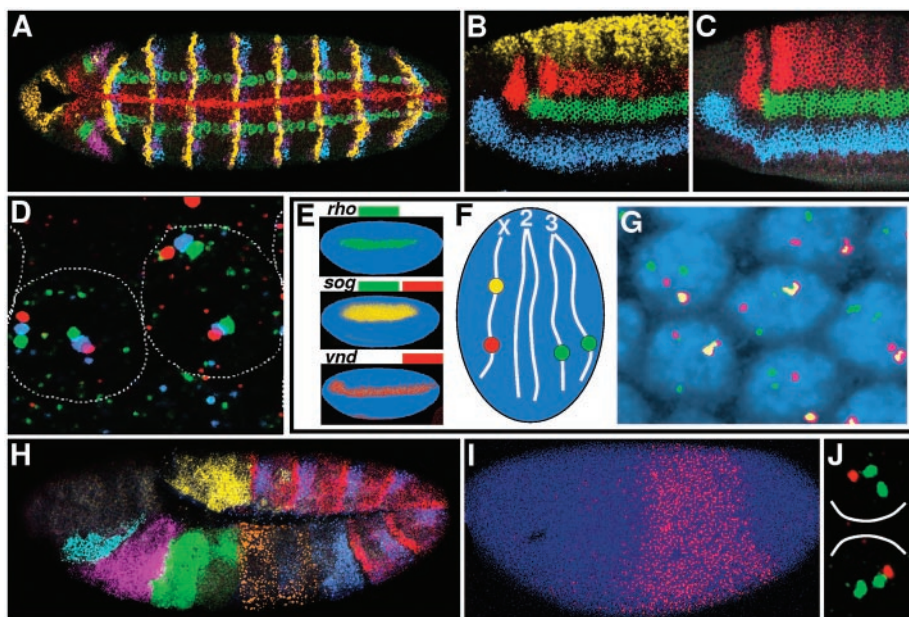


**Fig. 1.** (A) *Drosophila* embryo, stained for *sog* (direct label, red), *ind* (green), *msh* (magenta), *wg* (yellow), and *en* (blue) transcripts. (B) Anterior of a wild-type embryo stained for *vnd* (blue), *ind* (green), *msh* (red), and *dpp* (yellow). (C) Anterior of a *dpp*-deletion mutant stained as in (B). (D) Cells stained for *Dfd* (red), *Scr* (blue), and *ftz* (green). Nuclear borders are indicated by dotted lines. (E) Diagram of two-color combinatorial coding scheme to detect transcripts from three genes. (F) Diagram of a nucleus from a male embryo, displaying nascent transcripts from these three genes at their chromosome positions. (G) Nuclei (blue) from an embryo stained with a two-color coding scheme possess two nascent transcript signals for *rho* (green) and one each for *sog* (yellow) and *vnd* (red). (H) An embryo stained for seven Hox transcripts: *lab* (light blue), *Dfd* (magenta), *Scr* (green), *Antp* (orange), *Ubx* (dark blue), *abd-A* (red), and *Abd-B* (yellow). (I) *miR-10* transcripts (red) in a blastoderm embryo. (J) Close-up view of two nuclei from an embryo heterozygous for an *miR-10* deletion, revealing two sites of *Antp* transcription (green) and one site of *miR-10* transcription (red). White lines indicate nucleus borders.



## Mimicking Surface Plasmons with Structured Surfaces

J. B. Pendry,<sup>1\*</sup> L. Martín-Moreno,<sup>2</sup> F. J. Garcia-Vidal<sup>3</sup>

Metals such as silver support surface plasmons: electromagnetic surface excitations localized near the surface that originate from the free electrons of the metal. Surface modes are also observed on highly conducting surfaces perforated by holes. We establish a close connection between the two, showing that electromagnetic waves in both materials are governed by an effective permittivity of the same plasma form. The size and spacing of holes can readily be controlled on all relevant length scales, which allows the creation of designer surface plasmons with almost arbitrary dispersion in frequency and in space, opening new vistas in surface plasmon optics.

The interaction of light with a metal surface is dominated by the free electrons that behave like a plasma with a dielectric function,  $\epsilon = 1 - \omega_p^2/\omega^2$ , which is negative below the plasma frequency,  $\omega_p$ . As a consequence, metals support collective oscillations of the electrons bound to the surface (1). These are the surface plasmons, responsible for a host of phenomena unique to metals. Examples are the surface-enhanced Raman scattering experiments (2), in which the Raman signal is enhanced by the surface plasmon resonances (sometimes by as much as a factor of  $10^6$ ) and by the strong absorption of light in silver colloids (the black parts of photographic negatives). Previous work has investigated waveguiding in surface plasmon polariton band gap structures (3), plasmon propagation in metal stripes (4), and two-dimensional optics with surface plasmon polaritons (5). A useful summary of work appears in a recent review (6). More recently, experiments have been performed on the transmission of light through subwavelength holes in metal films (7). It has been established (8) that resonant excitation of surface plasmons creates huge electric fields at the surface that force light through the holes, giving very high transmission coefficients.

Other materials with quite different dielectric functions than the plasma form can also support electromagnetic surface modes. A perfect conductor is an exception,

but even such a material can be induced to support surface modes by drilling an array of holes in the surface. We show that these structured surfaces have many more properties in common with the electron plasma and that they can be described by an effective dielectric function of the plasma form, provided that the structure is on a scale much smaller than the wavelength of probing radiation. Reducing our description to a dielectric function of the plasma form has a conceptual elegance that unites all of these phenomena under the same umbrella. An effective response generated by the structure of the medium is commonly seen at microwave frequencies (9–11). Thus, it appears that surface structure may spoof surface plasmons, which provide an accurate paradigm for structured surfaces. Such a description allows us to unify a broad range of analogous phenomena. To illustrate these ideas, we begin with a simple model. Let us suppose that we have a surface that is a perfect conductor pierced by an array of holes. For simplicity, we shall assume a square cross section  $a \times a$  for the holes and a square array of side  $d$  (Fig. 1). We suppose that the holes and their spacing are much smaller than the wavelength of radiation,  $a < d \ll \lambda_0$ . An incident wave excites several waveguide modes in the holes but the fundamental mode will dominate because it is the least strongly decaying. Both electric and magnetic fields are zero inside the conductor but in the holes the electric field has the form

$$\mathbf{E} = E_0[0,1,0]\sin(\pi x/a)\exp(ik_z z - i\omega t),$$

$$0 < x < a, 0 < y < a \quad (1)$$

where  $E_0$  is a constant,  $x$ ,  $y$ , and  $z$  are cartesian coordinates,  $i = \sqrt{-1}$ ,  $\omega$  is the frequency,  $t$  is time,  $k_0$  is the free space wave vector, and

$$k_z = i\sqrt{\pi^2/a^2 - \epsilon_h \mu_h k_0^2} \quad (2)$$

where  $\epsilon_h$  and  $\mu_h$  are the permittivity and permeability, respectively, of any material that may be filling the holes. We take the  $z$  axis to be the surface normal. The magnetic fields along the  $x$  and  $z$  axes  $H_x$  and  $H_z$ , follow from this equation.

Externally incident radiation is insensitive to the details of the holes, which it cannot resolve, and sees only an average response that we shall describe by  $\epsilon_z$ ,  $\epsilon_x = \epsilon_y$ , and  $\mu_z$ ,  $\mu_x = \mu_y$ , for an anisotropic effective homogeneous medium. We can easily determine  $\epsilon_z$  and  $\mu_z$  by observing that the dispersion of the waveguide mode is unaffected by  $k_x$  or  $k_y$ , in either of the two possible polarizations and therefore

$$\epsilon_z = \mu_z = \infty \quad (3)$$

Suppose that the effective homogeneous fields in the medium are

$$\mathbf{E}' = E'_0[0,1,0]\exp(ik_x x + ik_z z - i\omega t) \quad (4)$$

We require that  $k_z$  is the same as in the waveguide and  $k_x$  is defined by the incident direction. If this effective field is to match to the incident and reflected fields external to the surface, Eq. 1 and Eq. 4 must give the same average fields at the surface. Hence, after matching to incident and reflected waves,

$$\bar{E}_y = E_0 \frac{a}{d^2} \int_0^a \sin(\pi x/a) dx = E_0 \frac{2a^2}{\pi d^2} = E'_0 \quad (5)$$

We argue that the instantaneous flow of energy across the surface,  $(\mathbf{E} \times \mathbf{H})_z$ , must be the

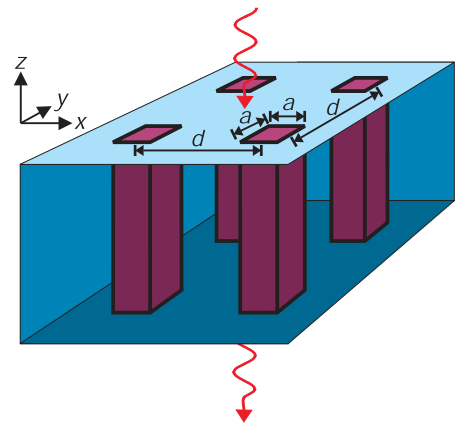


**Fig. 1.** Our model system:  $a \times a$  square holes arranged on a  $d \times d$  lattice are cut into the surface of a perfect conductor. Our theory predicts localized surface plasmon modes induced by the structure.

<sup>1</sup>Imperial College London, Department of Physics, The Blackett Laboratory, London, SW7 2AZ, UK.

<sup>2</sup>Departamento de Física de la Materia Condensada, Instituto de Ciencia de Materiales, Universidad de Zaragoza, E-50009 Zaragoza, Spain.

<sup>3</sup>Departamento de Física Teórica de la Materia Condensada, Universidad Autónoma de Madrid, E-28049 Madrid, Spain.

\*To whom correspondence should be addressed. E-mail: j.pendry@imperial.ac.uk

same inside and outside the surface, both for the real and effective media,

$$(\mathbf{E} \times \mathbf{H})_z = \frac{-k_z E_0^2}{\omega \mu_h \mu_0} \frac{a}{d^2} \int_0^a \sin^2(\pi x/a) dx = \frac{-k_z E_0^2}{\omega \mu_h \mu_0} \frac{a^2}{2d^2} = (\mathbf{E}' \times \mathbf{H}')_z = \frac{-k_z E_0'^2}{\omega \mu_0 \mu_x} \quad (6)$$

Finer details of the fields around the holes are matched by strongly evanescent fields in the vacuum. Because these fields do not escape from the surface and contain little energy, we neglect them. Substituting for  $E_0'^2$ , we deduce

$$\mu_x = \mu_y = \frac{2d^2 \mu_h \left[ \frac{2a^2}{\pi d^2} \right]^2}{a^2} = \frac{8a^2 \mu_h}{\pi^2 d^2} \quad (7)$$

We also know that

$$k_z = k_0 \sqrt{\epsilon_y \mu_x} = i \sqrt{\pi^2/a^2 - \epsilon_h \mu_h k_0^2} \quad (8)$$

and hence if  $c_0$  is the velocity of light in a vacuum

$$\epsilon_y = \epsilon_x = \frac{1}{\mu_x} \left( \epsilon_h \mu_h - \frac{\pi^2}{a^2 k_0^2} \right) = \frac{\pi^2 d^2 \epsilon_h \left( 1 - \frac{\pi^2 c_0^2}{a^2 \omega^2 \epsilon_h \mu_h} \right)}{8a^2} \quad (9)$$

which is the canonical plasmon form with a plasma frequency of

$$\omega_{pl} = \frac{\pi c_0}{1 \sqrt{\epsilon_h \mu_h}} \quad (10)$$

This is exactly the cut-off frequency of the wave guide. It is easy to see that this is a general result: Any array of closely spaced holes in a perfect conductor will have this form of effective response, with the plasma frequency given by the cut-off frequency of the waveguide mode.

This effective medium implies a bound surface state when there is a divergence in the reflection coefficient of the surface for large values of  $k_{||}$  where  $k_z' = i \sqrt{k_{||}^2 - k_0^2}$  is imag-

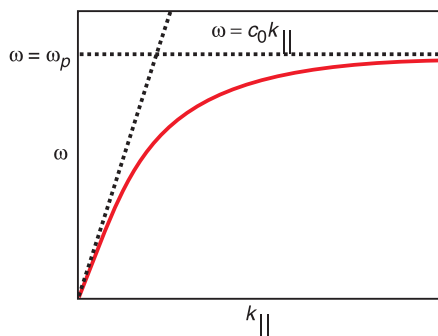


**Fig. 2.** Dispersion relation for spoof surface plasmons on a structured surface. The asymptotes of the light line at low frequencies and the plasma frequency at large values of  $k_{||}$  are shown.

inary. For the polarization where the magnetic field is parallel to the surface

$$r = \frac{k_z' - \epsilon_{||}^{-1} k_z}{k_z' + \epsilon_{||}^{-1} k_z} = \infty \quad (11)$$

which implies a dispersion relationship typical of a surface plasmon polariton

$$k_{||}^2 c_0^2 = \omega^2 + \frac{1}{\omega_{pl}^2 - \omega^2} \frac{64a^4 \omega^4}{\pi^4 d^4} \quad (12)$$

Figure 2 shows a sketch of the dispersion. Notably, at low frequencies the surface mode approaches the light line asymptotically, and the fields associated with the mode expand into the vacuum. At large  $k_{||}$  the frequency of the mode approaches  $\omega_p$ , in contrast to an isotropic plasma where the asymptote is  $\omega_p/\sqrt{2}$ . Although a flat perfectly conducting surface supports no bound states, the presence of holes, however small, produces a surface plasmon polariton-like bound surface state. Indeed, almost any disturbance of the flat surface will bind a state. Bound states are found in the following circumstances: a surface with an array of holes of finite depth, however shallow; a surface with an array of grooves of finite depth; and a surface covered by a layer of dielectric, however thin.

It is also possible to produce hybrid surface plasmons by cutting holes in metals such as silver that already have a surface plasmon. The holes will increase the penetration of fields into the metal and lower the frequency of existing surface plasmons. In this case, it is hard to distinguish between the “real” and the spoof surface plasmons as they merge one into the other.

Our theory as presented is valid when the spacing between the holes is much smaller than the wavelength, so that incident radiation cannot resolve the individual holes. However, the theory can be progressively extended to larger hole spacings by including diffracted waves, more of which appear as the spacing gets bigger. We can do this by including Fourier components of  $\epsilon$  and  $\mu$  so that the effective medium also gives rise to diffracted beams. The main effect of diffraction is to couple the spoof plasmons to incident radiation.

Our result resolves a longstanding debate over transmission through subwavelength holes. As mentioned above, when the anomalously high transmission was first observed (Eq. 7), it was attributed to resonant excitation of surface plasmons. Subsequent calculations (Eq. 8) showed that subwavelength holes in a perfect conductor also gave rise to similar anomalous transmission even though the free surface of an unperforated conductor has no surface modes, leading to discussion as to the true origin of the effect. Now we can see that there are not two separate mechanisms: The

holes will spoof surface plasmons which play the same resonant role as do the real ones on silver.

The ability to engineer a surface plasmon at almost any frequency (metals are nearly perfect conductors from zero frequency up to the threshold of the terahertz regime) where none existed before and to modify at will the frequency of surface plasmons on metals such as silver opens opportunities to control and direct radiation at surfaces over a wide spectral range. Unlike other schemes for creating metamaterials with a plasmalike response (9–11), the present scheme is readily implemented, given that hole drilling techniques are available over a range of length scales down to suboptical wavelengths. Invoking a picture of the surface plasmon as a wave in two dimensions, we now have the ability to control the refractive index perceived by this wave. We stress that this is not the refractive index of the underlying material but is given by the extent to which the surface plasmon wave vector deviates from the light line,  $n_{sp} = k_{||}/\omega_{sp}$ . We have the option to design a lens to focus surface plasmons. Alternatively, we could contour the refractive index,  $n_{sp}(x, y)$ , and, adopting a particle picture of the surface plasmon, imagine it rolling like a ball over this landscape. More prosaic applications such as creating channels to act as waveguides are also possible.

**References and Notes**

1. R. H. Ritchie, *Phys. Rev.* **106**, 874 (1957).
2. M. Fleischmann et al., *Chem. Phys. Lett.* **26**, 163 (1974).
3. S. I. Bozhevolnyi, J. Erland, K. Leosson, P. M. Skovgaard, J. M. Hvam, *Phys. Rev. Lett.* **86**, 3008 (2001).
4. J. C. Weeber, A. Dereux, C. Girard, J. R. Krenn, J. R. Goudonnet, *Phys. Rev. B* **60**, 9061 (1999).
5. H. Ditlbacher, J. R. Krenn, G. Schider, A. Leitner, F. R. Aussenegg, *Appl. Phys. Lett.* **79**, 3035 (2002).
6. W. L. Barnes, A. Dereux, T. W. Ebbesen, *Nature* **424**, 824 (2003).
7. T. W. Ebbesen, H. J. Lezec, H. F. Ghaemi, T. Thio, P. A. Wolff, *Nature* **391**, 667 (1998).
8. L. Martin-Moreno et al., *Phys. Rev. Lett.* **86**, 1114 (2001).
9. J. B. Pendry, A. J. Holden, D. J. Robbins, W. J. Stewart, *J. Phys. Condens. Matter* **10**, 4785 (1998).
10. J. B. Pendry, A. J. Holden, D. J. Robbins, W. J. Stewart, *IEEE Trans. Microw. Theory Tech.* **47**, 2075 (1999).
11. A. Grbic, G. V. Eleftheriades, *Phys. Rev. Lett.* **92**, 117403 (2004).
12. We thank the European Community (EC) under project FP6-NMP4-CT-2003-505699 for financial support. Additionally, J.B.P. acknowledges support from the The Engineering and Physical Sciences Research Council, from the Department of Defense/Office of Naval Research Multidisciplinary University Research Initiative grant N00014-01-1-0803, and from the EC Information Societies Technology program Development and Analysis of Left-Handed Materials, project number IST-2001-35511. L.M.-M. and F.J.G.-V. also acknowledge financial support from the Spanish Ministerio de Ciencia y Tecnologia under contracts MAT2002-01534, MAT2002-00139, and BFM2003-08532-C02-01.

9 April 2004; accepted 28 June 2004  
 Published online 8 July 2004;  
 10.1126/science.1098999  
 Include this information when citing this paper.



# The (Me<sub>5</sub>C<sub>5</sub>)Si<sup>+</sup> Cation: A Stable Derivative of HSi<sup>+</sup>

Peter Jutzi,\* Andreas Mix, Britta Rummel,  
Wolfgang W. Schoeller, Beate Neumann, Hans-Georg Stammler

The reaction of decamethylsilicocene, (Me<sub>5</sub>C<sub>5</sub>)<sub>2</sub>Si, with the proton-transfer reagent Me<sub>5</sub>C<sub>5</sub>H<sub>2</sub><sup>+</sup> B(C<sub>6</sub>F<sub>5</sub>)<sub>4</sub><sup>-</sup> produces the salt (Me<sub>5</sub>C<sub>5</sub>)Si<sup>+</sup> B(C<sub>6</sub>F<sub>5</sub>)<sub>4</sub><sup>-</sup> (**2**), which can be isolated as a colorless solid that is stable in the absence of air and moisture. The crystal structure reveals the presence of a cationic π complex with an η<sup>5</sup>-pentamethylcyclopentadienyl ligand bound to a bare silicon center. The <sup>29</sup>Si nuclear magnetic resonance at very high field (δ = -400.2 parts per million) is typical of a π complex of divalent silicon. The (η<sup>5</sup>-Me<sub>5</sub>C<sub>5</sub>)Si<sup>+</sup> cation in **2** can be regarded as the "resting state" of a silyliumylidene-type (η<sup>1</sup>-Me<sub>5</sub>C<sub>5</sub>)Si<sup>+</sup> cation. The availability of **2** opens new synthetic avenues in organosilicon chemistry. For example, **2** reacted with lithium bis(trimethylsilyl)amide to give the disilene E-[(η<sup>1</sup>-Me<sub>5</sub>C<sub>5</sub>)N(SiMe<sub>3</sub>)<sub>2</sub>Si]<sub>2</sub> (**3**).

The smallest polyatomic moiety in silicon chemistry is the silyliumylidene cation, HSi<sup>+</sup>. Because of its electronic structure (one lone pair and two vacant orbitals of silicon), it is presumably also one of the most reactive species. In 1970, SiH<sup>+</sup> was found by Douglas and Lutz in the spectrum of a discharge through helium mixed with a trace of silane, SiH<sub>4</sub>. It has been characterized by its emission spectrum (1). Shortly after its experimental observation, HSi<sup>+</sup> was identified in the solar spectrum (2), and it was postulated to be present also in interstellar space (3). The astrophysical importance of HSi<sup>+</sup> has made it the subject of detailed spectroscopic and theoretical investigations (4, 5).

Calculations have been performed to investigate the energy of several derivatives of RSi<sup>+</sup> in relation to the parent HSi<sup>+</sup> (isodesmic reaction: HSi<sup>+</sup> + RSiH<sub>3</sub> → RSi<sup>+</sup> + SiH<sub>4</sub>). Furthermore, the <sup>29</sup>Si nuclear magnetic resonance (NMR) shift, the effective nuclear charge of silicon, and the R-Si distance have been calculated (6, 7). The data presented in Table 1 indicate that a pentahapto (η<sup>5</sup>)-bonded pentamethylcyclopentadienyl (Me<sub>5</sub>C<sub>5</sub>, Cp\*) group is the most promising substituent for a stable derivative of HSi<sup>+</sup>: A stabilization energy of almost 100 kcal/mol is calculated for converting the parent HSi<sup>+</sup> into the (η<sup>5</sup>-Me<sub>5</sub>C<sub>5</sub>)Si<sup>+</sup> cation.

The concept of thermodynamic and/or kinetic stabilization has already been applied successfully in the class of divalent silicon compounds, where several stable derivatives of silylene, SiH<sub>2</sub>, could be synthesized (8–11). In this context, π complexation with the Cp\* ligand has turned out to be a useful

synthetic tool, as demonstrated with the synthesis of the silicon(II) complex decamethylsilicocene, (Me<sub>5</sub>C<sub>5</sub>)<sub>2</sub>Si (**1**) (12). This compound shows the reactivity expected for a nucleophilic silylene in that the η<sup>5</sup>-η<sup>1</sup> rearrangement processes of Cp\* groups easily take place (13, 14).

The initial evidence for the intermediate presence of an (Me<sub>5</sub>C<sub>5</sub>)Si<sup>+</sup> cation in the condensed phase (15) came from the reaction of decamethylsilicocene (**1**) with etheral HBF<sub>4</sub> (Scheme 1). Protonation of **1** led to the elimination of pentamethylcyclopentadiene and to the formation of the salt Me<sub>5</sub>C<sub>5</sub>Si<sup>+</sup> BF<sub>4</sub><sup>-</sup>, which instantaneously decomposed even at low temperatures under fluoride transfer to give BF<sub>3</sub> and the also short-lived silylene Me<sub>5</sub>C<sub>5</sub>SiF (16). This observation suggested the use of a proton source containing an anion with much lower nucleophilicity to prevent group transfer to the obviously highly electrophilic silicon atom.

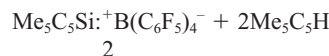
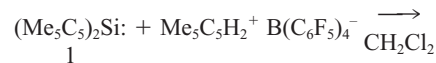
**Table 1.** Quantum chemical calculations for R-Si<sup>+</sup> in the isodesmic reaction SiH<sup>+</sup> + R-SiH<sub>3</sub> → SiH<sub>4</sub> + R-Si<sup>+</sup> + ΔE. The ΔE values and R-Si distances were calculated at the b3lyp/6-311 g(d,p) level. The values for δ Si were calculated at the RHF/6-311+g(2d,p)//b3lyp/6-311 g(d,p) level, and additional values in parentheses at the MP2/6-311+g(2d,p)//b3lyp/6-311 g(d,p) level. The atomic charges q were obtained from a natural population analysis.

R	ΔE (kcal mol <sup>-1</sup> )	δ Si (ppm)	q (Si)	R-Si (Å)
H	0.0	814 (773)	1.37	1.18
H <sub>3</sub> Si	-9.1	2688(2271)	1.06	2.421
H <sub>2</sub> P	-20.6	825 (814)	0.99	2.173
F	-23.2	-103(-111)	1.64	1.558
H <sub>3</sub> C	-23.3	827 (780)	1.47	1.818
Cl	-25.1	192 (154)	1.27	1.972
HC≡C	-26.9	308 (271)	1.43	1.772
HS	-29.1	546 (489)	1.12	2.072
Ph	-38.3	602 (589)	1.36	1.795
H <sub>2</sub> N	-47.5	186 (171)	1.47	1.661
HO	-48.0	-118(-153)	1.57	1.553
η <sup>5</sup> -H <sub>5</sub> C <sub>5</sub>	-83.2	-469(-473)	1.02	2.185
η <sup>5</sup> -Me <sub>5</sub> C <sub>5</sub>	-103.7	-431(-426)	0.99	2.171

Faculty of Chemistry, University of Bielefeld, Universitätsstrasse 25, D-33615 Bielefeld, Germany.

\*To whom correspondence should be addressed. E-mail: peter.jutzi@uni-bielefeld.de

We detected the (Me<sub>5</sub>C<sub>5</sub>)Si<sup>+</sup> cation in the <sup>1</sup>H NMR spectrum after reacting **1** with H(OEt)<sub>2</sub><sup>+</sup> B(C<sub>6</sub>F<sub>5</sub>)<sub>4</sub><sup>-</sup> (**17**) in CD<sub>2</sub>Cl<sub>2</sub> solution at -80°C; this reaction was performed directly in the spectrometer with a special "two-chamber" tube (**18**). The cation turned out to be quite stable in the reaction mixture even at room temperature. This stability initiated a number of experimental modifications. Finally, the compound Me<sub>5</sub>C<sub>5</sub>H<sub>2</sub><sup>+</sup> B(C<sub>6</sub>F<sub>5</sub>)<sub>4</sub><sup>-</sup> (**19**, **20**) turned out to be the protonation agent of choice under laboratory conditions: Reaction with **1** yielded exclusively the salt Me<sub>5</sub>C<sub>5</sub>Si<sup>+</sup> B(C<sub>6</sub>F<sub>5</sub>)<sub>4</sub><sup>-</sup> (**2**) and two equivalents of Me<sub>5</sub>C<sub>5</sub>H (Eq. 1).



Compound **2** was obtained as a colorless powder that is thermally stable but extremely air- and moisture-sensitive. Because of its ionic nature, **2** is poorly soluble in nonpolar solvents but readily soluble in dichloromethane. Its structure was determined by <sup>1</sup>H, <sup>13</sup>C, <sup>29</sup>Si, <sup>11</sup>B, and <sup>19</sup>F NMR spectroscopy and by x-ray crystallography (crystallization from CH<sub>2</sub>Cl<sub>2</sub>/hexane as 2\*0.75 CH<sub>2</sub>Cl<sub>2</sub>) (**21**, **22**). The structure (Fig. 1) is dominated by the large B(C<sub>6</sub>F<sub>5</sub>)<sub>4</sub><sup>-</sup> anions with the smaller Me<sub>5</sub>C<sub>5</sub>Si<sup>+</sup> cations and solvent molecules in the present voids. Rather long Si-F distances reflect only weak cation-anion interactions; the shortest Si-F distance was found to be 2.99 Å. Contacts between silicon and incorporated dichloromethane molecules are not observed (**23**). The structure of the Me<sub>5</sub>C<sub>5</sub>Si<sup>+</sup> cation deviates only to a very small extent from an ideal pentagonal-pyramidal arrangement. The distance of the Si atom to the center of the Cp\* ring is 1.76 Å; the Si-C(Cp\*) distances are 2.14 to 2.16 Å. Both parameters

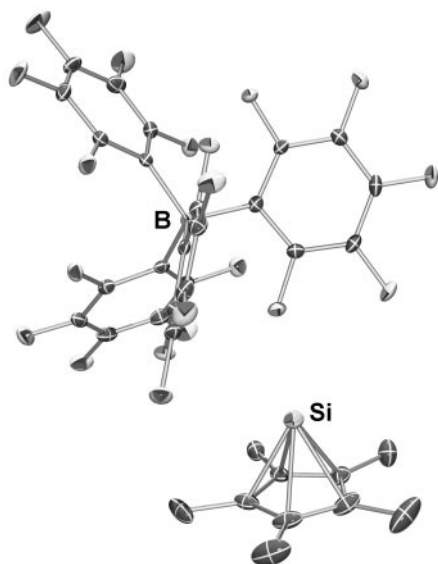


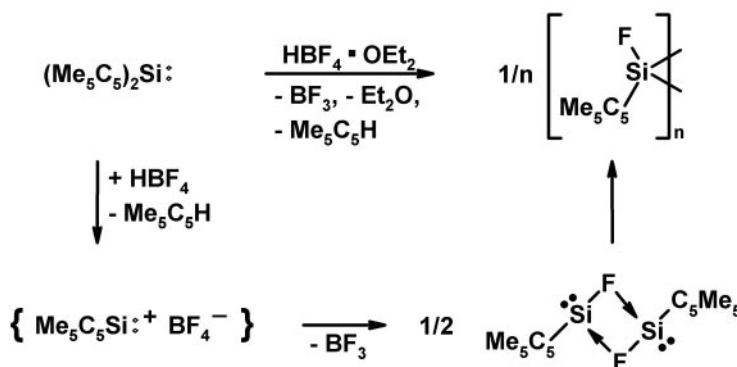
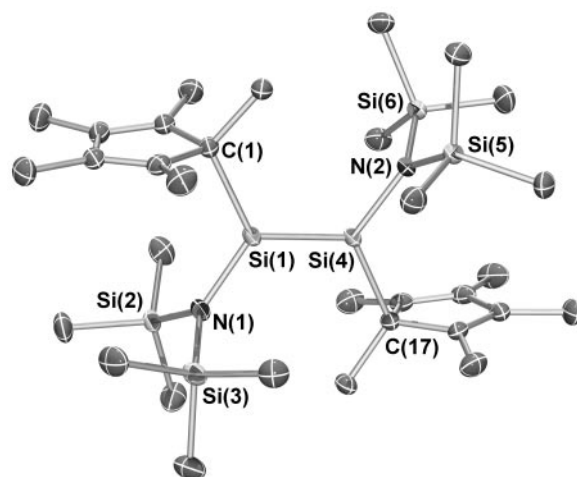
**Fig. 1.** Molecular structure of  $\text{Me}_5\text{C}_5\text{Si}^+ \text{B}(\text{C}_6\text{F}_5)_4^-$  (**2**)  $\cdot$  0.75  $\text{CH}_2\text{Cl}_2$ . Thermal ellipsoids are on the 50% probability level. Protons are omitted for clarity.

are substantially shorter than those in **1**. The C-C distances within the  $\text{Cp}^*$  unit are in the range of 1.43 to 1.44 Å (C-C) and of 1.50 to 1.51 Å (C-Me). The carbon atoms of the five methyl (Me) groups are positioned within the plane of the  $\text{C}_5$  perimeter. The structural parameters in the  $\text{B}(\text{C}_6\text{F}_5)_4^-$  anion are as expected (*17*). The parameters found for the  $(\eta^5\text{-Me}_5\text{C}_5)\text{Si}^+$  cation agree with those obtained by quantum chemical calculations (*18*).

The NMR spectra of **2** recorded in dichloromethane- $d_2$  as solvent indicate the presence of a pentagonal-pyramidal cation structure also in solution. In the  $^1\text{H}$  NMR spectrum, the five Me groups of the  $\text{Cp}^*$  unit give rise to only one sharp singlet at a chemical shift ( $\delta$ ) of 2.23 parts per million (ppm), even at low temperature. The downfield shift of 0.34 ppm compared with that for the 10 Me groups in **1** (*12*) is expected because of the cationic nature of the species. Similarly, one signal for the Me groups ( $\delta = 9.3$  ppm) and one for the carbon atoms of the  $\text{C}_5$  ring ( $\delta = 122.9$  ppm) are observed in the  $^{13}\text{C}$  NMR spectrum. The  $^{29}\text{Si}$  NMR signal appears at  $-400.2$  ppm, that is, in the very high-field region characteristic for a  $\pi$  complex of divalent silicon (*12*). As expected, no  $^{29}\text{Si}$ - $^{19}\text{F}$  coupling is observed. The room temperature  $^{29}\text{Si}$  heteronuclear multiple-bond correlation (HMBC) spectrum shows a cross peak at the corresponding  $^1\text{H}$  and  $^{29}\text{Si}$  chemical shift as a result of the presence of a permanent long-range coupling of all Me protons to silicon; thus, a  $\sigma$  structure with fast sigmatropic rearrangements at the given time scale can be excluded. The  $^{13}\text{C}$ ,  $^{11}\text{B}$ , and  $^{19}\text{F}$  NMR signals for the anion in **2** are found in the usual range (*17*).

The expected broad synthetic potential of the  $(\eta^5\text{-Me}_5\text{C}_5)\text{Si}^+$  cation is mainly based on

**Fig. 2.** Molecular structure of  $E\text{-Me}_5\text{C}_5[(\text{Me}_3\text{Si})_2\text{N}]\text{Si}=\text{Si}[\text{N}(\text{SiMe}_3)_2]\text{C}_5\text{Me}_5$  (**3**). Thermal ellipsoids are on the 50% probability level. Protons are omitted for clarity. Selected bond lengths (Å): Si(1)-Si(4), 2.1683  $\pm$  5; Si(1)-N(1), 1.7476  $\pm$  10; Si(4)-N(2), 1.7483  $\pm$  10; Si(2)-N(1), 1.7663  $\pm$  11; Si(3)-N(1), 1.7683  $\pm$  11; Si(4)-N(2), 1.7483  $\pm$  10; Si(5)-N(2), 1.7675  $\pm$  11; Si(6)-N(2), 1.7642  $\pm$  11. Selected bond angles ( $^\circ$ ): N(1)-Si(1)-C(1), 116.36  $\pm$  5; N(1)-Si(1)-Si(4), 121.52  $\pm$  4; C(1)-Si(1)-Si(4), 121.24  $\pm$  4; N(2)-Si(4)-C(17), 116.92  $\pm$  5; N(2)-Si(4)-Si(1), 121.29  $\pm$  4; C(17)-Si(4)-Si(1), 121.29  $\pm$  4. Twist angles ( $^\circ$ ):  $\phi = 9.0, 6.9$ ;  $\varphi = 4.9$ .



**Scheme 1.**

the following conceivable reaction types: (i) addition of a nucleophile (neutral donor or anionic  $\text{R}^-$ ) to give cationic donor-acceptor complexes  $\text{Me}_5\text{C}_5(\text{donor})\text{Si}^+$  or neutral silycon(II) compounds  $(\text{Me}_5\text{C}_5\text{SiR})_n$ , (ii) oxidative addition and formation of silicon(IV) cations  $\text{Me}_5\text{C}_5(\text{X})(\text{Y})\text{Si}^+$ , and (iii) one electron reduction to give silicon(I) compounds  $(\text{Me}_5\text{C}_5\text{Si})_n$ . In most cases, haptotropic shifts within the  $\text{Cp}^*$  silicon unit from  $\eta^5$  to  $\eta^{2,3}$  or  $\eta^1$  are a prerequisite for a successful reaction.

In an initial experiment with **2**, a novel access to the class of disilenes (*24*) was accomplished. Reaction with lithium bis(trimethylsilyl)amide led to the silylene  $(\text{Me}_5\text{C}_5)\text{SiN}(\text{SiMe}_3)_2$  as a reactive intermediate, which dimerizes to give the disilene  $E\text{-}\{(\eta^1\text{-Me}_5\text{C}_5)[\text{N}(\text{SiMe}_3)_2]\text{Si}\}_2$  (**3**). An x-ray crystal structure analysis of **3** (Fig. 2) (*25*) reveals a CNSiSiNC skeleton that is slightly twisted ( $\varphi = 4.9^\circ$ ) and trans bent ( $\phi = 9.0^\circ$  and  $6.9^\circ$ ). The  $\text{N}(\text{SiMe}_3)_2$  units are nearly perpendicular to the CNSiSiNC unit. The Si-Si distance of 2.17 Å corresponds to typical values for a Si-Si double bond (*24*).

The  $\text{Cp}^*$  group in **3** now is  $\sigma$  bonded to the silicon atom. This observation supports the concept that the  $(\eta^5\text{-Me}_5\text{C}_5)\text{Si}^+$  cation can be regarded as the “resting state” of a true

silyliumylidene-type cation  $(\eta^1\text{-Me}_5\text{C}_5)\text{Si}^+$ .

We note that the carbon analog of the title compound, the  $(\eta^5\text{-Me}_5\text{C}_5)\text{C}^+$  cation, is still unreported. By contrast, the  $(\eta^5\text{-Me}_5\text{C}_5)\text{E}^+$  cations with  $\text{E} = \text{Ge}, \text{Sn}, \text{Pb}$  are described in the literature and exist even in the presence of more nucleophilic anions such as  $\text{BF}_4^-$ ,  $\text{AlCl}_4^-$ ,  $\text{GeCl}_3^-$ , or  $\text{F}_3\text{CSO}_3^-$  (*26*). This behavior can be explained with the increased stability of the formal +2 oxidation state of the heavier homologs.

## References and Notes

- A. E. Douglas, B. L. Lutz, *Can. J. Phys.* **48**, 247 (1970).
- N. Grevesse, A. Sauval, *Astron. Astrophys.* **9**, 232 (1970).
- P. D. Singh, F. G. Vanlandingham, *Astron. Astrophys.* **66**, 87 (1978).
- P. J. Bruna, S. D. Peyerimhoff, *Bull. Soc. Chim. Belg.* **92**, 525 (1983).
- A. B. Sannigrahi, R. J. Buenker, G. Hirsch, Jian-Ping Gu, *Chem. Phys. Lett.* **237**, 204 (1995).
- M. J. Frisch *et al.*, *Gaussian 98*, revision A.1 (Gaussian, Inc., Pittsburgh, PA, 1998).
- Natural population analysis according to (*27*).
- P. P. Gaspar, R. West, in *The Chemistry of Organosilicon Compounds*, Vol. 2, Z. Rappoport, Y. Apeloig, Eds. Part 3, Chapt. 43, Wiley, New York, 1998.
- M. Haaf, A. Schwedake, R. West, *Acc. Chem. Res.* **33**, 704 (2000).
- B. Gehrhus, M. F. Lappert, *J. Organomet. Chem.* **209**, 617 (2001).
- T. Kühler, P. Putzi, *Adv. Organomet. Chem.* **49**, 1 (2003).



12. P. Jutzi, D. Kanne, C. Krüger, *Angew. Chem.* **98**, 163 (1986). [For a review, see (17).]
13. P. Jutzi, G. Reumann, *J. Chem. Soc., Dalton Trans.* **14**, 2237 (2000).
14. P. H. M. Budzelaar, J. J. Engelberts, J. H. van Lenthe, *Organometallics* **22**, 1562 (2003).
15. The gas-phase species  $(\text{Me}_5\text{C}_5\text{Si})^+$  has been observed in the mass spectrum of  $(\text{Me}_5\text{C}_5)_2\text{Si}$  (11).
16. P. Jutzi, U. Holtmann, H. Bögge, A. Müller, *J. Chem. Soc., Chem. Commun.* **1988**, 305, 1988.
17. P. Jutzi, C. Müller, A. Stämmler, H. G. Stämmler, *Organometallics* **19**, 1442 (2000).
18. P. Jutzi *et al.*, in *Organosilicon Chemistry: From Molecules to Materials*, Vol. VI, N. Auner, J. Weis, Eds., Wiley-VCH, Weinheim, in press.
19. M. Otto *et al.*, *Angew. Chem.* **114**, 2379 (2002).
20. Prepared by reaction of  $\text{Me}_5\text{C}_5\text{H}$  with  $\text{H}(\text{OEt})_2^+ \text{B}(\text{C}_6\text{F}_5)_4^-$  in  $\text{CH}_2\text{Cl}_2$ .  $^1\text{H}$  NMR data of the  $\text{Me}_5\text{C}_5\text{H}_2^+$  cation correspond to those given in (19).
21. NMR data of **2** in  $\text{CD}_2\text{Cl}_2$ ,  $\delta$  (ppm):  $^1\text{H}$  NMR (600.13 MHz) 2.23 (singlet, 15 H, methyl protons);  $^{13}\text{C}$  NMR (150.92 MHz) 9.0 (methyl carbons) 122.7 ( $\text{C}_5$ -ring carbons), 124.0 (broad), 136.6 [doublet,  $^1\text{J}(\text{C},\text{F}) = 245$  Hz], 138.5 [doublet,  $^1\text{J}(\text{C},\text{F}) = 244$  Hz], 148.4 [doublet,  $^1\text{J}(\text{C},\text{F}) = 239$  Hz (aromatic carbons)];  $^{29}\text{Si}$  NMR (99.34 MHz)  $-400.3$ ;  $^{11}\text{B}$  NMR (160.43 MHz)  $-16.7$ ;  $^{19}\text{F}$  NMR (470.46 MHz)  $-167.37$  (8 F),  $-163.51$  (4 F),  $-132.99$  (8 F).
22. A colorless crystal (approximate dimensions 0.30 by 0.21 by 0.20 mm) of  $2 \cdot 0.75 \text{CH}_2\text{Cl}_2$  used for x-ray diffraction on a Nonius KappaCCD (charge-coupled device) instrument equipped with monochromatized Mo  $\text{K}_\alpha$  radiation ( $\lambda = 0.71073$  Å). Crystal system triclinic; space group  $\text{P}^1$  with  $a = 10.6900 \pm 9$  Å,  $b = 17.4170 \pm 14$  Å,  $c = 19.940 \pm 3$  Å,  $\alpha = 101.416 \pm 10^\circ$ ,  $\beta = 102.745 \pm 9^\circ$ ,  $\gamma = 94.579 \pm 7^\circ$ ,  $V = 3519.7 \pm 7$  Å $^3$ , four molecules per unit cell, formula weight 906.05, calculated density 1.710 Mg/m $^3$ . Data were collected at 100 K,  $\Theta$  range from  $3.0^\circ$  to  $27.5^\circ$ . A total of 116,423 reflections were collected (16,140 unique,  $R_{\text{int}} = 0.04$ );  $R_f = 0.0399$  for 12,334 reflections, with  $I > 2\sigma$  (1), weighted  $R_{p2} = 0.0984$  for all reflections. More crystallographic data are available at the Cambridge Crystallographic Data Centre, CCDC number 242266.
23. The closest Si-Cl ( $\text{CH}_2\text{Cl}_2$ ) distance was determined to a resolution of 5.34 Å.
24. R. Okazaki, R. West, *Adv. Organomet. Chem.* **39**, 231 (1996).
25. A yellow crystal (approximate dimensions: 0.30 by 0.30 by 0.16 mm) of **3** used for x-ray diffraction on a Nonius KappaCCD instrument equipped with monochromatized Mo  $\text{K}_\alpha$  radiation ( $\lambda = 0.71073$  Å). Crystal system monoclinic; space group  $\text{P}2_1/\text{n}$  with  $a = 17.6670 \pm 2$  Å,  $b = 10.18800 \pm 10$  Å,  $c = 23.4380 \pm 2$  Å,  $\beta = 110.6080 \pm 6^\circ$ ,  $V = 3,948.69 \pm 7$  Å $^3$ , four molecules per unit cell, formula weight 647.41, calculated density 1.089 Mg/m $^3$ . Data were collected at 100 K (range from  $3.0^\circ$  to  $27.5^\circ$ ). A total of 69,748 reflections were collected (9,000 unique,  $R_{\text{int}} = 0.04$ );  $R_f = 0.0313$  for 7,739 reflections with  $I > 2\sigma$  (1), weighted  $R_{p2} = 0.0874$  for all reflections. More crystallographic data are available at the Cambridge Crystallographic Data Centre, CCDC number 242267.
26. P. Jutzi, N. Burford, *Chem. Rev.* **99**, 969 (1999).
27. A. Reed, L. A. Curtiss, F. Weinhold, *Chem. Rev.* **88**, 899 (1988).
28. We thank the Deutsche Forschungsgemeinschaft and the University of Bielefeld for financial support.

3 May 2004; accepted 23 June 2004

Published online 1 July 2004;

10.1126/science.1099879

Include this information when citing this paper.

# Climatic Control of Riverine and Seawater Uranium-Isotope Ratios

Laura F. Robinson,\*† Gideon M. Henderson, Lisa Hall,‡  
Iain Matthews

The large variation in the ratio of uranium-234 to uranium-238 ( $^{234}\text{U}/^{238}\text{U}$ ) in rivers is not well understood, but may provide information about past weathering and rainfall and is important because it controls seawater ( $^{234}\text{U}/^{238}\text{U}$ ). Here, we demonstrate the importance of physical weathering and rainfall for ( $^{234}\text{U}/^{238}\text{U}$ ), using rivers from South Island, New Zealand. These data allow interpretation of an existing speleothem ( $^{234}\text{U}/^{238}\text{U}$ ) record and suggest that New Zealand glacier advance 13,000 years ago was influenced by increased rainfall rather than by Younger Dryas-like cooling. A model of seawater ( $^{234}\text{U}/^{238}\text{U}$ ) during glacial cycles indicates that rejection of corals based on modern ( $^{234}\text{U}/^{238}\text{U}$ )  $\pm <0.01$  is not merited and may reject the highest quality ages.

The energetic alpha decay of  $^{238}\text{U}$  makes its great-granddaughter,  $^{234}\text{U}$ , relatively mobile and causes variability in the ratio of activities of  $^{234}\text{U}$  and  $^{238}\text{U}$  ( $^{234}\text{U}/^{238}\text{U}$ ) in the surface-Earth environment (1). Rivers, for instance, have ( $^{234}\text{U}/^{238}\text{U}$ ) varying from  $<1$  to  $>3$  (2). These surface-water ratios are recorded in precipitates such as riverine tufas or cave carbonates and are routinely measured during U/Th dating (3–5). Resulting ( $^{234}\text{U}/^{238}\text{U}$ ) records may contain information about past rainfall and continental weathering that could be deciphered if the controls on the ratio were fully understood.

Department of Earth Sciences, University of Oxford, Parks Road, Oxford, OX1 3PR, UK.

\*To whom correspondence should be addressed. E-mail: laurar@gps.caltech.edu

†Present address: California Institute of Technology, MS 100-23, 1200 East California Boulevard, Pasadena, CA 91125, USA.

‡Present address: RMS Inc., 7015 Gateway Boulevard, Newark, CA 94560, USA.

One example of such a record is Netlebed Cave in New Zealand (Fig. 1). A speleothem from this location contains a sharp change of initial ( $^{234}\text{U}/^{238}\text{U}$ ) 13 thousand years ago (ka) (3). This change is synchronous with the advance of some glaciers in New Zealand and, particularly, with the formation of the Waiho Loop moraine (6). The Waiho Loop advance is controversial because it suggests cooling of the Southern Hemisphere climate at the same time as Younger Dryas cooling in the Northern Hemisphere. Such Southern Hemisphere cooling differs from that seen in Antarctic ice cores and would complicate the idea of a bipolar seesaw as the cause for millennial climate changes (7).

Carbonate ( $^{234}\text{U}/^{238}\text{U}$ ) ratios are used routinely to assess the quality of coral U/Th ages (8) and, more recently, to correct for alpha-recoil processes (9, 10). Such an approach relies on a known history of ( $^{234}\text{U}/^{238}\text{U}$ ) in seawater. Understanding the controls on surface-water ( $^{234}\text{U}/^{238}\text{U}$ ) allows an assess-

ment of the magnitude of possible changes in this seawater ( $^{234}\text{U}/^{238}\text{U}$ ) history.

The South Island of New Zealand provides an ideal region to quantify the controls on surface water ( $^{234}\text{U}/^{238}\text{U}$ ) because it features considerable and independent variation in rainfall and physical weathering, with a reasonably constant rock chemistry (11). Rainfall is very asymmetric, with extremely high levels (up to 12,000 mm/year) on the western flanks of the Southern Alps and levels as low as 400 mm/year to the east (Fig. 1). Physical weathering also varies substantially because tectonic uplift rates range from zero to as high as 17 mm/year (Fig. 1) (12, 13). Higher uplift causes more rapid physical erosion and higher river sediment loading, commonly dominated by landslide-derived material (14). In general, catchments on the South Island are small, so rivers flow through a narrow range of rainfall and uplift environments. The rocks of the South Island have a rather uniform bulk chemistry and comprise predominantly Mesozoic silicates (15). Groundwater solute contributions also tend to be low (16, 17), so that complications due to high or variable groundwater input are avoided (18, 19).

We collected a suite of 27 river-water samples from the South Island (Fig. 1) in March 2001 and analyzed them for U concentration and isotope ratios (20, 21). The size and shape of the catchment for each of these samples were calculated from a hydrologically accurate digital elevation model (DEM) (22) (Fig. 1). This DEM also allows an estimate of the average rainfall and average uplift rate for each catchment by using digitized versions of available rainfall (23) and uplift maps (12, 24). A single groundwater sample was also analyzed to assess the possibility of an impor-

REPORTS

tant contribution to riverine U from this source. A seawater sample was analyzed to confirm analytical accuracy and allow data comparison with other laboratories.

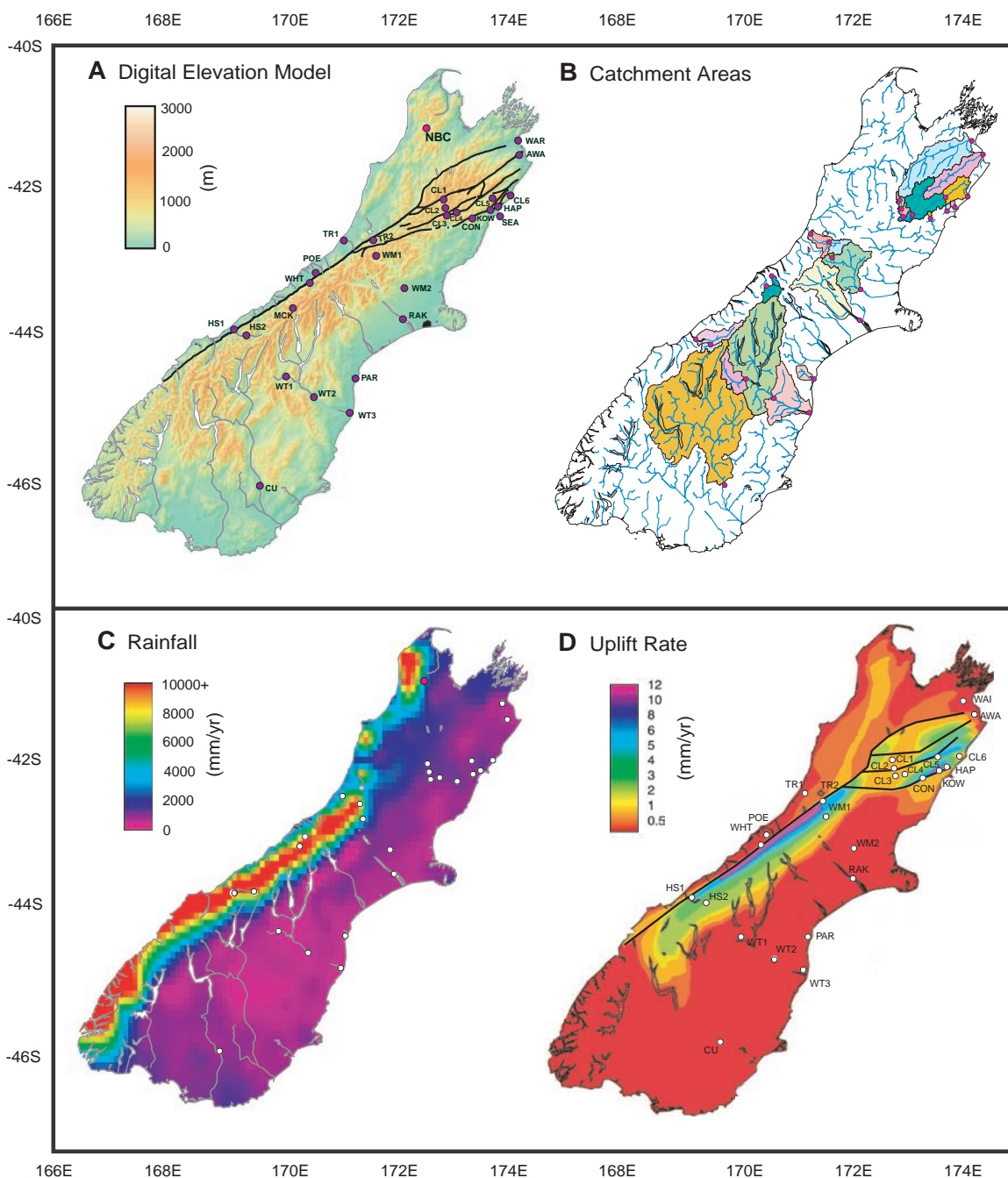
New Zealand rivers exhibit a very wide range of ( $^{234}\text{U}/^{238}\text{U}$ ), from 1.09 to 4.61 (Fig. 2 and table S1) (25). This range spans that previously measured in rivers from elsewhere and includes values further from secular equilibrium than have previously been reported. The wide range of values cannot be explained by changes in rock chemistry because the chemistry and grain size of the source rock for all rivers is similar (15). The high values also cannot be caused by groundwater input

as has been suggested in other regions (18, 19), because the measured groundwater has, as expected (16, 17), a low U concentration (2.7 parts per thousand) and also a reasonably low ( $^{234}\text{U}/^{238}\text{U}$ ) of 1.42. The high and variable ( $^{234}\text{U}/^{238}\text{U}$ ) must therefore be controlled by variations in the rate of mechanical erosion and rainfall.

Riverine ( $^{234}\text{U}/^{238}\text{U}$ ) on the dry eastern side of the South Island correlates strongly with uplift rate (Fig. 2). This correlation is not dependent on samples from a single river or region and indicates a first-order control on the ( $^{234}\text{U}/^{238}\text{U}$ ) ratio of surface waters by the rate of uplift-induced physical weather-

ing. The rivers with the highest ( $^{234}\text{U}/^{238}\text{U}$ ) are those draining uplifting fault scarps from the zone of high uplift in the north of the South Island. In this zone, bare rock is being eroded as the Kaikoura Range is being created (24). For example, the Kowhai River has a value of 4.60 and its catchment is uplifting at an average rate of  $\sim 7$  mm/year. By contrast, in the southern region where there is virtually no tectonic motion ( $< 1$  mm/year), the Clutha River exhibits values of  $< 1.10$ . At intermediate uplift rates, such as those of the Clarence River catchment ( $\sim 3$  mm/year), ( $^{234}\text{U}/^{238}\text{U}$ ) is intermediate, at  $\sim 2.60$ . The short recoil distance of  $^{234}\text{U}$  ( $\sim 500$  to 1000

**Fig. 1.** (A) Digital elevation model of South Island, New Zealand, with sample locations marked in purple and major faults shown in black. The location of Nettlebed Cave is labeled NBC. All other three-letter location names are tabulated in table S1. (B) Drainage network and catchments areas for each sample. (C) Contour map of the average yearly rainfall (23). (D) Uplift rates, based on the models of (72) and (24) and adapted to account for more recent studies (41). Although the precision of this model is limited, the relative variation in uplift rates correlates well with the observed spatial variation of denudation rates from fission-track data (42). Despite being a simple representation of the complex tectonic deformation of the South Island, the model acts as a good guide to the relative uplift of the region. The map shows many similar features to the DEM, but the latter cannot be used as a proxy for uplift because topographic height is related to the total uplift integrated over time, not to uplift rate. Furthermore, the relation between topographic height and uplift is nonlinear as a result of the increasing influence of erosional processes on the landscape at higher uplift rates (14).





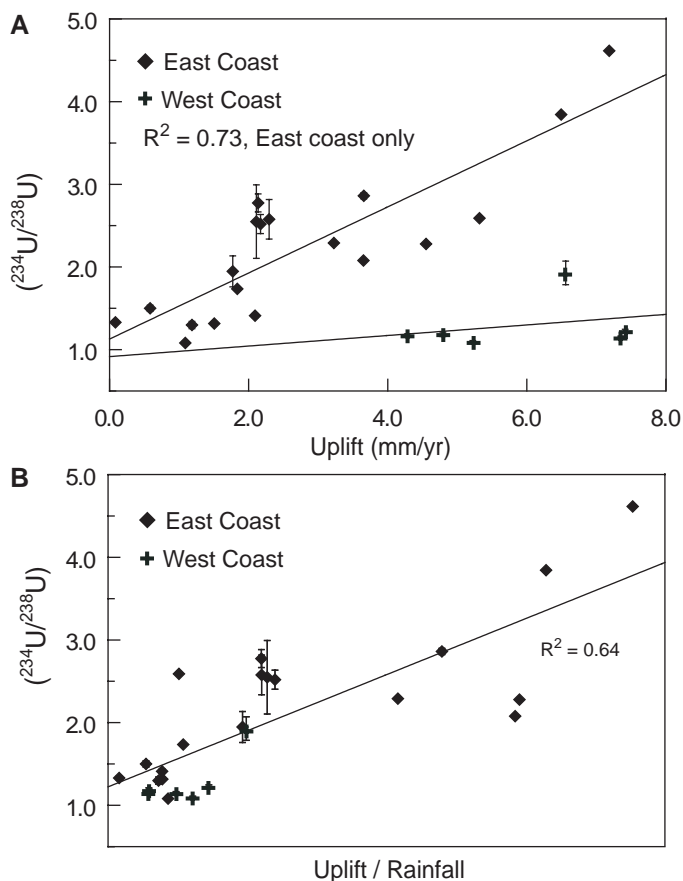
Å) (26) means that only a small fraction of  $^{234}\text{U}$  is recoiled. This fraction increases linearly as grain radius decreases, so that reduction of grain size during physical weathering increases the  $^{234}\text{U}$  release. Such physical weathering will also liberate  $^{234}\text{U}$  from decay-damaged lattice sites within the mineral grains (27) to further increase ( $^{234}\text{U}/^{238}\text{U}$ ). The New Zealand river data represent the first convincing evidence for the strong control that physical weathering exerts on surface water ( $^{234}\text{U}/^{238}\text{U}$ ).

Rivers draining the wet western side of the South Island also show a correlation with uplift rate (Fig. 2). The most striking feature of these rivers, however, is that they all have considerably lower ( $^{234}\text{U}/^{238}\text{U}$ ) than those draining to the east (Fig. 2). This is true even when comparing catchments with similar average uplift rates. The relation with rainfall reflects the constant rate of  $^{234}\text{U}$  recoil from mineral grains (26). In regions of high rainfall, recoil  $^{234}\text{U}$  will be washed away rapidly, whereas in regions of lower rainfall, it will have time to accumulate, resulting in higher  $^{234}\text{U}$  concentrations in the water. This leads to the expectation that excess  $^{234}\text{U}$  levels in rivers should have a reciprocal relation to rainfall (i.e., a doubling of rainfall should lead to a halving of the  $^{234}\text{U}$  excess). Such a relation is consistent with the New Zealand river data, although the relation is somewhat

masked because rainfall is only a secondary control on ( $^{234}\text{U}/^{238}\text{U}$ ).

These modern river data indicate that a temporal change of ( $^{234}\text{U}/^{238}\text{U}$ ) in catchment waters will result from a change either in the rate of physical weathering or in rainfall. Substrates that capture past drainage chemistry, such as tufas or near-surface cave carbonates, therefore provide a record of past weathering and/or rainfall. The abrupt change in ( $^{234}\text{U}/^{238}\text{U}$ ) observed at 13 ka in the Nettlebed Cave Speleothem (3) can be interpreted in this context. This record shows a reasonably consistent value of 1.43 during the last glacial and a sudden change at 13 ka to values of  $\sim 1.37$  (3). This abrupt shift is unlikely to represent a change in uplift rate and, because the location of Nettlebed Cave was not glaciated during the last glacial, changes in physical weathering due to ice grinding cannot be invoked. The shift is therefore very likely to be caused by an increase in rainfall. The continuous ( $^{234}\text{U}/^{238}\text{U}$ ) values observed in the Nettlebed record on either side of this shift indicate a single change in rainfall at 13 ka rather than a millennial-style oscillation. This shift, therefore, probably represents a response of the climate to global deglaciation, perhaps due to the poleward movement of wind systems as the planet warms.

**Fig. 2.** Filled diamonds show samples from the east coast, with crosses from the west coast. Error bars are all  $2\sigma$ . (A) Plot of ( $^{234}\text{U}/^{238}\text{U}$ ) against uplift rate. Solid and dashed best-fit lines are for the east ( $R^2 = 73$ ) and west coast data, respectively. (B) Plot of the same data, but with uplift rate normalized to rainfall and a best-fit line through all the data ( $R^2 = 64$ ).

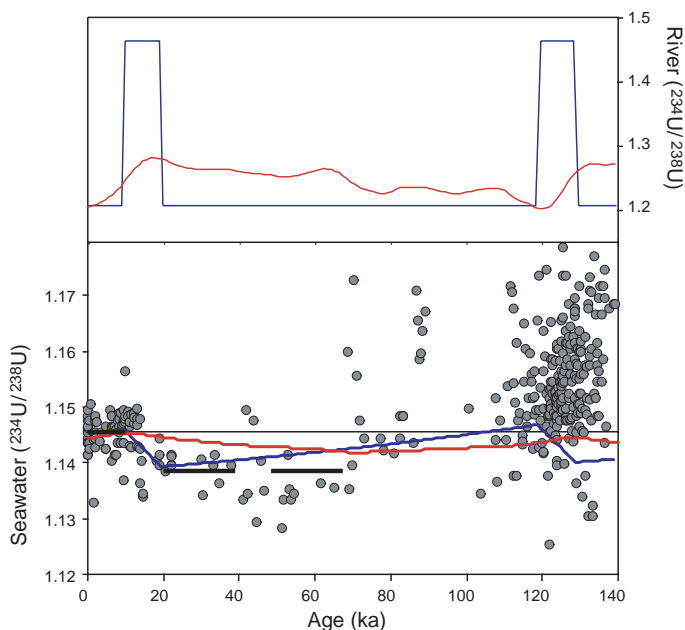


The timing of advance of some New Zealand glaciers dated at 13 ka (6) is not consistent with other Southern Hemisphere records, particularly those in the Antarctic ice cores, which show earlier cooling ( $\sim 13.8$  ka) followed by warming during the Younger Dryas (at  $\sim 13$  ka) (28). Glacier growth is controlled by both temperature and moisture supply, so that an increase in rainfall at constant temperature can explain the advance at 13 ka. Such an interpretation is consistent with other data from the Nettlebed speleothem, particularly the  $\delta^{18}\text{O}$  record (29) which, although complicated, can be interpreted as showing cooling at 13.8 ka rather than at 13.0 ka. Pollen records provide somewhat conflicting evidence for change at this time, with some showing little evidence for change (30) and others showing early cooling at  $\sim 13.7$  ka (31–33). Three pollen records in the vicinity of the Waiho Loop location suggest an increase in precipitation, but the chronology is not as precise as the U/Th ages of the Nettlebed speleothem (34). A strong rainfall control of glacial advance at 13 ka suggests that cooling during a Younger Dryas-like event is not likely to have been as important in the mid-latitudes of the South Pacific as in areas of the Northern Hemisphere.

Understanding the controls on surface water ( $^{234}\text{U}/^{238}\text{U}$ ) helps to interpret speleothem and tufa records from other regions and confirms the interpretation of a change in fluid regime suggested for the Soreq Cave, Israel (4). Care will be needed, however, in areas where major groundwater contributions to surface water are found because of the high and variable ( $^{234}\text{U}/^{238}\text{U}$ ) in groundwaters.

The observation of a strong climatic control on riverine ( $^{234}\text{U}/^{238}\text{U}$ ) also has implications for the value of seawater ( $^{234}\text{U}/^{238}\text{U}$ ) during glacial cycles. Such changes in seawater ( $^{234}\text{U}/^{238}\text{U}$ ) were first proposed by Esat and Yokoyama (35) on the basis of coral data but have remained controversial because of scatter of the coral data and the lack of a viable forcing mechanism. Existing coral data (Fig. 3) from the period 0 to 10 ka have an average initial ( $^{234}\text{U}/^{238}\text{U}$ ) of 1.146 ( $n = 67$ ), compared with a value of 1.139 for the period 10 to 70 ka ( $n = 29$ ). The scatter of values within both intervals cannot be explained by changes in seawater and indicates that diagenesis must have affected at least some of the corals. The difference between the average values, however, suggests an  $\sim 0.007$  change in seawater ( $^{234}\text{U}/^{238}\text{U}$ ) between the glacial and interglacial. The possibility that such a difference can result from changes in rainfall and weathering during a glacial cycle can be investigated with the New Zealand river data as a guide. Two simple models were constructed based on a model used

**Fig. 3.** A compilation of existing mass spectrometric initial ( $^{234}\text{U}/^{238}\text{U}$ ) for corals of the past 140,000 years, compared with two models of possible changes in ocean ( $^{234}\text{U}/^{238}\text{U}$ ) based on New Zealand river data. Thick dashed lines show the average coral values for the Holocene (1.146;  $n = 67$ ) and for 70 to 20 ka (1.139;  $n = 29$ ). The blue lines show a possible average riverine input (upper panel) and ocean response (lower panel) to a periodic release of high ( $^{234}\text{U}/^{238}\text{U}$ ) during deglaciation. The red lines show the expected riverine forcing and ocean response for a change in rainfall expected during different global climate states.



previously to understand the longer-term history of seawater ( $^{234}\text{U}/^{238}\text{U}$ ) (36).

The first model tests the effect of changes in physical weathering. The most important change in such weathering during a glacial cycle is that induced by subglacial grinding during glacials. We model this effect by assuming that 10,000-year deglaciations release pulses of high ( $^{234}\text{U}/^{238}\text{U}$ ) from freshly ground rock. We assume that a percentage of global rivers equivalent to the fraction of continent uncovered at the end of the glacial (~15%) had increased ( $^{234}\text{U}/^{238}\text{U}$ ) as a result of such subglacial grinding. The maximum possible value for these rivers based on the New Zealand data is 4.6, which predicts a seawater cycle in ( $^{234}\text{U}/^{238}\text{U}$ ) of amplitude 0.013, about twice that suggested by the average coral data. To generate the average glacial-interglacial difference observed in corals requires that rivers draining deglaciated crust had an average ( $^{234}\text{U}/^{238}\text{U}$ ) of ~3.0, well within the range observed for New Zealand rivers. Such a change would suggest a global average river ( $^{234}\text{U}/^{238}\text{U}$ ) during deglaciation ~0.27 higher than at other times. This analysis implies that the amplitude of seawater ( $^{234}\text{U}/^{238}\text{U}$ ) change suggested by coral data can be generated by changes in physical weathering.

The second model tests the expected seawater response to rainfall variability. The hydrological cycle during the glacial is thought to be ~70% of its Holocene strength. Assuming the expected reciprocal relationship between  $^{234}\text{U}$  excess and rainfall suggests a glacial riverine  $^{234}\text{U}$  excess 42% higher than during the Holocene. Scaling this change to climate using the SPECMAP curve

(37) suggests a seawater ( $^{234}\text{U}/^{238}\text{U}$ ) change of amplitude of ~4%, with a low at ~70 ka and a high in the early Holocene (Fig. 3) (38). It is probable that both effects—weathering and rainfall—played a role in controlling seawater ( $^{234}\text{U}/^{238}\text{U}$ ) during glacial cycles.

The two models indicate that seawater ( $^{234}\text{U}/^{238}\text{U}$ ) was likely to have been lower than today by as much as 0.01 at times during the past 80,000 years. With measurement precision on ( $^{234}\text{U}/^{238}\text{U}$ ) now routinely in the per mil range, there is a growing tendency to reject all corals with initial ( $^{234}\text{U}/^{238}\text{U}$ ) more than a few per mil different from the modern value. The new river data and modeling presented here suggest that this criterion is in error and may, in fact, lead to the rejection of those corals that have remained a closed system.

**References and Notes**

1. V. V. Cherdyn'tsev, *Uranium-234* (Israel Program for Scientific Translations, Jerusalem, 1971).
2. F. Chabaux, J. Riotte, O. Dequincey, *Rev. Mineral. Geochem.* **52**, 533 (2003).
3. J. C. Hellstrom, M. T. McCulloch, *Earth Planet. Sci. Lett.* **179**, 287 (2000).
4. A. Kaufman et al., *Earth Planet. Sci. Lett.* **156**, 141 (1998).
5. K. R. Ludwig et al., *Science* **258**, 284 (1992).
6. G. H. Denton, C. H. Hendy, *Science* **264**, 1434 (1994).
7. W. S. Broecker, *Paleoceanography* **13**, 119 (1998).
8. C. H. Stirling, T. M. Esat, K. Lambeck, M. T. McCulloch, *Earth Planet. Sci. Lett.* **160**, 745 (1998).
9. G. M. Henderson, N. C. Slowey, *Nature* **404**, 61 (2000).
10. W. G. Thompson, M. W. Spiegelman, S. L. Goldstein, R. C. Speed, *Earth Planet. Sci. Lett.* **210**, 365 (2003).
11. A. D. Jacobson, J. D. Blum, C. P. Chamberlain, D. Crav, P. O. Koons, *Geochim. Cosmochim. Acta* **67**, 29 (2003).
12. H. W. Wellman, in *The Origin of the Southern Alps*, R. I. Walcott, M. M. Cresswell, Eds. (Roy. Soc. of N. Z., Wellington, 1979), vol. 18, pp. 13–20.
13. J. Adams, *Geol. Soc. Am. Bull.*, Part 1, **91**, 2 (1980).
14. N. Hovius, C. P. Stark, P. A. Allen, *Geology* **25**, 231 (1997).

15. R. P. Suggate, *The Geology of New Zealand* (E. C. Keating, Wellington, 1978).
16. M. A. Mongillo, L. L. Clelland, "DSIR Geothermal Report" (Department of Scientific and Industrial Research, Wellington, vol. 9, 1984).
17. R. G. Allis, Y. Shi, *N. Z. J. Geol. Geophys.* **38**, 585 (1995).
18. F. Chabaux, J. Riotte, N. Clauer, C. France-Lanord, *Geochim. Cosmochim. Acta* **65**, 3201 (2001).
19. D. Porcelli, P. S. Andersson, G. J. Wasserburg, J. Ingri, M. Baskaran, *Geochim. Cosmochim. Acta* **61**, 4095 (1997).
20. L. F. Robinson, G. M. Henderson, N. C. Slowey, *Earth Planet. Sci. Lett.* **196**, 175 (2002).
21. Water samples of between 100 and 300 g were acidified and spiked with  $^{236}\text{U}$ . Iron co-precipitation was succeeded by chemical separation of U (39). Simultaneous measurements of  $^{238}\text{U}$ ,  $^{236}\text{U}$ ,  $^{235}\text{U}$  (Faraday collectors), and  $^{234}\text{U}$  (ion counting) were made on a Nu Instruments multi-collector inductively coupled plasma-mass spectrometer with two bracketing CRM 145 standards to correct for mass biases and ion counter-Faraday collector gain and to assess repeatability (20).
22. The DEM has a 200-m horizontal resolution and was created from digitized contour and drainage data, derived from 1:25,000 topographic maps. The contour interpolation process was conducted using the software ArcInfo, following the method of (40) to ensure hydrological accuracy.
23. National Institute of Water and Atmospheric Research Climate Database, South Island daily rainfall, 1980–2000. [www.niwa.co.nz/services/clidb](http://www.niwa.co.nz/services/clidb)
24. S. H. Lamb, H. M. Bibby, *J. Struct. Geol.* **11**, 473 (1989).
25. Uranium concentrations in the rivers show no systematic relation with uplift, rainfall, or ( $^{234}\text{U}/^{238}\text{U}$ ). This lack of correlation presumably reflects the active chemistry of uranium. Changes of redox, organic complexing, or carbonate concentration all influence the U concentration without directly changing ( $^{234}\text{U}/^{238}\text{U}$ ).
26. K. Kigoshi, *Science* **173**, 3991 (1971).
27. J. Kronfeld, J. C. Vogel, *Earth Planet. Sci. Lett.* **105**, 191 (1991).
28. T. Sowers, M. Bender, *Science* **269**, 210 (1995).
29. J. Hellstrom, M. McCulloch, J. Stone, *Quat. Res.* **50**, 167 (1998).
30. C. Singer, J. Shulmeister, B. McLea, *Science* **281**, 812 (1998).
31. C. S. M. Turney, M. S. McGlone, J. M. Wilmhurst, *Geology* **31**, 223 (2003).
32. A. Sandiford, R. Newnham, B. Alloway, J. Ogden, *Palaeogeogr. Palaeoclimatol. Palaeoecol.* **201**, 235 (2003).
33. R. M. Newnham, D. J. Lowe, *Geology* **28**, 759 (2000).
34. M. J. Vandergoes, S. J. Fitzsimons, *Quat. Sci. Rev.* **22**, 1461 (2003).
35. T. M. Esat, Y. Yokoyama, *Eos* **80**, 581 (1999).
36. G. M. Henderson, *Earth Planet. Sci. Lett.* **199**, 97 (2002).
37. D. G. Martinson et al., *Quat. Res.* **27**, 1 (1987).
38. Because the  $^{234}\text{U}$  recoil rate is constant, a global increase in riverine ( $^{234}\text{U}/^{238}\text{U}$ ) must be caused either by intermittent storage of recoil  $^{234}\text{U}$  on the continents or by a decrease in the global  $^{238}\text{U}$  flux to the oceans. Running the model with a simple ( $^{234}\text{U}/^{238}\text{U}$ ) change (to mimic storage) or with a coupled ( $^{234}\text{U}/^{238}\text{U}$ ) and U-flux change made no significant difference to the amplitude of the seawater ( $^{234}\text{U}/^{238}\text{U}$ ) predicted. In the latter case, only a very small (3%) amplitude cycle in seawater U concentration is observed.
39. R. L. Edwards, J. H. Chen, G. J. Wasserburg, *Earth Planet. Sci. Lett.* **81**, 175 (1986).
40. M. F. Hutchinson, *J. Hydrol.* **106**, 211 (1989).
41. Y. Ota et al., *N. Z. J. Geol. Geophys.* **39**, 51 (1996).
42. J. M. Tippet, P. J. J. Kamp, *J. Geophys. Res.* **16**, 16119 (1993).
43. We thank the Gary Comer Fellowship program for financial support and N. Belshaw for help in the laboratory.

**Supporting Online Material**

[www.sciencemag.org/cgi/content/full/305/5685/851/DC1](http://www.sciencemag.org/cgi/content/full/305/5685/851/DC1)  
Table S1

27 April 2004; accepted 7 July 2004



# A Plant Vacuolar Protease, VPE, Mediates Virus-Induced Hypersensitive Cell Death

Noriyuki Hatsugai,<sup>1,2,3</sup> Miwa Kuroyanagi,<sup>1</sup> Kenji Yamada,<sup>2,3</sup> Tetsuo Meshi,<sup>4</sup> Shinya Tsuda,<sup>5</sup> Maki Kondo,<sup>2</sup> Mikio Nishimura,<sup>2,3</sup> Ikuko Hara-Nishimura<sup>1\*</sup>

Programmed cell death (PCD) in animals depends on caspase protease activity. Plants also exhibit PCD, for example as a response to pathogens, although a plant caspase remains elusive. Here we show that vacuolar processing enzyme (VPE) is a protease essential for a virus-induced hypersensitive response that involves PCD. VPE deficiency prevented virus-induced hypersensitive cell death in tobacco plants. VPE is structurally unrelated to caspases, although VPE has a caspase-1 activity. Thus, plants have evolved a regulated cellular suicide strategy that, unlike PCD of animals, is mediated by VPE and the cellular vacuole.

Some regulatory mechanisms that underlie programmed cell death (PCD) are thought to be conserved in animals and plants, and many studies have provided evidence that PCD in both shares components that include caspase activity (1–4). However, there is only indirect evidence that caspases are present in plants. The identification of a protease exhibiting caspase activity is essential in elucidating the molecular mechanism that operates PCD in plants. In this study, we have identified VPE (5), a protein that has a proteolytic activity toward a caspase-1 substrate (a caspase-1 activity), as a key component underlying hypersensitive cell death, a typical PCD in plants (6). VPE, like a caspase, is a cysteine protease and was originally found as a processing enzyme responsible for the maturation of seed storage proteins (7, 8). Evidence indicates that VPE is responsible for the maturation or activation not only of various vacuolar proteins in plants (5, 9–11), but also of lysosomal proteins in the mouse (12). Previously, we reported that VPE was up-regulated during cell death in association with leaf senescence and lateral root formation of *Arabidopsis* (5, 13). This implied that VPE might be involved in plant cell death.

Hypersensitive response (HR) is caused by interactions between plants and incompatible pathogens, in association with rapid and localized cell death (hypersensitive cell death) at the infected sites of host tissues (14). The HR plays a role in preventing the growth and spread of the pathogens into healthy tissues. For this

study, we used *Nicotiana* plants that carried the *N* resistance gene to tobacco mosaic virus (TMV) to form synchronous lesions that showed hypersensitive cell death in the TMV-infected leaves after a temperature shift (supporting online text and fig. S1). We isolated

four VPE cDNAs [*NiVPE-1a* (DNA Data Bank of Japan, accession no. AB075947), *NiVPE-1b* (AB075948), *NiVPE-2* (AB075949), and *NiVPE-3* (AB075950)] from the TMV-infected leaves. Both mRNA and protein levels of VPE were rapidly and transiently increased at an early stage of HR in the leaves (supporting online text and fig. S1). To clarify the effect of VPE on lesion formation, we infected the tobacco leaves with TMV, and then infiltrated each protease inhibitor into the infected region 1 hour before the temperature shift. The characteristic lesion was observed in the TMV-infected region 24 hours after the temperature shift (Fig. 1A). Lesion formation was strongly inhibited by a VPE inhibitor, Ac-ESEN-CHO, and a caspase-1 inhibitor, Ac-YVAD-CHO (Fig. 1A). Other protease inhibitors used were unable to inhibit lesion formation. These results suggest that VPE activity and caspase-1 activity contribute to TMV-induced cell death.

To detect the protein that had caspase-1 activity, we developed a biotinylated-inhibitor blot analysis with an irreversible caspase inhibitor, biotin-xVAD-fmk. In this analysis, an enzyme that conjugates with the inhibitor becomes visible on the blot with streptavidin-

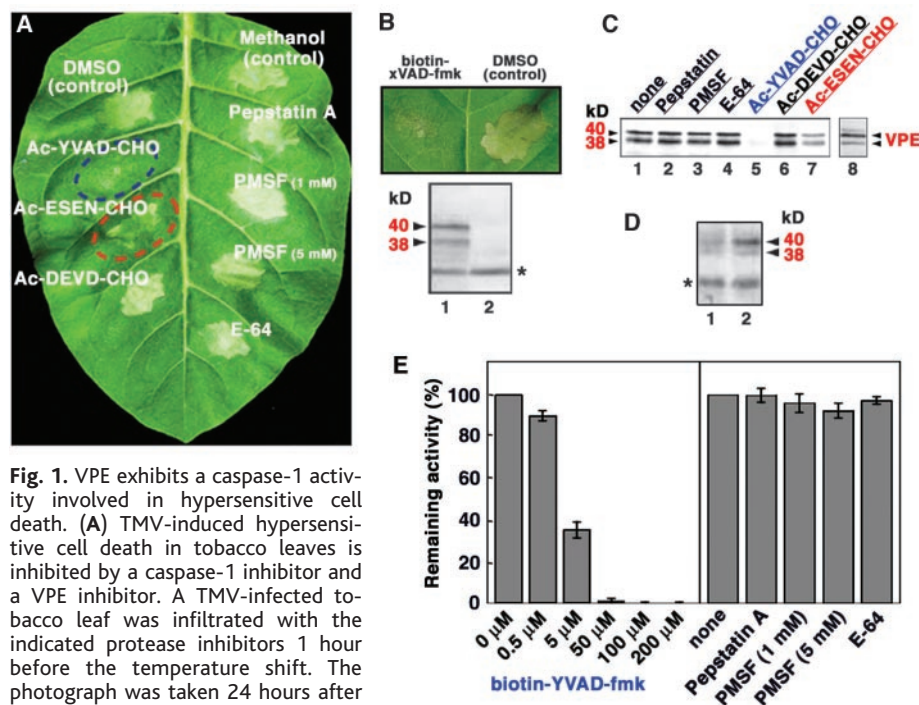
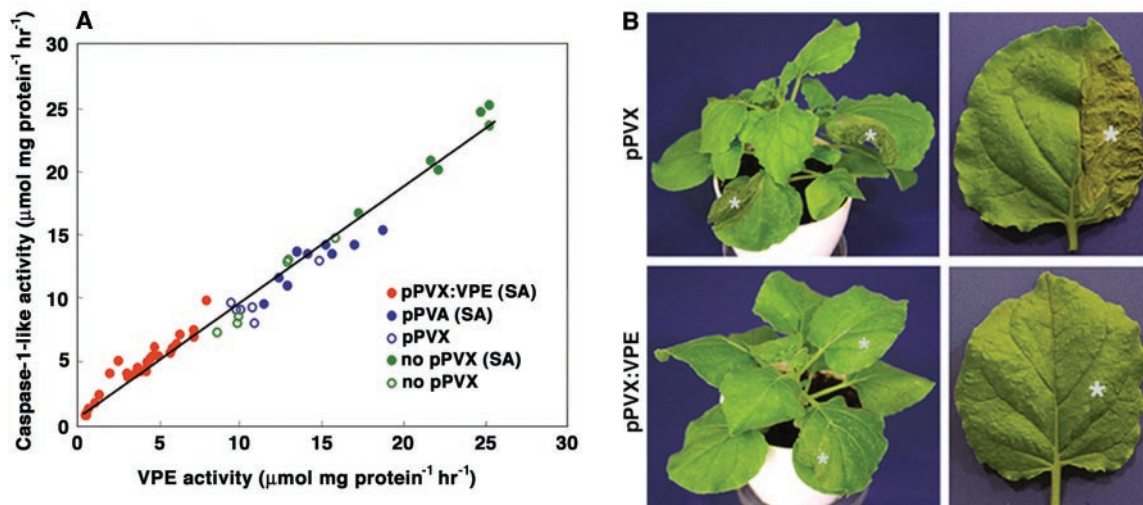


**Fig. 1.** VPE exhibits a caspase-1 activity involved in hypersensitive cell death. (A) TMV-induced hypersensitive cell death in tobacco leaves is inhibited by a caspase-1 inhibitor and a VPE inhibitor. A TMV-infected tobacco leaf was infiltrated with the indicated protease inhibitors 1 hour before the temperature shift. The photograph was taken 24 hours after the temperature shift. (B) Top: A TMV-infected leaf infiltrated with or without biotin-xVAD-fmk. Bottom: A biotinylated-inhibitor blot of the biotin-xVAD-fmk-infiltrated leaves (lane 1) and control leaves (lane 2). An asterisk indicates nonspecific signals. (C) A biotinylated-inhibitor blot of the TMV-infected leaves that were pre-incubated with each protease inhibitor before further incubation with biotin-xVAD-fmk (lanes 1 to 7) and an immunoblot of the leaf extracts with antibodies to VPE (lane 8). (D) A biotinylated-inhibitor blot of the leaf extract after immunodepletion with antibodies to VPE (lane 1) or with preimmune serum (lane 2). An asterisk indicates nonspecific signals. (E) Effects of various inhibitors on VPE activity in TMV-infected leaves 3 hours after the temperature shift. Each experiment was repeated three times, and vertical bars represent standard error. DMSO, dimethylsulfoxide; Ac-YVAD-CHO, a caspase-1 inhibitor; Ac-ESEN-CHO, a VPE inhibitor; Ac-DEVD-CHO, a caspase-3 inhibitor; Pepstatin A, an aspartic protease inhibitor; PMSF, a serine protease inhibitor; E-64, a papain-type-protease inhibitor.

<sup>1</sup>Graduate School of Science, Kyoto University, Sakyo-ku, Kyoto 606-8502, Japan. <sup>2</sup>Department of Cell Biology, National Institute for Basic Biology, Okazaki 444-8585, Japan. <sup>3</sup>School of Life Science, Graduate University for Advanced Studies, Okazaki 444-8585, Japan. <sup>4</sup>National Institute of Agrobiological Sciences, Tsukuba 305-8602, Japan. <sup>5</sup>National Agricultural Research Center, Tsukuba 305-8666, Japan.

\*To whom correspondence should be addressed. E-mail: ihnishi@gr.bot.kyoto-u.ac.jp

**Fig. 2.** *VPE* deficiency suppresses TMV-induced hypersensitive cell death. (A) Both *VPE* and caspase-1 activities were measured in the leaves that had been treated with (closed circles) or without (open circles) salicylic acid (SA) for 24 hours, in the *VPE*-silenced plants (pPVX:VPE, red) and in non-silenced plants including pPVX-inoculated (pPVX, blue) and non-inoculated (no pPVX, green) plants. (B) Non-silenced (pPVX) and *VPE*-silenced (pPVX:VPE) *N. benthamiana* plants were infected with TMV on halves of their leaves (indicated by asterisks). The photographs of the plants (left) and the leaves (right) were taken 24 hours after the temperature shift.



conjugated horseradish peroxidase. Like Ac-YVAD-CHO, biotin-xVAD-fmk strongly inhibited lesion formation (Fig. 1B, top). Two bands of 40 and 38 kD were detected specifically on the blot of the extract from the biotin-xVAD-fmk-infiltrated leaves (Fig. 1B, bottom). We examined the competitive effects of various inhibitors on in vitro formation of the enzyme-inhibitor complex with the TMV-infected leaf extracts. When Ac-YVAD-CHO was added as a competitor with biotin-xVAD-fmk, the 40- and 38-kD bands completely disappeared on the blot (Fig. 1C, lane 5). Their signal intensities were reduced with Ac-ESEN-CHO (Fig. 1C, lane 7). On the other hand, the 40- and 38-kD proteins were detected on an immunoblot of the TMV-infected leaves with antibodies to VPE (Fig. 1C, lane 8), which corresponded to the intermediate and mature forms of VPE, respectively (15, 16). The immunodepleted extract from the TMV-infected leaf with antibodies to VPE reduced the signal intensities of both the 40- and 38-kD bands on the in vitro biotinylated-inhibitor blot analysis (Fig. 1D), suggesting that the immunodepletion reduced the level of the active enzyme exhibiting caspase-1 activity. These results imply that the proteases that exhibited the caspase-1 activity in the TMV-infected leaves are both forms of VPE. VPE activity was detected in TMV-infected leaves in vitro (Fig. 1E). Biotin-YVAD-fmk completely inhibited the VPE activity at a concentration of 50  $\mu\text{M}$  and reduced it by 64% at a concentration of 5  $\mu\text{M}$  (Fig. 1E, left). The concentration of the inhibitor was comparable to the concentrations necessary to inhibit the authentic human caspase-1. Other inhibitors had no effect on the VPE activity (Fig. 1E, right). These results imply that the abolishment of lesion formation by the VPE and caspase-1 inhibitors was caused by the inhibition of VPE.

For an in planta analysis, we isolated two *VPE* homologs of *Nicotiana benthamiana* [*NbVPE-1a* (AB181187) and *NbVPE-1b* (AB181188)], which correspond to the most abundant *VPEs* in *N. tabacum* (*NtVPE-1a* and *NtVPE-1b*) from the TMV-infected leaves. We used the cDNAs for virus-induced gene silencing (VIGS) with a potato virus X vector (pPVX) to silence *VPE* genes in *N. benthamiana*, a species well-suited for VIGS (17). The expression of major *VPEs* was suppressed in four independent *VPE*-silenced plants that we generated (supporting online text and fig. S2). We measured the VPE activity on Ac-ESEN-MCA in the *VPE*-silenced and non-silenced leaves that had been treated with or without salicylic acid (Fig. 2A). VPE activity was reduced in all four independent *VPE*-silenced plants. These results revealed that the VIGS, which was caused by four independent sequences derived from *NbVPEs*, abolished both VPE expression and activity, indicating that the specificity to VPE was high in the VIGS. Each circle in Fig. 2A represents the VPE and caspase-1 activities in each of the *VPE*-silenced and non-silenced plants. The level of VPE activity completely paralleled that of the caspase-1 activity in each plant (Fig. 2A). This result and the immunodepletion analysis of VPE (Fig. 1D) show that VPE is the protease with caspase-1 activity. This was in agreement with our previous result that plant *VPEs* cleave a peptide bond at the C-terminal sides of not only asparagine residues but also aspartic acid residues (15, 18–20).

To determine how *VPE* deficiency affects hypersensitive cell death, both the *VPE*-silenced and non-silenced plants were infected with TMV on different halves of their leaves. The non-silenced plants formed typical visible lesions in the TMV-infected regions of the leaves 24 hours after the temperature shift (Fig. 2B, pPVX, indicated by asterisks). However,

the *VPE*-silenced plants formed no visible lesions in the TMV-infected regions (Fig. 2B, pPVX:VPE, indicated by asterisks). The *VPE* deficiency suppressed the hypersensitive cell death in response to TMV infection.

It has been shown that disintegration of the vacuolar membranes is the crucial event in plant cell death (21). For an ultrastructural analysis of the *VPE*-silenced and non-silenced *N. benthamiana* plants, we examined the TMV-infected leaves 0, 9, and 24 hours after the temperature shift (Fig. 3, A to G). This was because *N. benthamiana* leaves started to form lesions at 12 hours, which was later than for *N. tabacum* leaves. The vacuolar membranes were partially disintegrated in the leaves at 9 hours (Fig. 3, C to E), indicating that the disintegration of the vacuolar membranes occurred in the leaves before visible lesions were formed. The disintegration of the vacuolar membranes continued, resulting in complete vacuolar collapse in association with plasmolysis, and finally the cytoplasmic aggregations were left within the cells (Fig. 3B). However, in the *VPE*-silenced plants, the vacuoles and vacuolar membranes remained intact, even 24 hours after the temperature shift, and no morphological differences except for chloroplasts were found in the leaves before and after the temperature shift (Fig. 3, F and G). Chloroplasts accumulated starch granules in both the silenced and non-silenced leaves at 24 hours (Fig. 3, B and G).

To investigate vacuolar collapse during hypersensitive cell death, we infiltrated 2', 7'-bis-(2-carboxyethyl)-5(6)carboxyfluorescein acetoxymethyl ester (BCECF-AM) into TMV-infected leaves and then prepared protoplasts from the leaves 0, 9, and 12 hours after the temperature shift. We subjected the protoplasts to a diagnosis of vacuolar membrane disintegration with BCECF fluorescence and to a viability assay with trypan blue. Protoplasts that were prepared at 0 hours accumulated BCECF



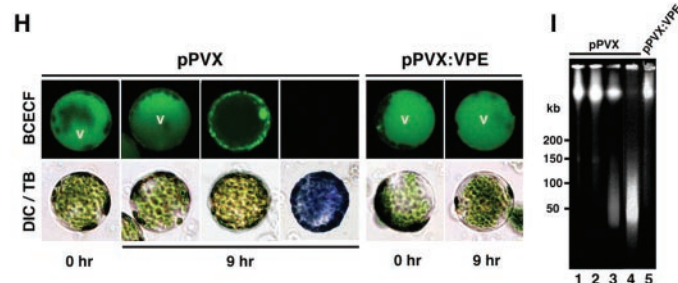
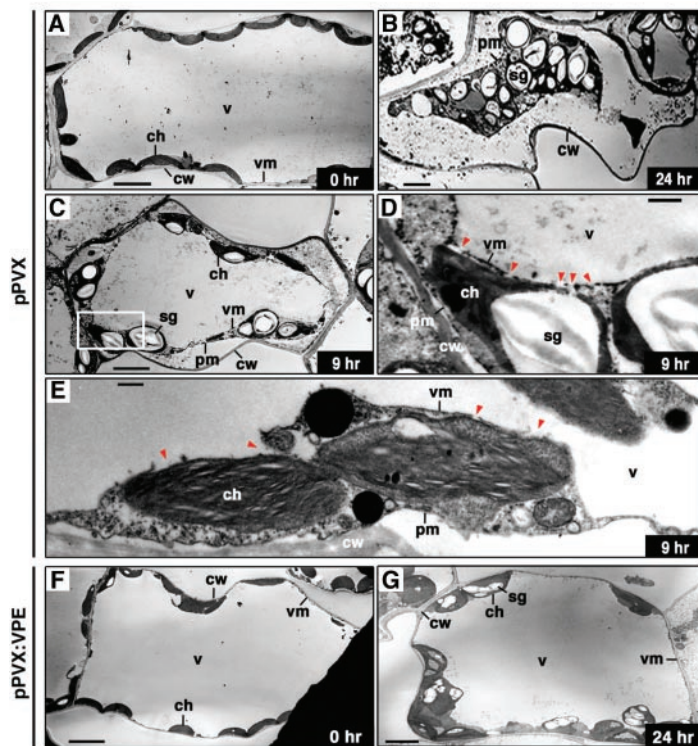


**Fig. 3.** *VPE* deficiency suppresses vacuolar collapse leading to TMV-induced hypersensitive cell death. (A to G) Morphological changes in the TMV-infected regions of the non-silenced leaves (pPVX) at (A) 0, [(C) to (E)] 9, and (B) 24 hours after the temperature shift, and of the *VPE*-silenced leaves (pPVX:VPE) at (F) 0 and (G) 24 hours, under the electron microscope. (D) A higher magnification view of the boxed area in (C). Scale bars, 5  $\mu$ m for (A) to (C), (F), and (G), and 1  $\mu$ m for (D) and (E). cw, cell wall; pm, plasma membrane; vm, vacuolar membrane; v, vacuole; ch, chloroplast; sg, starch granule. Red triangles indicate the disintegrated parts of vacuolar membranes. (H) The TMV-infected leaves of the non-silenced (pPVX) and *VPE*-silenced (pPVX:VPE) plants were infiltrated with the vital dye BCECF-AM. Protoplasts were prepared from the leaves at 0 and 9 hours after the temperature shift and then stained with trypan blue. The BCECF fluorescent images (BCECF) and differential interference contrast images after staining with trypan blue (DIC/TB) of the protoplasts were inspected. v, vacuole. (I) Pulsed-field gel electrophoresis of total DNA from TMV-infected leaves of the non-silenced plants at 0 (lane 1), 9 (lane 2), 12 (lane 3), and 24 (lane 4) hours after the temperature shift and of *VPE*-silenced plants at 24 hours (lane 5).

only in the vacuoles (Fig. 3H, pPVX, 0 hours). Protoplasts ( $n > 100$ ) that were prepared at 9 hours were separated into three staining types (Fig. 3H, pPVX): (I) BCECF-positive and trypan blue-negative (~70% of the protoplasts), (II) BCECF-negative and trypan blue-negative (~20%), and (III) BCECF-negative and trypan blue-positive (~10%). The staining indicates that type I protoplasts were alive and had intact vacuoles. Type II protoplasts were also alive even though the vacuolar membranes had disintegrated (as shown by distribution of BCECF throughout the cell and in the periphery regions inside the cells). Type III protoplasts were dead. At 12 hours after the temperature shift, the number of dead protoplasts in the population was greater (22). The finding that many of the protoplasts with degraded vacuolar membranes were alive suggests that cell death is preceded by vacuolar collapse. All protoplasts from the *VPE*-silenced leaves were alive and accumulated BCECF in the vacuoles at 9 hours (Fig. 3H, pPVX:VPE) and even at 12 hours (22), which indicates the integrity of the vacuoles in the silenced plants. *VPE* deficiency suppressed the disintegration of the vacuolar membranes in the TMV-infected leaves. These results suggest that *VPE* is involved in vacuolar collapse, which triggers hypersensitive cell death.

Plant PCDs are reported to be accompanied by DNA fragmentation (23, 24). Similarly, cleavage of nuclear DNA into ~50-kb fragments was detected in the TMV-infected leaves at 12 hours after the temperature shift, and the fragmentation was completed at 24 hours (Fig. 3I, pPVX). In contrast, such fragmentation was

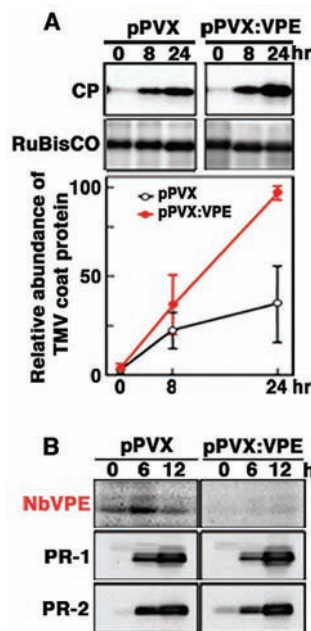


**Fig. 4.** *VPE* deficiency affects virus proliferation, although it does not affect the production of the PR proteins. (A) An immunoblot showing change in the protein levels of TMV coat protein (CP) in TMV-infected leaves of the non-silenced (pPVX) and *VPE*-silenced (pPVX:VPE) plants after the temperature shift (top). RuBisCO is a loading control of the immunoblot. The protein levels were densitometrically determined (bottom). Each experiment with a control was repeated with three independent samples, and vertical bars represent standard error. The relative abundance is given as a percentage of the maximum value. (B) Immunoblots showing changes in the protein levels of NbVPE, PR-1, and PR-2 in TMV-infected leaves of the non-silenced (pPVX) and *VPE*-silenced (pPVX:VPE) plants after the temperature shift.

completely suppressed in the *VPE*-silenced plants (Fig. 3I, pPVX:VPE). Vacuolar nucleases have been shown to be induced during plant PCD (21). *VPE*-mediated vacuolar collapse might be involved in the nuclear DNA fragmentation that occurs during hypersensitive cell death.

An immunoblot analysis with antibodies to TMV coat protein (Fig. 4A) showed that the virus was produced more abundantly in the *VPE*-silenced plants, which formed no visible lesions, than in the non-silenced plants. We densitometrically determined the levels of the

coat protein and ribulose-1,5-biphosphate carboxylase-oxygenase (RuBisCO) in three independent experiments (Fig. 4A, bottom). The level of RuBisCO as a loading control was fixed with less than 7% of error. The virus level in the *VPE*-silenced leaves increased for 24 hours after the temperature shift. In contrast, increase in the virus level in non-silenced leaves was suppressed after 8 hours. The virus level in the *VPE*-silenced leaves at 24 hours was definitely more than that in non-silenced leaves. Therefore, *VPE*

was involved in suppression of virus production during the HR. On the other hand, induction of pathogenesis-related (PR) proteins, PR-1 and PR-2, continued after the temperature shift in the VPE-silenced leaves as in the non-silenced plants (Fig. 4B). The VPE deficiency did not affect the production of the PR proteins, although it affected TMV-induced cell death. These results suggest that PCD and defense-protein induction are not coupled during the HR and that the HR is composed of two independent processes, PCD and defense-protein induction. VPE regulates PCD but not defense-protein induction. There has been a lot of discussion about whether PCD during the HR is really critical for resistance (25). Our results suggest that PCD contributes to resistance to a virus infection.

Although the *Arabidopsis* genome does not have a caspase family, it has a metacaspase family, which is distantly related to the caspase family. A metacaspase was reported to be involved in the cell death of yeast (26). The gene expression of metacaspase was found in pathogen-infected tomato leaves (27), and a proteolytic activity toward Ac-VEID-MCA (a metacaspase/caspase-6 substrate) was detected in dying suspensor cells of Norway spruce (28). Metacaspases might function in the cytosol during cell death as animal caspases. This is in contrast to the VPE functions in vacuole-mediated cell death. VPE is structurally unrelated to the caspase family, although it has caspase-1 activity and an ability to bind caspase-1 inhibitor.

In animals, dying cells are engulfed by phagocytes. However, in plants, which do not have phagocytes, cells surrounded by rigid cell walls must degrade their materials by themselves. Vacuolar collapse has been shown to trigger degradation of the cytoplasmic structures and lead to cell death (21), although its molecular mechanism is not known. Our findings suggest that VPE functions as a key player in vacuolar collapse-triggered cell death. VPEs are distributed in mono- and dicotyledonous plants. *Arabidopsis* VPE genes are up-regulated in dying cells during development and senescence of tissues (5, 13). Thus, VPE might regulate various types of PCD in higher plants. Identification of the VPE-target proteins, which are possibly associated with the vacuolar membranes, would help to unravel the molecular mechanism of VPE-mediated vacuolar collapse underlying plant PCD. Because VPE acts as a processing enzyme to activate various vacuolar proteins, it might also convert the inactive hydrolytic enzymes to the active forms, which are involved in the disintegration of vacuoles, to initiate the proteolytic cascade in plant PCD. Understanding the VPE-regulated mechanism, which operates in the early process of the HR, may also lead to practical applications for strengthening disease resistance in crops.

References and Notes

1. G. M. Cohen, *Biochem. J.* **326**, 1 (1997).
2. E. Lam, O. del Pozo, *Plant Mol. Biol.* **44**, 417 (2000).
3. E. Lam, N. Kato, M. Lawton, *Nature* **411**, 848 (2001).
4. E. J. Woltering, A. van der Bent, F. A. Hoeberichts, *Plant Physiol.* **130**, 1764 (2002).
5. I. Hara-Nishimura, M. Maeshima, in *Vacuolar Compartments in Plants*, A. D. G. Robinson, J. C. Rogers, Eds. (Sheffield, London, 2000), pp. 20–42.
6. J. T. Greenberg, *Annu. Rev. Plant Physiol. Plant Mol. Biol.* **48**, 525 (1997).
7. I. Hara-Nishimura, K. Inoue, M. Nishimura, *FEBS Lett.* **294**, 89 (1991).
8. I. Hara-Nishimura, Y. Takeuchi, M. Nishimura, *Plant Cell* **5**, 1651 (1993).
9. K. Yamada, T. Shimada, M. Kondo, M. Nishimura, I. Hara-Nishimura, *J. Biol. Chem.* **274**, 2563 (1999).
10. N. Mitsuhashi et al., *Plant Cell* **13**, 2361 (2001).
11. T. Shimada et al., *J. Biol. Chem.* **278**, 32292 (2003).
12. K. Shirahama-Noda et al., *J. Biol. Chem.* **278**, 33194 (2003).
13. T. Kinoshita, K. Yamada, N. Hiraiwa, M. Nishimura, I. Hara-Nishimura, *Plant J.* **19**, 43 (1999).
14. R. N. Goodman, A. J. Novacky, *The Hypersensitive Response Reaction in Plants to Pathogens: A Resistance Phenomenon* (American Phytopathological Society Press, St. Paul, MN, 1994).
15. N. Hiraiwa, M. Nishimura, I. Hara-Nishimura, *FEBS Lett.* **447**, 213 (1999).
16. M. Kuroyanagi, M. Nishimura, I. Hara-Nishimura, *Plant Cell Physiol.* **43**, 143 (2002).
17. S. M. Angell, D. C. Baulcombe, *Plant J.* **20**, 357 (1999).
18. I. Hara-Nishimura, in *Handbook of Proteolytic Enzymes*, A. J. Barrett, N. D. Rawlings, J. F. Woessner, Eds. (Academic Press, London, 1998), pp. 746–749.

19. I. Hara-Nishimura, T. Kinoshita, N. Hiraiwa, M. Nishimura, *J. Plant Physiol.* **152**, 668 (1998).
20. C. Becker et al., *Eur. J. Biochem.* **228**, 456 (1995).
21. A. M. Jones, *Plant Physiol.* **125**, 94 (2001).
22. N. Hatsugai et al., unpublished data.
23. R. Mittler, L. Simon, E. Lam, *J. Cell Sci.* **110**, 1333 (1997).
24. A. Levine, R. I. Pennell, M. E. Alvarez, R. Palmer, C. Lamb, *Curr. Biol.* **6**, 427 (1996).
25. J. T. Greenberg, N. Yao, *Cell. Microbiol.* **6**, 201 (2004).
26. F. Madeo et al., *Mol. Cell* **9**, 911 (2002).
27. F. A. Hoeberichts, A. ten Have, E. J. Woltering, *Planta* **217**, 517 (2003).
28. P. V. Bozhkov et al., *Cell Death Differ.* **11**, 175 (2004).
29. We thank B. Baker (University of California and USDA–Agriculture Research Service) for donating a binary vector with the TMV resistance gene *N*, D. C. Baulcombe (John Innes Centre, UK) for donating a *Potato virus X* vector (pgR107), and T. Kobayashi (National Institute for Basic Biology, Japan) for his help on pulsed-field gel electrophoresis. Supported by Core Research for Evolutional Science and Technology (CREST) of the Japan Science and Technology Corporation, and by Grants-in-Aid for Scientific Research (no. 12138205) and for 21st Century Center of Excellence Research, Kyoto University (A14), from the Ministry of Education, Culture, Sports, Science and Technology of Japan.

**Supporting Online Material**  
[www.sciencemag.org/cgi/content/full/305/5685/855/DC1](http://www.sciencemag.org/cgi/content/full/305/5685/855/DC1)  
 Materials and Methods  
 SOM Text  
 Figs. S1 and S2  
 References and Notes

3 May 2004; accepted 9 July 2004

## Structural Basis of Mitochondrial Tethering by Mitofusin Complexes

Takumi Koshiba,<sup>1</sup> Scott A. Detmer,<sup>1</sup> Jens T. Kaiser,<sup>2,3</sup> Hsiuchen Chen,<sup>1</sup> J. Michael McCaffery,<sup>4</sup> David C. Chan<sup>1\*</sup>

Vesicle fusion involves vesicle tethering, docking, and membrane merger. We show that mitofusin, an integral mitochondrial membrane protein, is required on adjacent mitochondria to mediate fusion, which indicates that mitofusin complexes act in trans (that is, between adjacent mitochondria). A heptad repeat region (HR2) mediates mitofusin oligomerization by assembling a dimeric, antiparallel coiled coil. The transmembrane segments are located at opposite ends of the 95 angstrom coiled coil and provide a mechanism for organelle tethering. Consistent with this proposal, truncated mitofusin, in an HR2-dependent manner, causes mitochondria to become apposed with a uniform gap. Our results suggest that HR2 functions as a mitochondrial tether before fusion.

Diverse membrane trafficking systems—including endoplasmic reticulum-to-Golgi transport, endosome fusion, Golgi-to-Golgi fusion, and synaptic vesicle fusion—use a common set of steps to mediate the targeting and fusion of intracellular vesicles to acceptor target membranes (1, 2). First, a vesicle

becomes “tethered” to its target membrane, although the two membranes remain separated by a considerable gap. This step is often mediated by the binding of activated Rab guanosine triphosphatases (GTPases) on the vesicle surface to effectors on the target membrane (3). Second, a SNARE (soluble *N*-ethylmaleimide-sensitive factor attachment protein receptor) protein on the tethered vesicle surface forms a complex with SNAREs on the target membrane; this leads to closer apposition of membranes, a state termed “docking.” Finally, the two bilayers fuse, probably because of the close proximity produced by SNARE complex

<sup>1</sup>Division of Biology, <sup>2</sup>Division of Chemistry, California Institute of Technology, 1200 East California Boulevard, MC114-96, Pasadena, CA 91125, USA. <sup>3</sup>Howard Hughes Medical Institute. <sup>4</sup>Integrated Imaging Center, Department of Biology, Johns Hopkins University, 3400 North Charles Street, Baltimore, MD 21218, USA.

\*To whom correspondence should be addressed. E-mail: dchan@caltech.edu



formation. Although much progress has been made in understanding the structural basis of docking and fusion by SNARE complexes (4, 5), less is understood about tethering, because of difficulty in obtaining structures of the large heterotypic protein complexes involved.

Mitochondria are dynamic organelles that undergo continual cycles of fusion and fis-

sion, opposing processes that control the overall morphology of the mitochondrial population (6–8). Reduced mitochondrial fusion causes greater autonomy for individual organelles in the mitochondrial population, a state that increases heterogeneity among organelles and results in dysfunction (9). Mitochondrial fusion is controlled by members of

the *fuzzy onions* (Fzo)/mitofusins (Mfn) family of large GTPases that are localized to the mitochondrial outer membrane (10). Mammals have two mitofusins, Mfn1 and Mfn2 (9, 11–14), that control mitochondrial fusion and are required for embryonic development (9). Mutations in *Mfn2* are responsible for most cases of Charcot-

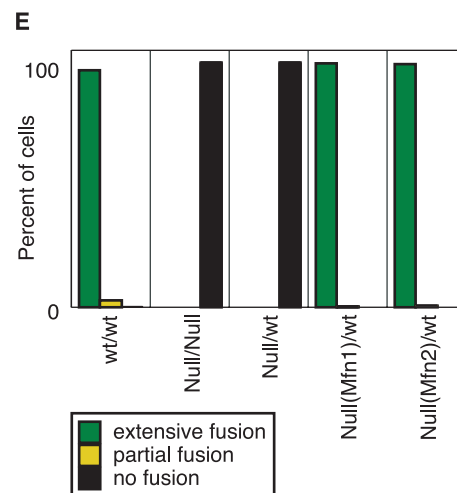
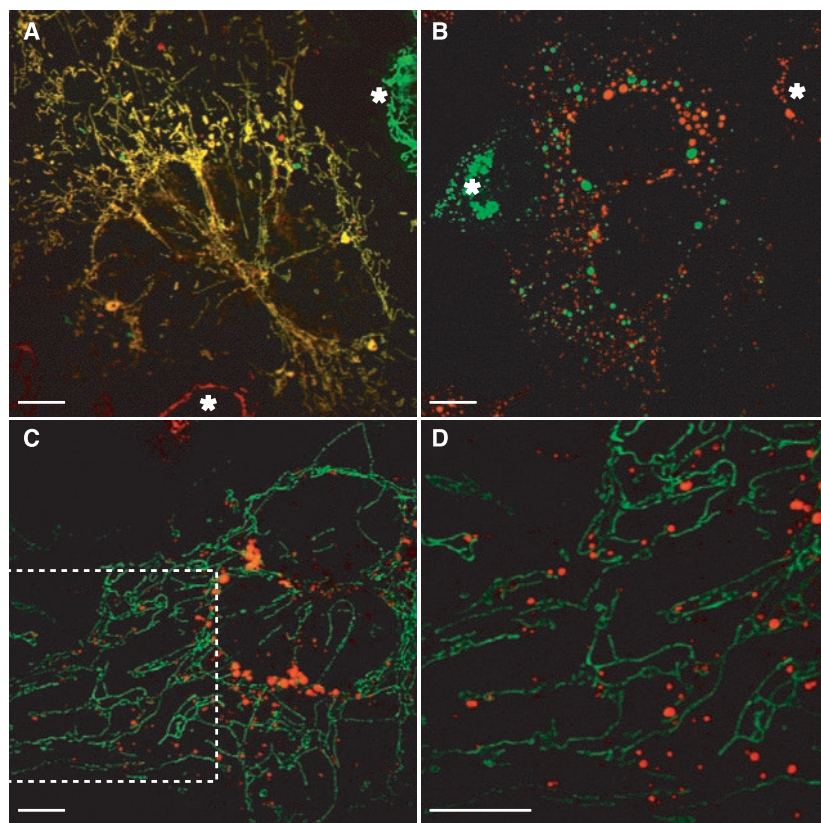


**Fig. 1.** Mitofusins are required on adjacent mitochondria. PEG-induced hybrids were generated between cells with GFP- and DsRed-labeled mitochondria. Representative cell hybrids are shown between (A) wild-type versus wild-type cells, (B) Mfn-null versus Mfn-null cells, and (C) wild-type (green mitochondria) versus Mfn-null (red) cells. (D) The boxed area in (C) magnified. Asterisks in (A) and (B) indicate unfused adjacent cells. Scale bar, 10  $\mu$ m. (E) Quantification of mitochondrial fusion in cell hybrids. The pairs of cell lines fused are indicated at the bottom. In each cell fusion experiment, at least 250 cell hybrids were scored for mitochondrial fusion. Null(Mfn), Mfn-null cells expressing an Mfn construct.

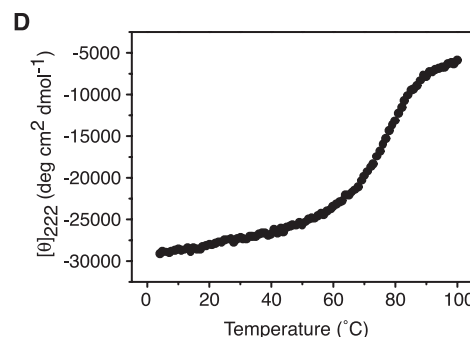
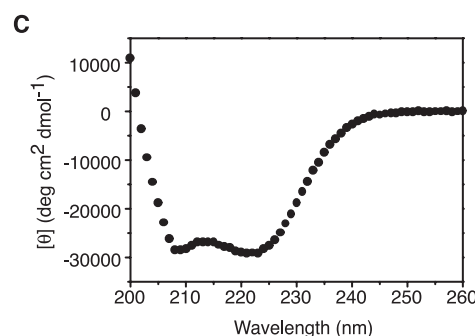
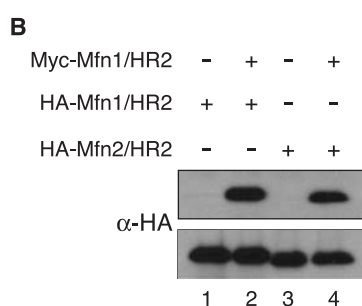
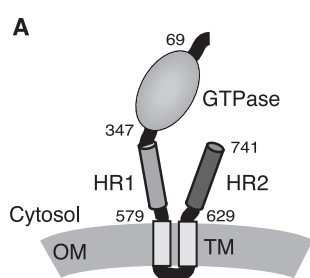


**Fig. 2.** The HR2 region of Mfn1 assembles into a helical, oligomeric complex. (A) Schematic of the Mfn1 molecule in the mitochondrial outer membrane, based on topology mapping studies (12). The GTPase domain, hydrophobic heptad repeats (HR), and transmembrane segments (TM) are shown. OM, mitochondrial outer membrane. (B) The HR2 domain of Mfn1 forms both homotypic (lane 2) and heterotypic (lane 4) complexes. Cell lysates were prepared from 293T cells expressing combinations of Myc- and hemagglutinin (HA)-tagged Mfn1/HR2 or Mfn2/HR2, as indicated. Western blots of Myc antibody-specific immunoprecipitates (top) or post-nuclear cell lysates (bottom) were probed with a monoclonal antibody against HA. (C) CD wavelength scan and (D) thermal denaturation profile of Mfn1/HR2<sub>660-735</sub>.

## REPORTS

Marie-Tooth type 2A disease, an inherited peripheral neuropathy (15). In spite of these insights, it is not known whether mitofusins directly mediate fusion and whether this process proceeds through the canonical steps of tethering, docking, and fusion.

To address this issue, we examined whether mitofusins are required on adjacent mitochondria during homotypic membrane fusion. Mitochondrial fusion in mammalian cells can be measured *in vivo* by using polyethylene glycol (PEG) to generate cell hybrids between cell lines with differentially marked mitochondria (16). When wild-type mouse embryonic fibroblasts with either mitochondrially targeted green fluorescent protein (GFP) or DsRed are fused in this manner, the vast majority of cell hybrids (97%) show extensively fused mitochondria by 7 hours (Fig. 1, A and E). We next tested fibroblasts containing targeted deletions in both *Mfn1* and *Mfn2*. Such *Mfn*-null cells

have completely fragmented mitochondria and show no detectable mitochondrial fusion (Fig. 1, B and E). In contrast, cells null for only *Mfn1* or *Mfn2* contain low but readily measured rates of fusion, with many hybrids showing partially fused mitochondrial populations (9). These results indicate that mitofusins are absolutely required for mitochondrial fusion. Most important, cell hybrids between *Mfn*-null cells and wild-type cells show no detectable mitochondrial fusion (Fig. 1, C to E). In such hybrids, the mitochondria derived from wild-type cells remain elongated tubules, clearly distinct from the spherical mitochondria derived from mutant cells. Reintroduction of either *Mfn1* or *Mfn2* into *Mfn*-null cells fully rescues mitochondrial fusion in cell hybrids with wild-type cells (Fig. 1E). These observations indicate that mitochondrial fusion requires mitofusins on adjacent mitochondria. Because these outer membrane proteins form both homotypic and

heterotypic complexes (9), the most likely explanation is that fusion requires mitofusin complexes acting in trans (that is, between adjacent mitochondria) (17–19).

We therefore attempted to identify domains of mitofusin that might mediate oligomerization. Both *Mfn1* and *Mfn2* contain two 4,3 hydrophobic heptad repeats (HR1 and HR2) that flank the bipartite transmembrane segment (Fig. 2A). Heptad repeats play central roles in membrane fusion mediated by SNARE proteins and many viral envelope glycoproteins (1, 20). Using immunoprecipitation, we found that isolated HR2 fragments expressed in 293T cells form stable complexes (Fig. 2B). *Mfn1*/HR2 forms stable complexes with itself, as well as with *Mfn2*/HR2. Therefore, the HR2 region can form homotypic and heterotypic complexes, which parallel the behavior of full-length *Mfn1* and *Mfn2* (9).

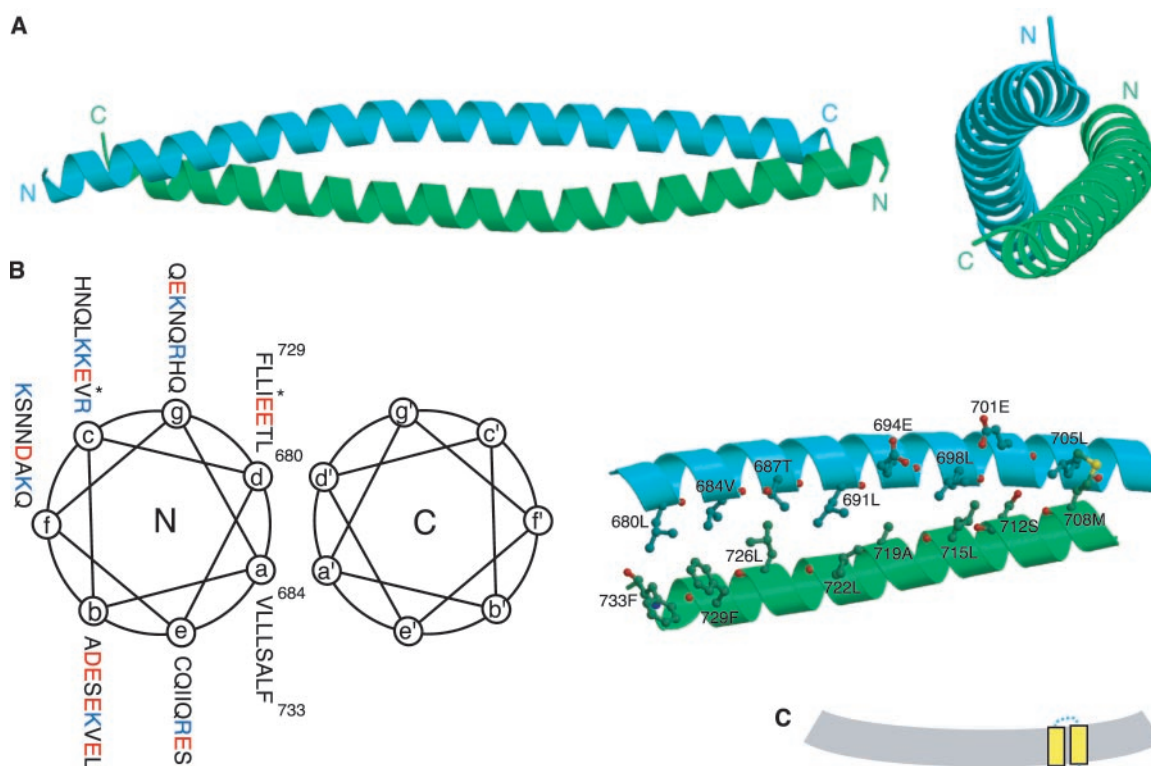


**Fig. 3.** Crystal structure of *Mfn1*/HR2 at 2.5 Å resolution. **(A)** Overall structure of *Mfn1*/HR2<sub>660-735</sub>. The left panel shows a side view of the dimeric, antiparallel coiled coil with the N and C termini labeled. The right panel shows an end-on view looking down the two-fold axis of the dimer. The first 14 residues were disordered; the figures depict residues 674 to 735. **(B)** Residues are projected onto helical wheels (left panel), and the *a* to *d'* layers in half of the symmetry-related interface are shown (right panel). Two residues were mutated to methionine to enable MAD phasing, as indicated (\*). In the left panel, positively and negatively charged residues are shown in blue and red, respectively. **(C)** Model of the HR2 domain in a trans-*Mfn1* complex in the mitochondrial outer membrane (OM). Formation of the HR2 antiparallel coiled coil would result in tethering of adjacent mitochondria. For simplicity, the GTPase and HR1 domains are not shown.



We investigated the biophysical properties of the Mfn1/HR2 region. Recombinant Mfn1/HR2 was subjected to limited proteolysis with a panel of proteases to yield a slightly smaller, stable domain (residues 660 to 735) that corresponded well with the predicted heptad repeat (fig. S1, A and B). The resulting fragment, Mfn1/HR2<sub>660-735</sub>, retains self-association in an immunoprecipitation assay (fig. S1C). Mfn1/HR2<sub>660-735</sub> appears to be well folded, because circular dichroism (CD) analysis indicates that it is highly helical (77%) and unfolds cooperatively, with a thermal transition midpoint of 78°C (Fig. 2, C and D).

We obtained crystals of Mfn1/HR2<sub>660-735</sub> and solved its atomic structure at 2.5 Å by multi-wavelength anomalous diffraction (MAD) analysis of a selenomethionine-substituted crystal

(table S1 and fig. S2). The HR2 polypeptide folds into a dimeric antiparallel coiled coil that is 95 Å long (Fig. 3A). Each of the two helices can be depicted in a helical wheel diagram (Fig. 3B), from which it can be readily observed that the *a* and *d* residues of the heptad repeat constitute a predominantly hydrophobic interaction interface. Complex formation involves typical “knobs-in-holes” packing, buries 2850 Å<sup>2</sup> of surface area, and results in a highly charged surface (fig. S3A).

An interesting feature of this coiled coil is the presence of two glutamic acids at consecutive *d* positions (Glu<sup>694</sup> and Glu<sup>701</sup>). These two charged residues may be important in specifying the antiparallel orientation of the HR2 coiled coil. In fact, the addition of a charged residue in the *d* position has been used as part of a design strategy to construct

artificial coiled coils with a strong tendency for the antiparallel orientation (21, 22). Among mitofusin homologs, these *d* positions contain either charged or polar residues (fig. S3B). Substitution of these positions with leucines reduces the ability of Mfn1 to restore tubular mitochondrial morphology in Mfn-null cells (fig. S4).

To test whether the HR2 coiled coil is essential for mitofusin function, we designed mutations expected to disrupt its structure. We introduced proline substitutions into recombinant Mfn1/HR2<sub>660-735</sub> at positions 691 and 705. CD, gel filtration, and immunoprecipitation analysis indicate that both mutations significantly reduce the stability of the HR2 coiled coil, with the proline replacement of leucine at residue 705 (L705P) much more severe than L691P (fig. S5). We studied the effects of these mutations on the ability of Mfn1 to restore mitochondrial tubules to Mfn-null cells. Expression of wild-type Mfn1 fully rescues the fragmented mitochondria of Mfn-null cells (Fig. 4A). Mfn1(L691P) can restore a subset of the mitochondrial population to tubules, but almost no cells show the fully tubular mitochondrial morphology observed with wild-type Mfn1. This result is consistent with the moderate effect of this mutation on the biophysical properties of Mfn1/HR2<sub>660-735</sub> (fig. S5). In contrast, the L705P mutant has little activity in vivo (Fig. 4A). Corresponding defects in mitochondrial fusion activity were observed using the PEG cell hybrid assay (Fig. 4B). Both mutants retain predominantly mitochondrial localization (fig. S6). These results indicate that the HR2 coiled coil is essential for the mitochondrial fusion activity of Mfn1.

Because of the antiparallel orientation of the HR2 coiled coil, a remarkable consequence is that the membrane-anchoring segments of mitofusin dimers would be located at opposite ends of the 95 Å coiled coil (Fig. 3C). In addition, there are more than 40 residues between each transmembrane anchor and the beginning of the coiled coil. In a trans complex of mitofusin dimers, this coiled coil would lock two mitochondria together but would likely leave a significant gap between the opposing outer membranes. It is not possible to predict precisely the dimensions of such a gap, because it would depend on the angle of the coiled coil in relation to the opposing bilayers.

In the course of examining the role of the GTPase domain of Mfn1, we found that amino terminal truncations that remove the GTPase domain result in extensive aggregation of mitochondria when expressed in NIH 3T3 cells (Fig. 4, C and D). Some constructs of human Mfn1 also cause mitochondrial aggregation (14), although it is unclear whether that effect is related to the results described here. The aggregation by truncated Mfn1 (residues 331 to 741)

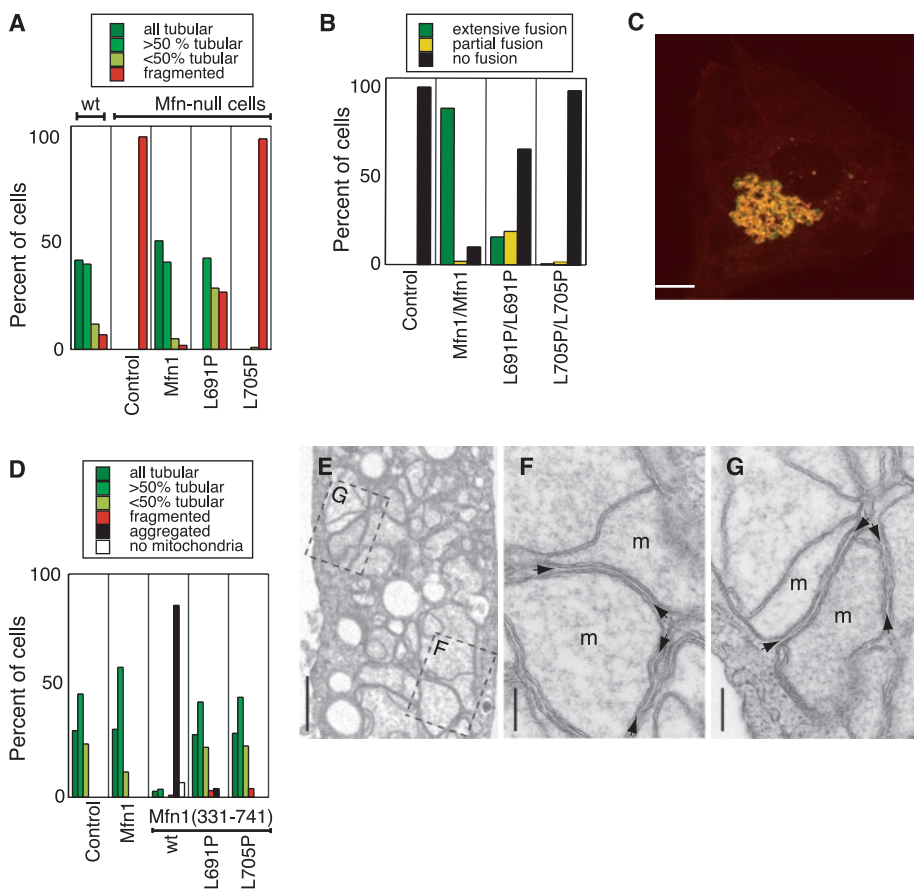


**Fig. 4.** Disruption of HR2 structure abolishes mitochondrial fusion by Mfn1 and mitochondrial tethering by truncated Mfn1. (A) Mitochondrial morphologies in Mfn-null mouse embryo fibroblasts (MEFs) infected with retrovirus expressing Myc-tagged Mfn1 mutants. (Left) For comparison, data from a wild-type cell line are also presented. Mitochondrial morphology is scored by mitochondrially targeted GFP, and infected cells were identified by immunofluorescence against the Myc tag. Control, empty retrovirus. (B) PEG fusion assay of Mfn1 mutants. Wild-type or mutant Mfn1 was expressed in Mfn-null cells. PEG-induced hybrids were generated between cells containing the same construct. Control, empty retrovirus. (C) Mitochondrial aggregation in an NIH 3T3 cell expressing truncated Mfn1 (Myc-tagged). Mitochondria are visualized by mitochondrially targeted GFP, and truncated Mfn1 by immunofluorescence (Cy3) against the Myc epitope. Scale bar, 10 μm. (D) Mitochondrial morphologies in NIH 3T3 cells infected with retrovirus expressing truncated Mfn1 (residues 331 to 741) or derivatives with HR2 mutations. Control, empty retrovirus. (E) Electron micrograph of mitochondrial tethering by truncated Mfn1. Scale bar, 1 μm. Rectangles indicate regions magnified in (F) and (G). Note the uniform gap (arrowheads) between adjacent double-membraned mitochondria (m). Scale bar, 0.2 μm.

is dependent on HR2 coiled-coil formation, because HR2-destabilizing mutations abolish the effect (Fig. 4D). Strikingly, electron microscopy revealed densely packed mitochondria that maintain a uniform gap between opposing outer mitochondrial membranes (Fig. 4, E to G). The average distance of this gap is 159 Å ( $n = 124$  measurements; SD = 30 Å). Taken together, these results suggest that, in the absence of the GTPase domain, Mfn1 is unable to promote full fusion. Instead, mitochondria are trapped in a tethered state mediated by the HR2 coiled coil. At present, we do not know if this trapped state remains competent for future fusion.

Because mitofusins are required on the outer membranes of adjacent mitochondria, it is likely that they act in trans and are directly involved in promoting membrane fusion. Moreover, our results suggest that mitochondrial fusion, like other intracellular membrane fusion events, proceeds through a tethering step before full fusion. The HR2 structure provides a structural understanding of how antiparallel coiled-coil formation can mediate organelle tethering by providing a large interaction interface while maintaining separation of the membrane anchors. In contrast, trans-SNARE complexes drive membrane-anchoring regions into close apposition (4) and may force bilayer merger. Many of the components mediating vesicle tethering are known in other membrane-trafficking systems, but those tethering events are far more complex, involving heterotypic interactions between Rab GTPases and large, coiled coil-containing proteins (3). As a result, they are poorly understood structurally, even though crystal structures of some individual components are available (23).

The HR2 structure provides a mechanism for the tethering of mitochondria, rather than for the closer apposition that must occur later during the fusion process (Fig. 3C). It is likely that mitofusins themselves mediate these downstream events, because genomic screens for mitochondrial fusion molecules have failed to identify molecules, besides the Fzo/Mfn proteins, that are both located in the outer membrane and conserved in vertebrates (24). In future work, it will be critical to understand how further mitofusin-mediated structural rearrangements, likely involving regulation by the GTPase domain, lead to full fusion.

References and Notes

1. J. S. Bonifacio, B. S. Glick, *Cell* **116**, 153 (2004).
2. I. Mellman, G. Warren, *Cell* **100**, 99 (2000).
3. J. R. Whyte, S. Munro, *J. Cell Sci.* **115**, 2627 (2002).
4. R. B. Sutton, D. Fasshauer, R. Jahn, A. T. Brunger, *Nature* **395**, 347 (1998).
5. T. Weber et al., *Cell* **92**, 759 (1998).
6. H. Chen, D. C. Chan, *Curr. Top. Dev. Biol.* **59**, 119 (2004).
7. M. Karbowski, R. J. Youle, *Cell Death Differ.* **10**, 870 (2003).
8. J. M. Shaw, J. Nunnari, *Trends Cell Biol.* **12**, 178 (2002).

9. H. Chen et al., *J. Cell Biol.* **160**, 189 (2003).
10. A. D. Mozdy, J. M. Shaw, *Nature Rev. Mol. Cell Biol.* **4**, 468 (2003).
11. A. Santel, M. T. Fuller, *J. Cell Sci.* **114**, 867 (2001).
12. M. Rojo, F. Legros, D. Chateau, A. Lombes, *J. Cell Sci.* **115**, 1663 (2002).
13. F. Legros, A. Lombes, P. Frachon, M. Rojo, *Mol. Biol. Cell* **13**, 4343 (2002).
14. A. Santel et al., *J. Cell Sci.* **116**, 2763 (2003).
15. S. Zuchner et al., *Nature Genet.* **36**, 449 (2004).
16. Materials and methods are available as supporting materials on Science Online.
17. A previous study using RNA interference to reduce mitofusin levels in rat cells concluded that mitofusins function in cis (on a single mitochondrial membrane) (18). These authors found that fusion of wild-type and mitofusin knockdown cells resulted in significant fusion of mitochondria. However, it is clear that the RNA interference in that study failed to completely deplete both mitofusins, because residual mitochondrial fusion was observed even in cell hybrids between double mitofusin knockdown cells [figure 5 of (18)]. In our study, the use of genetically defined, Mfn-null cells leads to definitive results. Yeast mitochondrial fusion also requires Fzo1 on adjacent membranes, on the basis of an in vitro mitochondrial fusion assay (19).
18. N. Ishihara, A. Jofuku, Y. Eura, K. Mihara, *Biochem. Biophys. Res. Commun.* **301**, 891 (2003).
19. S. Meeusen, J. M. McCaffery, J. Nunnari, manuscript in preparation.
20. D. M. Eckert, P. S. Kim, *Annu. Rev. Biochem.* **70**, 777 (2001).
21. M. G. Oakley, J. J. Hollenbeck, *Curr. Opin. Struct. Biol.* **11**, 450 (2001).
22. D. G. Gurmon, J. A. Whitaker, M. G. Oakley, *J. Am. Chem. Soc.* **125**, 7518 (2003).
23. J. J. Dumas et al., *Mol. Cell* **8**, 947 (2001).
24. K. S. Dimmer et al., *Mol. Biol. Cell* **13**, 847 (2002).
25. We are grateful to D. Rees, J. Nunnari, and R. Deshaies for helpful discussions. We thank the staff of the Advanced Light Source at Berkeley Lab. We thank P. Huang for advice on structural analysis. T.K. was supported by a Gosney Foundation postdoctoral fellowship; J.T.K. is an HHMI Research Associate. This work was supported by the National Institute of Health (R01 GM62967). D.C.C. is a Bren Scholar, Rita Allen Scholar, and Beckman Young Investigator. Atomic coordinates and structure factors have been deposited in the Protein Data Bank, accession code 1T3J.

Supporting Online Material  
[www.sciencemag.org/cgi/content/full/305/5685/858/DC1](http://www.sciencemag.org/cgi/content/full/305/5685/858/DC1)  
 Materials and Methods  
 Figs. S1 to S6  
 Table S1  
 References

30 April 2004; accepted 30 June 2004 .

## The Semaphorin 4D Receptor Plexin-B1 Is a GTPase Activating Protein for R-Ras

Izumi Oinuma, Yukio Ishikawa, Hironori Katoh, Manabu Negishi\*

Plexins are cell surface receptors for semaphorin molecules, and their interaction governs cell adhesion and migration in a variety of tissues. We report that the Semaphorin 4D (Sema4D) receptor Plexin-B1 directly stimulates the intrinsic guanosine triphosphatase (GTPase) activity of R-Ras, a member of the Ras superfamily of small GTP-binding proteins that has been implicated in promoting cell adhesion and neurite outgrowth. This activity required the interaction of Plexin-B1 with Rnd1, a small GTP-binding protein of the Rho family. Down-regulation of R-Ras activity by the Plexin-B1-Rnd1 complex was essential for the Sema4D-induced growth cone collapse in hippocampal neurons. Thus, Plexin-B1 mediates Sema4D-induced repulsive axon guidance signaling by acting as a GTPase activating protein for R-Ras.

Plexins constitute a large family of transmembrane proteins that function as receptors for semaphorins (1). Semaphorins were originally identified as repulsive axonal guidance molecules in the developing nervous system, but have recently been shown to control cell adhesion and migration in other tissues (2–5). The cytoplasmic domain of plexin family members has been highly conserved during evolution and shares sequence similarity with Ras family-specific GTPase activating proteins (GAPs), especially R-Ras GAP (6, 7). These homologous domains in plexins con-

tain two conserved arginine residues corresponding to those essential for the catalytic activity of common Ras GAPs (8); however, no GAP activity by plexins has been demonstrated so far. R-Ras has been shown to play a key role in cell adhesion by activating integrins and to promote cell migration and neurite outgrowth (9–12).

Rnd1, a constitutively active Rho family member (13), directly interacts with Plexin-B1, the receptor for Semaphorin 4D (Sema4D) (14). The Rnd1-binding region in Plexin-B1 is located between the two GAP-homologous domains (Fig. 1E). To evaluate whether the interaction of Rnd1 with Plexin-B1 could affect the GAP activity toward R-Ras, we examined the interaction between Plexin-B1 and R-Ras in the presence and the absence of Rnd1. Epitope (Myc)-tagged cy-

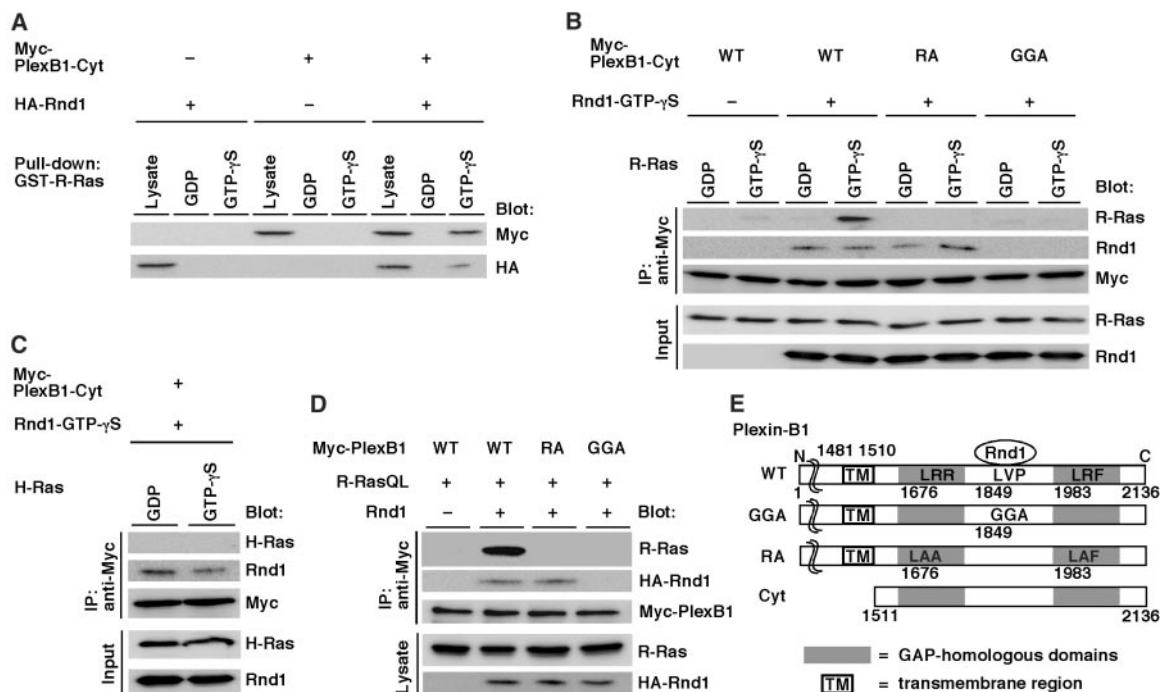
Laboratory of Molecular Neurobiology, Graduate School of Biostudies, Kyoto University, Sakyo-ku, Kyoto 606-8502, Japan.

\*To whom correspondence should be addressed. E-mail address: mnegishi@pharm.kyoto-u.ac.jp



**Fig. 1.** Interaction between Plexin-B1 and R-Ras requires Rnd1.

(A) Lysates from transfected COS-7 cells expressing the Myc-tagged cytoplasmic domain of Plexin-B1 (Myc-PlexB1-Cyt) and HA-tagged Rnd1 were used in a pull-down assay with GST-R-Ras preloaded with GDP or GTP- $\gamma$ S. Bound proteins and total cell lysates (Lysates) were analyzed by immunoblotting with antibodies against Myc and HA. (B and C) Recombinant Myc-PlexB1-Cyt, Rnd1, R-Ras, and H-Ras were purified from *E. coli*. Myc-PlexB1-Cyt and GTP- $\gamma$ S-loaded Rnd1 were incubated with R-Ras (B) or H-Ras (C) preloaded with GDP or GTP- $\gamma$ S, and then immunoprecipitated with an antibody against Myc. Bound and total proteins were analyzed by immunoblotting with antibodies against R-Ras, Rnd1, and Myc. (D) Lysates from transfected COS-7 cells expressing the indicated proteins were immunoprecipitated with an antibody against Myc, and bound



toplasmic domain of Plexin-B1 was expressed in COS-7 cells and used in a pull-down assay with purified glutathione *S*-transferase (GST)-fused R-Ras preloaded with guanosine 5'-diphosphate (GDP) or guanosine 5'-*O*-(3'-thiotriphosphate) (GTP- $\gamma$ S). No interaction was detected between R-Ras and the cytoplasmic domain of Plexin-B1 in the absence of Rnd1. In contrast, Plexin-B1 interacted with GTP-bound active R-Ras when it was coexpressed with Rnd1 (Fig. 1A). Rnd1 was also immunoprecipitated with GTP-bound R-Ras, indicating that Plexin-B1 interacted simultaneously with R-Ras and Rnd1. To determine whether the interaction between Plexin-B1 and R-Ras is direct, we purified the recombinant Rnd1, R-Ras, and Myc-tagged cytoplasmic domain of Plexin-B1 from *Escherichia coli* and used them in immunoprecipitation studies with an antibody against Myc. The cytoplasmic domain of Plexin-B1 interacted with GTP-bound R-Ras only in the presence of Rnd1 (Fig. 1B). A mutant of Plexin-B1 unable to interact with Rnd1 [Plexin-B1-GGA, in which Leu-Val-Pro is mutated to Gly-Gly-Ala at amino acids 1849 to 1851 (14)] did not bind to R-Ras. In addition, mutations in arginine residues in the Ras GAP-homologous domains conserved among Ras GAPs (Plexin-B1-RA, in which Arg is mutated to Ala at amino acids 1677, 1678, and 1984) abolished binding of Plexin-B1 to R-Ras, although Plexin-B1-RA could still bind to Rnd1 (Fig. 1B). Another Ras family member, H-Ras, did not interact with the Plexin-B1-

proteins were analyzed by immunoblotting with antibodies against R-Ras, HA, and Myc. (E) Plexin-B1 constructs. The Rnd1-binding region is indicated. Letters indicate specific amino acid residues within domains (A, Ala; F, Phe; G, Gly; L, Lys; P, Pro; R, Arg; V, Val). Numbers indicate amino acid position within the sequence.

proteins were analyzed by immunoblotting with antibodies against R-Ras, HA, and Myc. (E) Plexin-B1 constructs. The Rnd1-binding region is indicated. Letters indicate specific amino acid residues within domains (A, Ala; F, Phe; G, Gly; L, Lys; P, Pro; R, Arg; V, Val). Numbers indicate amino acid position within the sequence.

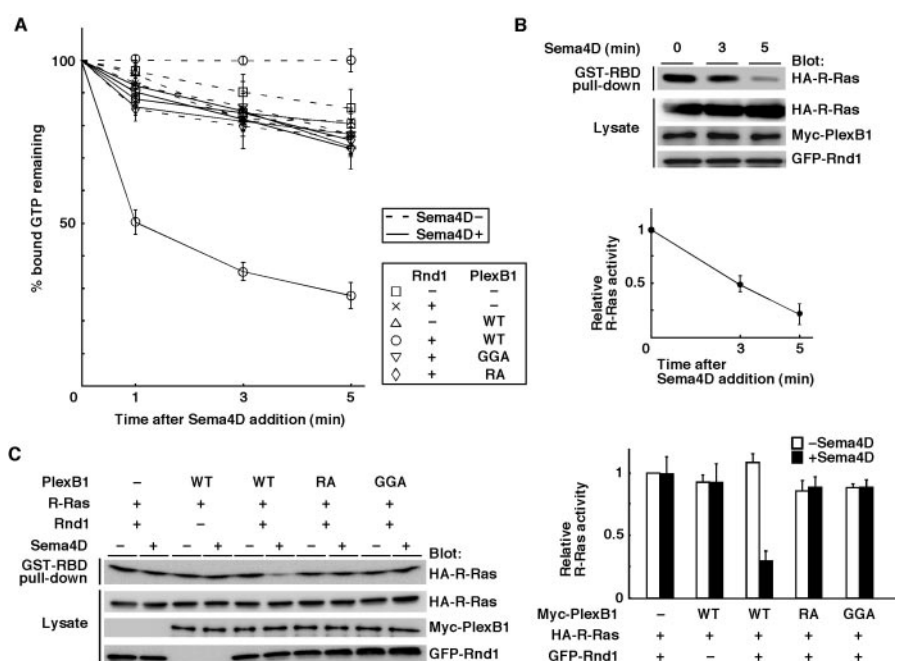


**Fig. 2.** Plexin-B1 stimulates the intrinsic GTPase activity of R-Ras in a ligand-dependent manner. (A) Purified R-Ras preloaded with [ $\gamma$ - $^{32}$ P]GTP was incubated with the membrane fraction from COS-7 cells transfected with the indicated plasmids in the presence (solid lines) or the absence (dashed lines) of Sema4D at 25°C for the indicated times. The radioactivity bound to R-Ras was determined by a nitrocellulose filtration assay. Results are the means  $\pm$  SEM of three independent experiments. (B) COS-7 cells transfected with expression plasmids encoding Myc-tagged Plexin-B1 (Myc-PlexB1), GFP-tagged Rnd1, and HA-tagged R-Ras were stimulated with Sema4D for the indicated times. The cell lysates were incubated with GST-fused Ras binding domain of c-Raf-1 (GST-RBD). Bound R-Ras and total cell lysates were analyzed by immunoblotting with antibodies against HA (R-Ras), Myc (Plexin-B1), and GFP (Rnd1). (C) COS-7 cells transfected with the indicated plasmids were stimulated with Sema4D for 5 min. The cell lysates were incubated with GST-RBD, and bound R-Ras and total cell lysates were analyzed by immunoblotting. Relative R-Ras activity was determined by the amount of R-Ras bound to GST-RBD normalized to the amount of R-Ras in cell lysates analyzed by NIH Image software (28). Results are the means  $\pm$  SEM of three or five independent experiments.

Rnd1 complex (Fig. 1C). The Rnd1-dependent interaction between active R-Ras and Plexin-B1 also occurred in transfected COS-7 cells expressing Myc-tagged full-length Plexin-B1, constitutively active R-Ras (R-Ras-QL), and hemagglutinin (HA) epitope-tagged Rnd1 (Fig. 1D). Neither Plexin-B1-GGA nor Plexin-B1-RA immunoprecipitated R-Ras-QL (Fig. 1D). These results suggest that Plexin-B1 interacts directly and specifically with active R-Ras through its Ras GAP-homologous domains, and that this interaction requires the binding of Rnd1 to Plexin-B1 at the region between the two GAP-homologous domains.

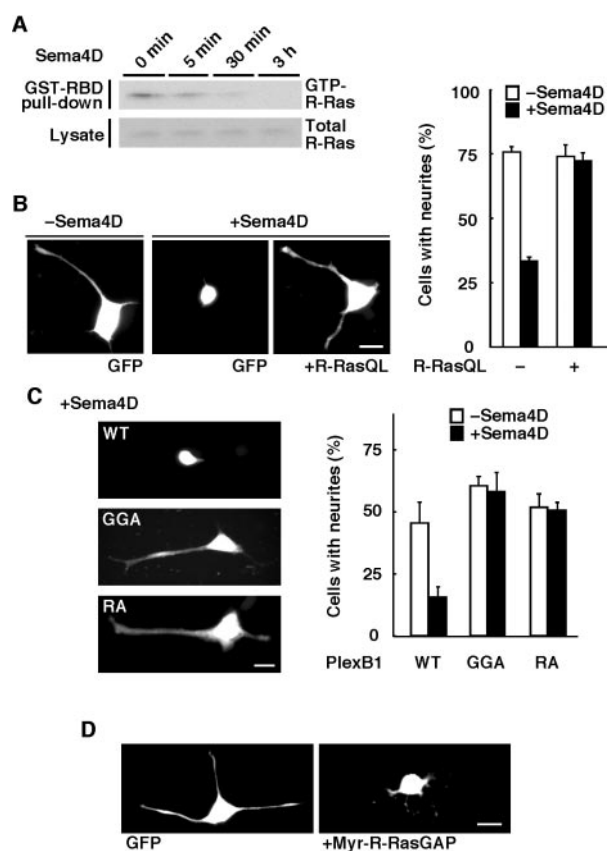
To determine whether Plexin-B1 promotes the intrinsic GTPase activity of R-Ras in vitro, we incubated purified R-Ras preloaded with [ $\gamma$ - $^{32}$ P]GTP with the membrane fraction from transfected COS-7 cells expressing full-length Plexin-B1 and Rnd1. Expression of Plexin-B1 or Rnd1 alone had little effect on the intrinsic GTPase activity of R-Ras in the presence and the absence of Sema4D. In contrast, stimulation of cells with Sema4D increased hydrolysis of bound GTP when R-Ras was incubated with the membrane fraction from COS-7 cells expressing Plexin-B1 and Rnd1 (Fig. 2A). Expression of Rnd1 and Plexin-B1-GGA or Plexin-B1-RA did not stimulate the GTPase activity of R-Ras in the presence and the absence of Sema4D (Fig. 2A). Expression of Plexin-B1 constructs in the membrane fractions was similar, as verified by immunoblot analysis (15).

To assess the GAP activity of Plexin-B1 in cells, we determined the presence of GTP-bound R-Ras in transfected COS-7 cells expressing Plexin-B1, Rnd1, and R-Ras by using a pull-down assay with a fusion protein containing GST and the Ras-binding domain of c-Raf-1, which selectively isolates active R-Ras (16). After stimulation of cells with Sema4D, GTP-bound R-Ras rapidly decreased to a minimum within 5 min (Fig. 2B). However, addition of Sema4D had no effect on GTP-bound R-Ras in the absence of Rnd1 or when Plexin-B1-GGA or Plexin-B1-RA was expressed (Fig. 2C). These data indicate that Plexin-B1 acts as a GAP toward R-Ras through the Ras GAP-homologous domains, and that the interaction of Rnd1 with Plexin-B1 and the ligand stimulation are essential for Plexin-B1 GAP activity in vitro and in cells.

It has been reported that Plexin-B1 binds to Rho-specific guanine nucleotide exchange factors PDZ-RhoGEF and LARG through the receptor's C-terminal PDZ domain-binding motif, thus activating RhoA (17–21). However, mutations in the Ras GAP-homologous domains in Plexin-B1 had no effect on the ability of Plexin-B1 to activate RhoA (fig. S1). Furthermore, deletion of the PDZ domain-binding motif

or expression of the dominant-negative form of PDZ-RhoGEF, both of which completely inhibited RhoA activation by Plexin-B1, had no effect on the R-Ras GAP activity (figs. S1 and S2). These results indicate that Plexin-B1 induces down-regulation of R-Ras activity separately from its activation of RhoA.

To address the biological role of the R-Ras GAP activity manifested by Plexin-B1, we used differentiated PC12 cells that express endogenous Plexin-B1 and exhibit neurite retraction in response to Sema4D (17). Stimulation of nerve growth factor (NGF)-differentiated PC12 cells with Sema4D decreased GTP-bound R-Ras in the cells (Fig. 3A). To determine whether the down-regulation of R-Ras activity is required for the Sema4D-induced neurite retraction, we used NGF to differentiate transfected PC12 cells expressing constitutively active R-Ras (R-Ras-QL), and then examined cell morphology after stimulation of the cells with Sema4D. Tips of neurites were detected by also expressing green fluorescent protein (GFP). PC12 cells expressing GFP alone retracted their neurites within 3 hours after stimulation with Sema4D. In contrast, expression of R-Ras-QL completely blocked the Sema4D-induced neurite retraction (Fig. 3B). To

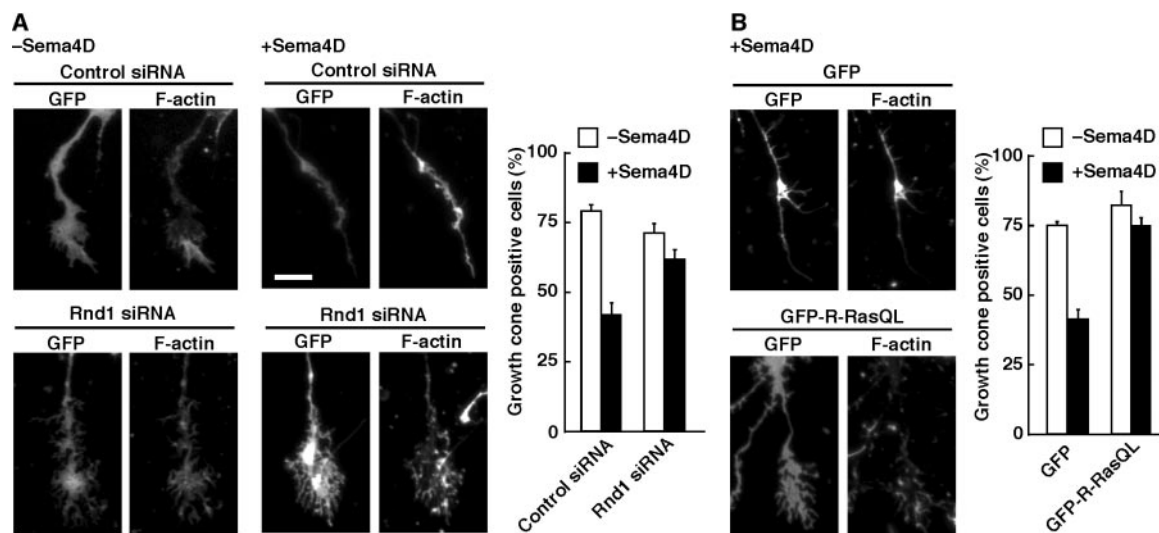


confirm that the Sema4D-induced neurite retraction depends on the GAP activity of Plexin-B1, we stimulated transfected PC12 cells expressing Plexin-B1-GGA or Plexin-B1-RA with Sema4D and compared their morphologies with that of cells expressing wild-type (WT) Plexin-B1. Similar to untransfected cells, differentiated PC12 cells expressing WT Plexin-B1 retracted their neurites in response to Sema4D. Expression of Plexin-B1-GGA or Plexin-B1-RA blocked the Sema4D-induced neurite retraction (Fig. 3C). In addition, expression of the myristoylated GAP domain of R-Ras GAP, which exhibits a specific GAP activity toward R-Ras (22), or knockdown of R-Ras expression by the use of an R-Ras-specific short interfering RNA (siRNA) expression vector, mimicked the Sema4D-induced morphological change (Fig. 3D and fig. S3). We also observed the involvement of Rnd1 in the Sema4D-induced neurite retraction with a Rnd1-specific siRNA expression vector that effectively reduced the amount of Rnd1 protein (fig. S4). These results indicate that the GAP activity exhibited by the Plexin-B1-Rnd1 complex toward R-Ras is essential for the Sema4D-induced neurite retraction. However, inhibition of RhoA signaling by expression of a mutant Plexin-B1 lacking the PDZ domain-

confirm that the Sema4D-induced neurite retraction depends on the GAP activity of Plexin-B1, we stimulated transfected PC12 cells expressing Plexin-B1-GGA or Plexin-B1-RA with Sema4D and compared their morphologies with that of cells expressing wild-type (WT) Plexin-B1. Similar to untransfected cells, differentiated PC12 cells expressing WT Plexin-B1 retracted their neurites in response to Sema4D. Expression of Plexin-B1-GGA or Plexin-B1-RA blocked the Sema4D-induced neurite retraction (Fig. 3C). In addition, expression of the myristoylated GAP domain of R-Ras GAP, which exhibits a specific GAP activity toward R-Ras (22), or knockdown of R-Ras expression by the use of an R-Ras-specific short interfering RNA (siRNA) expression vector, mimicked the Sema4D-induced morphological change (Fig. 3D and fig. S3). We also observed the involvement of Rnd1 in the Sema4D-induced neurite retraction with a Rnd1-specific siRNA expression vector that effectively reduced the amount of Rnd1 protein (fig. S4). These results indicate that the GAP activity exhibited by the Plexin-B1-Rnd1 complex toward R-Ras is essential for the Sema4D-induced neurite retraction. However, inhibition of RhoA signaling by expression of a mutant Plexin-B1 lacking the PDZ domain-



**Fig. 4.** Down-regulation of R-Ras activity by Plexin-B1 is required for the Sema4D-induced growth cone collapse in rat hippocampal neurons. **(A)** Hippocampal neurons transfected with control or the Rnd1-specific siRNA expression plasmid together with a plasmid encoding GFP were stimulated with Sema4D for 1 hour. **(B)** Hippocampal neurons transfected with expression plasmids encoding GFP or GFP-tagged R-RasQL were stimulated with Sema4D for 1 hour. Growth cones of the transfected cells are shown by the fluorescence of GFP. A growth cone was defined by the presence of lamellipodia and filopodia visualized by the staining of filamentous actin (F-actin) with Alexa 594-conjugated phalloidin.



Growth cone-positive cells were scored as a percentage of the total number of transfected cells, and results are the means  $\pm$  SEM of three independent experiments in which 30 cells were counted. Bar, 10  $\mu$ m.

binding motif also suppressed the Sema4D-induced neurite retraction (15), as reported previously (17). Thus, the Sema4D-induced neurite retraction requires both the R-Ras GAP activity and the PDZ-RhoGEF-mediated RhoA activation by Plexin-B1.

Sema4D induces growth cone collapse in primary hippocampal neurons from rat embryos (18). Plexin-B1 and Rnd1 are endogenously expressed in cultured hippocampal neurons (18, 23), and endogenous R-Ras protein was also detected by immunoblot analysis (15). To determine whether the GAP activity of Plexin-B1 toward R-Ras is involved in Sema4D-induced growth cone collapse in hippocampal neurons, we reduced expression of Rnd1 in rat hippocampal neurons by RNA interference (fig. S5). Similar to untransfected neurons, transfected neurons expressing GFP and control siRNA caused growth cone collapse in response to Sema4D. However, expression of GFP and the Rnd1 siRNA suppressed the Sema4D-induced growth cone collapse (Fig. 4A). Expression of R-Ras-QL also blocked Sema4D-induced growth cone collapse (Fig. 4B). In addition, expression of R-Ras siRNA promoted growth cone collapse (fig. S6). These results suggest that inactivation of R-Ras by the Plexin-B1-Rnd1 complex is necessary for the Sema4D-induced growth cone collapse in hippocampal neurons.

Rnd1 also binds to Plexin-A1 and is required for the Sema3A-Plexin-A1-mediated repulsion (6, 24). In addition, mutations in the GAP homologous domains in Plexin-A1 suppressed the Plexin-A1-mediated repulsion (24). To determine whether the down-regulation of R-Ras activity was also involved in Plexin-A-mediated growth cone collapse, we expressed GFP-tagged R-Ras-

QL in rat hippocampal neurons. R-Ras-QL suppressed the Sema3A-induced growth cone collapse (fig. S7), indicating that the down-regulation of R-Ras activity is also required for the Sema3A/Plexin-A-mediated growth cone collapse.

Direct regulation of R-Ras activity by Plexin-B1 acting as a GAP serves as a mechanism for transmembrane receptor-mediated signal transduction. The down-regulation of R-Ras activity is also involved in the Sema3A-induced repulsion. Activation of R-Ras promotes cell adhesion and controls cell migration and neurite outgrowth by activating integrins (9–12). It has been recently reported that Sema3A and Sema4D inhibited integrin-mediated cell adhesion and migration (25–27). Therefore, the down-regulation of R-Ras activity by plexins may suppress integrin activation and thereby reduce cell adhesiveness, leading to growth cone collapse and neurite retraction. Considering that the GAP-homologous domains are well conserved among different plexin subfamilies, direct regulation of R-Ras activity by plexin is likely to be a major signaling pathway for cellular functions mediated by semaphorins.

#### References and Notes

1. L. Tamagnone *et al.*, *Cell* **99**, 71 (1999).
2. F. Nakamura, R. G. Kalb, S. M. Strittmatter, *J. Neurobiol.* **44**, 219 (2000).
3. J. A. Raper, *Curr. Opin. Neurobiol.* **10**, 88 (2000).
4. L. Trusolino, P. M. Comoglio, *Nat. Rev. Cancer* **2**, 289 (2002).
5. Y. Goshima, T. Ito, Y. Sasaki, F. Nakamura, *J. Clin. Invest.* **109**, 993 (2002).
6. B. Rhom, B. Rahim, B. Kleiber, I. Hovatta, A. W. Püschel, *FEBS Lett.* **486**, 68 (2000).
7. H. Hu, T. F. Marton, C. S. Goodman, *Neuron* **32**, 39 (2001).
8. K. Scheffzek, M. R. Ahmadian, A. Wittinghofer, *Trends Biochem. Sci.* **23**, 257 (1998).

9. Z. Zhang, K. Vuori, H. Wang, J. C. Reed, E. Ruoslahti, *Cell* **85**, 61 (1996).
10. P. J. Keely, E. V. Rusyn, A. D. Cox, L. V. Parise, *J. Cell Biol.* **145**, 1077 (1999).
11. J. K. Ivins, P. D. Yurchenco, A. D. Lander, *J. Neurosci.* **20**, 6551 (2000).
12. K. Kinbara, L. E. Goldfinger, M. Hansen, F. L. Chou, M. H. Ginsberg, *Nat. Rev. Mol. Cell Biol.* **4**, 767 (2003).
13. C. D. Nobes *et al.*, *J. Cell Biol.* **141**, 187 (1998).
14. I. Oinuma, H. Katoh, A. Harada, M. Negishi, *J. Biol. Chem.* **278**, 25671 (2003).
15. I. Oinuma, Y. Ishikawa, H. Katoh, M. Negishi, data not shown.
16. M. van Triest, J. de Rooij, J. L. Bos, *Methods Enzymol.* **333**, 343 (2001).
17. V. Perrot, T. Vázquez-Prado, J. S. Gutkind, *J. Biol. Chem.* **277**, 43115 (2002).
18. J. M. Swiercz, R. Kuner, J. Behrens, S. Offermanns, *Neuron* **35**, 51 (2002).
19. M. H. E. Driessens *et al.*, *Curr. Biol.* **11**, 339 (2001).
20. J. Aurandt, H. G. Vikis, J. S. Gutkind, N. Ahn, K.-L. Guan, *Proc. Natl. Acad. Sci. U.S.A.* **99**, 12085 (2002).
21. M. H. E. Driessens, C. Olivo, K. Nagata, M. Inagaki, J. G. Collard, *FEBS Lett.* **529**, 168 (2002).
22. T. Yamamoto *et al.*, *J. Biol. Chem.* **270**, 30557 (1995).
23. Y. Ishikawa, H. Katoh, M. Negishi, *J. Neurosci.* **23**, 11065 (2003).
24. S. M. Zanta, I. Hovatta, B. Rohm, A. W. Püschel, *J. Neurosci.* **22**, 471 (2002).
25. G. Serini *et al.*, *Nature* **424**, 391 (2003).
26. T. Takahashi *et al.*, *Cell* **99**, 59 (1999).
27. D. Barberis *et al.*, *FASEB J.* **18**, 592 (2004).
28. <http://rsb.info.nih.gov/nih-image/>
29. We thank L. Tamagnone for Plexin-B1 cDNA and H. Kikutani for the soluble forms of Sema4D expression plasmids. This work was supported in part by Grants-in-Aid for Scientific Research from the Ministry of Education, Science, Sports, and Culture of Japan and a grant from Takeda Science Foundation. Molecular interaction data have been deposited in the Biomolecular Interaction Network Database with accession codes 149198, 149199, 149200, 149201, 149204, and 149207.

#### Supporting Online Materials

[www.sciencemag.org/cgi/content/full/305/5685/862/DC1](http://www.sciencemag.org/cgi/content/full/305/5685/862/DC1)  
Materials and Methods  
Figs. S1 to S7  
References

4 March 2004; accepted 9 July 2004

# The Binding Mode of Epothilone A on $\alpha,\beta$ -Tubulin by Electron Crystallography

James H. Nettles,<sup>1</sup> Huilin Li,<sup>2</sup> Ben Cornett,<sup>3</sup> Joseph M. Krahn,<sup>4</sup>  
James P. Snyder,<sup>3\*</sup> Kenneth H. Downing<sup>5\*</sup>

The structure of epothilone A, bound to  $\alpha,\beta$ -tubulin in zinc-stabilized sheets, was determined by a combination of electron crystallography at 2.89 angstrom resolution and nuclear magnetic resonance-based conformational analysis. The complex explains both the broad-based epothilone structure-activity relationship and the known mutational resistance profile. Comparison with Taxol shows that the longstanding expectation of a common pharmacophore is not met, because each ligand exploits the tubulin-binding pocket in a unique and independent manner.

The extraordinary clinical success achieved by Taxol (**1**) and related taxanes in treating a wide variety of cancers has been accompanied by delivery problems (1), resistance arising from various cellular factors, including increased P-glycoprotein expression (2), and numerous side effects (3). A search for alternative drug therapies that also operate by microtubule stabilization has led to a focus on a family of 16-membered ring macrocyclic lactones represented by epothilone A (EpoA, **2**) (Scheme 1). Discovered by Höfle and co-workers from the myxobacterium *Sorangium cellulosum* (4), epothilones are more water soluble than Taxol, appear to largely escape drug resistance encountered by taxanes, and cause tumor cell death by stabilizing microtubules and inducing apoptosis (5).

Since the discovery of the epothilones in 1993, an impressive structure-activity relationship (SAR) profile has emerged from the efforts of numerous synthetic teams (6). Epothilones, Taxol, and other microtubule stabilizers, including the endogenous neuronal tau protein (7), compete for the same binding pocket on  $\beta$ -tubulin. This has prompted attempts to describe a common pharmacophore for the structurally diverse taxanes and epothilones (8–11). This exercise, pursued primarily to facilitate the rational design of chemotherapeutic agents, is based on the assumption that superimposable polar and hydrophobic groups on the individ-

ual ligands interact with complementary subsites on the protein target.

Combining nuclear magnetic resonance (NMR) spectroscopy, electron crystallography (EC), and molecular modeling (12), we derived a structural model of the binding mode and conformation of EpoA in complex with the  $\beta$ -tubulin subunit in zinc-stabilized tubulin sheets (Fig. 1). A similar approach has led to the identification of T-Taxol: Taxol bound to  $\beta$ -tubulin in a conformer with approximately equal distances between the C-2 phenyl and the two C-3' aromatic substituents (13). The complex accommodates the extensive epothilone SAR data developed for microtubules composed of wild-type tubulin (TB) and the more limited resistance data from mutant tubulins. Importantly, the structure demonstrates that, whereas EpoA and Taxol overlap in their occupation of a rather expansive common binding site on tubulin, the expectation of a common pharmacophore is unmet, because each ligand exploits the

binding pocket in a unique and qualitatively independent manner (Fig. 2).

A variety of epothilone conformations and binding modes on tubulin have been proposed by pharmacophore mapping (10, 11), solution NMR (14, 15), and the superposition of epothilones on Taxol or Taxotere in the EC tubulin complex (8, 9). All proposals for the binding mode have assumed that the macrocyclic epothilone ring occupies common space with the baccatin core of Taxol, whereas the thiazole side chain superposes one of its three phenyl rings. Thus, He (8) and Giannakakou (9) placed the C-2 benzoyl phenyl, Giannakakou and Wang (9, 10) the C-3' phenyl, and Ojima (11) located the C-3' benzamido phenyl as coincident with the thiazole ring. Overlap of the two drugs' binding modes determined by EC illustrates that the thiazole of EpoA benzoyl phenyl resides in a region of the tubulin pocket unoccupied by Taxol (Fig. 2). Of the five oxygen-containing polar groups decorating the epothilone macrocycle, only C7-OH falls near the similar C7-OH moiety in paclitaxel (Fig. 2), making this center the only notable common nonbonded contact for the two molecules. With one exception (10), all previous proposals have directed the C12–C13 epoxide ring outward from the periphery of the molecule. This is in marked contrast to the C10–C15 fragment that is folded beneath the macrocycle and above the hydrophobic pocket in the present model (Figs. 1 and 3). As previously speculated (10), the lack of protein-ligand interaction with the epoxide ring is consistent with the activity of olefin analogs EpoC and EpoD lacking the oxygen. Complementing the epoxide fold is a near-parallel orientation of the C-O bonds at C3, C5, and C7, an alignment ideal for the ligand-tubulin interaction. This arrangement leads to a very different set of backbone torsion angles from

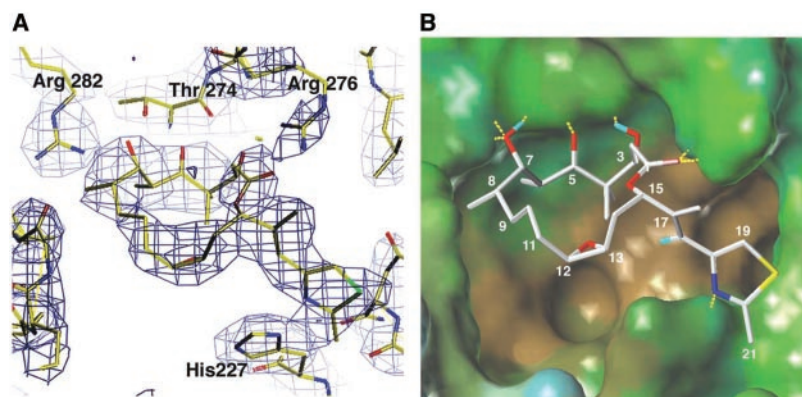


**Fig. 1.** (A) The density map (purple wireframe) resulting from Fourier synthesis of the EC diffractions ( $2F_{\text{obs}} - F_{\text{calc}}$ ) and associated model (stick figure is colored by atom type: yellow, C; red, O; blue, N; and green, S) derived from electron crystallographic analysis of epothilone A (**1**) bound to zinc-stabilized two-dimensional crystals of tubulin. (B) Hydrophobic (brown) to hydrophilic (blue) properties are mapped to the solvent-accessible  $\beta$ -tubulin surface at the ligand-binding site. Epothilone A (white, C; red, O; blue, N; and yellow, S) is shown with hydrogen bonds (yellow dashes) to associated centers on the  $\beta$ -tubulin protein. Select hydrogens (cyan) are also modeled.

<sup>1</sup>Molecular and Systems Pharmacology, Emory University, Atlanta, GA 30322, USA. <sup>2</sup>Department of Biology, Brookhaven National Laboratory, Upton, NY 11973, USA. <sup>3</sup>Department of Chemistry, Emory University, Atlanta, GA 30322, USA. <sup>4</sup>Laboratory of Structural Biology, National Institute of Environmental Health Sciences, Research Triangle Park, NC 27709, USA. <sup>5</sup>Life Sciences Division, Lawrence Berkeley National Laboratory, Berkeley, CA 94720, USA.

\*To whom correspondence should be addressed. E-mail: snyder@euch4e.chem.emory.edu (J.P.S.); kdowning@lbl.gov (K.H.D.)



C1 to C9 for epothilone A in comparison with either its single crystal x-ray structure or the transfer nuclear Overhauser effect NMR structure of EpoA, completed with an unpolymerized soluble form of the protein (14).

Six residues lining or adjacent to the ligand-binding pocket in  $\beta$ -tubulin undergo mutation under pressure from exposure of various cell lines to epothilones (Ala<sup>231</sup>, Thr<sup>274</sup>, Arg<sup>282</sup>, and Gln<sup>292</sup>) (9, 16, 17) or taxanes (Phe<sup>270</sup> and Ala<sup>364</sup>) (18). Superposition of the two ligands along with the corresponding  $\beta$ -tubulin side chains provides a graphical portrait of the origins of the observed differential acquired resistance (fig. S7). For example, Taxol's C3'-phenyl and C4-OAc are in van der Waals contact with the Phe<sup>270</sup>. Thus, the drug shows 24-fold less activity in a human ovarian carcinoma cell line with the Phe<sup>270</sup>→Val<sup>270</sup> (Phe270Val) mutation. EpoA is located a relatively benign 4 to 5 Å from the same residue and displays only threefold resistance. Taxol experiences substantially less cross-resistance to Thr<sup>274</sup> (10-fold) and Arg<sup>282</sup> (sevenfold) mutations, in strong contrast to the cellular response to EpoA [40- and 57-fold, respectively] (8, 16)]. In the present model, wild-type Thr<sup>274</sup> and Arg<sup>282</sup> are cooperatively engaged in a cluster of hydrogen bonds with the C3, C5, and C7 triad of oxygen atoms in EpoA (Fig. 3). Perturbation of either set of noncovalent interactions by elimination of an OH (Thr274Ile) or elonga-

tion of the distance between associated centers (Arg282Gln) dissipates the binding energy between the drug and the protein. The backbone NH of Thr<sup>274</sup> is likewise in the vicinity of the oxetane ring of Taxol, such that residue replacement might be expected to diminish ligand binding. However, as has been argued previously (19), this interaction is likely to be weak and not as influential in Taxol's binding. In the epothilone complex, Arg<sup>282</sup> is within conformational reach of C7-OH (Figs. 1 and 3). This differs from the tubulin-Taxol complex (13, 20), in which a variation in M-loop conformation directs Arg<sup>282</sup> into solvent, but is compatible with the mutation-induced resistance. An acquired mutation reported independently by two groups in lung and leukemia cancer cell lines is the Gln292Glu mutation (70- to 90-fold for EpoA and EpoB) (16, 17). The residue lies on the opposite side of the M-loop from EpoA and makes a hydrogen bond to the backbone NH of Leu<sup>275</sup> adjacent to Thr<sup>274</sup> (Fig. 3). Interchange of Gln for Glu most likely alters the M-loop conformation, disrupts the network of M-loop hydrogen bonds from Arg<sup>278</sup> to Arg<sup>282</sup>, and thereby prevents epothilone binding. Finally, the present model also explains the Epo-resistant Ala231Thr mutation. Ala<sup>231</sup> is within hydrogen bonding contact of His<sup>227</sup>, which anchors epothilone in the binding pocket. As has been implied previously (16,

17), the introduction of the polar threonine is predicted to perturb the His anchor and compromise ligand binding.

Our binding model for EpoA accommodates a range of epothilone structure-activity data (6, 21). We show this with the use of six diverse bioactive modifications.

First, alkyl chain extension at C12 from methyl (EpoB) to hexyl does not eliminate *in vitro* activity, although in general methyl appears optimal for biological activity (22, 23). The observation also applies to the desoxy epothilone series in which large groups such as CH<sub>2</sub>OC(O)Ph continue to show considerable tubulin polymerizing capacity. The folded orientation of the epoxide (Fig. 1B) directs the C12 substituent into the underlying hydrophobic basin, which readily accepts long and bulky hydrophobic groups. The same observation applies to the epothilone cyclopropanes (24) and cyclobutanes (25) that exhibit high activity (fig. S8).

Second, a more subtle effect is shown by the recently reported epimers of 14-methyl-epothilones B and D (15, 22). The R and S configurations, respectively, exhibit antiproliferative activity against several cell lines that are slightly lower than the parent compounds (epothilones B and D). In contrast, the corresponding S and R configurations are completely inactive. In the bound EC conformation, the active pair directs the methyl group outside the ring into a region unoccupied by protein (Fig. 4). For the inactive pair in the same conformer, the S/R methyl points inward and experiences a severe steric clash with the CH<sub>2</sub> at C10. The associated 1.8 to 2.2 Å H-H distances prevent the molecule from adopting the bound form. For similar reasons, (S)-C10-methyl epothilone C is unable to adopt the bound conformer in accord with its lack of cytotoxicity (15). The model depicted in Fig. 4 predicts that the (R)-enantiomer is active.

Third, the OH at C3 [(3S)-configuration] was replaced with a cyano group in EpoB without substantially altering either the microtubule-stabilizing effect or cell cytotoxicity. Although the OH hydrogen bond to Thr<sup>274</sup> is lost, the extension of the C3 substituent by an additional 1.2 Å brings it within favorable H-bonding contact with the backbone NH of Arg<sup>276</sup> (Figs. 3 and 4). The tradeoff accounts for the near equipotency with EpoB. By contrast, the unnatural cyano epimer [(3R)-configuration] is 86 times less active in the tubulin polymerization assay (26). The inverted cyano group experiences no undue intra- or intermolecular steric repulsion in the EC model, and it likewise makes no productive contacts. C3-OH inversion would seriously perturb the hydrogen-bonding network shown in Fig. 3.

Fourth, the EC model accommodates active unsaturated Epo analogs. Already mentioned are the cis-EpoC and -EpoD com-

**Fig. 2.** Superposition of EpoA (blue, C; red, O) and T-Taxol (gold, C; red, O) in  $\beta$ -tubulin as determined by electron crystallography. Hydrogen atoms have been eliminated for clarity. Side chains terminating in aromatic rings occupy distinctly different regions of the binding site. The single common center (<1.1 Å) between the molecules is C7-OH (blue arrows). The image in (A) corresponds to a 90° rotation of the image in (B) about an axis approximately parallel to the blue side chain of EpoA. The alignment shown here without tubulin is identical to those structures shown in Figs. 1 and 3 and figs. S1 to S7.

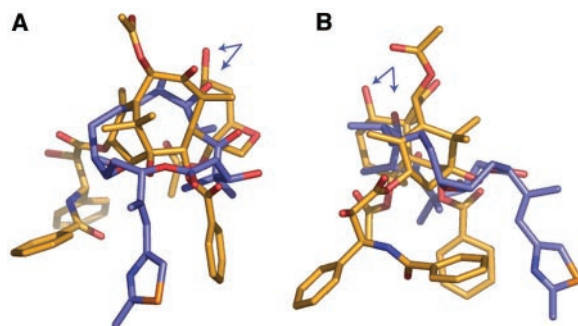
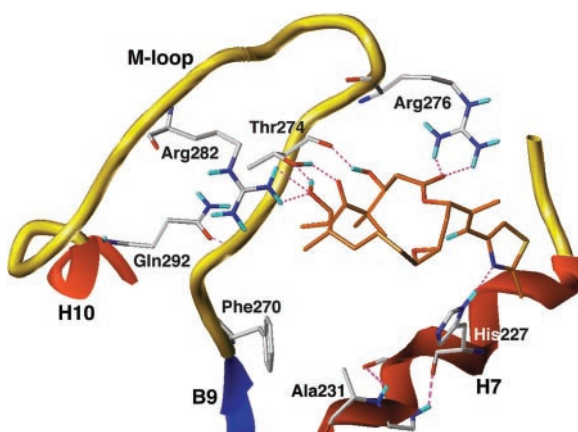


**Fig. 3.** Hydrogen bonding (violet) around EpoA in  $\beta$ -TB. Oxygens from C1 to C7 engage in network H bonds with M-loop residues. The thiazole is anchored by His<sup>227</sup>. Disruption of primary or secondary hydrogen bonds would occur upon mutation of Ala<sup>231</sup>, Thr<sup>274</sup>, Arg<sup>282</sup>, or Gln<sup>292</sup> to other residues as observed in epothilone-resistant cells. Protein secondary structure for helices is shown in red, sheets in blue, and loops in yellow. The protein side chains are colored by atom type: white, C; red, O; and blue, N. The EpoA ligand is colored by atom type: orange, C; red, O; blue, N; and yellow, S.



pounds. Conformational analysis for the corresponding trans-analog and docking into the binding site depicted in Fig. 1B assures that this isomer can participate in all key ligand-receptor interactions without steric congestion. Recent synthesis of second-generation epothilones targeted (E)-9,10-dehydro-12,13-desoxy-EpoB, a compound four times as active as desoxy-EpoB against several cell lines (27). The planar and trans C9–C10 center is naturally incorporated by the corresponding trans disposition of the saturated carbons in Figs. 1B and 4. The analog in which the C12 methyl is replaced by the relatively bulky  $\text{CF}_3$  is likewise as active as desoxy-EpoB. The folded epoxide directs this group comfortably into the occluded hydrophobic space. Finally, a slight conformational reorganization in the (E)-10,11-dehydro analog is compatible with both our binding model and the twofold reduction in activity relative to EpoA (28).

Fifth, a number of thiazole replacements have been shown to retain or improve epothilone activity. Specifically, Nicolaou and colleagues found that pyridines in which the nitrogen is ortho to the side chain connector are 10

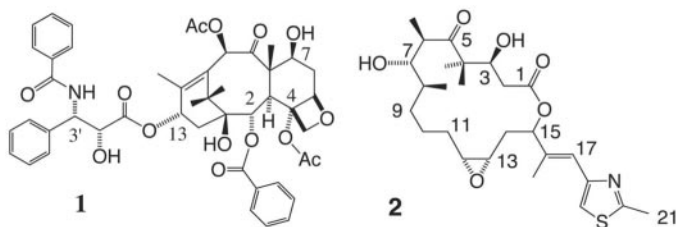
to 100 times more effective in cells than meta and para placement of the heteroatom (25, 29). Figs. 1 and 3 illustrate the origin of the effect to lie in hydrogen bonding of this group to His<sup>227</sup>. Other nitrogen placements are unable to anchor the side chain as illustrated. A particularly interesting set of analogs are Altman's benzoheterocycles, which result from fusion of the methyl at C16 to the terminal heterocycle (Fig. 4) (30). To maintain the H bond to His<sup>227</sup> in this set of analogs, the side chain of bound epothilone must position the C16 methyl and the C19 ring carbon in a syn orientation, and the nitrogen of the EpoB ring anti to the same methyl. The models depicted in Figs. 1 and 3 meet these requirements perfectly. A confirming experiment is the inactivity of a pyridine in which both nitrogen and a methyl substituent are ortho to the side chain connector. Maintenance of the H bond to His<sup>227</sup> would involve a severe steric clash between the pyridine methyl and that at C16. Obviously, the compound cannot adopt the proposed active conformation, consistent with its virtual inactivity against all cell lines (29). A particularly productive variation leading to an EpoB analog more active than the parent is replacement of the thiazole methyl at C21

with thiomethyl (SMe). In the present model, the SMe fits snugly into a small, shallow pocket unsuitable for larger substituents (Fig. 4). Accordingly, increased bulk diminishes activity (30).

Sixth, a series of active epoxide replacements in the form of aziridines has been prepared (31). For example, the bulky  $\text{NCOOC}_6\text{H}_5$  and  $\text{NCOC}_6\text{H}_5$  analogs show a tubulin polymerization and antiproliferative activity profile virtually identical to that of EpoB. The terminal phenyl rings are unlikely to be directed toward the surface of the protein exposed to water. Once again, the folded epoxide accommodates the observations by steering the N-substituent beneath the macrocyclic ring into the hydrophobic taxoid pocket (Fig. 4).

The SAR data described for the extended C12 substituents, epothilone cyclopropanes, and the aziridines suggests that the epothilone 16-membered ring and part of the side chain resides over a spacious but unfilled hydrophobic pocket on tubulin. Indeed, the present EpoA/tubulin model includes a generous cavity between the epothilone structure and the floor of the hydrophobic pocket surrounding Phe<sup>270</sup>. The cavity is likely filled with water molecules that are either displaced or reorganized upon binding by a substituted epothilone but are unobservable at  $\sim 3$  Å resolution.

In the EC model, EpoA that is bound to tubulin is anchored at two extremes by hydrogen bonds. C1=O, C3-OH, C5=O, and C7-OH on one flank of the molecule participate in a network of short contacts with Thr<sup>274</sup>, Arg<sup>278</sup>, and Arg<sup>282</sup>, residues on the M-loop, and nitrogen in the 10.5 Å distal thiazole ring serves as a proton acceptor for His<sup>227</sup> (Fig. 3). The remaining ligand-protein contacts are primarily hydrophobic, providing a tight surface-to-surface interaction from C3 to C11 (Fig. 1B). The Taxol-TB contacts are fundamentally different (fig. S6). The two phenyl C13 side chain termini and the C2' OH group associate with TB centers distant from epothilone (i.e., Ser<sup>234</sup>/Pro<sup>358</sup>, Val<sup>21</sup>, and Gly<sup>368</sup>, respectively), whereas the C2 and C3' phenyl groups sandwich His<sup>227</sup> in a three-ring stack (13), neither set of contacts is observed for epothilone. The ether oxygen of Taxol's oxetane ring interacts weakly with Thr<sup>274</sup> at one end of the M-loop, whereas an indirect hydrophobic chain to the other end operates by means of the C18 methyl. As mentioned above, the only notable common nonbonded contact for the two ligands appears to occur through C7-OH in each molecule. For Taxol, this affords a long and weak polar interaction with the C-OH of Thr<sup>274</sup>; for EpoA, it allows classic H bonds to Thr<sup>274</sup> and Arg<sup>284</sup>. Although M-loop arginines 278 and 282 in Taxol-TB are directed toward solvent (13), both have shifted by 6 to 8 Å in



Scheme 1.

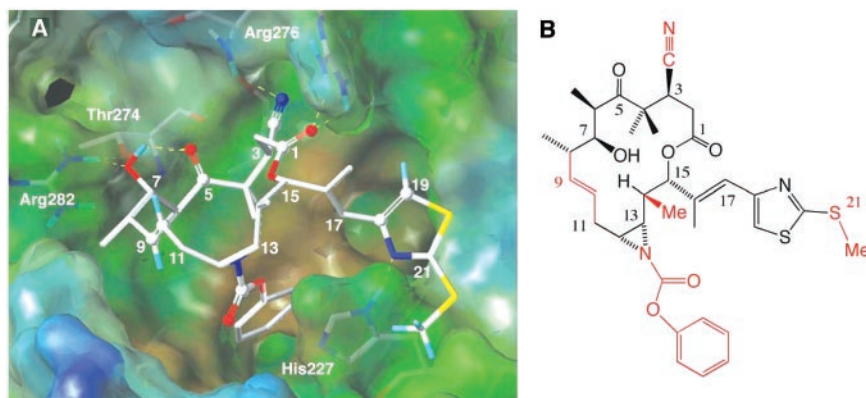


**Fig. 4.** An energy-optimized composite model of a fictionalized epothilone showing diverse features of the SARs in the context of the EC-derived model for TB and epothilone A. This single ligand structure docked into  $\beta$ -tubulin incorporates functional group modifications from five different analog studies that individually produced the same or better potency than epothilone A, including effects caused by changes of functionality at C3 (CN), C9–C10 (C=C), C12–C13 (N-Bz-aziridine), C14 ((S)-Me), and 21 (SMe). (A) The experimental conformation and binding mode of **1** in Figs. 1 to 3 used as a modeling template to illustrate geometric compatibility (C9=C10, C14-Me), hydrogen bonds (C3-CN), and hydrophobic complementarity (aziridine phenyl, S21-Me) for the five derivatives. Colors on the translucent protein surface range from brown (hydrophobic) to blue (hydrophilic). The ligand is colored by atom type: white, C; red, O; blue, N; and yellow, S. (B) Topological representation of the composite model; red corresponds to the five centers of substitution relative to epothilone A.



the Epo-TB complex so as to engage epothilone (Fig. 3). A similar arginine displacement (4 Å) has been observed in the binding of two epothilones to cytochrome P450-EpoK (32). The double arginine relocation reflects a subtle reorganization of M-loop residues not previously seen with taxanes, but both epothilone and Taxol bridge the M-loop and helix H7 adjacent to the nucleotide-binding site and thereby promote tubulin polymerization and microtubule stability.

Instead of a common pharmacophore (8–11), tubulin displays a promiscuous binding pocket with the bound molecules exploiting contacts with an optimal subset of binding pocket residues. Although this provides a unique challenge for “rational” ligand design, it can be anticipated that the promiscuity principle will apply to the binding of other ligands that occupy the taxane site on TB, namely, discodermolide, eleutherobin, and the sarcodictyins (33).

#### References and Notes

1. A. K. Singla, A. Garg, D. Aggarwal, *Int. J. Pharm.* **235**, 179 (2002).
2. M. M. Gottesman, *Annu. Rev. Med.* **53**, 615 (2002).

3. J. P. Guastalla, V. Diéras, *Br. J. Cancer* **89**, S16 (2003).
4. G. Höfle, N. Bedorf, K. Gerth, H. Reichenbach, *Chem. Abstr.* **120**, 52841 (1993).
5. D. Bollag et al., *Cancer Res.* **55**, 2325 (1995).
6. M. Wartmann, K. H. Altmann, *Curr. Med. Chem. Anti-Cancer Agents* **2**, 123 (2002).
7. S. Kar, J. Fan, M. J. Smith, M. Goedert, L. A. Amos, *EMBO J.* **22**, 70 (2003).
8. L. He et al., *Biochemistry* **39**, 3972 (2000).
9. P. Giannakakou et al., *Proc. Natl. Acad. Sci. U.S.A.* **97**, 2904 (2000).
10. M. Wang et al., *Org. Lett.* **1**, 43 (1999).
11. I. Ojima et al., *Proc. Natl. Acad. Sci. U.S.A.* **96**, 4256 (1999).
12. Materials and methods are available as supporting material on Science Online.
13. J. P. Snyder, J. H. Nettles, B. Cornett, K. H. Downing, E. Nogales, *Proc. Natl. Acad. Sci. U.S.A.* **98**, 5312 (2001).
14. T. Carlomagno et al., *Angew. Chem. Int. Ed. Engl.* **42**, 2511 (2003).
15. R. E. Taylor, Y. Chen, G. M. Galvin, P. K. Pabba, *Org. Biomol. Chem.* **2**, 127 (2004).
16. L. He, C.-P. H. Yang, S. B. Horwitz, *Mol. Cancer Ther.* **1**, 3 (2001).
17. N. M. Verrills et al., *Chem. Biol.* **10**, 597 (2003).
18. P. Giannakakou et al., *J. Biol. Chem.* **272**, 17118 (1997).
19. M. Wang, B. Cornett, J. Nettles, D. C. Liotta, J. P. Snyder, *J. Org. Chem.* **65**, 1059 (2000).
20. J. Lowe, H. Li, K. H. Downing, E. Nogales, *J. Mol. Biol.* **313**, 1045 (2001).
21. K. C. Nicolaou, F. Roschangar, D. Vourloumis, *Angew. Chem. Int. Ed. Engl.* **37**, 2014 (1998).

22. R. E. Taylor, Y. Chen, A. Beatty, D. C. Myles, Y. Zhou, *J. Am. Chem. Soc.* **125**, 26 (2003).
23. K. C. Nicolaou, A. Ritzén, K. Namoto, *Chem. Commun.* **2001**, 1523 (2001).
24. J. Johnson et al., *Org. Lett.* **2**, 1537 (2000).
25. K. C. Nicolaou et al., *J. Am. Chem. Soc.* **123**, 9313 (2001).
26. A. Regueiro-Ren et al., *Org. Lett.* **4**, 3815 (2002).
27. A. Rivkin et al., *J. Am. Chem. Soc.* **125**, 2899 (2003).
28. I. H. Hardt et al., *J. Nat. Prod.* **64**, 847 (2001).
29. K. C. Nicolaou et al., *Chem. Biol.* **7**, 593 (2000).
30. K. C. Nicolaou et al., *Angew. Chem. Int. Ed. Engl.* **42**, 3515 (2003).
31. A. Regueiro-Ren et al., *Org. Lett.* **3**, 2693 (2001).
32. S. Nagano et al., *J. Biol. Chem.* **278**, 44886 (2003).
33. J. Jimenez-Barbero, F. Amat-Guerri, J. P. Snyder, *Curr. Med. Chem. Anti-Cancer Agents* **2**, 91 (2002).
34. Supported in part by NIH and the Department of Energy. J.N., B.C., and J.P.S. thank D. Liotta (Emory University) for encouragement, discussion, and support during the course of the work. We thank P. Giannakakou, J. Gallivan, and D. Lynn (Emory University) for helpful discussions. Structure has been deposited in the Protein Data Bank under accession number 1TVK.

#### Supporting Online Material

www.sciencemag.org/cgi/content/full/305/5685/866/DC1

Materials and Methods

Figs. S1 to S8

References

15 April 2004; accepted 12 July 2004

## Multiple Rare Alleles Contribute to Low Plasma Levels of HDL Cholesterol

Jonathan C. Cohen,<sup>1,2,3,\*†</sup> Robert S. Kiss,<sup>5\*</sup>  
Alexander Pertsemlidis,<sup>1</sup> Yves L. Marcel,<sup>5†</sup> Ruth McPherson,<sup>5</sup>  
Helen H. Hobbs<sup>1,3,4</sup>

Heritable variation in complex traits is generally considered to be conferred by common DNA sequence polymorphisms. We tested whether rare DNA sequence variants collectively contribute to variation in plasma levels of high-density lipoprotein cholesterol (HDL-C). We sequenced three candidate genes (*ABCA1*, *APOA1*, and *LCAT*) that cause Mendelian forms of low HDL-C levels in individuals from a population-based study. Nonsynonymous sequence variants were significantly more common (16% versus 2%) in individuals with low HDL-C (<fifth percentile) than in those with high HDL-C (>95th percentile). Similar findings were obtained in an independent population, and biochemical studies indicated that most sequence variants in the low HDL-C group were functionally important. Thus, rare alleles with major phenotypic effects contribute significantly to low plasma HDL-C levels in the general population.

Many clinically important quantitative traits are highly heritable, but progress in the elucidation of their genetic architecture has been limited. Because quantitative traits do not segregate in Mendelian fashion in most families, their distribution in the population is presumed to reflect the cumulative contribution of multiple common DNA sequence variants that each has a small effect (1). Sequence variants with strong phenotypic effects may also contribute to variation in complex traits (2). Although these variants

are likely to be rare individually, they may be sufficiently common in aggregate to contribute to variation in common traits in the population. Whereas most Mendelian disorders are caused by a spectrum of different mutations in a gene (or genes) (3), the contribution of rare alleles to more common, quantitative traits has not been systematically evaluated.

In this study, we evaluated the hypothesis that rare sequence variations contribute significantly to low plasma levels of high-density lipoprotein cholesterol (HDL-C), a

major risk factor for coronary atherosclerosis. If this hypothesis is correct, then mutations that impair HDL production or enhance HDL catabolism should be significantly more common among individuals with low plasma levels of HDL-C than among those with high plasma levels of HDL-C. Furthermore, sequence variants with major phenotypic effects are likely to be found exclusively in one extreme or the other, whereas alleles found in both the high HDL-C and the low HDL-C groups are likely to be neutral with respect to plasma HDL-C levels. The prevalence of mutations with major effects on plasma HDL-C levels is not known. Molecular defects causing rare genetic forms of HDL deficiency have been identified in the genes encoding apolipoprotein AI (*APOA1*), the major protein component of HDL (4); the adenosine triphosphate binding cassette (ABC) transporter A1 (*ABCA1*), required for the efflux of cholesterol from cells to HDL particles (5); and lecithin cholesterol acyltransferase (*LCAT*), the enzyme that catalyzes the formation of

<sup>1</sup>Donald W. Reynolds Cardiovascular Clinical Research Center and McDermott Center for Human Growth and Development, <sup>2</sup>Center for Human Nutrition, <sup>3</sup>Department of Internal Medicine and Department of Molecular Genetics, <sup>4</sup>Howard Hughes Medical Institute, University of Texas Southwestern Medical Center, Dallas, TX, 75390, USA. <sup>5</sup>Lipoprotein and Atherosclerosis Research Group, University of Ottawa Heart Institute, Ottawa, Ontario K7Y4W7, Canada.

\*These authors contributed equally to this work.

†To whom correspondence should be addressed. E-mail: jonathan.cohen@utsouthwestern.edu (J.C.C.); ymarcel@ottawaheart.ca (Y.L.M.)

REPORTS

cholesteryl esters in HDL (6). Homozygotes for mutations in these genes have virtually no circulating HDL-C, whereas heterozygotes have about half the normal plasma level of HDL-C. Mutations in *ABCA1* have also been associated with a less severe form of familial hypoalphalipoproteinemia (7, 8), but systematic screening of these genes in population-based samples has not been reported.

To determine whether sequence variations in these three candidate genes contribute to low plasma levels of HDL-C in the general population, we sequenced the coding regions and consensus splice sites of each gene in 32 individuals from each of four gender and race groups [black men, white men, black women, and white women (table S1)] constituting the upper and lower 5% of the distribution of plasma HDL-C levels in a population-based study of Dallas County residents (9). Nonsynonymous sequence variations were significantly more common in the low HDL-C group than in the high HDL-C group (Table 1). Of the 128 individuals with low plasma levels of HDL-C, 21 (16%) had sequence variants not present in the high HDL-C group (Table 2). In contrast, only 3 (2%) of the individuals in the high HDL-C group had sequence variants not found in the low HDL-C group ( $P < 0.0001$ , Fisher's exact test). A total of 20 of the 21 mutant alleles found only in the low HDL-C group were in *ABCA1* (fig. S1) and two of these (W590S and N1800H) were previously identified in individuals with hypoalphalipoproteinemia (6).

Thus, one of six individuals with HDL-C levels below the fifth percentile in the Dallas Heart Study had a rare mutation in *ABCA1* or *APOA1*. Similar analyses were performed in a second sample comprising white Canadians who had either low (10 to 34 mg/dl) or high (58 to 116 mg/dl) levels of HDL-C (Table 3). A total of 21 (14%) of the 155 Canadians in the low HDL-C group had sequence variants that were not present in the 108 Canadians with a high plasma level of HDL-C. In contrast, only three individuals in the high HDL-C group (3%) had sequence variants not present in the low HDL-C group ( $P < 0.001$ , Fisher's exact test). Four sequence variants found in the Canadian low HDL-C group (*ABCA1* P85L, N1800H, S1731C, and R1851X) had been previously identified in subjects with hypoalphalipoproteinemia (10). One mutation (*ABCA1* N1800H) was found in both the Canadian and Dallas low HDL-C groups. In both Canadian and Dallas groups, almost all of the excess sequence variations in the low HDL-C group were in *ABCA1*. This may reflect the size of the coding sequence of *ABCA1*, which is three times larger than those of the other two genes; it is also possible that sequence changes occur more frequently at this locus or that mutations arising in *ABCA1* are more likely to persist in the population.

To test whether differences in population substructure between the low HDL-C and high

HDL-C groups contributed to the observed differences in the prevalence of rare sequence variants, we compared the frequency of synonymous substitutions in the high and low HDL-C groups. The frequency of synonymous substitutions was similar in the high HDL-C and low HDL-C groups in both the U.S. and Canadian populations (Table 1). Furthermore, the racial

composition of the low HDL-C and high HDL-C groups was matched. Thus, it is unlikely that the excess sequence variations in the low HDL-C group is attributable to either population stratification or chance variations in allele frequencies.

Analysis using a computer program [PolyPhen (11)] that predicts effects of amino acid changes on protein function (12) indicated that

**Table 1.** Sequence variations in the coding regions of *ABCA1*, *APOA1*, and *LCAT*. Values represent the numbers of sequence variants identified in 256 individuals from the Dallas Heart Study (DHS) (128 with low HDL-C and 128 with high HDL-C) and 263 Canadians (155 with low HDL-C and 108 with high HDL-C) (17). NS, nonsynonymous (nucleotide substitutions resulting in an amino acid change); S, synonymous (coding sequence substitutions that do not result in an amino acid change). GenBank accession numbers for DHS *ABCA1*, *APOA1*, and *LCAT* sequences are NM\_005502, NM\_000039, and NM\_000229, respectively.

	Sequence variants unique to one group				Sequence variants common to both groups	
	Low HDL-C		High HDL-C		NS	S
	NS	S	NS	S		
DHS						
<i>ABCA1</i>	14	6	2	5	10	19
<i>APOA1</i>	1	0	0	1	0	1
<i>LCAT</i>	0	1	1	0	1	1
Canadians						
<i>ABCA1</i>	14	2	2	3	7	5
<i>APOA1</i>	0	1	0	0	2	0
<i>LCAT</i>	6	1	0	0	0	0

**Table 2.** Nonsynonymous sequence variations in *ABCA1*, *APOA1*, and *LCAT* in Dallas Heart Study participants with low ( $n = 128$ ) or high ( $n = 128$ ) plasma HDL-C levels. The effect of each amino acid (18) substitution on protein function was predicted with the use of PolyPhen (11, 19). Substitutions affecting known functional residues in the protein or that resulted in large changes in surface accessibility or side chain volume of the affected amino acid were scored as probably damaging. Substitutions that negatively affected predicted transmembrane regions or that were predicted to have smaller effects on surface accessibility or side chain volume of the affected amino acid on the basis of inferred protein structure were scored as possibly damaging. Conservative substitutions at poorly conserved residues were scored as benign. NA, not applicable.

Nucleotide change	Amino acid change (18)	<i>n</i>	Race	Predicted effect
Low HDL-C <i>ABCA1</i>				
c.593C>A	S198X	1	Black	NA
c.742G>A	P248A	1	Black	Benign
c.1201A>C	K401Q	1	White	Benign
c.1769G>C	W590S*	1	Black	Probably damaging
c.1913G>A	R638Q	1	Black	Possibly damaging
c.2320A>T	T774S*	4	Black	Benign
c.2320A>T	E815G	1	White	Probably damaging
c.2444A>G	S1181F	1	White	Possibly damaging
c.3542C>T	R1341T	1	Black	Possibly damaging
c.4022G>C	S1376G	1	Black	Benign
c.4126A>G	R1615Q	1	Black	Possibly damaging
c.4844G>A	A1670T	1	Black	Possibly damaging
c.5008G>A	N1800H*	1	White	Possibly damaging
c.5398A>C	D2243E	4	Black	Benign
Low HDL-C <i>APOA1</i>				
c.152G>C	R51T	1	Black	Possibly damaging
Low HDL-C <i>LCAT</i>				
None				
High HDL-C <i>ABCA1</i>				
c.1486C>T	R496W	1	White	Probably damaging
c.5039G>A	R1680Q	1	White	Possibly damaging
High HDL-C <i>APOA1</i>				
None				
High HDL-C <i>LCAT</i>				
c.340G>A	V114M	1	Black	Benign

\*These sequence variations have been identified previously.



72% of the nonsynonymous sequence variants identified in the low HDL-C group were likely to adversely affect protein function. In a previous study (12), 69% of nonsynonymous mutations associated with a functional disorder were predicted to be damaging with the use of this algorithm, compared to 32% of nonsynonymous sequence variants identified in DNA samples from arbitrarily selected individuals. Thus, the proportion of nonsynonymous sequence variants predicted to be damaging in the low HDL-C groups with the use of PolyPhen was comparable to that obtained for disease-associated sequence variants (12, 13).

Biochemical measurement of cholesterol efflux rates in cells from Canadian subjects with nonsynonymous sequence variants in *ABCA1* provided further evidence that the sequence variants identified in this study were causally related to low plasma levels of HDL-C (Table 3). Eleven of 14 *ABCA1* sequence variants represented in the low HDL-C group were associated with cholesterol efflux rates that were two standard deviations or more below the mean value obtained in subjects with normal HDL-C levels [i.e.,  $\leq 38\%$  of total cellular cholesterol

per 2 hours (Table 3)]. Conversely, the cholesterol efflux was within the normal range in cells from two individuals in the high HDL-C group who had a missense mutation (Thr<sup>774</sup>→Pro<sup>774</sup>) in *ABCA1*. These findings are consistent with the notion that the excess of sequence variants in subjects with low HDL-C reflects an accumulation of damaging alleles in this group.

The results of this study provide direct evidence that rare variants contribute significantly to low plasma levels of HDL-C, a common quantitative trait. To determine whether any of the common sequence variants identified in this study influenced plasma levels of HDL-C, we tested for associations between sequence variations with frequencies  $> 10\%$  in at least one racial group and plasma levels of HDL-C in the Dallas Heart Study (table S1). Previously we showed that functionally significant sequence variations in *APOE* (14) and *APOA5* (15) are associated with plasma lipid levels in all four major gender and race groups in this population. In contrast to those results, we found no sequence variation in *ABCA1* that was systematically associated with plasma levels of HDL-C in men and women of both race groups

(table S2). Two sequence variants were associated with plasma HDL-C levels in two groups (white men and black men), but the effect of these variants on HDL-C levels was modest. For example, plasma HDL-C concentrations were  $52 \pm 17$  mg/dl in black men homozygous for the Met<sup>883</sup> allele of *ABCA1* and  $48 \pm 15$  mg/dl in homozygotes for the common allele (Ile<sup>883</sup>) at this locus. These data are consistent with haplotype analyses of the *ABCA1* gene (16) and with quantitative trait linkage mapping studies, which have not provided consistent support for common variants at any locus contributing to variation in plasma HDL-C levels. Nonetheless, our results do not exclude a role for common sequence variations in hypoalphalipoproteinemia. Because we screened primarily the coding sequences and flanking intronic regions of the three candidate genes, it is possible that common sequence variations in intronic or regulatory regions not sequenced in this study confer susceptibility to low plasma levels of HDL-C. Alternatively, specific haplotypes or combinations of alleles at these loci or common sequence variants at other loci may contribute to low plasma HDL-C levels.

The strategy used in this study can be generalized to analyze the relationships between sequence variations in candidate genes and other quantitative traits in humans. Screening individuals with low or high levels of a trait increases the likelihood of detecting functionally significant sequence variations. Comparison of the numbers of sequence variants found in individuals with trait levels at opposite ends of the distribution provides a method to assess the significance of the variants identified, including rare variants that are unlikely to be detected by haplotype-based association studies. The method is unbiased, because the selection of individuals has its basis solely in their phenotype and has the added advantage of not requiring ascertainment of families.

**Table 3.** Nonsynonymous sequence variations in *ABCA1*, *APOA1*, and *LCAT* in white Canadians with low ( $n = 155$ ) or high ( $n = 108$ ) plasma HDL-C levels. Cholesterol efflux data for the controls is the mean  $\pm$  SD. ND, not done; NA, not applicable. Functional effects of amino acid substitutions were estimated as described in the legend to Table 2.

Nucleotide change	Amino acid change (18)	n	Predicted effect	Cholesterol efflux (% of total cellular cholesterol/2 hours)
Low HDL-C <i>ABCA1</i>				
c.254C>T	P85L*	1	Probably damaging	0.8
c.917G>A	R306H	1	Benign	ND
c.1375A>C	T459P	1	Possibly damaging	0.28
c.1651C>G	H551D	1	Probably damaging	0.32
c.1769G>T	W590L	1	Probably damaging	0.31
c.2893T>C	R965C	1	Probably damaging	0.59
c.3077T>C	L1026P	1	Benign	0.25
c.3966G>A	W1322X	1	NA	0.38
c.4156G>C	E1386Q	1	Benign	0.51
c.4430G>T	C1477F	1	Probably damaging	0.34
c.5116G>A	D1706N	1	Possibly damaging	0.38
c.5192C>G	S1731C*	1	Possibly damaging	0.28
c.5398A>G	N1800H*	1	Possibly damaging	0.27
c.5864C>T	R1851X*	1	NA	0.26
c.6217A>G	T2073A	1	Possibly damaging	0.28
Controls ( $n = 46$ )				0.52 $\pm$ 0.07
Low HDL-C <i>APOA1</i>				
None				
Low HDL-C <i>LCAT</i>				
c.167T>C	L56P	1	Possibly damaging	ND
c.254G>A	W85X	1	NA	ND
c.382G>A	G128S	1	Probably damaging	ND
c.463A>G	N155D	1	Possibly damaging	ND
c.901G>A	D301N	1	Benign	ND
c.1103G>T	G396V	1	Probably damaging	ND
High HDL-C <i>ABCA1</i>				
c.1664A>C	K555T	1	Benign	ND
c.2320A>C	T774P*	2	Benign	0.63/0.57
High HDL-C <i>APOA1</i>				
None				
High HDL-C <i>LCAT</i>				
None				

\*These sequence variations have been identified previously.

**References and Notes**

1. K. E. Lohmueller, C. L. Pearce, M. Pike, E. S. Lander, J. N. Hirschhorn, *Nat. Genet.* **33**, 177 (2003).
2. J. K. Pritchard, *Am. J. Hum. Genet.* **69**, 124 (2001).
3. D. E. Reich, E. S. Lander, *Trends Genet.* **17**, 502 (2001).
4. G. Assmann, A. von Eckardstein, H. Funke, *Circulation* **87**, III28 (1993).
5. M. R. Hayden et al., *Curr. Opin. Lipidol.* **11**, 117 (2000).
6. J. A. Kuivenhoven et al., *J. Lipid Res.* **38**, 191 (1997).
7. G. K. Hovingh et al., *J. Lipid Res.* **44**, 1251 (2003).
8. S. Mott et al., *Atherosclerosis* **152**, 457 (2000).
9. R. G. Victor et al., *Am. J. Cardiol.* **93**, 1473 (2004).
10. R. R. Singaraja, L. R. Brunham, H. Visscher, J. J. Kastelein, M. R. Hayden, *Arterioscler. Thromb. Vasc. Biol.* **23**, 1322 (2003).
11. Information about this program is available at [www.bork.embl-heidelberg.de/PolyPhen/](http://www.bork.embl-heidelberg.de/PolyPhen/).
12. S. Sunyaev et al., *Hum. Mol. Genet.* **10**, 591 (2001).
13. V. Ramensky, P. Bork, S. Sunyaev, *Nucleic Acids Res.* **30**, 3894 (2002).
14. J. C. Cohen, H. H. Hobbs, unpublished observation.
15. L. A. Pennacchio et al., *Hum. Mol. Genet.* **11**, 3031 (2002).
16. D. A. Tregouet et al., *Arterioscler. Thromb. Vasc. Biol.* **24**, 775 (2004).
17. Details of each sequence variant are provided at <http://pga.swmed.edu>.
18. Single-letter abbreviations for the amino acid resi-

dues are as follows: A, Ala; C, Cys; D, Asp; E, Glu; F, Phe; G, Gly; H, His; I, Ile; K, Lys; L, Leu; M, Met; N, Asn; P, Pro; Q, Gln; R, Arg; S, Ser; T, Thr; V, Val; W, Trp; and Y, Tyr.  
 19. A detailed explanation of PolyPhen scoring criteria is available at [http://tux.embl-heidelberg.de/ramensky/doc/pph\\_help.html](http://tux.embl-heidelberg.de/ramensky/doc/pph_help.html).  
 20. We thank R. Wilson, S. Niu, and J. Horton for DNA sequencing; J. Schageman, N. Prikhodko, and A.

Patel for analysis of the sequence data; and M. Brown, J. Goldstein, and S. Sunyaev for helpful discussions. This study was supported by grants from NIH (HL53917), National Heart, Lung, and Blood Institute Program for Genomic Applications (UO1-HL66880), Fondation Le Ducq, Heart and Stroke Foundation of Canada, and Canadian Institutes of Health Research (64519, CIHR-RD, and DOP-51714).

**Supporting Online Material**  
[www.sciencemag.org/cgi/content/full/305/5685/869/DC1](http://www.sciencemag.org/cgi/content/full/305/5685/869/DC1)  
 Materials and Methods  
 Fig. S1  
 Tables S1 and S2

3 May 2004; accepted 12 July 2004

# HLA and NK Cell Inhibitory Receptor Genes in Resolving Hepatitis C Virus Infection

Salim I. Khakoo,<sup>1\*</sup> Chloe L. Thio,<sup>2</sup> Maureen P. Martin,<sup>3</sup> Collin R. Brooks,<sup>1</sup> Xiaojiang Gao,<sup>3</sup> Jacquie Astemborski,<sup>2</sup> Jie Cheng,<sup>3</sup> James J. Goedert,<sup>4</sup> David Vlahov,<sup>5</sup> Margaret Hilgartner,<sup>6</sup> Steven Cox,<sup>7</sup> Ann-Margeret Little,<sup>7</sup> Graeme J. Alexander,<sup>8</sup> Matthew E. Cramp,<sup>9</sup> Stephen J. O'Brien,<sup>10</sup> William M. C. Rosenberg,<sup>1</sup> David L. Thomas,<sup>2</sup> Mary Carrington<sup>3\*</sup>

Natural killer (NK) cells provide a central defense against viral infection by using inhibitory and activation receptors for major histocompatibility complex class I molecules as a means of controlling their activity. We show that genes encoding the inhibitory NK cell receptor KIR2DL3 and its human leukocyte antigen C group1 (HLA-C1) ligand directly influence resolution of hepatitis C virus (HCV) infection. This effect was observed in Caucasians and African Americans with expected low infectious doses of HCV but not in those with high-dose exposure, in whom the innate immune response is likely overwhelmed. The data strongly suggest that inhibitory NK cell interactions are important in determining antiviral immunity and that diminished inhibitory responses confer protection against HCV.

Natural killer (NK) cells are key components of the innate antiviral immune response. In vivo, they are under the constitutively dominant influence of inhibitory receptors for self-MHC class I ligands (1, 2), such that effector functions occur only when activating signals overcome inhibitory signals (3, 4). The killer cell immunoglobulin-like receptors (KIR) represent a diverse family of activating and inhibitory receptors that are integral in this model. As with their MHC class I ligands, the population diversity and rapid evolution of

the KIR genes strongly suggests that they are under pathogen-mediated selection (5–7). KIR haplotypes vary in number and type of genes present, and because HLA and KIR map to separate chromosomes, some individuals lack specific KIR-HLA receptor-ligand pairings. To date, only activating KIR have been associated with disease outcome (8–10), whereas the influence of inhibitory KIR on disease is undetermined. Hepatitis C virus (HCV) is a common infection worldwide, causing cirrhosis and hepatocellular carcinoma. About 20% of individuals

resolve acute infection, an outcome associated with specific components of the adaptive immune system (11), including HLA class I (12). Because resolution of HCV infection may also involve the innate immune system, including NK cells (13, 14), we examined the possible synergistic influence that corresponding KIR-HLA combinations might have on the outcome of HCV infection.

Individuals who were exposed to HCV (685 with persistent and 352 with resolved infection) (table S1, A to C) were categorized according to their KIR-binding motifs based on HLA-B and -C genotyping data (15). Group 1 HLA-C (HLA-C1) allotypes have asparagine at residue 80 and are ligands for the inhibitory receptors KIR2DL2 and KIR2DL3, which segregate as alleles of a single locus (Table 1). The remaining HLA-C allotypes (group 2, HLA-C2) have

<sup>1</sup>Liver Group, Division of Infection, Inflammation, and Repair, Southampton University, Southampton 5016 6YD, UK. <sup>2</sup>Department of Medicine, Johns Hopkins Medical Institutions, Baltimore, MD 21231, USA. <sup>3</sup>Basic Research Program, Scientific Applications International Corporation Frederick, Inc., Laboratory of Genomic Diversity, NCI Frederick, Frederick, MD 21702, USA. <sup>4</sup>Viral Epidemiology Branch, Division of Cancer Epidemiology and Genetics, National Cancer Institute, Rockville, MD 20852, USA. <sup>5</sup>New York Academy of Medicine, New York, NY 10029, USA. <sup>6</sup>Department of Pediatrics, New York Presbyterian Hospital–Cornell Medical Center, New York, NY 10021, USA. <sup>7</sup>Anthony Nolan Research Institute, The Royal Free Hospital, London NW3 2PF, UK. <sup>8</sup>Department of Medicine, University of Cambridge, Cambridge CD2 2QQ, UK. <sup>9</sup>Department of Gastroenterology, Derriford Hospital, Plymouth PL6 8DH, UK. <sup>10</sup>Laboratory of Genomic Diversity, National Cancer Institute, Frederick, MD 21702, USA.

\*To whom correspondence should be addressed: E-mail: [carringt@ncifcrf.gov](mailto:carringt@ncifcrf.gov) (M.C.); [sik@soton.ac.uk](mailto:sik@soton.ac.uk) (S.I.K.)

**Table 1.** Frequency of KIR and HLA receptor-ligand pairings in the population studied, stratified by race, study site, and route of infection.

	N	KIR2DL1- HLA-C2 N (%)	KIR2DL2- HLA-C1 N (%)	KIR2DL3- HLA-C1 N (%)	KIR2DS1- HLA-C2 N (%)	KIR2DS2- HLA-C1* N (%)	KIR3DL1- HLA-Bw4 N (%)	KIR3DS1- HLA-Bw4* N (%)
All	1037	689 (66.4)	591 (57.0)	754 (72.7)	231 (22.3)	441 (42.5)	635 (61.2)	216 (20.8)
				Race†				
UK Caucasian	340	219 (64.4)	144 (42.4)	271 (79.7)	78 (22.9)	144 (42.3)	205 (60.1)	83 (24.4)
USA Caucasian	355	220 (62.0)	163 (45.9)	265 (74.6)	88 (24.8)	167 (47.0)	205 (57.7)	89 (25.1)
USA African-American	271	205 (75.6)	108 (39.9)	166 (61.3)	47 (17.3)	99 (36.5)	188 (69.4)	31 (11.4)
USA other	69	44 (63.8)	30 (43.5)	52 (75.4)	17 (24.6)	30 (43.5)	35 (50.7)	12 (17.4)
				Route				
No blood products	543	372 (68.5)	229 (42.2)	382 (70.3)	115 (21.2)	222 (40.9)	344 (63.3)	105 (19.3)
Blood products	494	317 (64.2)	217 (43.9)	372 (75.3)	116 (23.5)	219 (44.3)	291 (59.0)	111 (22.5)

\*Receptor ligand pairing inferred by protein sequence but not directly demonstrated. †Excludes two non-Caucasian individuals from the United Kingdom.



lysine at position 80 and are ligands for KIR2DL1 (an inhibitory receptor) and KIR2DS1 (the homologous activating receptor). HLA-B Bw4 allotypes serve as ligands for KIR3DL1.

The frequency of individuals with two copies of *HLA-C1* alleles (*HLA-C1C1*) was higher in the group that had resolved infection (37.5%) relative to those with persistent infection (29.9%) ( $P = 0.01$ ; OR = 1.40). The reciprocal association of two *HLA-C2* alleles (*HLA-C2C2*) with viral persistence (14.5% in resolved versus 20.2% in persistent infection) was also observed ( $P = 0.02$ ; OR = 0.67) (Table 2). The frequency of *HLA-B Bw4* alleles did not differ significantly between the groups.

Although both KIR2DL3 and KIR2DL2 bind HLA-C1 allotypes, KIR2DL2 binds HLA-C1 with greater affinity than does KIR2DL3 (16). We hypothesized that a weaker inhibitory

receptor-ligand (KIR2DL3-HLA-C1) interaction would be protective, because it should be more easily overridden by activating signals than a stronger inhibitory interaction such as KIR2DL2-HLA-C1 or KIR2DL1-HLA-C2. Consistent with this model, the protective association of *HLA-C1C1* was significant only among individuals homozygous for *KIR2DL3* ( $P = 0.003$ ; OR = 1.71) and not among *KIR2DL2/KIR2DL3* heterozygotes or *KIR2DL2* homozygotes (Table 2). Thus, the presence of *KIR2DL2* appears to counteract *KIR2DL3-HLA-C1C1* protection. Further, *KIR2DL3* did not associate with HCV resolution in individuals who were lacking *HLA-C1C1*, which indicates a synergistic protective effect between *HLA-C1C1* and *KIR2DL3/KIR2DL3*, as opposed to additive, independent effects of each. All individuals in this study have at least one copy of *KIR2DL1*, so it was not possible to determine

whether the susceptible *HLA-C2C2* effect is independent of *KIR2DL1*. Neither *KIR2DS2* nor *KIR2DS1*, activating receptors with high sequence similarity to *KIR2DL2/KIR2DL3* and *KIR2DL1*, respectively, were associated with HCV resolution, but *KIR3DS1* displayed a weak protective effect in combination with *HLA-B Bw4+* alleles ( $P = 0.04$ ; OR = 1.39).

Resistance to murine cytomegalovirus infection is dependent on the NK cell receptor Ly49H (17) and can be overcome by increasing the size of the infecting inoculum (18). To investigate whether a similar dose-response relation could be detected with HCV infection, individuals were stratified by the expected inoculum size, assuming that individuals who contract HCV by transfusion of either blood or concentrated blood products ( $N = 494$ ) receive larger inocula than those infected by injection drug use and needle-stick injuries (nontransfused) ( $N = 543$ ) (table S1B) (19, 20).

Among nontransfused individuals, 20.4% of those resolving infection had the compound genotype *KIR2DL3/KIR2DL3-HLA-C1C1*, as compared with 9.9% with persistent infection ( $P = 0.001$ ; OR = 2.33) (Table 3). Further, homozygosity for *HLA-C1* was protective only among individuals who were homozygous for *KIR2DL3* ( $P = 0.0001$ ; OR = 3.01) but not in those with one or no *KIR2DL3* genes ( $P = 0.6$  and  $P = 0.3$ , respectively) (Table 4). Protection conferred by *KIR2DL3/KIR2DL3-HLA-C1C1* was stronger than any other *KIR-HLA* combination tested, indicating a direct, primary effect of this genotype on HCV clearance (tables S2 and S3). Alternatively, *KIR2DL3/KIR2DL3-HLA-C1C1* showed no protection among transfused individuals.

*KIR2DL3/KIR2DL3-HLA-C1C1* protection was observed in both nontransfused Caucasians and African Americans. Among Caucasians homozygous for *KIR2DL3* ( $N = 145$ ), 21.7% of persistently infected versus 49.1% of resolved individuals were *HLA-C1C1* ( $P = 0.0009$ ; OR = 3.47), as compared with 20.6% versus 36.4%, respectively, in African Americans ( $N = 106$ ;  $P = 0.096$ ; OR = 2.21). Although the protective effect did not reach significance in African Americans, the consistent trends across racial groups further suggest that a synergistic interaction between *KIR2DL3* and *HLA-C1* directly confers protection against HCV, rather than indirectly through linkage disequilibrium with neighboring loci.

Multiple variable logistic regression analyses of variables that were significant ( $p < 0.05$ ) in univariate analysis supported a protective effect of *HLA-C1C1* only in the context of *KIR2DL3* homozygosity and only among nontransfused individuals ( $P = 0.001$ ; OR = 2.24) (Table 5). Conversely, the adverse effect of *HLA-C2C2* alone and in combination with *KIR2DL1* was no longer significant, suggesting that its effect in univariate analysis derives from the absence of protective *HLA-C1* alleles. The weak effect of *KIR3DS1-Bw4* persisted, ap-

**Table 2.** *HLA-C* and *KIR-HLA-C* interactions are associated with resolution of HCV infection. Frequencies of *HLA-C* and *KIR-HLA-C* combinations among individuals with resolved and persistent HCV infection from all individuals combined are shown. *HLA-C1C1* indicates two group 1 *HLA-C* alleles, *HLA-C2C2* indicates two group 2 *HLA-C* alleles, and *HLA-C1C2* indicates one of each. *P* values were calculated by using the chi-square test from two-by-two contingency tables; a positive odds ratio indicates a protective association with resolution of infection.

Genetic factor	Frequency resolved N (%) N = 348–352	Frequency persistent N (%) N = 681–685	OR	95% CI	<i>P</i>
<i>HLA-C1C1</i>	132 (37.5)	205 (29.9)	1.40	1.07–1.84	0.01
<i>HLA-C1C2</i>	169 (48.0)	342 (49.9)	0.93	0.72–1.20	0.6
<i>HLA-C2C2</i>	51 (14.5)	138 (20.2)	0.67	0.47–0.95	0.02
<i>2DL2+ HLA-C1C1</i>	64 (18.2)	121 (17.7)	1.04	0.74–1.45	0.9
<i>2DL3+ HLA-C1C1</i>	119 (33.9)	182 (26.7)	1.41	1.06–1.86	0.02
<i>2DS2+ HLA-C1C1</i>	64 (18.2)	120 (17.5)	1.05	0.75–1.46	0.9
<i>2DL1+ HLA-C2C2</i>	50 (14.2)	135 (19.7)	0.68	0.47–0.96	0.03
<i>2DS1+ HLA-C2C2</i>	22 (6.3)	32 (4.7)	1.36	0.78–2.37	0.3
<i>3DS1+HLA-Bw4</i>	86 (24.7)	130 (19.1)	1.39	1.02–1.90	0.04
<i>2DL2/2DL2+ HLA-C1C1</i>	11 (3.1)	23 (3.4)	0.93	0.45–1.92	1.00
<i>2DL2/2DL3+ HLA-C1C1</i>	52 (14.8)	98 (14.4)	1.03	0.72–1.49	0.9
<i>2DL3/2DL3+ HLA-C1C1</i>	68 (19.4)	84 (12.3)	1.71	1.20–2.42	0.003
<i>2DL3/2DL3+ HLA-C1C2</i>	82 (23.3)	165 (24.2)	0.95	0.70–1.29	0.8
<i>2DL3/2DL3+ HLA-C2C2</i>	21 (6.0)	73 (10.7)	0.53	0.32–0.88	0.01

**Table 3.** Comparison of the frequencies of *HLA-C* and *KIR-HLA-C* combinations in individuals, stratified by history of transfusion of blood or plasma products. Definitions and calculations as for Table 2.

Genetic factor	Frequency resolved N (%)	Frequency persistent N (%)	OR	95% CI	<i>P</i>
Nontransfusion	N = 185–187	N = 353–356			
<i>HLA-C1C1</i>	72 (38.5)	93 (26.1)	1.77	1.21–2.58	0.003
<i>HLA-C1C2</i>	85 (45.4)	180 (50.6)	0.81	0.57–1.16	0.3
<i>HLA-C2C2</i>	30 (16.0)	83 (23.3)	0.63	0.40–1.00	0.06
<i>2DL2/2DL2+ HLA-C1C1</i>	3 (1.6)	14 (4.0)	0.40	0.11–1.40	0.2
<i>2DL2/2DL3+ HLA-C1C1</i>	30 (16.1)	44 (12.5)	1.35	0.82–2.23	0.2
<i>2DL3/2DL3+ HLA-C1C1</i>	38 (20.4)	35 (9.9)	2.33	1.42–3.85	0.001
Transfusion	N = 165	N = 328–329			
<i>HLA-C1C1</i>	60 (36.3)	112 (34.0)	1.11	0.75–1.63	0.6
<i>HLA-C1C2</i>	84 (50.9)	162 (49.2)	1.07	0.74–1.55	0.8
<i>HLA-C2C2</i>	21 (12.7)	55 (16.7)	0.73	0.42–1.25	0.3
<i>2DL2/2DL2+ HLA-C1C1</i>	8 (4.85)	9 (2.74)	1.81	0.68–4.77	0.3
<i>2DL2/2DL3+ HLA-C1C1</i>	22 (13.3)	54 (16.5)	0.78	0.46–1.33	0.4
<i>2DL3/2DL3+ HLA-C1C1</i>	30 (18.2)	49 (14.9)	1.27	0.77–2.08	0.4

REPORTS

pearing to be independent of *KIR2DL3/KIR2DL3-HLA-C1C1* (Table 5). The *KIR-HLA* associations detected in HCV resolution were not affected by hepatitis B virus (HBV) infection or human immunodeficiency virus (HIV) infection [both previously associated with differential HCV recovery (21)], age, or sex; correspondingly, the associations were more significant in the UK cohort, which contained a lower proportion of transfused individuals.

*KIR* are clonally expressed on NK cells in a stochastic manner such that each NK cell clone expresses only a portion of the genes within the genetic profile (2, 22). Thus, homozygotes for *KIR2DL3* will have more NK cells solely under the inhibitory control of *KIR2DL3* than will *KIR2DL2/KIR2DL3* heterozygotes. Similarly, individuals who have the *HLA-C1C1* genotype

(and are therefore missing the HLA-C2 ligand for *KIR2DL1*) will have more NK cells under the inhibitory control of *KIR2DL3* than individuals who have the *HLA-C1C2* genotype, in whom a proportion of NK cells will be inhibited by *KIR2DL1* (an inhibitory receptor that is present in virtually all individuals). Consistent with this thesis, we observed a linear trend between the number of *KIR2DL3-HLA-C1* interactions and the odds of resolving infection ( $\chi^2$  for trend = 12.33;  $P = 0.0004$ ) (Fig. 1).

In this quantitative model, protective NK cell activity may be mediated through weak inhibitory *KIR2DL3-HLA-C1* interactions (i.e., the lack of strong NK cell inhibition), perhaps in combination with one of the many nonvariable NK cell activating receptors (23). The protection was observed only among individuals presumably be-

ceiving low-dose HCV inocula, which suggests that the difference in the ability of distinct *KIR-HLA* genotypes to regulate NK cell activity is great enough to alter the outcome when faced with low-dose, but not high-dose, infection. The beneficial effect of lower inhibitory signals in HCV infection is consistent with other disease models in which activating interactions are advantageous against HIV disease (9) but disadvantageous in autoimmune disease (8, 10). In light of the protection conferred by *KIR2DL3-HLA-C1* against HCV, the known conservation of the MHC-C1 motif across primate species (24) may indicate a selective advantage of this genotype against viral disease in general.

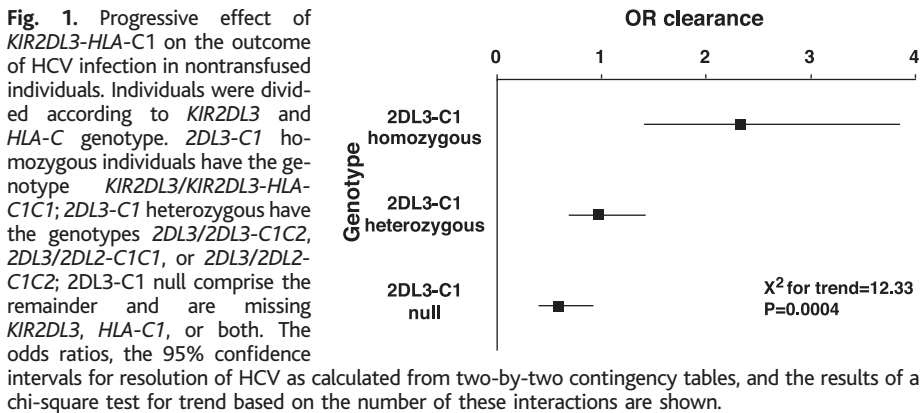


**Table 4.** Frequency of *HLA-C1C1* among nontransfused individuals stratified according to *KIR2DL2* and *KIR2DL3* genotype. Definitions and calculations as for Table 2.

<i>KIR</i> genotype	Frequency <i>HLA-C1C1</i>		OR	95% CI	<i>P</i>
	Resolved N (%)	Persistent N (%)			
<i>2DL2/2DL2</i> (N = 57)	3 (18.6)	14 (34.5)	0.45	0.11–1.83	0.3
<i>2DL2/2DL3</i> (N = 223)	30 (36.1)	44 (31.3)	1.24	0.70–2.19	0.6
<i>2DL3/2DL3</i> (N = 258)	38 (43.7)	35 (20.5)	3.01	1.72–5.29	0.0001

**Table 5.** *HLA-C1C1* protection is present only in the context of *KIR2DL3* homozygosity. Multiple variable logistic regression analyses of the effect of *KIR* and *HLA* effects in the resolution of HCV infection demonstrate that the protective effect of *HLA-C1C1* is due to its epistatic interaction with *KIR2DL3* and that this effect is present only among nontransfused individuals. Analysis was performed by stepwise logistic regression with the PROC LOGISTIC procedure (15), with the variables *KIR2DL3/KIR2DL3-HLA-C1C1*, *HLA-C1C1* (without *KIR2DL3/KIR2DL3*), *HLA-C2C2*, and *KIR3DS1-Bw4*.

Group	Genotype	OR	95% CI	<i>P</i>
All (N = 1023)	<i>HLA-C1C1</i>	1.05	0.73–1.50	0.80
	<i>HLA-C2C2</i>	0.75	0.51–1.08	0.12
	<i>2DL3/2DL3+ HLA-C1C1</i>	1.75	1.21–2.55	0.003
	<i>KIR3DS1-Bw4</i>	1.49	1.09–2.04	0.01
No transfusion (N = 533)	<i>HLA-C1C1</i>	1.2	0.73–1.98	0.48
	<i>HLA-C2C2</i>	0.78	0.48–1.28	0.33
	<i>2DL3/2DL3+ HLA-C1C1</i>	2.42	1.42–4.13	0.001
	<i>KIR3DS1-Bw4</i>	1.55	0.99–2.41	0.06
Transfusion (N = 490)	<i>HLA-C1C1</i>	0.92	0.55–1.53	0.24
	<i>HLA-C2C2</i>	0.71	0.40–1.26	0.75
	<i>2DL3/2DL3+ HLA-C1C1</i>	1.28	0.75–2.18	0.36
	<i>KIR3DS1-Bw4</i>	1.45	0.93–2.26	0.11

References and Notes

- H. G. Ljunggren, K. Karre, *Immunol. Today* **11**, 237 (1990).
- N. M. Valiante et al., *Immunity* **7**, 739 (1997).
- S. Bauer et al., *Science* **285**, 727 (1999).
- K. Karre, H. G. Ljunggren, G. Piontek, R. Kiessling, *Nature* **319**, 675 (1986).
- K. L. Hershberger, R. Shyam, A. Miura, N. L. Letvin, *J. Immunol.* **166**, 4380 (2001).
- S. I. Khakoo et al., *Immunity* **12**, 687 (2000).
- M. Uhrberg et al., *Immunity* **7**, 753 (1997).
- M. P. Martin et al., *J. Immunol.* **169**, 2818 (2002).
- M. P. Martin et al., *Nature Genet.* **31**, 429 (2002).
- J. H. Yen et al., *J. Exp. Med.* **193**, 1159 (2001).
- V. Racanelli, B. Rehermann, *Trends Immunol.* **24**, 456 (2003).
- C. L. Thio et al., *J. Virol.* **76**, 4792 (2002).
- S. Crotta et al., *J. Exp. Med.* **195**, 35 (2002).
- C. B. Bigger, K. M. Brasky, R. E. Lanford, *J. Virol.* **75**, 7059 (2001).
- Materials and methods are available as supporting material on Science Online.
- C. Winter, J. E. Gumperz, P. Parham, E. O. Long, N. Wagtmann, *J. Immunol.* **161**, 571 (1998).
- H. Arase, E. Mocarski, A. E. Campbell, A. B. Hill, L. L. Lanie Science **296**, 1323 (2002).
- A. A. Scalzo, N. A. Fitzgerald, A. Sim, G. R. Shellam, *J. Exp. Med.* **171**, 1469 (1990).
- P. Simmonds et al., *Lancet* **336**, 1469 (1990).
- Z. P. Guo, M. W. Yu, *Transfusion* **35**, 112 (1995).
- D. L. Thomas et al., *JAMA* **284**, 450 (2000).
- H. G. Shilling et al., *J. Immunol.* **169**, 239 (2002).
- F. Colucci, J. P. Di Santo, P. J. Leibson, *Nature Immunol.* **3**, 807 (2002).
- E. J. Adams, G. Thomson, P. Parham, *Immunogenetics* **49**, 865 (1999).

We would like to acknowledge the many individuals who assisted in collecting samples, the research participants, health care providers, and P. Karacki and J.-H. Lee for technical assistance. This publication has been funded in part with funds from the National Cancer Institute, National Institutes of Health, under contracts NO1-CO-12400, NO1-CP-33002, and NO1-CP-01004; NIH grants DA00441, DA04334, and DA13324; the Bureau of Maternal and Child Health and Resources Development (MCJ-060570); the National Institute of Child Health and Human Development (NO1-HD-4-3200); the Centers for Disease Control and Prevention; the National Institute of Mental Health; the Medical Research Council (UK); Hope Charity; and the National Health Service (UK) research and development program. The content of this publication does not necessarily reflect the views or policies of the U.S. Department of Health and Human Services, nor does mention of trade names, commercial products, or organizations imply endorsement by the U.S. government.

Supporting Online Material

www.sciencemag.org/cgi/content/full/305/5685/872/DC1  
Materials and Methods  
Figs. S1 and S2  
Tables S1 to S3  
References

8 March 2004; accepted 25 June 2004



# That's My Hand! Activity in Premotor Cortex Reflects Feeling of Ownership of a Limb

H. Henrik Ehrsson,<sup>1\*</sup> Charles Spence,<sup>2</sup> Richard E. Passingham<sup>1,2</sup>

When we look at our hands, we immediately know that they are part of our own body. This feeling of ownership of our limbs is a fundamental aspect of self-consciousness. We have studied the neuronal counterparts of this experience. A perceptual illusion was used to manipulate feelings of ownership of a rubber hand presented in front of healthy subjects while brain activity was measured by functional magnetic resonance imaging. The neural activity in the premotor cortex reflected the feeling of ownership of the hand. This suggests that multisensory integration in the premotor cortex provides a mechanism for bodily self-attribution.

The experience that the body is part of the self is critical for our daily interaction with the outside world and is a fundamental aspect of self-consciousness. Many of us take this ability for granted, but under certain pathological conditions (1–4) people demonstrate an inability to identify their own limbs as belonging to themselves. Although these observations suggest that the frontal and parietal lobes are somehow involved in the self-attribution of limbs, the underlying neural mechanism remains uncertain.

We used functional magnetic resonance imaging (fMRI) to investigate the brain mechanisms of the feeling of ownership of seen body parts. We manipulated ownership by making use of a perceptual illusion: the rubber hand illusion (5). During the experiment, the subject's real hand is hidden out of view (under a table) while a realistic life-sized rubber hand is placed in front of the subject. The experimenter uses two small paintbrushes to stroke the rubber hand and the subject's hidden hand, synchronizing the timing of the brushing as closely as possible. After a short period, the majority of subjects have the experience that the rubber hand is their own hand and that the rubber hand senses the touch (5, 6). This illusion happens as a result of the interaction of vision, touch, and position sense (proprioception) and the dominance of vision over proprioception (5).

To manipulate the feeling of ownership, we took advantage of the fact that the rubber hand illusion is only elicited when synchronous brushstrokes are applied to the real and fake hand (5, 6) and when the rubber hand is aligned with the subject's own hand (7). Thus, we defined four conditions where we

systematically manipulated the orientation of the seen rubber hand (aligned with the subject's own hand or rotated 180°, pointing toward the subject) and the timing of the brushstrokes applied to the real and fake hand (synchronous or alternating brushstrokes). In this 2 × 2 factorial design with four conditions—Synchronous Congruent, Asynchronous Congruent, Synchronous Incongruent, and Asynchronous Incongruent—the activation associated with the feeling of ownership of the fake hand corresponds to the interaction between hand orientation and brushstroke timing (8) (fig. S1).

We hypothesized that the multisensory activity in the parietal and premotor cortex would reflect the feeling of ownership of a seen hand. It has been suggested that the body is distinguished from the external world by its participation in specific types of multisensory perceptual correlations (5, 9–11). Self-attribution depends on a match between the look and feel of the body part. Relevant to this hypothesis is

the observation that neuronal populations in the parietal and ventral premotor cortex represent both the seen and felt position of the arm (12–16). But although these studies show that limb position can be computed in these areas on the basis of multisensory information, they do not inform us as to whether the activity in these areas is related to the conscious experience of ownership of the seen limb. This is because it is not possible to know what monkeys feel when looking at a fake limb (14, 15) and the feeling of ownership of the limbs was not experimentally manipulated in the human studies (16).

Before the brain scan, we tested the subjects to make sure that they experienced the rubber hand illusion (8) (fig. S2). The participants felt the illusion more strongly in the Synchronous Congruent condition relative to the other three control conditions [ $P < 0.05$  (8)].

We looked for brain activity related to the illusion in three ways. First, we analyzed the areas in which there was activity during the illusion condition that could not be accounted for by the summation of the effects of seeing the arm in a congruent position and feeling the synchronous brushstrokes [the interaction term (8)]. Such activity was detected in the bilateral inferior part of the precentral sulcus ( $P < 0.001$ ; Fig. 1) (table S1). The posterior bank of this sulcus corresponds to ventral premotor area 6, and the anterior bank to the posterior part of area 44. We also observed activation that reflected the illusion condition in the bilateral frontal operculum, which is a region located adjacent to the premotor cortex and area 44.

We then searched for areas in which the activity was related to the strength of the illusion as rated by the subjects just after the scan [using a linear regression analysis (8)]. The subjects who reported the strongest illusion during the Synchronous Congruent condition relative to the control conditions also

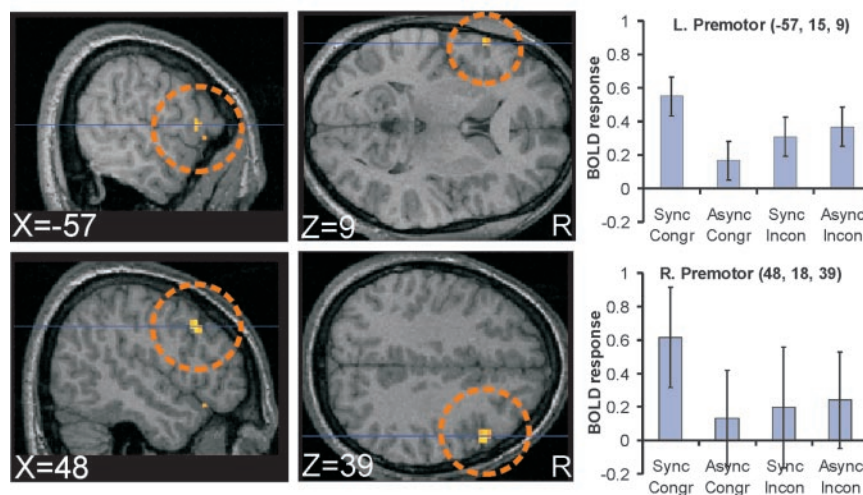


**Fig. 1.** Bilateral premotor activity that reflects the rubber hand illusion (interaction effect,  $P < 0.005$  for display purposes). The activation peaks are located in the inferior part of the precentral sulcus. R denotes right; coordinates in standard space are indicated at lower left. The plot shows the contrast estimates; error bars denote SEs. See (8) and table S1 for details.

<sup>1</sup>Wellcome Department of Imaging Neuroscience, Institute of Neurology, 12 Queen Square, London WC1N 3BG, UK. <sup>2</sup>Department of Experimental Psychology, University of Oxford, South Parks Road, Oxford OX1 3UD, UK.

\*To whom correspondence should be addressed. E-mail: h.ehrsson@fil.ion.ucl.ac.uk

## REPORTS

showed the strongest blood oxygen level–dependent (BOLD) signal in the bilateral premotor cortex [Fig. 2; left precentral sulcus;  $-48, 0, 39$  ( $x, y,$  and  $z$  coordinates in standard space);  $t = 3.25$ ;  $P < 0.003$ ; left precentral sulcus;  $-57, 15, 6$ ;  $t = 2.62$ ;  $P < 0.009$ ; right precentral sulcus;  $51, 0, 48$ ;  $t = 3.25$ ;  $P < 0.002$ ]. There was thus a linear relation between the subjective rating of the illusion and the level of neural activity in premotor cortex. There was also a significant relation between activity in the right lateral cerebellum and the strength of the illusion (crus I/lobule VI;  $48, -57, -27$ ;  $t = 4.0$ ;  $P < 0.001$ ).

Finally, we analyzed the temporal evolution of the premotor activity with respect to the time course of the illusion. Because it typically takes about 11 s for the illusion to start, we compared

the functional images obtained after the onset of the illusion with those collected before it commenced. The left premotor cortex showed enhanced activation after the subjects indicated that the illusion had started (left precentral sulcus;  $-33, 12, 30$ ;  $t = 4.49$ ;  $P < 0.001$ ; left precentral sulcus;  $-42, 12, 48$ ;  $t = 2.94$ ;  $P < 0.005$ ; see fig. S4). Also, such a response was observed in the right cerebellum (crus I;  $27, -81, -27$ ;  $t = 3.55$ ;  $P < 0.002$ ).

These three observations suggest that neural activity in the premotor cortex reflects the feeling of ownership of a seen hand. Thus, activity in this area is associated with the subjective experience that the body one sees belongs to oneself. This result provides evidence for the hypothesis that self-attribution of body parts depends on multisensory integration in the pre-

motor cortex. It may do so as part of a circuit that includes the parietal cortex and the cerebellum. There were trends for an interaction effect in both areas (left parietal  $P < 0.009$ , left cerebellum  $P < 0.003$ ); moreover, there was a significant relation between subjective ratings of the illusion and cerebellar activity.

The ventral premotor cortex is an ideal candidate for the multisensory representation of one's own body. It is anatomically connected to visual and somatosensory areas in the posterior parietal cortex and to frontal motor areas (17). Premotor neurons represent both the seen and felt position of the hand (12–14, 16) and discharge when the hand is touched or when a visual stimulus is presented near the hand (12–14, 18, 19). The receptive fields of the visual cells are “anchored” to the hand so that when the position of the hand changes, the receptive fields follow the hand; that is, these cells represent the space near the hand in a body-centered reference frame (12, 14). When the illusion arises, there is a change in the proprioceptive and tactile representations of the hand so that the somatic information from the hand matches the visual information. Thus, the premotor activity could reflect the matching of the visual and somatic signals, in line with the hypothesis that self-attribution is mediated by multisensory correlations (5, 9–11). Furthermore, when the illusion starts, it is likely that the hand-centered reference frame shifts from the hidden real hand to the rubber hand. Thus, the premotor activity might also reflect hand-centered cells that become active at the sight of the brush near the hand (in peripersonal space). In this, case the premotor activity would provide information about ownership by signaling that the object is close to one's own hand, thus defining the boundary zone between the body and the environment. These two interpretations are complementary and both suggest that the feeling of ownership is associated with the relocation of body space (intrapersonal and near-personal space), in this case to a nonbody object.

Multisensory information about arm orientation and binding of synchronous visuotactile events is represented in the parietal lobe. We found activity in the same intraparietal area both when we contrasted synchronous and asynchronous brushstrokes and when we contrasted the congruent and incongruent arm position (Fig. 3) (table S2). Given that activity in this area reflects the synchrony of the visual and tactile events as well as the seen orientation of the hand, this cortical area is probably critically important for the rubber hand illusion because this illusion depends on the integration of these types of information. The active area was located in the medial wall of the intraparietal sulcus in a location that might correspond to the medial intraparietal area in nonhuman primates. This region is connected to visual, somatosen-

**Fig. 2.** Significant relation between the bilateral premotor activity and the subjective ratings of the illusion (left:  $R^2 = 0.3969$ ,  $P < 0.003$ ; right:  $R^2 = 0.3982$ ,  $P < 0.002$ ). See (8) for details.

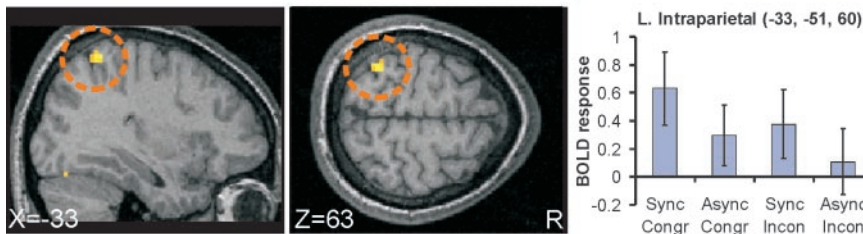
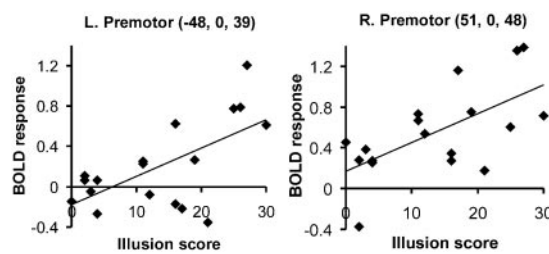
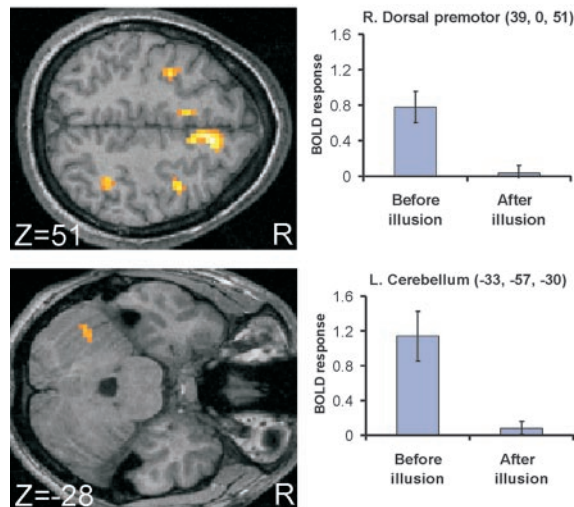


**Fig. 3.** Intraparietal activity that reflects the effects of both seeing the arm in a congruent position and perceiving synchronous brushstrokes [conjunction of the main effects,  $P < 0.001$  in each contrast; see (8) and table S2]. As evident from the plot, the parietal cortex displayed stronger activation during the Synchronous Congruent condition relative to the control conditions, but for this peak, the activity in this condition was no greater than would be accounted for by the combination of the effects of congruent arm orientation and synchrony.

**Fig. 4.** Activity associated with the recalibration period before the illusion started relative to the period after the illusion onset. See table S3 and (8) for details ( $P < 0.005$  for display purposes).





sory, and premotor areas (17, 20, 21), and neurons in this region integrate visual, tactile, and proprioceptive information from the hand (15, 16, 21–26). People with parietal lesions sometimes show an inability to identify their own limbs as part of the body (1). This could reflect impaired multisensory integration of body-related information. However, it is still somewhat unclear whether the activity in the intraparietal cortex reflects the feeling of ownership per se, because we only detected a trend for illusion-related activity in this region (interaction effect,  $-45, -54, 57$ ;  $P < 0.009$ ).

The elicitation of the rubber hand illusion depends on the integration of visual and tactile information and the resolution of differences between the visual and position sense representations. The period before the illusion develops is critical in this respect, and it probably involves a recalibration of position sense for the hand (5). Before the illusion started, we found increased levels of activity in the bilateral intraparietal cortex, bilateral dorsal premotor cortex, and supplementary motor area, as well as the left cerebellum, left putamen, and left ventral thalamus (Fig. 4) (table S3). Several of these areas are known to be involved in the processing of proprioceptive signals as revealed by tendon vibration experiments (27). Likewise, some of the areas are involved in arm reaching in humans and nonhuman primates (20, 28–30). Thus, the recalibration of limb position in a reaching circuit might be a key mechanism for the elicitation of the illusion, and indeed experiencing the illusion has behavioral consequences for arm movements. After having experienced the rubber hand illusion of their left hand, subjects make a reaching error (toward the location of the rubber hand) when asked to point toward their hidden left hand (5, 31).

In summary, the rubber hand illusion depends on three neural mechanisms: multisensory integration in parietocerebellar regions, recalibration of proprioceptive representations of the upper limb in a reaching circuit, and self-attribution in the premotor cortex (8). Our results associate activity in the premotor cortex with the feeling of ownership of a seen limb, and we suggest that multisensory integration in a body-centered reference frame is the underlying mechanism of self-attribution.

#### References and Notes

- M. Critchley, *The Parietal Lobes* (Edward Arnold, London, 1953).
- M. Critchley, *Mt. Sinai J. Med.* **41**, 82 (1974).
- T. E. Feinberg, *Semin. Neurol.* **17**, 129 (1997).
- K. J. Meador, D. W. Loring, T. E. Feinberg, G. P. Lee, M. E. Nichols, *Neurology* **55**, 816 (2000).
- M. Botvinick, J. Cohen, *Nature* **391**, 756 (1998).
- K. C. Armel, V. S. Ramachandran, *Proc. R. Soc. London Ser. B* **270**, 1499 (2003).
- F. Pavani, C. Spence, J. Driver, *Psychol. Sci.* **11**, 353 (2000).
- See supporting data at Science Online.
- R. W. Mitchell, in *The Self: From Soul to Brain*, J. LeDoux, Ed. (New York Academy of Sciences, New York, 2003), pp. 39–62.
- L. E. Bahrick, J. S. Watson, *Dev. Psychol.* **21**, 963 (1985).
- E. van den Bos, M. Jeannerod, *Cognition* **85**, 177 (2002).
- M. S. Graziano, G. S. Yap, C. G. Gross, *Science* **266**, 1054 (1994).
- M. S. Graziano, X. T. Hu, C. G. Gross, *J. Neurophysiol.* **77**, 2268 (1997).
- M. S. Graziano, *Proc. Natl. Acad. Sci. U.S.A.* **96**, 10418 (1999).
- M. S. Graziano, D. F. Cooke, C. S. Taylor, *Science* **290**, 1782 (2000).
- D. M. Lloyd, D. I. Shore, C. Spence, G. A. Calvert, *Nature Neurosci.* **6**, 17 (2003).
- G. Rizzolatti, G. Luppino, M. Matelli, *Electroencephalogr. Clin. Neurophysiol.* **106**, 283 (1998).
- G. Rizzolatti, C. Scandolara, M. Matelli, M. Gentilucci, *Behav. Brain Res.* **2**, 125 (1981).
- G. Rizzolatti, C. Scandolara, M. Matelli, M. Gentilucci, *Behav. Brain Res.* **2**, 147 (1981).
- P. B. Johnson, S. Ferraina, L. Bianchi, R. Caminiti, *Cereb. Cortex* **6**, 102 (1996).
- E. G. Jones, J. D. Coulter, S. H. Hendry, *J. Comp. Neurol.* **181**, 291 (1978).
- F. H. Duffy, J. L. Burchfiel, *Science* **172**, 273 (1971).
- H. Sakata, Y. Takaoka, A. Kawarasaki, H. Shibutani, *Brain Res.* **64**, 85 (1973).
- C. L. Colby, J. R. Duhamel, *Neuropsychologia* **29**, 517 (1991).
- M. S. Graziano, M. Botvinick, in *Common Mechanisms in Perception and Action, Attention and Performance XIX* (Oxford Univ. Press, Oxford, 2001), pp. 136–157.
- E. Macaluso, J. Driver, *Adv. Neurol.* **93**, 219 (2003).
- E. Naito, P. E. Roland, H. H. Ehrsson, *Neuron* **36**, 979 (2002).
- C. Kertzman, U. Schwarz, T. A. Zeffiro, M. Hallett, *Exp. Brain Res.* **114**, 170 (1997).
- Y. Burnod et al., *Exp. Brain Res.* **129**, 325 (1999).
- R. A. Andersen, L. H. Snyder, D. C. Bradley, J. Xing, *Annu. Rev. Neurosci.* **20**, 303 (1997).
- H. H. Ehrsson, C. Spence, R. E. Passingham, unpublished data.
- Supported by the Wellcome Trust and by postdoctoral grants from STINT (the Swedish Foundation for International Cooperation in Research and Higher Education) and the Human Frontier Science Program (H.E.E.). We thank R. Deichmann for advice on MRI. For further acknowledgments, see (8).

#### Supporting Online Material

www.sciencemag.org/cgi/content/full/1097011/DC1

Materials and Methods

SOM Text

Figs. S1 to S4

Tables S1 to S3

References

20 February 2004; accepted 2 June 2004

Published online 1 July 2004;

10.1126/science.1097011

Include this information when citing this paper.

## Brood Parasitic Cowbird Nestlings Use Host Young to Procure Resources

Rebecca M. Kilner,<sup>1\*</sup> Joah R. Madden,<sup>1</sup> Mark E. Hauber<sup>2,3</sup>

Young brood parasites that tolerate the company of host offspring challenge the existing evolutionary view of family life. In theory, all parasitic nestlings should be ruthlessly self-interested and should kill host offspring soon after hatching. Yet many species allow host young to live, even though they are rivals for host resources. Here we show that the tolerance of host nestlings by the parasitic brown-headed cowbird *Molothrus ater* is adaptive. Host young procure the cowbird a higher provisioning rate, so it grows more rapidly. The cowbird's unexpected altruism toward host offspring simply promotes its selfish interests in exploiting host parents.

Parents provisioning young commonly balance the effort they spend on rearing their current brood with the effort they might devote to future offspring (1, 2). Members of the current brood then become rivals for limited parental resources [intra-brood conflict (3, 4)] and must also compete with future offspring to increase the total effort that parents will devote to the current breeding attempt [inter-brood conflict (5)]. In theory, the intensity of both forms of

conflict should increase as offspring relatedness declines, all else being equal (3, 6–9). We used an avian brood parasite to test the importance of relatedness in determining interactions between broodmates.

Obligate avian brood parasites lay their eggs in nests belonging to other species, leaving each of their nestlings to grow up in a family to which it is entirely unrelated (10). The host's nestlings offer formidable competition for resources (11, 12). Nonetheless, in contrast to many cuckoo and honeyguide species, the *Clamator* cuckoos, *Vidua* finches, and parasitic cowbirds tolerate the company of host young in the nest. Nestmate tolerance is unlikely to be explained by kin selection because, although multiple parasitism of individual host nests is common (10), parasite siblings

<sup>1</sup>Department of Zoology, Downing Street, Cambridge CB2 3EJ, UK. <sup>2</sup>School of Biological Sciences, University of Auckland, PB 92019, Auckland, New Zealand. <sup>3</sup>Department of Integrative Biology, Museum of Vertebrate Zoology, University of California, Berkeley, CA 94720, USA.

\*To whom correspondence should be addressed. E-mail: rmk1002@hermes.cam.ac.uk

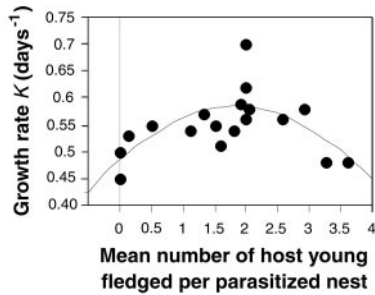


**Fig. 1.** Relationship between cowbird growth rate and mean number of host young fledged per successful parasitized nest, for cowbirds reared in the nests of 18 different host species. Each data point shows the cowbird's growth rate ( $K$ ) in one of the 18 host species. Cowbird growth rates were taken from (20). A second-order polynomial regression line is shown. Sources for the number of host young surviving in parasitized nests are given in table S1.

are not typically raised in the same nest (10). Host tolerance by brown-headed cowbird nestlings is especially intriguing because they have been filmed evicting young from the nest (13), yet they apparently refrain from this behavior on most other occasions.

One possibility is that host young bring parasites direct benefits because collectively they evoke a higher level of provisioning than the parasite could ever achieve alone (14–16). We tested this hypothesis with the brown-headed cowbird (44 g), a North American brood parasite that successfully victimizes more than 100 host species (10). Cowbirds reduce host reproductive success by removing eggs, lowering hatching success, and starving young (17, 18). To some degree, therefore, cowbirds (both mothers and young) can manipulate the competitive environment in which young parasites are raised. The extent of offspring mortality varies widely from host to host, but one or more host nestlings commonly survive to fledge with the cowbird (19).

We began by using data from the literature for cowbirds reared by 18 host species (20) to test whether cowbirds could ever profit from the survival of host young (21). We examined the association between the number of host young in the nest and cowbird growth rate, because growth rate is a correlate of post-fledging fitness in other songbirds (22). We found that the relationship could be explained by a quadratic regression curve [ $F_{2,17} = 6.32, P = 0.010, R^2 = 0.46$ : host young partial  $t_{17} = 3.54, P = 0.003$ ; (host young)<sup>2</sup> partial  $t_{17} = -3.44, P = 0.004$ ], which peaked at a growth rate corresponding with 1.8 host young (Fig. 1) (21). One interpretation of this result is that the brown-headed cowbird benefits from sharing the nest with host young, and that its optimal number of host companions is approximately two [see also (16)].

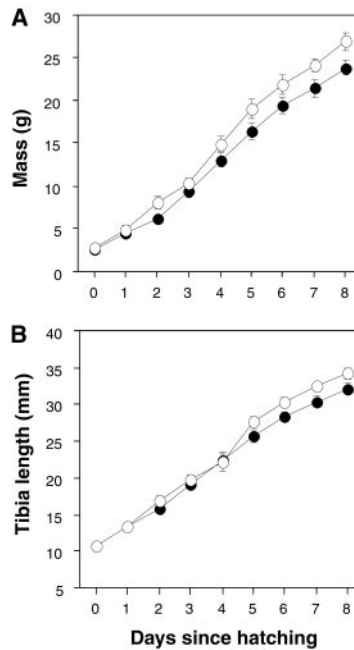


**Fig. 2.** Change in (A) mass and (B) tibia length with age for cowbirds reared alone ( $N = 10$ ; black circles) or with two phoebe young ( $N = 10$ ; white circles). Means with SE bars are shown.

We tested this interpretation with experiments that focused on the cowbird's interactions with one host, the Eastern phoebe *Sayornis phoebe* (20 g), a migrant flycatcher that typically rears broods of five phoebe young. At our study site in Tompkins County, New York, USA (19, 23), one to three host offspring survived to fledge at 62% of naturally parasitized nests ( $N = 29$  broods with one cowbird chick, 1999–2001). In April and May 2003, we monitored 81 phoebe nests during egg-laying and arranged for 20 nests to be parasitized with a single cowbird egg. At 10 of these nests, we removed host eggs on the day the cowbird nestling hatched so that it would be reared alone. At the remaining 10 nests, we removed host eggs and introduced two phoebe nestlings per nest, which had hatched either on same day as the cowbird chick ( $N = 8$ ) or a day later ( $N = 2$ ). Molecular sexing later revealed that we had assigned equal numbers of male and female cowbird nestlings to the two treatments by chance. On hatch day, and every day thereafter for 9 days, we weighed chicks and measured their tibia length, and calculated the instantaneous growth constant  $K$  to summarize rates of mass gain and skeletal growth (21).

We found that cowbird nestlings that were accompanied by host young in the nest gained mass at a greater rate (Mann-Whitney  $U$  test:  $Z = -2.003, P = 0.045$ ) and showed faster skeletal growth (unpaired  $t_{18} = -2.59,$

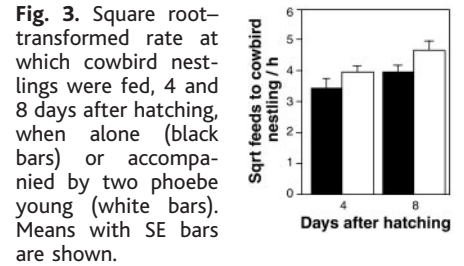


**Fig. 3.** Square root-transformed rate at which cowbird nestlings were fed, 4 and 8 days after hatching, when alone (black bars) or accompanied by two phoebe young (white bars). Means with SE bars are shown.

$P = 0.019$ ; Fig. 2) than those reared alone. By day 8, cowbirds reared with host young were, on average, 14% heavier than cowbirds reared alone (unpaired  $t_{16} = -2.23, P = 0.041$ ; Fig. 2A). To determine how the presence of host young benefited cowbird nestlings, we filmed each nest twice, 4 and 8 days after hatching, and scored the hourly provisioning rate to chicks in the nest. Pooling data from both days, we found that parents brought food to nests containing a cowbird and two phoebe nestlings more frequently (mean  $\pm$  SEM =  $36.4 \pm 3.85$  feeds/hour) than to nests containing a lone cowbird ( $14.2 \pm 1.62$  feeds/hour). Cowbirds took an average of  $55.7 \pm 2.9\%$  of feeds in mixed broods, which is a significantly greater share than the 33% expected by chance (Wilcoxon signed rank test,  $Z = 3.73, P < 0.001$ ). As a result, cowbirds reared with host young obtained more food in total than cowbirds reared without competitors [analysis of variance (ANOVA): brood manipulation effect,  $F_{1,30} = 5.14, P = 0.031$ ; Fig. 3]. Older broods were provisioned more frequently (ANOVA: chick age effect,  $F_{1,30} = 3.23, P = 0.029$ ), but the cowbird's share of the food did not change with age (ANOVA: brood manipulation  $\times$  chick age interaction,  $F_{1,30} = 0.17, P = 0.68$ ).

Accompanied cowbirds may have experienced a higher provisioning rate because the collective begging behavior of the brood presented a greater stimulus to parents, or because parents were more responsive to the begging behavior of their own young (24). Alternatively, it may have been that the longer periods of brooding experienced by lone cowbirds slowed the rate at which these parasites were fed (ANOVA, brood manipulation effect:  $F_{1,30} = 4.92, P = 0.034$ ) (21). However, the latter explanation seems unlikely because the brooding effort devoted to lone cowbirds was not significantly related to the rate at which they were fed (simple linear regression, time spent brooding versus provisioning rate:  $F_{1,16} = 0.07, P = 0.94$ ), probably because male phoebes continued to feed the cowbird as it was brooded by the female (23).

Our results show that cowbirds exploit host parents to a greater extent by using host young to procure food. Cowbirds capitalize on the increased provisioning that



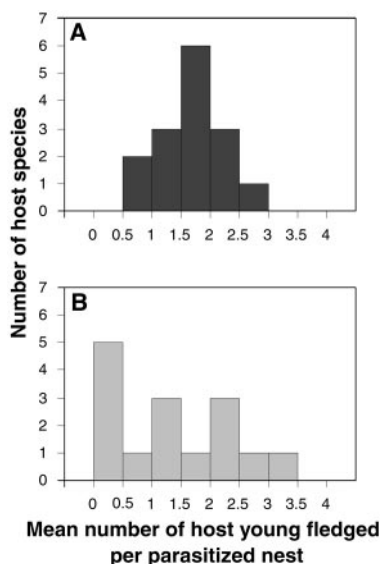


**Fig. 4.** Frequency distributions of mean numbers of host young fledging from successful nests of (A) hosts within the cowbird's historic range ("old" hosts) and (B) hosts victimized as a result of the cowbird's recent range expansion ("new" or "intermediate" hosts). The data set uses 30 of the species in (37) and their descriptions of the duration of host-cowbird sympatry. The sources of data for the mean host young fledged in parasitized nests of the different host species are given in (27). We calculated the difference between the "ideal" number of host young (= 1.8 from Fig. 1) and the observed numbers of host young for "old" and "new" hosts. The magnitude of difference was much greater for "new" hosts than for "old" hosts (unpaired  $t_{28} = 2.94$ ,  $P = 0.007$ ), even after controlling for phylogenetic effects with pairwise comparisons of closely related "new" and "old" host species (paired  $t_4 = 2.79$ ,  $P = 0.049$ ).

results from additional young in the nest by consistently outcompeting host nestlings to obtain extra parental feedings. Furthermore, there appears to be an optimal number of roughly two host young that are of use to the cowbird (Fig. 1). Larger numbers

of host nestlings may take too much of the additional food collectively solicited by the brood. We note that cowbirds reared in the nests of hosts within the cowbird's historic range are most frequently accompanied by an average of 1.5 to 2 host young (Fig. 4), but further experiments are required to explain this association fully.

Our study shows that there are costs associated with the loss of assistance in soliciting care, as hypothesized previously (14–16). It means that both the benign and virulent behavioral strategies of young brood parasites toward host nestmates can now be viewed as adaptive, each the result of a different balance between the costs of sharing resources with rivals and the benefits of retaining assistance in soliciting care. Our experiments also have implications beyond host-parasite interactions, suggesting that selection acts on avian broods at two levels (25, 26): through the competitive success of individual offspring, and through the parental provisioning rates evoked by the brood collectively. If offspring must restrain their selfishness in intrabrood conflict to attract a more frequent provisioning rate, then they cannot simultaneously "win" intrabrood conflict and interbrood conflict (27, 28). The extent of parent-offspring conflict seen in avian families may therefore depend on the interplay between intrabrood conflict and interbrood conflict (29, 30).

#### References and Notes

- R. L. Trivers, in *Sexual Selection and the Descent of Man 1871–1971*, B. Campbell, Ed. (Aldine, Chicago, 1972), pp. 136–179.
- L. Gustafsson, W. J. Sutherland, *Nature* **335**, 813 (1988).
- W. D. Hamilton, *J. Theor. Biol.* **7**, 1 (1964).
- M. Macnair, G. A. Parker, *Anim. Behav.* **27**, 1202 (1979).
- R. L. Trivers, *Am. Zool.* **14**, 249 (1974).
- G. A. Parker, M. Macnair, *Anim. Behav.* **27**, 1210 (1979).
- J. Maynard Smith, *Anim. Behav.* **42**, 1034 (1991).
- H. C. J. Godfray, *Nature* **376**, 133 (1995).
- R. A. Johnstone, *Proc. Natl. Acad. Sci. U.S.A.* **96**, 12644 (1999).

- N. B. Davies, *Cuckoos, Cowbirds and Other Cheats* (Poyser, London, 2000).
- D. C. Dearborn, *Behav. Ecol. Sociobiol.* **43**, 259 (1998).
- G. Lichtenstein, S. G. Sealy, *Proc. R. Soc. London Ser. B* **265**, 249 (1998).
- D. C. Dearborn, *Condor* **98**, 645 (1996).
- G. Lichtenstein, thesis, University of Cambridge (1997).
- A. Lotem, *Trends Ecol. Evol.* **13**, 342 (1998).
- R. M. Kilner, *Anim. Behav.* **66**, 569 (2003).
- S. I. Rothstein, *Condor* **77**, 250 (1975).
- R. M. May, S. K. Robinson, *Am. Nat.* **126**, 475 (1985).
- M. E. Hauber, *Behav. Ecol.* **14**, 227 (2003).
- A. M. Kilpatrick, *Can. J. Zool.* **80**, 145 (2002).
- See supporting data at Science Online.
- S. Gebhardt-Henrich, H. Richner, in *Avian Growth and Development: Evolution Within the Altricial-Precocial Spectrum*, J. M. Starck, R. E. Ricklefs, Eds. (Oxford Univ. Press, New York, 1998), pp. 324–339.
- M. E. Hauber, K. Montenegro, *Etologia* **10**, 1 (2002).
- R. B. Payne, J. L. Woods, L. L. Payne, *Anim. Behav.* **62**, 473 (2001).
- H. K. Reeve, L. Keller, in *Levels of Selection in Evolution*, L. Keller, Ed. (Princeton Univ. Press, Princeton, NJ, 1999), pp. 3–14.
- D. Sloan Wilson, A. B. Clark, in *The Evolution of Begging: Competition, Cooperation and Communication*, J. Wright, M. L. Leonard, Eds. (Kluwer Academic, Dordrecht, Netherlands, 2002), pp. 43–64.
- G. A. Parker, D. W. Mock, T. C. Lamey, *Am. Nat.* **133**, 846 (1989).
- L. S. Forbes, *Am. Nat.* **142**, 82 (1993).
- D. Haig, *J. Evol. Biol.* **9**, 357 (1996).
- M. A. Rodríguez-Gironés, *Proc. R. Soc. London Ser. B* **266**, 2399 (1999).
- S. A. Hosoi, S. I. Rothstein, *Anim. Behav.* **59**, 823 (2000).
- R.M.K. is supported by a Royal Society University Research Fellowship. J.R.M. is a postdoctoral research assistant to N. B. Davies (funded by the UK Natural Environment Research Council), and M.E.H. holds a Miller Research Fellowship. We thank C. Wilson, E. and C. Cramer, and the many residents of Tompkins County who kindly allowed us access to nests on their property; D. W. Winkler and his lab for logistical support; N. Flanders for assistance in the field; and M. de L. Brooke, N. B. Davies, E. H. DuVal, C. A. Hinde, S. Hunt, E. A. Lacey, N. E. Langmore, K. M. Pilz, T. D. Price, A. F. Russell, J. G. Schuetz, P. W. Sherman, three anonymous referees, and many others for discussion or comments on the manuscript.

#### Supporting Online Material

[www.sciencemag.org/cgi/content/full/305/5685/877/DC1](http://www.sciencemag.org/cgi/content/full/305/5685/877/DC1)

Materials and Methods

Table S1

References

30 March 2004; accepted 30 June 2004

Turn a new page to...

[www.sciencemag.org/books](http://www.sciencemag.org/books)

Science  
Books et al.  
HOME PAGE

- ▶ the latest book reviews
- ▶ extensive review archive
- ▶ topical books received lists
- ▶ buy books online

# NEW PRODUCTS

## Bioinformatics Solutions

For more information  
519-885-8288

[www.bioinformaticsolutions.com](http://www.bioinformaticsolutions.com)

[www.scienceproductlink.org](http://www.scienceproductlink.org)

## HOMOLOGY SEARCH TOOL

PatternHunter 2.0 is a general-purpose homology search tool. It now has the full functionalities of BLAST (Basic Local Alignment Search Tool) and input and output formats compatible with BLAST. In the 1980s, BLAST was designed to speed up the Smith-Waterman algorithm for homology search by trading sensitivity for speed. PatternHunter 2.0 now makes use of modern homology search technology to offer speed and sensitivity without compromise. PatternHunter can approach Smith-Waterman sensitivity and yet run 3000 times faster. Among its features, PatternHunter does gapped alignments and can search against arbitrarily large databases without running out of memory.

## Minitab

For more information  
800-488-3555

[www.minitab.com](http://www.minitab.com)

[www.scienceproductlink.org](http://www.scienceproductlink.org)

## STATISTICAL SOFTWARE

Release 14 of Minitab Statistical Software for Windows offers extensive graphical enhancements. Important advances in the new release include greatly expanded and simplified graph creation and editing; many new options to increase graph flexibility; new quality tools, including multivariate control charts and process capability analysis; new statistical features, including partial least squares and additional reliability analysis methods; and customizable menus, toolbars, and settings that can be used to create shareable profiles.

## Elchrom Scientific

For more information  
+41 41 747 25 50

[www.elchrom.com](http://www.elchrom.com)

[www.scienceproductlink.org](http://www.scienceproductlink.org)

## PURE siRNA OLIGONUCLEOTIDES

A novel purification technology for obtaining small-interfering RNA (siRNA) synthetic oligonucleotides delivers high performance in terms of purity (typically 98%), yield (typically 60% of the incoming full-length oligonucleotide), and turnaround time (typically 3 hours). A newly developed gel matrix allows purification of small RNA oligonucleotide duplexes as well as singleplexes. The new gel resolves RNA duplexes from singleplexes according to their structural differences, in addition to their size. These properties lead to ultrapure siRNA products. Labeled siRNA duplexes can also be purified effectively. Additional advantages enabled by the new technology are quality control by matrix-assisted laser desorption ionization-time of flight mass spectrometry analysis for all oligonucleotides up to 120 mer, and gel excision in blue light, which prevents degradation.

## Ariadne Genomics

For more information  
847-644-1557

[www.ariadnegenomics.com](http://www.ariadnegenomics.com)

[www.scienceproductlink.org](http://www.scienceproductlink.org)

## BIOLOGICAL PATHWAY VISUALIZATION AND ANALYSIS

PathwayAssist 2.5 desktop software is a state-of-the-art tool for building, analysis, expansion, and navigation of biological pathways, gene regulation networks, and protein interaction maps. It features the ResNet database of more than 200,000 biological interactions extracted from the scientific literature using MedScan, an advanced text mining tool. Integrated into the software, the MedScan tool enables researchers to update pathways with the latest information from scientific literature in real time. New features in the 2.5 version include the addition of molecular net-

work databases for four model organisms, the capability to map gene expression data onto KEGG pathways, and the ability to save pathways in HTML format as interactive, clickable maps. This version also features seamless integration with GeneSpring and ArrayAssist gene expression analysis software.

## Millipore

For more information  
800-MILLIPORE

[www.millipore.com](http://www.millipore.com)

[www.scienceproductlink.org](http://www.scienceproductlink.org)

## MALDI MS SAMPLE PREPARATION

The MALDIspot Kit is designed to improve the sensitivity of mass spectrometry (MS) by maximizing peptide recovery during sample preparation of gel spots. The kit is the second in a series of MS sample preparation products being developed through a proteomics partnership between Millipore and Applied Biosystems. The kit includes the new ZipPlate micro-solid-phase extraction plate, the first 96-well sample preparation tool for destaining, digesting, and concentrating proteins from either one-dimensional or two-dimensional gels in a single plate. Also included is an apparatus that allows direct elution of purified peptides onto an Applied Biosystems matrix-assisted laser desorption ionization (MALDI) target insert in a matrix solution of only 1–2  $\mu$ l. The insert is then placed into a sled that is compatible with Voyager-DE and other workstations.



## Finnzymes

For more information  
+358 9 584 121

[www.finnzymes.com](http://www.finnzymes.com)

[www.scienceproductlink.org](http://www.scienceproductlink.org)

## QUANTITATIVE PCR KIT

DyNamo Capillary SYBR Green qPCR Kit is a ready-to-use master mix for specific quantitative polymerase chain reaction (PCR) for instruments using capillary tubes. The master mix contains uniquely engineered hot start DyNamo DNA polymerase and all the other reagents needed for quantitative PCR. Only template DNA and PRC primers need to be added by the user.

## BioCal Technology

For more information  
714-639-2124

[www.biocal.com](http://www.biocal.com)

[www.scienceproductlink.org](http://www.scienceproductlink.org)

## LITERATURE

HDA-GT12 System for RNA Analysis is an application note that describes and illustrates a cost-effective, multi-channel capillary electrophoresis system to determine the quality and quantity of RNA as an essential step for any gene expression analysis. This affordable system can be used in research laboratories as an alternative to other methods of RNA analysis. Featuring a fluorescence detection mechanism, the unit's consumable multi-channel capillary gel cartridge automatically injects and analyzes 12 strips simultaneously.

Newly offered instrumentation, apparatus, and laboratory materials of interest to researchers in all disciplines in academic, industrial, and government organizations are featured in this space. Emphasis is given to purpose, chief characteristics, and availability of products and materials. Endorsement by *Science* or AAAS of any products or materials mentioned is not implied. Additional information may be obtained from the manufacturer or supplier by visiting [www.scienceproductlink.org](http://www.scienceproductlink.org) on the Web, where you can request that the information be sent to you by e-mail, fax, mail, or telephone.